Computational Methods in Applied Sciences

Manolis Papadrakakis
George Stefanou
Vissarion Papadopoulos *Editors*

Computational Methods in Stochastic Dynamics

Volume 2

ECCOMAS
European Community on Computational Methods in Applied Sciences

Springer

Computational Methods in Stochastic Dynamics

Computational Methods in Applied Sciences

Volume 26

Series Editor

E. Oñate
International Center for Numerical Methods in Engineering (CIMNE)
Technical University of Catalonia (UPC)
Edificio C-1, Campus Norte UPC
Gran Capitán, s/n
08034 Barcelona Spain
onate@cimne.upc.edu
www.cimne.com

For further volumes:
www.springer.com/series/6899

Manolis Papadrakakis • George Stefanou •
Vissarion Papadopoulos
Editors

Computational Methods in Stochastic Dynamics

Volume 2

Springer

Editors
Manolis Papadrakakis
Institute of Structural Analysis &
Antiseismic Research
National Technical University of Athens
Athens, Greece

Vissarion Papadopoulos
Institute of Structural Analysis &
Antiseismic Research
National Technical University of Athens
Athens, Greece

George Stefanou
Institute of Structural Analysis &
Antiseismic Research
National Technical University of Athens
Athens, Greece

ISSN 1871-3033 Computational Methods in Applied Sciences
ISBN 978-94-007-5133-0 ISBN 978-94-007-5134-7 (eBook)
DOI 10.1007/978-94-007-5134-7
Springer Dordrecht Heidelberg New York London

Library of Congress Control Number: 2012949417

Printed on acid-free paper

Springer is part of Springer Science+Business Media (www.springer.com)

This book is dedicated to the memory of Prof. Gerhart I. Schuëller, a pioneer in the field of Computational Stochastic Dynamics

Preface

The considerable influence of inherent uncertainties on structural behavior has led the engineering community to recognize the importance of a stochastic approach to structural problems. Issues related to uncertainty quantification and its influence on the reliability of the computational models, are continuously gaining in significance. In particular, the problems of dynamic response analysis and reliability assessment of structures with uncertain system and excitation parameters have been the subject of continuous research over the last two decades as a result of the increasing availability of powerful computing resources and technology. This book is a follow up of a previous book with the same subject and focuses on advanced computational methods and software tools which can highly assist in tackling complex problems in stochastic dynamic/seismic analysis and design of structures. The selected chapters are authored by some of the most active scholars in their respective areas and represent some of the most recent developments in this field.

This edited book is primarily intended for researchers and post-graduate students who are familiar with the fundamentals and wish to study or to advance the state of the art on a particular topic in the field of computational stochastic structural dynamics. Nevertheless, practicing engineers could benefit as well from it as most code provisions tend to incorporate probabilistic concepts in the analysis and design of structures. The book consists of 21 chapters which are extended versions of papers presented at the recent COMPDYN 2011 Conference. The chapters can be grouped into several thematic topics including dynamic analysis of stochastic systems, reliability-based design, structural control and health monitoring, model updating, system identification, wave propagation in random media, seismic fragility analysis and damage assessment.

In Chap. 1, A. Batou and C. Soize examine the random dynamic response of a multibody system with uncertain rigid bodies. A stochastic model of an uncertain rigid body is constructed by modeling the mass, the center of mass and the tensor of inertia by random variables. The prior probability distributions of these random variables are computed using the maximum entropy principle under the constraints defined by the available information. Several uncertain rigid bodies are linked to each other in order to calculate the random response of a multibody dynamic system.

A numerical application consisting of five rigid bodies is proposed to illustrate the theoretical developments.

In Chap. 2, V. Papadopoulos and O. Kokkinos extend the concept of Variability Response Functions (VRFs) to linear stochastic systems under dynamic excitation. An integral form for the variance of the dynamic response of stochastic systems is considered, involving a Dynamic VRF (DVRF) and the spectral density function of the stochastic field modeling the uncertain system properties. The uncertain property considered is the flexibility of the system. The same integral expression can be used to calculate the mean response of a dynamic system using a Dynamic Mean Response Function (DMRF) which is a function similar to the DVRF. These integral forms are used to efficiently compute the mean and variance of the transient system response along with time dependent spectral-distribution-free upper bounds.

A. Kundu and S. Adhikari provide the theoretical development and simulation results of a novel Galerkin subspace projection scheme for damped linear dynamic systems with stochastic coefficients and homogeneous Dirichlet boundary conditions (Chap. 3). The fundamental idea is to solve the stochastic dynamic system in the frequency domain by projecting the solution into a reduced finite dimensional spatio-random vector basis spanning the stochastic Krylov subspace to approximate the response. Galerkin weighting coefficients are employed to minimize the error induced by the use of the reduced basis. The statistical moments of the solution are evaluated at all frequencies to illustrate and compare the stochastic system response with the deterministic case. The results are validated with direct Monte Carlo simulation for different correlation lengths and variability of randomness.

An efficient approach for modeling nonlinear systems subjected to general non-Gaussian excitations is developed by X.F. Xu and G. Stefanou in Chap. 4. This chapter describes the formulation of an n-th order convolved orthogonal expansion (COE) method. For linear vibration systems, the statistics of the output are directly obtained as the first-order COE about the underlying Gaussian process. The COE method is next verified by its application on a weakly nonlinear oscillator. In dealing with strongly nonlinear dynamics problems, a variational method is presented by formulating a convolution-type action and using the COE representation as trial functions.

In Chap. 5 by L. Pichler et al., various finite difference (FD) and finite element methods (FEM) are discussed for the numerical solution of the Fokker–Planck equation allowing the investigation of the evolution of the probability density function of linear and nonlinear systems. The results are compared using various numerical examples. Despite the greater numerical effort, the FEM is preferable over FD, because it yields more accurate results. However, at this moment the FEM is only suitable for dimension less or equal to 3. In the case of 3D and 4D problems, a stabilized multi-scale FEM provides a tool with a high order of accuracy, preserving numerical efficiency due to the fact that a coarser mesh size can be used.

There are various approaches to deal with uncertainty propagation in stochastic dynamics. In Chap. 6, M. Corradi et al. examine some classical structural problems

in order to investigate which probabilistic approach better propagates the uncertainty from input to output, in terms of accuracy and computational cost. The examined methods are: Univariate Dimension Reduction methods, Polynomial Chaos Expansion, First-Order Second Moment method, and algorithms based on the Evidence Theory for epistemic uncertainty. The performances of these methods are compared in terms of moment estimations and probability density function construction corresponding to several scenarios of reliability-based design and robust design. The structural problems examined are: (i) the static, dynamic and buckling behavior of a composite plate, (ii) the reconstruction of the deformed shape of a beam from measured surface strains.

Chapter 7 by F. Steinigen et al. is devoted to enhanced computational algorithms to simulate the load-bearing behavior of reinforced concrete structures under dynamic loading. In order to take into account uncertain data of reinforced concrete, fuzzy and fuzzy stochastic analyses are presented. The capability of the fuzzy dynamic analysis is demonstrated by an example in which a steel bracing system and viscous damping connectors are designed to enhance the structural resistance of a reinforced concrete structure under seismic loading.

W. Verhaeghe et al. use the concept of interval fields to deal with uncertainties of spatial character arising in the context of groundwater transport models needed to predict the flow of contaminants (Chap. 8). The main focus of the chapter is on the application of interval fields to a geo-hydrological problem. The uncertainty taken into account is the material layers' hydraulic conductivity. The results presented are the uncertainties on the contaminant's concentration near a river. Another objective of the chapter is to define an input uncertainty elasticity of the output, i.e. to identify the locations in the model, whose uncertainties mostly influence the uncertainty on the output. Such a quantity indicates where to perform additional in situ point measurements to reduce the uncertainty on the output the most.

Although reliability analysis methods have matured in recent years, the problem of reliability-based structural design still poses a challenge in stochastic dynamics. In Chap. 9, A. Naess et al. extend their recently developed enhanced Monte Carlo approach to the problem of reliability-based design. The objective is to optimize a design parameter α so that the system, represented by a set of failure modes or limit states, achieves a target reliability. Monte Carlo sampling occurs at a range of values for α that result in failure probabilities larger than the target and thus the design problem essentially amounts to a statistical estimation of a high quantile. Several examples of the approach are provided in the chapter.

Chapter 10 by H. Jensen et al. presents a general framework for reliability-based design of base-isolated structural systems under uncertain conditions. The uncertainties about the structural parameters as well as the variability of future excitations are characterized in a probabilistic manner. Nonlinear elements composed by hysteretic devices are used for the isolation system. The optimal design problem is formulated as a constrained minimization problem which is solved by a sequential approximate optimization scheme. First excursion probabilities that account for the uncertainties in the system parameters as well as in the excitation are used to characterize the system reliability. The approach explicitly takes into account all nonlinear

characteristics of the combined structural system (superstructure-isolation system) during the design process. Numerical results highlight the beneficial effects of isolation systems in reducing the superstructure response.

The influence of structural uncertainties on actively controlled smart beams is investigated in Chap. 11 by A. Moutsopoulou et al. The dynamical problem of a model smart composite beam is treated using a simplified modeling of the actuators and sensors, both being realized by means of piezoelectric layers. In particular, a practical robust controller design methodology is developed, which is based on recent theoretical results on H_∞ control theory and μ-analysis. Numerical examples demonstrate the vibration-suppression property of the proposed smart beams under stochastic loading.

The field of Structural Health Monitoring (SHM) has significantly evolved in the last years due to the technological advances and the evolution of advanced smart systems for damage detection and signal processing. In Chap. 12, G. Saad and R. Ghanem present a robust data assimilation approach based on a stochastic variation of the Kalman Filter where polynomial functions of random variables are used to represent the uncertainties inherent to the SHM process. The presented methodology is combined with a non-parametric modeling technique to tackle SHM of a four-story shear building subjected to a base motion consistent with the El-Centro earthquake and undergoing a preset damage in the first floor. The purpose of the problem is localizing the damage in both space and time, and tracking the state of the system throughout and subsequent to the damage time. The application of the introduced data assimilation technique to SHM enhances its applicability to a wide range of structural problems with strongly nonlinear dynamic behavior and with uncertain and complex governing laws.

The accurate prediction of the response of spacecraft systems during launch and ascent phase is a crucial aspect in design and verification stages which requires accurate numerical models. The enhancement of numerical models based on experimental data is denoted model updating and focuses on the improvement of the correlation between finite element (FE) model and test structure. In aerospace industry, the examination of the agreement between model and real structure involves the comparison of the modal properties of the structure. Chapter 13 by B. Goller et al. is devoted to the efficient model updating of a satellite in a Bayesian setting based on experimental modal data. A detailed FE model of the satellite is used for demonstrating the applicability of the employed updating procedure to large-scale complex aerospace structures.

In Chap. 14, B. Rosič and H. Matthies deal with the identification of properties of stochastic elastoplastic systems in a Bayesian setting. The inverse problem is formulated in a probabilistic framework where the unknown uncertain quantities are embedded in the form of their probability distributions. With the help of stochastic functional analysis, a new update procedure is introduced as a direct, purely algebraic way of computing the posterior, which is comparatively inexpensive to evaluate. Such description requires the solution of the convex minimization problem in a stochastic setting for which the extension of the classical optimization algorithm

in predictor-corrector form is proposed as the solution procedure. The identification method is finally validated through a series of virtual experiments taking into account the influence of the measurement error and the order of the approximation on the posterior estimate.

Chapter 15 deals with the study of SH surface waves in a half space with random heterogeneities. C. Du and X. Su prove both theoretically and numerically that surface waves exist in a half space which has small, random density, but the mean value of the density is homogeneous. Historically, this type of half space is often treated as homogeneous using deterministic methods. In this investigation, a closed-form dispersion equation is derived stochastically and the frequency spectrum, dispersion equation and phase/group velocity are computed numerically to study how the random inhomogeneities will affect the dispersion properties of the half space with random density. The results of this research may find their application in various fields, such as in seismology and in non-destructive test/evaluation of structures with randomly distributed micro-cracks or heterogeneities.

The following six chapters are devoted to earthquake engineering applications. P. Jehel et al. (Chap. 16) investigate the seismic fragility of a moment-resisting reinforced concrete frame structure in the area of the Cascadia subduction zone situated in the South-West of Canada and the North-West of the USA. According to shaking table tests, the authors first validate the capability of an inelastic fiber beam/column element, using a recently developed concrete constitutive law, for representing the seismic behavior of the tested frame coupled to either a commonly used Rayleigh damping model or a proposed new model. Then, for each of the two damping models, they perform a structural fragility analysis and investigate the amount of uncertainty to be induced by damping models.

In Chap. 17 by Y. Vargas et al., a detailed study of the seismic response of a reinforced concrete building is conducted using a probabilistic approach in the framework of Monte Carlo simulation. The building is representative for office buildings in Spain but the procedures used and the results obtained can be extended to other types of buildings. The purpose of the work is twofold: (i) to analyze the differences when static and dynamic analysis techniques are used and (ii) to obtain a measure of the uncertainties involved in the assessment of structural vulnerability. The results show that static procedures are somehow conservative and that uncertainties increase with the severity of the seismic actions and with the damage. Low damage state fragility curves have little uncertainty while high damage state fragility curves show great scattering.

Seismic pounding can induce severe damage and losses in buildings. The corresponding risk is particularly relevant in densely inhabited metropolitan areas, due to the inadequate clearance between buildings. Chapter 18 by E. Tubaldi and M. Barbato proposes a reliability-based procedure for assessing the level of safety corresponding to a given value of the separation distance between adjacent buildings exhibiting linear elastic behavior. The seismic input is modeled as a non-stationary random process and the first-passage reliability problem corresponding to the pounding event is solved employing analytical techniques involving the determination of specific statistics of the response processes. The proposed procedure is applied to esti-

mate the probability of pounding between linear single-degree-of-freedom systems and to evaluate the reliability of simplified design code formulae used to determine building separation distances. Furthermore, the capability of the proposed method to deal with complex systems is demonstrated by assessing the effectiveness of the use of viscous dampers in reducing the probability of pounding between adjacent buildings modeled as multi-degree-of-freedom systems.

In Chap. 19, A. Elenas provides a methodology to quantify the relationship between seismic intensity parameters and structural damage. First, a computer-supported elaboration of ground motion records provides several peak, spectral and energy seismic parameters. After that, nonlinear dynamic analyses are carried out to provide the structural response for a set of seismic excitations. Among the several response characteristics, the overall structure damage indices after Park/Ang and the maximum inter-storey drift ratio are selected to represent the structural response. Correlation coefficients are evaluated to express the grade of interrelation between seismic acceleration parameters and structural damage. The presented methodology is applied to a reinforced concrete frame building, designed according to the rules of the recent Eurocodes, and the numerical results show that the spectral and energy parameters provide strong correlation to the damage indices.

As demonstrated in the previous chapter, there is interdependence between seismic intensity parameters and structural damage. In Chap. 20, A. Elenas et al. proceed to the classification of seismic damage in buildings using an adaptive neuro-fuzzy inference system. The seismic excitations are simulated by artificial accelerograms and their intensity is described by seismic parameters. The proposed system is trained using a number of seismic events and tested on a reinforced concrete structure. The results show that the proposed fuzzy technique contributes to the development of an efficient blind prediction of seismic damage. The recognition scheme achieves correct classification rates over 90%.

The book closes with a study on damage identification of historical masonry structures under seismic excitation by G. De Matteis et al. (Chap. 21). The seismic behavior of a physical 1:5.5 scaled model of the church of the Fossanova Abbey (Italy) is examined by means of numerical and experimental analyses. As it mostly influences the seismic vulnerability of the Abbey, the central transversal three-bay complex of the church was investigated in detail by means of a shaking table test on a 1:5.5 scaled physical model in the Laboratory of the Institute for Earthquake Engineering and Engineering Seismology in Skopje. In this chapter, a brief review of the numerical activity related to the prediction of the shaking table test response of the model is first proposed. Then, the identification of frequency decay during collapse is performed through decomposition of the measured power spectral density matrix. Finally, the localization and evolution of damage in the structure is analyzed and the obtained numerical results show a very good agreement with the experimental data.

The book editors would like to express their deep appreciation to all contributors for their active participation in the COMPDYN 2011 Conference and for the time and effort devoted to the completion of their contributions to this volume. Special thanks are also due to the reviewers for their constructive comments and suggestions

which enhanced the quality of the book. Finally, the editors would like to thank the personnel of Springer for their most valuable support during the publication process.

Athens, Greece
April 2012

Manolis Papadrakakis
George Stefanou
Vissarion Papadopoulos

Contents

1 Random Dynamical Response of a Multibody System with Uncertain Rigid Bodies 1
Anas Batou and Christian Soize

2 Dynamic Variability Response for Stochastic Systems 15
Vissarion Papadopoulos and Odysseas Kokkinos

3 A Novel Reduced Spectral Function Approach for Finite Element Analysis of Stochastic Dynamical Systems 31
Abhishek Kundu and Sondipon Adhikari

4 Computational Stochastic Dynamics Based on Orthogonal Expansion of Random Excitations 55
X. Frank Xu and George Stefanou

5 Numerical Solution of the Fokker–Planck Equation by Finite Difference and Finite Element Methods—A Comparative Study . . . 69
L. Pichler, A. Masud, and L.A. Bergman

6 A Comparative Study of Uncertainty Propagation Methods in Structural Problems 87
Manuele Corradi, Marco Gherlone, Massimiliano Mattone, and Marco Di Sciuva

7 Fuzzy and Fuzzy Stochastic Methods for the Numerical Analysis of Reinforced Concrete Structures Under Dynamical Loading 113
Frank Steinigen, Jan-Uwe Sickert, Wolfgang Graf, and Michael Kaliske

8 Application of Interval Fields for Uncertainty Modeling in a Geohydrological Case 131
Wim Verhaeghe, Wim Desmet, Dirk Vandepitte, Ingeborg Joris, Piet Seuntjens, and David Moens

9 Enhanced Monte Carlo for Reliability-Based Design and Calibration 149
Arvid Naess, Marc Maes, and Markus R. Dann

10 Optimal Design of Base-Isolated Systems Under Stochastic Earthquake Excitation 161
Hector A. Jensen, Marcos A. Valdebenito, and Juan G. Sepulveda

11 Systematic Formulation of Model Uncertainties and Robust Control in Smart Structures Using H_∞ and μ-Analysis 179
Amalia Moutsopoulou, Georgios E. Stavroulakis, and Anastasios Pouliezos

12 Robust Structural Health Monitoring Using a Polynomial Chaos Based Sequential Data Assimilation Technique 203
George A. Saad and Roger G. Ghanem

13 Efficient Model Updating of the GOCE Satellite Based on Experimental Modal Data 215
B. Goller, M. Broggi, A. Calvi, and G.I. Schuëller

14 Identification of Properties of Stochastic Elastoplastic Systems . . . 237
Bojana V. Rosić and Hermann G. Matthies

15 SH Surface Waves in a Half Space with Random Heterogeneities . . 255
Chaoliang Du and Xianyue Su

16 Structural Seismic Fragility Analysis of RC Frame with a New Family of Rayleigh Damping Models 267
Pierre Jehel, Pierre Léger, and Adnan Ibrahimbegovic

17 Incremental Dynamic Analysis and Pushover Analysis of Buildings. A Probabilistic Comparison 293
Yeudy F. Vargas, Luis G. Pujades, Alex H. Barbat, and Jorge E. Hurtado

18 Stochastic Analysis of the Risk of Seismic Pounding Between Adjacent Buildings 309
Enrico Tubaldi and Michele Barbato

19 Intensity Parameters as Damage Potential Descriptors of Earthquakes 327
Anaxagoras Elenas

20 Classification of Seismic Damages in Buildings Using Fuzzy Logic Procedures 335
Anaxagoras Elenas, Eleni Vrochidou, Petros Alvanitopoulos, and Ioannis Andreadis

21 Damage Identification of Masonry Structures Under Seismic Excitation 345
G. De Matteis, F. Campitiello, M.G. Masciotta, and M. Vasta

Chapter 1
Random Dynamical Response of a Multibody System with Uncertain Rigid Bodies

Anas Batou and Christian Soize

Abstract This work is devoted to the construction of the random dynamical response of a multibody system with uncertain rigid bodies. We construct a stochastic model of an uncertain rigid body by modeling the mass, the center of mass and the tensor of inertia by random variables. The prior probability distributions of these random variables are constructed using the maximum entropy principle under the constraints defined by the available information. A generator of independent realizations are then developed. Several uncertain rigid bodies can be linked each to the others in order to calculate the random response of a multibody dynamical system. An application is proposed to illustrate the theoretical development.

1 Introduction

This work is devoted to the construction of a probabilistic model of uncertainties for a rigid multibody dynamical system made up of uncertain rigid bodies. In some cases, the mass distribution inside a rigid body is not perfectly known and must be considered as random (for example, the distribution of passengers inside a vehicle) and therefore, this unknown mass distribution inside the rigid body induces uncertainties in the model of this rigid body. Here, we propose a new probabilistic modeling for uncertain rigid bodies in the context of the multibody dynamics. Concerning the modeling of uncertainties in multibody dynamical system, a very few previous researches have been carried out. These researches concerned parameters which describe the joints linking each rigid body to the others and the external sources (see [3, 8, 12, 13, 16]), but not rigid bodies themselves. In the field of uncertain rigid bodies, a first work has been proposed in [9, 10], in which the authors take into account uncertain rigid bodies for rotor dynamical systems using the nonparamet-

A. Batou (✉) · C. Soize
Laboratoire Modélisation et Simulation Multi Echelle, MSME UMR 8208 CNRS, Université Paris-Est, 5 bd Descartes, 77454 Marne-la-Vallee, France
e-mail: anas.batou@univ-paris-est.fr

C. Soize
e-mail: christian.soize@univ-paris-est.fr

M. Papadrakakis et al. (eds.), *Computational Methods in Stochastic Dynamics*, Computational Methods in Applied Sciences 26,
DOI 10.1007/978-94-007-5134-7_1,

ric probabilistic approach [19, 20] consisting in replacing the mass and gyroscopic matrices by random matrices.

In this paper, a general and complete stochastic model is constructed for an uncertain rigid body. The mass, the center of mass and the tensor of inertia which describe the rigid body are modeled by random variables. The prior probability distributions of the random variables are constructed using the maximum entropy principle [6, 7] from Information Theory [17, 18]. The generator of independent realizations corresponding to the prior probability distributions of these random quantities are developed and presented. Then, several uncertain rigid bodies can be linked each to the others in order to calculate the random response of an uncertain multibody dynamical system. The stochastic multibody dynamical equations are solved using the Monte Carlo simulation method.

Section 2 is devoted to the construction of the nominal model for the rigid multibody dynamical system by using the classical method. In Sect. 3, we propose a general probability model for an unconstrained uncertain rigid body and then, the uncertain rigid multibody dynamical system is obtained by joining this unconstrained uncertain rigid body to the other rigid bodies. The last section is devoted to an application which illustrates the proposed theory.

2 Nominal Model for the Rigid Multibody Dynamical System

In this paper, the usual model of a rigid multibody dynamical system for which all the mechanical properties are known will be called the nominal model. This section is devoted to the construction of the nominal model for a rigid multibody dynamical system. This nominal model is constructed as in [14, 15] and is summarized below.

2.1 Dynamical Equations for a Rigid Body of the Multibody System

Let RB_i be the rigid body occupying a bounded domain Ω_i with a given geometry. Let ξ be the generic point of the three dimensional space (see Fig. 1.1). Let $\mathbf{x} = (x_1, x_2, x_3)$ be the position vector of point ξ defined in a fixed inertial frame $(O, x_{0,1}, x_{0,2}, x_{0,3})$, such that $\mathbf{x} = \overrightarrow{O\xi}$. A rigid body is classically defined by three quantities.

1. The first one is the mass m_i of RB_i which is such that

$$m_i = \int_{\Omega_i} \rho(\mathbf{x})\, d\mathbf{x}, \tag{1.1}$$

where $\rho(\mathbf{x})$ is the mass density.

Fig. 1.1 Rigid body RB_i

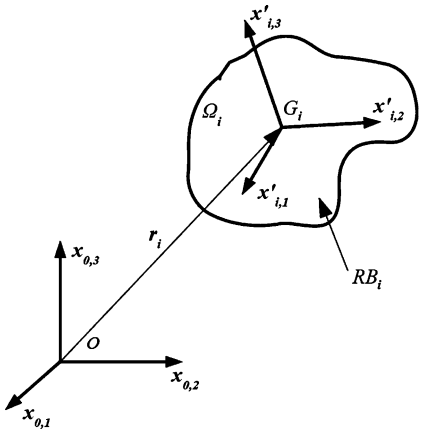

2. The second quantity is the position vector $\mathbf{r}_i$ of the center of mass G_i, defined in the fixed inertial frame, by

$$\mathbf{r}_i = \frac{1}{m_i} \int_{\Omega_i} \mathbf{x} \rho(\mathbf{x})\, d\mathbf{x}. \tag{1.2}$$

3. Let $(G_i, x'_{i,1}, x'_{i,2}, x'_{i,3})$ be the local frame for which the origin is G_i and which is deduced from the fixed frame $(O, x_{0,1}, x_{0,2}, x_{0,3})$ by the translation $\overrightarrow{OG_i}$ and a rotation defined by the three Euler angles α_i, β_i and γ_i. The third quantity is the positive-definite matrix $[J_i]$ of the tensor of inertia in the local frame such that

$$[J_i]\mathbf{u} = -\int_{\Omega_i} \mathbf{x}' \times \mathbf{x}' \times \mathbf{u} \rho\big(\mathbf{x}'\big)\, d\mathbf{x}', \quad \forall \mathbf{u} \in \mathbb{R}^3, \tag{1.3}$$

in which the vector $\mathbf{x}' = (x'_1, x'_2, x'_3)$ of the components of vector $\overrightarrow{G_i\xi}$ are given in $(G_i, x'_{i,1}, x'_{i,2}, x'_{i,3})$. In the above equation, $\mathbf{u} \times \mathbf{v}$ denotes the cross product between the vectors $\mathbf{u}$ and $\mathbf{v}$.

2.2 Matrix Model for the Rigid Multibody Dynamical System

The rigid multibody dynamical system is made up of n_b rigid bodies and ideal joints including rigid joints, joints with given motion (rheonomic constraints) and vanishing joints (free motion). The interactions between the rigid bodies are realized by these ideal joints but also by springs, dampers or actuators which produce forces between the bodies. In this paper, only n_c holonomic constraints are considered. Let $\mathbf{u}$ be the vector in $\mathbb{R}^{6n_b}$ such that $\mathbf{u} = (\mathbf{r}_1, \ldots, \mathbf{r}_{n_b}, \mathbf{s}_1, \ldots, \mathbf{s}_{n_b})$ in which $\mathbf{s}_i = (\alpha_i, \beta_i, \gamma_i)$ is the rotation vector. The n_c constraints are given by n_c implicit equations which are globally written as $\boldsymbol{\varphi}(\mathbf{u}, t) = 0$. The $(6n_b \times 6n_b)$ mass matrix $[M]$ is defined by

$$[M] = \begin{bmatrix} [M^r] & 0 \\ 0 & [M^s] \end{bmatrix}, \tag{1.4}$$

where the $(3n_b \times 3n_b)$ matrices $[M^r]$ and $[M^s]$ are defined by

$$[M^r] = \begin{bmatrix} m_1[I_3] & \cdots & 0 \\ \vdots & \ddots & \vdots \\ 0 & \cdots & m_{n_b}[I_3] \end{bmatrix}, \qquad [M^s] = \begin{bmatrix} [J_1] & \cdots & 0 \\ \vdots & \ddots & \vdots \\ 0 & \cdots & [J_{n_b}] \end{bmatrix}, \tag{1.5}$$

in which $[I_3]$ is the (3×3) identity matrix. The function $\{\mathbf{u}(t) \in [0, T]\}$ is then the solution of the following differential equation (see [15])

$$\begin{bmatrix} [M] & [\boldsymbol{\varphi}_{\mathbf{u}}]^T \\ [\boldsymbol{\varphi}_{\mathbf{u}}] & [0] \end{bmatrix} \begin{bmatrix} \ddot{\mathbf{u}} \\ \boldsymbol{\lambda} \end{bmatrix} = \begin{bmatrix} \mathbf{q} - \mathbf{k} \\ -\frac{d}{dt}\boldsymbol{\varphi}_t - [\frac{d}{dt}\boldsymbol{\varphi}_{\mathbf{u}}]\dot{\mathbf{u}} \end{bmatrix}, \tag{1.6}$$

with the initial conditions

$$\mathbf{u}(0) = \mathbf{u}_0, \qquad \dot{\mathbf{u}}(0) = \mathbf{v}_0, \tag{1.7}$$

in which $\mathbf{k}(\dot{\mathbf{u}})$ is the vector of the Coriolis forces and where $[\boldsymbol{\varphi}_{\mathbf{u}}(\mathbf{u}(t), t)]_{ij} = \partial\varphi_i(\mathbf{u}(t), t)/\partial u_j(t)$ and $\boldsymbol{\varphi}_t = \partial\boldsymbol{\varphi}/\partial t$. The vector $\mathbf{q}(\mathbf{u}, \dot{\mathbf{u}}, t)$ is constituted of the applied forces and torques induced by springs, dampers and actuators. The vector $\boldsymbol{\lambda}(t)$ is the vector of the Lagrange multipliers. Equation (1.6) can be solved using an adapted integration algorithm (see for instance [2]).

3 Stochastic Model for a Multibody Dynamical System with Uncertain Rigid Bodies

Firstly, a stochastic model for an uncertain rigid body of the multibody dynamical system is proposed and secondly, the stochastic model for the multibody dynamical system with uncertain rigid bodies is constructed joining the stochastic model of the uncertain rigid bodies.

3.1 Stochastic Model for an Uncertain Rigid Body of the Multibody Dynamical System

The properties of the nominal model of the rigid body RB_i are defined by its mass $\underline{m}_i$, the position vector $\underline{\mathbf{r}}_{0,i}$ of its center of mass $\underline{G}_i$ at initial time $t = 0$ and the matrix $[\underline{J}_i]$ of its tensor of inertia with respect to the local frame $(\underline{G}_i, \underline{x}'_{i,1}, \underline{x}'_{i,2}, \underline{x}'_{i,3})$. The probabilistic model of uncertainties for this rigid body is constructed by replacing these three parameters by the following three random variables: the random mass M_i, the random position vector $\mathbf{R}_{0,i}$ of its random center of mass $\mathbf{G}_i$ at initial time $t = 0$ and the random matrix $[\mathbf{J}_i]$ of its random tensor of inertia with respect to the random local frame $(\mathbf{G}_i, \underline{x}'_{i,1}, \underline{x}'_{i,2}, \underline{x}'_{i,3})$. The probability density functions

(PDF) of these three random variables are constructed using the maximum entropy principle (see [6, 7, 17]), that is to say, in maximizing the uncertainties in the model under the constraints defined by the available information.

3.1.1 Construction of the PDF for the Random Mass

(i) *Available information.*
Let $E\{\cdot\}$ be the mathematical expectation. The available information for the random mass M_i is defined as follows. Firstly, the random variable M_i must be positive almost surely. Secondly, the mean value of the random mass M_i must be equal to the value $\underline{m}_i$ of the nominal model. Thirdly, as it is proven in [20], the random mass must verify the inequality $E\{M_i^{-2}\} < +\infty$ in order that a second-order solution exists for the stochastic dynamical system. In addition, it is also proven that this constraint can be replaced by $|E\{\log M_i\}| < +\infty$.

(ii) *Maximum entropy principle.*
The probability density function $\mu \mapsto p_{M_i}(\mu)$ of the random variable M_i is constructed by maximizing the entropy under the constraints defined above. The solution of this optimization problem is the PDF of a gamma random variable defined on $]0, +\infty[$. This PDF depends on two parameters which are the nominal value $\underline{m}_i$ and the coefficient of variation δ_{M_i} of the random variable M_i such that $\delta_{M_i} = \sigma_{M_i}/\underline{m}_i$ where σ_{M_i} is the standard deviation of the random variable M_i. Therefore, the PDF of the random mass is completely defined by the mean value $\underline{m}_i$ and by the dispersion parameter δ_{M_i}.

3.1.2 Construction of the PDF for the Random Position Vector $\mathbf{R}_{0,i}$

In this subsection, the PDF of the random initial position vector $\mathbf{R}_{0,i}$ of the center of mass of RB_i at initial time $t = 0$ is constructed.

(i) *Available information.*
The position vector $\underline{\mathbf{r}}_{0,i}$ of the center of mass $\underline{G}_i$ at initial time $t = 0$ of the nominal model is given. However, the real position is not exactly known and $\underline{\mathbf{r}}_{0,i}$ only corresponds to a mean position. Consequently, there is an uncertainty about the real position and this is the reason why this position is modeled by the random vector $\mathbf{R}_{0,i}$. Some geometrical and mechanical considerations lead us to introduce an admissible domain D_i of random vector $\mathbf{R}_{0,i}$. We introduce the vector $\mathbf{h}$ of the parameters describing the geometry of domain D_i. In addition, the mean value of the random vector $\mathbf{R}_{0,i}$ must be equal to the value $\underline{\mathbf{r}}_{0,i}$ of the nominal model. Therefore, the available information for random variable $\mathbf{R}_{0,i}$ can be written as

$$\mathbf{R}_{0,i} \in D_i(\mathbf{h}) \quad \text{a.s.}, \tag{1.8a}$$

$$E\{\mathbf{R}_{0,i}\} = \underline{\mathbf{r}}_{0,i} \in D_i(\mathbf{h}). \tag{1.8b}$$

(ii) *Maximum entropy principle.*
The probability density function $\mathbf{a} \mapsto p_{\mathbf{R}_{0,i}}(\mathbf{a})$ of random variable $\mathbf{R}_{0,i}$ is then constructed by maximizing the entropy with the constraints defined by the available information in Eqs. (1.8a) and (1.8b). The solution of this optimization problem depends on two parameters which are $\underline{\mathbf{r}}_{0,i}$ and vector-valued parameter $\mathbf{h}$, and is such that

$$p_{\mathbf{R}_{0,i}}(\mathbf{a};\mathbf{h}) = \mathbb{1}_{D_i(\mathbf{h})}(\mathbf{a}) C_0 e^{-\langle \boldsymbol{\lambda}, \mathbf{a} \rangle}. \tag{1.9}$$

The positive valued parameter C_0 and vector $\boldsymbol{\lambda}$ are the unique solution of the equations

$$C_0 \int_{D_i(\mathbf{h})} e^{-\langle \boldsymbol{\lambda}, \mathbf{a} \rangle} \, d\mathbf{a} = 1, \tag{1.10a}$$

$$C_0 \int_{D_i(\mathbf{h})} \mathbf{a} e^{-\langle \boldsymbol{\lambda}, \mathbf{a} \rangle} \, d\mathbf{a} = \underline{\mathbf{r}}_{0,i}. \tag{1.10b}$$

(iii) *Generator of independent realizations.*
The independent realizations of random variable $\mathbf{R}_{0,i}$ must be generated using the constructed PDF $p_{\mathbf{R}_{0,i}}$. Such a generator can be obtained using the Monte Carlo Markov Chain (MCMC) method (Metropolis–Hastings algorithm [5]).

3.1.3 Random Matrix $[\mathbf{J}_i]$ of the Random Tensor of Inertia

In this subsection, the random matrix $[\mathbf{J}_i]$ of the random tensor of inertia with respect to $(\mathbf{G}_i, \underline{x}'_{i,1}, \underline{x}'_{i,2}, \underline{x}'_{i,3})$ is defined and an algebraic representation of this random matrix is constructed. The mass distribution around the random center of mass $\mathbf{G}_i$ is uncertain and consequently, the tensor of inertia is also uncertain. This is the reason why the matrix $[\underline{J}_i]$ of the tensor of inertia of the nominal model with respect to $(\underline{G}_i, \underline{x}'_{i,1}, \underline{x}'_{i,2}, \underline{x}'_{i,3})$ is replaced by a random matrix $[\mathbf{J}_i]$ which is constructed by using the maximum entropy principle. We introduce the positive-definite matrix $[Z_i]$ independent of m_i such that

$$[Z_i] = \frac{1}{m_i} \left\{ \frac{\mathrm{tr}([J_i])}{2} [I_3] - [J_i] \right\}. \tag{1.11}$$

Then $[J_i]$ can be calculated as a function of $[Z_i]$,

$$[J_i] = m_i \left\{ \mathrm{tr}\big([Z_i]\big)[I_3] - [Z_i] \right\}. \tag{1.12}$$

It can be proven that $[Z_i]$ is positive definite and that each positive definite matrix $[J_i]$ constructed using Eq. (1.12), where $[Z_i]$ is a given positive definite matrix, can be interpreted as the matrix of a tensor of inertia of a physical rigid body (see [1]). In the literature, the matrix $m_i[Z_i]$ is referred as to the Euler tensor. The probabilistic modeling $[\mathbf{J}_i]$ of $[J_i]$ consists in introducing the random matrix $[\mathbf{Z}_i]$ and in using Eq. (1.12) in which m_i is replaced by the random variable M_i and where $[Z_i]$ is replaced by $[\mathbf{Z}_i]$. We then obtain

$$[\mathbf{Z}_i] = \frac{1}{M_i}\left\{\frac{\mathrm{tr}([\mathbf{J}_i])}{2}[I_3] - [\mathbf{J}_i]\right\}, \tag{1.13}$$

$$[\mathbf{J}_i] = M_i\big\{\mathrm{tr}\big([\mathbf{Z}_i]\big)[I_3] - [\mathbf{Z}_i]\big\}. \tag{1.14}$$

(i) *Available information concerning random matrix* $[\mathbf{Z}_i]$.
Let us introduce (1) the nominal value $[\underline{Z}_i]$ of deterministic matrix $[Z_i]$ such that $[\underline{Z}_i] = (1/\underline{m}_i)\{\mathrm{tr}([\underline{J}_i])/2[I_3] - [\underline{J}_i]\}$ and (2) the upper bound $[Z_i^{\max}]$ of random matrix $[\mathbf{Z}_i]$. Then, the available information for $[\mathbf{Z}_i]$ can be summarized as follows,

$$\begin{aligned}
[\mathbf{Z}_i] &\in \mathbb{M}_3^+(\mathbb{R}) \quad \text{a.s.},\\
\big\{\big[Z_i^{\max}\big] - [\mathbf{Z}_i]\big\} &\in \mathbb{M}_3^+(\mathbb{R}) \quad \text{a.s.},\\
E\big\{[\mathbf{Z}_i]\big\} &= [\underline{Z}_i],\\
E\big\{\log\big(\det[\mathbf{Z}_i]\big)\big\} &= C_i^l, \quad \big|C_i^l\big| < +\infty,\\
E\big\{\log\big(\det\big(\big[Z_i^{\max}\big] - [\mathbf{Z}_i]\big)\big)\big\} &= C_i^u, \quad \big|C_i^u\big| < +\infty.
\end{aligned} \tag{1.15}$$

For more convenience, random matrix $[\mathbf{Z}_i]$ is normalized as follow. Matrix $[\underline{Z}_i]$ being positive definite, its Cholesky decomposition yields $[\underline{Z}_i] = [\underline{L}_{Z_i}]^T[\underline{L}_{Z_i}]$ in which $[\underline{L}_{Z_i}]$ is an upper triangular matrix in the set $\mathbb{M}_3(\mathbb{R})$ of all the (3×3) real matrices. Then, random matrix $[\mathbf{Z}_i]$ can be rewritten as

$$[\mathbf{Z}_i] = [\underline{L}_{Z_i}]^T[\mathbf{G}_i][\underline{L}_{Z_i}], \tag{1.16}$$

in which the matrix $[\mathbf{G}_i]$ is a random matrix for which the available information is

$$\begin{aligned}
[\mathbf{G}_i] &\in \mathbb{M}_3^+(\mathbb{R}) \quad \text{a.s.},\\
\big\{\big[G_i^{\max}\big] - [\mathbf{G}_i]\big\} &\in \mathbb{M}_3^+(\mathbb{R}) \quad \text{a.s.},\\
E\big\{[\mathbf{G}_i]\big\} &= [I_3],\\
E\big\{\log\big(\det[\mathbf{G}_i]\big)\big\} &= C_i^{l\prime}, \quad \big|C_i^{l\prime}\big| < +\infty,\\
E\big\{\log\big(\det\big(\big[G_i^{\max}\big] - [\mathbf{G}_i]\big)\big)\big\} &= C_i^{u\prime}, \quad \big|C_i^{u\prime}\big| < +\infty,
\end{aligned} \tag{1.17}$$

in which $C_i^{l\prime} = C_i^l - \log(\det[\underline{Z}_i])$, $C_i^{u\prime} = C_i^u - \log(\det[\underline{Z}_i])$ and where the matrix $[G_i^{\max}]$ is an upper bound for random matrix $[\mathbf{G}_i]$ and is defined by $[G_i^{\max}] = ([\underline{L}_{Z_i}]^T)^{-1}[Z_i^{\max}][\underline{L}_{Z_i}]^{-1}$.

(ii) *Maximum entropy principle.*
The probability distribution of random matrix $[\mathbf{G}_i]$ is constructed using the maximum entropy principle under the constraints defined by the available information given by Eq. (1.17). The probability density function $p_{[\mathbf{G}_i]}([G])$ with respect to the volume element $\widetilde{d}G$ of random matrix $[\mathbf{G}_i]$ is then written as

$$\begin{aligned}
p_{[\mathbf{G}_i]}\big([G]\big) = {} & \mathbb{1}_{\mathbb{M}_3^+(\mathbb{R})}\big([G]\big) \times \mathbb{1}_{\mathbb{M}_3^+(\mathbb{R})}\big(\big[G_i^{\max}\big] - [G]\big) \times C_{G_i} \times \big(\det[G]\big)^{-\lambda_l}\\
& \times \big(\det\big(\big[G_i^{\max}\big] - [G]\big)\big)^{-\lambda_u} \times e^{-\mathrm{tr}([\mu][G])},
\end{aligned} \tag{1.18}$$

in which the positive valued parameter C_{G_i} is a normalization constant, the real parameters $\lambda_l < 1$ and $\lambda_u < 1$ are Lagrange multipliers relative to the two last constraints defined by Eq. (1.17) and the symmetric real matrix $[\mu]$ is a Lagrange multiplier relative to the third constraint defined by Eq. (1.17). This probability density function is a particular case of the Kummer-Beta matrix variate distribution (see [4, 11]) for which the lower bound is a zero matrix. Parameters C_{G_i}, λ_l, λ_u and matrix $[\mu]$ are the unique solution of the equations

$$\begin{aligned} E\{\mathbb{1}_{\mathbb{M}_3^S(\mathbb{R})}([\mathbf{G}_i])\} &= 1, \\ E\{[\mathbf{G}_i]\} &= [I_3], \\ E\{\log(\det[\mathbf{G}_i])\} &= C_i^{l\prime}, \\ E\{\log(\det([G_i^{\max}] - [\mathbf{G}_i]))\} &= C_i^{u\prime}. \end{aligned} \tag{1.19}$$

For fixed values of λ_l and λ_u, parameters C_{G_i} and $[\mu]$ can be estimated using Eq. (1.19). In Eq. (1.19), since the parameters $C_i^{l\prime}$ and $C_i^{u\prime}$ have no real physical meaning, the parameters λ_l and λ_u are kept as parameters which then allows the "shape" of the PDF to be controlled. If experimental data are available for the responses of the dynamical system, then the two parameters λ_l and λ_u can be identified solving an inverse problem. If experimental data are not available, these two parameters allow a sensitivity analysis of the solution to be carried out with respect to the level of uncertainties.

(iii) *Properties for random matrix* $[\mathbf{J}_i]$.
It is proven in [1] that using Eq. (1.14) and the available information defined by Eq. (1.15), the following important properties for random matrix $[\mathbf{J}_i]$ can be deduced,

$$\left\{\frac{1}{2}\,\mathrm{tr}([\mathbf{J}_i])[I_3] - [\mathbf{J}_i]\right\} \in \mathbb{M}_3^+(\mathbb{R}) \quad \text{a.s.}, \tag{1.20a}$$

$$\{[\mathbf{J}_i^{\max}] - [\mathbf{J}_i]\} \in \mathbb{M}_3^+(\mathbb{R}) \quad \text{a.s.}, \tag{1.20b}$$

$$E\{[\mathbf{J}_i]\} = [\underline{J}_i], \tag{1.20c}$$

$$\{\lambda_l < -2\} \Rightarrow E\{\|[\mathbf{J}_i]^{-1}\|^2\} < +\infty, \tag{1.20d}$$

in which the random matrix $[\mathbf{J}_i^{\max}]$, which represents a random upper bound for random matrix $[\mathbf{J}_i]$, is defined by

$$[\mathbf{J}_i^{\max}] = M_i\{\mathrm{tr}([Z_i^{\max}])[I_3] - [Z_i^{\max}]\}. \tag{1.21}$$

It should be noted that Eq. (1.20a) implies that each realization of random matrix $[\mathbf{J}_i]$ corresponds to the matrix of a tensor of inertia of a physical rigid body. In addition, this equation implies that random matrix $[\mathbf{J}_i]$ is almost surely positive definite. Equation (1.20b) provides a random upper bound for random matrix $[\mathbf{J}_i]$. Equation (1.20c) corresponds to a construction for which the mean value of random matrix $[\mathbf{J}_i]$ is equal to the nominal value $[\underline{J}_i]$. Finally, Eq. (1.20d) is necessary for that the random solution of the nonlinear dynamical system be a second-order stochastic process.

(iv) *Generator of independent realizations for random matrix* $[\mathbf{J}_i]$.
The generator of independent realizations of random matrix $[\mathbf{G}_i]$ is based on the Monte Carlo Markov Chain (MCMC) (Metropolis–Hastings algorithm [5] with the PDF defined by Eq. (1.18). Then, independent realizations of random matrix $[\mathbf{Z}_i]$ are obtained using Eq. (1.16). Finally, independent realizations of random matrix $[\mathbf{J}_i]$ are obtained using Eq. (1.14) and independent realizations of random mass M_i.

3.2 Stochastic Matrix Model for a Multibody Dynamical System with Uncertain Rigid Bodies and Its Random Response

In order to limit the developments, it is assumed that only one of the n_b rigid bodies denoted by RB_i of the rigid multibody system is uncertain. The extension to several uncertain rigid bodies is straightforward. Let the $6n_b$ random coordinates be represented by the $\mathbb{R}^{6n_b}$-valued stochastic process $\mathbf{U} = (\mathbf{R}_1, \ldots, \mathbf{R}_{n_b}, \mathbf{S}_1, \ldots, \mathbf{S}_{n_b})$ indexed by $[0, T]$ and let the n_c random Lagrange multipliers be represented by the $\mathbb{R}^{n_c}$-valued stochastic process $\boldsymbol{\Lambda}$ indexed by $[0, T]$. The deterministic Eq. (1.6) becomes the following stochastic equation

$$\begin{bmatrix} [\mathbf{M}] & [\boldsymbol{\varphi}_{\mathbf{u}}]^T \\ [\boldsymbol{\varphi}_{\mathbf{u}}] & [0] \end{bmatrix} \begin{bmatrix} \ddot{\mathbf{U}} \\ \boldsymbol{\Lambda} \end{bmatrix} = \begin{bmatrix} \mathbf{q} - \mathbf{K} \\ -\frac{d}{dt}\boldsymbol{\varphi}_t - [\frac{d}{dt}\boldsymbol{\varphi}_{\mathbf{u}}]\dot{\mathbf{U}} \end{bmatrix}, \tag{1.22}$$

$$\mathbf{U}(0) = \mathbf{U}_0, \qquad \dot{\mathbf{U}}(0) = \mathbf{v}_0, \quad \text{a.s.} \tag{1.23}$$

in which the vector $\mathbf{U}_0 = (\mathbf{r}_{0,1}, \ldots, \mathbf{R}_{0,i}, \ldots, \mathbf{r}_{0,n_b}, \mathbf{s}_{0,1}, \ldots, \mathbf{s}_{0,n_b})$ is random due to the random vector $\mathbf{R}_{0,i}$. For all given real vector $\dot{\mathbf{u}}$, the vector $\mathbf{K}(\dot{\mathbf{u}})$ of the Coriolis forces is random due to the random matrix $[\mathbf{J}_i]$. The random mass matrix $[\mathbf{M}]$ is defined by

$$[\mathbf{M}] = \begin{bmatrix} [\mathbf{M}^r] & 0 \\ 0 & [\mathbf{M}^s] \end{bmatrix}, \tag{1.24}$$

in which the $(3n_b \times 3n_b)$ random matrices $[\mathbf{M}^r]$ and $[\mathbf{M}]^s$ are defined by

$$[\mathbf{M}^r] = \begin{bmatrix} m_1[I_3] & \cdots & 0 \\ & \ddots & \\ \vdots & M_i[I_3] & \vdots \\ & & \ddots \\ 0 & \cdots & m_{n_b}[I_3] \end{bmatrix}, \tag{1.25}$$

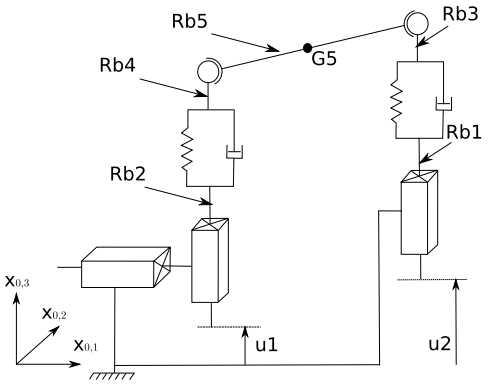

Fig. 1.2 Rigid multibody system

$$\left[\mathbf{M}^s\right] = \begin{bmatrix} [J_1] & \cdots & 0 \\ & \ddots & \\ \vdots & [\mathbf{J}_i] & \vdots \\ & \ddots & \\ 0 & \cdots & [J_{n_b}] \end{bmatrix}. \tag{1.26}$$

Random Eqs. (1.22) and (1.23) are solved using the Monte Carlo simulation method.

4 Application

In this section, we present a numerical application which validates the methodology presented in this paper.

4.1 Description of the Nominal Model

The rigid multibody model is made up of five rigid bodies and six joints which are described in the fixed frame $(O, x_{0,1}, x_{0,2}, x_{0,3})$ (see Fig. 1.2). The plan defined by $(O, x_{0,1}, x_{0,2})$ is identified below as the "ground". The gravity forces in the $x_{0,3}$-direction are taken into account.

(i) *Rigid bodies.*
In the initial configuration, the rigid bodies $Rb1$, $Rb2$, $Rb3$ and $Rb4$ are cylinders for which the axes follow the $x_{0,3}$-direction. In the initial configuration, the rigid body $Rb5$ is supposed to be symmetric with respect to the planes $(G5, x_{0,1}, x_{0,2})$ and $(G5, x_{0,1}, x_{0,3})$ in which $G5$ is the center of mass of $Rb5$.

(ii) *Joints.*

– The joint *Ground-Rb*1 is made up of a prismatic joint following $x_{0,3}$-direction. The displacement following $x_{0,3}$-direction (see Fig. 1.2), denoted

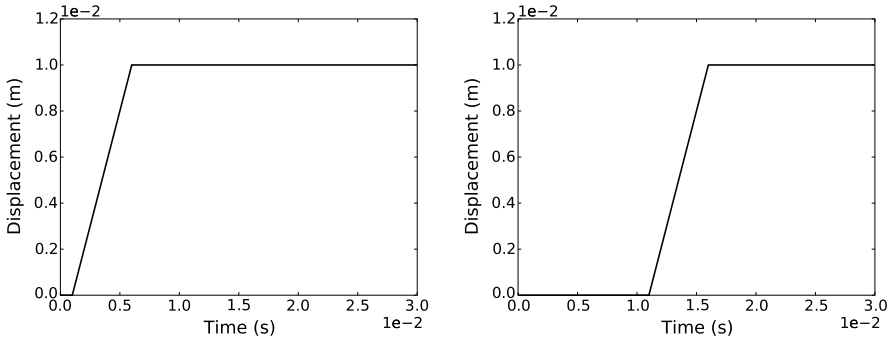

Fig. 1.3 Imposed displacement $u1(t)$ (*left figure*) and $u2(t)$ (*right figure*)

by $u1(t)$, is imposed. The joint *Ground*-$Rb2$ is a prismatic joint following $x_{0,3}$-direction. The displacement following $x_{0,3}$-direction (see Fig. 1.2), denoted by $u2(t)$, is imposed. The displacement following $x_{0,1}$-direction is unconstrained. Imposed displacements $u1(t)$ and $u2(t)$ are plotted in Fig. 1.3 for t in $[0, 0.03]$ s.

– The joints $Rb1$-$Rb3$ and $Rb2$-$Rb4$ are constituted of 6D spring-dampers.
– Finally, the joints $Rb3$-$Rb5$ and $Rb4$-$Rb5$ are $x_{0,2}$-direction revolute joints.

4.2 Random Response of the Stochastic Model

Rigid body $Rb5a$ is considered as uncertain and is therefore modeled by a random rigid body. As explained in Sect. 3, the elements of inertia of the uncertain rigid Body $Rb5$ are replaced by random quantities. The fluctuation of the response is controlled by four parameters δ_{M_5}, $\mathbf{h}$, λ_l and λ_u. A sensitivity analysis is carried out with respect to these four parameters. Statistics on the transient response are estimated using the Monte Carlo simulation method with 500 independent realizations. The initial velocities and angular velocities are zero. The observation point P_{obs} belongs to $Rb5$. Four different cases are analyzed:

1. *Case 1*: M_5 is random, $\mathbf{R}_{0,5}$ is deterministic and $[\mathbf{Z}_5]$ is deterministic.
   We choose $\delta_{M_5} = 0.5$. The confidence region, with a probability level $P_c = 0.90$, of the random acceleration of point P_{obs} is plotted in Fig. 1.4. It can be noted that the acceleration is sensitive to the mass uncertainties.
2. *Case 2*: M_i is deterministic, $\mathbf{R}_{0,5}$ is random and $[\mathbf{Z}_5]$ is deterministic.
   The domain of $\mathbf{R}_{0,5}$ is supposed to be a parallelepiped which is centered at point $(0, 0, 0.55)$ for which its edges are parallel to the directions $x_{0,1}$, $x_{0,2}$ and $x_{0,3}$ and for which the lengths following these three directions are respectively 0.5, 0.2 and 0.02. The confidence region, with a probability level $P_c = 0.90$, of the random acceleration of point P_{obs} is plotted in Fig. 1.5. We can remark that the angular acceleration is sensitive to uncertainties on initial center of mass of $Rb5$.

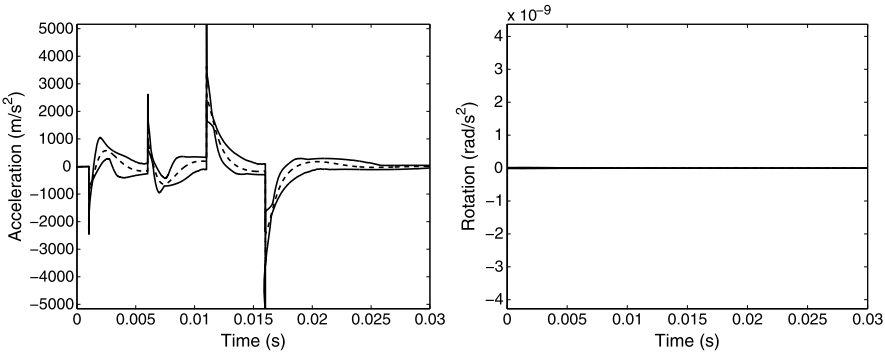

Fig. 1.4 Random transient acceleration of point P_{obs}, Case 1: confidence region (*upper* and *lower solid lines*) and mean response (*dashed line*); $x_{0,3}$-acceleration (*left figure*) and $x_{0,1}$-angular acceleration (*right figure*)

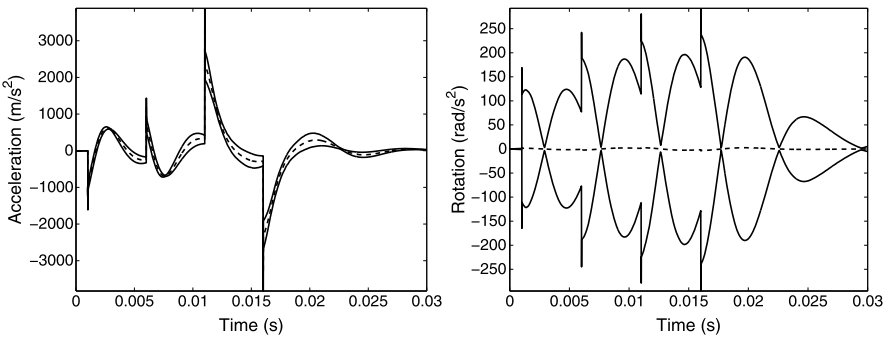

Fig. 1.5 Random transient acceleration of point P_{obs}, Case 2: confidence region (*upper* and *lower solid lines*) and mean response (*dashed line*); $x_{0,3}$-acceleration (*left figure*) and $x_{0,1}$-angular acceleration (*right figure*)

3. *Case 3*: M_5 is deterministic, $\mathbf{R}_{0,5}$ is deterministic and $[\mathbf{Z}_5]$ is random.
   We choose $\lambda_l = -5$ and $\lambda_u = -5$ for random matrix $[\mathbf{Z}_5]$. The confidence region, with a probability level $P_c = 0.90$, of the random acceleration of point P_{obs} is plotted in Fig. 1.6. We can remark, as it was expected, that the angular acceleration is very sensitive to uncertainties on the tensor of inertia. We can also remark a high sensitivity of the acceleration.
4. *Case 4*: M_5, $\mathbf{R}_{0,5}$ and $[\mathbf{Z}_5]$ are random.
   The values of the parameters of the PDF are those fixed in the three previous cases. The confidence region, with a probability level $P_c = 0.90$, of the random acceleration of point P_{obs} is plotted in Fig. 1.7. It can be viewed that (1) the randomness on the acceleration is mainly due to the randomness of mass M_5, (2) the randomness on the angular acceleration is mainly due to the randomness of the initial position $\mathbf{R}_{0,5}$ of the center of mass and the random tensor $[\mathbf{Z}_5]$.

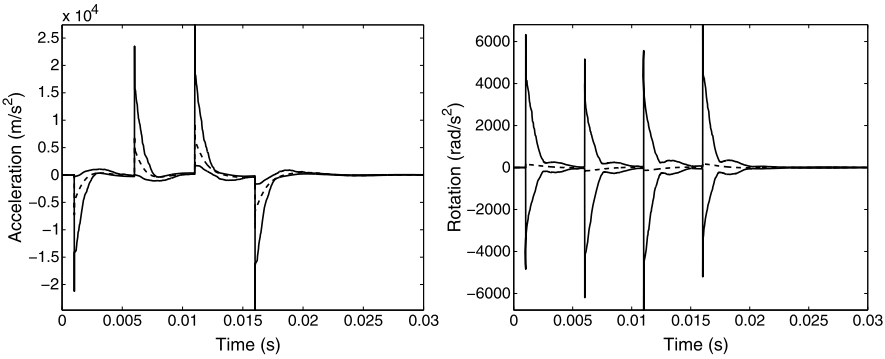

Fig. 1.6 Random transient acceleration of point P_{obs}, Case 3: confidence region (*upper* and *lower solid lines*) and mean response (*dashed line*); $x_{0,3}$-acceleration (*left figure*) and $x_{0,1}$-angular acceleration (*right figure*)

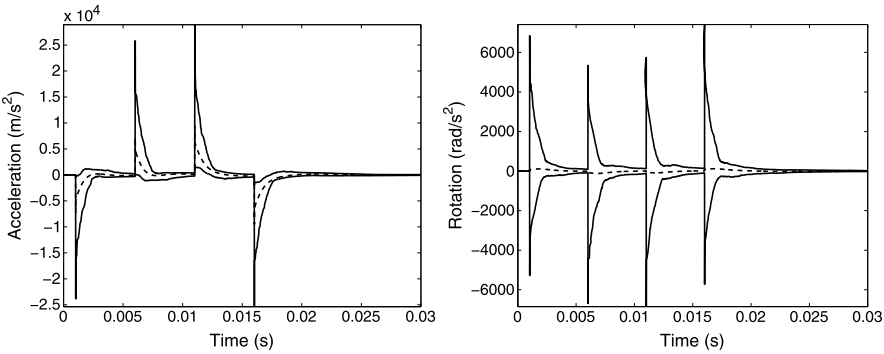

Fig. 1.7 Random transient acceleration of point P_{obs}, Case 4: confidence region (*upper* and *lower solid lines*) and mean response (*dashed line*); $x_{0,3}$-acceleration (*left figure*) and $x_{0,1}$-angular acceleration (*right figure*)

5 Conclusion

We have presented a complete and general probabilistic modeling of uncertain rigid bodies taking into account all the known mechanical and mathematical properties defining a rigid body. This probabilistic model of uncertainties is used to construct the stochastic equations of uncertain multibody dynamical systems. The random dynamical responses can then be calculated. In the proposed probabilistic model, the mass, the center of mass and the tensor of inertia are modeled by random variables for which the prior probability density functions are constructed using the maximum entropy principle under the constraints defined by all the available mathematical, mechanical and design properties. Several uncertain rigid bodies can be linked each to the others in order to obtain the stochastic dynamical model of the uncertain multibody dynamical system. The theory proposed has been illustrated analyzing a simple example. The results obtained clearly show the role played by uncertainties

and the sensitivity of the responses due to uncertainties on (1) the mass (2) the center of mass and (3) the tensor of inertia. Such a prior stochastic model allows the robustness of the responses to be analyzed with respect to uncertainties. If experimental data were available on the responses, then the parameters which control the level of uncertainties could be estimated by solving an inverse stochastic problem.

References

1. Batou, A., Soize, C.: Rigid multibody system dynamics with uncertain rigid bodies. Multibody Syst. Dyn. **27**, 285–319 (2012)
2. Baumgarte, J.: Stabilization of constraints and integrals of motion in dynamical systems. Comput. Methods Appl. Mech. Eng. **1**(1), 1–16 (1972)
3. Carrarini, A.: Reliability based analysis of the crosswind stability of railway vehicles. J. Wind Eng. Ind. Aerodyn. **95**, 493–509 (2007)
4. Das, S., Ghanem, R.: A bounded random matrix approach for stochastic upscaling. Multiscale Model. Simul. **8**(1), 296–325 (2009)
5. Hastings, W.K.: Monte Carlo sampling methods using Markov chains and their applications. Biometrika **109**, 57–97 (1970)
6. Jaynes, E.T.: Information theory and statistical mechanics. Phys. Rev. **106**(4), 620–630 (1957)
7. Jaynes, E.T.: Information theory and statistical mechanics. II. Phys. Rev. **108**(2), 171–190 (1957)
8. Li, L., Corina Sandu, C.: On the impact of cargo weight, vehicle parameters, and terrain characteristics on the prediction of traction for off-road vehicles. J. Terramech. **44**, 221–238 (2007)
9. Murthy, R., Mignolet, M.P., El-Shafei, A.: Nonparametric stochastic modeling of uncertainty in rotordynamics—part I: formulation. J. Eng. Gas Turbines Power **132**(9), 092501 (2010)
10. Murthy, R., Mignolet, M.P., El-Shafei, A.: Nonparametric stochastic modeling of uncertainty in rotordynamics—part II: applications. J. Eng. Gas Turbines Power **132**(9), 092502 (2010)
11. Nagar, D.K., Gupta, A.K.: Matrix-variate Kummer-Beta distribution. J. Aust. Math. Soc. A **73**, 11–25 (2002)
12. Negrut, D., Datar, M., Gorsich, D., Lamb, D.: A framework for uncertainty quantification in nonlinear multi-body system dynamics. In: Proceedings of the 26th Army Science Conference, Orlando, FL (2008)
13. Sandu, A., Sandu, C., Ahmadian, M.: Modeling multibody dynamic systems with uncertainties. Part I: theoretical and computational aspects. Multibody Syst. Dyn. **23**, 375–395 (2006)
14. Schiehlen, W.: Multibody Systems Handbook. Springer, Berlin (1990)
15. Schiehlen, W.: Multibody system dynamics: roots and perspectives. Multibody Syst. Dyn. **1**, 149–188 (1997)
16. Schmitt, K.P., Anitescu, M., Negrut, D.: Efficient sampling for spatial uncertainty quantification in multibody system dynamics applications. Int. J. Numer. Methods Eng. **80**, 537–564 (2009)
17. Shannon, C.E.: A mathematical theory of communication. Bell Syst. Tech. J. **27**, 379–423 (1948)
18. Shannon, C.E.: A mathematical theory of communication. Bell Syst. Tech. J. **27**, 623–656 (1948)
19. Soize, C.: A nonparametric model of random uncertainties on reduced matrix model in structural dynamics. Probab. Eng. Mech. **15**(3), 277–294 (2000)
20. Soize, C.: Maximum entropy approach for modeling random uncertainties in transient elastodynamics. J. Acoust. Soc. Am. **109**(5), 1979–1996 (2001)

Chapter 2
Dynamic Variability Response for Stochastic Systems

Vissarion Papadopoulos and Odysseas Kokkinos

Abstract In this study we implement the concept of Variability Response Functions (VRFs) in dynamic systems. The variance of the system response can be readily estimated by an integral involving the Dynamic VRF (DVRF) and the uncertain system parameter power spectrum. With the proposed methodology spectral and probability distribution-free upper bounds can be easily derived. Also an insight is provided with respect to the mechanisms controlling the system's response. The necessarily asserted conjecture of independence of the DVRF to the spectral density and the marginal probability density is validated numerically through brute-force Monte Carlo simulations.

Keywords Dynamic Variability Response Functions · Stochastic finite element analysis · Upper bounds · Stochastic dynamic systems

1 Introduction

Over the past two decades a lot of research has been dedicated to the stochastic analysis of structural systems involving uncertain parameters in terms of material or geometry with the implementation of stochastic finite element methodologies. Although these methods have proven to be highly accurate and computationally efficient for a variety of problems, there is still a wide range of problems in stochastic mechanics involving combinations of strong non-linearities and/or large variations of system properties as well as non-Gaussian system properties that can be solved with reasonable accuracy only through a computationally expensive Monte Carlo simulation approach [3–5, 12].

In all aforementioned cases, the spectral/correlation characteristics and the marginal probability distribution function (pdf) of the stochastic fields describing

V. Papadopoulos (✉) · O. Kokkinos
Institute of Structural Analysis and Antiseismic Research, National Technical University of Athens, 9 Iroon Polytechneiou, Zografou Campus, Athens 15780, Greece
e-mail: vpapado@central.ntua.gr

O. Kokkinos
e-mail: okokki@central.ntua.gr

M. Papadrakakis et al. (eds.), *Computational Methods in Stochastic Dynamics*, Computational Methods in Applied Sciences 26,
DOI 10.1007/978-94-007-5134-7_2,

the uncertain system parameters are required in order to estimate the response variability of a stochastic static or dynamic system. As there is usually a lack of experimental data for the quantification of such probabilistic quantities, a sensitivity analysis with respect to various stochastic parameters is often implemented. In this case, however, the problems that arise are the increased computational effort, the lack of insight on how these parameters control the response variability of the system and the inability to determine bounds of the response variability.

In this framework and to tackle the aforementioned issues, the concept of the variability response function (*VRF*) has been proposed in the late 1980s [10], along with different aspects and applications of the *VRF* [1, 13]. A development of this approach was presented in a series of papers [7–9], where the existence of closed-form integral expressions for the variance of the response displacement of the form

$$\mathrm{Var}[u] = \int_{-\infty}^{\infty} VRF(\kappa, \sigma_{ff}) S_{ff}(\kappa)\, d\kappa \tag{2.1}$$

was demonstrated for linear stochastic systems under static loads using a flexibility-based formulation. It was shown that the *VRF* depends on standard deviation σ_{ff} but appears to be independent of the functional form of the spectral density function $S_{ff}(\kappa)$ modeling the inverse of the elastic modulus. The existence however of this integral expression had to be conjectured for statically indeterminate as well as for general stochastic finite element systems. A rigorous proof of such existence is available only for statically determinate systems for which *VRF* is independent of σ_{ff} as well [8]. Further investigations [6] verified the aforementioned results but showed that *VRF* has a slight dependence on the marginal pdf of the stochastic field modeling the flexibility.

The present paper extends the aforementioned approach to linear statically determinate stochastic systems under dynamic excitations. Although the derivation of an analytic expression for the variability response function of the dynamic system (*DVRF*), if possible at all, is extremely cumbersome, a numerical computation of the *DVRF* can be easily achieved to provide results for the variance time history of the dynamic system response. As in previous works [7–9], the existence of the *DVRF* and a similar to Eq. (2.1) integral form expression has to be conjectured. This assumption is numerically validated by comparing the results from Eq. (2.1) with brute force Monte Carlo simulations. It is demonstrated that the *DVRF* is highly dependent on the standard deviation σ_{ff} of the inverse of the elastic modulus and, based on numerical evidence further presented but, to this point, not to a full proof verification technique, appears to be almost independent of the functional form of $S_{ff}(\kappa)$ as well as of the marginal *pdf* of the flexibility. In addition, an integral expression similar to that of Eq. (2.1) is proposed for the mean system response involving a Dynamic Mean Response Function (*DMRF*), which is a function similar to the *DVRF*.

Both integral forms for the mean and variance can be used to efficiently compute the first and second order statistics of the transient system response with reasonable accuracy, together with time dependant spectral-distribution-free upper bounds.

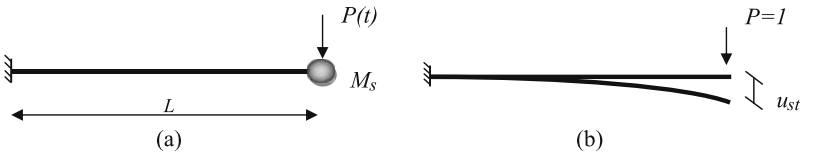

Fig. 2.1 One degree of freedom oscillator: (**a**) Geometry and loading (**b**) Static displacement for unit load

They also provide an insight into the mechanisms controlling the uncertainty propagation with respect to both space and time and in particular the mean and variability time histories of the stochastic system dynamic response.

2 Dynamic Analysis of a Stochastic Single Degree of Freedom Oscillator

For the single degree of freedom statically determinate stochastic oscillator of length L and mass M_s in Fig. 2.1(a), loaded with a dynamic deterministic load $P(t)$, the inverse of the elastic modulus is considered to vary randomly along the length of the beam according to the following expression:

$$\frac{1}{E(x)} = F_0\big(1 + f(x)\big) \tag{2.2}$$

is the elastic modulus, F_0 is the mean value of the inverse of $E(x)$, and $f(x)$ is a zero-mean homogeneous stochastic field modeling the variation of $1/E(x)$ around its mean value F_0.

The displacement time history $u(t)$ of the oscillator can be derived from the solution of Duhamel's integral:

$$u(t) = \frac{1}{\omega_D}\int_0^t P(\tau)e^{-\xi\omega(t-\tau)}\sin\big(\omega_D(t-\tau)\big)\,d\tau \tag{2.3}$$

where ξ is the damping ratio and $\omega_D = \omega\sqrt{1-\xi^2}$ with ω being the circular frequency of the system. Due to the system uncertainty in Eq. (2.2), the circular frequency ω is a random variable given by the following relation:

$$\omega = \sqrt{k/M_s} \tag{2.4}$$

where k is the stiffness of the oscillator which can be derived from the static displacement of the oscillator for a unit static deterministic load at the end of the beam (Fig. 2.1(b)) as follows:

$$k = \frac{1}{u_{st}} = \left[-\frac{F_0}{I}\int_0^L (x-\alpha)M(\alpha)\big(1+f(\alpha)\big)\,d\alpha\right]^{-1} \tag{2.5}$$

where I is the moment of inertia of the beam and $M(\alpha)$ is the moment at position α.

In the general case where the load is arbitrary and the system is initially at rest, the deterministic displacement at the right end of the beam can be derived by numerically solving the Duhamel's integral. In the special case of a sinusoidal $P(t) = P_0 \sin(\bar{\omega} t)$ the solution of Eq. (2.3) leads to the following expression for $u(t)$:

$$u(t) = u_0(t) + u_p(t) \tag{2.6}$$

where

$$u_0(t) = e^{-\xi \omega t}(A \sin \omega_D t + B \cos \omega_D t) \tag{2.7a}$$

$$u_p(t) = C_1 \sin \bar{\omega} t + C_2 \cos \bar{\omega} t \tag{2.7b}$$

$$A = \frac{P_0}{K} * \frac{1}{(1-\beta^2)^2 + (2\xi\beta)^2} * \frac{2\beta\xi^2 - (1-\beta^2)\beta}{\sqrt{1-\xi^2}} \tag{2.7c}$$

$$\mathrm{B} = -\frac{P_0}{K} * \frac{2\xi\beta}{(1-\beta^2)^2 + (2\xi\beta)^2} \tag{2.7d}$$

$$C_1 = \frac{P_0}{K} * \frac{1}{(1-\beta^2)^2 + (2\xi\beta)^2}\left(1-\beta^2\right) \tag{2.7e}$$

$$C_2 = -\frac{P_0}{K} * \frac{1}{(1-\beta^2)^2 + (2\xi\beta)^2}(2\xi\beta) \tag{2.7f}$$

$$\beta = \bar{\omega}/\omega \tag{2.7g}$$

In the trivial case in which a static load $P(t) = P_0$ is suddenly applied, the response displacement is given by

$$u(t) = \frac{P_0}{k}\left[1 - \left(\cos \omega_D t + \frac{\xi}{\sqrt{1-\xi^2}} \sin \omega_D t\right) e^{-\xi \omega t}\right] \tag{2.7h}$$

3 Response Variance and Mean Value of the Dynamic Response

Following a procedure similar to the one presented in [8] for linear stochastic systems under static loading, it is possible to express the variance of the dynamic response of the stochastic system in the following integral form expression:

$$\mathrm{Var}\big[u(t)\big] = \int_{-\infty}^{\infty} DVRF(t, \kappa, \sigma_{ff}) S_{ff}(\kappa)\, d\kappa \tag{2.8a}$$

where *DVRF* is the dynamic version of a *VRF*, assumed to be a function of deterministic parameters of the problem related to geometry, loads and (mean) material properties and the standard deviation σ_{ff} of the stochastic field that models the system flexibility. A similar integral expression can provide an estimate for the mean value of the dynamic response of the system using the Dynamic Mean Response Function (*DMRF*) [9]:

$$\varepsilon\big[u(t)\big] = \int_{-\infty}^{\infty} DMRF(t, \kappa, \sigma_{ff}) S_{ff}(\kappa)\, d\kappa \tag{2.8b}$$

DMRF is assumed to be a function similar to the *DVRF* in the sense that it also depends on deterministic parameters of the problem as well as σ_{ff}. It is extremely difficult however, to prove that the *DVRF* (same counts for *DMRF*) is independent (or even approximately independent) of the marginal pdf and the functional form of the power spectral density of the stochastic field $f(x)$. As in [7–9], the aforementioned assumptions are considered to form a conjecture which is numerically validated here by comparing the results from Eqs. (2.8a) and (2.8b) with brute force MCS.

The derivation of an analytic expression for the *DVRF* and *DMRF*, if possible at all, is an extremely cumbersome task. A numerical computation, however can be easily achieved, as described in the following section and then fed into the Eqs. (2.8a) and (2.8b) to provide estimates of the mean and variance of the dynamic system response.

3.1 Numerical Estimation of the DVRF and the DMRF Using Fast Monte Carlo Simulation

The numerical estimation of DVRF and DMRF involves a fast Monte Carlo simulation (FMCS) whose basic idea is to consider the random field $f(x)$ as a random sinusoid [7, 8] and plug its monochromatic power spectrum into Eqs. (2.8a) and (2.8b), in order to compute the respective mean and variance response at various wave numbers. The steps of the FMCS approach are the following:

(i) Generate N (10–20) sample functions of the below random sinusoid with standard deviation σ_{ff} and wave number $\bar{\kappa}$ modeling the variation of the inverse of the elastic modulus $1/E$ around its mean F_0:

$$f_j(x) = \sqrt{2}\sigma_{ff}\cos(\bar{\kappa}x + \varphi_j) \tag{2.9}$$

where $j = 1, 2, \ldots, N$ and φ_j varies randomly under uniform distribution in the range $[0, 2\pi]$.

(ii) Using these N generated sample functions it is straightforward to compute their respective dynamic mean and response variance, $\varepsilon[u(t)]_{\bar{\kappa}}$ and $\mathrm{Var}[u(t)]_{\bar{\kappa}}$, respectively for a given time step t.

(iii) The value of the *DMRF* at wave number $\bar{\kappa}$ can then be computed as follows

$$DMRF(t, \bar{\kappa}, \sigma_{ff}) = \frac{\varepsilon[u(t)]_{\bar{\kappa}}}{\sigma_{ff}^2} \tag{2.10a}$$

and likewise the value of the *DVRF* at wave number $\bar{\kappa}$

$$DVRF(t, \bar{\kappa}, \sigma_{ff}) = \frac{\mathrm{Var}[u(t)]_{\bar{\kappa}}}{\sigma_{ff}^2} \tag{2.10b}$$

Both previous equations are direct consequences of the integral expressions in Eqs. (2.8a) and (2.8b) in the case that the stochastic field becomes a random sinusoid.

(iv) Get *DMRF* and *DVRF* as a function of both time t and wave number κ by repeating previous steps for various wave numbers and different time steps. The entire procedure can be repeated for different values of the standard deviation σ_{ff} of the random sinusoid.

3.2 Bounds of the Mean and Variance of the Dynamic Response

Upper bounds on the mean and variance of the dynamic response of the stochastic system can be established directly from Eqs. (2.8a) and (2.8b), as follows:

$$\begin{aligned}\varepsilon\big[u(t)\big] &= \int_{-\infty}^{\infty} DMRF(t,\kappa,\sigma_{ff})S_{ff}(\kappa)\,d\kappa \\ &\le DMRF\big(t,\kappa^{\max}(t),\sigma_{ff}\big)\sigma_{ff}^2 \qquad (2.11a)\\ \mathrm{Var}\big[u(t)\big] &= \int_{-\infty}^{\infty} DVRF(t,\kappa,\sigma_{ff})S_{ff}(\kappa)\,d\kappa \\ &\le DVRF\big(t,\kappa^{\max}(t),\sigma_{ff}\big)\sigma_{ff}^2 \qquad (2.11b)\end{aligned}$$

where $\kappa^{\max}(t)$ is the wave number at which *DMRF* and *DVRF*, corresponding to a given time step t and value of σ_{ff}, reach their maximum value. An envelope of time evolving upper bounds on the mean and variance of the dynamic system response can be extracted from Eqs. (2.11a) and (2.11b). As in the case of linear stochastic systems under static loads [7–9], this envelope is physically realizable since the form of the stochastic field that produces it is the random sinusoid of Eq. (2.9) with $\bar{\kappa} = \kappa^{\max}(t)$.

4 Numerical Example

For the cantilever beam shown in Fig. 2.1 with length $L = 4$ m, the inverse of the modulus of elasticity is assumed to vary randomly along its length according to Eq. (2.2) with $F_0 = (1.25 \times 10^8\ \mathrm{kN/m})^{-1}$ and $I = 0.1\ \mathrm{m}^4$. A concentrated mass $M_s = 3.715 \times 10^3$ kg is assumed at the right end of the beam. The damping ratio is taken as $\xi = 5\%$ and the mean eigenperiod of this one d.o.f. oscillator is calculated at $T_0 = 0.5$ s.

Two load cases are considered: LC1 consisting of a concentrated dynamic periodic load $P(t) = 100\sin(\bar{\omega}t)$ and LC2 consisting of $P(t) = -M_s\ddot{U}_g(t)$ where $\ddot{U}_g(t)$ is the acceleration time history of the 1940 El Centro earthquake.

The spectral density function (*SDF*) of Fig. 2.2 was used for the modeling of the inverse of the elastic modulus stochastic field, given by:

$$S_{ff}(\kappa) = \frac{1}{4}\sigma^2 b^3 \kappa^2 e^{-b|\kappa|} \qquad (2.12)$$

with $b = 10$ being a correlation length parameter.

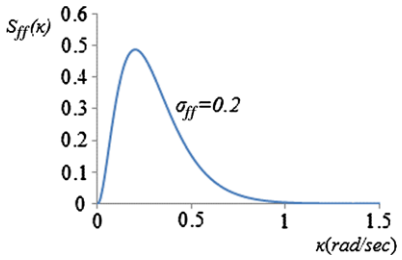

Fig. 2.2 Spectral density function for stochastic field $f(x)$ standard deviation $\sigma_{ff} = 0.2$

In order to demonstrate the validity of the proposed methodology, a truncated Gaussian and a lognormal pdf were used to model $f(x)$. For this purpose, an underlying Gaussian stochastic field denoted by $g(x)$ is generated using the spectral representation method [11] and the power spectrum of Eq. (2.12). The truncated Gaussian field $f_{\mathrm{TG}}(x)$ is obtained by simply truncating $g(x)$ in the following way: $-0.9 \leq g(x) \leq 0.9$, while the lognormal $f_{\mathrm{L}}(x)$ is obtained from the following transformation as a translation field [2]:

$$f_{\mathrm{L}}(x) = F_{\mathrm{L}}^{-1}\{G[g(x)]\} \tag{2.13}$$

The *SDF* of the underlying Gaussian field in Eq. (2.12) and the corresponding spectral densities of the truncated Gaussian and the Lognormal fields denoted $S_{f_{\mathrm{TG}} f_{\mathrm{TG}}}(\kappa)$ and $S_{f_{\mathrm{L}} f_{\mathrm{L}}}(\kappa)$, respectively, will be different. These are computed from the following formula

$$S_{f_i f_i}(\kappa) = \frac{1}{2\pi L_x}\left|\int_0^{L_x} f_i(x) e^{-i\kappa x}\, dx\right|^2; \quad i = \mathrm{TG}, \mathrm{L} \tag{2.14}$$

where L_x is the length of the sample functions of the non-Gaussian fields modeling flexibility. As the sample functions of the non-Gaussian fields are non-ergodic, the estimation of power spectra in Eq. (2.14) is performed in an ensemble average sense [2].

LC1: Dynamic Periodic Load at the End of the Beam Figures 2.3 and 2.4 present *DMRF* and *DVRF*, respectively, computed with FMCS for a periodic load with frequency $\bar{\omega} = 2$ and three different values of the standard deviation $\sigma_{ff} = 0.2$, $\sigma_{ff} = 0.4$ and $\sigma_{ff} = 0.6$. From these figures it can be observed that *DVRF* do not follow any particular pattern with respect to any increase or decrease of σ_{ff} in contrast to *DMRF* and to what has been observed in Papadopoulos and Deodatis [7] for the corresponding static problem, albeit the mean and variability response increases as σ_{ff} increases, as shown in Fig. 2.4. Figures 2.5(a) and (b) present plots of *DMRF* and *DVRF* as a function of t for a fixed wave number $\kappa = 2$ and $\sigma_{ff} = 0.2$. From the above Figs. 2.3, 2.4 and 2.5 it appears that *DMRF* and *DVRF* have a significant variation along the wave number κ axis and the time axis t. Both functions and especially *DVRF* have an initial transient phase and then appear to be periodic. It is reminded here that *DVRF* and *DMRF* are functions of the imposed dynamic loading. This explains the fact that they do not approach zero with t increasing, since the applied dynamic load is periodic with constant amplitude which does not decay.

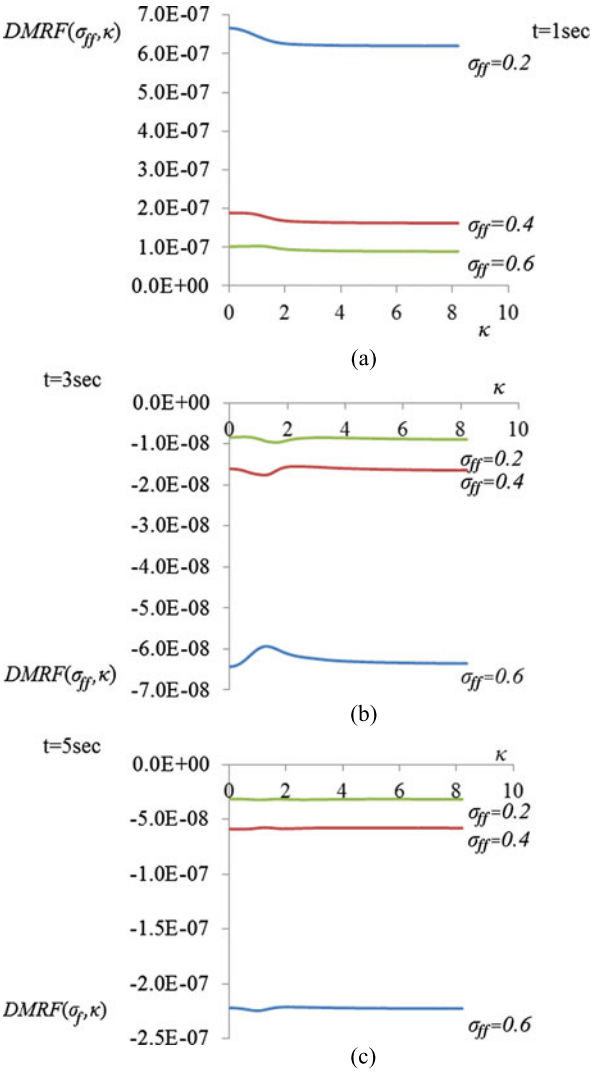

Fig. 2.3 *DMRF* as a function of σ_{ff} for (**a**) $t = 1$ s, (**b**) $t = 3$ s and (**c**) $t = 5$ s

Figures 2.6(a) and (b) present comparatively the results of the computed response variance time histories using the integral expression of Eq. (2.8a) and MCS, for two different standard deviations of a truncated Gaussian stochastic field used for the modeling of flexibility. The underlying Gaussian field is modeled with the power spectral density of Eq. (2.12) and two different standard deviations $\sigma_{gg} = 0.4$ and $\sigma_{gg} = 0.6$. The corresponding standard deviations of the truncated Gaussian field $f(x)$ are computed as $\sigma_{ff} = 0.3912$ and $\sigma_{ff} = 0.5286$, respectively. Figures 2.7(a) and (b) present the same results with Fig. 2.8 but for the mean response of the oscillator. The deterministic displacement time history is also plotted in Fig. 2.7(c) for comparison purposes. From these figures it can be observed that the mean and

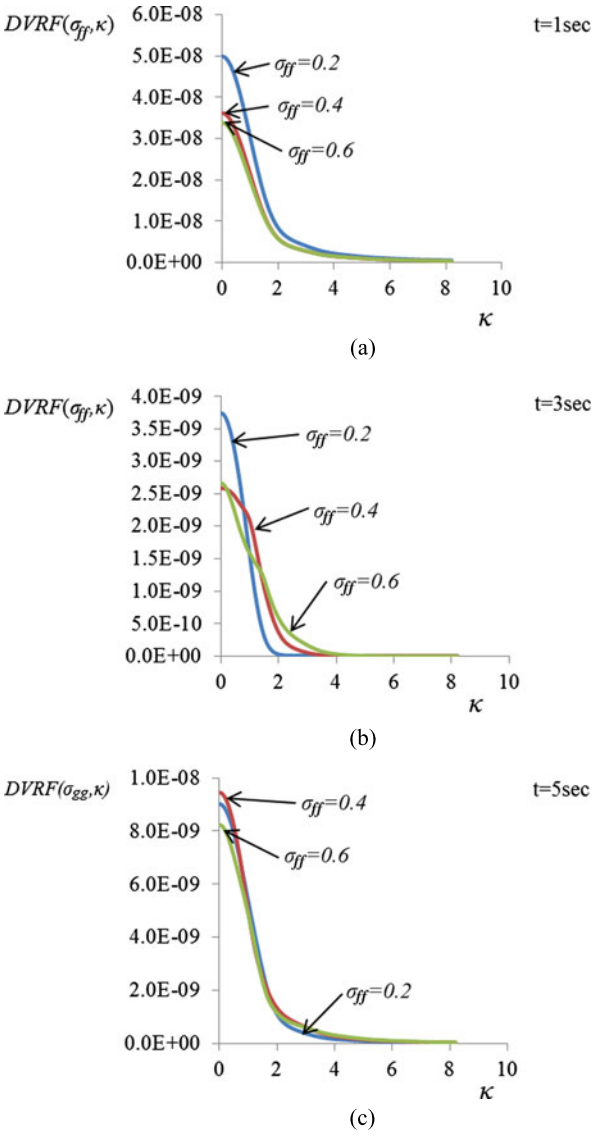

Fig. 2.4 *DVRF* as a function of the σ_{ff} for (**a**) $t = 1$ s, (**b**) $t = 3$ s and (**c**) $t = 5$ s

variability response time histories obtained with the integral expressions of Eqs. (2.8a) and (2.8b) are in close agreement with the corresponding MCS estimates. In all cases examined the maximum error in the computed Var$[u(t)]$, observed at the peak values of the variance, is less than 25%, while in all other time steps this error is less than 3–4%. In the case of $\varepsilon[u(t)]$, the predictions of Eq. (2.8b) are almost identical to the ones obtained with MCS, with an error of less than 3% in all cases. From Figs. 2.7(a)–(c), it can be observed that in all cases, the mean response time

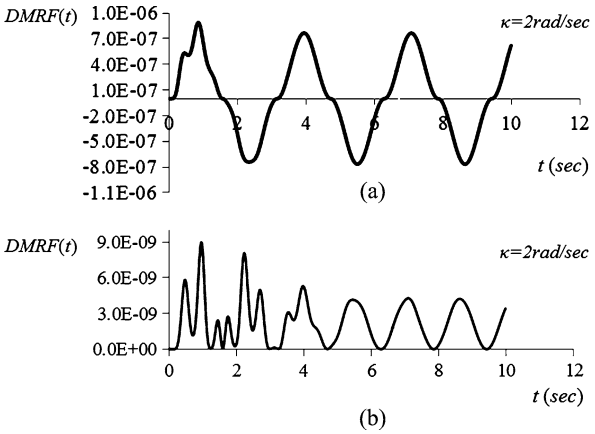

Fig. 2.5 *DMRF* (**a**) and *DVRF* (**b**) as a function of t for $\kappa = 2$ rad/s and $\sigma_{ff} = 0.2$

history for all cases examined is almost identical to the deterministic one, with the exception of the first cycle where slight differences in the peak values are observed.

Figures 2.8(a) and (b) repeat the same comparisons with the previous Figs. 2.6 and 2.7 but for the case of a lognormal stochastic field used for the modeling of flexibility with $\sigma_{ff} = 0.2$ and lower bound $l_b = -0.8$. The conclusions extracted previously for the case of truncated Gaussian fields also apply here.

LC2: El Centro Earthquake Figures 2.9(a) and (b) present 3D plots of the *DMRF* and *DVRF* as a function of frequency κ and time t (s) for $\sigma_{ff} = 0.2$. From these figures it can be observed that *DMRF* and *DVRF* have a significant variation in both κ and t axis, without being periodic in contrast to what has been observed in LC1. In addition, both *DMRF* and *DVRF* approach a zero value with time increasing due to the fact that ground accelerations decay and vanish after some time.

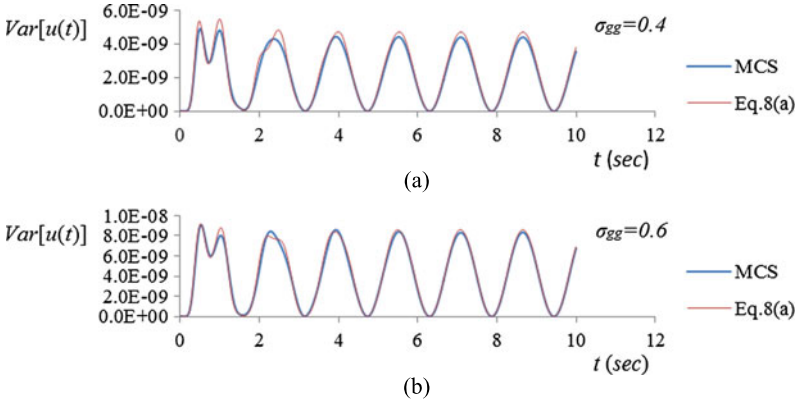

Fig. 2.6 Time histories of the variance of the response displacement for a truncated Gaussian field with (**a**) $\sigma_{gg} = 0.4$, and (**b**) $\sigma_{gg} = 0.6$. Comparison of results obtained from Eq. (2.11a) and MCS

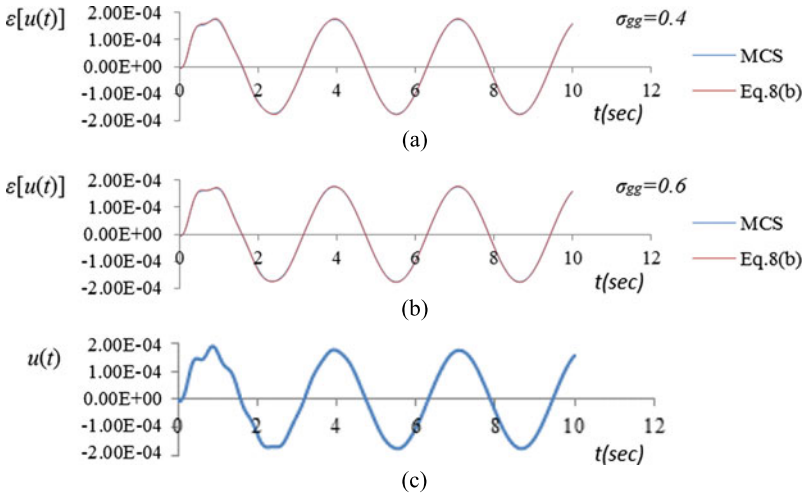

Fig. 2.7 Time histories of: (**a**) mean response displacement for a truncated Gaussian field with $\sigma_{gg} = 0.4$, (**b**) $\sigma_{gg} = 0.6$ and (**c**) the deterministic displacement. Comparison of results obtained from Eq. (2.11b) and MCS

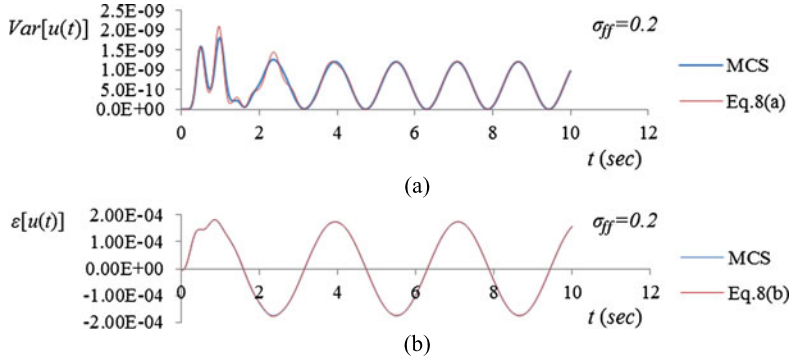

Fig. 2.8 Comparative results from Eqs. (2.11a) and (2.11b) and MCS for a lognormal field with $\sigma_{ff} = 0.2$ for (**a**) the variance and (**b**) the mean of the response displacement time history

Figures 2.10(a) and (b) present a comparison of the response variance computed with Eq. (2.8a) and MCS, in the case of a truncated Gaussian stochastic field modeling flexibility with $\sigma_{gg} = 0.4$ and 0.6, while Figs. 2.11(a) and (b) present the same results for the mean dynamic response of the stochastic oscillator along with the corresponding deterministic displacement time history (Fig. 2.11(c)). Figures 2.12(a) and (b) repeat the same comparisons for the case of a lognormal stochastic field used for the modeling of flexibility and $\sigma_{ff} = 0.3$ and lower bound $l_b = -0.8$.

From the above figures it can be observed that, as in LC2, the mean and variability response time histories obtained with the integral expressions of Eqs. (2.8a)

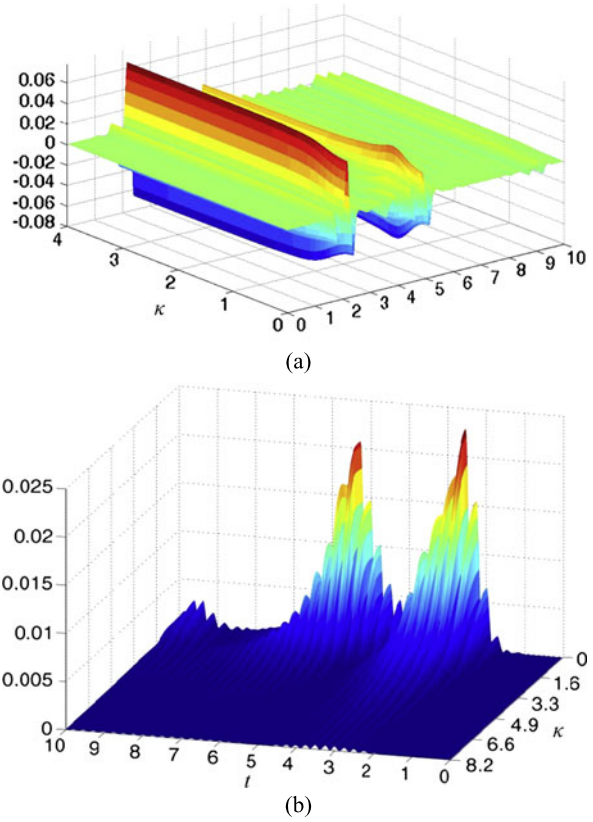

Fig. 2.9 3D plots of (**a**) *DMRF* and (**b**) *DVRF*, as a function of frequency κ (rad/m) and time t (s) for LC2 and $\sigma_{ff} = 0.2$

and (2.8b) are in close agreement with the corresponding MCS estimates, in all cases. Again, the maximum error in the computed Var$[u(t)]$ was observed at the peak values of the variance and is less than 25%, while in all other time steps this error is less than 3–4%. In the case of $\varepsilon[u(t)]$, the predictions of Eq. (2.8b) are very close to the ones obtained with MCS, with a error of less than 3% in all cases. From Figs. 2.9(a)–(c), it can be observed that, in contrast to what was observed in LC2, the mean response time history differs significantly from the corresponding deterministic one, in terms of both frequencies and amplitudes.

Upper Bounds on the Mean and Variance of the Response of LC3 Spectral-distribution-free upper bounds on both the mean and variance of the response are obtained via Eqs. (2.11a) and (2.11b), respectively. Results of this calculation are presented in Figs. 2.13(a) and (b), in which the time dependant upper bounds on the mean and variance of the response displacement are plotted against time for a standard deviation $\sigma_{ff} = 0.4$.

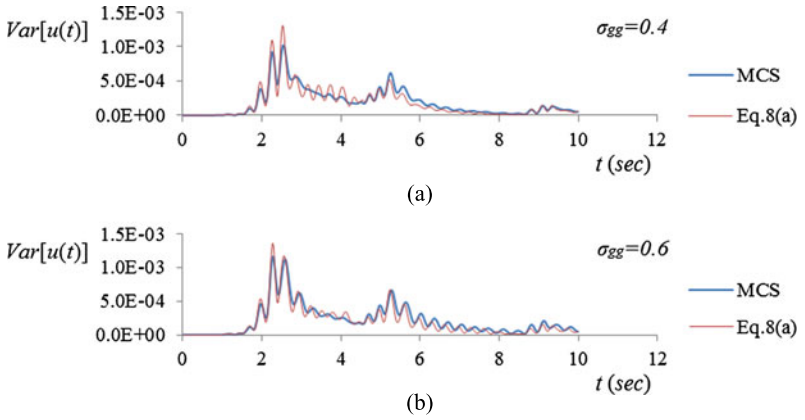

Fig. 2.10 Time histories of the variance of the response displacement for a truncated Gaussian field for (**a**) $\sigma_{gg} = 0.4$ and (**b**) $\sigma_{gg} = 0.6$. Comparison of results obtained from Eq. (2.8a) and MCS

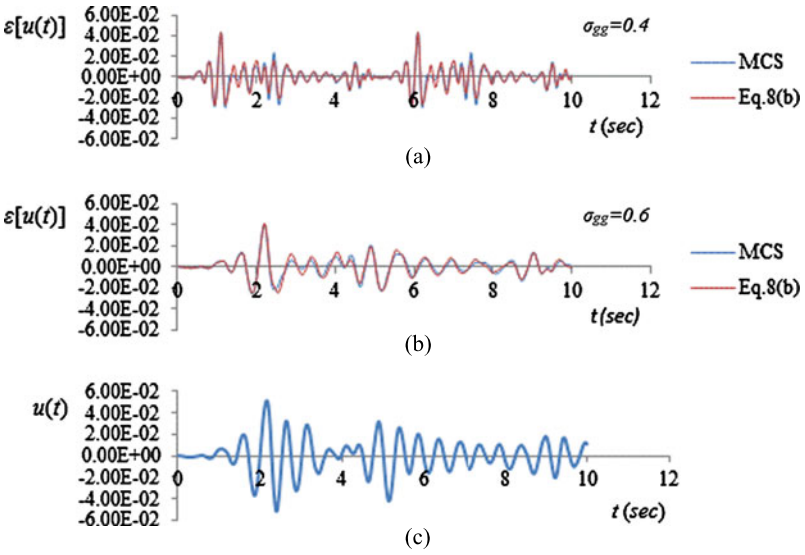

Fig. 2.11 Time histories of the mean response displacement for a truncated Gaussian field with (**a**) $\sigma_{gg} = 0.4$, (**b**) $\sigma_{gg} = 0.6$ and (**c**) of the deterministic response displacement. Comparison of results obtained from Eq. (2.8b) and MCS

Sensitivity Analysis for LC3 Using the Integral Expressions in Eqs. (2.8a) and (2.8b) Finally, a sensitivity analysis is performed using Eqs. (2.8a) and (2.8b) at minimum computational cost, with respect to three different values of the correlation length parameter of the *SDF* in Eq. (2.12) and $\sigma_{ff} = 0.2$. Respective results are shown in Figs. 2.14(a) and (b).

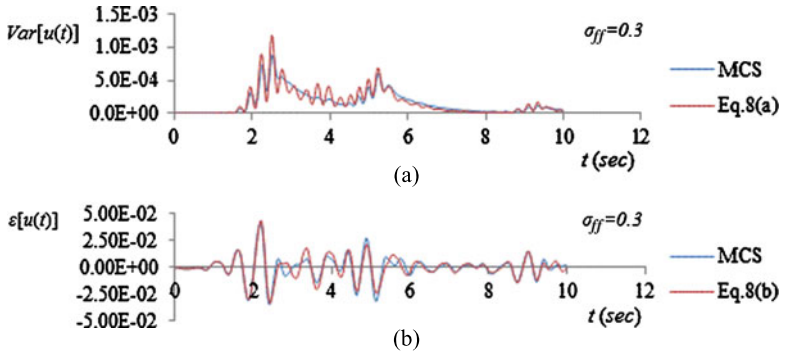

Fig. 2.12 Comparative results from Eqs. (2.11a) and (2.11b) and MCS for a lognormal field with $\sigma_{ff} = 0.2$ for (**a**) the variance and (**b**) the mean of the response displacement time history

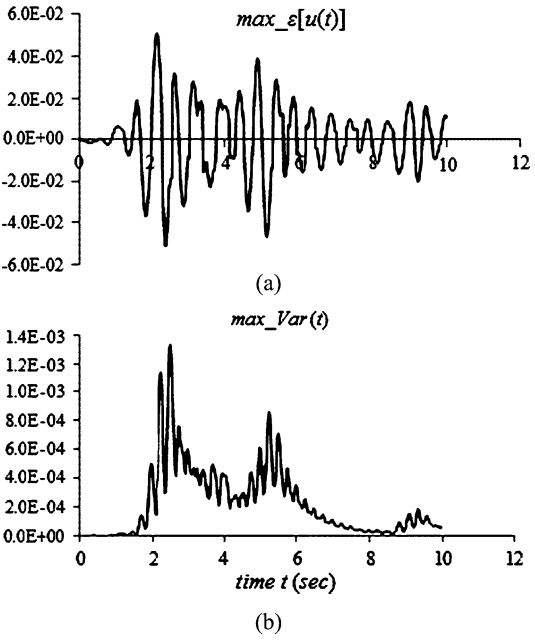

Fig. 2.13 Upper bounds on the (**a**) mean and (**b**) variance of the response displacement for LC2 and $\sigma_{gg} = 0.4$

5 Concluding Remarks

In the present work, Dynamic Variability Response Functions and Dynamic Mean Response Functions are obtained for a linear stochastic single d.o.f. oscillator with random material properties under dynamic excitation. The inverse of the modulus of elasticity was considered as the uncertain system parameter.

It is demonstrated that, as in the case of stochastic systems under static loading, *DVRF* and *DMRF* depend on the standard deviation of the stochastic field modeling the uncertain parameter but appear to be almost independent of its power spectral

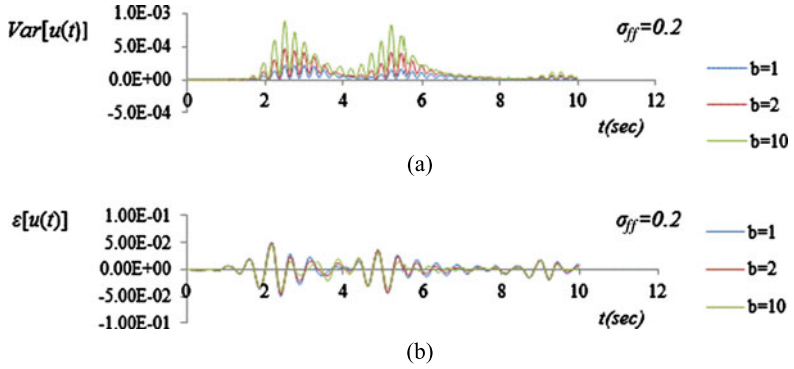

Fig. 2.14 (**a**) Mean and (**b**) variance time histories of the response displacement computed from Eqs. (2.8b) and (2.8a), respectively for three different values of the correlation length parameter b of the *SDF* in Eq. (2.12)

density and marginal *pdf*. The results obtained from the integral expressions are close to those obtained with MCS reaching a maximum error of the order of 20–25%.

As in the case of stochastic systems under static loading, the *DVRF* and *DMRF* provide with an insight of the dynamic system sensitivity to the stochastic parameters and the mechanisms controlling the response mean and variability and their evolution in time.

References

1. Graham, L., Deodatis, G.: Weighted integral method and variability response functions for stochastic plate bending problems. Struct. Saf. **20**, 167–188 (1998)
2. Grigoriu, M.: Applied Non-Gaussian Processes: Examples, Theory, Simulation, Linear Random Vibration, and MATLAB Solutions. Prentice Hall, New York (1995)
3. Grigoriu, M.: Evaluation of Karhunen–Loève, spectral and sampling representations for stochastic processes. J. Eng. Mech. **132**, 179–189 (2006)
4. Liu, W.K., Belytschko, T., Mani, A.: Probabilistic finite elements for nonlinear structural dynamics. Comput. Methods Appl. Mech. Eng. **56**, 61–86 (1986)
5. Matthies, H.G., Brenner, C.E., Bucher, C.G., Guedes Soares, C.: Uncertainties in probabilistic numerical analysis of structures and solids—stochastic finite elements. Struct. Saf. **19**, 283–336 (1997)
6. Miranda, M.: On the response variability of beam structures with stochastic parameters. Ph.D. thesis, Columbia University (2008)
7. Papadopoulos, V., Deodatis, G.: Response variability of stochastic frame structures using evolutionary field theory. Comput. Methods Appl. Mech. Eng. **195**(9–12), 1050–1074 (2006)
8. Papadopoulos, V., Deodatis, G., Papadrakakis, M.: Flexibility-based upper bounds on the response variability of simple beams. Comput. Methods Appl. Mech. Eng. **194**(12–16), 1385–1404 (2005)
9. Papadopoulos, V., Papadrakakis, M., Deodatis, G.: Analysis of mean response and response variability of stochastic finite element systems. Comput. Methods Appl. Mech. Eng. **195**(41–43), 5454–5471 (2006)

10. Shinozuka, M.: Structural response variability. J. Eng. Mech. **113**(6), 825–842 (1987)
11. Shinozuka, M., Deodatis, G.: Simulation of stochastic processes by spectral representation. Appl. Mech. Rev. **44**(4), 191–203 (1991)
12. Stefanou, G.: The stochastic finite element method: past, present and future. Comput. Methods Appl. Mech. Eng. **198**, 1031–1051 (2009)
13. Wall, F.J., Deodatis, G.: Variability response functions of stochastic plane stress/strain problems. J. Eng. Mech. **120**(9), 1963–1982 (1994)

Chapter 3
A Novel Reduced Spectral Function Approach for Finite Element Analysis of Stochastic Dynamical Systems

Abhishek Kundu and Sondipon Adhikari

Abstract This work provides the theoretical development and simulation results of a novel Galerkin subspace projection scheme for damped dynamic systems with stochastic coefficients and homogeneous Dirichlet boundary conditions. The fundamental idea involved here is to solve the stochastic dynamic system in the frequency domain by projecting the solution into a reduced finite dimensional spatio-random vector basis spanning the stochastic Krylov subspace to approximate the response. Subsequently, Galerkin weighting coefficients have been employed to minimize the error induced due to the use of the reduced basis and a finite order of the spectral functions and hence to explicitly evaluate the stochastic system response. The statistical moments of the solution have been evaluated at all frequencies to illustrate and compare the stochastic system response with the deterministic case. The results have been validated with direct Monte-Carlo simulation for different correlation lengths and variability of randomness.

1 Introduction

Due to the significant development in computational hardware it is now possible to solve very high resolution models in various computational physics problems, ranging from fluid mechanics to nano-bio mechanics. However, the spatial resolution is not enough to determine the credibility of the numerical model, the physical model as well its parameters are also crucial. Since neither of these may not be exactly known, there has been increasing research activities over the past three decades to model the governing partial differential equations within the framework of stochastic equations. We refer to few recent review papers [5, 25, 32]. Consider a bounded domain $\mathcal{D} \in \mathbb{R}^d$ with piecewise Lipschitz boundary $\partial\mathcal{D}$, where $d \leq 3$ is the spatial dimension and $t \in \mathbb{R}^+$ is the time. Further, consider that $(\Theta, \mathcal{F}, P)$ is a probability

A. Kundu (✉) · S. Adhikari
Swansea University, Singleton Park, Swansea, SA2 8PP, UK
e-mail: a.kundu.577613@swansea.ac.uk

S. Adhikari
e-mail: s.adhikari@swansea.ac.uk

M. Papadrakakis et al. (eds.), *Computational Methods in Stochastic Dynamics*, Computational Methods in Applied Sciences 26,
DOI 10.1007/978-94-007-5134-7_3,

space where $\theta \in \Theta$ is a sample point from the sampling space Θ, $\mathcal{F}$ is the complete σ-algebra over the subsets of Θ and P is the probability measure. We consider a linear stochastic partial differential equation (PDE) of the form

$$\mathfrak{F}_\alpha\big[u(\mathbf{r},t,\theta)\big] + \mathfrak{L}_\beta\big[u(\mathbf{r},t,\theta)\big] = p(\mathbf{r},t); \quad \mathbf{r} \text{ in } \mathcal{D} \tag{3.1}$$

with the associated Dirichlet condition

$$u(\mathbf{r},t,\theta) = 0; \quad \mathbf{r} \text{ on } \partial\mathcal{D}. \tag{3.2}$$

These second order time varying equations typically arise in case of structural vibration problems in mechanical engineering. Here $\mathfrak{F}_\alpha$ and $\mathfrak{L}_\beta$ denote the linear stochastic differential operators with coefficients $\alpha(\mathbf{r},\theta)$ and $\beta(\mathbf{r},\theta)$ as the second order random fields such that $\alpha, \beta : \mathbb{R}^d \times \Theta \to \mathbb{R}$. We assume the random fields to be stationary and square integrable. Depending on the physical problem the random fields $\alpha[u(\mathbf{r},\theta)]$ and $\beta[u(\mathbf{r},\theta)]$ can be used to model different physical quantities. $p(\mathbf{r},t)$ denotes the deterministic excitation field for which the solution $u(\mathbf{r},t,\theta)$ is sought. The purpose of this paper is to investigate a new solution approach for Eq. (3.1) after the discretization of the spatio-random fields using the well established techniques of stochastic finite element method (SFEM) as can be found in references [10, 14, 21].

The random fields in Eq. (3.1) can be discretized to represent them as spectral functions using a finite number of random variables using one of the established techniques available in literatures [10, 16]. Hence the stochastic PDE along with the boundary conditions would result in an equation of the form

$$\mathbf{M}(\theta)\ddot{\mathbf{u}}(\theta,t) + \mathbf{C}(\theta)\dot{\mathbf{u}}(\theta,t) + \mathbf{K}(\theta)\mathbf{u}(\theta,t) = \mathbf{f}_0(t) \tag{3.3}$$

where $\mathbf{M}(\theta) = \mathbf{M}_0 + \sum_{i=1}^{p_1} \mu_i(\theta)\mathbf{M}_i \in \mathbb{R}^{n\times n}$ is the random mass matrix, $\mathbf{K}(\theta) = \mathbf{K}_0 + \sum_{i=1}^{p_2} \nu_i(\theta)\mathbf{K}_i \in \mathbb{R}^{n\times n}$ is the random stiffness matrix along with $\mathbf{C}(\theta) \in \mathbb{R}^{n\times n}$ as the random damping matrix. Here the mass and stiffness matrices have been expressed in terms of their deterministic components ($\mathbf{M}_0$ and $\mathbf{K}_0$) and the corresponding random contributions ($\mathbf{M}_i$ and $\mathbf{K}_i$) obtained from discretizing the stochastic field with a finite number of random variables ($\mu_i(\theta)$ and $\nu_i(\theta)$) and their corresponding spatial basis functions. This has been elaborated in Sect. 2.1. In the present work proportional damping is considered for which $\mathbf{C}(\theta) = \zeta_1\mathbf{M}(\theta) + \zeta_2\mathbf{K}(\theta)$, where ζ_1 and ζ_2 are deterministic scalars. For the harmonic analysis of the structural system considered in Eq. (3.3), it is represented in the frequency domain as

$$\big[-\omega^2\mathbf{M}(\theta) + i\omega\mathbf{C}(\theta) + \mathbf{K}(\theta)\big]\widetilde{\mathbf{u}}(\theta,\omega) = \widetilde{\mathbf{f}}_0(\omega) \tag{3.4}$$

where $\widetilde{\mathbf{u}}(\theta,\omega)$ is the complex frequency domain system response amplitude and $\widetilde{\mathbf{f}}_0(\omega)$ is the amplitude of the harmonic force. Now we group the random variables associated with the mass and damping matrices of Eq. (3.3) as

$$\xi_i(\theta) = \mu_i(\theta) \quad \text{for } i = 1, 2, \ldots, p_1$$

and

$$\xi_{i+p_1}(\theta) = \nu_i(\theta) \quad \text{for } i = 1, 2, \ldots, p_2.$$

Thus the total number of random variables used to represent the mass and the stiffness matrices becomes $p = p_1 + p_2$. Following this, the expression for the linear structural system in Eq. (3.4) can be expressed as

$$\left(\mathbf{A}_0(\omega) + \sum_{i=1}^{p} \xi_i(\theta)\mathbf{A}_i(\omega)\right)\widetilde{\mathbf{u}}(\omega, \theta) = \widetilde{\mathbf{f}}_0(\omega) \tag{3.5}$$

where $\mathbf{A}_0$ and $\mathbf{A}_i \in \mathbb{C}^{n\times n}$ represent the complex deterministic and stochastic parts respectively of the mass, the stiffness and the damping matrices ensemble. For the case of proportional damping the matrices $\mathbf{A}_0$ and $\mathbf{A}_i$ can be written as

$$\mathbf{A}_0(\omega) = \left[-\omega^2 + i\omega\zeta_1\right]\mathbf{M}_0 + [i\omega\zeta_2 + 1]\mathbf{K}_0 \tag{3.6}$$

and

$$\begin{aligned} \mathbf{A}_i(\omega) &= \left[-\omega^2 + i\omega\zeta_1\right]\mathbf{M}_i \quad \text{for } i = 1, 2, \ldots, p_1 \\ \mathbf{A}_{i+p_1}(\omega) &= [i\omega\zeta_2 + 1]\mathbf{K}_i \quad \text{for } i = 1, 2, \ldots, p_2. \end{aligned} \tag{3.7}$$

The paper has been arranged as follows. In Sect. 2 a brief overview of spectral stochastic finite element method is presented. The projection theory in the vector space is developed in Sect. 3. In Sect. 4 an error minimization approach in the Hilbert space is proposed. The idea of the reduced orthonormal vector basis is introduced in Sect. 5. The post processing of the results to obtain the response moments are discussed in Sect. 6. Based on the theoretical results, a simple computational approach is shown in Sect. 7 where the proposed method of reduced orthonormal basis is applied to the stochastic mechanics of an Euler–Bernoulli beam. From the theoretical developments and numerical results, some conclusions are drawn in Sect. 8.

2 Overview of the Spectral Stochastic Finite Element Method

2.1 Discretization of the Stochastic PDE

First consider $a(\mathbf{r}, \theta)$ is a Gaussian random field with a covariance function $C_a : \mathbb{R}^d \times \mathbb{R}^d \to \mathbb{R}$ defined in the domain $\mathcal{D}$. Since the covariance function is square bounded, symmetric and positive definite, it can be represented by a spectral decomposition in an infinite dimensional Hilbert space. Using this spectral decomposition, the random process $a(\mathbf{r}, \theta)$ can be expressed [see for example, [10, 27]] in a generalized Fourier type of series known as the Karhunen–Loève (KL) expansion

$$a(\mathbf{r}, \theta) = a_0(\mathbf{r}) + \sum_{i=1}^{\infty} \sqrt{\nu_i}\widetilde{\xi}_i(\theta)\varphi_i(\mathbf{r}) \tag{3.8}$$

Here $a_0(\mathbf{r})$ is the mean function, $\widetilde{\xi}_i(\theta)$ are uncorrelated standard Gaussian random variables, ν_i and $\varphi_i(\mathbf{r})$ are eigenvalues and eigenfunctions satisfying the integral equation

$$\int_{\mathcal{D}} C_a(\mathbf{r}_1, \mathbf{r}_2)\varphi_j(\mathbf{r}_1)\,\mathrm{d}\mathbf{r}_1 = \nu_j\varphi_j(\mathbf{r}_2), \quad \forall j = 1, 2, \ldots \tag{3.9}$$

The Gaussian random field model is not applicable for strictly positive quantities arising in many practical problems. Equation (3.8) could also represent the Karhunen–Loève expansion of a non-Gaussian random field, which is also well defined. Alternatively, when $a(\mathbf{r}, \theta)$ is a general non-Gaussian random field, it can be expressed in a mean-square convergent series in random variables and spatial functions using the polynomial chaos expansion. For example Ghanem [9] expanded log-normal random fields in a polynomial chaos expansion. In general, non Gaussian random fields can be expressed in a series like

$$a(\mathbf{r}, \theta) = a_0(\mathbf{r}) + \sum_{i=1}^{\infty} \xi_i(\theta) a_i(\mathbf{r}) \tag{3.10}$$

using Wiener–Askey chaos expansion [33–35]. Here $\xi_i(\theta)$ are in general non-Gaussian and correlated random variables and $a_i(\mathbf{r})$ are deterministic functions. In this paper we use this general form of the decomposition of the random field.

Truncating the series in Eq. (3.10) upto the M-th term and using the same approach for the governing PDE (3.1) with boundary conditions, the discretized system equation in the frequency domain (3.3) can be represented by Eq. (3.5), with $M = p$. It is given here once again for convenience.

$$\left[\mathbf{A}_0(\omega) + \sum_{i=1}^{M} \xi_i(\theta)\mathbf{A}_i(\omega)\right]\mathbf{u}(\theta, \omega) = \mathbf{f}_0(\omega). \tag{3.11}$$

The 'tilde' sign has been omitted from the notations of the frequency domain quantities of $\mathbf{u}(\theta, \omega)$ and $\mathbf{f}_0(\omega)$ for the sake of notational convenience and this shall be followed henceforth. The global matrices in Eq. (3.11) can be expressed as

$$\mathbf{A}_i = \sum_e \mathbf{A}_i^{(e)}; \quad i = 0, 1, 2, \ldots, M \tag{3.12}$$

The element matrices $\mathbf{A}_i^{(e)}$ are defined over an element domain $\mathcal{D}_e \in \mathcal{D}$ such that $\mathcal{D}_e \cap \mathcal{D}_{e'} = \varnothing$ for $e \neq e'$ and $\bigcup_{\forall e} \mathcal{D}_e = \mathcal{D}$ and can be given by

$$\mathbf{A}_0^{(e)} = \int_{\mathcal{D}_e} a_0(\mathbf{r})\mathbf{B}^{(e)^T}(\mathbf{r})\mathbf{B}^{(e)}(\mathbf{r})\,\mathrm{d}\mathbf{r} \tag{3.13}$$

and

$$\mathbf{A}_i^{(e)} = \sqrt{\nu_i}\int_{\mathcal{D}_e} a_i(\mathbf{r})\mathbf{B}^{(e)^T}(\mathbf{r})\mathbf{B}^{(e)}(\mathbf{r})\,\mathrm{d}\mathbf{r}; \quad i = 1, 2, \ldots, M \tag{3.14}$$

In the above equations the $\mathbf{B}^{(e)}(\mathbf{r})$ is a deterministic matrix related to the shape function used to interpolate the solution within the element e. For the elliptic problem it can be shown [37] that $\mathbf{B}^{(e)}(\mathbf{r}) = \nabla \mathbf{N}^{(e)}(\mathbf{r})$. The necessary technical details to obtain the discrete stochastic algebraic equations from the stochastic partial differential equation (3.1) have become standard in the literature. Excellent references, for example [2, 3, 10, 20] are available on this topic. In Eq. (3.11), $\mathbf{A}_0(\omega) \in \mathbb{C}^{n\times n}$ and $\mathbf{A}_i(\omega) \in \mathbb{C}^{n\times n}$; $i = 1, 2, \ldots, M$ are symmetric matrices which are deterministic in nature, $\mathbf{u}(\omega, \theta) \in \mathbb{C}^n$ is the solution vector and $\mathbf{f}_0 \in \mathbb{C}^n$ in the input vector. We assume that the eigenvalues of the generalized eigenvalue problem with the deterministic mass ($\mathbf{M}_0$) and stiffness matrices $\mathbf{K}_0$ are distinct. The number of terms M in Eq. (3.11) can be selected based on the accuracy desired for the representation of the underlying random field. One of the main aim of a stochastic finite element analysis is to obtain $\mathbf{u}(\omega, \theta)$ for $\theta \in \Theta$ from Eq. (3.11) in an efficient manner and is the main topic of this paper. We propose a solution technique for Eq. (3.11) when $\xi_i(\theta)$ are in general non-Gaussian and correlated random variables.

2.2 Brief Review of the Solution Techniques

The solution of the set of stochastic linear algebraic equations (3.11) is a key step in the stochastic finite element analysis. As a result, several methods have been proposed. These methods include, first- and second-order perturbation methods [14, 18], Neumann expansion method [1, 36], Galerkin approach [11], linear algebra based methods [6, 7, 17] and simulation methods [26]. More recently efficient collocation methods have been proposed [8, 19]. Another class of methods which have been used widely in the literature is known as the spectral methods (see [25] for a recent review). These methods include the polynomial chaos (PC) expansion [10], stochastic reduced basis method [22, 29, 30] and Wiener–Askey chaos expansion [33–35]. According to the polynomial chaos expansion, second-order random variables $u_j(\theta)$ can be represented by the mean-square convergent expansion

$$
\begin{aligned}
u_j(\theta) = u_{i_0} h_0 + \sum_{i_1=1}^{\infty} u_{i_1} h_1\big(\xi_{i_1}(\theta)\big) \\
+ \sum_{i_1=1}^{\infty} \sum_{i_2=1}^{i_1} u_{i_1,i_2} h_2\big(\xi_{i_1}(\theta), \xi_{i_2}(\theta)\big) \\
+ \sum_{i_1=1}^{\infty} \sum_{i_2=1}^{i_1} \sum_{i_3=1}^{i_2} u_{i_1 i_2 i_3} h_3\big(\xi_{i_1}(\theta), \xi_{i_2}(\theta), \xi_{i_3}(\theta)\big)
\end{aligned}
$$

$$+\sum_{i_1=1}^{\infty}\sum_{i_2=1}^{i_1}\sum_{i_3=1}^{i_2}\sum_{i_4=1}^{i_3} u_{i_1 i_2 i_3 i_4} h_4\big(\xi_{i_1}(\theta), \xi_{i_2}(\theta), \xi_{i_3}(\theta), \xi_{i_4}(\theta)\big) + \cdots, \tag{3.15}$$

where $u_{i_1,\ldots,i_r}$ are deterministic constants to be determined and $h_r(\xi_{i_1}(\theta), \ldots, \xi_{i_r}(\theta))$ is the r^{th} order homogeneous Chaos. When $\xi_i(\theta)$ are Gaussian random variables, the functions $h_r(\xi_{i_1}(\theta), \ldots, \xi_{i_r}(\theta))$ are the r^{th} order Hermite polynomial so that it becomes orthonormal with respect to the Gaussian probability density function. The same idea can be extended to non-Gaussian random variables, provided more generalized functional basis are used [33–35] so that the orthonormality with respect to the probability density functions can be retained. When we have a random vector, as in the case of the solution of Eq. (3.11), then it is natural to replace the constants $u_{i_1,\ldots,i_r}$ by vectors $\mathbf{u}_{i_1,\ldots,i_r} \in \mathbb{R}^n$. Suppose the series is truncated after P number of terms. The value of P depends on the number of basic random variables M and the order of the PC expansion r as

$$P = \sum_{j=0}^{r} \frac{(M+j-1)!}{j!(M-1)!} = \binom{M+r}{r} \tag{3.16}$$

After the truncation, there are P number of unknown vectors of dimension n. Then a mean-square error minimization approach can be applied and the unknown vectors can be solved using the Galerkin approach [10]. Since P increases very rapidly with the order of the chaos r and the number of random variables M, the final number of unknown constants Pn becomes very large. As a result several methods have been developed (see for example [4, 22, 29–31]) to reduce the computational cost. In the polynomial chaos based solution approach, the *only* information used to construct the basis is the probability density function of the random variables. In the context of the discretized Eq. (3.11), more information such as the matrices $\mathbf{A}_i$, $i = 0, 1, 2, \ldots, M$ are available. It may be possible to construct alternative basis using these matrices. Here we investigate such an approach, where instead of projecting the solution in the space of orthonormal polynomials, the solution is projected in an orthonormal vector basis generated from the coefficient matrices.

3 Spectral Decomposition in the Vector Space

3.1 Derivation of the Spectral Functions

Following the spectral stochastic finite element method, or otherwise, an approximation to the solution of Eq. (3.11) can be expressed as a linear combination of functions of random variables and deterministic vectors. Recently Nouy [23, 24]

discussed the possibility of an optimal spectral decomposition. The aim is to use small number of terms to reduce the computation without loosing the accuracy. Here an orthonormal vector basis is considered. Fixing a value of θ, say $\theta = \theta_1$, the solution of Eq. (3.11) $\mathbf{u}(\theta_1)$ can be expanded in a complete basis as $\mathbf{u}(\theta_1) = \alpha_1^{(1)}\boldsymbol{\phi}_1 + \alpha_2^{(1)}\boldsymbol{\phi}_2 + \cdots + \alpha_n^{(1)}\boldsymbol{\phi}_n$. Repeating this for $\theta_1, \theta_2, \ldots$ eventually the whole sample-space can be covered and it would be possible to expand $\mathbf{u}(\theta)$, $\forall\theta \in \Theta$ as a linear combination of $\boldsymbol{\phi}_1, \boldsymbol{\phi}_2, \ldots, \boldsymbol{\phi}_n$.

We use the eigenvectors $\boldsymbol{\phi}_k \in \mathbb{R}^n$ of the generalized eigenvalue problem

$$\mathbf{K}_0\boldsymbol{\phi}_k = \lambda_k\mathbf{M}_0\boldsymbol{\phi}_k; \quad k = 1, 2, \ldots, n \tag{3.17}$$

Since the matrices $\mathbf{K}_0$ and $\mathbf{M}_0$ are symmetric and generally non-negative definite, the eigenvectors $\boldsymbol{\phi}_k$ for $k = 1, 2, \ldots, n$ form an orthonormal basis. Note that in principle any orthonormal basis can be used. This choice is selected due to the analytical simplicity as will be seen later. For notational convenience, define the matrix of eigenvalues and eigenvectors

$$\boldsymbol{\lambda}_0 = \text{diag}\,[\lambda_1, \lambda_2, \ldots, \lambda_n] \in \mathbb{R}^{n\times n} \quad \text{and} \quad \boldsymbol{\Phi} = [\boldsymbol{\phi}_1, \boldsymbol{\phi}_2, \ldots, \boldsymbol{\phi}_n] \in \mathbb{R}^{n\times n} \tag{3.18}$$

Eigenvalues are ordered in the ascending order so that $\lambda_1 < \lambda_2 < \cdots < \lambda_n$. Since $\boldsymbol{\Phi}$ is an orthonormal matrix we have $\boldsymbol{\Phi}^{-1} = \boldsymbol{\Phi}^T$ so that the following identities can easily be established

$$\begin{aligned}
\boldsymbol{\Phi}^T\mathbf{A}_0\boldsymbol{\Phi} &= \boldsymbol{\Phi}^T\big(\big[-\omega^2 + i\omega\zeta_1\big]\mathbf{M}_0 + [i\omega\zeta_2 + 1]\mathbf{K}_0\big)\boldsymbol{\Phi} \\
&= \big(-\omega^2 + i\omega\zeta_1\big)\mathbf{I} + (i\omega\zeta_2 + 1)\boldsymbol{\lambda}_0 \quad \text{which gives,} \\
\boldsymbol{\Phi}^T\mathbf{A}_0\boldsymbol{\Phi} &= \boldsymbol{\Lambda}_0; \qquad \mathbf{A}_0 = \boldsymbol{\Phi}^{-T}\boldsymbol{\Lambda}_0\boldsymbol{\Phi}^{-1} \quad \text{and} \quad \mathbf{A}_0^{-1} = \boldsymbol{\Phi}\boldsymbol{\Lambda}_0^{-1}\boldsymbol{\Phi}^T
\end{aligned} \tag{3.19}$$

where $\boldsymbol{\Lambda}_0 = (-\omega^2 + i\omega\zeta_1)\mathbf{I} + (i\omega\zeta_2 + 1)\boldsymbol{\lambda}_0$ and $\mathbf{I}$ is the identity matrix. Hence, $\boldsymbol{\Lambda}_0$ can also be written as

$$\boldsymbol{\Lambda}_0 = \text{diag}\,[\lambda_{0_1}, \lambda_{0_2}, \ldots, \lambda_{0_n}] \in \mathbb{C}^{n\times n} \tag{3.20}$$

where $\lambda_{0_j} = (-\omega^2 + i\omega\zeta_1) + (i\omega\zeta_2 + 1)\lambda_j$ and λ_j is as defined in Eq. (3.18). We also introduce the transformations

$$\widetilde{\mathbf{A}}_i = \boldsymbol{\Phi}^T\mathbf{A}_i\boldsymbol{\Phi} \in \mathbb{C}^{n\times n}; \quad i = 0, 1, 2, \ldots, M. \tag{3.21}$$

Note that $\widetilde{\mathbf{A}}_0 = \boldsymbol{\Lambda}_0$ is a diagonal matrix and

$$\mathbf{A}_i = \boldsymbol{\Phi}^{-T}\widetilde{\mathbf{A}}_i\boldsymbol{\Phi}^{-1} \in \mathbb{C}^{n\times n}; \quad i = 1, 2, \ldots, M. \tag{3.22}$$

Suppose the solution of Eq. (3.11) is given by

$$\hat{\mathbf{u}}(\omega, \theta) = \left[\mathbf{A}_0(\omega) + \sum_{i=1}^{M}\xi_i(\theta)\mathbf{A}_i(\omega)\right]^{-1}\mathbf{f}_0(\omega) \tag{3.23}$$

Using Eqs. (3.18)–(3.22) and the orthonormality of $\boldsymbol{\Phi}$ one has

$$\begin{aligned}\hat{\mathbf{u}}(\omega,\theta) &= \left[\boldsymbol{\Phi}^{-T}\boldsymbol{\Lambda}_0(\omega)\boldsymbol{\Phi}^{-1} + \sum_{i=1}^{M}\xi_i(\theta)\boldsymbol{\Phi}^{-T}\widetilde{\mathbf{A}}_i\boldsymbol{\Phi}^{-1}\right]^{-1}\mathbf{f}_0(\omega)\\ &= \boldsymbol{\Phi}\boldsymbol{\Psi}\big(\omega,\boldsymbol{\xi}(\theta)\big)\boldsymbol{\Phi}^{T}\mathbf{f}_0(\omega)\end{aligned} \tag{3.24}$$

where

$$\boldsymbol{\Psi}\big(\omega,\boldsymbol{\xi}(\theta)\big) = \left[\boldsymbol{\Lambda}_0(\omega) + \sum_{i=1}^{M}\xi_i(\theta)\widetilde{\mathbf{A}}_i(\omega)\right]^{-1} \tag{3.25}$$

and the M-dimensional random vector

$$\boldsymbol{\xi}(\theta) = \big\{\xi_1(\theta),\xi_2(\theta),\ldots,\xi_M(\theta)\big\}^{T} \tag{3.26}$$

Now we separate the diagonal and off-diagonal terms of the $\widetilde{\mathbf{A}}_i$ matrices as

$$\widetilde{\mathbf{A}}_i = \boldsymbol{\Lambda}_i + \boldsymbol{\Delta}_i, \quad i = 1,2,\ldots,M \tag{3.27}$$

Here the diagonal matrix

$$\boldsymbol{\Lambda}_i = \mathrm{diag}\,[\widetilde{\mathbf{A}}_i] = \mathrm{diag}\,[\lambda_{i_1},\lambda_{i_2},\ldots,\lambda_{i_n}] \in \mathbb{C}^{n\times n} \tag{3.28}$$

and the matrix containing only the off-diagonal elements $\boldsymbol{\Delta}_i = \widetilde{\mathbf{A}}_i - \boldsymbol{\Lambda}_i$ is such that Trace $(\boldsymbol{\Delta}_i) = 0$. Using these, from Eq. (3.25) one has

$$\boldsymbol{\Psi}\big(\omega,\boldsymbol{\xi}(\theta)\big) = \Bigg[\underbrace{\boldsymbol{\Lambda}_0(\omega) + \sum_{i=1}^{M}\xi_i(\theta)\boldsymbol{\Lambda}_i(\omega)}_{\boldsymbol{\Lambda}(\omega,\boldsymbol{\xi}(\theta))} + \underbrace{\sum_{i=1}^{M}\xi_i(\theta)\boldsymbol{\Delta}_i(\omega)}_{\boldsymbol{\Delta}(\omega,\boldsymbol{\xi}(\theta))}\Bigg]^{-1} \tag{3.29}$$

where $\boldsymbol{\Lambda}(\omega,\boldsymbol{\xi}(\theta)) \in \mathbb{C}^{n\times n}$ is a diagonal matrix and $\boldsymbol{\Delta}(\omega,\boldsymbol{\xi}(\theta))$ is an off-diagonal only matrix. In the subsequent expressions we choose to omit the inclusion of frequency dependence of the individual matrices for the sake of notational simplicity, so that $\boldsymbol{\Psi}(\omega,\boldsymbol{\xi}(\theta)) \equiv \boldsymbol{\Psi}(\boldsymbol{\xi}(\theta))$ and so on. Hence,we rewrite Eq. (3.29) as

$$\boldsymbol{\Psi}\big(\boldsymbol{\xi}(\theta)\big) = \big[\boldsymbol{\Lambda}\big(\boldsymbol{\xi}(\theta)\big)\big[\mathbf{I}_n + \boldsymbol{\Lambda}^{-1}\big(\boldsymbol{\xi}(\theta)\big)\boldsymbol{\Delta}\big(\boldsymbol{\xi}(\theta)\big)\big]\big]^{-1} \tag{3.30}$$

The above expression can be represented using a Neumann type of matrix series [36] as

$$\boldsymbol{\Psi}\big(\boldsymbol{\xi}(\theta)\big) = \sum_{s=0}^{\infty}(-1)^s\big[\boldsymbol{\Lambda}^{-1}\big(\boldsymbol{\xi}(\theta)\big)\boldsymbol{\Delta}\big(\boldsymbol{\xi}(\theta)\big)\big]^s\boldsymbol{\Lambda}^{-1}\big(\boldsymbol{\xi}(\theta)\big) \tag{3.31}$$

Taking an arbitrary r-th element of $\hat{\mathbf{u}}(\theta)$, Eq. (3.24) can be rearranged to have

$$\hat{u}_r(\theta) = \sum_{k=1}^{n} \Phi_{rk} \left(\sum_{j=1}^{n} \Psi_{kj}\big(\boldsymbol{\xi}(\theta)\big)\big(\boldsymbol{\phi}_j^T \mathbf{f}_0\big) \right) \tag{3.32}$$

Defining

$$\Gamma_k\big(\boldsymbol{\xi}(\theta)\big) = \sum_{j=1}^{n} \Psi_{kj}\big(\boldsymbol{\xi}(\theta)\big)\big(\boldsymbol{\phi}_j^T \mathbf{f}_0\big) \tag{3.33}$$

and collecting all the elements in Eq. (3.32) for $r = 1, 2, \ldots, n$ one has

$$\hat{\mathbf{u}}(\theta) = \sum_{k=1}^{n} \Gamma_k\big(\boldsymbol{\xi}(\theta)\big)\boldsymbol{\phi}_k \tag{3.34}$$

This shows that the solution vector $\hat{\mathbf{u}}(\theta)$ can be projected in the space spanned by $\boldsymbol{\phi}_k$.

Now assume the series in Eq. (3.31) is truncated after m-th term. We define the truncated function

$$\boldsymbol{\Psi}^{(m)}\big(\boldsymbol{\xi}(\theta)\big) = \sum_{s=0}^{m} (-1)^s \big[\boldsymbol{\Lambda}^{-1}\big(\boldsymbol{\xi}(\theta)\big)\boldsymbol{\Delta}\big(\boldsymbol{\xi}(\theta)\big)\big]^s \boldsymbol{\Lambda}^{-1}\big(\boldsymbol{\xi}(\theta)\big) \tag{3.35}$$

From this one can obtain a sequence for different m

$$\hat{\mathbf{u}}^{(m)}(\theta) = \sum_{k=1}^{n} \Gamma_k^{(m)}\big(\boldsymbol{\xi}(\theta)\big)\boldsymbol{\phi}_k; \quad m = 1, 2, 3, \ldots \tag{3.36}$$

Since $\theta \in \Theta$ is arbitrary, comparing (3.11) and (3.23) we observe that $\hat{\mathbf{u}}^{(m)}(\theta)$ is the solution of Eq. (3.11) for every θ when $m \to \infty$. This implies that

$$\text{Prob}\left\{\theta \in \Theta : \lim_{m\to\infty} \hat{\mathbf{u}}^{(m)}(\theta) = \hat{\mathbf{u}}(\theta)\right\} = 1 \tag{3.37}$$

Therefore, $\hat{\mathbf{u}}(\theta)$ is the solution of Eq. (3.11) in probability. In this derivation, the probability density function of the random variables has not been used. Therefore, the random variables can be general as long as the solution exists.

Remark 1 The matrix power series in (3.31) is different from the classical Neumann series [36]. The classical Neumann series is a power series in $\mathbf{A}_0^{-1}[\boldsymbol{\Delta}\mathbf{A}(\boldsymbol{\xi}(\theta))]$, where the first term is deterministic and the second term is random. The elements of this matrix series are polynomials in $\xi_i(\theta)$. In contrast, the series in (3.31) is in terms of $[\boldsymbol{\Lambda}^{-1}(\boldsymbol{\xi}(\theta))][\boldsymbol{\Delta}(\boldsymbol{\xi}(\theta))]$, where both terms are random. The elements of this matrix series are not simple polynomials in $\xi_i(\theta)$, but are in terms of a ratio of polynomials as seen in Eq. (3.39). The convergence of this series depends on the spectral

radius of

$$\mathbf{R} = \boldsymbol{\Lambda}^{-1}\big(\boldsymbol{\xi}(\theta)\big)\boldsymbol{\Delta}\big(\boldsymbol{\xi}(\theta)\big) \tag{3.38}$$

A generic term of this matrix can be obtained as

$$R_{rs} = \frac{\Delta_{rs}}{\Lambda_{rr}} = \frac{\sum_{i=1}^{M}\xi_i(\theta)\Delta_{i_{rs}}}{\lambda_{0_r} + \sum_{i=1}^{M}\xi_i(\theta)\lambda_{i_r}} = \frac{\sum_{i=1}^{M}\xi_i(\theta)\widetilde{A}_{i_{rs}}}{\lambda_{0_r} + \sum_{i=1}^{M}\xi_i(\theta)\widetilde{A}_{i_{rr}}}; \quad r \neq s \tag{3.39}$$

Since $\mathbf{A}_0$ is positive definite, $\lambda_{0_r} > 0$ for all r. It can be seen from Eq. (3.39) that the spectral radius of $\mathbf{R}$ is also controlled by the diagonal dominance of the $\widetilde{\mathbf{A}}_i$ matrices. If the diagonal terms are relatively larger than the off-diagonal terms, the series will converge faster even if the relative magnitude of λ_{0_r} is not large.

The series in (3.36) approaches to the exact solution of the governing Eq. (3.11) for every $\theta \in \Theta$ for $m \to \infty$. For this reason it converges in probability 1.

Definition 1 The functions $\Gamma_k(\boldsymbol{\xi}(\theta))$, $k = 1, 2, \ldots, n$ are called the spectral functions as they are expressed in terms of the spectral properties of the coefficient matrix $\mathbf{A}_0$ arising in the discretized equation.

For certain class of problems the series in Eq. (3.34) can give useful physical insights into the uncertainty propagation. For structural mechanics problems, the matrix $\mathbf{A}_0$ is the stiffness matrix and its eigenvectors $\boldsymbol{\phi}_k$ are proportional to vibrational mode with a lumped mass assumption [28]. Equation (3.34) says that the response of a stochastic system is a linear combination of fundamental deformation modes weighted by the random variables Γ_k.

3.2 Properties of the Spectral Functions

In this section we discuss some important properties of these functions. From the series expansion in Eq. (3.31) we have

$$\begin{aligned}\boldsymbol{\Psi}\big(\boldsymbol{\xi}(\theta)\big) = {} & \boldsymbol{\Lambda}^{-1}\big(\boldsymbol{\xi}(\theta)\big) - \boldsymbol{\Lambda}^{-1}\big(\boldsymbol{\xi}(\theta)\big)\boldsymbol{\Delta}\big(\boldsymbol{\xi}(\theta)\big)\boldsymbol{\Lambda}^{-1}\big(\boldsymbol{\xi}(\theta)\big) \\ & + \boldsymbol{\Lambda}^{-1}\big(\boldsymbol{\xi}(\theta)\big)\boldsymbol{\Delta}\big(\boldsymbol{\xi}(\theta)\big)\boldsymbol{\Lambda}^{-1}\big(\boldsymbol{\xi}(\theta)\big)\boldsymbol{\Delta}\big(\boldsymbol{\xi}(\theta)\big)\boldsymbol{\Lambda}^{-1}\big(\boldsymbol{\xi}(\theta)\big) \\ & + \cdots\end{aligned} \tag{3.40}$$

Since $\boldsymbol{\Lambda}(\boldsymbol{\xi}(\theta))$ is a diagonal matrix, its inverse is simply a diagonal matrix containing the inverse of each of the diagonal elements. Also recall that the diagonal of $\boldsymbol{\Delta}(\boldsymbol{\xi}(\theta))$ contains only zeros. Different terms of the series in (3.40) can be obtained using a simple recursive relationship [36]. The numerical computation of the series is therefore computationally very efficient. For further analytical results, truncating the series upto different terms, we define spectral functions of different order.

Definition 2 The first-order spectral functions $\Gamma_k^{(1)}(\boldsymbol{\xi}(\theta))$, $k = 1, 2, \ldots, n$ are obtained by retaining one term in the series (3.40).

Retaining one term in (3.40) we have

$$\boldsymbol{\Psi}^{(1)}\big(\boldsymbol{\xi}(\theta)\big) = \boldsymbol{\Lambda}^{-1}\big(\boldsymbol{\xi}(\theta)\big) \quad \text{or} \quad \Psi_{kj}^{(1)}\big(\boldsymbol{\xi}(\theta)\big) = \frac{\delta_{kj}}{\lambda_{0_k} + \sum_{i=1}^{M} \xi_i(\theta)\lambda_{i_k}} \tag{3.41}$$

Using the definition of the spectral function in Eq. (3.33), the first-order spectral functions can be explicitly obtained as

$$\Gamma_k^{(1)}\big(\boldsymbol{\xi}(\theta)\big) = \sum_{j=1}^{n} \Psi_{kj}^{(1)}\big(\boldsymbol{\xi}(\theta)\big)\big(\boldsymbol{\phi}_j^T \mathbf{f}_0\big) = \frac{\boldsymbol{\phi}_k^T \mathbf{f}_0}{\lambda_{0_k} + \sum_{i=1}^{M} \xi_i(\theta)\lambda_{i_k}} \tag{3.42}$$

From this expression it is clear that $\Gamma_k^{(1)}(\boldsymbol{\xi}(\theta))$ are correlated non-Gaussian random variables. Since we assumed that all eigenvalues λ_{0_k} are distinct, every $\Gamma_k^{(1)}(\boldsymbol{\xi}(\theta))$ in Eq. (3.42) are different for different values of k.

Definition 3 The second-order spectral functions $\Gamma_k^{(2)}(\boldsymbol{\xi}(\theta))$, $k = 1, 2, \ldots, n$ are obtained by retaining two terms in the series (3.40).

Retaining two terms in (3.40) we have

$$\boldsymbol{\Psi}^{(2)}\big(\boldsymbol{\xi}(\theta)\big) = \boldsymbol{\Lambda}^{-1}\big(\boldsymbol{\xi}(\theta)\big) - \boldsymbol{\Lambda}^{-1}\big(\boldsymbol{\xi}(\theta)\big)\boldsymbol{\Delta}\big(\boldsymbol{\xi}(\theta)\big)\boldsymbol{\Lambda}^{-1}\big(\boldsymbol{\xi}(\theta)\big) \tag{3.43}$$

or

$$\begin{aligned}\Psi_{kj}^{(2)}\big(\boldsymbol{\xi}(\theta)\big) = &\frac{\delta_{kj}}{\lambda_{0_k} + \sum_{i=1}^{M} \xi_i(\theta)\lambda_{i_k}} \\ &- \frac{\sum_{i=1}^{M} \xi_i(\theta)\Delta_{i_{kj}}}{(\lambda_{0_k} + \sum_{i=1}^{M} \xi_i(\theta)\lambda_{i_k})(\lambda_{0_j} + \sum_{i=1}^{M} \xi_i(\theta)\lambda_{i_j})}\end{aligned} \tag{3.44}$$

Using the definition of the spectral function in Eq. (3.33), the second-order spectral functions can be obtained in closed-form as

$$\begin{aligned}\Gamma_k^{(2)}\big(\boldsymbol{\xi}(\theta)\big) = &\frac{\boldsymbol{\phi}_k^T \mathbf{f}_0}{\lambda_{0_k} + \sum_{i=1}^{M} \xi_i(\theta)\lambda_{i_k}} \\ &- \sum_{\substack{j=1 \\ j\neq k}}^{n} \frac{(\boldsymbol{\phi}_j^T \mathbf{f}_0)\sum_{i=1}^{M} \xi_i(\theta)\Delta_{i_{kj}}}{(\lambda_{0_k} + \sum_{i=1}^{M} \xi_i(\theta)\lambda_{i_k})(\lambda_{0_j} + \sum_{i=1}^{M} \xi_i(\theta)\lambda_{i_j})}\end{aligned} \tag{3.45}$$

The second-order function can be viewed as adding corrections to the first-order expression derived in Eq. (3.42).

Definition 4 The vector of spectral functions of order s can be obtained by retaining s terms in the series (3.40) and can be expressed as

$$\boldsymbol{\Gamma}^{(s)}\big(\boldsymbol{\xi}(\theta)\big) = \big[\mathbf{I}_n - \mathbf{R}\big(\boldsymbol{\xi}(\theta)\big) + \mathbf{R}\big(\boldsymbol{\xi}(\theta)\big)^2 - \mathbf{R}\big(\boldsymbol{\xi}(\theta)\big)^3 \ldots s^{\text{th}} \text{ term}\big]\boldsymbol{\Gamma}^{(1)}\big(\boldsymbol{\xi}(\theta)\big) \quad (3.46)$$

where $\mathbf{I}_n$ is the n-dimensional identity matrix and $\mathbf{R}$ is defined in Eq. (3.38) as $\mathbf{R}(\boldsymbol{\xi}(\theta)) = [\boldsymbol{\Lambda}^{-1}(\boldsymbol{\xi}(\theta))][\boldsymbol{\Delta}(\boldsymbol{\xi}(\theta))]$. Different terms of this series can be obtained recursively from the previous term [36].

4 Error Minimization Using the Galerkin Approach

In Section 3.1 we derived the spectral functions such that a projection in an orthonormal basis converges to the exact solution in probability 1. The spectral functions are expressed in terms of a convergent infinite series. First, second and higher order spectral functions obtained by truncating the infinite series have been derived. We have also showed that they have the same functional form as the exact solution of Eq. (3.11). This motivates us to use these functions as 'trial functions' to construct the solution. The idea is to minimize the error arising due to the truncation. A Galerkin approach is proposed where the error is made orthogonal to the spectral functions.

We express the solution vector by the series representation

$$\hat{\mathbf{u}}(\theta) = \sum_{k=1}^{n} c_k \widehat{\Gamma}_k\big(\boldsymbol{\xi}(\theta)\big)\boldsymbol{\phi}_k \quad (3.47)$$

Here the functions $\widehat{\Gamma}_k : \mathbb{C}^M \to \mathbb{C}$ are the spectral functions and the constants $c_k \in \mathbb{C}$ need to be obtained using the Galerkin approach. The functions $\widehat{\Gamma}_k(\boldsymbol{\xi}(\theta))$ can be the first-order (3.42), second-order (3.45) or any higher-order spectral functions (3.46) and $\boldsymbol{\phi}_k$ are the eigenvectors introduced earlier in Eq. (3.17). Substituting the expansion of $\hat{\mathbf{u}}(\theta)$ in the governing equation (3.11), the error vector can be obtained as

$$\boldsymbol{\varepsilon}(\theta) = \left(\sum_{i=0}^{M} \mathbf{A}_i \xi_i(\theta)\right)\left(\sum_{k=1}^{n} c_k \widehat{\Gamma}_k\big(\boldsymbol{\xi}(\theta)\big)\boldsymbol{\phi}_k\right) - \mathbf{f}_0 \in \mathbb{C}^n \quad (3.48)$$

where $\xi_0 = 1$ is used to simplify the first summation expression. The expression (3.47) is viewed as a projection where $\{\widehat{\Gamma}_k(\boldsymbol{\xi}(\theta))\boldsymbol{\phi}_k\} \in \mathbb{C}^n$ are the basis functions and c_k are the unknown constants to be determined. We wish to obtain the coefficients c_k using the Galerkin approach so that the error is made orthogonal to the basis functions, that is, mathematically

$$\boldsymbol{\varepsilon}(\theta) \perp \big(\widehat{\Gamma}_j\big(\boldsymbol{\xi}(\theta)\big)\boldsymbol{\phi}_j\big) \quad \text{or} \quad \big\langle \widehat{\Gamma}_j\big(\boldsymbol{\xi}(\theta)\big)\boldsymbol{\phi}_j, \boldsymbol{\varepsilon}(\theta)\big\rangle = 0 \quad \forall j = 1, 2, \ldots, n \quad (3.49)$$

Here $\langle \mathbf{u}(\theta), \mathbf{v}(\theta) \rangle = \int_\Theta P(\mathrm{d}\theta)\mathbf{u}(\theta)\mathbf{v}(\theta)$ defines the inner product norm. Imposing this condition and using the expression of $\boldsymbol{\varepsilon}(\theta)$ from Eq. (3.48) one has

$$\mathrm{E}\Bigg[\big(\widehat{\Gamma}_j\big(\boldsymbol{\xi}(\theta)\big)\boldsymbol{\phi}_j\big)^T \Bigg(\sum_{i=0}^{M} \mathbf{A}_i \xi_i(\theta)\Bigg)\Bigg(\sum_{k=1}^{n} c_k \widehat{\Gamma}_k\big(\boldsymbol{\xi}(\theta)\big)\boldsymbol{\phi}_k\Bigg) - \big(\widehat{\Gamma}_j\big(\boldsymbol{\xi}(\theta)\big)\boldsymbol{\phi}_j\big)^T \mathbf{f}_0 \Bigg] = 0 \tag{3.50}$$

Interchanging the $\mathrm{E}[\cdot]$ and summation operations, this can be simplified to

$$\sum_{k=1}^{n}\Bigg(\sum_{i=0}^{M}\big(\boldsymbol{\phi}_j^T \mathbf{A}_i \boldsymbol{\phi}_k\big)\mathrm{E}\big[\xi_i(\theta)\widehat{\Gamma}_j^T\big(\boldsymbol{\xi}(\theta)\big)\widehat{\Gamma}_k\big(\boldsymbol{\xi}(\theta)\big)\big]\Bigg)c_k = \mathrm{E}\big[\widehat{\Gamma}_j^T\big(\boldsymbol{\xi}(\theta)\big)\big]\big(\boldsymbol{\phi}_j^T \mathbf{f}_0\big) \tag{3.51}$$

or

$$\sum_{k=1}^{n}\Bigg(\sum_{i=0}^{M} \widetilde{A}_{i_{jk}} D_{ijk}\Bigg)c_k = b_j \tag{3.52}$$

Defining the vector $\mathbf{c} = \{c_1, c_2, \ldots, c_n\}^T$, these equations can be expressed in a matrix form as

$$\mathbf{S}\mathbf{c} = \mathbf{b} \tag{3.53}$$

with

$$S_{jk} = \sum_{i=0}^{M} \widetilde{A}_{i_{jk}} D_{ijk}; \quad \forall j,k = 1,2,\ldots,n \tag{3.54}$$

where

$$\widetilde{A}_{i_{jk}} = \boldsymbol{\phi}_j^T \mathbf{A}_i \boldsymbol{\phi}_k, \tag{3.55}$$

$$D_{ijk} = \mathrm{E}\big[\xi_i(\theta)\widehat{\Gamma}_j^T\big(\boldsymbol{\xi}(\theta)\big)\widehat{\Gamma}_k\big(\boldsymbol{\xi}(\theta)\big)\big] \tag{3.56}$$

and

$$b_j = \mathrm{E}\big[\widehat{\Gamma}_j^T\big(\boldsymbol{\xi}(\theta)\big)\big]\big(\boldsymbol{\phi}_j^T \mathbf{f}_0\big). \tag{3.57}$$

Higher order spectral functions can be used to improve the accuracy and convergence of the series (3.47). This will be demonstrated in the numerical examples later in the paper.

Remark 2 (Comparison with the classical spectral SFEM) We compare this Galerkin approach with the classical spectral stochastic finite element approach for further insight. The number of equations to be solved for the unknown coefficients in Eq. (3.53) is n, the same dimension as the original governing equation

(3.11). There are only n unknown constants, as opposed to nP unknown constants arising in the polynomial chaos expansion. The coefficient matrix $\mathbf{S}$ and the vector $\mathbf{b}$ in Eq. (3.53) should be obtained numerically using the Monte Carlo simulation or other numerical integration technique. In the classical PC expansion, however, the coefficient matrix and the associated vector are obtained exactly in closed-form. In addition, the coefficient matrix is a sparse matrix whereas the matrix $\mathbf{S}$ in Eq. (3.53) is in general a fully populated matrix.

The series in Eq. (3.47) can also be viewed as an enhanced Neumann expansion method where the approximating functions have been generated using a Neumann type expansion. It can be observed that the matrix $\mathbf{S}$ in Eq. (3.53) is symmetric. Therefore, one need to determine $n(n+1)/2$ number of coefficients by numerical methods. Any numerical integration method, such as the Gaussian quadrature method, can be used to obtain the elements of D_{ijk} and b_j in Eq. (3.55). In this paper Monte Carlo simulation is used. The samples of the spectral functions $\widehat{\Gamma}_k(\boldsymbol{\xi}(\theta))$ can be simulated from Eqs. (3.42), (3.45) or (3.46) depending on the order. These can be used to compute D_{ijk} and b_j from Eq. (3.55). The simulated spectral functions can also be 'recycled' to obtain the statistics and probability density function (pdf) of the solution. In summary, compared to the classical spectral stochastic finite element method, the proposed Galerkin approach results in a smaller size matrix but requires numerical integration techniques to obtain its entries. The numerical method proposed here therefore can be considered as a hybrid analytical-simulation approach.

5 Model Reduction Using a Reduced Number of Basis

The Galerkin approach proposed in the previous section requires the solution of $n \times n$ algebraic equations. Although in general this is smaller compared to the polynomial chaos approach, the computational cost can still be high for large n as the coefficient matrix is in general a dense matrix. The aim of this section is to reduce it further so that, in addition to large number of random variables, problems with large degrees of freedom can also be solved efficiently.

Suppose the eigenvalues of $\mathbf{A}_0$ are arranged in an increasing order such that

$$\lambda_{0_1} < \lambda_{0_2} < \cdots < \lambda_{0_n} \tag{3.58}$$

From the expression of the spectral functions observe that the eigenvalues appear in the denominator:

$$\Gamma_k^{(1)}\big(\boldsymbol{\xi}(\theta)\big) = \frac{\boldsymbol{\phi}_k^T \mathbf{f}_0}{\lambda_{0_k} + \sum_{i=1}^{M} \xi_i(\theta)\lambda_{i_k}} \tag{3.59}$$

The numerator $(\boldsymbol{\phi}_k^T \mathbf{f}_0)$ is the projection of the force on the deformation mode. Since the eigenvalues are arranged in an increasing order, the denominator of $|\Gamma_{k+r}^{(1)}(\boldsymbol{\xi}(\theta))|$

is larger than the denominator of $|\Gamma_k^{(1)}(\boldsymbol{\xi}(\theta))|$ according a suitable measure. The numerator $(\boldsymbol{\phi}_k^T \mathbf{f}_0)$ depends on the nature of forcing and the eigenvectors. Although this quantity is deterministic, in general an ordering cannot be easily established for different values of k. Because all the eigenvectors are normalized to unity, it is reasonable to consider that $(\boldsymbol{\phi}_k^T \mathbf{f}_0)$ does not vary significantly for different values of k. Using the ordering of the eigenvalues, one can select a small number ε such that $\lambda_1/\lambda_q < \varepsilon$ for some value of q, where λ_j is the eigenvalue of the generalized eigenvalue problem defined in Eq. (3.17). Based on this, we can approximate the solution using a truncated series as

$$\hat{\mathbf{u}}(\theta) \approx \sum_{k=1}^{q} c_k \widehat{\Gamma}_k\big(\boldsymbol{\xi}(\theta)\big)\boldsymbol{\phi}_k \tag{3.60}$$

where c_k, $\widehat{\Gamma}_k(\boldsymbol{\xi}(\theta))$ and $\boldsymbol{\phi}_k$ are obtained following the procedure described in the previous section by letting the indices j, k only upto q in Eqs. (3.54) and (3.55). The accuracy of the series (3.60) can be improved in two ways, namely, (a) by increasing the number of terms q, or (b) by increasing the order of the spectral functions $\widehat{\Gamma}_k(\boldsymbol{\xi}(\theta))$.

Model reduction techniques have been widely used within the scope of proper orthogonal decomposition (POD) method [12, 13, 15]. Here the eigenvalues of a symmetric positive definite matrix (the covariance matrix of a snapshot the system response) are used for model reduction. In spite of this similarity, the reduction method proposed here is different from a POD since it only considers the operator and not the solution itself. Reduction based on eigen-solution is of classical nature in various areas of applied mathematics, engineering and physics and extensive studies exist on this topic. It should be noted that the truncation in series (3.60) introduces errors. A rigorous mathematical quantification of error arising due to this truncation is beyond the scope of this article. The ratio of the eigenvalues λ_1/λ_q gives a good indication, but the projection of the force on the eigenvector $(\boldsymbol{\phi}_k^T \mathbf{f}_0)$ is also of importance. Since this quantity is problem dependent, care should be taken while applying this reduction method.

Remark 3 The reduction of the original problem by a projection on the set of dominant eigenvectors of a part of the operator is rather classical in model reduction techniques. It relies on the strong hypothesis that the solution can be well represented on this set of vectors. The impact of this truncation on the solution or a quantity of interest is not estimated in the article. The truncation criteria is based on the spectral decay of a part of the operator but not on the solution itself. By introducing this reduction, some essential features of the solution may not be always captured. The proposed method will only capture the projection of the solution $\mathbf{u}$ on the reduced basis $\boldsymbol{\phi}_k$, $k = 1, 2, \ldots, q$, which could be unadapted to the complete representation of $\mathbf{u}$.

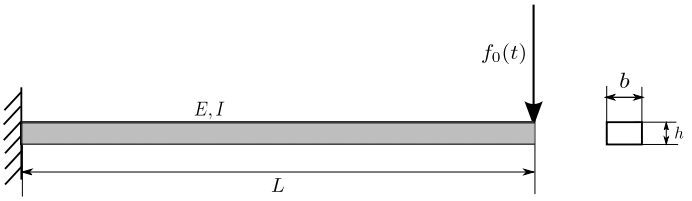

Fig. 3.1 Schematic diagram of the Euler–Bernoulli beam with a point load at the free end

6 Post Processing: Moments of the Solution

For the practical application of the method developed here, the efficient computation of the response moments and pdf is of crucial importance. A simulation based algorithm is proposed in this section. The coefficients c_k in Eq. (3.51) can be calculated from a reduced set of equations given by (3.53). The reduced equations can be obtained by letting the indices j, k upto $q < n$ in Eqs. (3.54) and (3.55). After obtaining the coefficient vector $\mathbf{c} \in \mathbb{C}^q$, the statistical moments of the solution can be obtained from Eqs. (3.61) and (3.62) using the Monte Carlo simulation. The spectral functions used to obtain the vector $\mathbf{c}$ itself, can be reused to obtain the statistics and pdf of the solution. The mean vector can be obtained as

$$\bar{\mathbf{u}} = \mathrm{E}\big[\big|\hat{\mathbf{u}}(\theta)\big|\big] = \sum_{k=1}^{q} |c_k| \mathrm{E}\big[\big|\widehat{\Gamma}_k\big(\boldsymbol{\xi}(\theta)\big)\big|\big]\boldsymbol{\phi}_k \tag{3.61}$$

where $|\cdot|$ is the absolute value of the complex quantities. The covariance of the solution vector can be expressed as

$$\boldsymbol{\Sigma}_u = \mathrm{E}\big[\big(\big|\hat{\mathbf{u}}(\theta)\big| - \bar{\mathbf{u}}\big)\big(\big|\hat{\mathbf{u}}(\theta)\big| - \bar{\mathbf{u}}\big)\big] = \sum_{k=1}^{q}\sum_{j=1}^{q} |c_k c_j| \Sigma_{\Gamma_{kj}} \boldsymbol{\phi}_k \boldsymbol{\phi}_j \tag{3.62}$$

where the elements of the covariance matrix of the spectral functions are given by

$$\Sigma_{\Gamma_{kj}} = \mathrm{E}\big[\big(\big|\widehat{\Gamma}_k\big(\boldsymbol{\xi}(\theta)\big)\big| - \mathrm{E}\big[\big|\widehat{\Gamma}_k\big(\boldsymbol{\xi}(\theta)\big)\big|\big]\big)\big(\big|\widehat{\Gamma}_k\big(\boldsymbol{\xi}(\theta)\big)\big| - \mathrm{E}\big[\big|\widehat{\Gamma}_k\big(\boldsymbol{\xi}(\theta)\big)\big|\big]\big)\big] \tag{3.63}$$

Based on the results derived in the paper, a hybrid reduced simulation-analytical approach can thus be realized in practice. The method is applicable to general structural dynamics problems with general non-Gaussian random fields. In the following section this approach has been applied to a physical problem.

7 Illustrative Application: The Stochastic Mechanics of an Euler–Bernoulli Beam

In this section we apply the computational method to a cantilever beam with stochastic bending modulus. Figure 3.1 shows the configuration of the cantilever beam with

a harmonic point load at its free end. We assume that the bending modulus is a homogeneous stationary Gaussian random field of the form

$$EI(x,\theta) = EI_0\big(1 + a(x,\theta)\big) \tag{3.64}$$

where x is the coordinate along the length of the beam, EI_0 is the estimate of the mean bending modulus, $a(x,\theta)$ is a zero mean stationary Gaussian random field. The autocorrelation function of this random field is assumed to be

$$C_a(x_1,x_2) = \sigma_a^2 e^{-(|x_1-x_2|)/\mu_a} \tag{3.65}$$

where μ_a is the correlation length and σ_a is the standard deviation. We use the base-line parameters as the length $L = 1$ m, cross-section $(b \times h)$ 39×5.93 mm^2 and Young's modulus $E = 2 \times 10^{11}$ Pa. In study we consider deflection of the tip of the beam under harmonic loads of amplitude $\tilde{f}_0 = 1.0$ N. The correlation length considered in this numerical study is $\mu_a = L/2$. The number of terms retained (M) in the Karhunen–Loève expansion (3.8) is selected such that $\nu_M/\nu_1 = 0.01$ in order to retain 90% of the variability. For this correlation length the number of terms M comes to 18. For the finite element discretization, the beam is divided into 40 elements. Standard four degrees of freedom Euler–Bernoulli beam model is used [37]. After applying the fixed boundary condition at one edge, we obtain the number of degrees of freedom of the model to be $n = 80$.

7.1 Results

The proposed method has been compared with a direct Monte Carlo Simulation (MCS), where both have been performed with 10,000 samples. For the direct MCS, Eq. (3.23) is solved for each sample and the mean and standard deviation is derived by assembling the responses. The calculations have been performed for all the four values of σ_a to simulate increasing uncertainty. This is done to check the accuracy of the proposed method against the direct MCS results for varying degrees of uncertainty.

Figure 3.2(a) presents the ratio of the eigenvalues of the generalized eigenvalue problem (3.17) for which the ratio of the eigenvalues is taken with the first eigenvalue. We choose the reduced basis of the problem based on $\lambda_1/\lambda_q < \varepsilon$, where $\varepsilon = 0.01$, and they are highlighted in the figure. Figure 3.2(b) shows the frequency domain response of the deterministic system for both damped and undamped conditions. We have applied a constant modal damping matrix with the damping coefficient $\alpha = 0.02$ (which comes to 1% damping). It is also to be noted that the mass and damping matrices are assumed to be deterministic in nature, while it has to be emphasized that the approach is equally valid for random mass, stiffness and damping matrices. The frequency range of interest for the present study is 0–600 Hz with an interval of 2 Hz. In Fig. 3.2(b), the tip deflection is shown on a log scale for a unit

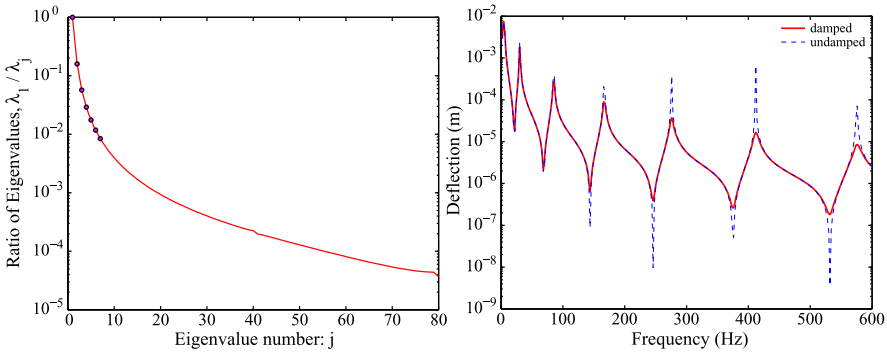

(a) Ratio of eigenvalues of the generalized eigenvalue problem.

(b) Frequency domain reponse of the tip of the beam under point load for the undamped and damped conditions (constant modal damping)

Fig. 3.2 The eigenvalues of the generalized eigenvalue problem involving the mass and stiffness matrices given in Eq. (3.17). For $\varepsilon = 0.01$, the number of reduced eigenvectors $q = 7$ such that $\lambda_1/\lambda_j < \varepsilon$

amplitude harmonic force input. The resonance peak amplitudes of the response of the undamped system definitely depends on the frequency resolution of the plot.

The frequency response of the mean deflection of the tip of the beam is shown in Fig. 3.3 for the cases for cases of $\sigma_a = \{0.05, 0.10, 0.15, 0.20\}$. The figures show a comparison of the direct MCS simulation results with different orders of the solution following Eq. (3.31), where the orders $s = 2, 3, 4$. A very good agreement between the MCS simulation and the proposed spectral approach can be observed in the figures. All the results have been compared with the response of the deterministic system which shows that the uncertainty has an added damping effect at the resonance peaks. This can be explained by the fact that the parametric variation of the beam, results in its peak response for the different samples to get distributed around the resonance frequency zones instead of being concentrated at a particular frequency, and when the subsequent averaging is applied, it smooths out the response peaks to a fair degree. The same explanation holds for the anti-resonance frequencies. It can also be observed that increased variability of the parametric uncertainties (as is represented by the increasing value of σ_a) results in an increase of this added damping effect which is consistent with the previous explanation.

The standard deviation of the frequency domain response of the tip deflection for different spectral order of solution of the reduced basis approach is compared with the direct MCS and is shown in Fig. 3.4, for different values of σ_a. We find that the standard deviation is maximum at the resonance frequencies which is expected due to the differences in the resonance peak of each sample. It is again observed that the direct MCS solution and the reduced order approach give almost identical results, which demonstrate the effectiveness of the proposed approach.

Figure 3.5 shows the standard deviation of the response of the beam at two frequencies 154 Hz and 412 Hz, which correspond to the anti-resonance and reso-

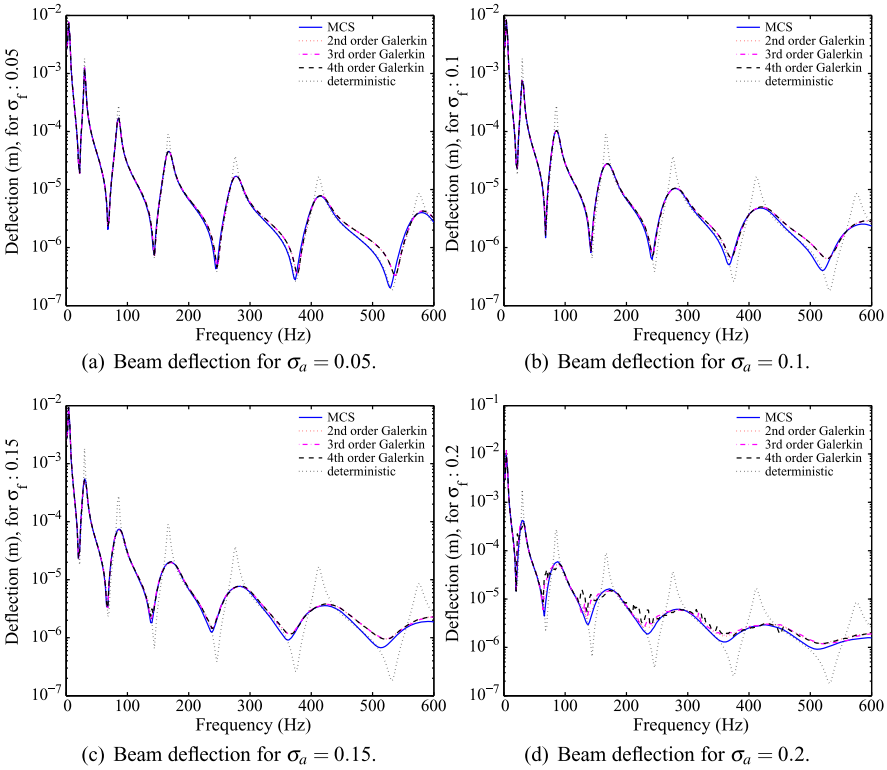

(a) Beam deflection for $\sigma_a = 0.05$.
(b) Beam deflection for $\sigma_a = 0.1$.
(c) Beam deflection for $\sigma_a = 0.15$.
(d) Beam deflection for $\sigma_a = 0.2$.

Fig. 3.3 The frequency domain response of the deflection of the tip of the Euler–Bernoulli beam under unit amplitude harmonic point load at the free end. The response is obtained with 10,000 sample MCS and for $\sigma_a = \{0.05, 0.10, 0.15, 0.20\}$. The proposed Galerkin approach requires the solution of a 7×7 linear system of equation only

nance frequencies of the cantilever beam respectively. The standard deviation values have been obtained for a set of 4 values of σ_a, which represents the different degrees of variability of the system uncertainty. The results obtained with the Galerkin approach for the different order of spectral functions have been compared to the direct MCS, and a good agreement between the two results have been obtained. It is interesting to point out here that the standard deviation decreases with the values of σ_a for the anti-resonance frequency while it increases for the resonance frequencies. This is consistent with the results shown in Fig. 3.4 which shows that an increased value of the variance of the random field has the effect of an increasing added damping on the system, when an averaging is done over the sample space. Thus the resonance response is expected to reduce with the increased variability of the random field while the anti-resonance response will increase.

The probability density function of the deflection of the tip of the cantilever beam for different degrees of variability of the random field is shown in Fig. 3.6.

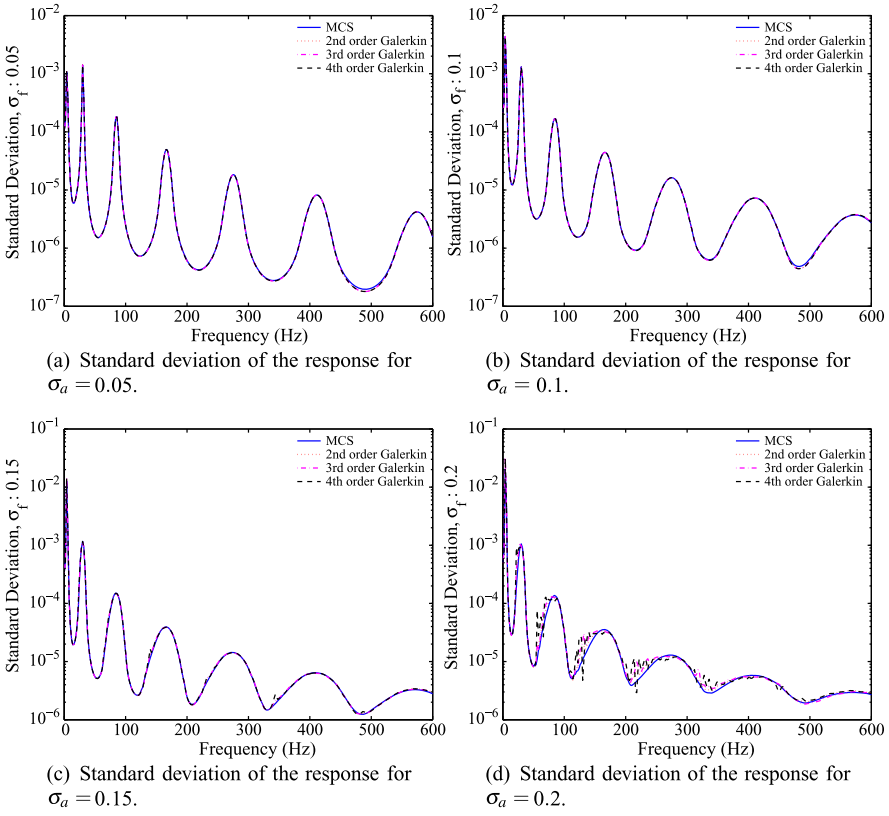

(a) Standard deviation of the response for $\sigma_a = 0.05$.

(b) Standard deviation of the response for $\sigma_a = 0.1$.

(c) Standard deviation of the response for $\sigma_a = 0.15$.

(d) Standard deviation of the response for $\sigma_a = 0.2$.

Fig. 3.4 The standard deviation of the tip deflection of the Euler–Bernoulli beam under unit amplitude harmonic point load at the free end. The response is obtained with 10,000 sample MCS and for $\sigma_a = \{0.05, 0.10, 0.15, 0.20\}$

The probability density functions have been calculated at the frequency of 412 Hz, which is a resonance frequency of the beam. The results indicate that with the increase in the degree of uncertainty (variance) of the system, the lower values of deflection has a higher probability which is absolutely consistent with the standard deviation curve shown in Fig. 3.5(a) and the comparison of the mean deflection of the stochastic system with the deterministic response in Fig. 3.3. This shows that the increase in the variability of the stochastic system has a damping effect on the response.

The results establish the applicability of this spectral reduced basis method with Galerkin error minimization technique as a satisfactory working model for providing solution of the stochastic structural systems. The method is found to be consistent with the direct MCS approach, while being much more computationally efficient than the latter.

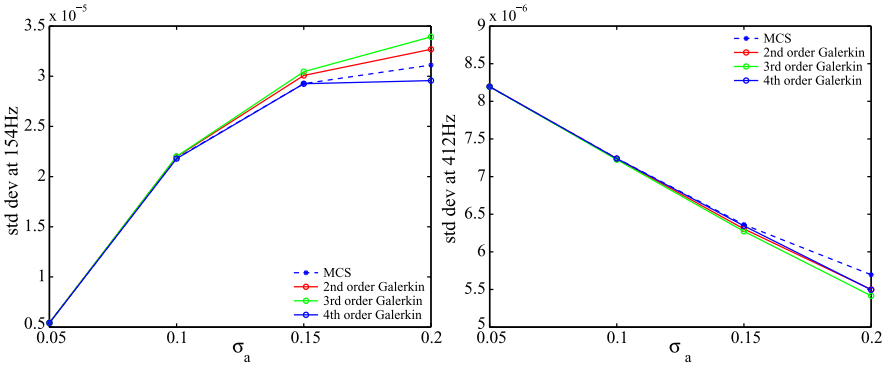

(a) Standard deviation of the response at 154 Hz. (b) Standard deviation of the response at 412 Hz.

Fig. 3.5 The standard deviation of the deflection of the tip versus the variability (σ_a) of the random field of the Euler–Bernoulli beam under unit amplitude harmonic point load at the free end at two frequencies 154 Hz and 412 Hz, which correspond to off-resonance and resonance frequencies respectively. The plots are shown for 4 different values of $\sigma_a = \{0.05, 0.10, 0.15, 0.20\}$ and calculated with 10,000 random samples

8 Conclusions

Here we have considered the discretized stochastic partial differential equation for structural systems with generally non-Gaussian random fields. In the classical spectral stochastic finite element approach, the solution is projected into an infinite dimensional orthonormal basis functions and the associated constant vectors are obtained using the Galerkin type of error minimization approach. Here an alternative approach is proposed. The solution is projected into a finite dimensional reduced vector basis and the associated coefficient functions are obtained. The coefficient functions, called as the *spectral functions*, are expressed in terms of the spectral properties of the matrices appearing in the discretized governing equation. It is shown that then the resulting series converges to the exact solution in probability 1. This is a stronger convergence compared to the classical polynomial chaos which converges in the mean-square sense in the Hilbert space. Using an analytical approach, it is shown that the proposed spectral decomposition has the same functional form as the exact solution, which is not a polynomial, but a ratio of polynomials where the denominator has a higher degree than the numerator.

Using the spectral functions, a Galerkin error minimization approach has been developed. It is shown that the number of unknown constants can be obtained by solving a system of linear equations which have a dimension much smaller than the dimension of the original discretized equation. A simple numerical approach to obtain the reduced dimension has been suggested based on the ratio of the eigenvalues of the generalized eigenvalue problem involving the deterministic mass and stiffness matrices of the baseline model. A numerical approach using a general-

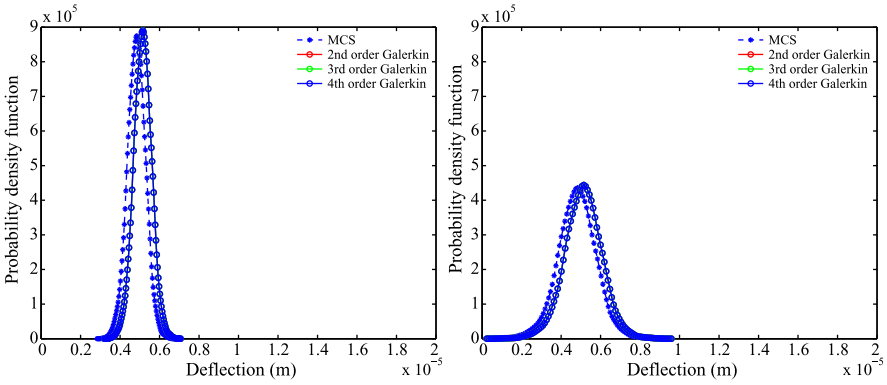

(a) PDF of the response at 210Hz for $\sigma_a = 0.05$. (b) PDF of the response at 210Hz for $\sigma_a = 0.1$.

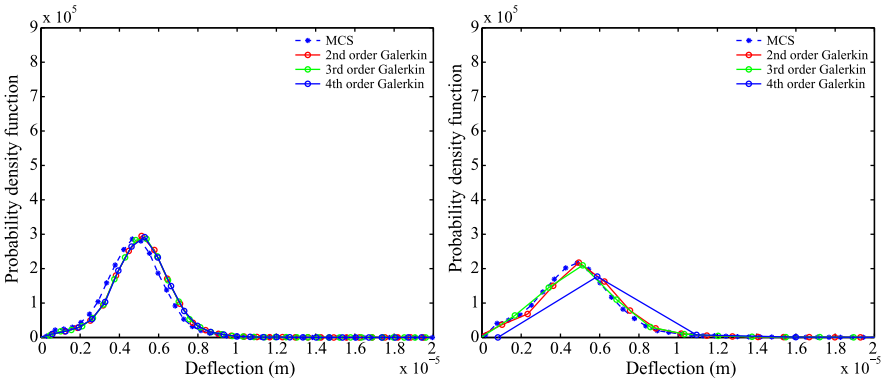

(c) PDF of the response at 210Hz for $\sigma_a = 0.15$. (d) PDF of the response at 210Hz for $\sigma_a = 0.2$.

Fig. 3.6 The probability density function (PDF) of the tip deflection of the Euler–Bernoulli beam at 210 Hz under unit amplitude harmonic point load at the free end. The response is obtained with 10,000 samples and for $\sigma_a = \{0.05, 0.10, 0.15, 0.20\}$

order spectral function has been developed. Based on these, a hybrid analytical-simulation approach is proposed to obtain the statistical properties of the solution.

The computational efficiency of the proposed reduced spectral approach has been demonstrated for large linear systems with non-Gaussian random variables. It may be possible to extend the underlying idea to the class of non-linear problems. For example, the proposed spectral approach can be used for every linearisation step or every time step. Further research is necessary in this direction.

Acknowledgements AK acknowledges the financial support from the Swansea University through the award for Zienkiewicz scholarship. SA acknowledges the financial support from The Royal Society of London through the Wolfson Research Merit Award.

References

1. Adhikari, S., Manohar, C.S.: Dynamic analysis of framed structures with statistical uncertainties. Int. J. Numer. Methods Eng. **44**(8), 1157–1178 (1999)
2. Babuska, I., Tempone, R., Zouraris, G.E.: Galerkin finite element approximations of stochastic elliptic partial differential equations. SIAM J. Numer. Anal. **42**(2), 800–825 (2004)
3. Babuska, I., Tempone, R., Zouraris, G.E.: Solving elliptic boundary value problems with uncertain coefficients by the finite element method: the stochastic formulation. Comput. Methods Appl. Mech. Eng. **194**(12–16), 1251–1294 (2005)
4. Blatman, G., Sudret, B.: An adaptive algorithm to build up sparse polynomial chaos expansions for stochastic finite element analysis. Probab. Eng. Mech. **25**(2), 183–197 (2010)
5. Charmpis, D.C., Schuëller, G.I., Pellissetti, M.F.: The need for linking micromechanics of materials with stochastic finite elements: a challenge for materials science. Comput. Mater. Sci. **41**(1), 27–37 (2007)
6. Falsone, G., Impollonia, N.: A new approach for the stochastic analysis of finite element modelled structures with uncertain parameters. Comput. Methods Appl. Mech. Eng. **191**(44), 5067–5085 (2002)
7. Feng, Y.T.: Adaptive preconditioning of linear stochastic algebraic systems of equations. Commun. Numer. Methods Eng. **23**(11), 1023–1034 (2007)
8. Ganapathysubramanian, B., Zabaras, N.: Sparse grid collocation schemes for stochastic natural convection problems. J. Comput. Phys. **225**(1), 652–685 (2007)
9. Ghanem, R.: The nonlinear Gaussian spectrum of log-normal stochastic processes and variables. J. Appl. Mech. **66**, 964–973 (1989)
10. Ghanem, R., Spanos, P.D.: Stochastic Finite Elements: A Spectral Approach. Springer, New York (1991)
11. Grigoriu, M.: Galerkin solution for linear stochastic algebraic equations. J. Eng. Mech. **132**(12), 1277–1289 (2006)
12. Kerfriden, P., Gosselet, P., Adhikari, S., Bordas, S.: Bridging the proper orthogonal decomposition methods and augmented Newton–Krylov algorithms: an adaptive model order reduction for highly nonlinear mechanical problems. Comput. Methods Appl. Mech. Eng. **200**(5–8), 850–866 (2011)
13. Khalil, M., Adhikari, S., Sarkar, A.: Linear system identification using proper orthogonal decomposition. Mech. Syst. Signal Process. **21**(8), 3123–3145 (2007)
14. Kleiber, M., Hien, T.D.: The Stochastic Finite Element Method. Wiley, Chichester (1992)
15. Lenaerts, V., Kerschen, G., Golinval, J.C.: Physical interpretation of the proper orthogonal modes using the singular value decomposition. J. Sound Vib. **249**(5), 849–865 (2002)
16. Li, C.C., Kiureghian, A.D.: Optimal discretization of random fields. J. Eng. Mech. **119**(6), 1136–1154 (1993)
17. Li, C.F., Feng, Y.T., Owen, D.R.J.: Explicit solution to the stochastic system of linear algebraic equations $(\alpha_1 A_1 + \alpha_2 A_2 + \cdots + \alpha_m A_m)x = b$. Comput. Methods Appl. Mech. Eng. **195**(44–47), 6560–6576 (2006)
18. Liu, W.K., Belytschko, T., Mani, A.: Random field finite-elements. Int. J. Numer. Methods Eng. **23**(10), 1831–1845 (1986)
19. Ma, X., Zabaras, N.: An adaptive hierarchical sparse grid collocation algorithm for the solution of stochastic differential equations. J. Comput. Phys. **228**(8), 3084–3113 (2009)
20. Matthies, H.G., Keese, A.: Galerkin methods for linear and nonlinear elliptic stochastic partial differential equations. Comput. Methods Appl. Mech. Eng. **194**(12–16), 1295–1331 (2005)
21. Matthies, H.G., Brenner, C.E., Bucher, C.G., Soares, C.G.: Uncertainties in probabilistic numerical analysis of structures and solids—stochastic finite elements. Struct. Saf. **19**(3), 283–336 (1997)
22. Nair, P.B., Keane, A.J.: Stochastic reduced basis methods. AIAA J. **40**(8), 1653–1664 (2002)
23. Nouy, A.: A generalized spectral decomposition technique to solve a class of linear stochastic partial differential equations. Comput. Methods Appl. Mech. Eng. **196**(45–48), 4521–4537 (2007)

24. Nouy, A.: Generalized spectral decomposition method for solving stochastic finite element equations: invariant subspace problem and dedicated algorithms. Comput. Methods Appl. Mech. Eng. **197**(51–52), 4718–4736 (2008)
25. Nouy, A.: Recent developments in spectral stochastic methods for the numerical solution of stochastic partial differential equations. Arch. Comput. Methods Eng. **16**, 251–285 (2009). doi:10.1007/s11831-009-9034-5
26. Papadrakakis, M., Papadopoulos, V.: Robust and efficient methods for stochastic finite element analysis using Monte Carlo simulation. Comput. Methods Appl. Mech. Eng. **134**(3–4), 325–340 (1996)
27. Papoulis, A., Pillai, S.U.: Probability, Random Variables and Stochastic Processes, 4th edn. McGraw-Hill, Boston (2002)
28. Petyt, M.: Introduction to Finite Element Vibration Analysis. Cambridge University Press, Cambridge (1998)
29. Sachdeva, S.K., Nair, P.B., Keane, A.J.: Comparative study of projection schemes for stochastic finite element analysis. Comput. Methods Appl. Mech. Eng. **195**(19–22), 2371–2392 (2006)
30. Sachdeva, S.K., Nair, P.B., Keane, A.J.: Hybridization of stochastic reduced basis methods with polynomial chaos expansions. Probab. Eng. Mech. **21**(2), 182–192 (2006)
31. Sarkar, A., Benabbou, N., Ghanem, R.: Domain decomposition of stochastic PDEs: theoretical formulations. Int. J. Numer. Methods Eng. **77**(5), 689–701 (2009)
32. Stefanou, G.: The stochastic finite element method: past, present and future. Comput. Methods Appl. Mech. Eng. **198**(9–12), 1031–1051 (2009)
33. Wan, X.L., Karniadakis, G.E.: Beyond Wiener–Askey expansions: handling arbitrary pdfs. J. Sci. Comput. **27**(1–3), 455–464 (2006)
34. Xiu, D.B., Karniadakis, G.E.: The Wiener–Askey polynomial chaos for stochastic differential equations. SIAM J. Sci. Comput. **24**(2), 619–644 (2002)
35. Xiu, D.B., Karniadakis, G.E.: Modeling uncertainty in flow simulations via generalized polynomial chaos. J. Comput. Phys. **187**(1), 137–167 (2003)
36. Yamazaki, F., Shinozuka, M., Dasgupta, G.: Neumann expansion for stochastic finite element analysis. J. Eng. Mech. **114**(8), 1335–1354 (1988)
37. Zienkiewicz, O.C., Taylor, R.L.: The Finite Element Method, 4th edn. McGraw-Hill, London (1991)

Chapter 4
Computational Stochastic Dynamics Based on Orthogonal Expansion of Random Excitations

X. Frank Xu and George Stefanou

Abstract A major challenge in stochastic dynamics is to model nonlinear systems subject to general non-Gaussian excitations which are prevalent in realistic engineering problems. In this work, an n-th order convolved orthogonal expansion (COE) method is proposed. For linear vibration systems, the statistics of the output can be directly obtained as the first-order COE about the underlying Gaussian process. The COE method is next verified by its application on a weakly nonlinear oscillator. In dealing with strongly nonlinear dynamics problems, a variational method is presented by formulating a convolution-type action and using the COE representation as trial functions.

1 Introduction

To evaluate the probabilistic response of a structural dynamic system subject to parametric and external excitations, there are generally two approaches [6]. The first approach uses Fokker–Planck–Kolmogorov (FPK) equation to directly find the probability density function (PDF) by assuming a white noise excitation. To solve FPK equation especially for nonlinear systems, various techniques have been proposed, including weighted residual, path integral, etc., which however are all limited to systems of low dimension. The second approach includes perturbation method, moment closure method, and statistical equivalent techniques. While the perturbation method is limited to weak nonlinearity, the accuracy of moment closure method and statistical equivalent techniques on highly nonlinear problems remains an open question. Solutions of nonlinear random oscillators subject to stochastic forcing

X.F. Xu (✉)
Department of Civil, Environmental and Ocean Engineering, Stevens Institute of Technology, Hoboken, NJ 07030, USA
e-mail: xxu1@stevens.edu

G. Stefanou
Institute of Structural Analysis & Antiseismic Research, National Technical University of Athens, 15780 Athens, Greece
e-mail: stegesa@mail.ntua.gr

M. Papadrakakis et al. (eds.), *Computational Methods in Stochastic Dynamics*, Computational Methods in Applied Sciences 26,
DOI 10.1007/978-94-007-5134-7_4,

have also been obtained by means of the generalized polynomial chaos expansion, as described in [5].

A major deficiency of the existing approaches is their incapability in dealing with general non-Gaussian excitations which are prevalent in realistic engineering problems [8]. The marginal PDF and power spectral density (PSD) of a loading process play a major role in determining the response of systems, e.g. seismic wave in earthquake engineering. Therefore, a new approach to model dynamic systems subject to non-Gaussian excitations is highly desired.

A novel stochastic computation method based on orthogonal expansion of random fields has been recently proposed [10]. In this study, the idea of orthogonal expansion is extended to the so-called n-th order convolved orthogonal expansions (COE) especially in dealing with nonlinear dynamics. The COE is first verified by its application on a weakly nonlinear oscillator. Next in dealing with strongly nonlinear dynamics problems, a variational method is presented by formulating the convolution-type action and using the COE representation as trial functions [12]. Theoretically, substitution of the trial response function into the stochastic action will lead to the optimal solution. The effect of using different trial functions (COE of different orders) on the accuracy and efficiency of the proposed approach will be the subject of future investigation.

2 Convolved Orthogonal Expansions

2.1 The Zero-th Order Convolved Orthogonal Expansion

An underlying stationary Gaussian excitation $h_1(t,\vartheta)$ is characterized with the autocorrelation function $\rho(t)$ and unit variance, where $\vartheta \in \Theta$ indicates a sample point in random space. Based on the so-called diagonal class of random processes [1], the zero-th order convolved (or memoryless) orthogonal expansion of $h_1(t,\vartheta)$ is proposed as [10]

$$u(t,\vartheta) = \sum_{i=0} u_i(t) h_i(t,\vartheta) \tag{4.1}$$

where the random basis function h_i corresponds to the i-th degree Hermite polynomial with $h_0 = 1$. According to the generalized Mehler's formula [7] the correlations among the random basis functions are given as

$$\begin{aligned} &R_{s_1 s_2 \cdots s_n}(t_1, t_2, \ldots, t_n) \\ &= \overline{h_{s_1}(t_1,\vartheta) \cdots h_{s_n}(t_n,\vartheta)} \\ &= \sum_{\nu_{12}=0}^{\infty} \cdots \sum_{\nu_{n-1,n}=0}^{\infty} \delta_{s_1 r_1} \cdots \delta_{s_n r_n} \prod_{j<k} \frac{\rho^{\nu_{jk}}(t_j - t_k)}{\nu_{jk}!} s_1! \cdots s_n! \end{aligned} \tag{4.2}$$

where

$$r_k = \sum_{j \neq k} \nu_{jk}, \quad \nu_{jk} = \nu_{kj}, \qquad \delta_{s_k r_k} = \begin{cases} 1, & s_k = r_k \\ 0, & s_k \neq r_k \end{cases}$$

and the overbar denotes ensemble average. Following Eq. (4.2), the two-point and three-point correlation functions are specifically obtained as

$$R_{ij}(t_1 - t_2) = \overline{h_i(t_1, \vartheta) h_j(t_2, \vartheta)} = \delta_{ij} i! \rho^i(t_1 - t_2) \tag{4.3}$$

$$\begin{aligned} R_{ijk}(t_1 - t_2, t_1 - t_3, t_2 - t_3) &= \overline{h_i(t_1, \vartheta) h_j(t_2, \vartheta) h_k(t_3, \vartheta)} \\ &= \frac{i! j! k!}{i'! j'! k'!} \rho^{k'}(t_1 - t_2) \rho^{j'}(t_1 - t_3) \rho^{i'}(t_2 - t_3) \end{aligned} \tag{4.4}$$

$$i' = \frac{j + k - i}{2}, \qquad j' = \frac{i + k - j}{2}, \qquad k' = \frac{i + j - k}{2}$$

where i', j', k' must be non-negative integers, otherwise $R_{ijk} = 0$.

The correlation relations can be extended to the derivatives of the random basis functions, e.g.

$$\begin{aligned} R_{ij,pq}(t_1 - t_2) &= \overline{h^{(0)}_{i,p}(t_1, \vartheta) h^{(0)}_{j,q}(t_2, \vartheta)} = \delta_{ij} i! \frac{\partial^{p+q}}{\partial t_1^p \, \partial t_2^q} \rho^i(t_1 - t_2) \\ &= \delta_{ij} (-1)^q i! \frac{\partial^{p+q}}{\partial \tau^{p+q}} \rho^i(\tau) \end{aligned} \tag{4.5}$$

where $\tau = t_1 - t_2$, and the subscripts p, q denote p-th and q-th derivatives. Similarly, the derivations can be made for the convolution of the random basis functions, e.g.

$$\begin{aligned} C_{ij} &= \overline{h_i(t_1, \vartheta) * h_j(t_2, \vartheta)} = \delta_{ij} i! \int_{-\infty}^{\infty} \rho^i(t_1 - 2t_2) \, dt_2 = \delta_{ij} i! \tau_i \\ C_{ij,11} &= \overline{h_{i,1}(t_1, \vartheta) * h_{j,1}(t_2, \vartheta)} = \delta_{ij} i! \int_{-\infty}^{\infty} \frac{\partial^2}{\partial t_1 \, \partial t_2} \rho^i(t_1 - 2t_2) \, dt_2 = 0 \end{aligned} \tag{4.6}$$

where $\tau_i = \int_0^\infty \rho^i(t) \, dt$ is the correlation time.

2.2 n-th Order Convolved Orthogonal Expansion

The idea of the memoryless orthogonal expansion presented above can be generalized to an n-th order convolved orthogonal expansion (COE) for representation of nonlinear output processes

$$u(t, \vartheta) = \sum_{n=0} \sum_{i=0} u_i^{(n)}(t) h_i^{(n)}(t, \vartheta) \tag{4.7}$$

$$h_i^{(n)}(t,\vartheta) = \overbrace{g * g * \cdots * g}^{n} * h_i = g^{*n} * h_i \tag{4.8}$$

where g is a given kernel, and the symbol * denotes the convolution operator. For notational simplicity, the superscript (0) of the zero-th order COE is usually omitted throughout the paper. The memoryless orthogonal expansion thus corresponds to the zero-th order COE with $n = 0$ in (4.7). The correlation functions of the n-th order basis functions are therefore obtained as

$$\begin{aligned} &R_{s_1\cdots s_n}^{m_1\cdots m_n}(t_1, t_2, \ldots, t_n) \\ &= \overline{h_{s_1}^{(m_1)}(t_1,\vartheta)\cdots h_{s_n}^{(m_n)}(t_n,\vartheta)} \\ &= \sum_{\nu_{12}=0}^{\infty}\cdots\sum_{\nu_{n-1,n}=0}^{\infty}\delta_{s_1r_1}\cdots\delta_{s_nr_n}\int_{-\infty}^{\infty}\cdots\int_{-\infty}^{\infty} g^{*m_1}(t_1,\tau_1)\cdots g^{*m_n}(t_n,\tau_n) \\ &\quad\times\prod_{j<k}\frac{\rho^{\nu_{jk}}(t_j - t_k)}{\nu_{jk}!}s_1!\cdots s_n!\,d\tau_1\cdots d\tau_n \end{aligned} \tag{4.9}$$

with the two-point correlations

$$\begin{aligned} R_{ij}^{mn}(t_1,t_2) &= \overline{h_i^{(m)}(t_1,\vartheta)h_j^{(n)}(t_2,\vartheta)} \\ &= \delta_{ij}i!\int_{-\infty}^{\infty}\int_{-\infty}^{\infty} g^{*m}(t_1,\tau_1)g^{*n}(t_2,\tau_2)\rho^i(\tau_1-\tau_2)\,d\tau_1\,d\tau_2 \end{aligned} \tag{4.10}$$

The derivatives of the n-th order basis functions can be similarly obtained, e.g.

$$\begin{aligned} &R_{ij,pq}^{mn}(t_1,t_2) \\ &= \overline{h_{i,p}^{(m)}(t_1,\vartheta)h_{j,q}^{(n)}(t_2,\vartheta)} \\ &= \delta_{ij}i!\frac{\partial^{p+q}}{\partial\tau_1^p\,\partial\tau_2^q}\int_{-\infty}^{\infty}\int_{-\infty}^{\infty} g^{*m}(t_1,\tau_1)g^{*n}(t_2,\tau_2)\rho^i(\tau_1-\tau_2)\,d\tau_1\,d\tau_2 \end{aligned} \tag{4.11}$$

When the kernel g is stationary, by letting $U = \mathcal{F}(u)$, $H = \mathcal{F}(h)$, $S = \mathcal{F}(R)$, $G^n = \mathcal{F}(g^{*n})$ and $\hat{\rho}^{*i} = \mathcal{F}(\rho^i)$, with $\mathcal{F}$ being the Fourier transform operator, we specially rewrite the two-point correlation functions of the COE basis functions in frequency domain

$$S_{ij}^{mn}(\omega) = \overline{H_i^{(m)}(\omega,\vartheta)H_j^{(n)}(\omega,\vartheta)} = \delta_{ij}i!G^m(\omega)\tilde{G}^n(\omega)\hat{\rho}^{*i}(\omega) \tag{4.12}$$

$$\begin{aligned} S_{ij,pq}^{mn}(\omega) &= (\omega\sqrt{-1})^{p+q}\overline{H_i^{(m)}(\omega,\vartheta)\tilde{H}_j^{(n)}(\omega,\vartheta)} \\ &= \delta_{ij}i!(\omega\sqrt{-1})^{p+q}G^m(\omega)\tilde{G}^n(\omega)\hat{\rho}^{*i}(\omega) \end{aligned} \tag{4.13}$$

where the tilde denotes complex conjugate.

Remark The advantage of the n-th order COE (4.7) can be demonstrated by comparing it with the classical Volterra series expansion [9]

$$u(t,\vartheta) = \sum_{n=0} \frac{1}{n!} \int_{-\infty}^{\infty} \cdots \int_{-\infty}^{\infty} k^{(n)}(t_1, t_2, \ldots, t_n) \times h(t-t_1,\vartheta)h(t-t_2,\vartheta)\cdots h(t-t_n,\vartheta)\, dt_1\, dt_2 \cdots dt_n \quad (4.14)$$

and the random variable-based polynomial chaos expansion (PCE)

$$u(t,\vartheta) = \sum_{n=0} u_n(t)\xi_n(\vartheta) \quad (4.15)$$

The Volterra representation typically suffers from severe difficulties in solving for the unknown kernels $k^{(n)}$. In the COE representation, the kernels are all explicitly given, and the problem is significantly reduced to solving of the unknown coefficients $u_i^{(n)}$. The random variable-based PCE, on the other hand, suffers from curse of dimensionality in using random variables $\xi_n(\vartheta)$ to represent random processes. By using random process-based expansions, the COE (4.7) circumvents much of this deficiency.

3 The COE Method in Random Vibration

3.1 Linear Oscillators

Suppose the linear oscillator

$$\begin{aligned} &\ddot{u} + 2\zeta\omega_n\dot{u} + \omega_n^2 u = f/m \\ &u(0) = \dot{u}(0) = 0 \end{aligned} \quad (4.16)$$

is subjected to a non-stationary non-Gaussian translation input, i.e.

$$f(t,\vartheta) = \sum_{i=0} f_i(t)h_i(t,\vartheta) \quad (4.17)$$

By using the Green function

$$\begin{aligned} g(t) &= \frac{1}{\omega_n\sqrt{1-\zeta^2}} e^{-\zeta\omega_n t}\sin\left(\omega_n\sqrt{1-\zeta^2}t\right) \\ G(\omega) &= \frac{1}{\omega_n^2 - \omega^2 + \sqrt{-1}2\zeta\omega\omega_n} \end{aligned} \quad (4.18)$$

the first three correlations of the non-stationary output u can be directly calculated from

$$\bar{u}(t) = \int_0^t g(t-\tau) f_0(\tau)\, d\tau \tag{4.19}$$

$$R_{uu}(t_1, t_2) = \int_0^{t_2} \int_0^{t_1} g(t_1-\tau_1) g(t_2-\tau_2) \times \sum_{i=0} i! \rho^i(\tau_1-\tau_2) f_i(\tau_1) f_i(\tau_2)\, d\tau_1\, d\tau_2 \tag{4.20}$$

$$R_{uuu}(t_1, t_2, t_3) = \int_0^{t_3} \int_0^{t_2} \int_0^{t_1} g(t_1-\tau_1) g(t_2-\tau_2) g(t_3-\tau_3) \times \sum_{i,j,k=0} R_{ijk}(\tau_1-\tau_2, \tau_1-\tau_3, \tau_2-\tau_3)\, d\tau_1\, d\tau_2\, d\tau_3 \tag{4.21}$$

where R_{ijk} is given in Eq. (4.4).

When the excitation in Eq. (4.16) is stationary, each term f_i of Eq. (4.17) becomes constant and the output can be directly given as

$$u(t, \vartheta) = \sum_{i=0} f_i h_i^{(1)}(t, \vartheta) \tag{4.22}$$

which is a special case of the COE representation (4.7). Note that, with the Green function g and the underlying Gaussian process being given, the stationary PDF of the output in Eq. (4.22) can be rapidly estimated by using Monte Carlo method in the frequency domain.

A numerical example of application of the COE on linear oscillator is given in [10]. Hereby we extend this example to provide a parametric study demonstrating the effect of the PSD of the excitation on the output statistics. The excitation force f is assumed to be a stationary lognormal random process $f(t, \vartheta) = \exp(\sigma_z Z(t, \vartheta))$, with the underlying process Z being Gaussian–Markov with the correlation function

$$\rho(\tau) = \exp\left(-\frac{|\tau|}{t_c}\right) \tag{4.23}$$

The lognormal excitation can be represented as a zeroth-order COE

$$f(t, \vartheta) = \sum_{i=0}^{N} f_i h_i(t, \vartheta) \tag{4.24}$$

with

$$f_n = \frac{1}{\sqrt{2\pi n!}} \int_{-\infty}^{+\infty} \exp(\sigma_z z) \Phi_n(z) e^{-z^2/2}\, dz = \frac{\sigma_z^n}{n!} \exp\left(\frac{\sigma_z^2}{2}\right) \tag{4.25}$$

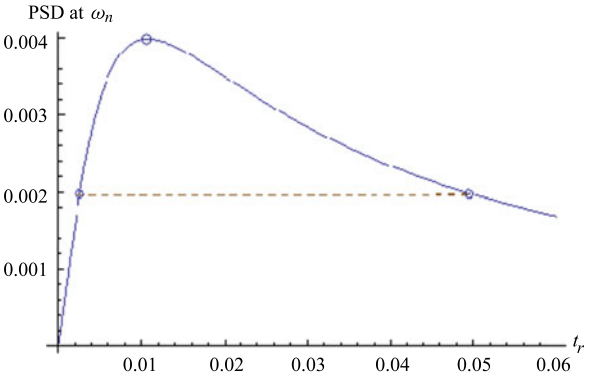

Fig. 4.1 The three points selected corresponding to a fast mode, probabilistic resonance and a slow mode, respectively (from left to right)

The correlation function of the lognormal process can be derived from Eqs. (4.24)–(4.25) as $\rho_f(\tau) = [\exp(\sigma_z^2 \rho(\tau)) - 1]/[\exp(\sigma_z^2) - 1]$ with the corresponding PSD expressed in terms of Gamma function and incomplete Gamma function

$$\hat{\rho}_f(\omega) = -\frac{\delta(\omega)}{e^{\sigma_z^2} - 1} + \frac{t_c}{(e^{\sigma_z^2} - 1)\pi}\Big[\big(-\sigma_z^2\big)^{\sqrt{-1}\omega t_c}\big(\Gamma(-\sqrt{-1}\omega t_c) - \Gamma\big(-\sqrt{-1}\omega t_c, -\sigma_z^2\big)\big) + \big(-\sigma_z^2\big)^{-\sqrt{-1}\omega t_c}\big(\Gamma(\sqrt{-1}\omega t_c) - \Gamma\big(\sqrt{-1}\omega t_c, -\sigma_z^2\big)\big)\Big], \quad \omega \geq 0 \tag{4.26}$$

Let the mass be normalized as $m = 1/\omega_n$, $\sigma_z = 1$, and choose the natural frequency $\omega_n = 40\pi$. To study the effect of PSD of the non-Gaussian lognormal excitation on the response, we modulate the PSD of the lognormal process by using three values of t_c, i.e. 0.0108, 0.05 and 0.00254 (Fig. 4.1). The first value corresponds to the maximum of the PSD at $\omega_n = 40\pi$, i.e. to "probabilistic resonance". The excitation with $t_c = 0.00254$ the smallest correlation time is highly fluctuating, and is termed as a fast mode. Accordingly the excitation with $t_c = 0.05$ is termed as a slow mode. Note the above t_c values are selected based on the undamped frequency, which approximate well the damped cases in most of engineering applications.

As shown in Fig. 4.2, the mean displacement of Eq. (4.19) is independent of PSD. Figure 4.3 shows that the variance of probabilistic resonance is the largest for lightly damped cases. The fast mode has the smallest variance, which is similar to the amplitude of the harmonic motion. It is interesting to note that in the moderately damped case (when ζ is larger than approximately 0.2), the variance of probabilistic resonance is smaller than that of the slow mode. In Fig. 4.4, the coefficient of variation consistently decreases from probabilistic resonance to slow mode, and to fast mode, respectively.

The third centered moment (Fig. 4.5) decreases with the frequency mode, i.e. the fast mode has very small values of the third centered moment. As expected, this trend is also observed for the skewness in Fig. 4.6, where it is shown that, when the

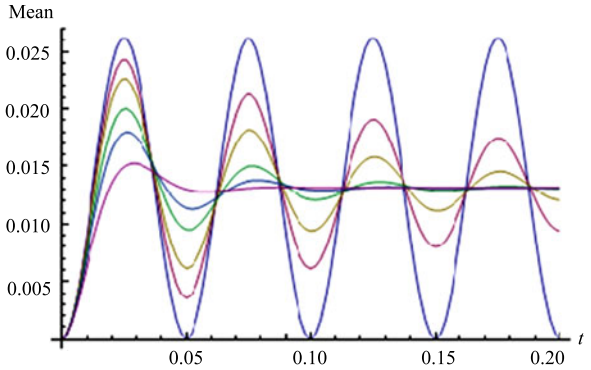

Fig. 4.2 Mean of displacement with the *curves* from exterior to interior corresponding to damping ratio $\zeta = 0, 0.05, 0.1, 0.2, 0.3, 0.5$, respectively

excitation mode becomes faster, the displacement output tends to the Gaussian case in terms of skewness.

With regard to the multi-degree-of-freedom linear systems, the oscillator equations given above can be directly applied by using the modal decomposition as shown in [11].

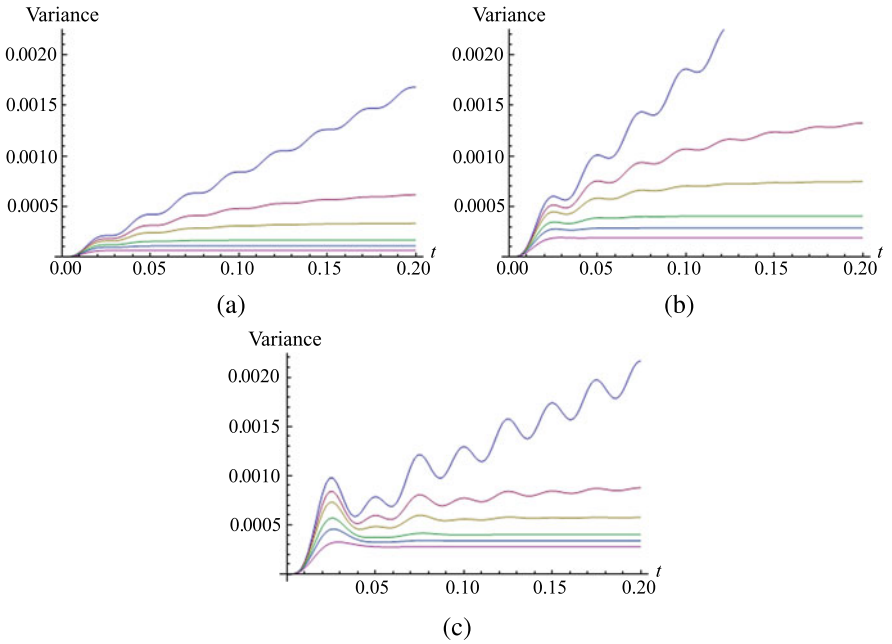

Fig. 4.3 Variance of displacement with the *curves* from top to bottom corresponding to damping ratio $\zeta = 0, 0.05, 0.1, 0.2, 0.3, 0.5$, respectively. (**a**) fast mode, (**b**) probabilistic resonance, (**c**) slow mode

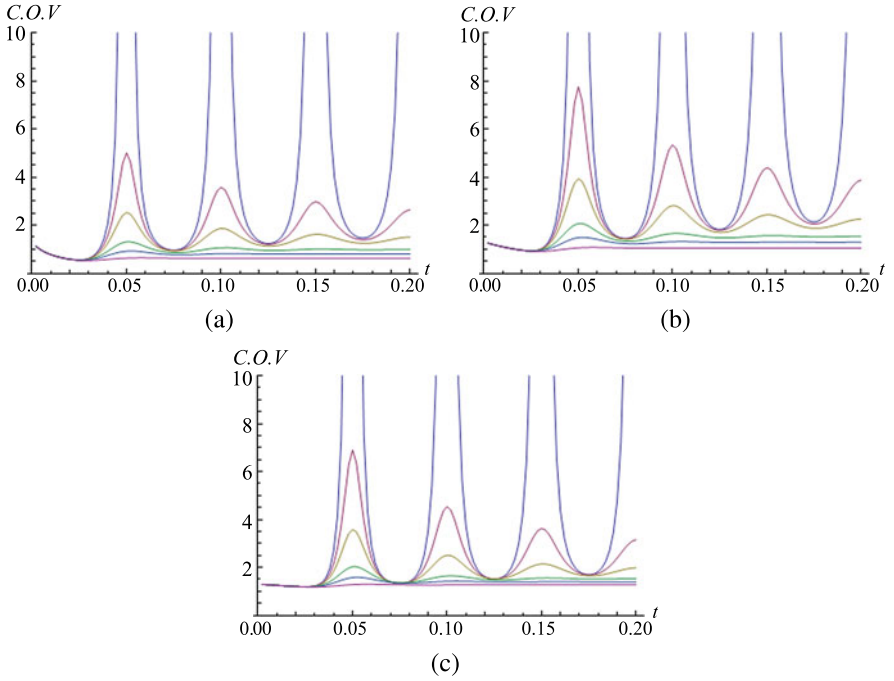

Fig. 4.4 Coefficient of variation of displacement with the *curves* from top to bottom corresponding to damping ratio $\zeta = 0, 0.05, 0.1, 0.2, 0.3, 0.5$, respectively. (**a**) fast mode, (**b**) probabilistic resonance, (**c**) slow mode

3.2 Weakly Nonlinear Oscillators

The accurate computation of the response of nonlinear single-degree-of-freedom (SDOF) oscillators under stochastic loading is important in earthquake engineering where equivalent nonlinear SDOF systems are often used in order to avoid the computationally intensive nonlinear response history analysis of MDOF systems, see e.g. [3].

In this section, a Duffing oscillator subjected to a Gaussian white noise excitation with intensity D is considered

$$\ddot{u} + 2\zeta\omega_n\dot{u} + \omega_n^2\left(u + \alpha u^3\right) = W \tag{4.27}$$

The Gaussian response of the linear filter can be given as $u_0 = \sigma_0 h_1$ where h_1 is characterized by unit variance and PSD [2]

$$S = \frac{D}{\sigma_0^2}\left|G(\omega)\right|^2 \tag{4.28}$$

$$\sigma_0^2 = \frac{1}{2\pi} D \int_{-\infty}^{\infty} \left| \frac{1}{\omega_n^2 - \omega^2 + \sqrt{-1}2\zeta\omega\omega_n} \right|^2 d\omega = \frac{D}{4\zeta\omega_n^3} \tag{4.29}$$

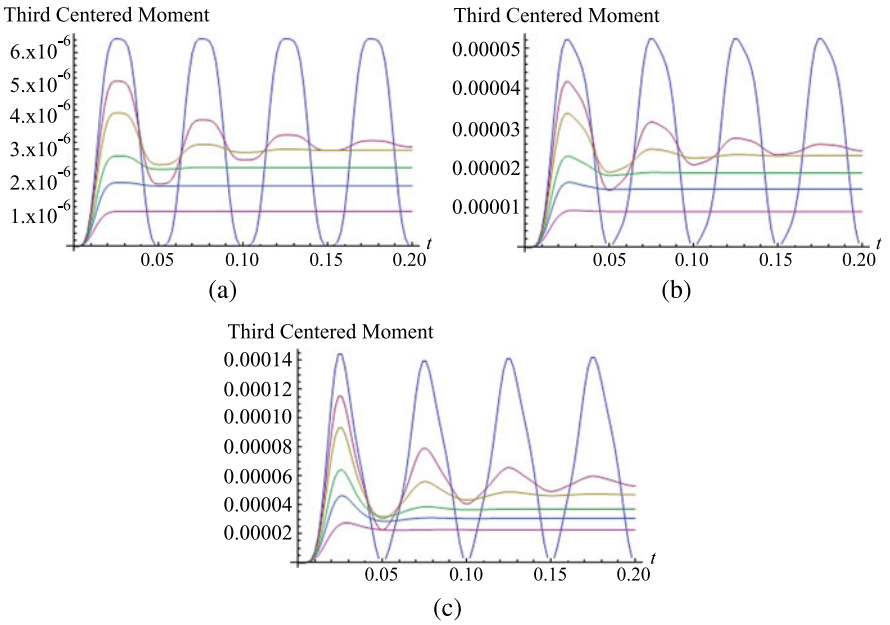

Fig. 4.5 Third centered moment of displacement with the *curves* from top to bottom corresponding to damping ratio $\zeta = 0, 0.05, 0.1, 0.2, 0.3, 0.5$, respectively. (**a**) fast mode, (**b**) probabilistic resonance, (**c**) slow mode

For small α, the nonlinear output of Eq. (4.27) can be approximated as

$$u = \sigma_0 h_1 - \alpha\omega_n^2\sigma_0^3 g * h_1^3 + 3\alpha^2\omega_n^4\sigma_0^5 g * \left(h_1^2 g * h_1^3\right) + O\left(\alpha^3\right) \tag{4.30}$$

By noting $h_1^3 = h_3 + 3h_1$ and $h_1^2 = h_2 + 1$, Eq. (4.30) can be rewritten in terms of the random basis functions

$$\begin{aligned} u = {} & \sigma_0 h_1 - \alpha\omega_n^2\sigma_0^3 g * (h_3 + 3h_1) \\ & + 3\alpha^2\omega_n^4\sigma_0^5 g * \left[(h_2 + 1)g * (h_3 + 3h_1)\right] + O\left(\alpha^3\right) \end{aligned} \tag{4.31}$$

$$\begin{aligned} U = {} & \sigma_0 H_1 - \alpha\omega_n^2\sigma_0^3 G(H_3 + 3H_1) \\ & + 3\alpha^2\omega_n^4\sigma_0^5 G\left[\left(H_2 + \delta(0)\right) * G(H_3 + 3H_1)\right] + O\left(\alpha^3\right) \end{aligned} \tag{4.32}$$

By using the correlations of Eqs. (4.3)–(4.4) and (4.12), it follows that the stationary mean

$$\bar{u} = O\left(\alpha^3\right) \tag{4.33}$$

and the stationary PSD

$$S_{UU} = U\tilde{U} = \sigma_0^2 S - 3\alpha\omega_n^2\sigma_0^4(G + \tilde{G})S + O\left(\alpha^2\right) \tag{4.34}$$

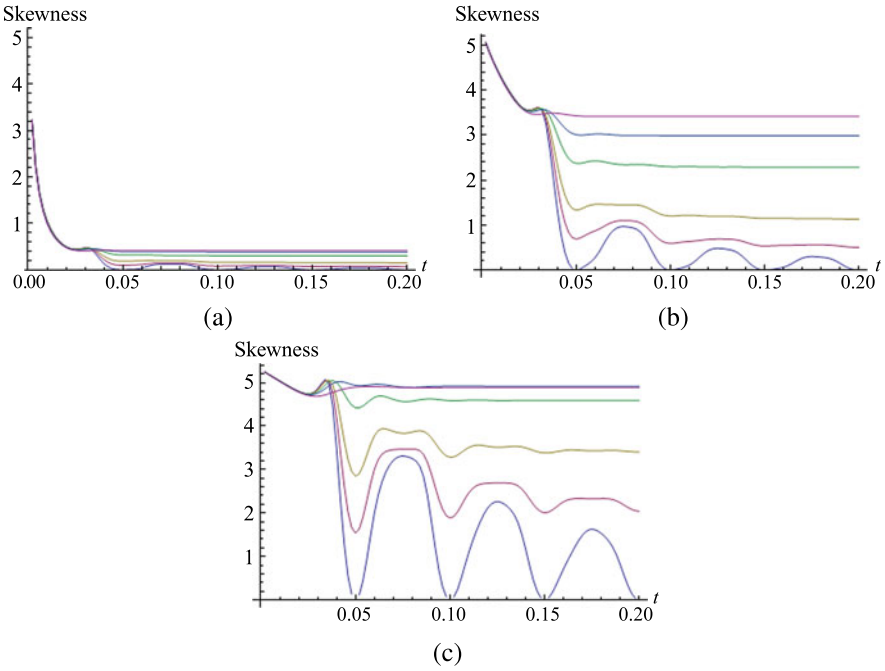

Fig. 4.6 Skewness of displacement with the *curves* from bottom to top corresponding to damping ratio $\zeta = 0, 0.05, 0.1, 0.2, 0.3, 0.5$, respectively. (**a**) fast mode, (**b**) probabilistic resonance, (**c**) slow mode

Since

$$\int_{-\infty}^{\infty} \frac{2(\omega_n^2 - \omega^2)}{(\omega_n^2 - \omega^2)^2 + (2\zeta\omega\omega_n)^2} \left| \frac{1}{\omega_n^2 - \omega^2 + \sqrt{-1}2\zeta\omega\omega_n} \right|^2 d\omega = \frac{\pi}{2\zeta\omega_n^5} \tag{4.35}$$

(see e.g. [2]) the variance calculated from the first two terms of Eq. (4.34) is simply obtained as

$$\sigma^2 = \sigma_0^2\left(1 - 3\alpha\sigma_0^2\right) \tag{4.36}$$

which is identical to the result obtained using other approaches e.g. [4, 6]. In addition to serving as verification to the COE method, this example shows simplicity and efficiency of the orthogonal expansions in nonlinear problems.

3.3 Strongly Nonlinear Oscillators

For strongly nonlinear systems, the perturbation method is inapplicable. In this part, a variational method will be presented following the variational principles formulated for random media elastodynamics [12]. The variational functional, or action,

of a nonlinear oscillator

$$\ddot{u} + 2\zeta\omega_n\dot{u} + \omega_n^2\big(u + g(u,\dot{u})\big) = f \tag{4.37}$$

can be formulated by using the convolution form

$$\delta\ell = \delta u * \big[\ddot{u} + 2\zeta\omega_n\dot{u} + \omega_n^2\big(u + g(u,\dot{u})\big) - f\big] = 0 \tag{4.38}$$

For a convolved nonlinear term $g(u,\dot{u}) = \alpha u^{*3}$, the action is derived from Eq. (4.38) as

$$\begin{aligned}\ell(u) = {} & \frac{1}{2}\dot{u} * \dot{u} + \zeta u * \dot{u} + \frac{1}{2}\omega_n^2 u * u \\ & + \frac{1}{4}\alpha\omega_n^2(u * u * u * u) - f * u + \dot{u}(0)u\end{aligned} \tag{4.39}$$

where any trial function u satisfies the specified initial condition $u(0)$. To the authors' knowledge, the action (4.39) is the first convolution-type variational form formulated for nonlinear dissipative systems. It is especially noted that the classical point-wise Lagrangian form does not work on the dissipative term.

For nonlinear random vibrations, the stochastic action is directly obtained by taking ensemble average of Eq. (4.39), i.e.

$$\delta\bar{\ell} = 0 \tag{4.40}$$

with the trial function u based on the COE representation (4.7).

For stationary solutions, Eq. (4.40) can be rewritten in frequency domain as

$$\begin{aligned}&\delta\bar{L}(U) = 0 \\ &\bar{L}(U) = \left(-\frac{1}{2}\omega^2 + \sqrt{-1}\omega\zeta + \frac{1}{2}\omega_n^2\right)\overline{U^2} + \frac{1}{4}\alpha\omega_n^2\overline{U^4} - \overline{FU}\end{aligned} \tag{4.41}$$

Suppose the excitation is stationary

$$f(t,\vartheta) = \sum_{i=0} f_i h_i(t,\vartheta) \tag{4.42}$$

and choose the zeroth-order COE

$$u(t,\vartheta) = \sum_{i=0} u_i h_i(t,\vartheta) \tag{4.43}$$

as the trial function for the stationary solution. By substituting Eq. (4.43) into Eqs. (4.39)–(4.40) and taking derivative with respect to u_i, it leads to a series of equations to solve for u_i

$$\frac{\partial\bar{\ell}}{\partial u_i} = 0 \tag{4.44}$$

Similarly the first- or higher-order COE can be chosen as the trial function. The detail of numerical examples and investigation of accuracy and computational efficiency of the different trial functions will be the subject of future research.

4 Conclusion

By developing a diagonal class of random fields/stochastic processes to represent high-dimensional uncertainty, the proposed convolved orthogonal expansion method opens a new direction to deal with nonlinear stochastic dynamics. The advantages of the proposed method over the classical Volterra series representation and the random variable-based polynomial chaos expansions have been highlighted in the preceding sections. Future work will be devoted to the investigation of its efficiency in computing of large and strongly nonlinear dynamical systems.

References

1. Barrett, J.F., Lampard, D.G.: An expansion for some second-order probability distributions and its application to noise problems. IRE Trans. Inf. Theory **IT-I**, 10–15 (1955)
2. Elishakoff, I.: Probabilistic Theory of Structures, 2nd edn. Dover, New York (1999)
3. Han, S.W., Wen, Y.K.: Method of reliability-based seismic design. I: equivalent nonlinear systems. J. Struct. Eng. **123**(3), 256–263 (1997)
4. Lin, Y.K.: Probabilistic Theory of Structural Dynamics. Krieger, Melbourne (1976)
5. Lucor, D., Karniadakis, G.E.: Adaptive generalized polynomial chaos for nonlinear random oscillators. SIAM J. Sci. Comput. **26**(2), 720–735 (2005)
6. Manolis, G.D., Koliopoulos, P.K.: Stochastic Structural Dynamics in Earthquake Engineering. WIT Press, Ashurst (2001)
7. Slepian, D.: On the symmetrized Kronecker power of a matrix and extensions of Mehler's formula for Hermite polynomials. SIAM J. Math. Anal. **3**, 606–616 (1972)
8. Stefanou, G.: The stochastic finite element method: past, present and future. Comput. Methods Appl. Mech. Eng. **198**, 1031–1051 (2009)
9. Volterra, V.: Theory of Functionals and of Integral and Integro-Differential Equations. Dover, New York (1959)
10. Xu, X.F.: Stochastic computation based on orthogonal expansion of random fields. Comput. Methods Appl. Mech. Eng. **200**(41–44), 2871–2881 (2011)
11. Xu, X.F.: Quasi-weak and weak formulations of stochastic finite element methods. Probab. Eng. Mech. **28**(Special issue on CSM 6), 103–109 (2012)
12. Xu, X.F.: Variational principles of random media elastodynamics. In preparation

Chapter 5
Numerical Solution of the Fokker–Planck Equation by Finite Difference and Finite Element Methods—A Comparative Study

L. Pichler, A. Masud, and L.A. Bergman

Abstract Finite element and finite difference methods have been widely used, among other methods, to numerically solve the Fokker–Planck equation for investigating the time history of the probability density function of linear and nonlinear 2d and 3d problems; also the application to 4d problems has been addressed. However, due to the enormous increase in computational costs, different strategies are required for efficient application to problems of dimension ≥ 3. Recently, a stabilized multi-scale finite element method has been effectively applied to the Fokker–Planck equation. Also, the alternating directions implicit method shows good performance in terms of efficiency and accuracy. In this paper various finite difference and finite element methods are discussed, and the results are compared using various numerical examples.

1 Introduction

The response of linear systems subjected to additive Gaussian white noise or linearly filtered Gaussian white noise is Gaussian. The derivation for an N-dimensional system can be found, e.g. in [11]. For the case of nonlinear systems subjected to additive Gaussian white noise, analytical solutions are restricted to certain scalar systems. It has been shown (see [2]), that the response of a multi-dimensional memoryless nonlinear system subjected to additive Gaussian white noise forms a vector Markov process, with transition probability density function satisfying both the forward (Fokker–Planck) and backward Kolmogorov equations for which numerical

L. Pichler · L.A. Bergman (✉)
Department of Aerospace Engineering, University of Illinois at Urbana-Champaign, 104 S. Wright Street, Urbana, IL 61801, USA
e-mail: lbergman@illinois.edu

L. Pichler
e-mail: Lukas.Pichler@ymail.com

A. Masud
Department of Civil and Environmental Engineering, University of Illinois at Urbana-Champaign, 205 N. Mathews Avenue, Urbana, IL 61801, USA
e-mail: amasud@illinois.edu

M. Papadrakakis et al. (eds.), *Computational Methods in Stochastic Dynamics*, Computational Methods in Applied Sciences 26,
DOI 10.1007/978-94-007-5134-7_5,

approximations in terms of finite element and finite difference methods can be pursued.

1.1 Scope of This Work

A number of numerical methods have been introduced over the past five decades to obtain approximate results for the solution of the Fokker–Planck equation (FPE). Many of these approximations can be shown to be accurate. This work deals with a review of several finite element and finite difference methods. A comparison and assessment of different methods is carried out by means of various numerical examples including a 2d linear, 2d unimodal and bimodal Duffing oscillators, 3d linear and 3d Duffing oscillators.

The goal is to evaluate the transient solution for the probability density function (PDF) of the oscillator due to stochastic (white noise) excitation. Thus, the forward Kolmogorov or Fokker–Planck equation is of interest and will be approximated within the numerical methods.

1.2 Background

The finite element method was first applied by [1] to determine the reliability of the linear, single degree-of-freedom oscillator subjected to stationary Gaussian white noise. The initial-boundary value problem associated with the backward Kolmogorov equation was solved numerically using a Petrov–Galerkin finite element method.

Reference [10] solved the stationary form of the FPE adopting the finite element method (FEM) to calculate the stationary probability density function of response. The weighted residual statement for the Fokker–Planck equation was first integrated by parts to yield the weak form of the equation.

The transient form of the FPE was analyzed in [16] using a Bubnov–Galerkin FEM. It was shown that the initial-boundary value problem can be modified to evaluate the first passage problem. A comparison for the reliability was carried out with the results obtained from the backward Kolmogorov equation.

A drawback of the FEM is the quickly increasing computational cost with increasing dimension. Thus, while 2 and 3 dimensional systems have been analyzed in the literature, the analysis of 4d or 5d problems reaches the limits of today's computational capabilities and are not yet feasible.

Computationally more economical—in terms of memory requirements, and when considering the effort spent for the assembly of the mass and stiffness matrices—are finite difference methods. The application of central differences is, as expected, only feasible for the case of 2d linear systems because of stability issues. The stability is a function of the nonlinearity and the dimension (ratio Δt and $\prod_{i=1}^{n} \Delta x_i$), thus being unfavorable for the use of this simple method.

A successful approach to overcome the limitations of simple finite differences was achieved by [20] in terms of higher order finite differences. The solution of a 4d system using higher order finite differences is reported in [20]. A comparison of various higher order FD formulations is presented in [9].

A viable approach to achieve higher accuracy is the application of operator splitting methods. Their capabilities with respect to the numerical solution of the FPE has so far received little attention. Operator splitting methods provide a tool to reduce the computational costs by the reduction of the solution to a series of problems of dimension one order less than the original problem. Thus, more efficiency, required for the solution of problems of larger dimension ($\geq$3), can be achieved. An operator splitting method for the solution of the 2d Duffing oscillator is presented in [23]. An operator splitting scheme for 3d oscillators subjected to additive and multiplicative white noise is given by [22]. The method consists of a series of consecutive difference equations for the three fluxes and is numerically stable. The alternating directions implicit method (ADI) [15] is adopted in this paper for a series of problems, and acceptably accurate results are achieved at low cost. The implementation of the method is straightforward and can be readily extended to higher dimensions.

Recent work by Masud et al. introduced a stabilized multi-scale finite element method which allows for a reduction of the number of elements for given accuracy and, thus, the efficiency of the computation can be increased by an order of magnitude when solving a 3d problem.

Several four-state dynamical systems were studied in [17, 18] in which the Fokker–Planck equation was solved using a global weighted residual method and extended orthogonal functions.

Meshless methods were proposed in [6, 7] to solve the transient FPE and [8] for the stationary FPE. Considerable reduction of the memory storage requirements is expected due to coarse meshes employed, and thus a standard desktop PC suffices to carry out the numerical analysis.

In addition, many numerical packages now provide the capability to solve partial differential equations by means of finite element and finite difference methods. However, in most cases these tools are limited to 2d and can only solve special forms of elliptic, parabolic or hyperbolic partial differential equations (PDE). The implementation of FD and FEM into computational software is shown for the cases of COMSOL (2d linear) and FEAP (general 3d).

2 The Fokker–Planck Equation

The Fokker–Planck equation for a n-dimensional system subjected to external Gaussian white noise excitation is given by

$$\frac{\partial p}{\partial t} = -\sum_{j=1}^{n} \frac{\partial}{\partial x_j}(z_j p) + \frac{1}{2}\left(\sum_{i=1}^{n}\sum_{j=1}^{n} \frac{\partial^2}{\partial x_i \, \partial x_j}(H_{ij} p)\right) \tag{5.1}$$

where p denotes the transition probability density function, $\mathbf{x}$ the n-dimensional state space vector and $\mathbf{z}(\mathbf{x})$ and $\mathbf{H}(\mathbf{x})$ denote the drift vector and diffusion matrix, respectively.

The normalization condition for the probability density function is given by

$$\int p_X(\mathbf{x}, t)\, d\mathbf{x} = 1, \tag{5.2}$$

and the initial conditions are given by $p_X(\mathbf{x}_0, 0)$. Examples for initial conditions are, e.g., deterministic, given by the Dirac delta function

$$p_X(\mathbf{x}_0, 0) = \prod_{i=1}^{n} \delta\big((x_i - x_{0i})\big) \tag{5.3}$$

and the n-dimensional Gaussian distribution

$$p_X(\mathbf{x}_0, 0) = \frac{1}{(2\pi)^{n/2} |\boldsymbol{\Sigma}|^{1/2}} \exp\left(-\frac{1}{2}(\mathbf{x} - \boldsymbol{\mu})^T \boldsymbol{\Sigma}^{-1} (\mathbf{x} - \boldsymbol{\mu})\right) \tag{5.4}$$

in the random case.

At infinity, a zero-flux condition is imposed

$$p(x_i, t) \to 0 \quad \text{as } x_i \to \pm\infty, i = 1, 2, \ldots, n \tag{5.5}$$

Without loss of generality, and for a better comparison, the various methods introduced will be examined for the 2d linear case,

$$\begin{Bmatrix} \dot{x_1} \\ \dot{x_2} \end{Bmatrix} = \begin{bmatrix} x_2 \\ -2\xi\omega x_2 - \omega^2 x_1 \end{bmatrix} + \begin{bmatrix} 0 \\ 1 \end{bmatrix} w(t) \tag{5.6}$$

The corresponding FPE is

$$\frac{\partial p}{\partial t} = -\frac{\partial (x_2 p)}{\partial x_1} + \frac{\partial [(2\xi\omega x_2 + x_1) p]}{\partial x_2} + D\frac{\partial^2 p}{\partial x_2^2} \tag{5.7}$$

which, after application of the chain rule, becomes

$$\frac{\partial p}{\partial t} = -x_2 \frac{\partial p}{\partial x_1} + (2\xi\omega x_2 + x_1)\frac{\partial p}{\partial x_2} + 2\xi\omega p + D\frac{\partial^2 p}{\partial x_2^2} \tag{5.8}$$

3 Finite Difference and Finite Element Methods

Many references deal with the application of FE and FD methods to the numerical solution of the Fokker–Planck equation (see e.g. [9, 19]).

3.1 Central Finite Differences

In terms of central finite differences, Eq. (5.8) becomes

$$\begin{aligned}\frac{p_{i,j}^{m+1}-p_{i,j}^{m}}{\Delta t} = &-x_2\frac{p_{i+1,j}^{m}-p_{i-1,j}^{m}}{2\Delta x_1}\\ &+2\xi\omega p_{i,j}^{m}+(2\xi\omega x_2)\frac{p_{i,j+1}^{m}-p_{i,j-1}^{m}}{2\Delta x_2}\\ &+D\frac{p_{i,j+1}^{m}-2p_{i,j}^{m}+p_{i,j-1}^{m}}{\Delta x_2^2}\end{aligned} \tag{5.9}$$

and an explicit formulation is obtained for the probability density function

$$\begin{aligned}p_{i,j}^{m+1} = p_{i,j}^{m}+\Delta t\Bigg(&-x_2\frac{p_{i+1,j}^{m}-p_{i-1,j}^{m}}{2\Delta x_1}\\ &+2\xi\omega p_{i,j}^{m}+(2\xi\omega x_2)\frac{p_{i,j+1}^{m}-p_{i,j-1}^{m}}{2\Delta x_2}\\ &+D\frac{p_{i,j+1}^{m}-2p_{i,j}^{m}+p_{i,j-1}^{m}}{\Delta x_2^2}\Bigg)\end{aligned} \tag{5.10}$$

The boundary conditions are given by $p_{i,j}=0$ for $i,\,j=1,N$. The discretization using central finite differences leads to an explicit scheme, which means that the values $p_{i,j}^{m+1}$ can be calculated directly from values $p_{i,j}^{m}$. Thus, the linear system of equations can be solved directly, and no inversion of the matrix relating $p_{i,j}^{m}$ to $p_{i,j}^{m+1}$ is required.

Explicit finite differences represent the simplest approximation; however, due to stability issues, implicit FD formulations are generally required.

Implicit, higher order finite difference schemes to solve Fokker–Planck equations have been developed by [20]. Higher order FD lead to more accurate results, but they are not used for comparison herein.

3.2 Alternating Directions Implicit Method

The alternating directions implicit method (ADI) is a finite difference scheme, for which the finite difference steps in each direction are resolved separately and in each step implicitly for one dimension and explicitly for the others, leading to a stable formulation. The main advantages are that the resulting operational matrix is tridiagonal and, thus, its inverse can be computed efficiently. Moreover, the dimensionality of the problem is reduced by one, and the problem is reduced to the solution of a series of problems of dimension of one order lower.

In Eq. (5.8), finite differences are first applied implicitly to the x_1-direction

$$\frac{p_{i,j}^{m+1/2} - p_{i,j}^{m}}{\Delta(t/2)} = -x_2 \frac{p_{i+1,j}^{m+1/2} - p_{i-1,j}^{m+1/2}}{2\Delta x_1} + 2\xi\omega p_{i,j}^{m} + (2\xi\omega x_2) \frac{p_{i,j+1}^{m} - p_{i,j-1}^{m}}{2\Delta x_2} + D \frac{p_{i,j+1}^{m} - 2p_{i,j}^{m} + p_{i,j-1}^{m}}{\Delta x_2^2} \tag{5.11}$$

and then to the x_2-direction.

$$\frac{p_{i,j}^{m+1} - p_{i,j}^{m+1/2}}{\Delta(t/2)} = -x_2 \frac{p_{i+1,j}^{m+1/2} - p_{i-1,j}^{m+1/2}}{2\Delta x_1} + 2\xi\omega p_{i,j}^{m+1/2} + (2\xi\omega x_2) \frac{p_{i,j+1}^{m+1} - p_{i,j-1}^{m+1}}{2\Delta x_2} + D \frac{p_{i,j+1}^{m+1} - 2p_{i,j}^{m+1} + p_{i,j-1}^{m+1}}{\Delta x_2^2} \tag{5.12}$$

Both Eq. (5.11) and Eq. (5.12) give $M-2$ tridiagonal linear systems of equations in x_1 for the $j = 2, \ldots, M-1$ values of x_2, and in case of Eq. (5.11) $M-2$ tridiagonal linear systems of equations in x_2 for the $i = 2, \ldots, M-1$ values of x_1.

The computational cost is mainly due to the n times N matrix inversions which are encountered in the n-loops solution for a full time step; n denotes the dimension of the problem and N the number of nodes per dimension.

3.3 Finite Element Method

Reduction of Eq. (5.1) to the weak form and the introduction of shape functions of C^0 continuity lead to

$$\mathbf{C}\dot{p} + Kp = 0 \tag{5.13}$$

where

$$C_{rs}^{e} = \int_{\Omega^e} N_r(\mathbf{x}) N_s(\mathbf{x})\, d\mathbf{x} \tag{5.14}$$

and

$$K_{rs}^{e} = \int_{\Omega^e} \left(\sum_{i=1}^{n} z_i(\mathbf{x}) N_s \frac{\partial}{\partial x_i} N_r \, d\mathbf{x} - \sum_{i=1}^{n} \sum_{j=1}^{n} \frac{\partial}{\partial x_i} N_r \frac{\partial}{\partial x_i} [H_{ij} N_s] \, d\mathbf{x} \right) \times N_r(\mathbf{x}) N_s(\mathbf{x})\, d\mathbf{x} \tag{5.15}$$

The integration over time can be performed in a suitable way using the Crank–Nicholson scheme ($\theta = 0.5$).

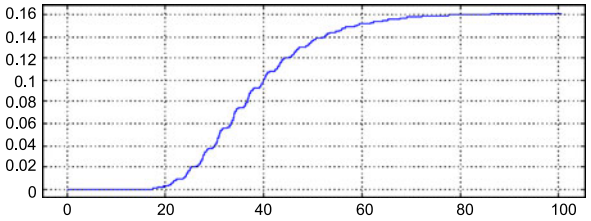

Fig. 5.1 Probability density function $p(0, 0, t)$ at central node over time

3.4 Multi-scale Finite Element Method

The multi-scale FEM used herein was introduced by [14] for the numerical treatment of advection-diffusion equations in fluid dynamics. Then, the methodology was extended by [13] to the special case of the Fokker–Planck equation. Finally, the method was applied to the numerical solution of the Fokker–Planck equation of a 3d linear system [12]; [5] provide an overview of stabilized finite element methods and recent developments of their application to the advection-diffusion equation.

For a description of the method the reader is referred to the aforementioned references. Basically, a multi-scale FEM means that an approximation of the error term from the traditional FE formulation is included at a fine scale into the formulation; the probability density function is then given by

$$p = \hat{p} + p' \tag{5.16}$$

where $\hat{p}$ represents the contribution of the coarse scale and p' the contribution of the fine scale.

3.5 Implementation Within COMSOL/FEAP

The FE code COMSOL provides the possibility to solve partial differential equations by finite differences. For an extensive discussion, refer to the COMSOL documentation [4]. Figure 5.1 shows the results obtained for the FPE for the 2d linear oscillator with parameters to be discussed later.

The multiscale finite element method was implemented by Masud and coworkers into the finite element code FEAP and is used herein for comparison of the 3d examples.

4 Numerical Examples

The numerical methods used in this comparison are:

1. central finite differences (FD)
2. alternating directions implicit method (ADI)

Table 5.1 Parameter for the linear oscillator

μ	σ	ξ	ω	D
$[5, 5]$	$\frac{1}{9}\mathbf{I}(2)$	0.05	1	0.1

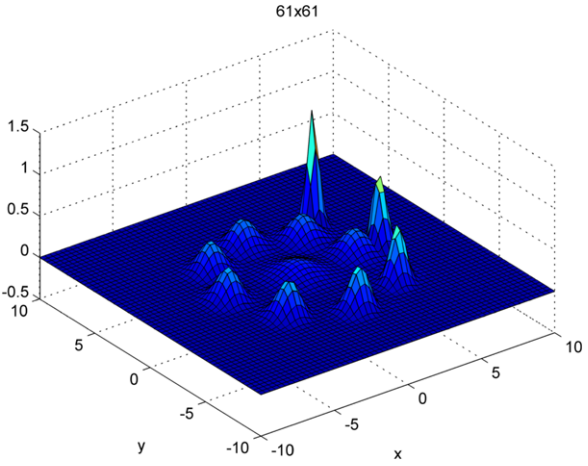

Fig. 5.2 FEM: 61×61—Probability density function $p(t)$ over time

3. Bubnov–Galerkin finite element method (FEM)
4. stabilized multiscale finite element method (MSFEM)

The methods 1–3 are coded in MATLAB and the analysis was carried out on a 64-bit Windows server (32 GB). The results for method 4 are obtained on 32 bit Linux or Windows machines with 2 GB memory using an implementation within FEAP [13].

4.1 2-d Linear Oscillator

The different methods are applied to solve the FPE for the linear oscillator (see Eq. (5.6)). The parameters of the oscillator are chosen according to [16] and are described in Table 5.1, were $\mathbf{I}(2)$ denotes the identity matrix in 2-d:

Finite element results obtained using a 61×61 mesh are shown in Fig. 5.2 and Fig. 5.3. All results are calculated with a time increment of $\Delta t = 0.001$ and a total time of $\tau = 20$ natural periods. The state space is discretized on the domain $[-10, 10] \times [-10, 10]$;

Figure 5.2 shows the evolution of the probability density function over time. In Fig. 5.3 the transient solution for the PDF at the origin is given. The exact stationary value at the origin is $p_{stat}(0, 0) = 1.5915e - 1$.

The accuracy of the numerical solutions are compared at stationarity (i.e., after $t = 20$ cycles) using two error measures. The first, the maximum norm

$$\|e\|_\infty = \left\| p^{ex} - p^{num} \right\|_\infty \tag{5.17}$$

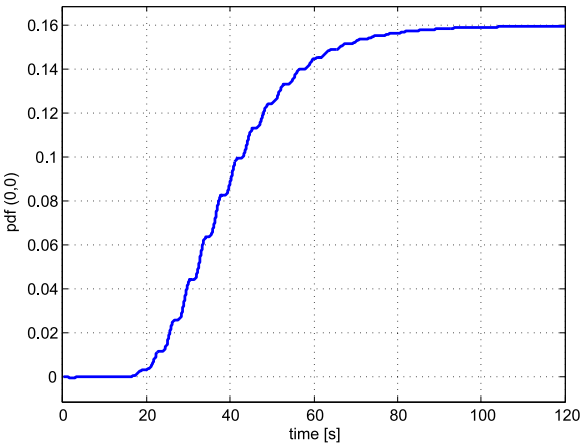

Fig. 5.3 FEM: 61×61—Probability density function at central node $p(0, 0, t)$ over time

is a measure of the maximum error across the entire mesh. The second, the Euclidean norm

$$\|e\|_2 = \left\| p^{ex} - p^{num} \right\|_2 \tag{5.18}$$

can be used to describe the average nodal error $\overline{e} = \|e\|_2 / n_{nodes}$, where n_{nodes} is the total number of nodes.

Table 5.2 correctly visualizes the increasing accuracy for all methods when the mesh is refined. It can also be seen that the FD and ADI deliver similar results. The advantage of the ADI over FD is that the stability of the method allows one to use larger time steps. The FEM provides more accurate results for the same mesh refinement as the finite difference methods. The FEM is the preferable method to investigate the first passage problem in case small probabilities of failure are involved and a highly accurate method is required.

Alternatively, the accuracy of the solution at stationarity can also be represented by comparison of the exact and numerical covariance matrices K_{xx}, the latter computed from FE/FD results for the PDF.

The transient solution for the probability density at the center node can be obtained with all three methods as listed in Table 5.2. Figure 5.4 shows a comparison for the PDF at the origin using finite difference method and different mesh sizes.

Table 5.2 Comparison of the accuracy for the linear oscillator

Method/Mesh	61×61		81×81		101×101		121×121	
	$\|e\|_\infty$	$\|e\|_2$	$\|e\|_\infty$	$\|e\|_2$	$\|e\|_\infty$	$\|e\|_2$	$\|e\|_\infty$	$\|e\|_2$
FD	7.05e-3	2.99e-2	4.169e-3	2.405e-2	2.983e-3	2.201e-2	2.371e-3	2.199e-2
ADI	1.66e-2	4.61e-2	4.144e-3	2.375e-2	2.931e-3	2.149e-2	2.305e-3	2.124e-2
FEM	2.04e-3	1.00e-2	1.712e-3	1.152e-2	1.550e-3	1.370e-2	1.464e-3	1.613e-2

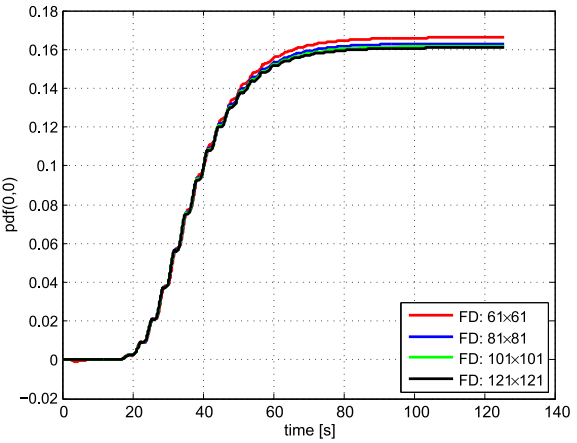

Fig. 5.4 FD—Comparison for probability density function at central node $p(0, 0, t)$ over time

Table 5.3 Parameters for the unimodal Duffing oscillator

μ	σ	ξ	ω	D	γ
$[0, 10]$	$\frac{1}{2}\mathbf{I}(2)$	0.2	1	0.4	0.1

4.2 2-d Duffing Oscillator

Both, the unimodal Duffing-oscillator and the bimodal Duffing-oscillator as well are investigated in the following.

4.2.1 Unimodal

The unimodal Duffing oscillator is considered next:

$$\begin{bmatrix} \dot{x_1} \\ \dot{x_2} \end{bmatrix} = \begin{bmatrix} x_2 \\ -2\xi\omega x_2 - \omega^2 x_1 - \omega^2 \gamma x_1^3 \end{bmatrix} + \begin{bmatrix} 0 \\ 1 \end{bmatrix} w(t) \tag{5.19}$$

The parameters of the oscillator are chosen as in Table 5.3.

The state space is discretized on the domain $[-15, 15] \times [-15, 15]$.

It is known that central finite differences are not suitable in case of nonlinearities, but ADI can be utilized nonetheless. When the Duffing-oscillator is analyzed, it is found that the ADI can be used due to its implicit formulation with the largest time step Δt, thus providing a good compromise between accuracy and efficiency as can be seen from Table 5.4. The time steps used are $\Delta t = 1e-2$ (ADI), $\Delta t = 1e-3$ (FEM) and $\Delta t = 5e-4$ (FEM: mesh 101).

Table 5.4 Comparison of the accuracy for the unimodal Duffing oscillator

Method/Mesh	61×61		81×81		101×101	
	$\|e\|_\infty$	$\|e\|_2$	$\|e\|_\infty$	$\|e\|_2$	$\|e\|_\infty$	$\|e\|_2$
ADI	1.7832e-2	4.9323e-2	9.6731e-3	3.5553e-2	6.1694e-3	2.8444e-2
FEM	2.6002e-3	1.1587e-2	1.3999e-3	8.5297e-3	9.3290e-4	6.8215e-3

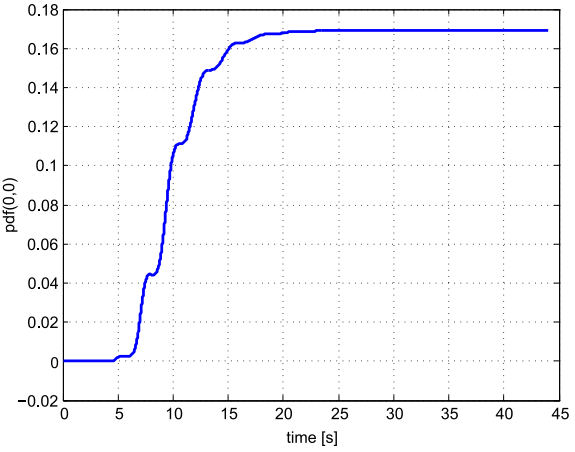

Fig. 5.5 FEM: 101×101—Probability density function at central node $p(0, 0, t)$ over time

The exact analytical expression for the stationary PDF of the unimodal Duffing oscillator of Eq. (5.19) is given by

$$\begin{aligned} \sigma_{x_0}^2 &= \frac{\pi G_0}{4\xi\omega_0^3} \\ \sigma_{v_0}^2 &= \omega_0^2 \sigma_{x_0}^2 \\ p_X(\mathbf{x}) &= C \exp\left(-\frac{1}{2\sigma_{x_0}^2}\left(x^2 + \frac{\gamma}{2}x^4\right) - \frac{1}{2}\sigma_{v_0}^2 v^2\right) \end{aligned} \tag{5.20}$$

The value of the stationary probability density function at the central node is $p_{stat}(0, 0) = 1.6851e - 1$. Figure 5.5 shows the evolution of the PDF at central node $p(0, 0, t)$ over time using the FEM and a mesh of 101×101.

4.2.2 Bimodal

The equations for the bimodal Duffing oscillator are characterized by the changed sign of the term $\omega^2 x_1$.

$$\begin{bmatrix} \dot{x_1} \\ \dot{x_2} \end{bmatrix} = \begin{bmatrix} x_2 \\ -2\xi\omega x_2 + \omega^2 x_1 - \omega^2 \gamma x_1^3 \end{bmatrix} + \begin{bmatrix} 0 \\ 1 \end{bmatrix} w(t) \tag{5.21}$$

Table 5.5 Parameter for the bimodal Duffing oscillator

μ	σ	ξ	ω	D	γ
$[0, 10]$	$\frac{1}{2}\mathbf{I}(2)$	0.2	1	0.4	0.1

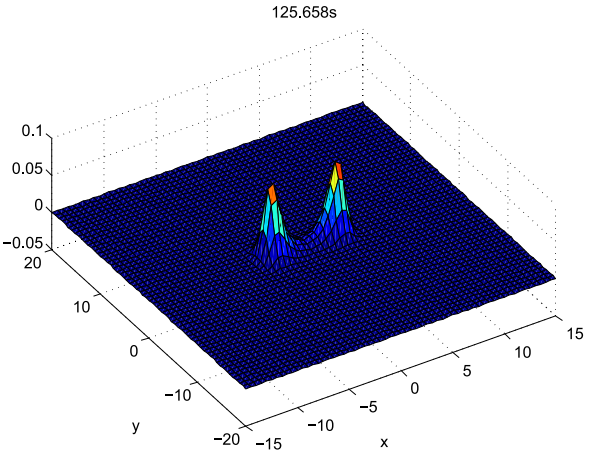

Fig. 5.6 61×61: Stationary probability density function p_{stat}

The parameters of the oscillator are chosen according to [16] and are given in Table 5.5.

The state space is discretized on the domain $[-15, 15] \times [-15, 15]$. Again, the ADI provides a tool for obtaining accurate results rather quickly.

In Fig. 5.6 the PDF is depicted for stationary conditions and a 61×61 mesh. A comparison of the evolution of the probability density function at the origin is shown in Fig. 5.7 for FEM and different meshes.

To compare the solution, the analytical expression according to [3] should be used. The exact analytical expression for the bimodal Duffing oscillator of Eq. (5.21) is given as

$$p_X(\mathbf{x}) = C \exp\left(-\frac{1}{2\sigma_{x_0}^2}\left(-x^2 + \frac{\gamma}{2}x^4\right) - \frac{1}{2}\sigma_{v_0}^2 v^2\right)$$

The value of the stationary PDF at the central node is $p_{stat}(0, 0) = 8.3161e-3$. Table 5.6 shows a comparison of the accuracy for different mesh sizes for the bimodal Duffing oscillator. The maximum value of the stationary PDF of the bimodal oscillator at $x_{1,2} = \pm\sqrt{1/\gamma} = \pm 3.1623$ and $y_{1,2} = 0$ is $p_{stat}(x_{1,2}, 0) = 0.1013$. A comparison of the evolution of the probability density function at the mesh point $(x = 3,\ y = 0)$ which is closest to the maximum of the PDF is shown in Fig. 5.8 for FEM and different meshes; $p_{stat}(3, 0) = 0.0988$.

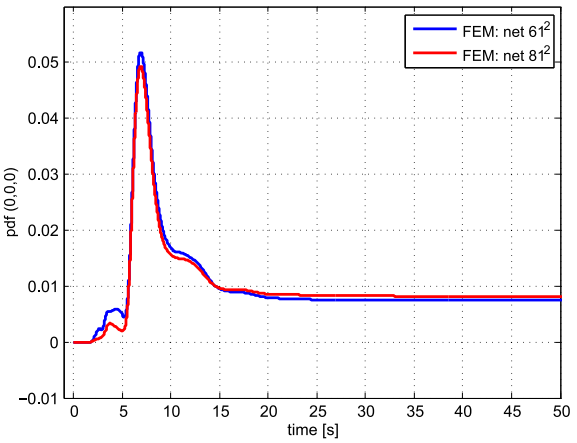

Fig. 5.7 FEM: Comparison of the probability density function at the central node $p(0,0,t)$ over time

4.3 3-d Linear Oscillator

A 3-rd state variable is introduced in terms of a low pass filter for the white noise excitation which is applied to the linear 2d system.

$$\begin{bmatrix} \dot{x_1} \\ \dot{x_2} \\ \dot{x_3} \end{bmatrix} = \begin{bmatrix} x_2 \\ -2\xi\omega x_2 - \omega^2 x_1 + x_3 \\ -\alpha x_3 \end{bmatrix} + \begin{bmatrix} 0 \\ 0 \\ 1 \end{bmatrix} w(t) \tag{5.22}$$

The parameters of the 3d linear oscillator are given in Table 5.7.

Tables 5.8 and 5.9 show a comparison of the accuracy of the results for the linear oscillator. The time step is chosen to be $\Delta t = 0.01$, and only for FEM (net 81^3) $\Delta t = 0.001$ is required. The exact stationary value of the PDF at the origin is $p_{stat}(0,0,0) = 0.2409$. Figure 5.9 shows a comparison for the evolution of the PDF at the central node. The exact analytical solution is compared with the ADI and the FEM using various mesh sizes.

Table 5.6 Comparison of the accuracy for the bimodal Duffing oscillator

Method/Mesh	61×61		81×81		101×101	
	$\|e\|_\infty$	$\|e\|_2$	$\|e\|_\infty$	$\|e\|_2$	$\|e\|_\infty$	$\|e\|_2$
ADI	4.7186e-2	1.8229e-1	1.1899e-2	4.2491e-2	7.5077e-3	3.0640e-2
FEM	6.8085e-3	1.9074e-2	2.6024e-3	1.1265e-2	2.8419e-3	1.3709e-2

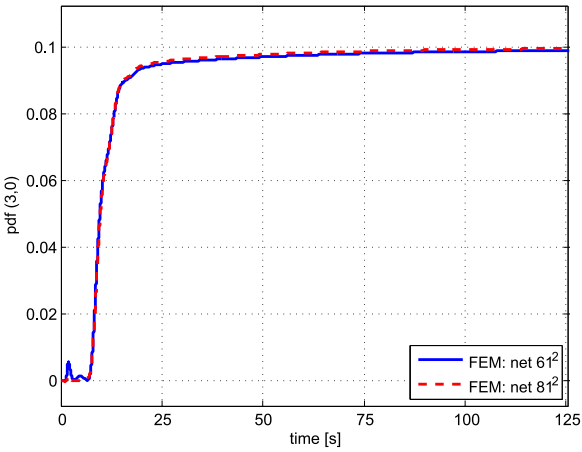

Fig. 5.8 FEM: Comparison of the probability density function at the node $p(3,0,t)$ over time

Table 5.7 Parameter for the 3d linear oscillator

μ	σ	ξ	ω	D	α
$[0,0,0]$	$0.2\mathbf{I}(3)$	0.2	1	0.4	1

4.4 3-d Duffing Oscillator

$$\begin{bmatrix} \dot{x_1} \\ \dot{x_2} \\ \dot{x_3} \end{bmatrix} = \begin{bmatrix} x_2 \\ -2\xi\omega x_2 - \omega^2 x_1 - \omega^2 \gamma x_1^3 + x_3 \\ -\alpha x_3 \end{bmatrix} + \begin{bmatrix} 0 \\ 0 \\ 1 \end{bmatrix} w(t) \tag{5.23}$$

The parameters of the 3d Duffing oscillator are given in Table 5.10.

Table 5.8 Comparison of the accuracy for the 3-d linear oscillator

Method/Mesh	25^3		41^3	
	$\|e\|_\infty$	$\|e\|_2$	$\|e\|_\infty$	$\|e\|_2$
ADI	1.8009e-1	3.6649e+0	4.8336e-2	4.8748e-1
FEM	6.5802e-3	4.6480e-2	3.5574e-3	4.6357e-2
MSFEM	1.2533e-2	5.0262e-2	—	—

Table 5.9 Comparison of the accuracy for the 3-d linear oscillator

Method/Mesh	61^3		81^3		101^3	
	$\|e\|_\infty$	$\|e\|_2$	$\|e\|_\infty$	$\|e\|_2$	$\|e\|_\infty$	$\|e\|_2$
ADI	1.2542e-2	2.1170e-1	6.9165e-3	1.8067e-1	4.3899e-3	1.6063e-1
FEM	1.4081e-3	3.4554e-2	3.9016e-4	2.4920e-2	—	—

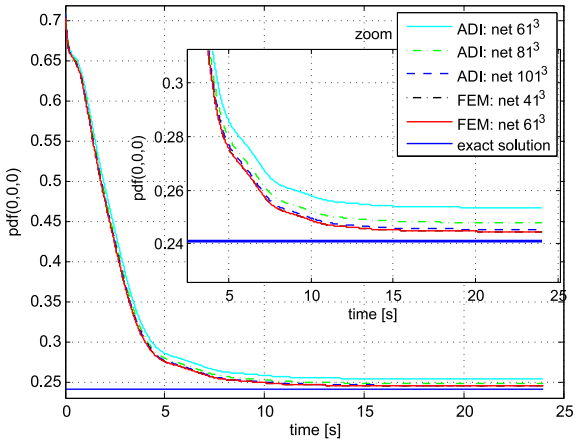

Fig. 5.9 Probability density function at the central node $p(0, 0, 0, t)$ over time

Table 5.10 Parameters for the 3d Duffing oscillator

μ	σ	ξ	ω	D	α	γ
$[0, 0, 0]$	$0.2\mathbf{I}(3)$	0.2	1	0.4	1	0.1

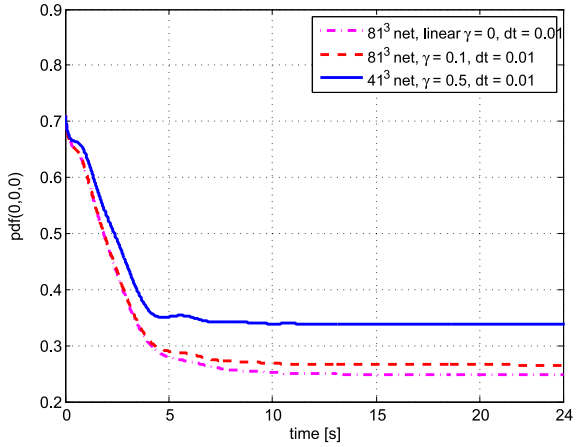

Fig. 5.10 Probability density function at the central node $p(0, 0, 0, t)$ over time

Figure 5.10 shows converged results for the evolution of the PDF at the origin over time using ADI for two different degrees of nonlinearity and for the corresponding linear system ($\gamma = 0$).

5 Discussion

Despite the greater numerical effort, the FEM is preferable over FD, because it yields more accurate results. However, at this time the FEM is only suitable for

dimension ≤ 3. In the case of 3d and 4d problems, the stabilized multi-scale FEM provides a tool with a high order of accuracy, preserving numerical efficiency due to the fact that a coarser mesh size can be used.

The first effective numerical solution for 4d problems was reported by [21] in terms of high-order finite differences. The advantage of operator splitting methods including the ADI is the stability of the method, meaning that larger time steps (when compared to FEM) can be used, thus speeding up the analysis as the dimensionality of the problem is reduced by one.

The recently introduced PUFEM (see Kumar et al.) represents a possibility to obtain good results with coarse mesh sizes. The price paid is the computational overhead required in order to allow for the proposed coarse mesh size.

From the above discussion it is clear that future developments will be bounded by the so-called curse of dimensionality for some time.

Acknowledgements This research was partially supported by the Austrian Research Council FWF under Project No. J2989-N22 (LP, Schrödinger scholarship).

References

1. Bergman, L.A., Heinrich, J.C.: On the reliability of the linear oscillator and systems of coupled oscillators. Int. J. Numer. Methods Eng. **18**(9), 1271–1295 (1982)
2. Caughey, T.K.: Derivation and application of the Fokker–Planck equation to discrete nonlinear dynamic systems subjected to white random excitation. J. Acoust. Soc. Am. **35**(11), 1683–1692 (1963)
3. Caughey, T.K.: Nonlinear Theory of Random Vibrations. Elsevier, Amsterdam (1971)
4. COMSOL 5.5: Theory manual. COMSOL (2011)
5. Franca, L.P., Hauke, G., Masud, A.: Revisiting stabilized finite element methods for the advective-diffusive equation. Comput. Methods Appl. Mech. Eng. **195**(13–16), 1560–1572 (2006)
6. Kumar, M., Chakravorty, S., Junkins, J.L.: A homotopic approach to domain determination and solution refinement for the stationary Fokker–Planck equation. Probab. Eng. Mech. **24**(3), 265–277 (2009)
7. Kumar, M., Chakravorty, S., Junkins, J.L.: A semianalytic meshless approach to the transient Fokker–Planck equation. Probab. Eng. Mech. **25**(3), 323–331 (2010)
8. Kumar, M., Chakravorty, S., Singla, P., Junkins, J.L.: The partition of unity finite element approach with hp-refinement for the stationary Fokker–Planck equation. J. Sound Vib. **327**(1–2), 144–162 (2009)
9. Kumar, P., Narayana, S.: Solution of Fokker–Planck equation by finite element and finite difference methods for nonlinear systems. Sâdhana **31**(4), 445–461 (2006)
10. Langley, R.S.: A finite element method for the statistics of non-linear random vibration. J. Sound Vib. **101**(1), 41–54 (1985)
11. Lin, Y.K.: Probabilistic Theory of Structural Dynamics. Krieger, Melbourne (1976)
12. Masud, A., Bergman, L.A.: Solution of the four dimensional Fokker–Planck equation: still a challenge. In: Augusti, G., Schuëller, G.I., Ciampoli, M. (eds.) ICOSSAR 2005. Millpress, Rotterdam (2005)
13. Masud, A., Bergman, L.A.: Application of multi-scale finite element methods to the solution of the Fokker–Planck equation. Comput. Methods Appl. Mech. Eng. **194**(12–16), 1513–1526 (2005)

14. Masud, A., Khurram, R.A.: A multiscale/stabilized finite element method for the advection-diffusion equation. Comput. Methods Appl. Mech. Eng. **193**(21–22), 1997–2018 (2004)
15. Peaceman, D.W., Rachford, H.H.: The numerical solution of parabolic and elliptic differential equations. J. Soc. Ind. Appl. Math. **3**, 28–41 (1955)
16. Spencer, B.F., Bergman, L.A.: On the numerical solutions of the Fokker–Planck equations for nonlinear stochastic systems. Nonlinear Dyn. **4**, 357–372 (1993)
17. von Wagner, U., Wedig, W.V.: On the calculation of stationary solutions of multi-dimensional Fokker–Planck equations by orthogonal functions. Nonlinear Dyn. **21**(3), 289–306 (2000)
18. Wedig, W.V., von Wagner, U.: Extended Laguerre polynomials for nonlinear stochastic systems. In: Computational Stochastic Mechanics. Balkema, Rotterdam (1999)
19. Wijker, J.: Random Vibrations in Spacecraft Structures Design: Theory and Applications. Solid Mechanics and Its Applications, vol. 165. Springer, Berlin (2009)
20. Wojtkiewicz, S.F., Bergman, L.A., Spencer, B.F.: High fidelity numerical solutions of the Fokker–Planck equation. In: Seventh International Conference on Structural Safety and Reliability (ICOSSAR'97) (1998)
21. Wojtkiewicz, S.F., Bergman, L.A., Spencer, B.F., Johnson, E.A.: Numerical solution of the four-dimensional nonstationary Fokker–Planck equation. In: Narayanan, S., Iyengar, R.N. (eds.) IUTAM Symposium on Nonlinearity and Stochastic Structural Dynamics (1999)
22. Xie, W.-X., Cai, L., Xu, W.: Numerical simulation for a Duffing oscillator driven by colored noise using nonstandard difference scheme. Physica A **373**, 183–190 (2007)
23. Zorzano, M., Mais, H., Vázquez, L.: Numerical solution of two dimensional Fokker–Planck equations. Appl. Math. Comput. **98**, 109–117 (1999)

Chapter 6
A Comparative Study of Uncertainty Propagation Methods in Structural Problems

Manuele Corradi, Marco Gherlone, Massimiliano Mattone, and Marco Di Sciuva

Abstract Several uncertainty propagation algorithms are available in literature: (i) MonteCarlo simulations based on response surfaces, (ii) approximate uncertainty propagation algorithms, and (iii) non probabilistic algorithms. All of these approaches are based on some a priori assumptions about the nature of design variables uncertainty and on the models and systems behavior. Some of these assumptions could misrepresent the original problem and, consequently, could yield to erroneous design solutions, in particular where the prior information is poor or inexistent (complete ignorance). Therefore, when selecting a method to solve an uncertainty based design problem, several aspects should be considered: prior assumptions, non-linearity of the performance function, number of input random variables and required accuracy. It could be useful to develop some guidelines to choose an appropriate method for a specific situation.

In the present work some classical structural problems will be studied in order to investigate which probabilistic approach, in terms of accuracy and computational cost, better propagates the uncertainty from input to output data. The methods under analysis will be: Univariate Dimension Reduction methods, Polynomial Chaos Expansion, First-Order Second Moment method, and algorithms based on the Evidence Theory for epistemic uncertainty. The performances of these methods will be compared in terms of moment estimations and probability density function construction corresponding to several scenarios of reliability based design and robust design. The structural problems presented will be: (1) the static, dynamic and buck-

M. Corradi (✉) · M. Gherlone · M. Mattone · M. Di Sciuva
Department of Aeronautics and Space Engineering, Politecnico di Torino, Corso Duca degli Abruzzi 24, 10129 Torino, Italy
e-mail: manuele.corradi@polito.it

M. Gherlone
e-mail: marco.gherlone@polito.it

M. Mattone
e-mail: massimiliano.mattone@polito.it

M. Di Sciuva
e-mail: marco.disciuva@polito.it

M. Papadrakakis et al. (eds.), *Computational Methods in Stochastic Dynamics*, Computational Methods in Applied Sciences 26,
DOI 10.1007/978-94-007-5134-7_6,

ling behavior of a composite plate, (2) the reconstruction of the deformed shape of a structure from measured surface strains.

1 Introduction

The design for reliability, as well as robust design, is phased in over last decades in the structural design. Although these concepts are well-known in many engineering fields, the high computational cost of the mathematical approaches needed to perform these kinds of analysis, have set back their application in the aerospace structural design. Although in this last field, the problems that deal with the input variable uncertainties are known since the beginning of the aviation history, they are coped with deterministic methods based on the safety factor approach. The diffusion of components based on composite materials, in secondary and primary aerospace structures, and the dropping of aerospace and aviation companies' profit have reawaken the interest in design philosophies that deal with the uncertainty in a more effective way. For this reason, mathematicians and researchers have been urged on the study of new numerical approaches for an accurate Uncertainty Propagation (UP) from input to output data. Traditionally, both the reliability and the robustness of a design configuration have been studied using the MonteCarlo simulation; although it is the most accurate method, its computational cost could be prohibitive. For this reason several alternative approaches have been developed to face UP.

Most of the available UP algorithms have particular characteristics that make them appropriate for some specific problems but their capabilities are not fully exploited in all kinds of applications. First of all it is possible to distinguish between algorithms for the study of aleatory uncertainty and approaches that deal with the epistemic uncertainty. This classification can be based on the prior hypotheses needed to simulate the prior uncertainty. In order to model the epistemic uncertainty by means of probabilistic (aleatory) algorithms, some prior hypotheses should be adopted to transform the epistemic information into a probability distribution function (epistemic algorithms need not such assumptions). On the other hand, a probabilistic problem may be studied by means of an epistemic algorithm if the prior probability density functions are transformed into set-based information.

The UP algorithms based on the probability theory are usually classified into five categories [1]: (1) Simulation based methods: these techniques are based on the simulation of the problem in proper trial points, selected according to the stochastic characteristics of the input variables. MonteCarlo Simulation (MCS) is certainly the most known and used of these methods. (2) Local expansion based methods: these algorithms, also known as perturbation methods, are based on the local series expansion of output functions in terms of input random parameters. The methods based on Taylor expansion, such as the FOSM (First Order Second Moment) or the SOSM (Second Order Second Moment) methods, belong to this class. (3) Most Probable Points (MPP) based methods: this class includes the First and Second Order Reliability Methods (FORM and SORM, respectively). (4) Functional expansion

based methods: they rely on a stochastic expansion of the performance function. The most known method of this class is the Polynomial Chaos Expansion (PCE). (5) Numerical integration based methods: these techniques are based on the numerical solving of integral equations for the statistical moments. These methods don't yield directly the performance joint probability function, but the corresponding statistical moments; by using the Pearson System and knowing the first four statistical moments, the probability distribution function can be obtained.

Several factors affect the choice of a suitable UP approach: (i) the identification and the classification of the input uncertainty, (ii) the definition of the required outputs (the first two statistical moments in robust design and the probability density function or the most probable points in a reliability based analysis), and (iii) the mathematical characteristics of the studied model (if the first order interactions cannot be neglected the Univariate Dimension Reduction method does not yield accurate prediction while if the performance function is non linear the methods based in Taylor local expansion are not accurate). This last information can be obtained using some numerical tools, such as the sensitivity analysis.

The main objective of this work is a comparative study of some of the most common and newest UP algorithms for both aleatory and epistemic uncertainties. As far as the first ones, the limits and merits of the Univariate Dimension Reduction method (UDR), of the Polynomial Chaos Expansion (PCE), and of the First Order Second Moments algorithm (FOSM) will be analyzed and discussed. These methods will be tested and compared on some numerical test functions and a classical structural problem: the probabilistic study of static, dynamic and buckling behavior of a composite plate. The sensitivity analysis has been performed in order to study the mathematical characteristics of the model. In the second part of the present work a probabilistic approach based on the UDR is compared with an epistemic approach based on the evidence theory. The structural application used as a test case for the comparison is an inverse problem: reconstruction of the deformed shape of a beam from measured surface strains using the inverse Finite elements Method (iFEM) [2, 3].

2 Uncertainty Propagation Algorithms

In this section, a review of some uncertainty propagation algorithms will be presented in order to set the framework for the assessment and comparison, through some structural applications, discussed in Sect. 3.

2.1 The Univariate Dimension Reduction Method (UDR)

This method involves an additive decomposition of a multidimensional integral function to multiple one-dimensional integral functions. The technique is suitable

for calculating the stochastic moments of a system response function, as Rahman and Xu have shown [4–6].

The stochastic moments of a probability distribution may be calculated as follows

$$m_l = \zeta\left[Y^l(X)\right] = \int_{-\infty}^{+\infty} \cdots \int_{-\infty}^{+\infty} y^l(x) f_X(x)\, dx \quad l = 0, 1, \ldots, L \tag{6.1}$$

where m_l is the l^{th}-order statistical moment (i.e., $l = 1$ is the mean value, $l = 2$ is the variance, etc.), $f_X(X)$ is the system response joint probability density function, $y(X)$ is the deterministic response when the input variables assume the values collected in the vector $X = \{x_1, \ldots, x_n\}^T$, and $Y(X) = y^l(X) f_X(X)$ is the performance function. The latter can be approximated as the sum of univariate functions, each one depending on only one random variable at a time and the other variables being fixed to nominal values

$$\begin{aligned} Y(x_1, \ldots, x_n) &\cong \tilde{Y}(X) \\ &\equiv \sum_{j=1}^{N} Y(\mu_1, \ldots, \mu_{j-1}, x_j, \mu_{j+1}, \ldots, \mu_N) - \cdots \\ &\quad + (N-1) \cdot y(\mu_1, \ldots, \mu_N) \end{aligned} \tag{6.2}$$

where $\mu_j$is the first moment of the stochastic variable x_j, $Y(\mu_1, \ldots, \mu_{j-1}, x_j, \mu_{j+1}, \ldots, \mu_N)$ is the stochastic response of the system only depending on the x_j random variable, and $y(\mu_1, \ldots, \mu_N)$ is the deterministic response of the system depending on the nominal value of the N input variables. Adopting the dimension-reduction procedure, the expression of statistical moments (6.1) can be rewritten as:

$$m_l = \int_{-\infty}^{+\infty} \cdots \int_{-\infty}^{+\infty} \sum_{j=1}^{N} \begin{pmatrix} Y(\mu_1, \ldots, \mu_{j-1}, x_j, \mu_{j+1}, \ldots, \mu_N) - \\ +(N-1) \cdot y(\mu_1, \ldots, \mu_N) \end{pmatrix}^l dx \tag{6.3}$$

To solve the univariate integration in the context of the UDR method, Xu and Rahman [4] suggest the use of the moment based quadrature rule. The evaluation of integration points x_j involves the solution of the following equation

$$x_j^n - r_{j,1} x_j^{n-1} + r_{j,2} x_j^{n-2} - \cdots + (-1)^n r_{j,n} = 0 \tag{6.4}$$

where the coefficients r_j are solution of the following linear system of equations

$$\begin{bmatrix} \mu_{j,n-1} & -\mu_{j,n-2} & \mu_{j,n-3} & \cdots & (-1)^{n-1}\mu_{j,0} \\ \mu_{j,n} & -\mu_{j,n-1} & \mu_{j,n-2} & \cdots & (-1)^{n-1}\mu_{j,1} \\ \mu_{j,n+1} & -\mu_{j,n} & \mu_{j,n-1} & \cdots & (-1)^{n-1}\mu_{j,2} \\ \cdots & \cdots & \cdots & \cdots & \cdots \\ \mu_{j,2n-2} & -\mu_{j,2n-3} & \mu_{j,2n-4} & \cdots & (-1)^{n-1}\mu_{j,n-1} \end{bmatrix} \begin{bmatrix} r_{j,1} \\ r_{j,2} \\ r_{j,3} \\ \cdots \\ r_{j,n} \end{bmatrix} = \begin{bmatrix} \mu_{j,n} \\ \mu_{j,n+1} \\ \mu_{j,n+2} \\ \cdots \\ \mu_{j,2n-1} \end{bmatrix} \tag{6.5}$$

$\mu_{j,i}$ $(i = 1, \ldots, n)$ represents the i$^{\text{th}}$ stochastic moment of the j$^{\text{th}}$ input variable. Thus, the univariate integral can be numerically solved as

$$\int_{-\infty}^{\infty} y^l(\mu_{1,}, \ldots, x_j, \ldots, \mu_N) f_{X_j}(x_j) \cdot dx_j \cong \sum_{i=1}^{n} w_{j,i} y^l(\mu_{1,}, \ldots, x_j, \ldots, \mu_N) \tag{6.6}$$

where f_{x_j} is the probability density function of input variable x_j. The weight $w_{j,i}$ appearing in Eq. (6.6) are evaluated using the following expression

$$w_{i,j} = \frac{\sum_{k=0}^{n-1}(-1)^k \mu_{j,(n-h-1)} \cdot q_{j,(ik)}}{\prod_{k=1,k\neq 1}^{n}(x_{j,i} - x_{j,k})} \qquad q_{j,i_0} = 1; \qquad q_{j,ik} = r_{j,k} - x_{j,i} \cdot q_{j,i(k-1)} \tag{6.7}$$

2.2 The Polynomial Chaos Expansion (PCE)

The Polynomial Chaos Expansion was introduced by Wiener [7] and is based on the approximation of each random variable by means of a suitable polynomial expansion about centered normalized Gaussian variables.

Any set $X = \{x_1, \ldots, x_n\}^T$ of independent variables (i.e. a set of Gaussian variables) can be expressed as function of a set $\xi = \{\xi_1, \ldots, \xi_n\}$ of independent normal variables; this is also known as normalization process.

$$X = f(\xi) \tag{6.8}$$

Hence, a performance function $y = Y(X)$ could be transformed into a function expressed in terms of ξ and, afterwards, approximated by means of the Polynomial Chaos Expansion (PCE) on the vector space

$$Y(X) = a_0\Gamma_0 + \sum_{i_1=1}^{\infty} a_{i_1}\Gamma_1(\xi_1) + \sum_{i_1=1}^{\infty}\sum_{i_2=1}^{i_1} a_{i_1 i_2}\Gamma_2(\xi_{i_1}, \xi_{i_2}) + \sum_{i_1=1}^{\infty}\sum_{i_2=1}^{i_1}\sum_{i_3=1}^{i_2} a_{i_1 i_2 i_3}\Gamma_3(\xi_{i_1}, \xi_{i_2}, \xi_{i_3}) + \cdots \tag{6.9}$$

where $a = [a_0, \ldots, a_n]$ is the vector of the expansion unknown terms and $\Gamma_p(\xi_1, \ldots, \xi_n)$ are the multidimensional Hermite polynomials (only if the input random variables are defined by a normal probability distribution) of order p.

Cameron and Martin have shown that this kind of series is convergent in the L_2-sense [8]. In order to simplify the notation a univocal relation between the functional

Γ and a new functional Ψ is defined. Hence, the PCE expansion, expressed by Eq. (6.9), can be rewritten as follows

$$Y(X) = \sum_{k=0}^{\infty} \beta_k \Psi_k\big(\xi(X)\big) \tag{6.10}$$

In the present work the classical convention is adopted:

- $\Psi_0 = 1$: is the 0^{th}-order polynomial
- β_k are the constant coefficients of the expansion
- Ψ_k are multivariate Hermite polynomials, orthogonal in the L_2-space. These polynomials are the product of the proper set of univariate Hermite polynomials [9].

The expansion is normally truncated at a selected order P

$$Y(X) \approx \hat{Y}(X) = \sum_{k=0}^{P} \beta_k \Psi(\xi)_k \tag{6.11}$$

The number of unknown coefficients β_k (6.11) can be evaluated using the following expression

$$P + 1 = \frac{(p+n)!}{p!n!} \tag{6.12}$$

The procedure described above is general, but the Hermite polynomials can be used only in the case of input variables with Gaussian probability distribution function. Xiu and Karniadakis [9] have extended the PCE applicability to all kinds of input distribution function, adopting the Wiener–Askey scheme for non Gaussian input distribution. They have proposed to use the Askey scheme to combine the non Gaussian input distribution with orthogonal polynomial family; in this way the expansion convergence is guaranteed for all kind of input PDF. As well as the Hermite polynomials are orthogonal in the Hilbert space, in the same way all polynomials, adopted in the Wiener–Askey [9] scheme are orthogonal in the Hilbert space and form an Hilbert basis of the corresponding space.

The set $\beta = \{\beta_0, \ldots, \beta_n\}^T$ of the PCE unknown coefficients, can be approximated by a new vector $\hat{\beta}$, obtained solving the following least squares problem

$$\hat{\beta} = \arg\min_{\beta} \sum_{i=1}^{N} \left(Y(X_i) - \sum_{k=0}^{P} \beta_k \psi_k(\xi_i) \right)^2 \tag{6.13}$$

where N is the training points set size; generally, it is convenient that $N > p + 1$.

2.3 The First Order Second Moment Algorithm (FOSM)

In this approach a performance function $Y(X)$ is approximated by means of a first order Taylor-series expansion around the design point [10]

$$Y(X) \cong Y(\bar{X}) + \sum_{i=1}^{n} \left.\frac{\partial Y}{\partial x_i}\right|_{\bar{X}} (x_i - \bar{x}_i) \tag{6.14}$$

Substituting Eq. (6.14) in the expectation definition (mean)

$$E\big[Y(X)\big] = E\big[Y(\bar{X})\big] + E\left[\sum_{i=1}^{n} \left.\frac{\partial Y}{\partial x_i}\right|_{\bar{X}} (x_i - \bar{x}_i)\right] \tag{6.15}$$

and considering that:

$$E\left[\sum_{i=1}^{n} \left.\frac{\partial Y}{\partial x_i}\right|_{\bar{X}} (x_i - \bar{x}_i)\right] = \sum_{i=1}^{n} \left.\frac{\partial Y}{\partial x_i}\right|_{\bar{X}} E\big[(x_i - \bar{x}_i)\big] = 0 \tag{6.16}$$

$$E\big[(x_i - \bar{x}_i)\big] = E(x_i) - \bar{x}_i = \bar{x}_i - \bar{x}_i = 0 \tag{6.17}$$

the performance function mean value, estimated by means of FOSM, assumes the following expression

$$E\big[Y(X)\big] = Y(\bar{X}) \tag{6.18}$$

Now, given the variance definition

$$Var\big[Y(X)\big] = E\big[\big(Y(X) - E\big(Y(X)\big)^2\big)\big] \equiv \sigma^2\big[Y(X)\big] \tag{6.19}$$

and substituting in it Eq. (6.14), the variance assumes the following expression

$$\sigma\big[Y(X)\big] = \sum_{i=1}^{n}\sum_{j=1}^{m} \left.\frac{\partial Y}{\partial x_i}\right|_{\bar{x}_i} \left.\frac{\partial Y}{\partial x_j}\right|_{x_j} \cdot COV(x_i, x_j) \tag{6.20}$$

where $COV(x_i, x_j)$ is the covariance matrix.

2.4 The Evidence Theory

The Evidence Theory is a non probabilistic approach used to characterize the effect of epistemic uncertainty on a system.

Given a design variable x_1, the prior information, or evidence, consists of n intervals, obtained from s sources $[x_{1,i}^l, x_{1,i}^u]$ (with $i = 1, \ldots, s$) that enclose the supposed true value. Clearly, the traditional probability theory cannot handle this type of evidence, without making some assumptions that can misrepresent the nature of the information. Several combination rules have been formulated to handle this kind

of prior information [11, 12]; in this work, the Dempster–Shafer combination rule is adopted.

When a source provides a set of information, this means that the variable can assume any value inside the interval. The probability that a variable x_1 assumes the value $\bar{x}_1$ is not defined by a probability distribution function but is included between a maximum probability (plausibility), and a minimum probability (belief). In order to define the plausibility and the belief, the basic probability assignment (m) must be introduced; m defines a mapping of the variable prior information. Formally the basic probability assignment function is defined by means of the following expressions

$$m : \mathrm{P}(x_1) \rightarrow [0, 1] \tag{6.21}$$

$$m(\varnothing) = 0 \tag{6.22}$$

$$m = 1 \quad \text{if } \bar{x}_1 \in S_i \text{ with } i = 1, \ldots, s \tag{6.23}$$

where $\mathrm{P}(x_1)$ represents the power set of x_1 (defined, according to the axiomatic set theory [12] as the set of all subset of S), while $\varnothing$ is the null set and S_i is the i^{th} evidence set. According to the previous equations, the basic probability assignment (BPA) assumes any value included between 0 and 1; if $\bar{x}_1$ does not belong to any subset, the basic probability assignment assumes value 0 while if $\bar{x}_1$ belongs to every subset, it assumes the value 1. Once defined the basic probability assignment m, the plausibility and belief probability measures can be introduced. Given a set $C = [D(x_1)^-, \bar{x}_1]$, where $\bar{x}_1$ is a generic value of the variable x_1 on its domain $D(x_1)$, while $D(x_1)^-$ represents the lower domain boundary, the plausibility can be expressed by

$$Pl(C_1) = \sum_{C_1 \cap s^i_{x_1} \neq 0} m_{x_{1,i}}\left(S^i_{x_1}\right) \tag{6.24}$$

while the belief is defined as

$$Bel(C_1) = \sum_{S^i_{x_1} \subseteq C_1} m_{x_1}\left(S^i_{x_1}\right) \tag{6.25}$$

In other words, the plausibility is the sum of all BPA of the sets $S^i_{x_1}$ which intersect the set of interest C_1, hence it represents the maximum probability that a variable x_1 assumes a given value $\bar{x}_1$. On the other hand, the belief is defined as the sum of all BPA of the sets $S^i_{x_1}$ that $S^i_{x_1} \subseteq C_1$ hence it is a measure of the minimum probability that a variable x_1 assumes a given value $\bar{x}_1$.

The probability lies between the plausibility and the belief

$$Bel(C_1) \leq P(C_1) \leq Pl(C_1) \tag{6.26}$$

and, only when plausibility and belief are overlapped, it can be univocally defined.

In a problem with n input variables there is the need to transfer the BPA values m_{x_j}, evaluated for each variable, into an equivalent information in the n-dimensional

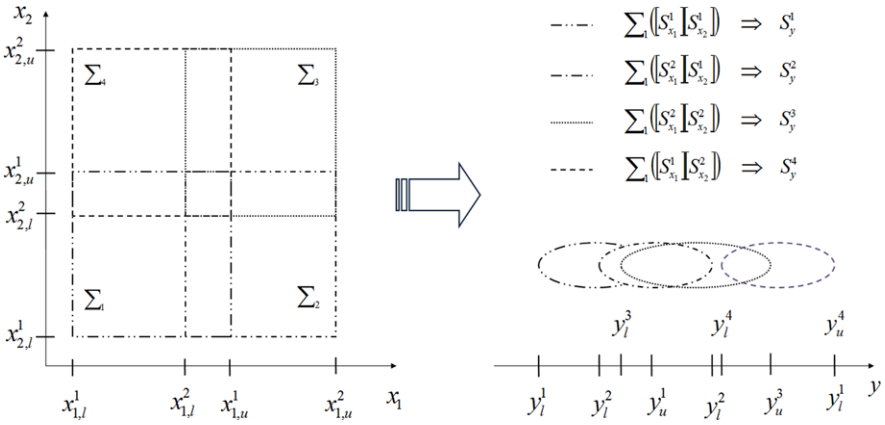

Fig. 6.1 Propagation of evidence from input to output space

design variables space. Assuming that all the variables are uncorrelated, the probability of each elementary set in the design variables space is defined by

$$m_{x_1,x_2,\ldots,x_n}\left(\left[S_{x_1}^j\right],\ldots,\left[S_{x_{n1}}^j\right]\right) = m_{x_1}\left(\left[S_{x_1}^j\right]\right)\cdot\cdots\cdot m_{x_1}\left(\left[S_{x_n}^j\right]\right) \tag{6.27}$$

Once defined the uncertainty acting on the design variables, its effects on the performance function can be evaluated. Given a generic function $y = Y(X)$, linking the output with the input variables $X = \{x_1,\ldots,x_n\}$, the evidence about y must be estimated from the joint body of evidence previously described in Eq. (6.27). By means of two optimization problems, for each evidence-set of the input variables space, the lower and upper boundary of the corresponding set into the output space are evaluated

$$\begin{aligned} &\textit{find } \bar{X} = \{\bar{x}_1,\ldots,\bar{x}_n\} \in \Sigma_j\left(\left[S_{x_1}^j\right],\left[S_{x_2}^j\right],\ldots,\left[S_{x_n}^j\right]\right)\\ &t.c\ \max/\min y = f(X)\\ &\Downarrow\\ &S_y^j = \left[y_l^j, y_u^j\right] \end{aligned} \tag{6.28}$$

The above optimization problems yield an evidence set on output-space S_y^j for each set Σ_j of the joint body of evidence (Fig. 6.1). Hence, in order to propagate the uncertainty from input to output, two optimizations for each set Σ_j have to be performed.

3 Numerical Examples

In this section some numerical examples will be presented in order to verify the accuracy of the UP methods described above. Some test functions and a structural

Table 6.1 Test functions used to test the UP methods

Function	PDF	PDF Parameters
$y = x_1^k x_2^k + 2x_3^4, k = 2, 3, 5$	Gaussian	$\mu = [1, 1, 1]$
		$\sigma = 0.1, 0.2, 0.4, 0.8$
$y = \sin x_1 + a \sin^2 x_2 + b x_3^4 \sin x_1$	Gaussian	$\mu = [\pi/4, \pi/4, \pi/4]$
		$\sigma = 0.05, 0.1, 0.2, 0.5$

problem (static, dynamic and buckling behavior of a composite plate) will be the test cases considered for assessing the methods for stochastic uncertainty. A comparison between stochastic and epistemic approaches when applied to a structural shape sensing problem will be then discussed.

3.1 Test Functions

Two test functions are used to compare the performance of the UP methods introduced in the previous paragraphs (Table 6.1).

The first example is a three-variate function, chosen to compare the performance of the UP algorithms against the first order effects of the input variables. In order to better understand this example and the capabilities of each method can be useful defined what are the main and high order effects. They deal with how the uncertainty on input parameters influences the output. In detail the main effects measure the influence of each single input parameter on the output, while the high order effects give information about the influence of each possible combination of input parameters (i.e. X_1X_2, X_1X_3) on the output. More details about the numerical methods used to evaluate these measures are beyond the purpose of this paper refer to [13] for further details.

The input variables follow a Gaussian distribution centered in $X = [1, 1, 1]$ and four values of standard deviation are tested ($\sigma = 0.1, 0.2, 0.4, 0.8$). In addition, the effect of the interactions among the variables is studied changing the value of k. The analysis of the accuracy of each method is performed comparing the predicted values of the statistical moments with those evaluated using a MonteCarlo Simulation, based on 10^6 observations. In this example the effect of an increasing input variability is combined with that of an increasing interaction effect.

In Table 6.2 the main effects and the interactions are listed for each value of k. These indices are evaluated by means of the Polynomial Chaos Expansion [14]. We can observe that changing the value of k the interaction x_1x_2 increases its effect on the output, becoming gradually the most important factor.

In Fig. 6.2 the errors in the estimation of the mean value are plotted as function of the input variables standard deviation for different values of k. As a general rule, when the input variability increases, all the UP methods here discussed become less accurate. This phenomenon is negligible if the first order interactions are marginal;

Table 6.2 Main and first order effects

	Main and First Order Effects		
	k = 2	k = 3	k = 5
X_1	0.011	0.0838	0.0575
X_2	0.011	0.0838	0.0572
X_3	0.9587	0.4734	0.0006
X_1X_2	0.01927	0.359	0.8808
X_1X_3	9.60E-25	8.78E-25	5.82E-04
X_2X_3	4.84E-26	8.34E-25	1.22E-03

on the contrary, in problems where the interaction effects are more important ($k = 3$ or $k = 5$) the results become more sensitive to the input variability.

As shown in Fig. 6.2(A), the UDR yields a good estimation of the mean values when the interaction between the variables is low ($k = 2$), also in the case of high

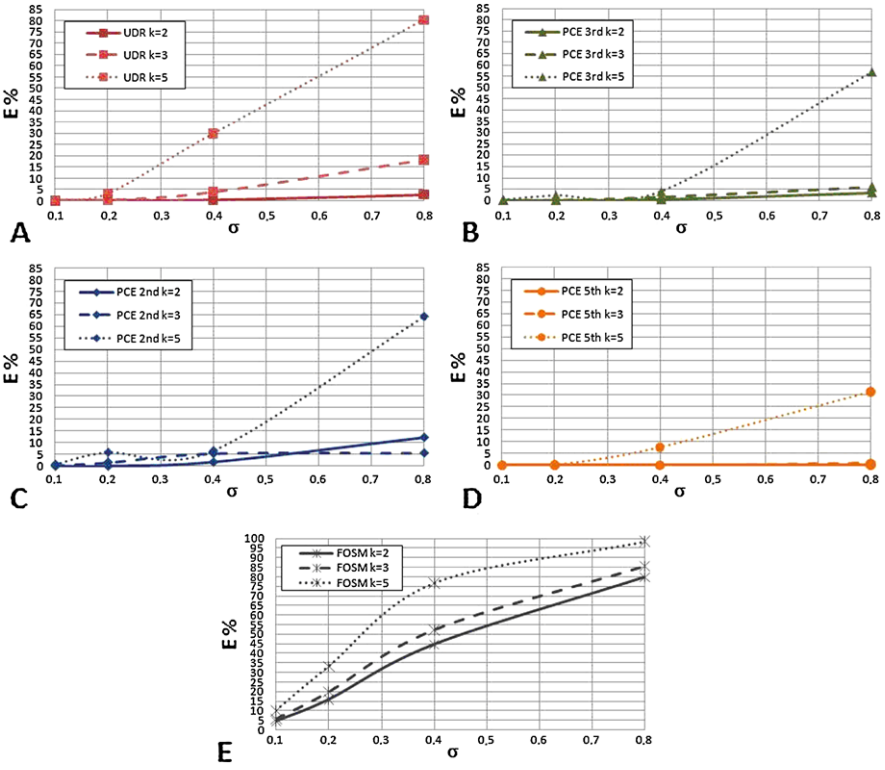

Fig. 6.2 Error in the estimation of the output mean value: (**A**) Error due to the UDR method (**B**)–(**D**) Error due to the PCE of 2nd, 3rd and 5th order, respectively. (**E**) Error due to the FOSM alghorithm

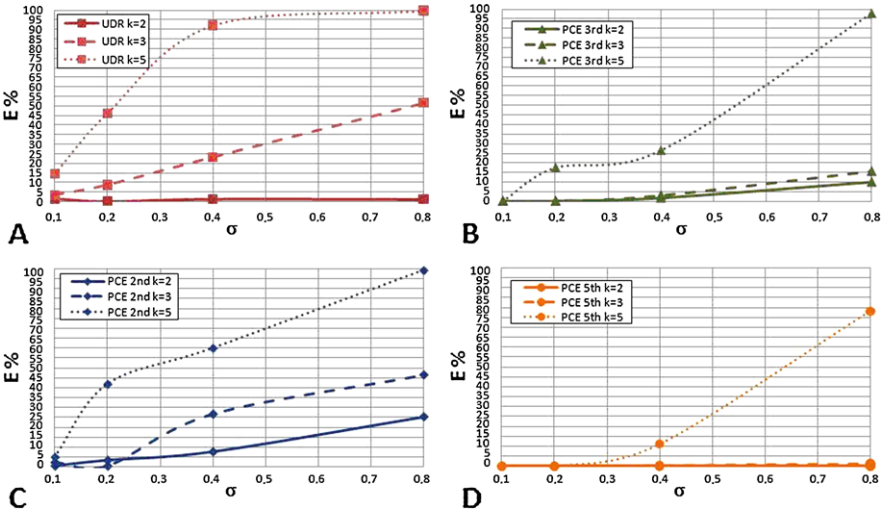

Fig. 6.3 Error in the estimation of the output variance: (**A**) Error due to the UDR method (**B**)–(**D**) Error due to the PCE of 2nd, 3rd and 5th order, respectively

input variability ($\sigma = 0.8$). Increasing the effect of interaction, the accuracy of this method greatly decays, in particular for higher values of input variability.

Similar behaviors are shown in Fig. 6.2(B)–(D); the output function is approximated with the Polynomial Chaos Expansion, truncated at different orders. Also in this case, for higher values of k and for a higher input uncertainty, the mean value is poorly approximated. When using the PCE, however, the reduced accuracy is not due to the interaction effects, but it is caused by the non-linearity of the output function: for example, if $k = 2$ we have a 4^{th} order function, while if $k = 3$ we have a 6^{th} order function. Hence, it is clear that a Polynomial Chaos Expansion truncated at the 5^{th} order better describes the problem than an expansion truncated at the 2^{nd} order, but, for $k = 5$, it does not guarantee adequate accuracy. Increasing the order of the expansion, the error in the prediction gradually vanishes.

Therefore, there is a substantial difference between the UDR and the PCE. In the UDR the lack of accuracy is inherent to its mathematical formulation and cannot be reduced. On the other hand, the accuracy of the PCE results can be improved increasing the order of the expansion.

In Fig. 6.2(E) the errors are shown on the output function mean value when computed using the FOSM algorithm. In this case the approximation is based on the hypothesis that the output function has a linear behavior in the studied domain; the errors are quite high also for small input variability levels.

The decay of UDR accuracy in the prediction of the statistical moments (due mainly to the first order effects) is more evident in the evaluation of the variance, Fig. 6.3(A) and of the higher order moments: Skewness Fig. 6.4(A) and Kurtosis Fig. 6.5(A). As already observed in the evaluation of mean value, for quite small

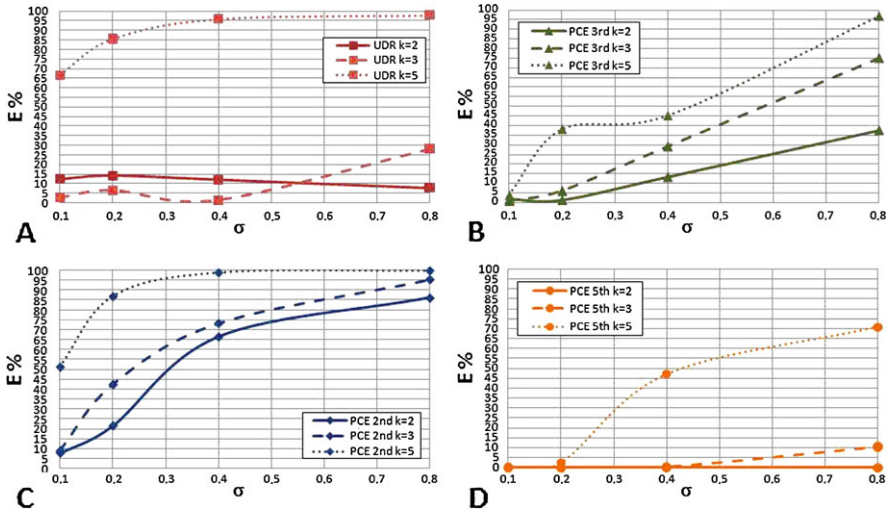

Fig. 6.4 Error in the estimation of the output skewness: (**A**) Error due to the UDR method (**B**)–(**D**) Error due to the PCE of 2nd, 3rd and 5th order, respectively

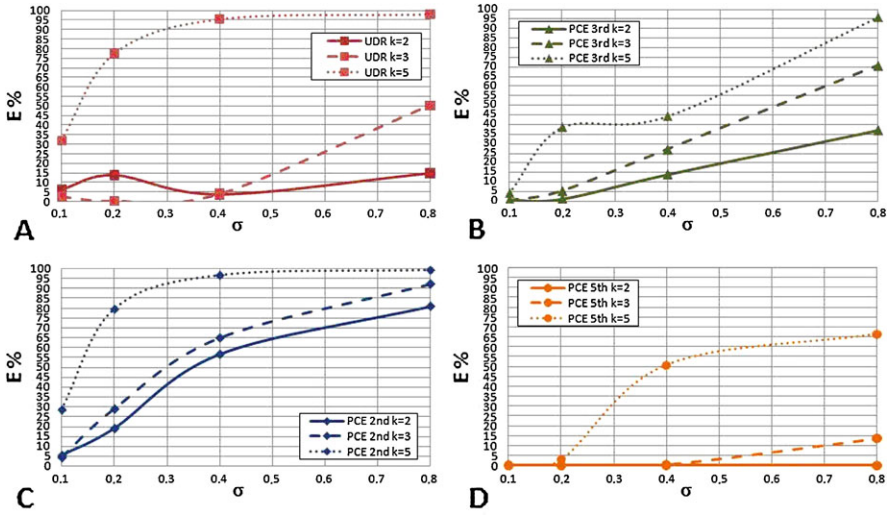

Fig. 6.5 Error in the estimation of the output kurtosis: (**A**) Error due to the UDR method (**B**)–(**D**) Error due to the PCE of 2nd, 3rd and 5th order, respectively

interaction effects ($k = 2$), the UDR approximation does not affect the accuracy of the results. This is not true for the higher order moments.

Results regarding higher order statistical moments (Figs. 6.3(B)–(D), 6.5(B)–(D), 6.6(B)–(D)) confirm that the interaction between the variables does not affect

Table 6.3 Number of observations for each method

FOSM	UDR	PCE 2nd	PCE 3rd	PCE 5th
49	16	31	61	168

the accuracy of the Polynomial Chaos Expansion; anyhow, a higher order expansion is required in order to have a good estimation of the variance, skewness and kurtosis.

In Table 6.3 the number of observation points needed to perform each analysis are listed. The UDR method needs only 16 observed data (it requires only $5n + 1$, where n are the stochastic input variables).

The UDR method is the cheapest one and, as seen in the present example, if there is a negligible interaction between the input variables, it yields a good estimation of the statistical moments. The computational cost of the PCE grows considerably increasing the order of expansion and the problem dimension. The number of unknown coefficients of PCE is $P + 1$, as given by Eq. (6.12); these coefficients are evaluated using a least-squares based method, Eq. (6.13). The number of training points must be at least equal to $P + 1$, but for and adequate accuracy of the solution, a higher number of points is usually adopted; this number (Table 6.3) is evaluated by a convergence study on the β values.

The second function here considered (see Table 6.1) is the Ishigami function, commonly used to test the uncertainty propagation algorithms and the sensitivity in order to understand their behavior with non-linear and non-monotonic functions. The three variables follow a Gaussian distribution, centered in $X = [\pi/4, \pi/4, \pi/4]$; the standard deviation ranges from 0.05 to 0.5. The accuracy of each method is assessed comparing the predicted values of the statistical moments with those evaluated using a MonteCarlo Simulation, based on 10^6 observations.

In Table 6.4 the percentage errors on the estimation of the mean value and variance are listed for different values of the input standard deviation. All methods yield a good estimation of the mean value (the error is always less than 1%). The differences between the methods are more evident when considering the variance evaluation. The FOSM method yields a very poor estimation in particular for high values of input variability: for example, the error with an input standard deviation of $\sigma = 0.2$ is around 12.3%, while with $\sigma = 0.5$ is around 56%. The UDR method leads to a good estimation of the variance (error around 2%); there is no evident correlation between the input variability and the estimation error. The PCE is very accurate, if the order of the expansion is sufficient to describe the problem; we can observe that a 5th order expansion is very accurate in the prediction of variance, and that the 7th order expansion yields the exact solution.

In a robust design framework it is important the accurate evaluation of the first two statistical moments (mean and variance), but for the evaluation of the reliability degree this information is not enough. Hence, the knowledge of the probability distribution function is needed. One of the main problems of the UDR approach is that it does not yield directly the probability distribution, but only the statistical moments. Anyway, it is possible to obtain the PDF, knowing the first four statistical moments, by means of the Pearson System. In Fig. 6.6 and Fig. 6.7 the probability

Table 6.4 Mean values and variance estimation errors

Standard Deviation Input	FOSM		UDR		PCE 2nd	
	Mean	Variance	Mean	Variance	Mean	Variance
0.05	3.336E-02	1.204E+00	2.515E-02	1.934E+00	2.363E-03	2.398E-01
0.1	7.351E-02	1.968E+00	4.734E-02	1.952E+00	2.837E-02	1.997E+00
0.2	1.609E-01	1.235E+01	7.092E-02	2.162E+00	1.754E-01	2.334E+00
0.5	5.364E-01	5.575E+01	3.560E-01	1.818E+00	5.596E-01	6.521E+00
Standard Deviation Input	PCE 3rd		PCE 5th		PCE 7th	
	Mean	Variance	Mean	Variance	Mean	Variance
0.05	0.000E+00	0.000E+00	0.000E+00	0.000E+00	0.000E+00	0.000E+00
0.1	0.000E+00	2.058E-02	0.000E+00	0.000E+00	0.000E+00	0.000E+00
0.2	4.731E-03	3.456E-02	0.000E+00	3.456E-02	0.000E+00	0.000E+00
0.5	1.189E-01	2.878E+00	4.749E-03	1.641E-02	0.000E+00	2.553E-02

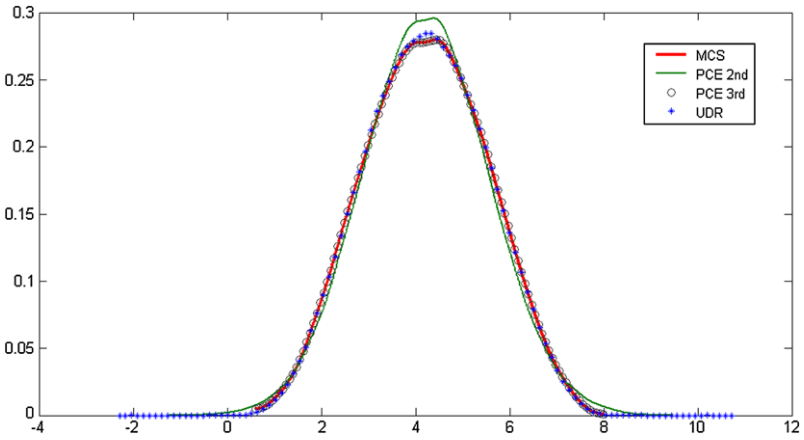

Fig. 6.6 Probability density function (all input variables have a standard deviation of 0.2)

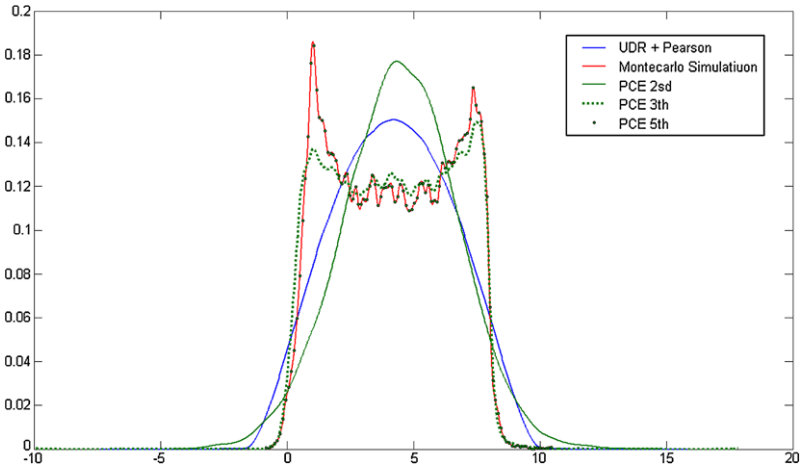

Fig. 6.7 Probability density function (all input variables have a standard deviation of 0.5)

distribution function, evaluated with the UDR and the Pearson System, is compared with the PDF obtained using the PCE with different expansion orders and the one obtained by means of MCS (10^6 training points). The curves plotted in Fig. 6.6 and in Fig. 6.7 are referred, respectively, to the case of an input standard deviation of $\sigma = 0.2$ and of $\sigma = 0.5$. In the first case (Fig. 6.5) a good agreement among all plotted curves can be observed. The UDR method coupled with the Pearson System yields a very good approximation of the probability density function. There is only a small discrepancy in the description of the tails: the tails of PDFs, obtained with the UDR method and the 2^{nd} order PCE, end with an asymptotic behavior, while in the one obtained with MCS the tails are limited. On the contrary there is a perfect

correspondence between the probability function obtained with a 3rd order PCE and the one obtained with the MonteCarlo Simulation.

In the second case ($\sigma = 0.5$) it is possible to appreciate a bigger discrepancy among the methods (Fig. 6.6(A)). Although the UDR method is able to predict with a good accuracy the mean and the variance of the output, it fails in the estimation of the PDF. This is mainly due to the fact that the higher order moments are predicted with low-accuracy and, as well known, the Pearson System is based on the relation between skewness and kurtosis. Also the 3rd order PCE gives not an accurate probability distribution. Only by means of a 5th order PCE a good PDF approximation can be obtained.

In this example we have seen that, although the UDR approach is adequately accurate to be used in a robust design problem, it cannot be used in a reliability based problem.

3.2 Composite Plate Mechanical Behavior

In this example the performances of UDR and PCE are tested on the static and dynamic response analysis of a symmetric composite plate ($0°/90°/90°/0°$) with all edges clamped. The material properties, the fiber orientation, and the plies thickness are considered affected by uncertainty and are described by means of Gaussian distributions. In Table 6.5 all plate properties are reported in terms of mean value and standard deviation. The stochastic moments of the maximum deflection ($\boldsymbol{w}$), the first natural frequency ($\boldsymbol{f}$), the maximum Von Misses stress ($\boldsymbol{\sigma}_{VM}$), the maximum transverse shear stresses, τ_{xz} and τ_{yz}, are evaluated by means of the UDR and of the PCE. The static and dynamic responses of the plate have been obtained using the Refined Zigzag Theory (RZT) for plates [15–19]; a Rayleigh–Ritz solution procedure has been adopted to find maximum deflection, first natural frequency and stresses distribution. The first four statistical moments, evaluated using the UDR and PCE, are compared with those obtained by a MonteCarlo Simulation based on 10^5 observations (Table 6.6). In Table 6.6 one can observe that approximately all approaches give the same results, the main difference between the UDR and the 2nd order PCE is in the computational cost needed to perform the analysis, indeed are needed 71 observations and 360 training points, respectively.

3.3 Structural Shape Sensing

The inverse Finite Element Method (iFEM), developed by Tessler for plate and shell structures [19] and specialized by Gherlone for beams and frames [2], is aimed at the reconstruction of the displacement field of a structure starting from in situ measurements of surface strains [2]; this represents an inverse problem [3]. A description of the iFEM approach is not within the scopes of the present paper, refer to [2, 3, 19] for further details.

Table 6.5 Plate properties: θ_1 is the fiber orientation of the first ply, t_1 is its thickness

		Mean	PDF	SD
Mechanical properties	E_{11} [Mpa]	1.58E+05	Gaussian	7.895
	E_{22} [Mpa]	9.58E+03	Gaussian	0.4792
	E_{33} [Mpa]	9.58E+03	Gaussian	0.4792
	G_{12} [Mpa]	5.93E+03	Gaussian	0.2965
	G_{13} [Mpa]	5.93E+03	Gaussian	0.2965
	G_{23} [Mpa]	3.23E+03	Gaussian	0.1613
	v_{12}	0.32	Deterministic	-
	v_{13}	0.32	Deterministic	-
	v_{23}	0.49	Deterministic	-
	ρ [T/mm^3]	1.90E-09	Deterministic	-
Fiber orientation	θ_1	0	Gaussian	3
	θ_2	90	Gaussian	3
	θ_3	90	Gaussian	3
	θ_4	0	Gaussian	3
Thickness	t_1 [mm]	1	Gaussian	0.05
	t_2 [mm]	1	Gaussian	0.05
	t_3 [mm]	1	Gaussian	0.05
	t_4 [mm]	1	Gaussian	0.05

In the present work a cantilevered aluminum beam (length L = 200 mm) with a circular thin-walled cross-section (radius r = 1 cm) and subjected to different load conditions has been studied. In lieu of the experimental measures of surface strains, high-fidelity direct FE analyses (MSC/NASTRAN) have been carried out for the example problem (Table 6.7). These results have also been used to verify the accuracy of the nodal displacements and rotations obtained by iFEM.

The position of a strain gauge, used to measure a surface strain, is defined by three coordinates: the first one, x, indicates the position along the longitudinal beam axis, the second one, θ, is an angle representing the circumferential position on the beam and the coordinate β indicates the strain gauge orientation (i.e., it represents the rotation of the strain gauge with respect to the beam axis (Fig. 6.8). For the current application, six strain gauges are used; their nominal positions are reported in Table 6.8 and their location is also represented in Fig. 6.9.

In this example three different load conditions are considered (Fig. 6.10(A)): (1) a shear force applied along y-axis, (2) a torque moment and (3) a bending moment around the z-axis. The free end displacements and rotations (Fig. 6.10(B)) are computed by means of the iFEM and are compared with the ones obtained using the direct MSC/NASTRAN FEM solution. Hence, the iFEM accuracy is evaluated by

Table 6.6 Stochastic moments: SD is the standard deviation, SKW is the skewness, KURT is the Kurtosis, w is the maximum deflection, f is the fundamental frequency, σ_{VM} is the maximum Von Mises stress, τ_{xz} and τ_{yz} are the maximum transverse shear stresses

		w	f	σ_{VM}	τ_{yz}	τ_{xz}
MCS	Mean	21.37	434.24	2194.65	28.76	14.01
	Variance	3.36	200.36	13570.68	0.70	0.45
	SD	1.84	14.15	116.49	0.84	0.67
	SKW	0.01	0.04	0.23	0.15	0.16
	KURT	3.05	3.03	3.06	3.01	3.03
UDR	Mean	21.36	434.24	2194.50	28.76	14.01
	Variance	3.35	201.67	13570.68	0.78	0.45
	SD	1.83	14.20	116.49	0.88	0.67
	SKW	0.00	0.00	0.23	0.15	0.16
	KURT	3.03	3.03	3.00	3.02	3.03
2^{nd} PCE	Mean	21.37	434.24	2194.64	28.76	14.01
	Variance	3.34	205.67	13570.68	0.72	0.45
	SD	1.83	14.34	116.49	0.85	0.67
	SKW	0.01	0.00	0.23	0.15	0.16
	KURT	3.03	3.03	3.00	3.02	3.03

Table 6.7 High-fidelity FE discretization of the thin-walled beam problem

Element type (name)	N° of elements along the external circumference	N° of elements along the beam length	Total N° of elements	Total N° of nodes
Shell element (QUAD4)	114	360	41.040	41.156

means of the following error:

$$E \equiv \frac{Value(FEM) - Value(FEM)}{Value(FEM)} \tag{6.29}$$

The aim of the present application is to verify the robustness of the iFEM in evaluating the displacement field when the sensor positions are considered affected by uncertainty. For this purpose, a probabilistic approach is compared with a non-probabilistic method based on the evidence theory. The main issue is the definition of the uncertainty that affects the coordinate values describing the sensors position. In order to obtain this kind of information, three technicians have been interviewed They have given three different estimations of the error in the strain gauge location; all these experts are equally trusted. The second expert (see Table 6.9) defined the errors using disjoint sets.

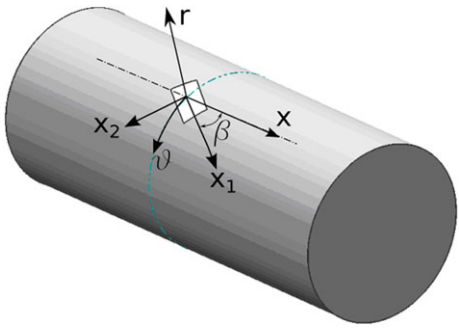

Fig. 6.8 Location of a strain gauge on the beam external surface [20]

Table 6.8 Strain gauge nominal positions

Strain gauges	x	θ	β
1	10	−120	0
2	10	−120	45
3	10	0	0
4	10	0	45
5	10	120	0
6	10	120	45

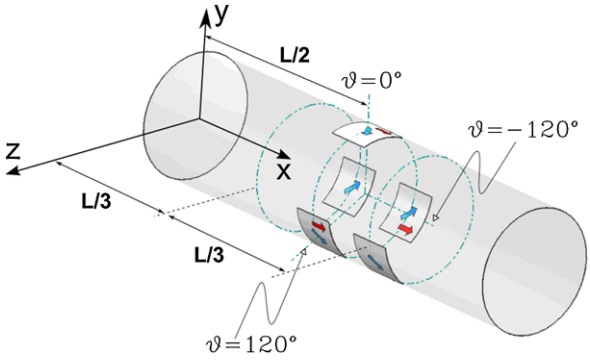

Fig. 6.9 Sensors position [20]

In order to use a probabilistic approach to propagate the uncertainty from input to output, there is the need to transform the input epistemic uncertainty into probabilistic information. Several hypotheses are then needed about the shape of the probability distribution and its standard deviation. In the present example we have assumed that the uncertainty in the sensor position is described by means of a Gaussian distribution, having the standard deviations listed in Table 6.10.

The information obtained by the sensitivity analysis [20] are used to select which input variables should be considered and which could be neglected during the uncertainty propagation process, performed both using the evidence theory and a probabilistic approach (the UDR method, having verified that there are not significant

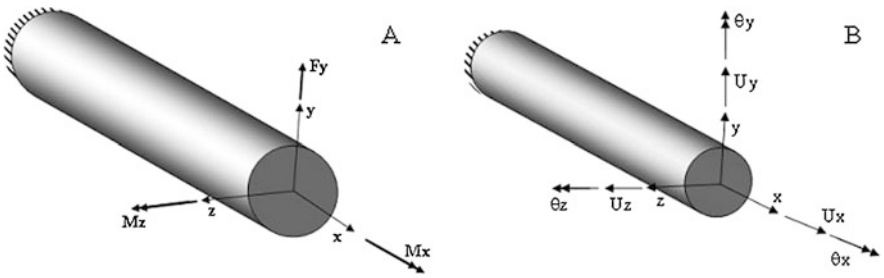

Fig. 6.10 (**A**) Applied load, (**B**) Studied degrees of freedom

Table 6.9 Sensor coordinates defined by means of interval sets

Expert	x [mm]		θ [°]		β [°]	
	LOWER	UPPER	LOWER	UPPER	LOWER	UPPER
1	−5	5	−5	5	−4	4
2	−5	−1	−5	5	−4	−1.5
	1	5	−5	5	1.5	4
3	−1	1	−5	5	−1.5	1.5

Table 6.10 Probabilistic assumptions about sensor position

Input variables	PDF	Standard Deviation
x	Gaussian	0.0233
θ	Gaussian	1.1666
β	Gaussian	1.3333

interactions between variables). Then, once the first four statistical moments are known, the corresponding probability distribution function is evaluated by means of the Pearson System.

The probability that the iFEM error w.r.t. the FEM reference displacements and rotations is greater than a given threshold value, is finally evaluated.

The evidence theory does not furnish a unique measure of the probability, but it gives two different probability curves: the plausibility, that describes the curve of the maximum reliability of the system, and the belief, that describes the minimum reliability of the system (Figs. 6.11, 6.12, and 6.13). According to what was said previously, the true reliability curve is included between the plausibility and the belief. Actually, the area included between the maximum reliability curve and the minimum one represents a region of uncertainty; this means that, without further information, no prediction about the actual behavior of the model can be made (we only know that the true error is included between the two probability curves). For this reason, the belief curve, that represents a conservative estimation of the model behavior, is used during the design phase. In this study we have compared the results

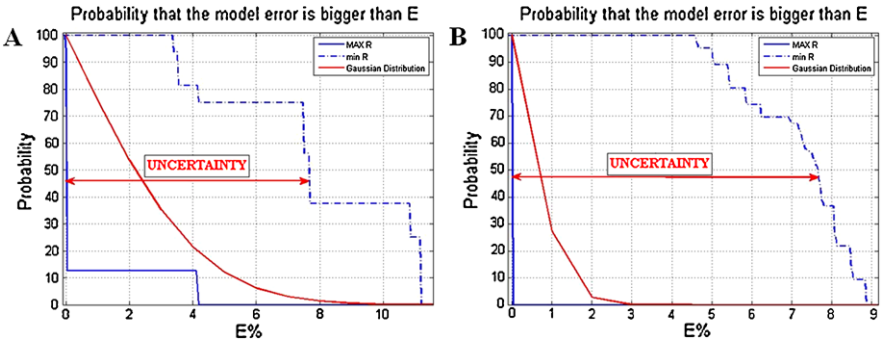

Fig. 6.11 Shear load (Fy): Probability that the error E about u_y (**A**) and θ_z (**B**) is bigger than a given threshold value. *Three curves* are plotted: the *first* one represents the maximum model reliability (labeled with *MAX R*), the *second* one represents the minimum reliability of the model (labeled with *min R*), the *red* one represents the curve obtained using the assumption of the Gaussian distribution

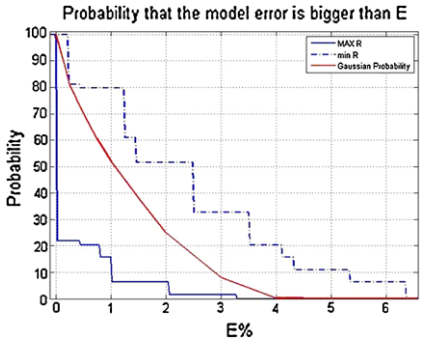

Fig. 6.12 Torque Moment: Probability that the error E about θ_x (**B**) is bigger than a given threshold value. *Three curves* are plotted: the *first* one represents the maximum model reliability (labeled with *MAX R*), the second one represents the minimum reliability of the model (labeled with *min R*), the *red* one represents the curve obtained using the assumption of the Gaussian distribution

obtained assuming that the position error is described by means of Gaussian distributions with those obtained assuming that each sensor is located inside an interval. In this last case no hypothesis has been made about the probability that a sensor is in a given point (inside the region). As shown in Figs. 6.11, 6.12, and 6.13, the maximum reliability curves give almost null prediction errors, whereas the minimum reliability curves indicate bigger probability to have large errors; in particular, the evaluation of the y-displacement and z-rotation is quite sensible to the sensor position uncertainty, Fig. 6.11 and Fig. 6.13. In most cases the reliability curves, based on the Gaussian distribution hypothesis, underestimate considerably the prediction errors. In particular the Gaussian hypothesis furnishes probability values close to those given by the maximum reliability curves.

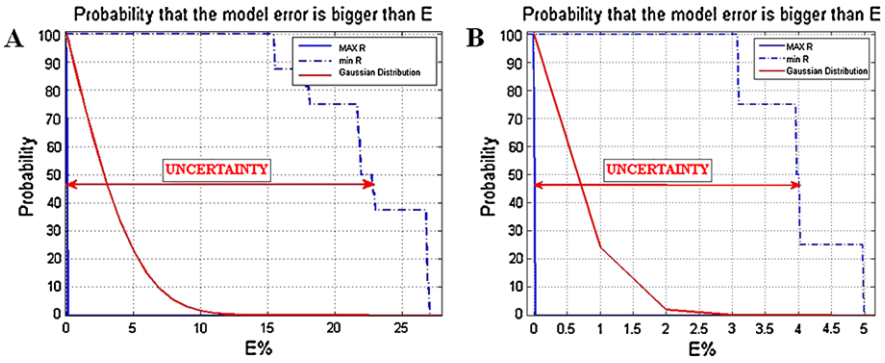

Fig. 6.13 Bending Moment around z: Probability that the error E about u_y (**A**) and θ_z (**B**) is bigger than a given threshold value. *Three curves* are plotted: the *first* one represents the maximum model reliability (labeled with *MAX R*), the second one represents the minimum reliability of the model (labeled with *min R*), the *red* one represents the curve obtained using the assumption of the Gaussian distribution

4 Conclusion

In the present work a comparative study of some uncertainty propagation algorithms is performed and discussed.

Methods for both aleatory and epistemic uncertainty are considered; in particular, a brief review of Univariate Dimension Reduction method (UDR), Polynomial Chaos Expansion (PCE), and First Order Second Moments algorithm (FOSM)—for aleatory uncertainty—and of Evidence Theory—for epistemic uncertainty—is presented.

Then, selected example problems are considered to assess and compare the available methods; some test functions are used as preliminary test cases, then structural applications are studied, ranging from the mechanical behavior of a composite plate to the shape sensing of a beam starting from measured surface strains. As for the latter application, an epistemic uncertainty propagation approach (Evidence Theory) has been compared with a probabilistic uncertainty propagation algorithm (UDR); the considered problem is a classical example of epistemic uncertainty, therefore probabilistic approaches may be applied after introducing some prior assumptions whose correctness may not be guaranteed.

Although this study is limited to some particular examples, interesting general conclusions can be drawn.

If there is no significant interaction between variables, the UDR is the most efficient method for statistical moments estimation. Its accuracy decreases when the interactions cannot be neglected; in particular, the evaluation of the 3rd and 4th statistical moments is more sensitive to the interaction effects and, therefore, also the evaluation of the corresponding Probability Distribution Function (PDF), by means of the Pearson System, can be compromised. The accuracy and the computational cost of the PCE depend on the truncation order of the expansion. However, the PCE is a useful approach when the knowledge of the PDF is desired. Moreover, the

UDR method leads to the best compromise between accuracy and computational cost when performing a probabilistic study of the mechanical behavior of a composite plate.

The transformation of the epistemic knowledge into a probabilistic knowledge could often cause a loss of information and consequently the underestimation of the uncertainty effects. The evidence theory, in the particular case of the shape sensing problem, seems to be a more robust and conservative approach. The use of a probabilistic approach is not wrong but it requires too strong prior assumptions. In other words, the correct use of the probabilistic approach would require the experimental probabilistic characterization of the sensors position.

References

1. Lee, S.H., Chen, W.: A Comparative study of uncertainty propagation methods for black-box-type problems. Struct. Multidiscip. Optim. **37**(3), 239–253 (2009)
2. Cerracchio, P., Gherlone, M., Mattone, M., Di Sciuva, M., Tessler, A.: Shape sensing of three-dimensional frame structures using the inverse finite element method. In: Proc. Fifth European Workshop on Structural Health Monitoring, Sorrento, Italy, pp. 615–620 (2010)
3. Cerracchio, P., Gherlone, M., Mattone, M., Di Sciuva, M., Tessler, A.: Inverse finite element method for three-dimensional frame structures. DIASP Report Politecnico di Torino 285 (2010)
4. Xu, H., Rahman, S.: A moment-based stochastic method for response moment and reliability analysis. In: Proc. Second MIT Conference on Computational Fluid and Solid Mechanics (2003)
5. Rahman, S., Xu, H.: A univariate dimension-reduction method for multi-dimensional integration in stochastic mechanics. Probab. Eng. Mech. **19**(1), 393–408 (2004)
6. Xu, H., Rahman, S.: A generalized dimension-reduction method for multidimensional integration in stochastic mechanics. Int. J. Numer. Methods Eng. **65**(13), 1992–2019 (2004)
7. Wiener, N.: The homogeneous chaos. Am. J. Math. **60**, 897–936 (1938)
8. Cameron, R.H., Martin, W.T.: The orthogonal development of nonlinear functionals in series of Fourier–Hermite functionals. Ann. Math. **48**(2), 385–392 (1947)
9. Xiu, D., Karniadakis, G.M.: The Wiener–Askey polynomial chaos for stochastic differential equations. SIAM J. Sci. Comput. **24**(2), 619–644 (2002)
10. Ticky, M.: Applied Methods of Structural Reliability. Springer, Berlin (1993)
11. Helton, J.C., Johnson, J.D., Oberkampf, W.L., Storli, C.B.: A sampling-based computational strategy for the representation of epistemic uncertainty in model predictions with evidence theory. Sandia report SAND2006-5557, Sandia National Laboratories (2006). http://prod.sandia.gov/techlib/access-control.cgi/2006/065557.pdf
12. Sentz, K., Ferson, S.: Combination of evidence in Dempster–Shafer theory. Sandia report SAND2002-083, Sandia National Laboratories (2002). http://www.sandia.gov/epistemic/Reports/SAND2002-0835.pdf
13. Saltelli, A., Chan, K., Scott, E.M.: Sensitivity Analysis. Wiley, New York (2008)
14. Crestaux, T., Le Maitre, O., Martinez, J.M.: Polynomial chaos expansion for sensitivity analysis. Reliab. Eng. Syst. Saf. **94**(7), 1161–1172 (2009)
15. Tessler, A., Di Sciuva, M., Gherlone, M.: Refined zigzag theory for laminated composite and sandwich plates. NASA/TP-2009-215561, Langley Research Center (2009)
16. Tessler, A., Di Sciuva, M., Gherlone, M.: A consistent refinement of first-order shear-deformation theory for laminated composite and sandwich plates using improved zigzag kinematics. J. Mech. Mater. Struct. **5**, 341–367 (2010). doi:10.2140/jomms.2010.5.341

17. Tessler, A., Di Sciuva, M., Gherlone, M.: A shear-deformation theory for composite and sandwich plates using improved zigzag kinematics. In: IX International Conference on Computational Structural Technology, 2–5 September, Greece, Proceedings on Cd, Paper 30 (2008)
18. Tessler, A., Di Sciuva, M., Gherlone, M.: Refined zigzag theory for homogeneous, laminate composite, and sandwich plates: a homogeneous limit methodology for zigzag function selection. Numer. Methods Partial Differ. Equ. **27**(1), 208–229 (2011)
19. Tessler, A., Spangler, J.L.: A least-squares variational method for full-field reconstruction of elastic deformations in shear-deformable plates and shells. Comput. Methods Appl. Mech. Eng. **94**, 327–339 (2005)
20. Corradi, M.: Uncertainty management techniques for aerospace structural design. Ph.D. thesis, Politecnico di Torino (2011)

Chapter 7
Fuzzy and Fuzzy Stochastic Methods for the Numerical Analysis of Reinforced Concrete Structures Under Dynamical Loading

Frank Steinigen, Jan-Uwe Sickert, Wolfgang Graf, and Michael Kaliske

Abstract This paper is mainly devoted to enhanced computational algorithms to simulate the load-bearing behavior of reinforced concrete structures under dynamical loading. In order to take into account uncertain data of reinforced concrete, fuzzy and fuzzy stochastic analyses are presented. The capability of the fuzzy dynamical analysis is demonstrated by an example in which a steel bracing system and viscous damping connectors are designed to enhance the structural resistance of a reinforced concrete structure under seismic loading.

1 Introduction

The numerical analysis of reinforced concrete (RC) structures under dynamical loads requires realistic nonlinear structural models and computational algorithms. Furthermore, the engineer/designer has to deal with uncertainty which results from variations in material parameters as well as incomplete knowledge about further excitations and the quality of the numerical model itself. The variations in material parameters may be assessed by the uncertainty measure probability. However, the stochastic model cannot be determined precisely because of rare information in most cases. Therefore, an imprecise probability approach is suggested in this contribution which is based on the uncertainty measure fuzzy probability resulting in a set of probability models assessed by membership values. Using this approach, input variables may be also modeled as fuzzy quantities and considered as a special case, if only subjective or linguistic assessments are available.

F. Steinigen (✉) · J.-U. Sickert · W. Graf · M. Kaliske
Institute for Structural Analysis, TU Dresden, Dresden 01062, Germany
e-mail: frank.steinigen@tu-dresden.de

J.-U. Sickert
e-mail: jan-uwe.sickert@tu-dresden.de

W. Graf
e-mail: wolfgang.graf@tu-dresden.de

M. Kaliske
e-mail: michael.kaliske@tu-dresden.de

M. Papadrakakis et al. (eds.), *Computational Methods in Stochastic Dynamics*, Computational Methods in Applied Sciences 26,
DOI 10.1007/978-94-007-5134-7_7,

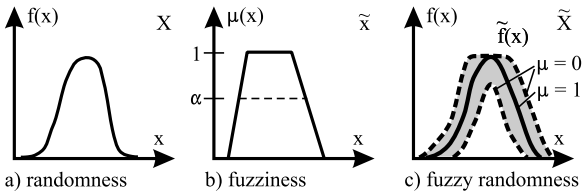

Fig. 7.1 Models of uncertainty

The incorporation of uncertain input variables within a dynamic structural analysis leads to uncertain structural responses representing the uncertain structural performance close to reality. The uncertain structural responses are determined using fuzzy stochastic dynamic analyses. Thereby, fuzzy stochastic processes result due to the specific dynamic actions. The fuzzy stochastic structural analysis of practical problems requires high performance computational tools in order to deal with a large number of uncertain input variables as well as complex nonlinear structural models. An efficient approach is introduced which is based on α-level optimization and Monte-Carlo simulation using meta-models which partly replace the dynamic structural analyses.

2 Uncertainty in Structural Dynamics

2.1 Data Models

The input variables—for geometry, material, load etc.—of the numerical simulations of structural behavior are generally uncertain. In order to describe this uncertainty, traditional stochastic and non-stochastic models are available [8]. In Fig. 7.1, the models randomness, fuzziness and fuzzy randomness are displayed. The choice of the model depends on the available data. If sufficient statistical data exist for a parameter and the reproduction conditions are constant, the parameter may be described stochastically. Thereby, the choice of type of probability distribution function affects the result considerably.

Overcoming the traditional probabilistic uncertainty model enables the suitable consideration of imprecision (epistemic uncertainty). Thereby, epistemic uncertainty is associated with human cognition, which is not limited to a binary measure. Advanced uncertainty concepts allow a gradual assessment of intervals. This extension can be realized with the uncertainty characteristic fuzziness. The combination of fuzziness and probabilistic leads to the generalized model fuzzy randomness.

2.1.1 Fuzzy Variables

Often, the uncertainty description for parameters is based on pure expert judgment or samples which are not validated statistically. Then, the description by the uncertainty model fuzziness is recommended. The model comprehends both objective and

subjective information. The uncertain parameters are characterized with the aid of a membership function $\mu(x)$ (see Fig. 7.1b and Eq. (7.1)). The membership function $\mu_x(x)$ assesses the gradual membership of elements to a set. Fuzzy variables

$$\tilde{x} = \left\{ \left(x; \mu_x(x) \right) \mid x \in X \right\}; \quad \mu_x(x) \geq 0 \; \forall x \in X \tag{7.1}$$

may be utilized to describe the imprecision of structural parameters directly as well as to specify the parameters of fuzzy random variables.

2.1.2 Fuzzy Random Variables

If, e.g. reproduction conditions vary during the period of observation or if expert knowledge completes the statistical description of data, an adequate uncertainty quantification succeeds with fuzzy random variables. The theory of fuzzy random variables is based on the uncertain data model fuzzy randomness representing a generalized model due to the combination of stochastic and non-stochastic characteristics. A fuzzy random variable $\tilde{X}$ is defined as the fuzzy set of their originals, whereby each original is a real-valued random variable X.

The representation of fuzzy random variables presented in this paper is based on [13]. The space of the random elementary events Ω is introduced. Here, e.g. the measurement of a structural parameter may be an elementary event ω. Each elementary event $\omega \in \Omega$ generates not only a crisp realization but a fuzzy realization $\tilde{x}(\omega) = \tilde{x}$, in which $\tilde{x}$ is an element of the set $\mathbf{F}(\mathbb{R})$ of all fuzzy variables on $\mathbb{R}$. Each fuzzy variable is defined as a convex, normalized fuzzy set, whose membership function $\mu_x(x)$ is at least segmentally continuous. Accordingly, a fuzzy random variable $\tilde{X}$ is a fuzzy result of the mapping given by

$$\tilde{X} : \Omega \mapsto \mathbf{F}(\mathbb{R}). \tag{7.2}$$

Based on this formal definition, a fuzzy random variable is described by its fuzzy cumulative distribution function (fuzzy cdf) $\tilde{F}(x)$. The function $\tilde{F}(x)$ is defined as the set of real-valued cumulative distribution functions F(x) which are gradually assessed by the membership $\mu_F(F(x))$. F(x) is the cdf of the original X and is referred to as trajectory of $\tilde{F}(x)$. As result, a fuzzy functional value $\tilde{F}(x_i)$ belongs to each value x_i (see Fig. 7.2). Thus, $\tilde{F}(x)$ represents a fuzzy function as defined in Sect. 2.2.1. A fuzzy probability density function

$$\tilde{f}(x) = \left\{ \left(f(x); \mu_f\left(f(x)\right) \right) \mid f \in \mathbf{f} \right\}; \quad \mu_f\left(f(x)\right) \geq 0 \; \forall f \in \mathbf{f} \tag{7.3}$$

is defined accordingly. In that, $\mathbf{f}$ represents the set of all probability density functions defined on X.

2.2 Uncertain Functions and Processes

2.2.1 Fuzzy Function

In case that fuzzy parameters depend on crisp or uncertain conditions, they are modeled as fuzzy functions $\tilde{x}(\underline{\tilde{t}}) = \tilde{x}(\underline{\tilde{\theta}}, \tilde{\tau}, \underline{\tilde{\varphi}})$ or in the special case of pure time depen-

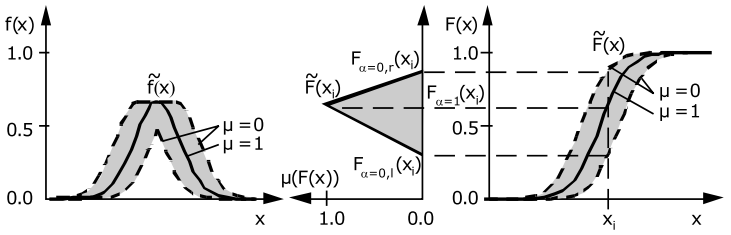

Fig. 7.2 Fuzzy probability density and cumulative distribution function

Fig. 7.3 Fuzzy process $\tilde{x}(\tau)$

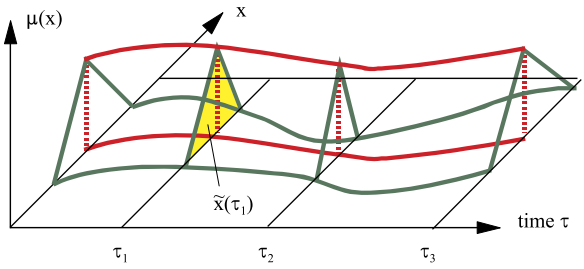

dency as fuzzy processes $\tilde{x}(\tilde{\tau})$. Arguments may be the time $\tilde{\tau}$, the spatial coordinates $\underline{\tilde{\theta}}$ and further parameters $\underline{\tilde{\varphi}}$, e.g. temperature. A fuzzy function $\tilde{x}(\underline{\tilde{t}})$ enables the formal description of at least piecewise continuous uncertain structural parameters in $\mathbb{R}$. In the following, a definition of fuzzy functions is introduced. Given are

- the fundamental sets $\mathbf{T} \subseteq \mathbb{R}$ and $\mathbf{X} \subseteq \mathbb{R}$,
- the set $\mathbf{F}(\mathbf{T})$ of all fuzzy variables $\underline{\tilde{t}}$ on the fundamental set $\mathbf{T}$,
- the set $\mathbf{F}(\mathbf{X})$ of all fuzzy variables $\tilde{x}$ on the fundamental set $\mathbf{X}$.

Then, the uncertain mapping of $\mathbf{F}(\mathbf{T})$ into $\mathbf{F}(\mathbf{X})$ that assigns exactly one $\tilde{x} \in \mathbf{F}(\mathbf{X})$ to each $\underline{\tilde{t}} \in \mathbf{F}(\mathbf{T})$ is referred to as a fuzzy function denoted by

$$\tilde{x}(\underline{\tilde{t}}) : \mathbf{F}(\mathbf{T}) \tilde{\mapsto} \mathbf{F}(\mathbf{X}), \tag{7.4}$$

$$\tilde{x}(\underline{\tilde{t}}) = \left\{ \tilde{x}_t = \tilde{x}(\underline{\tilde{t}}) \; \forall \underline{\tilde{t}} \mid \underline{\tilde{t}} \in \mathbf{F}(\mathbf{T}) \right\}. \tag{7.5}$$

In Fig. 7.3, a fuzzy process $\tilde{x}(\tau)$ is presented, which assigns a fuzzy quantity $\tilde{x}(\tau_i)$ to each time τ_i. For the numerical simulation, a bunch parameter representation of a fuzzy function

$$x(\underline{\tilde{s}}, \underline{t}) = \tilde{x}(\underline{\tilde{t}}) \tag{7.6}$$

is applied. Therewith, the fuzziness of both $\tilde{x}$ and $\tilde{t}$ is concentrated in the bunch parameter vector $\underline{\tilde{s}}$.

For each crisp bunch parameter vector $\underline{s} \in \underline{\tilde{s}}$ with the assigned membership value $\mu(\underline{s})$, a crisp function $x(\underline{t}) = x(\underline{s}, \underline{t}) \in \tilde{x}(\underline{t})$ with $\mu(x(\underline{t})) = \mu(\underline{s})$ is obtained. The fuzzy function

$$\tilde{x}(\underline{t}) = \tilde{x}(\underline{\tilde{s}}, \underline{t}) = \left\{ \left(x(\underline{s}, \underline{t}), \mu\left(x(\underline{s}, \underline{t})\right) \right) \mid \mu\left(x(\underline{s}, \underline{t})\right) = \mu(\underline{s}) \; \forall \underline{s} \mid \underline{s} \in \underline{\tilde{s}} \right\} \tag{7.7}$$

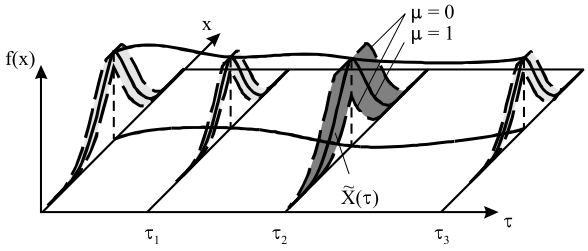

Fig. 7.4 Fuzzy random process $\tilde{X}(\underline{\theta}_j, \tau)$

may thus be represented by the fuzzy set of all real valued functions $x(\underline{s}, \underline{t})$ which may be generated from all possible real vectors $\underline{s} \in \tilde{\underline{s}}$. For every $\underline{t} \in \mathbf{T}$, each of the crisp functions $x(\underline{s}, \underline{t})$ yields values x_t which are contained in the associated fuzzy functional values $\tilde{x}_t$. The real functions $x(\underline{s}, \underline{t})$ of $\tilde{x}(\underline{t})$ are referred to as trajectories. Numerical processing of fuzzy functions $\tilde{x}(\underline{t}) = x(\tilde{\underline{s}}, \underline{t})$ demands the discretization of their arguments $\underline{t}$ in space and time.

2.2.2 Fuzzy Random Function

According to Eqs. (7.2) and (7.4), as well as Fig. 7.4, a fuzzy random function is the result of an uncertain mapping

$$\tilde{X}(\underline{t}) : \mathbf{F}(\mathbf{T}) \times \Omega \rightarrow \mathbf{F}(\mathbb{R}). \tag{7.8}$$

Thereby, $\mathbf{F}(\mathbf{X})$ and $\mathbf{F}(\mathbf{T})$ denote the sets of all fuzzy variables in $\mathbf{X}$ and $\mathbf{T}$ respectively [15, 16]. At a specific point $\underline{t}$, the mapping of Eq. (7.8) leads to the fuzzy random variable $\tilde{X}_t = \tilde{X}(\underline{t})$. Therefore, fuzzy random functions are defined as a family of fuzzy random variables

$$\tilde{X}(\underline{t}) = \left\{ \tilde{X}_t = \tilde{X}(\underline{t}) \; \forall \underline{t} \mid \underline{t} \in \mathbf{T} \right\}. \tag{7.9}$$

For the numerical simulation, again the bunch parameter representation of a fuzzy random function is applied. For each crisp bunch parameter vector $\underline{s} \in \tilde{\underline{s}}$ with the assigned membership value $\mu(\underline{s})$, a real random function $X(\underline{t}) = X(\underline{s}, \underline{t}) \in \tilde{X}(\underline{t})$ with $\mu(X(\underline{t})) = \mu(\underline{s})$ is obtained. The fuzzy random function $\tilde{X}(\underline{t})$ may thus be represented by the fuzzy set of all real random functions $X(\underline{t}) \in \tilde{X}(\underline{t})$

$$X(\tilde{\underline{s}}, \underline{t}) = \left\{ \left(X(\underline{t}), \mu\left(X(\underline{t})\right) \right) \mid X(\underline{t}) = X(\underline{s}, \underline{t}); \mu\left(X(\underline{t})\right) = \mu(\underline{s}) \; \forall \underline{s} \mid \underline{s} \in \tilde{\underline{s}} \right\} \tag{7.10}$$

which may be generated from all possible real vectors $\underline{s} \in \tilde{\underline{s}}$. The real random function $X(\underline{t}) \in \tilde{X}(\underline{t})$ is defined for all $\underline{t} \in \mathbf{T}$ and referred to as original function. A numerical processing of a fuzzy random function $\tilde{X}(\underline{t}) = X(\tilde{\underline{s}}, \underline{t})$ requires the discretization of their arguments $\underline{t}$ in space and time.

3 Fuzzy Stochastic Analysis

Fuzzy stochastic analysis is an appropriate computational approach for processing uncertain data using the uncertainty model fuzzy randomness. Basic terms and def-

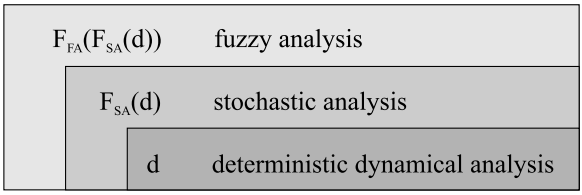

Fig. 7.5 Fuzzy stochastic analysis (FSA)

initions related to fuzzy randomness have been introduced, inter alia, by [13]. The formal description of fuzzy randomness chosen by [13] is however not suitable to formulating uncertainty encountered in engineering tasks. A suitable form of representation with the scope of numerical engineering tasks is given with the so-called α-discretization by [7] and [8].

The numerical simulation under consideration of fuzzy variables and fuzzy functions (fuzzy analysis) may formally be described by the mapping

$$F_{FA}(d) : \underline{\tilde{x}}(\underline{t}) \mapsto \underline{\tilde{z}}(\underline{t}). \tag{7.11}$$

According to Eq. (7.11), the fuzzy variables $\underline{\tilde{x}}$ and the fuzzy functions $\underline{\tilde{x}}(\underline{t})$ are mapped onto the fuzzy results $\underline{\tilde{z}}(\underline{t})$ with aid of the crisp analysis algorithm d. Every arbitrary deterministic fundamental solution may be used as algorithm d. On the basis of space and time discretization, fuzzy functional values $x(\underline{\tilde{s}}, \underline{\theta}_j, \tau_i, \underline{\varphi}_k)$ of the function $x(\underline{\tilde{s}}, \underline{\theta}, \tau, \underline{\varphi})$ are determined at points in space $\underline{\theta}_j$, time τ_i, and a realization of $\underline{\varphi}_k$.

The numerical simulation is carried out with the aid of the α-level optimization [7]. For fuzzy variables $\tilde{x}$ and fuzzy bunch parameter $\underline{\tilde{s}}$ of the fuzzy functions $x(\underline{\tilde{s}}, \underline{\theta}, \tau, \underline{\varphi})$, an input subspace $\underline{E}_\alpha$ is formed and assigned to the level α. By multiple application of the deterministic analysis, the extreme values $z_{\alpha,l}(\underline{\theta}_j, \tau_i, \underline{\varphi}_k)$ and $z_{\alpha,r}(\underline{\theta}_j, \tau_i, \underline{\varphi}_k)$ of the fuzzy result variable $\tilde{z}(\underline{\theta}_j, \tau_i, \underline{\varphi}_k)$ are computed. These points are interval bounds of the α-level sets and enable the numerical description of the convex membership function of the fuzzy result variable $\tilde{z}(\underline{\theta}_j, \tau_i, \underline{\varphi}_k)$. For the computation of $\tilde{z}(\underline{\theta}_j, \tau_{i+1}, \underline{\varphi}_k)$ at the time point τ_{i+1}, the procedure must be restarted at $\tau = 0$ due to the interaction within the mapping model.

Fuzzy stochastic analysis allows the mapping of fuzzy random input variables onto fuzzy random result variables. The fuzzy stochastic analysis can be applied for static and dynamic structural analysis and for assessment of structural safety, durability as well as robustness. Two different approaches for computation of the fuzzy random result variables have been developed. The first variant (Fig. 7.5) bases on the bunch parameter representation of fuzzy random variables by [16]. The second variant utilizes the $l_\alpha r_\alpha$-representation of fuzzy random variables. The variant to be preferred depends on the engineering task, the available uncertain data and the aspired results [10].

The fuzzy stochastic analysis is called fuzzy stochastic finite element method (FSFEM), if the deterministic dynamical analysis is based on a finite element (FE) model.

4 Deterministic Dynamical Analysis of RC Structures

4.1 1D-Beams

Plane and spatial beam structures are called 1D-structures. For the physical nonlinear analysis, the cross-sections of the beams are subdivided into layers (plane structures) or fibers (spatial structures). In contrast to the widespread finite element formulations, solutions based on the differential equations for the straight or imperfectly straight beam also exist. A respective approach for plane beam structures is presented here.

The geometrical and physical nonlinear analysis of plane reinforced concrete, prestressed concrete, and steel beam structures is chosen as fundamental model [14]. The beams are subdivided into integration sections, the cross-sections are subdivided into layers. On this basis, an incrementally formulated system of second order differential equations for the straight or imperfectly straight beam is solved

$$\left[\frac{d\Delta\underline{z}(\theta_1)}{d\theta_1}\right]^{[k]}_{(n)} = \underline{A}(\theta_1,\underline{z})_{(n-1)}\cdot\Delta\underline{z}(\theta_1)^{[k]}_{(n)} + \Delta\underline{b}(\theta_1)^{[k-1]}_{(n)} + \underline{d}(\theta_1)_{(n-1)}\cdot\Delta\dot{\underline{z}}(\theta_1)^{[k]}_{(n)} + \underline{m}(\theta_1)_{(n-1)}\cdot\Delta\ddot{\underline{z}}(\theta_1)^{[k]}_{(n)} \quad (7.12)$$

where $[k]$—counter of iteration steps; (n)—counter of increments; θ_1—bar coordinate; Δ—increment; $\underline{z} = \{\underline{z}_1, \underline{z}_2\} = \{uv\phi; NQM\}$—vector of structural responses; $\underline{A}$—matrix of coefficients (constant within the increment); $\underline{b}$—"right hand side" of the system of differential equations with loads and varying parts resulting from geometrical and physical nonlinearities as well as with forces from unbonded prestressing; $\underline{d}$—damping matrix; and $\underline{m}$—mass matrix.

The implicit nonlinear system of differential equations for the differential beam sections is linearized by increments. All geometrically and physically nonlinear components in the $\Delta\underline{b}$-vector are recalculated after every iteration step, and the $\underline{A}$-, $\underline{d}$-, and $\underline{m}$-matrix are recalculated after the completion of the iteration within the increment.

The solution of the system of differential equations by a Runge–Kutta integration results in the system of differential equations

$$\underline{K}_{T(n-1)}\cdot\Delta\underline{v}^{[k]}_{(n)} + \underline{D}_{T(n-1)}\cdot\Delta\dot{\underline{v}}^{[k]}_{(n)} + \underline{M}_{T(n-1)}\cdot\Delta\ddot{\underline{v}}^{[k]}_{(n)} = \Delta\underline{P}_{(n)} - \Delta\overset{o}{\underline{F}}{}^{[k]}_{(n)} + \Delta\Delta\underline{F}_{(n-1)} \quad (7.13)$$

of the unknown incremental displacements $\Delta\underline{v}$, velocities $\Delta\dot{\underline{v}}$, and accelerations $\Delta\ddot{\underline{v}}$ of the nodes.

4.2 2D-Folded Plate RC Structures

Shells, folded plates, shear panels and plates are called 2D-structures. Here, we focus on folded plates which represent the general case for plane 2D structures. They

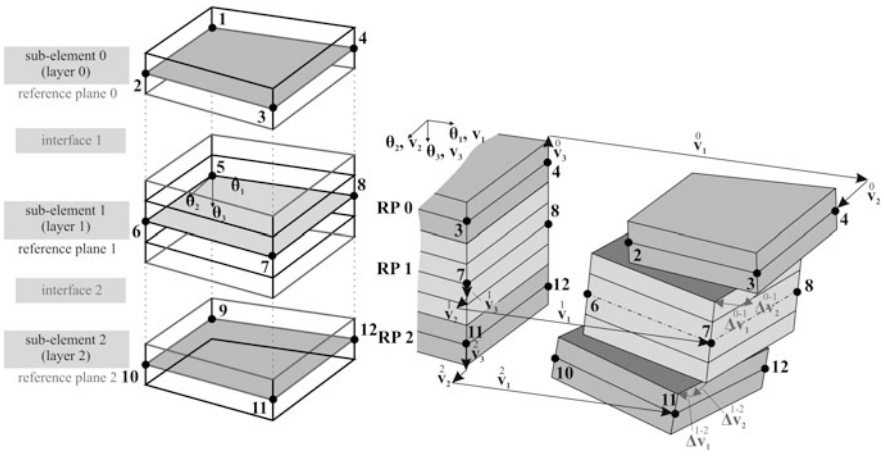

Fig. 7.6 MRM discretization and kinematics

can further be applied to approximate the shape of slightly curved structures. The internal forces are related to the reference plane, which is not stringently the midplane. The cross-section is subdivided into layers to describe the physical nonlinear behavior of reinforced concrete. Over the past years, a new strengthening technology for damaged RC structures has been developed. The thin strengthening layers consist of fine-grained concrete reinforced with textiles made of AR-glass or carbon, see e.g. [1] and [18]. The classical layered model with one reference plane for folded plate structures is enhanced to take into account the later applied strengthening layers.

An extended layer model with specific kinematics, the so-called multi-reference-plane model (MRM), is used to describe the load-bearing behavior of RC constructions with textile strengthening. The MRM consists of concrete layers and steel reinforcement layers of the old construction, the strengthening layers comprised of the inhomogeneous material textile concrete (TRC), and the interface layers (Fig. 7.6). This multilayer continuum has the following kinematic peculiarities. Due to the fact that the modification of the concrete layer thickness is very small and can be neglected, we have $\varepsilon_{33} = 0$. Furthermore, the transverse shear stresses in the concrete layers have no significant influence on the deformation, which means that $\varepsilon_{13} = 0$ and $\varepsilon_{23} = 0$ can be set to zero. The deformation state of the concrete layers may be described by Kirchhoff kinematics. The independent degrees of freedom are assigned to a reference plane which can be selected arbitrarily.

The very thin strengthening layers are subject to the same kinematic assumptions. Kirchhoff kinematic with a reference plane is also assigned to each strengthening layer. The independent degrees of freedom of the strengthening layer lie in the reference plane. The bond between the layers of reinforced concrete and an arbitrary strengthening layer is modeled by an interface. The interface is an immaterial layer of zero thickness. The bonding state is assessed with the help of the relative displacements $\Delta v_1, \Delta v_2, \Delta v_3$ between the contact surfaces. In conjunction with a bonding

matrix, the relative displacements enable assumptions regarding delamination and shear failure.

The FE discretization of the MRM is based on the functional of the complementary energy extended by the static transition conditions $\Delta\tilde{\underline{p}} - \overset{+}{\tilde{\underline{p}}} = 0$ to O_p^r and the equilibrium conditions $\tilde{\underline{G}} \cdot \underline{\sigma}_{el}^e + \overset{+}{\underline{p}}^e - \rho^e \cdot \ddot{\underline{v}}^e = 0$ in V^e

$$\begin{aligned} \Pi_{mh} = \int_{\tau_1}^{\tau_2} \sum_{e=1}^{n} \Bigg\{ & \int_{V^e} \left[w_c\left(\underline{\sigma}_{el}^e\right) + \left(\tilde{\underline{G}} \cdot \underline{\sigma}_{el}^e + \overset{+}{\underline{p}}^e - \rho^e \cdot \ddot{\underline{v}}^e\right)^T \cdot \underline{v}^e \right] dV \\ & + \int_{V^e} \left(\underline{\sigma}_{el}^e\right)^T \cdot \underline{\varepsilon}_0^e \, dV - \int_{O_p^{r,e}} \left(\underline{p}^{r,e} - \overset{+}{\tilde{\underline{p}}}^{r,e}\right)^T \cdot \underline{v}^{r,e} \, dO \\ & - \int_{O_v^{r,e}} \left(\underline{p}^{r,e}\right)^T \cdot \overset{+}{\underline{v}}^{r,e} \, dO \Bigg\} d\tau \end{aligned} \tag{7.14}$$

with $w_c(\underline{\sigma}_{el}^e)$—internal complementary energy; $\tilde{\underline{G}}$—matrix of differential operators; $\overset{+}{\tilde{\underline{p}}}$—external forces in V^e; ρ^e—density in; $\ddot{\underline{v}}^e$—internal acceleration in V^e; ρ^e; $\underline{\varepsilon}_0^e$—initial strain; $\underline{p}^{r,e}$—internal forces in the boundary surface $O_p^{r,e}$; $\overset{+}{\tilde{\underline{p}}}^{r,e}$—external forces along the boundary surface $O_p^{r,e}$; $\underline{v}^{r,e}$—displacements of the boundary surface $O_p^{r,e}$; $\overset{+}{\tilde{\underline{v}}}^{r,e}$—prescribed displacements of the boundary surface $O_v^{r,e}$; τ—time.

After some transformations, the quasi-static part of the equilibrium conditions $(\tilde{\underline{G}} \cdot \underline{\sigma}_{el}^e + \overset{+}{\underline{p}}^e)$ and the kinetic energy become visible in the mixed hybrid functional

$$\begin{aligned} \Pi_{mh} = \int_{\tau_1}^{\tau_2} \sum_{e=1}^{n} \Bigg\{ & \int_{V^e} \left[w_c\left(\underline{\sigma}_{el}^e\right) + \left(\tilde{\underline{G}} \cdot \underline{\sigma}_{el}^e + \overset{+}{\underline{p}}^e\right)^T \cdot \underline{v}^e + \frac{1}{2} \rho^e \cdot \left(\dot{\underline{v}}^e\right)^T \cdot \dot{\underline{v}}^e \right] dV \\ & + \int_{V^e} \left(\underline{\sigma}_{el}^e\right)^T \cdot \underline{\varepsilon}_0^e \, dV - \int_{O_p^{r,e}} \left(\underline{p}^{r,e} - \overset{+}{\tilde{\underline{p}}}^{r,e}\right)^T \cdot \underline{v}^{r,e} \, dO \\ & - \int_{O_v^{r,e}} \left(\underline{p}^{r,e}\right)^T \cdot \overset{+}{\underline{v}}^{r,e} \, dO \Bigg\} d\tau. \end{aligned} \tag{7.15}$$

In extension to the static case [9, 18], this functional may be applied to a layered continuum with dynamic loads. Following the procedure described in [9, 18], the steady-state condition of the mixed hybrid functional

$$\begin{aligned} \delta \Pi_{mh,NC} &= \frac{1}{2} \delta\left(d^2 \Pi_{mh}\right) \\ &= \sum_{i=0}^{k} \delta\left(d^2\left({}^{(R_i)}\Pi_{mh,NC}\right)\right) + \sum_{j=1}^{k} \delta\left(d^2\left({}^{(I_j)}\Pi_{mh,NC}\right)\right) = 0 \end{aligned} \tag{7.16}$$

with

$$
\begin{aligned}
{}^{(R_i)}\Pi_{mh,NC} = \int_{\tau_1}^{\tau_2} \Bigg\{ \sum_{e_i=1}^{n} \Bigg(\frac{1}{2} \sum_{m=0}^{s_i-1} \Bigg[& \int_{V^{e_i,m}} \left(d\underline{\sigma}_{el}^{e_i,m} \right)^T \cdot d\underline{\varepsilon}_{el}^{e_i,m} \, dV \\
& + 2 \int_{V^{e_i,m}} \left(\tilde{\underline{G}} \cdot d\underline{\sigma}_{el}^{e_i,m} + d \overset{+}{\tilde{\underline{p}}}{}^{e_i,m} \right)^T \cdot d\underline{v}^{e_i,m} \, dV \\
& + \int_{V^{e_i,m}} \rho^{e_i,m} \cdot \left(d\dot{\underline{v}}^{e_i,m} \right)^T \cdot d\dot{\underline{v}}^{e_i,m} \, dV \\
& + 2 \int_{V^{e_i,m}} \left(d\underline{\sigma}_{el}^{e_i,m} \right)^T \cdot d\underline{\varepsilon}_{0}^{e_i,m} \, dV \Bigg] \\
& - \int_{({}^{R_i})O_p^{r,e_i}} \left(d\underline{p}^{r,e_i} - d \overset{+}{\tilde{\underline{p}}}{}^{r,e_i} \right)^T \cdot d\underline{v}^{r,e_i} \, dO \\
& - \int_{({}^{R_i})O_v^{r,e_i}} \left(d\underline{p}^{r,e_i} \right)^T \cdot d \overset{+}{\tilde{\underline{v}}}{}^{r,e_i} \, dO \Bigg) \Bigg\} d\tau
\end{aligned}
\tag{7.17}
$$

$$
\begin{aligned}
{}^{(I_j)}\Pi_{mh,NC} = \int_{\tau_1}^{\tau_2} \Bigg\{ \sum_{e_j=1}^{n} \int_{({}^{I_j})O_p^{e_j}} & \left(d^I\underline{\sigma}^{e_j} \right)^T \\
& \cdot \left({}^{(j|j)}d\underline{v}^{r,e_j} - {}^{(j-1|j)}d\underline{v}^{r,e_{j-1}} \right) dO \Bigg\} d\tau
\end{aligned}
\tag{7.18}
$$

for a layered continuum with k layers is obtained from Eq. (7.15). Equation (7.17) describes the functional for the sub-element R_i whereas Eq. (7.18) depicts the functional for the interface I_j. Compared to [9, 18] Eqs. (7.16), (7.17) and (7.18) are extended by inertial forces. In order to account for physical nonlinearities of the layered continuum, the layer i with the reference plane R_i is subdivided into s_i sub-layers in Eq. (7.17).

On the basis of Eq. (7.16), the differential equation of motion can be derived. Thereby, the same stress shape functions, the same boundary displacement shape functions and the same element displacement shape function are chosen within all layers of the continuum. The stress shape functions are chosen in such a way, that they fulfill strongly the quasi-static part of the equilibrium conditions

$$
\tilde{\underline{G}} \cdot d\underline{\sigma}_{el}^{e_i,m} + d \overset{+}{\tilde{\underline{p}}}{}^{e_i,m} = 0. \tag{7.19}
$$

The evaluation of the steady-state condition, Eq. (7.16) yields the MRM element and leads to the differential equation of motion

$$
\tilde{\underline{K}}_T \cdot d\tilde{\underline{q}} + \tilde{\underline{M}} \cdot d\ddot{\tilde{\underline{q}}} - d\tilde{\underline{R}} - d\underline{R}_K = 0 \tag{7.20}
$$

with $\tilde{\underline{K}}_T$—tangential system stiffness matrix, $\tilde{\underline{M}}$—system mass matrix, $d\tilde{\underline{R}}$, $d\underline{R}_K$—differential load contributions, and $\tilde{\underline{q}}$—nodal displacement degrees of freedom. The matrix $\tilde{\underline{K}}_T$ and the vectors $d\tilde{\underline{R}}$, and $d\underline{R}_K$ are identical to the corresponding values of the hybrid procedure in [9]. The system mass matrix $\tilde{\underline{M}}$ is specified in [19].

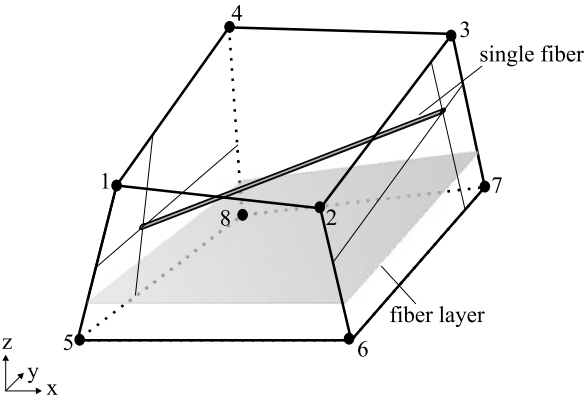

Fig. 7.7 Eight-node solid element with embedded reinforcements

4.3 3D-Compact RC Structures

Hybrid eight-node hexagonal solid elements for the physical linear static analysis are described in [12]. For the physically nonlinear analysis of reinforced concrete and textile reinforced concrete (TRC), respectively, two kinds of reinforcement are introduced—single fibers and fiber layers (see Fig. 7.7). The formulation of the hybrid eight-node hexagonal solid element with embedded (textile) reinforcement is outlined in the following.

Starting point is the functional of Hellinger–Reissner

$$\Pi_{HR} = \int_V \left(\underline{\sigma}^T \cdot (\underline{G} \cdot \underline{v}) - \frac{1}{2} \underline{\sigma}^T \cdot \underline{\varepsilon} - \overset{+}{\underline{p}}{}_V^T \cdot \underline{v} \right) dV - \int_{O_p} \overset{+}{\underline{p}}{}^T \cdot \underline{v} \, dO \qquad (7.21)$$

with $\underline{\sigma}, \underline{\varepsilon}, \underline{v}$—stresses, strains and displacements in the volume V, $\overset{+}{\underline{p}}{}_V^T$—external forces in V and $\overset{+}{\underline{p}}{}^T$—external forces along the boundary surface O_p, and the matrix of differential operators $\underline{G}$.

Based on it, the Hamilton functional is build

$$H = \delta \int_{\tau_1}^{\tau_2} (K - \Pi_{HR}) \, d\tau = \delta \int_{\tau_1}^{\tau_2} \left(\frac{1}{2} \int_V \rho \cdot (\dot{v})^T \cdot \dot{v} \, dV - \Pi_{HR} \right) d\tau \qquad (7.22)$$

with the kinetic energy K.

The physical nonlinear analysis of reinforced concrete is a non-conservative problem arising e.g. from crack formation, nonlinear material behavior, bonding and damage. In order to solve this non-conservative problem, a differential load change is considered. Under such load change, the existence of a potential is assumed. The differential load change leads to a transition of the structure from the basic condition to a differentially adjacent neighboring condition (NC). The steady-state condition of the neighboring condition is therefore

$$\delta H_{NC} = \frac{1}{2} \delta \left(d^2 H \right) = 0 \qquad (7.23)$$

with

$$H_{NC} = \int_{\tau_1}^{\tau_2} \left(\frac{1}{2} \int_V \rho \cdot (d\dot{\underline{v}})^T \cdot d\dot{\underline{v}} \, dV \right.$$
$$- \int_V \left(d\underline{\sigma}^T \cdot (\underline{G} \cdot d\underline{v}) - \frac{1}{2} d\underline{\sigma}^T \cdot d\underline{\varepsilon} - d\underline{p}^{+T}_V \cdot d\underline{v} \right) dV$$
$$\left. + \int_{O_p} d\underline{p}^{+T} \cdot d\underline{v} \, dO \right) d\tau. \tag{7.24}$$

The continuum is subdivided into n finite 3D elements. The volume V^e of one finite 3D element e consists of the matrix volume V_m^e and the reinforcement volume V_b^e. Single fibers (sf) and fiber layers (fl) are taken into account. The volume of the reinforcement V_b^e consists then of n_{sf} single fibers and n_{fl} fiber layers. For a function F (e.g. stresses, strains, displacements) holds

$$\int_{V^e} F \, dV = \int_{V_m^e} F_m \, dV + \int_{V_b^e} F_b \, dV = \int_{V^e} F_m \, dV + \int_{V_b^e} F_b \, dV - \int_{V_b^e} F_m \, dV$$
$$= \int_{V^e} F_m \, dV + \sum_{i=1}^{n_{sf}} \int_{V_{sf}^{e,i}} F_{sf}^{e,i} \, dV + \sum_{j=1}^{n_{fl}} \int_{V_{fl}^{e,j}} F_{fl}^{e,j} \, dV$$
$$- \sum_{i=1}^{n_{sf}} \int_{V_{sf}^{e,i}} F_m^{e,i} \, dV - \sum_{j=1}^{n_{fl}} \int_{V_{fl}^{e,j}} F_m^{e,j} \, dV. \tag{7.25}$$

With Eq. (7.25), the reinforcement is taken into account in Eq. (7.24).

5 Model Reduction

The computational cost of a fuzzy stochastic structural analysis of RC structures under dynamic loads is almost completely caused by the nonlinear FE analysis. Thus, the most effective measure to increase the numerical efficiency is to replace the costly deterministic computational model (innermost loop in Fig. 7.5) by a fast approximation solution based on a reasonable amount of initial deterministic computational results. The fuzzy stochastic analysis can then be performed with that surrogate model, which enables the utilization of an appropriate sample size for the simulation. The surrogate model is designed to describe a functional dependency between the structural parameters $\underline{x}$ and the structural responses $\underline{z}$ in the form of a response surface approximation

$$\underline{z} = f_{RS}(\underline{x}). \tag{7.26}$$

For response surface approximation, a variety of options exist (see [11, 17]). The suitability of the particular developments primarily depends on the properties of the computational model. Due to the very general properties of the FE analysis in structural analysis of textile strengthened RC structures, which can hardly be limited to convenient cases, a high degree of generality and flexibility of the approximation is demanded. In this context, an artificial neural network provides a

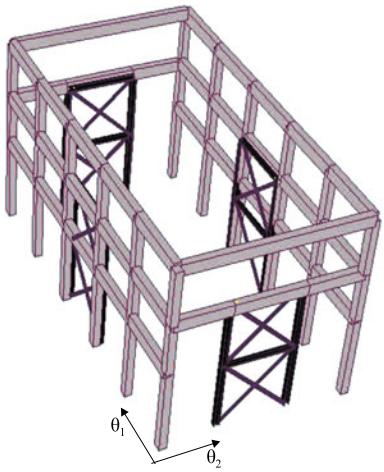

Fig. 7.8 3D pictorial view of the upgraded structure with scheme of the bracing system configuration

powerful basis for response surface approximation. This approach can extract information from initial deterministic computational results and can subsequently reproduce the structural response based on the extracted information only. According to the universal function approximation theorem, artificial neural networks are capable of uniformly approximating any kind of nonlinear functions over a compact domain of definition to any degree of accuracy. There is virtually no restriction for a response surface approximation with the aid of artificial neural networks.

In the case, that the global structural behavior is dominated from few eigen modes, the number of degrees of freedom can be reduced. In the following example, a simplified 2-DOF model is used as equivalent system for the whole structure.

6 Example

6.1 Investigated Structure

The investigated building (Fig. 7.8) has a rectangular plan whose dimensions are 10.80×20.40 m^2. The elevation of the first floor is 7.40 m, whereas the second one is at 11.10 m. It is characterized by a RC structure framed in the longitudinal direction only and is designed against vertical loads without account for seismic action. Columns and beams have rectangular 40×50 cm^2 and 40×70 cm^2 cross-sections, respectively. The T-shaped hollow tile RC floors have a 6 cm thick concrete slab, so that the total depth of the first floor is 36 cm, whereas the second, at the roof level, is 30 cm.

In [5], the results of the vulnerability evaluation have been published. Thereby, a three-dimensional FEM model with beam elements of the structure has been created considering floors like rigid diaphragms in the horizontal plane. Two nonlinear

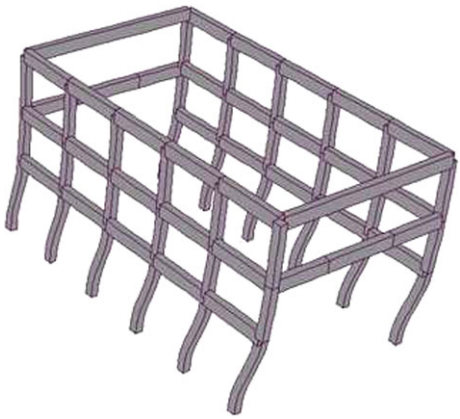

Fig. 7.9 Deformed shapes of the fundamental vibration modes for one principal direction

static analyses and a set of linear and nonlinear time history analyses have allowed to evaluate the vulnerability of the structure in the as-built condition and the effectiveness of the upgrading interventions. First of all, a calculation of the natural frequencies of the system has been carried out. Relevant values are 2.075 s^{-1} in Θ_1 direction (longitudinal, see Fig. 7.9) and 0.796 s^{-1} in Θ_2 direction (transverse). The mass participation factors are higher than 95% for such modes, so that the structure can be assumed as a matter of fact as made of two mutually independent SDOF systems in both Θ_1 and Θ_2 direction. This consideration assumes relevance in the determination of the optimal value of the damping devices. In fact, a design procedure for viscous devices based on simplified 2-DOF system can be used when the structural dynamic behavior can be interpreted through two SDOF systems [2, 6].

A peak ground acceleration (PGA) of 0.25 g has been assumed in the analysis, considering the combination of site effect and the importance of the structure with regard to collapse.

The time history analysis has shown an excessive deformability of the original structure, not compatible with the structural safety and immediate occupancy requirement after seismic events [3, 4]. The assumed upgrading interventions are aimed at reducing the lateral floor displacements of the structure by means of steel braces fitted with additional energy dissipation devices. Such devices connect the original structure at the first floor level with rigid steel braces and act due to the relative displacements occurring between the original structure and the steel braces. The study, presented in this paper, has been carried out considering the connection with purely viscous devices. As shown in [5], the reduction of horizontal floor displacements obtained thanks to the addition of this kind of devices is greater than the one obtained with a rigid connection of the original structure to the steel braces.

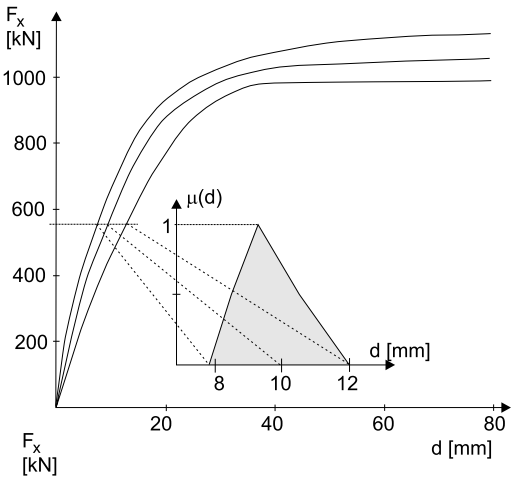

Fig. 7.10 Fuzzy load-displacement dependency of the existing RC frame structure

6.2 Uncertain Input Parameters

No technical documentation regarding the history of the structure is available, apart from the period of erection, which can be dated at the end of the 60's of XX century, on the basis of oral testimony.

Because of the lack of technical data and in order to find information about, the quality of structural materials, some characterization tests have been carried out on concrete core bored specimens and steel bars taken out of the structure. In result of the tests, the mechanical resistance of concrete is evaluated by means of fuzzy quantities. The concrete compressive and tensile strength are modeled as fuzzy triangular numbers $\tilde{f}_{ck} = \langle 14, 16.5, 20\rangle$ N/mm^2 and $\tilde{f}_t = \langle 1.5, 2.0, 2.5\rangle$ N/mm^2, respectively. A magneto-metric survey has been also carried out in order to locate the position and the diameter of steel bars in beams and columns. For the numerical study, twelve steel bars with a fuzzy cross-sectional area $\tilde{A} = \langle 2.69, 3.14, 3.21\rangle$ cm^2 are considered. In order to assess the seismic vulnerability of the existing structure, nonlinear static analyses have been carried out under consideration of fuzzy resistance variables. The response of the as-built structure along both principal directions has then been evaluated in terms of fuzzy capacity curves F-d (Fig. 7.10). These curves have been represented in an approximate way by means of equivalent SDOF nonlinear relationships. Thereby, the kernel curve with $\mu(d(F)) = 1$ is scaled according to

$$\tilde{d}(F) = {}_{1.0}d(F) + \tilde{a} \cdot F \tag{7.27}$$

with $\tilde{a} = \langle -3.3, 0.0, 6.0\rangle 10^{-3}$. The steel braces are also modeled as SDOF system with fuzzy stiffness $\tilde{K}$ and fuzzy mass $\tilde{M}$. Two variants are investigated especially: Variant 1 $\tilde{K}_1 = \langle 39, 40.8, 43\rangle$ MN/m with $\tilde{M}_1 = \langle 1.1, 1.3, 1.5\rangle$ t and Variant 2 $\tilde{K}_1 = \langle 50, 52.5, 55\rangle$ MN/m with $\tilde{M}_1 = \langle 1.2, 1.55, 1.8\rangle$ t. The uncertainty of the viscosity c_x of the connecting devices is with a fuzzy scaling factor according to $\tilde{c} = \tilde{b} \cdot c_x$ with $\tilde{b} = \langle 0.9, 1.0, 1.1\rangle$.

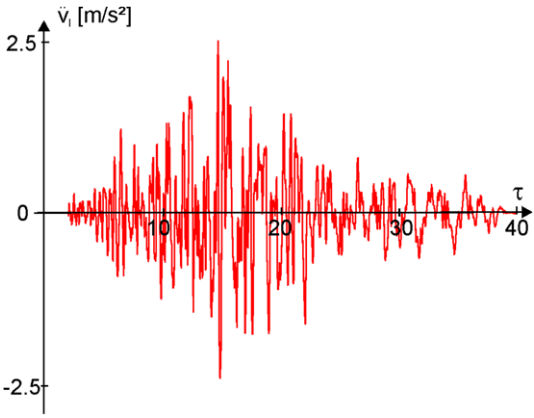

Fig. 7.11 Acceleration of the Taiwan earthquake scaled to PGA value of 0.25 g

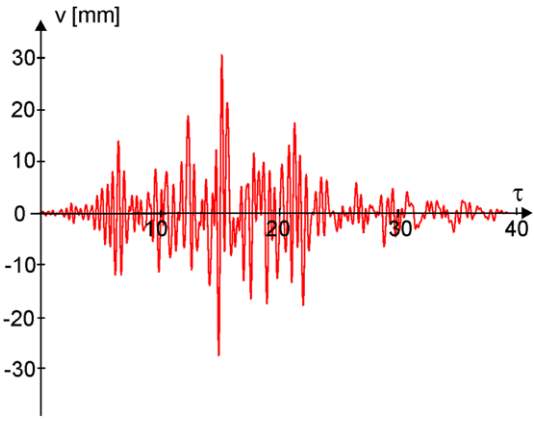

Fig. 7.12 Realization of the fuzzy displacement-time dependency due to the Taiwan earthquake

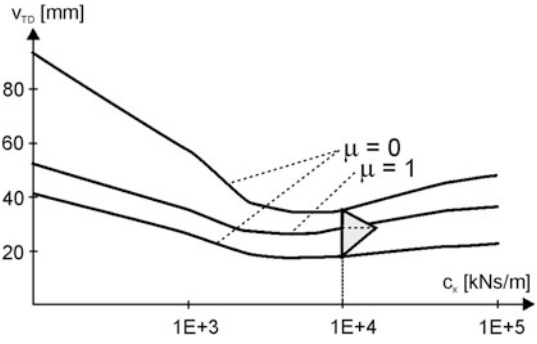

Fig. 7.13 Fuzzy top displacement in dependency of the viscosity

6.3 Fuzzy Structural Analysis

Nonlinear time-history analyses of the simplified 2-DOF system have then been performed considering the seismic input of Taiwan (1999) earthquake, scaled to PGA

value of 0.25 g. Figure 7.11 displays the time-history of the ground acceleration of the Taiwan earthquake. The fuzzy maximum displacement $\tilde{v}_{TD}$ at the top of the structure has been calculated on the basis of the fuzzy displacement-time dependency, as shown for one realization in Fig. 7.12. The parameter study with variation of the viscosity of damping devices yields a fuzzy function $\tilde{v}_{TD}(c_x)$ as presented in Fig. 7.13 for the Taiwan earthquake.

Acknowledgements Authors gratefully acknowledge the support of the German Research Foundation (DFG) within the framework of the Collaborative Research Center (SFB) 528 and the contribution of Alberto Mandara (Second University of Naples).

References

1. Kaliske, M., Graf, W., Sickert, J.-U., Steinigen, F.: Numerische Prognose des Tragverhaltens textilverstärkter Stahlbetontragwerke. Bauingenieur **86**, 371–380 (2011)
2. Mandara, A., Mazzolani, F.M.: On the design of retro-fitting by means of energy dissipation devices. In: 7th International Seminar on Seismic Isolation, Passive Energy Dissipation and Active Control of Vibrations of Structures, Assisi (2001)
3. Mandara, A., Ramundo, F., Spina, G.: Seismic up-grading of an existing r.c. building by steel braces and energy dissipation devices. In: XXI National Congress of CTA, Catania (2007)
4. Mandara, A., Ramundo, F., Spina, G.: Steel bracing for the optimal seismic control of existing r.c. structures. In: 5th European Conference on Steel and Composite Structures, Graz (2008)
5. Mandara, A., Ramundo, F., Spina, G.: Seismic up-grading of r.c. structures with innovative bracing systems. In: Proceedings of PROHITEC, London (2009)
6. Mazzolani, F.M., Mandara, A.: Seismic up-grading of an old industrial building by dissipative steel roofing. In: International Seminar on Structural Analysis of Historical Constructions, Padova (2004)
7. Möller, B., Graf, W., Beer, M.: Fuzzy structural analysis using α-level optimization. Comput. Mech. **26**, 547–565 (2000)
8. Möller, B., Beer, M.: Fuzzy Randomness—Uncertainty in Civil Engineering and Computational Mechanics. Springer, Berlin (2004)
9. Möller, B., Graf, W., Hoffmann, A., Steinigen, F.: Numerical simulation of RC structures with textile reinforcement. Comput. Struct. **83**, 1659–1688 (2005)
10. Möller, B., Graf, W., Sickert, J.-U., Reuter, U.: Numerical simulation based on fuzzy stochastic analysis. Math. Comput. Model. Dyn. Syst. **13**, 349–364 (2007)
11. Myers, R.H., Montgomery, D.C.: Response Surface Methodology: Process and Product Optimization Using Designed Experiments. Wiley, New York (1995)
12. Pian, H.H.T., Wu, C.-C.: Hybrid and Incompatible Finite Element Methods. Chapman & Hall, Boca Raton (2006)
13. Puri, M.L., Ralescu, D.: Fuzzy random variables. J. Math. Anal. Appl. **114**, 409–422 (1986)
14. Schneider, R.: Stochastische Analyse und Simulation des nichtlinearen Verhaltens ebener Stabtragwerke mittels M-N-Q-Interaktionsmodell. Dissertation, Technische Universität Dresden, Veröffentlichungen des Lehrstuhls für Statik, Heft 2 (2001)
15. Sickert, J.-U.: Fuzzy-Zufallsfunktionen und ihre Anwendung bei der Tragwerksanalyse und Sicherheitsbeurteilung. Dissertation, Technische Universität Dresden, Veröffentlichungen Institut für Statik und Dynamik der Tragwerke, Heft 9 (2005)
16. Sickert, J.-U., Beer, M., Graf, W., Möller, B.: Fuzzy probabilistic structural analysis considering fuzzy random functions. In: 9th International Conference on Applications of Statistics and Probability in Civil Engineering. Millpress, Rotterdam (2003)
17. Simpson, T., Poplinski, J., Koch, P.N., Allen, J.: Metamodels for computer-based engineering design: survey and recommendations. Eng. Comput. **17**, 129–150 (2001)

18. Steinigen, F.: Numerische Simulation des Tragverhaltens textilverstärkter Bauwerke. Dissertation, Technische Universität Dresden, Veröffentlichungen Institut für Statik und Dynamik der Tragwerke, Heft 11 (2006)
19. Steinigen, F., Möller, B., Graf, W., Hoffmann, A.: Numerical simulation of textile reinforced concrete considering dynamic loading process. In: Hegger, J., Brameshuber, W., Will, N. (eds.) Textile Reinforced Concrete—Proceedings of the 1st International RILEM Conference, Aachen (2006)

Chapter 8
Application of Interval Fields for Uncertainty Modeling in a Geohydrological Case

Wim Verhaeghe, Wim Desmet, Dirk Vandepitte, Ingeborg Joris, Piet Seuntjens, and David Moens

Abstract In situ soil remediation requires a good knowledge about the processes that occur in the subsurface. Groundwater transport models are needed to predict the flow of contaminants. Such a model must contain information on the material layers. This information is obtained from in situ point measurements which are costly and thus limited in number. The overall model is thus characterised by uncertainty. This uncertainty has a spatial character, i.e. the value of an uncertain parameter can vary based on the location in the model itself. In other words the uncertain parameter is non-uniform throughout the model. On the other hand the uncertain parameter

W. Verhaeghe (✉) · W. Desmet · D. Vandepitte · D. Moens
Department of Mechanical Engineering, K.U. Leuven, Celestijnenlaan 300B, 3001 Heverlee, Belgium
e-mail: wim.verhaeghe@mech.kuleuven.be

W. Desmet
e-mail: wim.desmet@mech.kuleuven.be

D. Vandepitte
e-mail: dirk.vandepitte@mech.kuleuven.be

D. Moens
e-mail: david.moens@mech.kuleuven.be

I. Joris · P. Seuntjens
VITO, Boeretang 200, 2400 Mol, Belgium

P. Seuntjens
e-mail: piet.seuntjens@vito.be

P. Seuntjens
Department of Soil Management, Ghent University, Coupure Links 653, 9000 Gent, Belgium

P. Seuntjens
Department of Bioscience Engineering, University of Antwerp, Groenenborgerlaan 171, 2020 Antwerpen, Belgium

D. Moens
Dept. of Applied Engineering, Lessius Hogeschool—Campus De Nayer, K.U. Leuven Association, J. De Nayerlaan 5, 2860 Sint-Katelijne-Waver, Belgium

M. Papadrakakis et al. (eds.), *Computational Methods in Stochastic Dynamics*, Computational Methods in Applied Sciences 26,
DOI 10.1007/978-94-007-5134-7_8,

does have some spatial dependency, i.e. the particular value of the uncertainty in one location is not totally independent of its value in a location adjacent to it. To deal with such uncertainties the authors have developed the concept of interval fields. The main advantage of the interval field is its ability to represent a field uncertainty in two separate entities: one to represent the uncertainty and one to represent the spatial dependency. The main focus of the paper is on the application of interval fields to a geohydrological problem. The uncertainty taken into account is the material layers' hydraulic conductivity. The results presented are the uncertainties on the contaminant's concentration near a river. The second objective of the paper is to define an input uncertainty elasticity of the output. In other words, identify the locations in the model, whose uncertainties influence the uncertainty on the output the most. Such a quantity will indicate where to perform additional in situ point measurements to reduce the uncertainty on the output the most.

1 Introduction

In recent years, the study of uncertainties in numerical modeling has gained a lot of attention. Probabilistic and non-probabilistic methods were developed for dealing with scalar parameter uncertainties. However, scalar parameter uncertainties are not the only kind of uncertainties influencing numerical models. Often scalar parameter uncertainties represent uncertainties that have uncertainty on a smaller scale spatial dimension too. The spatial influence of such uncertainties is often neglected, as it is assumed captured by assumptions of uniformity and homogeneity. This neglect is not without reasons, for a thorough discretisation of an uncertain property over the spatial domain would result in an explosion of independent uncertainties and thus a drastic increase in the computation time for the uncertainty analysis. However, a go-between approach is possible when certain patterns describing the spatial behaviour of an uncertainty are available. Taking into account the patterns reduces the explosion of uncertainties in going from one spatially uniform uncertainty to a thorough discretisation of the spatial domain. The authors have developed an interval field approach [6] to formalize these notions.

The paper first presents the general problem of interval finite element analysis and the interval field approach to it. Secondly, a section details the choice of certain spatial patterns in the interval field approach, based on random field analogies. Next, the concept of input uncertainty elasticity of the output is introduced in the context op spatial uncertainties. In the next section the geohydrological problem is introduced and the obtained results are presented. The paper concludes with some suggestions for further research.

2 Interval Finite Element and Interval Field Analysis

This section first describes the general concept of Interval Finite Element (IFE) analysis and the method used to deal with it. Next the interval field concept is introduced to deal with dependent uncertain quantities.

2.1 Interval Finite Element Analysis

Generally an IFE problem can be represented by [5]:

$$\mathbf{y}^s = \left\{ \mathbf{y} \mid \left(\mathbf{x} \in \mathbf{x}^I \right) \left(\mathbf{y} = f(\mathbf{x}) \right) \right\} \tag{8.1}$$

with $\mathbf{x}^I$ the interval vector representing the bounds on the input uncertainties and $f(\mathbf{x})$ the function representing the input-output relationship. The solution is expressed as a set $\mathbf{y}^s$, rather than an interval vector $\mathbf{y}^I$ to stress that certain value combinations of components within a hypercubic approximation of the uncertain vector result $\mathbf{y}$ are not necessarily physically coherent. However in most cases the individual ranges of only some components of $\mathbf{y}$ are really of interest. Several implementation strategies for interval numerical analysis have been proposed. Because global optimisation based strategies yield physically correct results, they are more and more acknowledged as the standard approach for non-intrusive IFE analysis. The core of this analysis (the $f(\mathbf{x})$) is a black-box FE calculation which can roughly be any analysis (for example a static or dynamic structural analysis, but also a heat-conductivity problem, hydrogeological problem or vibro-accoustic problem), limited only by the capabilities of the FE solver. The global optimisation based solution strategies actively search in the non-deterministic input interval space for the combination that results in the minimum or maximum value of an output quantity. In theory, the global optimisation approach results in the exact interval vector.

However, despite the smooth behaviour of typical objective functions, the computational cost of the global optimisation based approach remains high. Hence, most research on this method focuses on fast approximate optimisation techniques. The approximating technique used in this paper starts by building a Kriging response surface based on a number of initial sample points. From this preliminary response surface the optimal additional samples are determined by focusing on the location of the possible extremes of the approximated output quantity in the uncertainty space [2]. The response surface is thus improved by additionally sampling the core FE-model till a pre-specified maximum number of samples are taken. Subsequently, global optimisation and anti-optimisation is performed on this response surface model to yield the bounds on the considered output quantity. For a thorough discussion of this adaptive response surface optimisation method, the interested reader is referred to [1].

For completeness the extension of an interval number to a fuzzy set is presented. A fuzzy set [12] is a set in which every member has a degree of membership, represented by the membership function $\mu_x(x)$, associated with it. If $\mu_x(x) = 1$, x is definitely a member of the fuzzy set. If $\mu_x(x) = 0$, x is definitely not a member of the fuzzy set. Analysis using fuzzy sets is very often done by using so-called α-cuts. An α-cut contains all the x for which $\mu_x(x) > \alpha$ is true. These α-cuts are essentially classical intervals, which means that the interval analysis is the basis of a fuzzy analysis.

2.2 Interval Fields

The interval field framework as developed in [6] has an explicit and an implicit implementation. For the application presented here the explicit implementation is needed.

For a spatially dependent uncertainty, the interval vector $\mathbf{x}^I$ containing an independent interval component for every spatial location is not a realistic description. Furthermore, it would result in an unfeasibly high dimensional optimisation problem. To describe spatially dependent variation, numerical modelling approaches often use some type of shape functions (e.g. the modes used to represent the dynamic behaviour of a structure using the modal superposition technique). The actual solution is a linear combination of these shape functions.

Accordingly, the explicit interval field $\mathbf{x}^F$ is defined as a superposition of n_b base vectors $\boldsymbol{\psi}_i$ using interval factors α_i^I:

$$\mathbf{x}^F = \sum_{i=1}^{n_b} \alpha_{x,i}^I \boldsymbol{\psi}_{x,i} \tag{8.2}$$

The base vectors represent a limited set of reference patterns over the spatial domain, each of which is scaled by an interval factor. The components of the interval fields themselves (the local value of the uncertainty) are coupled through the reference patterns. Once the reference patterns are chosen, the definition of the interval field requires the specification of the interval factors that define the field on x, which can be assembled in a classical (hypercubic) interval vector $\boldsymbol{\alpha}_x^I$. In matrix notation, the interval field is denoted as:

$$\mathbf{x}^F = [\boldsymbol{\psi}_x]\boldsymbol{\alpha}_x^I \tag{8.3}$$

The application of an explicit interval field on the input side of an analysis is rather straightforward. Since expert knowledge about the modelled system dominates the definition of the uncertainties, the freedom in choosing the base vectors is ideal to reflect this knowledge (for example: the sinusoidal (= base vector) deviation of the thickness of a rolled plate with uncertain amplitude (= interval factor)). The main limitation of the explicit interval field is that its definition only allows a linear relation between the base vectors and the interval factors.

The application of an explicit interval field on the output side of an analysis is less straightforward. The base vectors and interval factors are determined by the analysis itself. Furthermore, in order to obtain an explicit interval field that introduces no conservatism in its derived response variables (i.e. derivatives of the primary response variables), the output interval factors should be completely independent. An analysis of the application of the interval field approach to the output of static FE analysis is presented in [10].

Once the spatially dependent uncertainty on the input side of an analysis is defined by means of an explicit interval field, the dimensions of the uncertainty space are drastically reduced. This allows for the use of the adaptive response surface technique as described in the above subsection.

3 The Choice of Base Vectors

The use of the explicit interval field on the input side of an analysis requires the selection of appropriate base vectors and interval factors. This section first presents the factors influencing the selection of these base vectors and interval factors. The choice for base vectors and interval factors based on random field expansions is explained in the next subsection.

3.1 Factors Influencing the Choice of Base Vectors

- The bounds on the uncertainty on a model parameter $\mathbf{x}$ are specified by two functions of the spatial coordinate $\mathbf{r}$, one function for the upper bound $\overline{x}(\mathbf{r})$ and one for the lower bound $\underline{x}(\mathbf{r})$ of the uncertainty. The linear combination of the base vectors with the interval factors that makes up an interval field must remain within these bounds for any value of the interval factors.
- The base vectors must represent the expert's knowledge of the spatial dependency of the model parameter. Most often knowledge about this dependency is limited and the set of base vectors preferably allows for a range of small and large scale dependency.
- The number of base vectors and corresponding interval factors to represent the input uncertainty will influence the calculation time to get the output uncertainty.

3.2 Base Vectors Derived from Random Field Expansion

In an attempt to construct a base vector set that takes into account the above described factors, the expansion of a random field is studied.

The objective of a random field is to represent a spatial variation of a specific model property by a stochastic variable defined over the region on which the variation occurs [9]. A random field can thus be denoted as $H(\mathbf{r}, \theta)$ with $\mathbf{r}$ the spatial coordinate and θ the outcome of a random phenomenon. A random field is a random variable for a given $\mathbf{r_0}$ and is a realization of the field for a given θ_0. The specification of a random field generally comes down to the specification of the spatial evolution of the first two statistical moments of the field variable and a corresponding covariance function, expressing the spatial dependency of the field variable. In most cases the random field is considered to be weakly stationary, resulting in a constant for the first few statistical moments throughout the spatial domain (i.e. zero mean and unit variance). Furthermore the covariance function for weakly stationary random fields depends only on the distance between observation points, not on their actual location.

The application of the concept of random fields in a numerical modelling framework requires some sort of discretisation of the spatially varying stochastic field

over the defined geometry. A good overview of methods can be found in the report by Sudret and Der Kiureghian [8]. The technique studied here is the Karhunen-Loève expansion [3] that has gained particular attention in literature. This approach is based on the spectral decomposition of the autocovariance function $C_{HH}(\mathbf{r_1}, \mathbf{r_2})$. The set of deterministic functions over which any realization of the field $H(\mathbf{r}, \theta_0)$ is expanded is defined by the eigenvalue problem:

$$\int_{\omega} C_{HH}(\mathbf{r_1}, \mathbf{r_2})\varphi_i(\mathbf{r_1})\, d\omega_{\mathbf{r_2}} = \lambda_i \varphi_i(\mathbf{r}) \tag{8.4}$$

with ω the spatial domain and $i = 1, \ldots$. Once the eigenfunctions are found, the zero-mean random field can be expressed as:

$$H(\mathbf{r}, \theta) = \sum_{i=1}^{\infty} \sqrt{\lambda_i}\xi_i(\theta)\varphi_i(\mathbf{r}) \tag{8.5}$$

with $\{\xi_i\}$ a set of orthonormal random variables. In stochastic analysis, this expansion is truncated after N terms to reduce the computational costs.

Several features of the random field expansion can be used in the interval field implementation after some adaptations. To begin, an off-set function $f_{mid}(\mathbf{r})$ to describe the mid value of the model parameter throughout the spatial domain is calculated

$$x_{mid}(\mathbf{r}) = \frac{\overline{x}(\mathbf{r}) + \underline{x}(\mathbf{r})}{2} \tag{8.6}$$

The eigenfunctions $\varphi_i(\mathbf{r})$ of the covariance function are then used as base vectors $\boldsymbol{\psi}_i(\mathbf{r})$ for the interval field with

$$\boldsymbol{\psi}_i(\mathbf{r}) = \lambda_i \varphi_i(\mathbf{r}) \left|\varphi_i(\mathbf{r})\right| \tag{8.7}$$

and replacing the orthonormal random variables $\{\xi_i\}$ by interval factors $\alpha_i^I \in \lfloor -1\ 1 \rceil$. These adaptations make sure that for $N \to \infty$ the interval field will assign a value from the interval $\lfloor -1\ 1 \rceil$ to the model parameter throughout the spatial domain. This unit interval is then scaled by the difference function

$$x_{dif}(\mathbf{r}) = \overline{x}(\mathbf{r}) - \underline{x}(\mathbf{r}) \tag{8.8}$$

describing the actual range of uncertainty on the model parameter for every location in the model. The description of the model parameter by the interval field is thus

$$\mathbf{x}^F = x_{mid}(\mathbf{r}) + \sum_{i=1}^{N} \left(\lambda_i \varphi_i(\mathbf{r}) \left|\varphi_i(\mathbf{r})\right| \alpha_i^I\right)\left(x_{dif}(\mathbf{r})\right) \tag{8.9}$$

With this equation the considerations from the first and last item in the list of influencing factors is accounted for. Next is the issue of uncertainty about the spatial dependency.

The base vectors taken from the expansion of a random field with a given autocovariance function only take into account the given correlation length L. In [11] a method is described to take into account interval correlation lengths with interval fields. Essentially the method relies on building an interval field description for the

base vectors themselves in the correlation length space using a limited number of autocovariance functions. In this way the base vectors are depending on the correlation length and can be calculated by a simple matrix vector product. The resulting interval field for the model parameter can thus be summarised by

$$\mathbf{x}^F = x_{mid}(\mathbf{r}) + \sum_{i=1}^{N} \left(\lambda_i(L)\varphi_i(\mathbf{r}, L)\middle|\varphi_i(\mathbf{r}, L)\middle|\alpha_i^I\right)\left(x_{dif}(\mathbf{r})\right) \quad L \in \lfloor L_{min}\ L_{max} \rceil \tag{8.10}$$

This approach only introduces one additional interval to represent the uncertainty about the amount of spatial dependency. The solution strategy to find the uncertainty on the output remains the same, for example a response surface based optimisation and anti-optimisation, with only one additional dimension in the uncertainty space.

4 Input Uncertainty Elasticity of the Output

To assess the relative importance of an input uncertainty on an output uncertainty, the concept of input uncertainty elasticity of the output is introduced in general terms and then applied to the case of spatial uncertainty.

4.1 General Concept

As in economics, an elasticity R is defined as the ratio of the relative change (more precisely, the derivative with respect to some quantity) in one parameter Y to the relative change in an other parameter X

$$R_X^Y = \frac{\Delta Y}{\Delta X}\frac{X}{Y} \tag{8.11}$$

Let Y be the range of the uncertain output and X be the range of the uncertain input. The reduction (i.e. the Δ) on the range of the interval for the input X, will affect the range of the interval for the output Y to a greater or lesser extent. The relative magnitude of this influence is described by the input uncertainty elasticity of the output R_X^Y.

4.2 Spatial Uncertainty Context

In the context of spatial uncertainty, the influence of an input uncertainty on an output uncertainty has a spatial component. The influence of an uncertain input parameter will depend on the spatial distribution of its uncertainty. Figure 8.1 shows

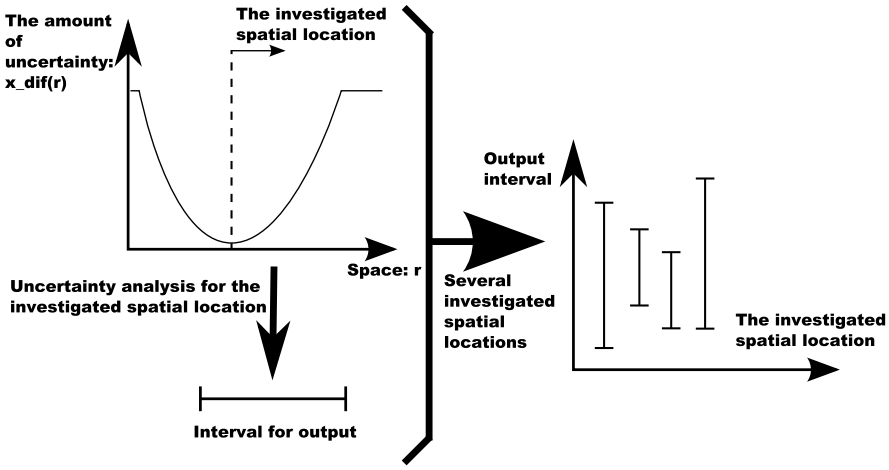

Fig. 8.1 Concept to determine R_X^Y in a spatial context

in a generic way the influence of the spatial uncertainty distribution. For an investigated spatial location the amount of uncertainty $x_{dif}(\mathbf{r})$ is reduced and some sort of coherent distribution of the uncertainty is assumed over the spatial domain (as illustrated at the top left in the figure). The uncertainty analysis is carried out for this spatial uncertainty distribution and a resulting uncertainty (an interval) for the output is found (bottom left). By repeating this for other investigated spatial locations, one finds the combined result which is shown at the right of the figure. It presents the different output uncertainties for several investigated spatial locations. This data is then used to calculate the input uncertainty elasticity of the output over the spatial domain. In this context the R_X^Y is in particular useful to identify the spatial location where an input uncertainty influences the output uncertainty the most. In allocating resources to reduce the uncertainty, the spatial location with the highest R_X^Y should get priority.

An appropriate selection of the $\overline{x}(\mathbf{r})$ and $\underline{x}(\mathbf{r})$ is needed to make a study over the spatial domain to give a scalar field of input uncertainty elasticities of the output. Important choices to be made in the selection of $\overline{x}(\mathbf{r})$ and $\underline{x}(\mathbf{r})$ to investigate a particular spatial location's uncertainty influence are listed below. Figure 8.2 shows $\overline{x}(\mathbf{r})$ and $\underline{x}(\mathbf{r})$ for three cases. The first case, at the left on the figure, is the reference case. The two other cases illustrate particular choices for $\overline{x}(\mathbf{r})$ and $\underline{x}(\mathbf{r})$ explained in the list below.

Important choices to be made in the selection of $\overline{x}(\mathbf{r})$ and $\underline{x}(\mathbf{r})$:

- the magnitude of the reduction of $x_{dif}(\mathbf{r})$ for the investigated spatial location. The second case in Fig. 8.2 shows a reduction of 50% for $x_{dif}(0.2)$, the third case shows a reduction of 90% for $x_{dif}(0.7)$.
- the magnitude of the reduction of $x_{dif}(\mathbf{r})$ in the local influence zone of the investigated spatial location. By reducing the amount of uncertainty for the investigated spatial location, the amount of uncertainty for the region around the investigated

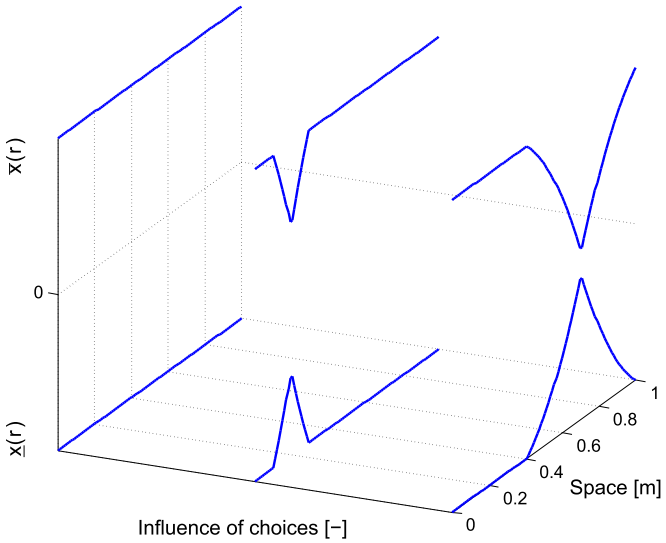

Fig. 8.2 Choices in the selection of $\overline{x}(\mathbf{r})$ and $\underline{x}(\mathbf{r})$

spatial location is also affected. In this so called local influence zone, a transition from the reduced amount of uncertainty to the reference amount of uncertainty is needed. In this paper a quadratic transition is suggested.

- the magnitude of the local influence zone of the investigated spatial location. The second case in Fig. 8.2 shows a zone of influence from -0.1 to $+0.1$ around the investigated spatial location 0.2. The third case shows a zone of influence from -0.3 to $+0.3$ around the investigated spatial location 0.7.
- the change in $x_{mid}(\mathbf{r})$. If $\overline{x}(\mathbf{r})$ and $\underline{x}(\mathbf{r})$ are not changed symmetrically with respect to $x_{mid}(\mathbf{r})$ in the reference case, then $x_{mid}(\mathbf{r})$ is affected as well. For simplicity this influence is not presented here.

These notions are explained further in the case study.

5 Geohydrological Case Study

A geohydrological case study was chosen to apply the above presented techniques. The case study deals with a groundwater pollution problem where benzene was spilled and is now being transported in groundwater to a river. To characterize the flow and transport of the benzene spill, a groundwater flow and transport model was built in HYDRUS3D. First, the problem together with its uncertainty is described and the results of a fuzzy analysis without taking into account the spatial dependency are presented. Next, the spatial dependency is introduced and an investigation of the input uncertainty elasticity of the output is performed.

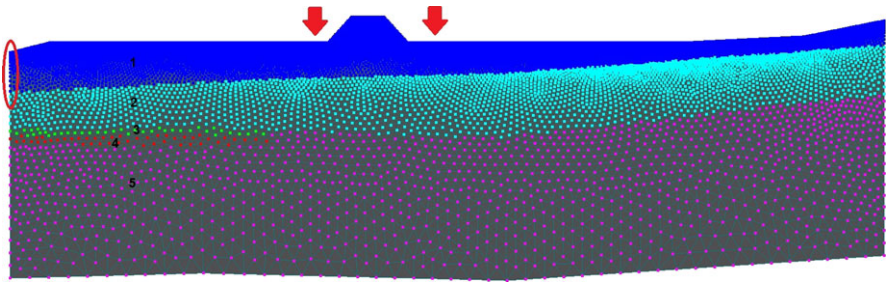

Fig. 8.3 FE-model for solute and ground water flow showing the five different material layers

Table 8.1 Intervals for the hydraulic conductivity K [m/day], ordered from top to bottom

Material Layer	Minimum K	Maximum K
1	1.4	2.1
2	8	12
3	3.6	5.4
4	2.6	3.9
5	4	6

5.1 Problem Description

The governing equation for solute transport in groundwater is a convection-diffusion equation based on conservation of mass. Convection is determined by groundwater flow which is based on the constitutive equation for variably saturated flow in porous media, called the Darcy Buckingham equation. For the solute (the contaminant: Benzene) and ground water flow problem at hand the following input was given:

- FE-model (14661 nodes) for the HYDRUS3D [7] solver (see Fig. 8.3). The dimensions of the problem are 1100 m in the length direction and between 32 and 36.5 m in the depth direction. In the time domain a period of 11000 days (approximately 30 years) is calculated. A deterministic run of this model takes 10 minutes.
- Intervals for the material properties, i.e. the saturated hydraulic conductivity K (see Table 8.1) of the five different material layers.

A river is situated at the left side of the domain (see the red ellipse on Fig. 8.3) and the two sources of the contaminant are in the middle of the domain (see the red arrows on Fig. 8.3). The requested output is the concentration of the contaminant over time at the river given the uncertainties on the material properties.

5.2 Fuzzy Analysis Without Spatial Uncertainty

In the first fuzzy analysis, the uncertainty on the material properties is represented by fuzzy numbers. The hydraulic conductivity of each layer is considered independent

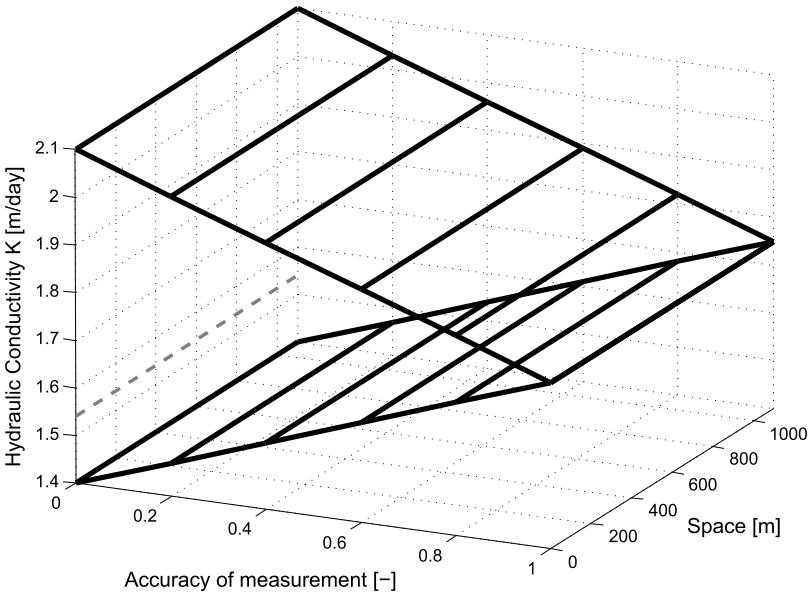

Fig. 8.4 The spatial fuzzy number in *black solid* line and a sample of it in *dashed grey* for the hydraulic conductivity of material layer 1, assuming homogeneity

and modelled as a triangular fuzzy number with the given intervals (see Table 8.1) as base and the mid value as the top of the triangle. In each material layer the hydraulic conductivity is considered homogeneous through space. Figure 8.4 shows for example the spatial fuzzy number in black and a possible sample of the fuzzy number in dashed grey for the hydraulic conductivity of material layer 1. Two types of fuzzy analyses were performed:

- Reduced Transformation Method (TM) [4] with 5 alpha-cuts, resulting in 161 samples.
- An optimisation on a Kriging response surface (ARSM) [1] that was built using 32 initial latinhypercube samples and 32 additional samples.

Additionally, a reference Monte Carlo Simulation using 200 samples was performed at each alpha-level, based on a uniform distribution within the interval at each alpha-level Fig. 8.5 shows the fuzzy concentration through time for location 11 (at the river, 3 m below the surface). In black solid line is the result of the reduced transformation method ($5 * 32 + 1$ samples); in dotted grey line is the result of the optimisation on a Kriging response surface (32 initial + 32 additional samples); in dashed grey line is the result of the Monte Carlo Simulation ($5 * 200$ samples). From these results it is clear that the TM and ARSM results are close to each other. The MCS result, despite being the computationally most expensive, does not yield good results for the maxima: the value given by the TM is an actual solution of the problem (i.e. a genuine sample) and results in higher maxima. The ARSM has problems identifying the proper minima since it tends to give negative (non-physical) results.

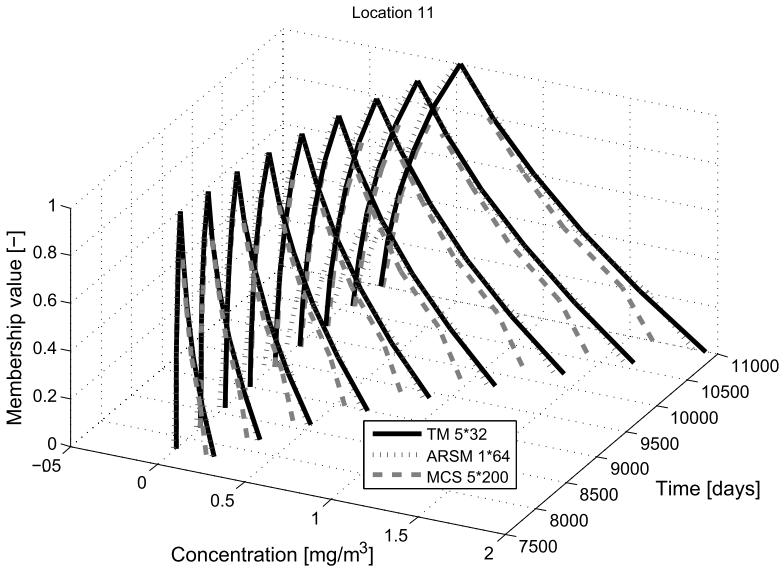

Fig. 8.5 The fuzzy concentration at the river, 3 m below the surface

5.3 Fuzzy Analysis with Spatial Uncertainty

In this fuzzy analysis, only the uncertainty on the hydraulic conductivity in material layer 1 is taken into account. The other hydraulic conductivities are set at their minimal value. To model the spatial uncertainty for the hydraulic conductivity of material layer 1, the following assumptions are made:

- The upper bound $\overline{x}(\mathbf{r})$ and lower bound $\underline{x}(\mathbf{r})$ are given by a constant, namely the maximum and minimum of the interval given in Table 8.1.
- The base vectors are derived from an exponential autocovariance function

$$C_{HH}(x_1, x_2) = e^{-|x_1 - x_2|/L} \tag{8.12}$$

  as described in Sect. 3.2. The first four eigenfunctions are used. Since a limited number of base vectors is used, the upper and lower bound on the uncertainty are not exactly satisfied throughout the domain. A scaling factor to adjust the maximal possible value of the interval field in the spatial domain to the requested bounds is applied. For a correlation length $L = 500$ m, the resulting base vectors are shown in Fig. 8.6.

To check the influence of taking into account the spatial uncertainty, two analyses (TM and ARSM) with the non-spatial uncertainty (i.e. uncertain, but homogeneous hydraulic conductivity of material layer 1) are performed as well. In total, the following types of analyses were performed:

- non-spatial uncertainty, Reduced Transformation Method (TM) with 5 alpha-cuts, resulting in 11 samples.

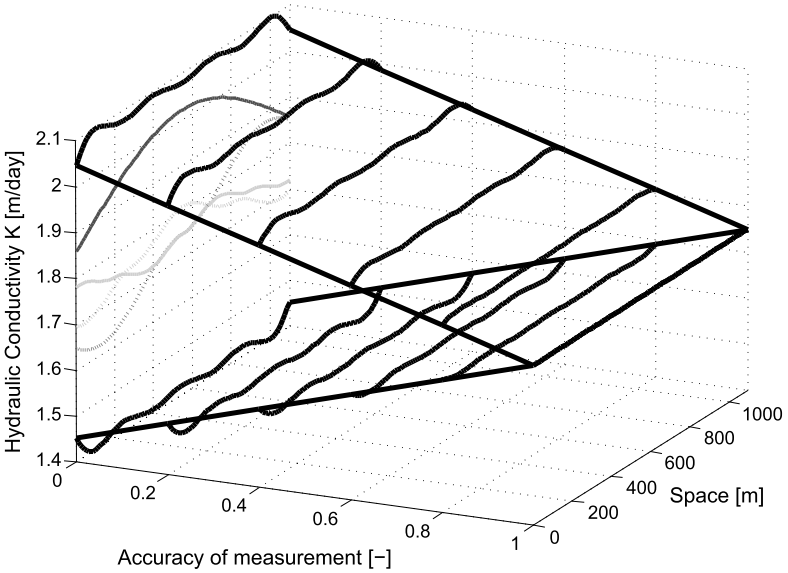

Fig. 8.6 The spatial fuzzy number in *black* and the four base vectors for membership level 0 in *grey* for the hydraulic conductivity of material layer 1, including spatial uncertainty

- non-spatial uncertainty, optimisation on a Kriging response surface (ARSM) that was built using 6 initial latinhypercube samples and 12 additional samples.
- spatial uncertainty, with correlation length between 500 and 2000 m, optimisation on a Kriging response surface (ARSM) that was built using 20 initial latinhypercube samples and 30 additional samples.

Figure 8.7 shows the fuzzy concentration through time for location 11 (at the river, 3 m below the surface). The influence of taking into account the spatial uncertainty results in slightly narrower fuzzy numbers. This suggests that assuming homogeneity for the hydraulic conductivity of material layer 1 gives conservative bounds on the contaminant's concentration for the studied case.

5.4 Input Uncertainty Elasticity of the Output

By performing an additional point measurement to determine the hydraulic conductivity in one location, the uncertainty on the contaminant's concentration will be reduced. To determine the optimal measurement location an input uncertainty elasticity of the output is calculated. The following assumptions, referring to Sect. 4.2 and Fig. 8.8, are made:

- The magnitude of the reduction of the uncertainty for the considered measurement location is a design parameter. By selecting a more accurate measurement

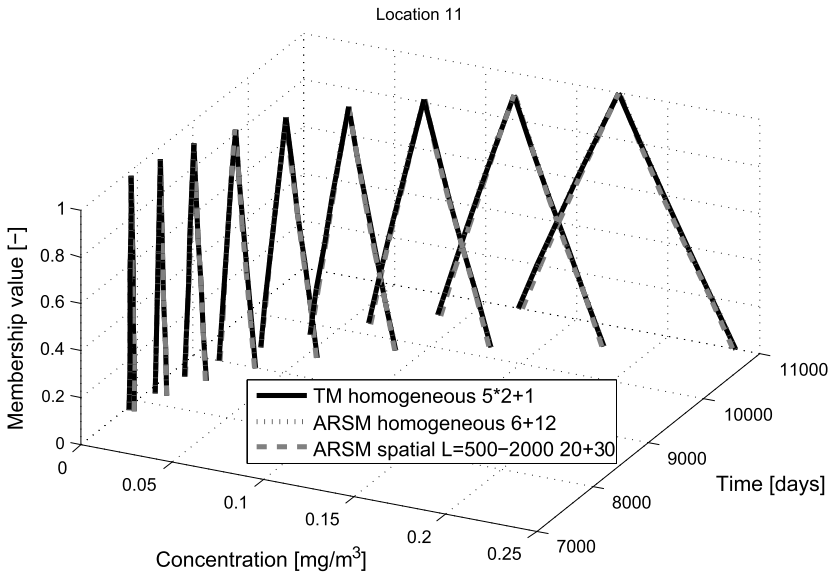

Fig. 8.7 The fuzzy concentration at the river, 3 m below the surface

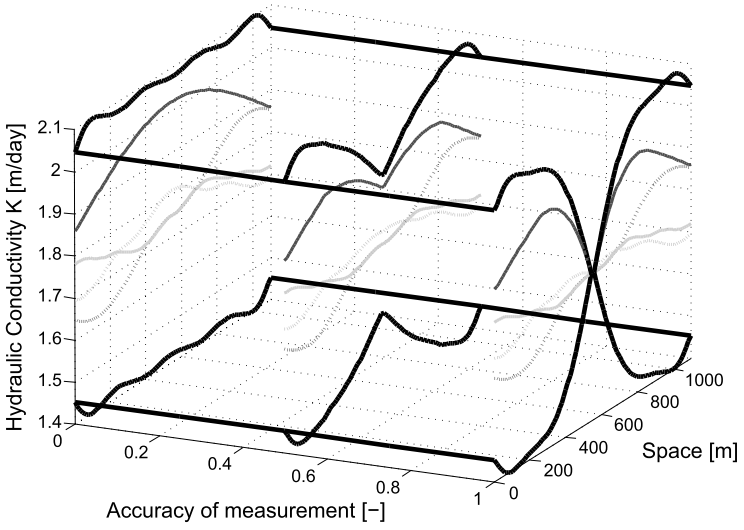

Fig. 8.8 The influence of a measurement in the middle of the domain on the bounds of the uncertainty (in *black*) and the base vectors (in *grey*), with a zone of influence of 330 m to both sides of the measurement location

device, the uncertainty remaining after measurement is a choice of the expert. In Fig. 8.8 the influence of an increasing measurement accuracy on the bounds and the base vectors is shown.

Table 8.2 Parameters in the input uncertainty elasticity of the output analysis

Design Parameter	Sampled values
Measurement location	110, 330 and 550 m from river
Measurement accuracy	50% reduction and 100% reduction of uncertainty
Uncertain Parameter	**Range**
Extent of influence	value chosen is 330 m
Correlation length	⌊500 2000⌉ m

- The magnitude of the reduction of the uncertainty in the local influence zone is an uncertainty. $f_{dif}(\mathbf{r})$ increases from the value at the measurement location to the reference value at the end of the local influence zone. In the presented analysis a quadratic function of the distance to the measurement location is chosen.
- The magnitude of the local zone of influence is an uncertainty. What is the extent of the influence of a measurement in one location on the rest of the spatial domain? Since a comparison between the input uncertainty elasticities of the output for different locations is of interest, the magnitude of this local zone of influence is chosen to be a fixed value. In Fig. 8.8 the bounds and base vectors for an influence up to 330 m to both sides is shown, as it is used in the analysis.
- The actual outcome of the measurement gives a value for $f_{mid}(\mathbf{r})$ in the measurement location. Until the measurement is done, this is also an uncertainty that influences the actual bounds on the output uncertainty. In the presented analysis the value of $f_{mid}(\mathbf{r})$ is considered a constant and unchanged by a measurement.

To summarize: the measurement location and the accuracy of the measurement are design parameters, whereas the influence of the measurement and the spatial correlation length are uncertainties. For the influence of the measurement a fixed magnitude is assumed and the correlation length is modelled as an interval. The values used in the analysis are presented in Table 8.2. For a choice of the design parameters, the uncertainty analysis was carried out using the ARSM method with 20 initial samples and 30 additional samples. The results are presented in Fig. 8.9. The bounds on the contaminant's concentration are presented for location 11 (at the river, 3 m below the surface) at the end time of the simulation (approx. 30 years) as a function of the measurement location and the accuracy of the measurement. Based on this information the input uncertainty elasticity of the output is calculated using Eq. (8.11) with X and Y respectively the range on the hydraulic conductivity and the range on the contaminant's concentration. The results are presented in Table 8.3, the reference is the range on the uncertainty before measurement. From this Table 8.3 it becomes clear that performing an input uncertainty reduction (i.e. a measurement of the hydraulic conductivity in material layer 1) at 110 m from the river provides the greatest reduction in uncertainty on the output (i.e. the concentration of the contaminant at the considered location and time). Furthermore, for this measurement location increasing the uncertainty reduction from 50% to 100% will not decrease

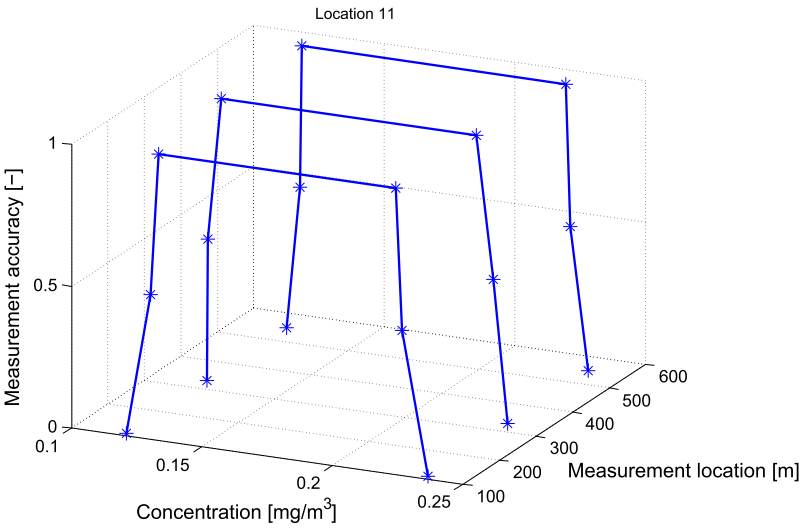

Fig. 8.9 The results of the uncertainty analysis to determine the input uncertainty elasticity of the output

Table 8.3 The input uncertainty elasticity of the output

Measurement accuracy [-]	Measurement location [m]		
	110	330	550
0.5	0.33	0.10	0.20
1.0	0.21	0.15	0.13

the uncertainty on the output with the same amount. In other words, a measurement with an uncertainty reduction of 50% will have a $\frac{0.33}{0.21} \simeq 1.5$ times higher relative uncertainty reduction on the output than a measurement with an uncertainty reduction of 100%. For a measurement at 330 m from the river the inverse is true: the extra effort of reducing the input uncertainty from 50% to 100% gives a 1.5 times higher relative uncertainty reduction on the output. Based on this information and knowledge of the actual costs of a measurement campaign an informed decision can be made concerning where and how accurate to measure.

6 Conclusion

From a methodological point of view, the paper introduces interval fields as an easy conceptual tool to deal with spatial uncertainty. The implementation of the interval field based on correlation length is made possible by deriving certain base vectors from the random field expansion technique. This allows for taking into account un-

certainty on the correlation length. Furthermore, the concept of input uncertainty elasticity of the output is introduced in a spatial uncertainty context.

From an applied point of view, the paper shows the applicability of the interval field to a geohydrological problem of realistic complexity. The adaptive response surface technique proves to be very useful in practice. Certainty on the value of the correlation length often is a problem. The feasibility of dealing with the correlation length as an interval is shown. The concept of input uncertainty elasticity of the output in a spatial uncertainty context is proven to be useful to determine the optimal location of a measurement (i.e. an uncertainty reduction) to reduce uncertainty on the output.

Acknowledgements The support of the Flemish Government through IWT-SBO project no. 060043: Fuzzy Finite Element Method is gratefully acknowledged.

References

1. De Munck, M.: Efficient optimization approaches for interval and fuzzy finite element analysis. Ph.D. thesis, Katholieke Universiteit Leuven (2009)
2. De Munck, M., Moens, D., Desmet, W., Vandepitte, D.: An efficient response surface based optimisation method for non-deterministic harmonic and transient dynamic analysis. Comput. Model. Eng. Sci. **47**(2), 119–166 (2009)
3. Ghanem, R., Spanos, P.: Stochastic Finite Elements: A Spectral Approach. Springer, New York (1991)
4. Hanss, M.: Applied Fuzzy Arithmetic—An Introduction with Engineering Applications. Springer, Berlin (2005)
5. Moens, D., De Munck, M., Farkas, L., De Gersem, H., Desmet, W., Vandepitte, D.: Recent advances in interval finite element analysis in applied mechanics. In: Proceedings of the First Leuven Symposium on Applied Mechanics in Engineering LSAME.08, Leuven, pp. 553–568 (2008)
6. Moens, D., De Munck, M., Desmet, W., Vandepitte, D.: Numerical dynamic analysis of uncertain mechanical structures based on interval fields. In: IUTAM Symposium on Vibration Analysis of Structures with Uncertainties, Saint Petersburg (2009)
7. Sejna, M., Simunek, J., Van Genuchten, R.: Software package for simulating water, heat and solute movement in two- and three-dimensional variably saturated media. PC-Progress s.r.o, Prague. www.hydrus3D.com
8. Sudret, B., Der Kiureghian, A.: Stochastic finite element methods and reliability: a state-of-the-art report. Technical report, Department of Civil & Environmental Engineering, University of California, Berkley, Institute of Structural Engineering, Mechanics and Materials (2010)
9. Vanmarcke, E.: Random Fields: Analysis and Synthesis. MIT Press, Cambridge (1993)
10. Verhaeghe, W., Rousounelos, A., Desmet, W., Vandepitte, D., Moens, D.: Interval fields to represent uncertainty on input and output side of a FE analysis. In: Proceedings of the 3rd International Conference on Uncertainty in Structural Dynamics, pp. 5067–5078 (2010)
11. Verhaeghe, W., Desmet, W., Vandepitte, D., Moens, D.: Uncertainty assessment in random field representations: an interval approach. In: Proceedings of NAFIPS 2011, El Paso, TX (2011)
12. Zadeh, L.: Fuzzy sets. Inf. Control **8**, 338–353 (1965)

Chapter 9
Enhanced Monte Carlo for Reliability-Based Design and Calibration

Arvid Naess, Marc Maes, and Markus R. Dann

Abstract This paper extends the recently developed enhanced Monte Carlo approach to the problem of reliability-based design. The objective is to optimize a design parameter(s) so that the system, represented by a set of failure modes or limit states, achieves a target reliability. In a large majority of design and/or calibration contexts, the design parameter α itself can be used to parameterize the system safety margin $M(\alpha)$. The lower tail of this random variable behaves in a regular way and is therefore amenable to straightforward parametric analysis. In contrast to the original Naess et al. method (Naess et al. in Struct. Saf. 31:349–355, 2009), the intention is to estimate the value α_T that corresponds to a (very) small target system failure probability p_{fT}. Monte Carlo sampling occurs at a range of values for α that result in larger failure probabilities, and so the design problem essentially amounts to a statistical estimation of a high quantile. Bounds for α_T can easily be constructed. Several examples of the approach are given in the paper.

1 Introduction

A new Monte Carlo (MC) based method for estimating system reliability was recently developed in [1]. The aim of this method is to reduce computational cost while maintaining the advantages of crude MC simulation, specifically, its ease in dealing with complex systems. The key idea is to exploit the regularity of tail probabilities to enable an approximate prediction of far tail failure probabilities based on

A. Naess (✉)
Centre for Ships and Ocean Structures & Dept. of Mathematical Sciences, NTNU, Trondheim 7491, Norway
e-mail: arvidn@math.ntnu.no

M. Maes · M.R. Dann
University of Calgary, Calgary T2N 1N4, Canada

M. Maes
e-mail: mamaes@ucalgary.ca

M.R. Dann
e-mail: markusdann@gmx.de

M. Papadrakakis et al. (eds.), *Computational Methods in Stochastic Dynamics*, Computational Methods in Applied Sciences 26,
DOI 10.1007/978-94-007-5134-7_9,

small Monte-Carlo sample results obtained for much more moderate levels of reliability. The motivation behind this approach is that systems with multiple and complex failure modes or limit states are often exceedingly difficult to analyze using traditional methods of structural reliability. While direct MC does not suffer from this problem, it is computationally burdensome for small probabilities. Hence originates the idea of sampling in a different less reliable range and performing a statistical extrapolation unto the tail. A similar but somewhat different idea is presented in [2].

The fundamentals of the method proposed in [1] are as follows. A safety margin $M = G(X_1, \ldots, X_n)$ expressed in terms of n basic variables, is extended to a parameterized class of safety margins using a scaling parameter λ ($0 \leq \lambda \leq 1$):

$$M(\lambda) = M - (1 - \lambda)\mu_M. \tag{9.1}$$

The failure probability is then assumed to behave as follows:

$$p_f(\lambda) = \text{Prob}\big(M(\lambda) \leq 0\big) \underset{\lambda \to 1}{\approx} q(\lambda) \exp\big\{-a(\lambda - b)^c\big\}, \tag{9.2}$$

where the function $q(\lambda)$ is slowly varying compared with the exponential function $\exp\{-a(\lambda - b)^c\}$. It may be pointed out that the assumed behaviour of the failure probability applies to any safety margin for which FORM or SORM approximations can be used, but actually its range of applicability is much wider than that.

Clearly, the target failure probability $p_f = p_f(1)$ can be obtained from values of $p_f(\lambda)$ for $\lambda < 1$. It is now far easier to estimate the (larger) failure probabilities $p_f(\lambda)$ for $\lambda < 1$ accurately than the target value itself, since they are larger and hence require less simulations. Fitting the parametric function given by Eq. (9.2) for $p_f(\lambda)$ to the estimated values would then allow us to provide an estimate of the target value by extrapolation. The viability of this approach is demonstrated by both analytical and numerical examples in [1] and [3].

In the next sections, the Naess et al. [1] approach is extended to reliability-based design and calibration.

2 Using Enhanced Monte Carlo to Optimize a Design Parameter

First consider a typical component design, the reliability of which is governed by the safety margin:

$$M(\alpha) = G(X_1, \ldots, X_n; \alpha) \tag{9.3}$$

with

$$p_f(\alpha) = \text{Prob}\big(M(\alpha) \leq 0\big), \tag{9.4}$$

where α acts as a design factor which "controls" the reliability of the component. The objective is now to determine the (assumed to be unique) value of $\alpha = \alpha_T$ that corresponds to a specified (target) component failure probability p_{fT}, i.e.:

$$\alpha_T : \text{Prob}\big(M(\alpha_T) \leq 0\big) = p_{fT}, \tag{9.5}$$

This assumes that the function $p_f(\alpha)$ is a monotonic function, that is, that the safety of the system either strictly increases or strictly decreases as the design factor

α increases and approaches α_T. In practical design situations, α may represent a safety factor, a partial load or resistance factor, or some exceedance level and, the condition of monotonicity is generally speaking satisfied, unless the problem relates to a poor or an unfeasible design.

A more general situation, typical in the context of calibration of design specifications, consists of having the safety margin controlled by a design check function $c(\alpha) = c(x_{1c}, \ldots, x_{nc}; \alpha)$ involving characteristic values x_{ic} of each basic variable X_i. Admissible designs are such that $c(\alpha) \leq 0$. Minimal acceptable designs are marked by $c(\alpha) = 0$, an assumption which is made throughout this paper. Often the design check function $c(\alpha)$ is selected to be the same mathematical function as G but this is not required—all that matters is that the resulting safety margin $M(\alpha) = G(X_1, \ldots, X_n | c(x_{1c}, \ldots, x_{nc}; \alpha) = 0)$ is monotonic with respect to α in its approach to the target α_T. Hence the objective is to determine α_T as follows:

$$\alpha_T : \text{Prob}\big(G\big(X_1, \ldots, X_n | c(x_{1c}, \ldots, x_{nc}; \alpha_T) = 0\big) \leq 0\big) = p_{fT}. \tag{9.6}$$

Typically, p_{fT} is a very small target probability and hence the behavior of p_f as a function of α is similar to a deep tail estimation problem so that it is reasonable to assume that:

$$p_f(\alpha) \underset{\alpha \to 1}{\approx} q(\alpha) \exp\big\{-a(\alpha - b)^c\big\}, \tag{9.7}$$

where $q(\alpha)$ is slowly varying compared to the exponential expression.

To illustrate this premise, consider a basic load and resistance safety margin $M(\alpha) = R(\alpha) - S$ controlled by a design check function $c(\alpha) = (r_c(\alpha)/\alpha) - s_c$, where r_c and s_c are characteristic values of a resistance R and a load S, and α acts as a partial resistance factor ($\alpha > 1$). Assume the load S is Weibull distributed with exponent d and scale parameter s_0, then the characteristic load s_c at its $(1-\theta)$ quantile, is equal to $s_c = (-\ln\theta)^{1/d} s_0 = k s_0$ where k is a known positive constant > 1. First consider the limiting case where the variance of R is zero, $\sigma_R^2 = 0$, hence $r_c(\alpha) = \alpha s_c$ such that $p_f(\alpha) = \text{Prob}(M(\alpha) \leq 0) = \exp(-(\alpha k)^d)$ which is fully consistent with Eq. (9.7) above. If the variance of $R(\alpha)$ now increases, then the mean resistance will shift even further down the tail since $r_c(\alpha)$ is a small quantile of R. But, the function $p_f(\alpha)$ will only be slightly "contaminated" by a much slower varying function of α; however, and this is certainly valid in the tail area as $\alpha \to \alpha_T$, the general form in Eq. (9.7) will persist and it is amenable to be fitted to data pairs $(p_f(\alpha), \alpha)$ obtained for (much) higher failure probabilities.

Once a satisfactory fit is achieved, the target value α_T corresponding to p_{fT} needs to be estimated, a problem which is similar to a high quantile estimation.

3 Extension to System Reliability

Using Monte Carlo methods for system reliability analysis has several attractive features, the most important being that the failure criterion is relatively easy to check almost irrespective of the complexity of the system. In order to limit the amount of

computational effort that may be involved, it is useful to extend the above approach to systems.

Let $M_j(\alpha) = G_j(X_1, \ldots, X_n, \alpha)$, $j = 1, \ldots, m$ be a set of m given safety margins expressed in terms of n basic variables and a single design parameter α. The series system reliability expressed in terms of the failure probability can then be written as,

$$p_f(\alpha) = \text{Prob}\left(\bigcup_{j=1}^{m} \{M_j(\alpha) \le 0\}\right), \tag{9.8}$$

while for the parallel system,

$$p_f(\alpha) = \text{Prob}\left(\bigcap_{j=1}^{m} \{M_j(\alpha) \le 0\}\right). \tag{9.9}$$

In general, any system can be written as a series system of parallel subsystems. The failure probability would then be given as,

$$p_f(\alpha) = \text{Prob}\left(\bigcup_{j=1}^{l} \bigcap_{i \in C_j} \{M_i(\alpha) \le 0\}\right), \tag{9.10}$$

Here each C_j is a subset of $1, \ldots, m$, for $j = 1, \ldots, l$. The C_js denote the index sets defining the parallel subsystems.

We then make the assumption that $p_f(\alpha)$ can also be represented as in Eq. (9.7) for the system reliability problems. Again, the objective is to determine the value α_T that achieves a stated overall system reliability.

4 Implementation

The method to be described in this section is based on the assumption expressed by Eq. (9.7). For practical applications it is implemented in the following form:

$$p_f(\alpha) \approx q(\alpha) \exp\{-a(\alpha - b)^c\}, \quad \text{for } \alpha_0 \le \alpha \le \alpha_T, \tag{9.11}$$

for a suitable value of α_0. An important part of the method is therefore to identify a suitable range for α so that the right hand side of Eq. (9.7) represents a good approximation of $p_f(\alpha)$ for $\alpha \in [\alpha_0, \alpha_T]$.

For a sample of size N of the vector of basic random variables $\mathbf{X} = (X_1, \ldots, X_n)$, let $N_f(\alpha)$ denote the number of outcomes of the random vector in the failure domain of $M(\alpha)$. The estimate of the failure probability is then

$$\hat{p}_f(\alpha) = \frac{N_f(\alpha)}{N}. \tag{9.12}$$

The coefficient of variation C_v of this estimator is

$$C_v\big(\hat{p}_f(\alpha)\big) = \sqrt{\frac{1 - \hat{p}_f(\alpha)}{\hat{p}_f(\alpha) N}}. \tag{9.13}$$

A fair approximation of the 95% confidence interval for the value $\hat{p}_f(\alpha)$ can be obtained as $\mathrm{CI}_{0.95} = (C^-(\alpha), C^+(\alpha))$, where

$$C^{\pm}(\alpha) = \hat{p}_f(\alpha)\big[1 \pm 1.96 C_v\big(\hat{p}_f(\alpha)\big)\big]. \tag{9.14}$$

Assuming now that we have obtained empirical Monte Carlo estimates of the failure probability, the problem then becomes one of optimal use of the information available. By plotting $\log|\log \hat{p}_f(\alpha)/q(\alpha)|$ versus $\log(\alpha - b)$, it is expected that an almost perfectly linear tail behavior will be obtained according to Eq. (9.11). Recalling that the function $q(\alpha)$ was assumed to be slowly varying compared with the exponential function $\exp\{-a(\alpha - b)^c\}$ for values of α close to α_T, it is now tentatively proposed to replace $q(\alpha)$ by a suitable constant value, q say, for tail values of α, say $\alpha > \alpha_1$ ($\geq \alpha_0$). Hence, we will investigate the viability of the following simpler version of Eq. (9.11):

$$p_f(\alpha) \approx q \exp\big\{-a(\alpha - b)^c\big\}, \quad \text{for } \alpha_1 \leq \alpha \leq \alpha_T, \tag{9.15}$$

for a suitable choice of α_1.

The problem of finding the optimal values of the parameters a, b, c, q is carried out by optimizing the fit on the log level by minimizing the following mean square error function with respect to all four arguments [4],

$$F(a, b, c, q) = \sum_{j=1}^{M} w_j \big(\log \hat{p}_f(\alpha_j) - \log q + a(\alpha_j - b)^c\big)^2, \tag{9.16}$$

where $\alpha_1 < \cdots < \alpha_M$ denotes the set of α values where the failure probability is empirically estimated. The w_j denote weight factors that put more emphasis on the more reliable data points, alleviating the heteroscedasticity of the estimation problem at hand. The choice of weight factor is to some extent arbitrary. In this paper, we use $w_j = (\log C^+(\alpha_j) - \log C^-(\alpha_j))^{-\theta}$ with the values $\theta = 1$ and 2, combined with a Levenberg–Marquardt least squares optimization method [5]. Note that the form of w_j puts some restriction on the use of the data. Usually, there is a level α_j beyond which w_j is no longer defined. Hence, the summation in Eq. (9.16) has to stop before that happens. Also, the data should be preconditioned by establishing the tail marker α_1 in a sensible way.

Although the Levenberg–Marquardt method as described above generally works well, it may be simplified by exploiting the structure of F. It is realized by scrutinizing Eq. (9.16) that if b and c are fixed, the optimization problem reduces to a standard weighted linear regression problem. That is, with both b and c fixed, the optimal values of a and $\log q$ are found using closed form weighted linear regression formulas in terms of w_j, $y_j = \log \hat{p}_f(\alpha_j)$ and $x_j = (\alpha_j - b)^c$.

It is obtained that the optimal values of a and q are given by the relations,

$$a^*(b, c) = -\frac{\sum_{j=1}^{M} w_j (x_j - \overline{x})(y_j - \overline{y})}{\sum_{j=1}^{M} w_j (x_j - \overline{x})^2}, \tag{9.17}$$

and

$$\log q^*(b, c) = \overline{y} + a^*(b, c)\overline{x}, \tag{9.18}$$

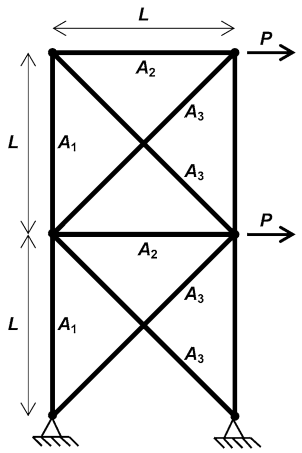

Fig. 9.1 Ten-bar truss structure

where $\overline{x} = \sum_{j=1}^{M} w_j x_j / \sum_{j=1}^{M} w_j$, with a similar definition of $\overline{y}$.

The Levenberg–Marquardt method may now be used on the function $\tilde{F}(b, c) = F(a^*(b, c), b, c, q^*(b, c))$ to find the optimal values b^* and c^*, and then the corresponding a^* and q^* can be calculated from Eqs. (9.17) and (9.18).

For estimation of the confidence interval for the predicted target quantile α_T provided by the optimal curve, the empirical confidence band is reanchored to the optimal curve. The range of fitted curves that stay within the reanchored confidence band will determine an optimized confidence interval of the predicted value.

5 Numerical Examples

The examples in the following two sections all have simple explicit limit state functions in terms of the basic random variables. The computational issue is therefore minor and no effort has been made to investigate the possibility of implementing more effective sampling strategies. If the proposed method were to be used in combination with computationally demanding procedures involving e.g. a FE method for calculating the sample, it would be necessary in general to use more effective sampling strategies than the brute force procedure used here.

5.1 Component Load Factor Calibration

In this first example, the 10-bar truss structure shown in Fig. 9.1 is studied. An enhanced Monte-Carlo reliability analysis of this truss is given in [1]. Here a load factor for a transversal load P is calibrated in order to achieve a target reliability of (10^{-6}) with respect to the horizontal sway of the truss. The ten truss members are cut from three different aluminum rods with cross-sectional areas A_1, A_2 and

Table 9.1 Basic variables

	Mean value	Coef. of var.	Prob. distr.	Char. value in (20)
A_1	10^{-2} m^2	0.05	Normal	1% quantile
A_2	$1.5 \cdot 10^{-3}$ m^2	0.05	Normal	1% quantile
A_3	$6.0 \cdot 10^{-3}$ m^2	0.05	Normal	1% quantile
B	1.0	0.10	Normal	mean
E	$6.9 \cdot 10^4$ MPa	0.05	Lognormal	1% quantile
P	based on Eq. (9.21)	0.10	Gumbel	95% quantile
d_0	0.1 m	-	-	-
L	9.0 m	-	-	-

A_3, as shown in Fig. 9.1. The structure is subjected to external loads P as shown in Fig. 9.1. The horizontal displacement D at the upper right hand corner of the truss structure can be written as [6]:

$$D = \frac{BPL}{A_1 A_3 E}\left\{\frac{4\sqrt{2}A_1^3(24A_2^2 + A_3^2) + A_3^3(7A_1^2 + 26A_2^2)}{D_T} + 4A_1A_2A_3\frac{20A_1^2 + 76A_1A_2 + 10A_3^2}{D_T} + 4\sqrt{2}A_1A_2A_3^2\frac{25A_1 + 29A_2}{D_T}\right\} \tag{9.19}$$

where $D_T = 4A_2^2(8A_1^2 + A_3^2) + 4\sqrt{2}A_1A_2A_3(3A_1 + 4A_2) + A_1A_3^2(A_1 + 6A_2)$ and E is Young's modulus. The random variable B accounts for model uncertainties. It is assumed that A_1, A_2, A_3, B, P, E are independent basic random variables. Their properties are summarized in Table 9.1. Also shown are the characteristic values used in the design check Eq. (9.21).

The safety margin

$$M(\alpha) = d_0 - D\big(A_1, A_2, A_3, B, E, P(\alpha)\big), \tag{9.20}$$

and the design check constraint is

$$c(\alpha) = d_0 - D\big(A_{1c}, A_{2c}, A_{3c}, B_c, E_c, \alpha P_c(\alpha)\big), \tag{9.21}$$

where α represents the transversal load factor.

Figures 9.2 and 9.3 show the optimized fitted parametric curve to the empirical data in a log plot for sample size 10^5 and for weighted regression coefficients $\theta = 2$ and $\theta = 1$, respectively. The difference between the two tail extrapolations is minimal. Applying the proposed procedure with a sample of size 10^5 gives the estimated value for α_T with the 95% confidence interval shown in Table 9.2 for both $\theta = 2$ and 1. Note that a crude Monte Carlo simulation verification of ($\alpha_T = 1.46$, $p_{fT} = 10^{-6}$) using $3 \cdot 10^9$ samples to within 2.5% at 95% confidence requires a computation time of about 24 h on a laptop computer. The CPU time for the results shown in Table 9.2 was only about 40 seconds on a standard laptop.

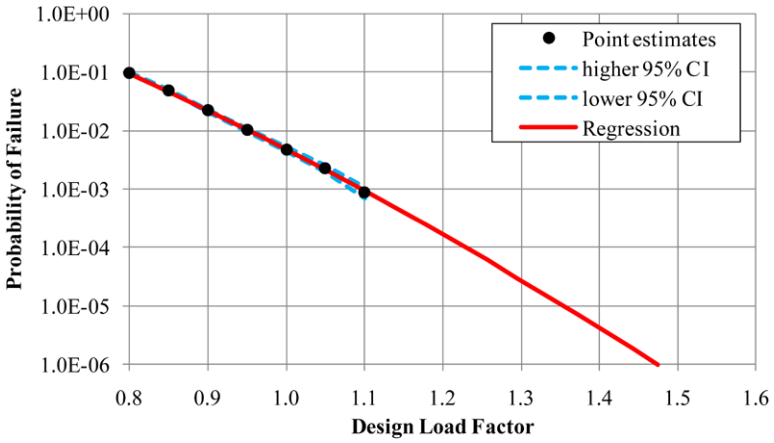

Fig. 9.2 Ten-bar truss structure. Sample size 10^5—weighted regression $\theta = 2$

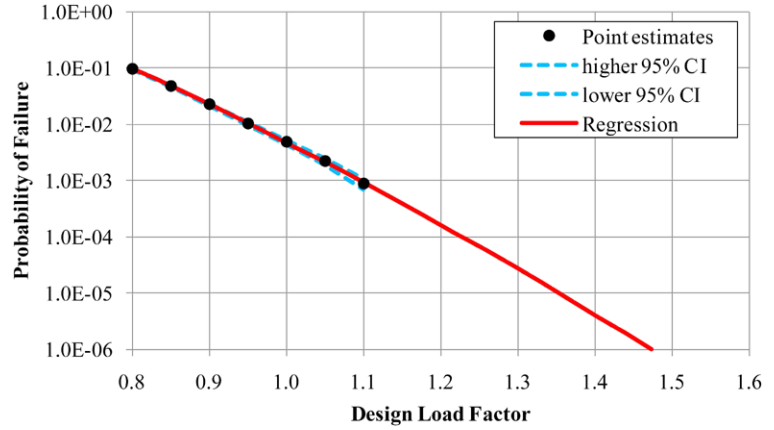

Fig. 9.3 Ten-bar truss structure. Sample size 10^5—weighted regression $\theta = 1$

Table 9.2 Optimal load factor α_T corresponding to $p_{fT} = 10^{-6}$ using sample size 10^5

	$\theta = 2$	$\theta = 1$
higher 95% CI	1.48	1.48
α_T	1.47	1.47
lower 95% CI	1.46	1.46

5.2 Design Resistance Safety Factor in a Series System

This example concerns the maximum internal forces in the members of a statically determinate 13-member truss structure subjected to external loading. The structure

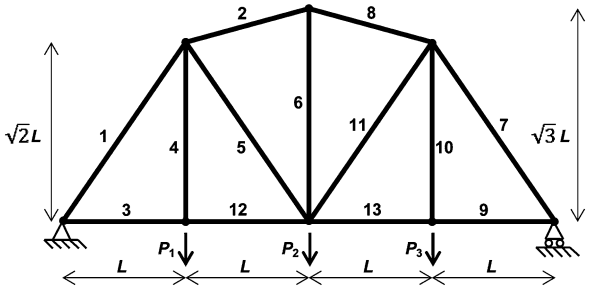

Fig. 9.4 Truss bridge example

is shown in Fig. 9.4, which also displays the numbering of the truss elements from 1 to 13.

The external loads P_1, P_2, P_3 which are acting on the structure as shown in Fig. 9.4, are modelled as independent Gaussian variables. The capacity for axial stress of truss element number j is expressed as $R_j = \sigma_{yj} A_j$ where σ_{yj} = the yield stress (MPa) and A_j = the cross-sectional area of this element (cm^2), and α is a resistance safety factor >1 used as a division factor in the design check equation below. It is assumed that $A_1 = A_7 = 18.7$, $A_2 = A_8 = 13.1$, $A_3 = A_9 = A_{12} = A_{13} = 11.7$, $A_4 = A_{10} = 11.3$, $A_5 = A_{11} = 3.3$, $A_6 = 8.0$. The 13 yield stresses are assumed to be independent Gaussian variables. The 16 basic random variables in this problem are listed in Table 9.3.

$$
\begin{aligned}
M_1 &= R_1 - 0.9186P_1 - 0.6124P_2 - 0.3062P_3 \\
M_2 &= R_2 - 0.3029P_1 - 0.6058P_2 - 0.3029P_3 \\
M_3 &= R_3 - 0.5303P_1 - 0.3535P_2 - 0.1768P_3 \\
M_4 &= R_4 - P_1 \\
M_5 &= R_5 + 0.4186P_1 - 0.3876P_2 - 0.1938P_3 \\
M_6 &= R_6 - 0.1835P_1 - 0.3670P_2 - 0.1835P_3 \\
M_7 &= R_7 - 0.3062P_1 - 0.6124P_2 - 0.9186P_3 \\
M_8 &= R_8 - 0.3029P_1 - 0.6058P_2 - 0.3029P_3 \\
M_9 &= R_9 - 0.1768P_1 - 0.3535P_2 - 0.5303P_3 \\
M_{10} &= R_{10} - P_1 \\
M_{11} &= R_{11} - 0.1938P_1 - 0.3876P_2 + 0.4186P_3
\end{aligned}
\tag{9.22}
$$

Table 9.3 The 16 basic variables

	Mean Value	Coef. of Var.	Prob. distr.	Char. value in Eq. (9.22)
P_j, $j = 1, 2, 3$	89 kN	0.15	Normal	99% quantile
σ_{yj}, $j = 1, \ldots, 13$	based on Eq. (9.23)	0.15	Normal	5% quantile
L	2.54 m	-	-	-

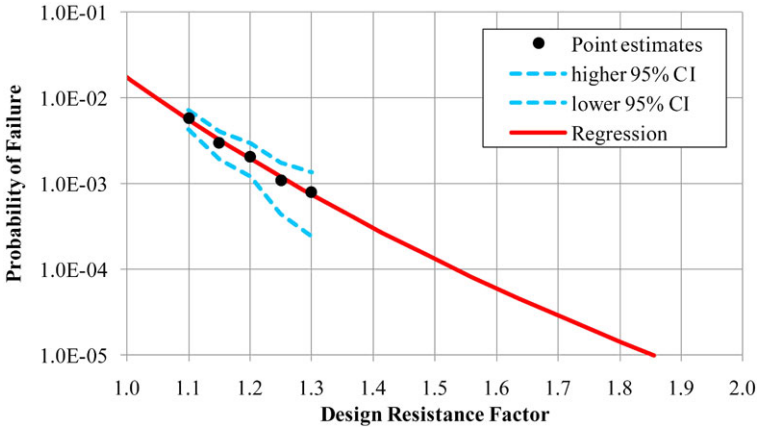

Fig. 9.5 Truss bridge. Sample size 10^4—weighted regression with $\theta = 1$

$$M_{12} = R_{12} - 0.5303P_1 - 0.3536P_2 - 0.1768P_3$$
$$M_{13} = R_{13} - 0.1768P_1 - 0.3536P_2 - 0.5303P_3$$

The 13 design check equations have the same mathematical set of 13 equations except that the deterministic characteristic values of Table 9.3 are used and a resistance safety factor is involved. The most severe constraint is the compressive stress in members 1 and 7 which therefore governs the design of the system as a whole:

$$\frac{\sigma_{yc}(\alpha)A_1}{\alpha} - 1.8372P_c = 0, \tag{9.23}$$

The objective is to find the value α_T such that the series system failure probability given by Eq. (9.8) is equal to a target $p_{fT} = 10^{-5}$. The log plot of $p_f(\alpha)$ versus α is shown in Figs. 9.5 and 9.6 for $\theta = 1$ and for samples of size 10^4 and 10^5, respectively. The estimated α_T corresponding to $p_f = 10^{-5}$ together with their CIs are shown in Table 9.4. A Winbugs script runs the entire analysis in under 1 min for 10^5 samples. As a contrast, crude Monte Carlo simulation with $5 \cdot 10^9$ samples confirms ($\alpha_T = 1.89$, $p_f = 10^{-5}$) for the series system accurate to within about 0.5% with 95% confidence, but requires a computation time of about 24 h on a laptop computer.

6 Conclusions

In this paper, we have described a Monte Carlo based method for a reliability-based calibration of design parameters such as load/resistance factors, safety factors or specification levels of structural systems. It has been shown that the method may provide good estimates of design factors for structural systems with a moderate computational effort. It has been pointed out that the use of Monte Carlo methods

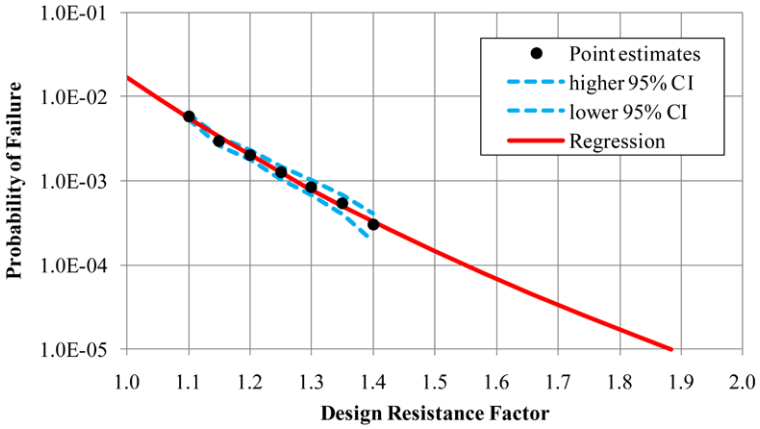

Fig. 9.6 Truss bridge. Sample size 10^5—weighted regression with $\theta = 1$

Table 9.4 Optimal resistance safety factor α_T corresponding to a system $p_{fT} = 10^{-5}$ using sample size 10^4 and 10^5 with $\theta = 1$

	$N = 10^4$	$N = 10^5$
higher 95% CI	1.95	1.92
α_T	1.85	1.88
lower 95% CI	1.69	1.80

for system reliability analysis has several very attractive features, the most important being that the failure criterion is usually relatively easy to check almost irrespective of the complexity of the system and the number of basic random variables.

Acknowledgements The first author is grateful for the financial support from the Research Council of Norway (NFR) through the Centre for Ships and Ocean Structures (CeSOS) at the Norwegian University of Science and Technology. The second and third authors gratefully acknowledge financial support from NSERC Canada.

References

1. Naess, A., Leira, B.J., Batsevych, O.: System reliability analysis by enhanced Monte Carlo simulation. Struct. Saf. **31**, 349–355 (2009)
2. Bucher, C.: Asymptotic sampling for high-dimensional reliability analysis. Probab. Eng. Mech. **24**, 504–510 (2009)
3. Naess, A., Leira, B.J., Batsevych, O.: Efficient reliability analysis of structural systems with a high number of limit states. In: Proceedings 29th International Conference on Offshore Mechanics and Arctic Engineering, pp. 809–814, OMAE–2010–21179. ASME, New York (2010)
4. Naess, A., Gaidai, O.: Estimation of extreme values from sampled time series. Struct. Saf. **31**, 325–334 (2009)
5. Gill, P., Murray, W., Wright, M.H.: Practical Optimization. Academic Press, London (1981)
6. Choi, S.-K., Grandhi, R.V., Canfield, R.A.: Reliability-Based Structural Design. Springer, London (2007)

Chapter 10
Optimal Design of Base-Isolated Systems Under Stochastic Earthquake Excitation

Hector A. Jensen, Marcos A. Valdebenito, and Juan G. Sepulveda

Abstract The development of a general framework for reliability-based design of base-isolated structural systems under uncertain conditions is presented. The uncertainties about the structural parameters as well as the variability of future excitations are characterized in a probabilistic manner. Nonlinear elements composed by hysteretic devices are used for the isolation system. The optimal design problem is formulated as a constrained minimization problem which is solved by a sequential approximate optimization scheme. First excursion probabilities that account for the uncertainties in the system parameters as well as in the excitation are used to characterize the system reliability. The approach explicitly takes into account all non-linear characteristics of the combined structural system (superstructure-isolation system) during the design process. Numerical results highlight the beneficial effects of isolation systems in reducing the superstructure response.

1 Introduction

There has been a growing interest during the last years in the application of base isolation techniques in order to improve the earthquake resistant performance of civil structures such as buildings, bridges, nuclear reactors, etc. [8, 10, 23, 30, 33]. In fact, the potential advantages of seismic isolation and the recent advancements in isolation-system products have lead to the design and construction of an increasing number of seismically isolated structural systems. Also, seismic isolation is extensively used for seismic retrofitting of existing structures [11, 26]. One of the difficulties in the design of base-isolated structural systems is the explicit consideration of the nonlinear behavior of the isolators during the design process. Similarly, the consideration of uncertainty about the structural model and the potential variability of future ground motions is a major challenge in the analysis and design of these

H.A. Jensen (✉) · M.A. Valdebenito · J.G. Sepulveda
Santa Maria University, Av. España 1680, Valparaiso, Chile
e-mail: hector.jensen@usm.cl

M.A. Valdebenito
e-mail: marcos.valdebenito@usm.cl

M. Papadrakakis et al. (eds.), *Computational Methods in Stochastic Dynamics*, Computational Methods in Applied Sciences 26,
DOI 10.1007/978-94-007-5134-7_10,

systems. The goal of this work is the development of a general framework for reliability based design of base-isolated systems under uncertain conditions. In particular, base-isolated building structures subject to earthquake excitation are considered in this study. A probabilistic approach is adopted for addressing the uncertainties about the structural model as well as the variability of future excitations. The uncertain earthquake excitation is modeled as a non-stationary stochastic process with uncertain model parameters. Specifically, a point-source model characterized by the moment magnitude and epicentral distance is adopted in this formulation [6]. Isolation elements composed by hysteretic devices are used for the isolation system. The hysteretic behavior of the devices is characterized by a Bouc–Wen type model [5]. The model provides general parametric hysteresis rules that gives a smooth transition of the change of stiffness as the deformation of the nonlinear elements changes. The reliability-based optimization problem is formulated as the minimization of an objective function subject to multiple design requirements including reliability constraints. First excursion probabilities are used as measures of system reliability. Such probabilities are estimated by an adaptive Markov Chain Monte Carlo procedure [4]. A sequential optimization approach based on global conservative, convex and separable approximations is implemented for solving the optimization problem [14, 18, 21]. The approach explicitly takes into account all non-linear characteristics of the structural response and it allows for a complex characterization of structural systems and excitation models. The solution of the equation of motion of the combined system (superstructure-isolation system) required during the simulation process is computed by a modified Runge–Kutta scheme of fourth-order. A numerical example is presented in order to illustrate the applicability and effectiveness of the proposed framework for reliability-based design of base-isolated buildings.

2 Reliability-Based Design Problem

The optimal design problem is defined as the identification of a vector $\{\phi\}$ of design variables that minimizes an objective function, that is

$$\text{Minimize } f\left(\{\phi\}\right) \tag{10.1}$$

subject to design constraints

$$h_j\left(\{\phi\}\right) \leq 0, \quad j = 1, \ldots, n_c \tag{10.2}$$

and side constraints

$$\phi_i^l \leq \phi_i \leq \phi_i^u, \quad i = 1, \ldots, n_d \tag{10.3}$$

The objective function is defined in terms of quantities such as initial, construction, repair, or downtime costs. On the other hand, the design constraints are given in terms of reliability constraints and/or constrains related to deterministic design requirements. In a stochastic setting the reliability constraints are usually defined in terms of failure probabilities. These probabilities provide a measure of the plausibility of the occurrence of unacceptable behavior (failure) of the system, based on the

available information. The probability of failure $P_{F_j}(\{\phi\})$ corresponding to a failure event F_j evaluated at the design $\{\phi\}$ can be expressed in terms of the multidimensional probability integral [13, 15]

$$P_{F_j}(\{\phi\}) = \int_{\Theta} I_{F_j}(\{\phi\}, \{\theta\}) q(\{\theta\})\, d\{\theta\} \tag{10.4}$$

where $I_{F_j}(\{\phi\}, \{\theta\})$ is the indicator function for failure, which is equal to one if the system fails and zero otherwise, and $\{\theta\}$, θ_i, $i = 1, \ldots, n_u$ is the vector that represents the uncertain system parameters involved in the problem (structural parameters and excitation). The uncertain system parameters $\{\theta\}$ are modeled using a prescribed probability density function $q(\{\theta\})$ which incorporates available knowledge about the system. Note, that the failure probability function $P_{F_j}(\{\phi\})$ accounts for the uncertainty in the system parameters as well as the uncertainties in the excitation. A model prediction error, that is, the error between the response of the actual system and the response of the model, can also be considered in the formulation [12, 31]. In this case the prediction error may be modeled probabilistically by augmenting the vector $\{\theta\}$ to form an uncertain parameter vector composed of both the structural and excitation model parameters as well as the model prediction-error. The failure domain $\Omega_{F_j}(\{\phi\})$ corresponding to the failure event F_j evaluated at the design $\{\phi\}$ is typically described in terms of a performance function g_j as

$$\Omega_{F_j}(\{\phi\}) = \{\{\theta\} \mid g_j(\{\phi\}, \{\theta\}) \geq 0\} \tag{10.5}$$

Then, the probability of failure can also be expressed as the integral of the probability density function $q(\{\theta\})$ over the failure domain in the form

$$P_{F_j}(\{\phi\}) = \int_{\Omega_{F_j}(\{\phi\})} q(\{\theta\})\, d\{\theta\} \tag{10.6}$$

With the previous notation, a reliability constraint can be written as $h_j(\{\phi\}) = P_{F_j}(\{\phi\}) - P^*_{F_j} \leq 0$, where $P^*_{F_j}$ is the target failure probability. The last inequality expresses the requirement that the probability of system failure must be smaller than an appropriate tolerance. It is noted that in the context of stochastic design a system that corresponds to a feasible design can not be certified with complete certainty, but with a tolerance $P^*_{F_j}$. In other words, the system will operate safely within the pre-specified probability of failure tolerance.

3 Structural Model

In general, base-isolated buildings are designed such that the superstructure remains elastic. Hence, the structure is modeled as a linear elastic system in the present formulation. The base and the floors are assumed to be infinitely rigid in plane. The superstructure and the base are modeled using three degrees of freedom per floor at the center of mass. Each nonlinear isolation element is modeled explicitly using the Bouc–Wen model. Let $\{x_s(t)\}$ be the n-th dimensional vector of displacements

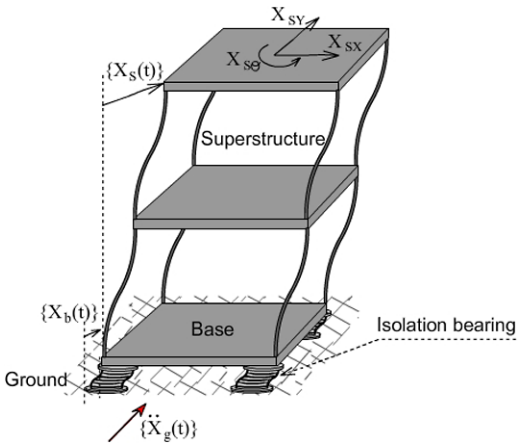

Fig. 10.1 Schematic representation of the base-isolated structural model

for the superstructure with respect to the base, and $[M_s]$, $[C_s]$, and $[K_s]$ be the corresponding mass, damping and stiffness matrices. Also, let $\{x_b(t)\}$ be the vector of base displacements with respect to the ground and $[G_s]$ be the matrix of earthquake influence coefficients of dimension $n \times 3$, that is, the matrix that couples the excitation components of the vector $\{\ddot{x}_g(t)\}$ to the degrees of freedom of the superstructure. The schematic representation of the base-isolated structural system as well as the displacement coordinates are shown in Fig. 10.1. The equation of motion of the elastic superstructure is then expressed in the form

$$\begin{aligned}&[M_s]\{\ddot{x}_s(t)\} + [C_s]\{\dot{x}_s(t)\} + [K_s]\{x_s(t)\} \\ &\quad = -[M_s][G_s]\big(\{\ddot{x}_b(t)\} + \{\ddot{x}_g(t)\}\big)\end{aligned} \tag{10.7}$$

where $\{\ddot{x}_b(t)\}$ is the vector of base accelerations relative to the ground. On the other hand, the equation of motion of the base can be written as

$$\begin{aligned}&\big([G_s]^T[M_s][G_s] + [M_b]\big)\big(\{\ddot{x}_b(t)\} + \{\ddot{x}_g(t)\}\big) \\ &\quad + [G_s]^T[M_s]\{\ddot{x}_s(t)\} + \{f_{is}\} = \{0\}\end{aligned} \tag{10.8}$$

where $[M_b]$ is the diagonal mass matrix of the rigid base, and $\{f_{is}\}$ is the vector containing the linear and nonlinear isolation elements forces (three components). The characterization of such forces is treated in a subsequent Section. Rewriting the previous equations, the combined equation of motion of the base-isolated structure system can be formulated in the form

$$\begin{aligned}&\begin{bmatrix}[M_s] & [M_s][G_s] \\ [G_s]^T[M_s] & [M_b] + [G_s]^T[M_s][G_s]\end{bmatrix}\begin{Bmatrix}\{\ddot{x}_s(t)\} \\ \{\ddot{x}_b(t)\}\end{Bmatrix} + \begin{bmatrix}[C_s] & [0] \\ [0]^T & [0]\end{bmatrix}\begin{Bmatrix}\{\dot{x}_s(t)\} \\ \{\dot{x}_b(t)\}\end{Bmatrix} \\ &\quad + \begin{bmatrix}[K_s] & [0] \\ [0]^T & [0]\end{bmatrix}\begin{Bmatrix}\{x_s(t)\} \\ \{x_b(t)\}\end{Bmatrix} \\ &= -\begin{Bmatrix}[M_s][G_s] \\ [M_b] + [G_s]^T[M_s][G_s]\end{Bmatrix}\{\ddot{x}_g(t)\} - \begin{Bmatrix}\{0\} \\ \{f_{is}(t)\}\end{Bmatrix}\end{aligned} \tag{10.9}$$

It is noted that elastic and viscous isolation elements can also be incorporated in the isolation model. Also, the above formulation can be directly extended to more complex cases, for example, to nonlinear models for the superstructure.

4 Earthquake Excitation Model

The ground acceleration is modeled as a non-stationary stochastic process. In particular, a point-source model characterized by the moment magnitude M and epicentral distance r is considered here [3, 6]. The model is a simple, yet powerful means for simulating ground motions and it has been successfully applied in the context of earthquake engineering. The time-history of the ground acceleration for a given magnitude M and epicentral distance r is obtained by modulating a white noise sequence by an envelope function and subsequently by a ground motion spectrum through the following steps: (1) generate a discrete-time Gaussian white noise sequence $\omega(t_j) = \sqrt{I/\Delta t}\theta_j,\ j = 1, \ldots, n_T$, where $\theta_j,\ j = 1, \ldots, n_T$, are independent, identically distributed standard Gaussian random variables, I is the white noise intensity, Δt is the sampling interval, and n_T is the number of time instants equal to the duration of the excitation T divided by the sampling interval; (2) the white noise sequence is modulated by an envelope function $h(t, M, r)$ at the discrete time instants; (3) the modulated white noise sequence is transformed to the frequency domain; (4) the resulting spectrum is normalized by the square root of the average square amplitude spectrum; (5) the normalized spectrum is multiplied by a ground motion spectrum (or radiation spectrum) $S(f, M, r)$ at discrete frequencies $f_l = l/T, l = 1, \ldots, n_T/2$; (6) the modified spectrum is transformed back to the time domain to yield the desired ground acceleration time history. Details of the characterization of the envelope function $h(t, M, r)$ and the ground acceleration spectrum $S(f, M, r)$ are provided in the subsequent sections. The probabilistic model for the seismic hazard at the emplacement is complemented by considering that the moment magnitude M and epicentral distance r are also uncertain. The uncertainty in moment magnitude is modeled by the Gutenberg–Richter relationship truncated on the interval $[6.0, 8.0]$, which leads to the probability density function [24]

$$p(M) = \frac{be^{-bM}}{e^{-6.0b} - e^{-8.0b}}, \quad 6.0 \le M \le 8.0 \tag{10.10}$$

where b is a regional seismicity factor. For the uncertainty in the epicentral distance r, a lognormal distribution with mean value $\bar{r}$ (km) and standard deviation σ_r (km) is used. The point source stochastic model previously described is well suited for generating the high-frequency components of the ground motion (greater than 0.1 Hz). Low-frequency components can also be introduced in the analysis by combining the above methodology with near-fault ground motion models [25].

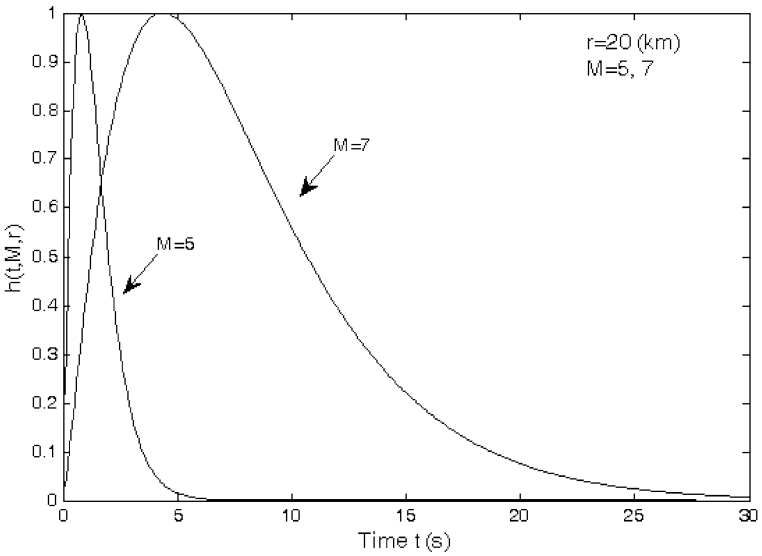

Fig. 10.2 Envelope function for epicentral distance $r = 20$ km and moment magnitudes $M = 5$ and $M = 7$

4.1 Envelope Function

The envelope function for the ground acceleration is represented by [6, 28]

$$h(t, M, r) = a_1 \left(\frac{t}{t_n}\right)^{a_2} e^{-a_3(t/t_n)} \tag{10.11}$$

where

$$a_2 = \frac{-0.2\ln(0.05)}{1 + 0.2(\ln(0.2) - 1)}, \qquad a_3 = \frac{a_2}{0.2}, \qquad a_1 = \left(\frac{e^1}{0.2}\right)^{a_2} \tag{10.12}$$

The envelope function has a peak equal to unity when $t = 0.2t_n$, and $h(t, M, r) = 0.05$ when $t = t_n$, with $t_n = 2.0T_{gm}$, where T_{gm} is the duration of ground motion, expressed as a sum of a path dependent and source dependent component $T_{gm} = 0.05\sqrt{r^2 + h^2} + 0.5/f_a$, where r is the epicentral distance, and the parameters h and f_a (corner frequency) are moment dependent given by $\log(h) = 0.15M - 0.05$ and $\log(f_a) = 2.181 - 0.496M$ [3]. As an example Fig. 10.2 shows the envelope function for $r = 20$ km, and $M = 5$ and $M = 7$. Note that increasing the moment magnitude increases the duration of the envelope function, as expected.

4.2 Ground Motion Spectrum

The total spectrum of the motion at a site $S(f, M, r)$ is expressed as the product of the contribution from the earthquake source $E(f, M)$, path $P(f, r)$, site $G(f)$ and type of motion $I(f)$, i.e.

$$S(f, M, r) = E(f, M)P(f, r)G(f)I(f) \tag{10.13}$$

The source component is given by

$$E(f, M) = CM_0(M)S_a(f, M) \tag{10.14}$$

where C is a constant, $M_0(M) = 10^{1.5M+10.7}$ is the seismic moment, and the factor S_a is the displacement source spectrum given by [3]

$$S_a(f, M) = \frac{1-\varepsilon}{1+(f/f_a)^2} + \frac{\varepsilon}{1+(f/f_b)^2} \tag{10.15}$$

where the corner frequencies f_a and f_b, and the weighting parameter ε are defined, respectively, as $\log(f_a) = 2.181 - 0.496M$, $\log(f_b) = 2.41 - 0.408M$, and $\log(\varepsilon) = 0.605 - 0.255M$. The constant C is given by $C = UR_\Phi VF/4\pi\rho_s\beta_s^3 R_0$, where U is a unit dependent factor, R_Φ is the radiation pattern, V represents the partition of total shear-wave energy into horizontal components, F is the effect of the free surface amplification, ρ_s and β_s are the density and shear-wave velocity in the vicinity of the source, and R_0 is a reference distance.

Next, the path effect $P(f, r)$ which is another component of the process that affects the spectrum of motion at a particular site it is represented by functions that account for geometrical spreading and attenuation

$$P(f, r) = Z\big(R(r)\big)e^{-\pi f R(r)/Q(f)\beta_s} \tag{10.16}$$

where $R(r)$ is the radial distance from the hypocenter to the site given by $R(r) = \sqrt{r^2 + h^2}$. The attenuation quantity $Q(f)$ is taken as $Q(f) = 180f^{0.45}$ and the geometrical spreading function is selected as $Z(R(r)) = 1/R(r)$ if $R(r) < 70.0$ km and $Z(R(r)) = 1/70.0$ otherwise [3]. The modification of seismic waves by local conditions, site effect $G(f)$, is expressed by the multiplication of a diminution function $D(f)$ and an amplification function $A(f)$. The diminution function accounts for the path-independent loss of high frequency in the ground motions and can be accounted for a simple filter of the form $D(f) = e^{-0.03\pi f}$ [2]. The amplification function $A(f)$ is based on empirical curves given in [7] for generic rock sites. An average constant value equal to 2.0 is considered. Finally, the filter that controls the type of ground motion $I(f)$ is chosen as $I(f) = (2\pi f)^2$ for ground acceleration. The particular values of the different parameters of the stochastic ground acceleration model are given in Table 10.1 (see Application Problem Section). For illustration purposes Fig. 10.3 shows the ground acceleration spectrum for a nominal distance $r = 20$ km, moment magnitudes $M = 5$ and $M = 7$, and model parameters

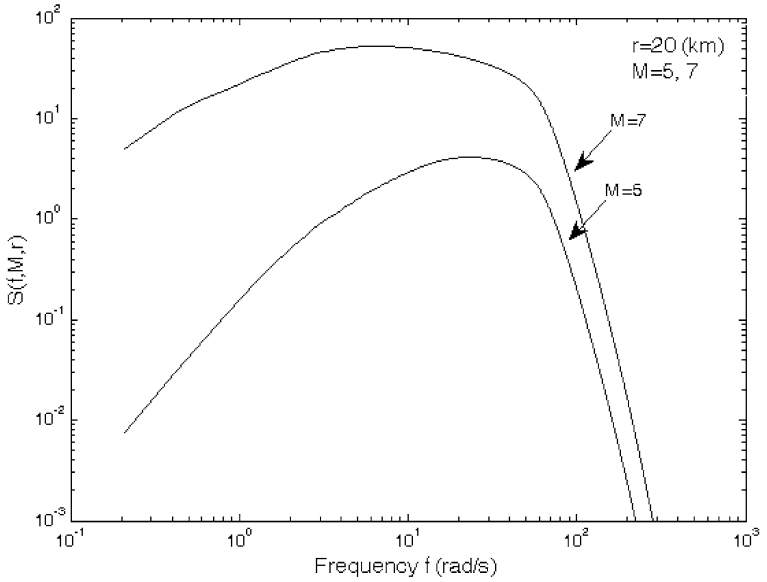

Fig. 10.3 Ground acceleration spectrum for epicentral distance $r = 20$ km and moment magnitudes $M = 5$ and $M = 7$

given in Table 10.1. As the moment magnitude increases, the spectral amplitude increases at all frequencies, with a shift of dominant frequency content towards the lower frequency regime, as anticipated.

5 Isolation Model

Several isolation elements can be used to model isolation systems. They include elastic, viscous, nonlinear fluid dampers, hysteretic (uniaxial or biaxial) elements for bilinear elastomeric bearings, hysteretic (uniaxial or biaxial) elements for sliding bearings, etc. Uniaxial elastomeric bearings with hysteretic behavior, such as lead rubber bearings, are considered in the present implementation. They are modeled using the Bouc–Wen model as [5]

$$U^y \dot{z}(t) = \begin{cases} \dot{x}_b(t)[\alpha - z^n(t)(\gamma \operatorname{sgn}(\dot{x}_b(t)z(t)) + \beta)] & \text{if n is even} \\ \dot{x}_b(t)[\alpha - z^n(t)(\gamma \operatorname{sgn}(\dot{x}_b(t)) + \beta \operatorname{sgn}(z(t)))] & \text{if n is odd} \end{cases} \tag{10.17}$$

where $z(t)$ is a dimensionless hysteretic variable, α, β, and γ are dimensionless quantities, U^y is the yield displacement, $x_b(t)$ and $\dot{x}_b(t)$ represent the base displacement and velocity, respectively, and $\operatorname{sgn}(\cdot)$ is the sign function. The forces activated in the elastomeric isolation bearing are modeled by an elastic-viscoplastic model

with strain hardening

$$f_{is}(t) = k_p x_b(t) + c_v \dot{x}_b(t) + (k_e - k_p) U^y z(t) \tag{10.18}$$

where k_e is the pre-yield stiffness, k_p is the post-yield stiffness, c_v is the viscous damping coefficient of the elastomeric bearing, and U^y is the yield displacement. If the post-yield stiffness is written as $k_p = \alpha_L k_e$, where α_L is a factor which defines the extent to which the force is linear, the isolator forces can be expressed as

$$f_{is}(t) = \alpha_L k_e x_b(t) + c_v \dot{x}_b(t) + (1 - \alpha_L) k_e U^y z(t) \tag{10.19}$$

6 Sequential Approximate Optimization

The solution of the reliability-based optimization problem given by Eqs. (10.1)–(10.3) is obtained by transforming it into a sequence of sub-optimization problems having a simple explicit algebraic structure. Thus, the strategy is to construct successive approximate analytical sub-problems. To this end, the objective and the constraint functions are represented by using approximate functions dependent on the design variables. In particular, a hybrid form of linear, reciprocal and quadratic approximations is considered in the present formulation [14, 20, 27]. The approximate discrete sub-optimization problems take the form ($k = 1, 2, \ldots$)

$$\text{Minimize } \tilde{f}_k\big(\{\phi\}\big) \tag{10.20}$$

subject to

$$\tilde{h}_{jk}\big(\{\phi\}\big) \le 0, \quad j = 1, \ldots, n_c \tag{10.21}$$

with side constraints

$$\phi_i^l \le \phi_i \le \phi_i^u, \quad i = 1, \ldots, n_d \tag{10.22}$$

where $\tilde{f}_k$ and $\tilde{h}_{jk}$, $j = 1, \ldots, n_c$ represent the approximate objective and constraint functions at the current point $\{\phi^k\}$ in the design space, respectively. The approximate objective function is obtained as

$$\tilde{f}_k\big(\{\phi\}\big) = f_{1k}\big(\{\phi\}\big) + f_{2k}\big(\{\phi\}\big) + f_{3k}\big(\{\phi\}\big) \tag{10.23}$$

where $f_{1k}(\{\phi\})$ is a linear function in terms of the design variables, $f_{2k}(\{\phi\})$ is a linear function with respect to the reciprocal of the design variables, and $f_{3k}(\{\phi\})$ is a quadratic function of the design variables. They are given by

$$f_{1k}\big(\{\phi\}\big) = \sum_{(i^+)} \frac{\partial f(\{\phi^k\})}{\partial \phi_i} \phi_i, \qquad f_{2k}\big(\{\phi\}\big) = -\sum_{(i^-)} \frac{\partial f(\{\phi^k\})}{\partial \phi_i} \frac{(\phi_i^k)^2}{\phi_i} \tag{10.24}$$

$$f_{3k}\big(\{\phi\}\big) = -2\chi^f \sum_{(i^-)} \frac{\partial f(\{\phi^k\})}{\partial \phi_i} \phi_i \left(\frac{\phi_i}{\phi_i^k} - 2 \right) \tag{10.25}$$

where (i^+) is the group that contains the variables for which the partial derivative of the objective function is positive at the expansion point $\{\phi^k\}$, (i^-) is the group that includes the remaining variables, and χ^f is a user-defined positive scalar that control the conservatism of the approximation [17, 18]. On the other hand, the constraint functions involving reliability measures (reliability constraints) are first transformed as $h_j^t(\{\phi\}) = \ln[P_{F_j}(\{\phi\})]$. Then the transformed constraint functions are approximated in the form

$$\tilde{h}_{jk}^t\big(\{\phi\}\big) = h_{j1k}^t\big(\{\phi\}\big) + h_{j2k}^t\big(\{\phi\}\big) + h_{j3k}^t\big(\{\phi\}\big) + \bar{h}_{jk}^t\big(\{\phi^k\}\big) \tag{10.26}$$

where

$$h_{j1k}^t\big(\{\phi\}\big) = \sum_{(i_j^+)} \frac{\partial h_j^t(\{\phi^k\})}{\partial \phi_i}\phi_i, \qquad h_{j2k}^t\big(\{\phi\}\big) = -\sum_{(i_j^-)} \frac{\partial h_j^t(\{\phi^k\})}{\partial \phi_i}\frac{(\phi_i^k)^2}{\phi_i} \tag{10.27}$$

$$h_{j3k}^t\big(\{\phi\}\big) = -2\chi^{h_j^t}\sum_{(i_j^-)} \frac{\partial h_j^t(\{\phi^k\})}{\partial \phi_i}\phi_i\left(\frac{\phi_i}{\phi_i^k} - 2\right) \tag{10.28}$$

$$\begin{aligned}\bar{h}_{jk}^t\big(\{\phi^k\}\big) = h_j^t\big(\{\phi^k\}\big) &- \sum_{(i_j^+)} \frac{\partial h_j^t(\{\phi^k\})}{\partial \phi_i}\phi_i^k \\ &- \big(2\chi^{h_j^t} - 1\big)\sum_{(i_j^-)} \frac{\partial h_j^t(\{\phi^k\})}{\partial \phi_i}\phi_i^k\end{aligned} \tag{10.29}$$

where $\sum_{(i_j^+)}$ and $\sum_{(i_j^-)}$ mean summation over the variables belonging to group (i_j^+) and (i_j^-), respectively, and $\chi^{h_j^t}$ is as before a user-defined positive scalar that control the conservatism of the approximations. Group (i_j^+) contains the variables for which $\partial h_j^t(\{\phi^k\})/\partial\phi_i$ is positive, and group (i_j^-) includes the remaining variables. The same type of approximations can be applied to the deterministic constraint functions. The explicit discrete sub-optimization problems (10.20)–(10.22) are solved by standard methods that treat the problem directly in the primal design variable space such as evolution-based optimization techniques [16]. The level of effectiveness of the above sequential optimization scheme depends on the degree of convexity of the functions involved in the optimization problem. For example, if the curvatures are not too large and relatively uniform throughout the design space the proposed algorithm converges within few iterations [9, 21, 29]. For more general cases methods based on trust regions and line search methodologies may be more appropriate [1, 19, 22].

7 Reliability and Sensitivity Assessment

The characterization of the sub-optimization problems (10.20)–(10.22) requires the estimation of first excursion probabilities and their sensitivities. In order to estimate the excursion probabilities at a given design high-dimensional integrals need to be evaluated. This difficulty favors the application of Monte Carlo Simulation as fundamental approach to cope with the probability integrals. However, in most engineering applications the probability that a particular system fails is expected to be small, e.g. between 10^{-4}–10^{-6}. Direct Monte Carlo is robust to the type and dimension of the problem, but it is not suitable for finding small probabilities. Therefore, advanced Monte Carlo strategies are needed to reduce the computational efforts. In particular a generally applicable method, called subset simulation, is implemented in this work [4]. On the other hand, the sensitivity of the failure probability functions with respect to the design variables is estimated by an approach recently introduced in [32]. The approach is based on the approximate local representation of two different quantities. The first approximation involves the performance functions that define the failure domains while the second includes the probability of failure in terms of the maximum response levels for safe system operation. For a detailed discussion of the approach the reader is referred to [22, 32].

8 Application Problem

8.1 Description

A four-story building with a base-isolation system under earthquake motion is considered as an application problem. The plan view, as well as the dimensions for each floor are shown in Fig. 10.4. The elevation of one resistant element (A-axis) is illustrated in Fig. 10.5. Each of the four floors is supported by 80 columns of square cross section. The first floor has a height equal to 3.5 m while the other floors have a constant height equal to 3.0 m, leading to a total height of 12.5 m.

As previously pointed out (see Structural Model Section) each floor is represented by three degrees of freedom, i.e. two translational displacements in the direction of the x axis and y axis, and a rotational displacement. The associated active masses in the x and y direction are taken constant for the first three floors and equal to 2.50×10^6 kg and 1.50×10^6 kg for the last floor. The corresponding mass moments of inertia are taken as 2.10×10^9 kg·m^2 and 1.20×10^9 kg·m^2, respectively. On the other hand, the mass of the base is equal to 6.0×10^6 kg, and its mass moment of inertia 5.00×10^9 kg·m^2. The Young's modulus and the modal damping ratios are treated as uncertain system parameters. The Young's modulus is modeled by a truncated normal random variable with most probable value $\bar{E} = 2.50 \times 10^{10}$ N/m^2 and coefficient of variation of 20%. Moreover, the damping ratios are modeled by independent Log-normal random variables with mean value $\bar{\zeta} = 0.03$ and coefficient of variation of 40%. The base isolation system is composed of 80 uniaxial lead rubber

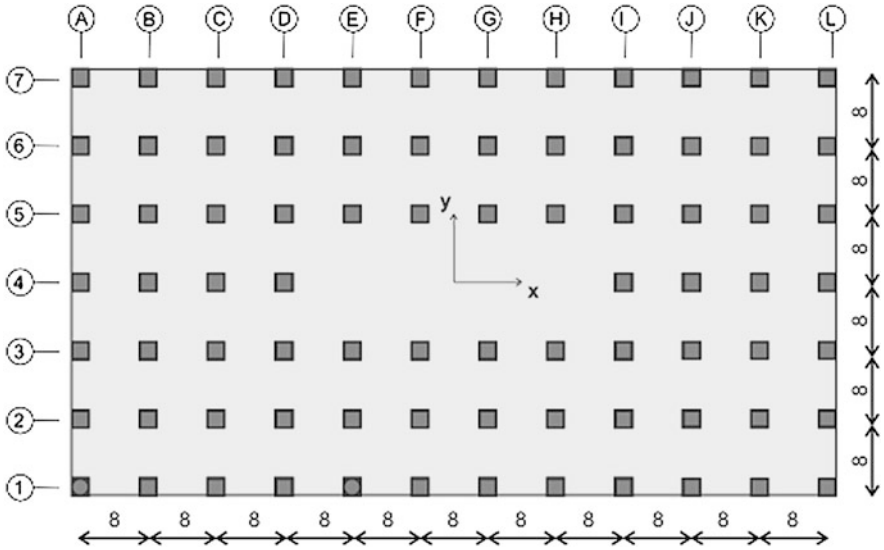

Fig. 10.4 Plan view of the structural model

Fig. 10.5 Elevation view of axis A

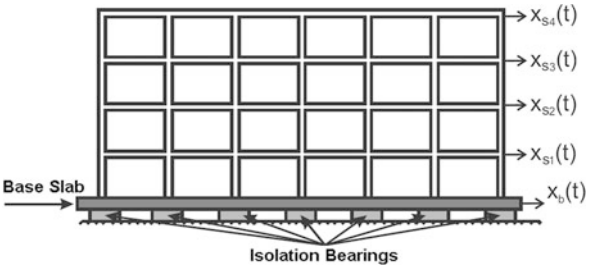

bearings with hysteretic behavior. The nonlinear behavior of these devices is modeled using the equations described in Sect. 5 with model parameters $n = 1$, $\alpha = 1.0$, $\beta = -0.65$, $\gamma = 0.5$, $U^y = 0.5$ cm, $\alpha_L = 0.1$, $k_e = 3 \times 10^6$ N/m, and $c_v = 0.0$. Figures 10.6 and 10.7 show a schematic representation of a lead rubber bearing and a typical displacement-restoring force curve of the isolation element, respectively. The structural system is excited horizontally by a ground acceleration applied in the y direction. The induced ground acceleration is characterized as in Sect. 4, with model parameters listed in Table 10.1.

8.2 Optimal Design Problem

The objective function f is defined as the volume of the column elements of the structural system. The design variables $\{\phi\}$ are chosen as the dimensions of the

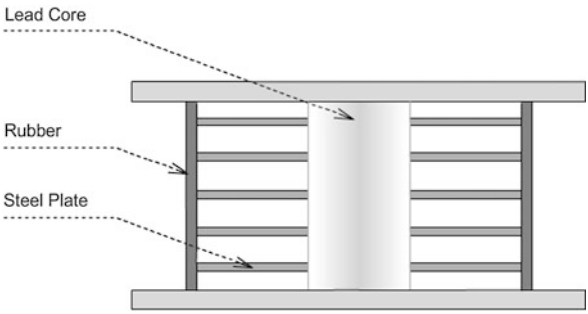

Fig. 10.6 Lead rubber bearing

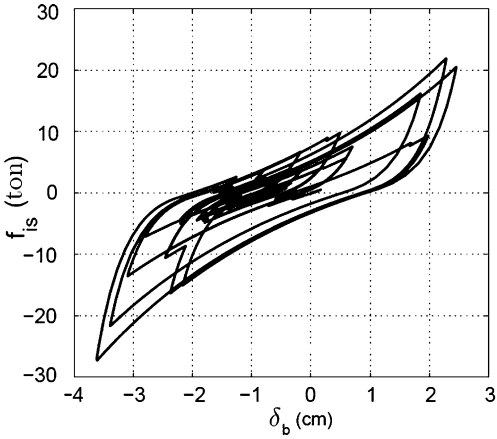

Fig. 10.7 Typical displacement-restoring force curve of the isolation element (lead rubber bearing)

columns throughout the height, grouped in four design variables, i.e. the dimensions of the columns of each floor constitute each of the design groups. The failure event is formulated as a first passage problem during the duration of the ground acceleration. The structural responses to be controlled are the 4 interstorey drift displacements. The threshold value is chosen equal to 0.2% of the floor height for the interstorey drift displacements. Thus, the failure domains evaluated at the design $\{\phi\}$ are given

Table 10.1 Parameters for the stochastic ground acceleration model

Parameter	Numerical Value	Parameter	Numerical Value
$\bar{r}$ (km)	20.0	σ_r (km)	9.0
b	1.8	U	10^{-20}
ρ_s (gm/cc)	2.8	β_s (km/s)	3.5
V	$1/\sqrt{2}$	R_Φ	0.55
F	2.0	R_0 (km)	1.0
T (s)	20.0	Δt (s)	0.01

Table 10.2 Initial and final designs

Design variable	Initial design	Final design	
		Problem 1	Problem 2
ϕ_1 (m)	0.90	0.68	0.85
ϕ_2 (m)	0.80	0.59	0.75
ϕ_3 (m)	0.75	0.57	0.72
ϕ_4 (m)	0.70	0.51	0.64
Normalized objective function	1.00	0.56	0.88

by

$$\Omega_{F_j}\left(\{\phi\}\right) = \left\{\{\theta\} \mid \max_{t_k, k=1,\ldots,2001} \left|\delta_j\left(t_k, \{\phi\}, \{\theta\}\right)\right| - \delta^* \geq 0\right\}, \quad j = 1, \ldots, 4 \tag{10.30}$$

where $\delta_j(t_k, \{\phi\}, \{\theta\})$ is the relative displacement between the $(j-1, j)$-th floor evaluated at the design $\{\phi\}$, t_k are the discrete time instants, δ^* is the critical threshold level, and $\{\theta\}$ is the vector that represents the uncertain system parameters (structural parameters and excitation). Note that more than two thousand random variables are involved in the characterization of the uncertain model parameters. The reliability-based optimization problem is defined as

$$\text{Min } f\left(\{\phi\}\right)$$

subject to

$$\begin{aligned} P_{F_j}\left(\{\phi\}\right) &\leq P_F^*, \quad j = 1, 2, 3, 4 \\ 0.30 \leq \phi_i &\leq 1.10, \quad i = 1, \ldots, 4 \end{aligned} \tag{10.31}$$

Two target failure probabilities are considered: $P_F^* = 10^{-2}$ and $P_F^* = 10^{-4}$. The first case can be interpreted as a design problem with a moderate level of reliability while the second case corresponds to a high level of reliability. In what follows the first case will be referred as Problem 1 while the second case as Problem 2.

8.3 Results

The initial and final designs of Problems 1 and 2 are given in Table 10.2. The results of the optimization process are presented in Figs. 10.8, 10.9 and 10.10 in terms of the evolution of the objective function and failure probabilities, respectively.

The objective function is normalized by its value at the initial design. It is observed that only a few optimization cycles are required for obtaining convergence. Moreover, most of the improvement of the objective function takes place in the first 3 iterations. It is also seen that the method generates a series of steadily improved

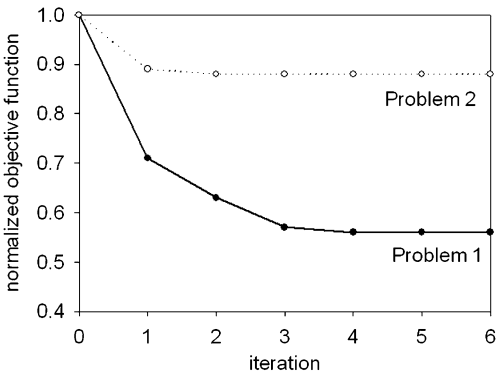

Fig. 10.8 Iteration history in terms of the objective function. Problem 1: moderate level of reliability. Problem 2: high level of reliability

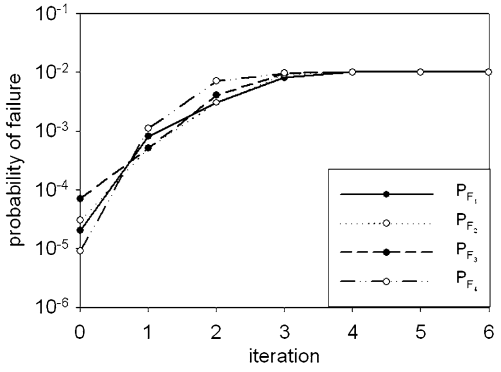

Fig. 10.9 Iteration history in terms of the reliability constraints. Problem 1

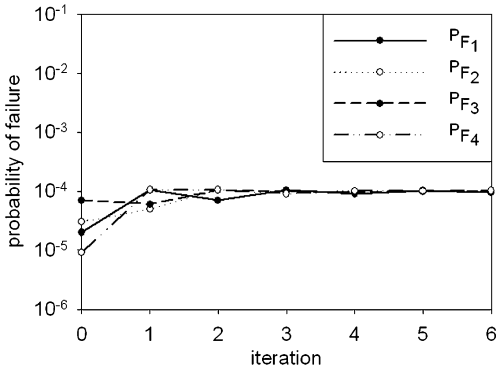

Fig. 10.10 Iteration history in terms of the reliability constraints. Problem 2

feasible designs that move toward the optimum. The results indicate that the value of the objective function at the final design of Problem 2 is greater than the corresponding value of Problem 1. This is turn implies that the structural components (columns) at the final design of Problem 2 are bigger than the corresponding components of Problem 1, as expected. The beneficial effects of the base isolation system are shown in Table 10.3. This table shows the value of the objective function at the

Table 10.3 Objective function value of models with and without the base isolation system

Model	Normalized objective function at the final design	
	Problem 1	Problem 2
With base isolation system	0.56	0.88
Without base isolation system	0.78	1.21
Difference	39%	38%

Table 10.4 Constraint violations

	Problem 2
P_{F_1}/P_F^*	103
P_{F_2}/P_F^*	55
P_{F_3}/P_F^*	20
P_{F_4}/P_F^*	2
$P_F^* = 10^{-4}$	

final designs of Problems 1 and 2 for models with and without the isolation system. The effect of the isolation system is clear from these results. The difference between the values of the objective functions is almost 40% in both Problems.

Finally, the effect of the base isolation system can also be observed from a constraint violation viewpoint. Table 10.4 shows the probability of occurrence of the failure events associated with the final design of Problem 2 (see Table 10.2) for the case where no base isolation is considered. The probability is normalized by the target failure probability $P_F^* = 10^{-4}$. It is seen for example that the probability of occurrence of failure event F_1 is more than 100 times greater than the target failure probability. Once again, the effect of the isolation system is evident from these results.

9 Conclusions

A general framework for reliability-based design of base-isolated buildings under uncertain conditions has been presented. The reliability-based design problem is formulated as an optimization problem with a single objective function subject to multiple reliability constraints. First excursion probabilities that account for the uncertainties in the system parameters as well as in the excitation are used to characterize the system reliability. The high computational cost associated with the solution of the optimization problem is addressed by the use of approximate reliability analyses during portions of the optimization process. The proposed approach takes into account all nonlinear characteristics of the structural response in the design process and it allows for a complex characterization of structural systems and excitation

models. At the same time, uncertainties in structural and excitation model parameters are considered explicitly during the design process. The numerical results and additional validation calculations highlight the beneficial effects of base-isolation systems in reducing the superstructure response. This in turn implies more robust and safer designs.

Acknowledgements This research was partially supported by CONICYT (National Commission for Scientific and Technological Research) under grant 1110061. This support is gratefully acknowledged by the authors.

References

1. Alexandrov, N.M., Dennis, J.E. Jr., Lewis, R.M., Torczon, V.: A trust-region framework for managing the use of approximation models in optimization. Struct. Optim. **15**(1), 16–23 (1998)
2. Anderson, J.G., Hough, S.E.: A model for the shape of fhe Fourier amplitude spectrum of acceleration at high frequencies. Bull. Seismol. Soc. Am. **74**(5), 1969–1993 (1984)
3. Atkinson, G.M., Silva, W.: Stochastic modeling of California ground motions. Bull. Seismol. Soc. Am. **90**(2), 255–274 (2000)
4. Au, S.K., Beck, J.L.: Estimation of small failure probabilities in high dimensions by subset simulation. Probab. Eng. Mech. **16**(4), 263–277 (2001)
5. Baber, T.T., Wen, Y.: Random vibration hysteretic, degrading systems. J. Eng. Mech. Div. **107**(6), 1069–1087 (1981)
6. Boore, D.M.: Simulation of ground motion using the stochastic method. Pure Appl. Geophys. **160**(3–4), 635–676 (2003)
7. Boore, D.M., Joyner, W.B., Fumal, T.E.: Equations for estimating horizontal response spectra and peak acceleration from western North American earthquakes: a summary of recent work. Seismol. Res. Lett. **68**(1), 128–153 (1997)
8. Ceccoli, C., Mazzotti, C., Savoia, M.: Non-linear seismic analysis of base-isolated rc frame structures. Earthquake Eng. Struct. Dyn. **28**(6), 633–653 (1999)
9. Chickermane, H., Gea, H.C.: Structural optimization using a new local approximation method. Int. J. Numer. Methods Eng. **39**, 829–846 (1996)
10. Chopra, A.K.: Dynamics of Structures: Theory and Applications to Earthquake Engineering. Prentice Hall, New York (1995)
11. De Luca, A., Mele, E., Molina, J., Verzeletti, G., Pinto, A.V.: Base isolation for retrofitting historic buildings: evaluation of seismic performance through experimental investigation. Earthquake Eng. Struct. Dyn. **30**(8), 1125–1145 (2001)
12. Der Kiureghian, A.: Analysis of structural reliability under parameter uncertainties. Probab. Eng. Mech. **23**(4), 351–358 (2008)
13. Ditlevsen, O., Madsen, H.O.: Structural Reliability Methods. Wiley, New York (1996)
14. Fleury, C., Braibant, V.: Structural optimization: a new dual method using mixed variables. Int. J. Numer. Methods Eng. **23**(3), 409–428 (1986)
15. Freudenthal, A.M.: Safety and the probability of structural failure. Trans. Am. Soc. Civ. Eng. **121**, 1337–1397 (1956)
16. Goldberg, D.: Genetic Algorithms in Search, Optimization, and Machine Learning. Addison-Wesley, Reading (1989)
17. Groenwold, A.A., Etman, L.F.P., Snyman, J.A., Rooda, J.E.: Incomplete series expansion for function approximation. Struct. Multidiscip. Optim. **34**(1), 21–40 (2007)
18. Groenwold, A.A., Wood, D.W., Etman, L.F.P., Tosserams, S.: Globally convergent optimization algorithm using conservative convex separable diagonal quadratic approximations. AIAA J. **47**(11), 2649–2657 (2009)

19. Haftka, R.T., Gürdal, Z.: Elements of Structural Optimization, 3rd edn. Kluwer Academic, Norwell (1992)
20. Jensen, H.A.: Structural optimization of non-linear systems under stochastic excitation. Probab. Eng. Mech. **21**(4), 397–409 (2006)
21. Jensen, H.A., Sepulveda, J.G.: Structural optimization of uncertain dynamical systems considering mixed-design variables. Probab. Eng. Mech. **26**(2), 269–280 (2011)
22. Jensen, H.A., Valdebenito, M.A., Schuëller, G.I., Kusanovic, D.S.: Reliability-based optimization of stochastic systems using line search. Comput. Methods Appl. Mech. Eng. **198**(49–52), 3915–3924 (2009)
23. Kelly, J.M.: Aseismic base isolation: review and bibliography. Soil Dyn. Earthq. Eng. **5**(4), 202–216 (1986)
24. Kramer, S.L.: Geotechnical Earthquake Engineering. Prentince Hall, New York (2003)
25. Mavroeidis, G.P., Papageorgiou, A.S.: A mathematical representation of near-fault ground motions. Bull. Seismol. Soc. Am. **93**(3), 1099–1131 (2003)
26. Mokha, A.S., Amin, N., Constantinou, M.C., Zayas, V.: Seismic isolation retrofit of large historic building. J. Struct. Eng. **122**(3), 298–308 (1996)
27. Prasad, B.: Approximation, adaptation and automation concepts for large scale structural optimization. Eng. Optim. **6**(3), 129–140 (1983)
28. Saragoni, G.R., Hart, G.C.: Simulation of artificial earthquakes. Earthquake Eng. Struct. Dyn. **2**(3), 249–267 (1974)
29. Schittkowski, K., Zillober, C., Zotemantel, R.: Numerical comparison of nonlinear programming algorithms for structural optimization. Struct. Optim. **7**(1–2), 1–19 (1994)
30. Taflanidis, A.A.: Robust stochastic design of viscous dampers for base isolation applications. In: Computational Methods in Structural Dynamics and Earthquake Engineering (COMPDYN), 22–24 June, Rhodes, Greece (2009)
31. Taflanidis, A.A., Beck, J.L.: Stochastic subset optimization for optimal reliability problems. Probab. Eng. Mech. **23**(2–3), 324–338 (2008)
32. Valdebenito, M.A., Schuëller, G.I.: Efficient strategies for reliability-based optimization involving non linear, dynamical structures. Comput. Struct. **89**(19–20), 1797–1811 (2011)
33. Zou, X.-K., Wang, Q., Li, G., Chan, C.-M.: Integrated reliability-based seismic drift design optimization of base-isolated concrete buildings. J. Struct. Eng. **136**(10), 1282–1295 (2010)

Chapter 11
Systematic Formulation of Model Uncertainties and Robust Control in Smart Structures Using H_∞ and μ-Analysis

Amalia Moutsopoulou, Georgios E. Stavroulakis, and Anastasios Pouliezos

Abstract The influence of structural uncertainties on actively controlled smart beams is investigated in this paper. The dynamical problem of a model smart composite beam is based on a simplified modelling of the actuators and sensors, both being realized by means of piezoelectric layers. In particular, a practical robust controller design methodology is developed, which is based on recent theoretical results on H_∞ control theory and μ-analysis. Numerical examples demonstrate the vibration-suppression property of the proposed smart beams.

Keywords Uncertainty · Smart beam · Robust performance · Robust analysis · Robust synthesis

1 Introduction

The use of active control techniques in smart structures is a modern research area [1, 5, 6, 9, 11, 15, 16, 21]. Vibration control of beams may serve as a model problem, since the beam is a fundamental structural element [6, 11, 15, 21]. A number of different control schemes have been proposed, where the main class of controllers is based on linear feedback laws. In real life applications there are always differences between the physical plant that is controlled and the model on which the controller design is based (for instance, neglected higher frequency dynamics). Therefore, robustness must be an important goal for any applicable feedback controller design

A. Moutsopoulou (✉)
Department of Civil Engineering, Technological Educational Institute of Crete, Estavromenos, 71004, Heraklion, Greece
e-mail: amalia@staff.teicrete.gr

G.E. Stavroulakis · A. Pouliezos
Department of Production Engineering and Management, Technical University of Crete, Kounoupidiana, 73100, Chania, Greece

G.E. Stavroulakis
e-mail: gestavr@dpem.tuc.gr

A. Pouliezos
e-mail: tasos@dpem.tuc.gr

M. Papadrakakis et al. (eds.), *Computational Methods in Stochastic Dynamics*, Computational Methods in Applied Sciences 26,
DOI 10.1007/978-94-007-5134-7_11,

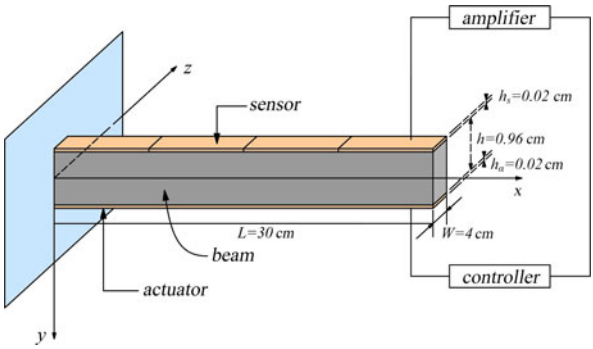

Fig. 11.1 Schematic picture with data used in the example

[5, 8, 10, 14, 16, 21]. The performance specifications, which the control system must fulfill and the class of uncertainties for which the control system must be robust against, determine the robust controller design methodology for any particular vibration control problem. In this study a vibration control problem in flexible structure (smart beam) is considered and the performance specification is stated in terms of a disturbance attenuation requirement for particular class of external disturbances acting on the structure. The paper illustrates H_∞ robust controller design techniques by considering the problem of active vibration control in a flexible cantilever beam using piezoelectric patches as sensors and actuators. This work demonstrates that the proposed robust control design schemes are suited to broadband vibration disturbances, which can be modelled as Gaussian white noise (e.g., in earthquake modelling), wind-like pressure, as well as structured uncertainties. Uncertainty denotes the difference between the model and the reality. By adopting the mechanical model described previously, we consider uncertainties in the parameters of the model. The H_∞ approach begins with an uncertain system model for the plant to be controlled [1, 5, 8, 9, 11]. In this section we will consider an uncertain system model whose primary purpose is to account for the uncertainty introduced by varying the nominal plant parameters.

First, for a simplified model, the governing equations of a beam with bonded piezoelectric sensors and actuators are formulated. After the finite element discretization, H_∞ robust control and m-analysis of the beam vibration is investigated. Numerical results obtained by using MATLAB routines demonstrate that these two robust control laws can effectively suppress the vibration of lower modes of the beam as well as avoid spillover from the higher frequency modes.

2 Mathematical Modelling

A cantilever slender beam with rectangular cross-section is considered. Four pairs of piezoelectric patches are embedded symmetrically at the top and the bottom surfaces of the beam, as shown in Fig. 11.1. The beam is made from graphite-epoxy T300–976 and the piezoelectric patches are $PZTG1195N$. The top patches act like

Table 11.1 Parameters of the composite beam

Parameters	Values
Beam length, L	0.3 m
Beam width, W	0.04 m
Beam thickness, h	0.0096 m
Beam density, ρ	1600 kg/m^3
Young's modulus of the beam, E	1.5×10^{11} N/m^2
Piezoelectric constant, d_{31}	254×10^{-12} m/V
Electric constant, ξ_{33}	11.5×10^{-3} Vm/N
Young's modulus of the piezoelectric element	1.5×10^{11} N/m^2
Width of the piezoelectric element	$b_S = b_a = 0.04$ m
Thickness of the piezoelectric element	$h_S = h_a = 0.0002$ m

sensors and the bottom like actuators. The resulting composite beam is modelled by means of the classical laminated technical theory of bending. Furthermore, we assume that the mechanical properties of both the piezoelectric material and the host beam are independent in time. The thermal effects are considered to be negligible as well [16].

The beam has length L, width b and thickness h. The sensors and the actuators have width b_S and b_A and thickness h_S and h_A, respectively. The electromechanical parameters of the beam used for the application of the method in this paper are given in Table 11.1.

2.1 Piezoelectric Equations

In order to derive the basic equations for piezoelectric sensors and actuators (S/As), we assume that:

- The piezoelectric S/A are bonded perfectly on the host beam;
- The piezoelectric layers are much thinner then the host beam;
- The piezoelectric material is homogeneous, transversely isotropic and linearly elastic;
- The piezoelectric S/A are transversely polarized (in the z-direction) [16].

Under these assumptions the three-dimensional linear constitutive equations are given by [5],

$$\begin{Bmatrix} \sigma_{xx} \\ \sigma_{xz} \end{Bmatrix} = \begin{bmatrix} Q_{11} & 0 \\ 0 & Q_{55} \end{bmatrix} \left(\begin{Bmatrix} \varepsilon_{xx} \\ \varepsilon_{xz} \end{Bmatrix} - \begin{bmatrix} d_{31} \\ 0 \end{bmatrix} E_z \right) \tag{11.1}$$

$$D_z = Q_{11} d_{31} \varepsilon_{xx} + \xi_{xx} E_z \tag{11.2}$$

where σ_{xx}, σ_{xz} denote the axial and shear stress components, D_z, denotes the transverse electrical displacement; ε_{xx} and ε_{xz} are axial and shear strain components; Q_{11}, and Q_{55}, denote elastic constants; d_{31}, and ξ_{33}, denote piezoelectric and dielectric constants, respectively. Equation (11.1) describes the inverse piezoelectric effect and equation (11.2) describes the direct piezoelectric effect. E_z, is the transverse component of the electric field that is assumed to be constant for the piezoelectric layers and its components in the xy-plain are supposed to vanish. If no electric field is applied in the sensor layer, the direct piezoelectric equation (11.2) is simplified to

$$D_z = Q_{11} d_{31} \varepsilon_{xx} \tag{11.3}$$

and it is used to calculate the output charge created by the strains in the beam [8].

2.2 Equations of Motion

We assume that:

- The beam centroidal and elastic axis coincides with the x-coordinate axis so that no bending-torsion coupling is considered;
- The axial vibration of the host beam is considered negligible;
- The displacement field $\{u\} = (u_1, u_2, u_3)$ is obtained based on the usual Timoshenko assumptions [11],

$$\begin{aligned} u_1(x, y, z) &\approx z\phi(x, t) \\ u_2(x, y, z) &\approx 0 \\ u_3(x, y, x) &\approx w(x, t) \end{aligned} \tag{11.4}$$

  where ϕ is the rotation of the beam's cross-section about the positive y-axis and w is the transverse displacement of a point of the centroidal axis ($y = z = 0$).

The strain displacement relations can be applied to equation (11.4) to give,

$$\varepsilon_{xx} = z\frac{\vartheta\phi}{\vartheta x} \qquad \varepsilon_{xz} = \phi + \frac{\vartheta w}{\vartheta x} \tag{11.5}$$

We suppose that the transverse shear deformation ε_{xx} is equal to zero [6].

In order to derive the equations of the motion of the beam we use Hamilton's principle [17],

$$\int_{t_2}^{t_1} (\delta T - \delta U + \delta W)\, dt = 0, \tag{11.6}$$

where T is the total kinetic energy of the system, U is the potential (strain) energy and W is the virtual work done by the external mechanical and electrical loads and

moments. The first variation of the kinetic energy is given by,

$$\begin{aligned}\delta T &= \frac{1}{2}\int_V \rho\left\{\frac{\vartheta u}{\vartheta t}\right\}^r\left\{\frac{\vartheta u}{\vartheta t}\right\}dV \\ &= \frac{b}{2}\int_0^L\int_{-h/2-h_a}^{h/2+h_s}\rho\left(z\frac{\vartheta\phi}{\vartheta t}\delta\frac{\vartheta\phi}{\vartheta t}+\frac{\vartheta w}{\vartheta t}\delta\frac{\vartheta w}{\vartheta t}\right)dz\,dx\end{aligned} \tag{11.7}$$

The first variation of the kinetic energy is given by,

$$\begin{aligned}\delta U &= \frac{1}{2}\int_V \delta\{\varepsilon\}^T\{\sigma\}\,dV \\ &= \frac{b}{2}\int_0^L\int_{-h/2-h_a}^{h/2+h_s}\left[Q_{11}\left(z\frac{\vartheta w}{\vartheta x}\delta\right)\left(z\frac{\vartheta w}{\vartheta x}\right)\right]dz\,dx\end{aligned} \tag{11.8}$$

If the load consists only of moments induced by piezoelectric actuators and since the structure has no bending twisting couple then the first variation of the work has the form [17],

$$\delta W = b\int_0^L M^a\delta\left(\frac{\vartheta\phi}{\vartheta x}\right)dx \tag{11.9}$$

where M^a is the moment per unit length induced by the actuator layer and is given by,

$$\begin{aligned}M^a &= \int_{-h/2-h_a}^{-h/2} z\sigma_{xx}^a\,dz = \int_{-h/2-h_a}^{-h/2} zQ_{11}d_{31}E_z^a\,dz \\ &\left(E_z^a = \frac{V_a}{h_a}\right)\end{aligned} \tag{11.10}$$

2.3 Finite Element Formulation

We consider a beam element of length L_e, which has two mechanical degrees of freedom at each node: one translational ω_1 (respectively ω_2) in direction y and one rotational ψ_1 (respectively ψ_2), as it is shown in Fig. 11.2. The vector of nodal displacements and rotations q_e is defined as [5],

$$q_e = [\omega_1, \psi_1, \omega_2, \psi_2] \tag{11.11}$$

The transverse deflection $\omega(x,t)$ and rotation $\psi(x,t)$ along the beam are continuous and they are interpolated by Hermitian linear shape functions H_i^{ω} and H_i^{ψ} as

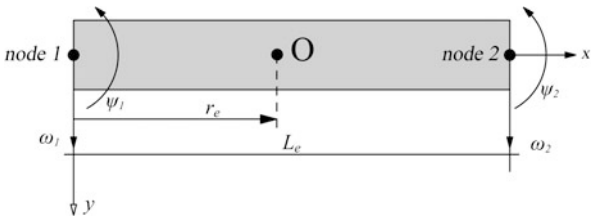

Fig. 11.2 Beam finite element

follows [10],

$$\begin{aligned} \omega(x,t) &= \sum_{i=1}^{4} H_i^{\omega}(x) q_i(t) \\ \psi(x,t) &= \sum_{i=1}^{4} H_i^{\psi}(x) q_i(t) \end{aligned} \tag{11.12}$$

This classical finite element procedure leads to the approximate (discretized) problem. For a finite element the discrete differential equations are obtained by substituting the discretized expressions (11.12) into equations (11.7) and (11.8) to evaluate the kinetic and strain energies. Integrating over spatial domains and using the Hamilton's principle (11.6) the equation of motion for a beam element are expressed in terms of nodal variable q as follows [5, 6, 14],

$$M\ddot{q}(t) + D\dot{q}(t) + Kq(t) = f_m(t) + f_e(t) \tag{11.13}$$

where M is the mass matrix, D is the viscous damping matrix, K is the stiffness matrix, f_m is the external loading vector and f_e is the generalized control force vector produced by electromechanical coupling effects. The independent variable vector $q(t)$ is composed of transversal deflections ω_i and rotations ψ_i, i.e. [21],

$$q(t) = \begin{bmatrix} \omega_1 \\ \psi_1 \\ \vdots \\ \omega_n \\ \psi_n \end{bmatrix} \tag{11.14}$$

where n is the number of nodes used in the analysis. Vectors w and f_m are positive upwards. For the state-space control transformation,we are presented with,

$$\dot{x}(t) = \begin{bmatrix} q(t) \\ \dot{q}(t) \end{bmatrix} \tag{11.15}$$

Furthermore to express $f_e(t)$ in the form of $Bu(t)$ we write it as the product $f_e^* u$, where f_e^* is the piezoelectric force for a unit applied on the corresponding actuator, and u represents the voltages on the actuators. Finally, $d(t) = f_m(t)$ is the distur-

bance vector [15]. Then,

$$\dot{x}(t) = \begin{bmatrix} 0_{2n\times 2n} & I_{2n\times 2n} \\ -M^{-1}K & -M^{-1}D \end{bmatrix} x(t) + \begin{bmatrix} 0_{2n\times n} \\ M^{-1} f_e^* \end{bmatrix} u(t) + \begin{bmatrix} 0_{2n\times 2n} \\ M^{-1} \end{bmatrix} \tag{11.16}$$

$$= Ax(t) + Bu(t) + Gd(t) = Ax(t) + \begin{bmatrix} B & G \end{bmatrix} \begin{bmatrix} u(t) \\ d(t) \end{bmatrix}$$

$$= Ax(t) + \tilde{B}\tilde{u}(t) \tag{11.17}$$

The previous description of the dynamical system will be augmented with the output equation, under the assumption that only displacements are measured [10]

$$y(t) = \begin{bmatrix} x_1(t) & x_3(t) & \cdots & x_{n-1}(t) \end{bmatrix}^T = Cx(t) \tag{11.18}$$

In this formulation u is $n \times 1$ (at most, but can be smaller), while d is $2n \times 1$. The units used are compatible for instance m, rad, s and N [5, 14].

3 Design Objectives and System Specifications

The structured singular value of the transfer function is defined as,

$$\mu(M) = \begin{cases} \frac{1}{\min_{k_m}\{\det(I - k_m M\Delta)=0, \bar{\sigma}(\Delta)\leq 1\}} \\ 0, \quad \Delta \det(I - M\Delta) = 0 \end{cases} \tag{11.19}$$

This quantity defines the smallest structured $\mu(M)$ (measured in terms of $\bar{\sigma}(\Delta)$) which makes $\det(I - M\Delta) = 0$: then $\mu(M) = \frac{1}{\bar{\sigma}(\Delta)}$. It follows that values of μ smaller than 1 are desired [2, 4].

The design objectives fall into two categories:

1. Stability of closed loop system (plant+controller).
   a. Disturbance attenuation with satisfactory transient characteristics (overshoot, settling time).
   b. Small control effort.
2. Robust performance

Stability of closed loop system (plant+controller) should be satisfied in the face of modelling errors [3].

In order to obtain the required system specifications with respect to the above objectives we need to represent our system in the so-called—Δ structure. Let us start with the simple typical diagram of Fig. 11.3 [7, 12].

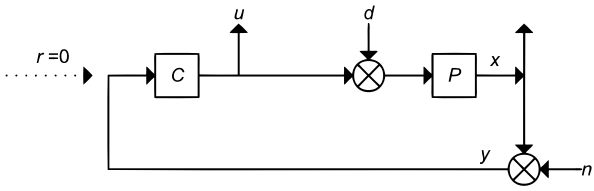

Fig. 11.3 Classical control block diagram (P: plant dynamical system, C: controller)

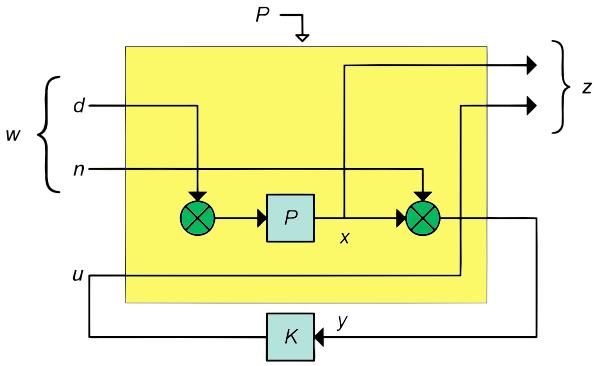

Fig. 11.4 Detailed two-port diagram (with a linear feedback control K)

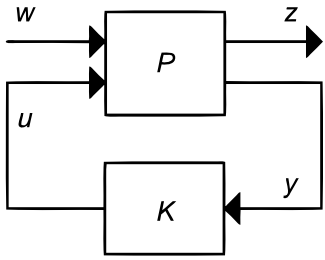

Fig. 11.5 Two-port diagram

In this diagram there are two inputs, d and n, and two outputs, u and x. In what follows it is assumed that,

$$\left\| \begin{matrix} d \\ n \end{matrix} \right\|_2 \leq 1, \qquad \left\| \begin{matrix} x \\ u \end{matrix} \right\|_2 \leq 1 \tag{11.20}$$

If this is not the case, appropriate frequency-dependent weights can transform original signals so that the transformed signals have this property. The details of the system are given in Fig. 11.4 or in less details Fig. 11.5:

In this description,

$$z = \begin{bmatrix} u \\ x \end{bmatrix}, \qquad w = \begin{bmatrix} d \\ n \end{bmatrix} \tag{11.21}$$

where z are the output variables to be controlled, and w the exogenous inputs.

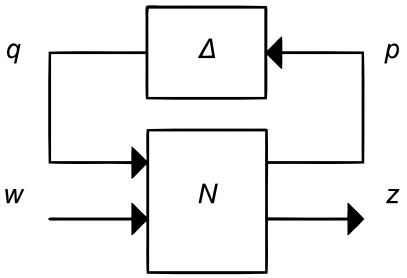

Fig. 11.6 Two port diagram with uncertainty

Given that P has two inputs and two outputs it is, as usual, naturally partitioned as,

$$\begin{bmatrix} z(s) \\ y(s) \end{bmatrix} = \begin{bmatrix} P_{zw}(s) & P_{zu}(s) \\ P_{yw}(s) & P_{yu}(s) \end{bmatrix} \begin{bmatrix} w(s) \\ u(s) \end{bmatrix} = P(s) \begin{bmatrix} w(s) \\ u(s) \end{bmatrix} \tag{11.22}$$

In addition the controller is written,

$$u(s) = K(s)y(s) \tag{11.23}$$

Substituting (11.22) in (11.23) gives the closed loop transfer function $N_{zw}(s)$,

$$N_{zw}(s) = P_{zw}(s) + P_{zu}(s)K(s)\big(I - P_{yu}(s)K(s)\big)^{-1}P_{yw}(s) \tag{11.24}$$

To deduce robustness specifications one more diagram is needed, namely that of Fig. 11.6: where N is defined by (11.24) and the uncertainty modelled in Δ satisfies $\|\Delta\|_\infty \leq 1$ (details are given later on in this paper). Here,

$$z = \mathcal{F}_u(N, \Delta)w = \big[N_{22} + N_{21}\Delta(I - N_{11}\Delta)^{-1}N_{12}\big]w = Fw \tag{11.25}$$

Given this structure we can state the following definitions:

$$\begin{aligned} \text{Nominal stability } (NS) \quad &\Leftrightarrow \quad N \text{ internally stable} \\ \text{Nominal performance } (NP) \quad &\Leftrightarrow \quad \|N_{22}(j\omega)\|_\infty \leq 1 \forall \omega \text{ and } NS \\ \text{Robust stability } (RS) \quad &\Leftrightarrow \quad F = \mathcal{F}_u(N, \Delta) \text{ stable } \forall \Delta, \|\Delta\|_\infty < 1 \text{ and } NS \\ \text{Robust performance } (RP) \quad &\Leftrightarrow \quad \|F\|_\infty < 1, \forall \Delta, \|\Delta\|_\infty < 1 \text{ and } S \end{aligned} \tag{11.26}$$

It has been proved that the following conditions hold in the case of block-diagonal real or complex perturbations Δ:

1. The system is nominally stable if M is internally stable.
2. The system exhibits nominal performance if $\bar{\sigma}(N_{22}(j\omega)) < 1$
3. The system (M, Δ) is robustly stable if and only if,

$$\sup_{\omega \in \mathbb{R}} \mu_\Delta\big(N_{11}(j\omega)\big) < 1 \tag{11.27}$$

where μ_{Δ} is the structured singular value of N given the structured uncertainty set Δ. This condition is known as the generalized small gain theorem.

4. The system (N, Δ) exhibits robust performance if and only if,

$$\sup_{\omega \in \mathbb{R}} \mu_{\Delta_a}\big(N(j\omega)\big) < 1 \tag{11.28}$$

where,

$$\Delta_a = \begin{bmatrix} \Delta_p & 0 \\ 0 & \Delta \end{bmatrix} \tag{11.29}$$

and Δ_p is full complex, has the same structure as Δ and dimensions corresponding to w, z [12].

Unfortunately, only bounds on μ can be estimated.

3.1 Controller Synthesis

All the above results support the analysis problem and provide tools to judge the performance of any controller or to compare different controllers. However it is possible to approximately synthesize a controller that achieves given performance in terms of the structured singular value μ.

In this procedure, which is called $(D, G - K)$ iteration [20] the problem of finding an μ-optimal controller K such that $\mu(\mathcal{F}_u(F(j\omega)), K(j\omega)) \leq \beta$, $\forall\omega$ is transformed into the problem of finding transfer function matrices $D(\omega) \in \mathcal{D}$ and $G(\omega) \in \mathcal{G}$, such that,

$$\sup_{\omega} \bar{\sigma}\left[\left(\frac{D(\omega)\mathcal{F}_u(F(j\omega), K(j\omega))D^{-1}(\omega)}{\gamma} - jG(\omega)\right) \times \left(I + G^2(\omega)\right)^{-1/2}\right] \leq 1, \quad \forall\omega \tag{11.30}$$

Unfortunately this method does not guarantee even finding local maxima. However for complex perturbations a method known as $D - K$ iteration is available (implemented in MATLAB) [20]. It combines H_∞ synthesis and μ-analysis and often yields good results. The starting point is an upper bound on μ in terms of the scaled singular value,

$$\mu(N) \leq \min_{D \in \mathcal{D}} \bar{\sigma}\left(DND^{-1}\right) \tag{11.31}$$

The idea is to find the controller that minimizes the peak over the frequency range namely,

$$\min_{K}\left(\min_{D \in \mathcal{D}} \left\| DN(K)D^{-1} \right\|_\infty\right) \tag{11.32}$$

by alternating between minimizing $\|DN(K)D^{-1}\|_\infty$ with respect to either K or D (while holding the other fixed).

1. *K-step*. Synthesize an $\mathcal{H}_\infty$ controller for the scaled problem $\min_K \|DN(K) \times D^{-1}\|_\infty$ with fixed $D(s)$.
2. *D-step*. Find $D(j\omega)$ to minimize at each frequency $\bar{\sigma}(DND^{-1}(j\omega))$ with fixed N.
3. Fit the magnitude of each element of $D(j\omega)$ to a stable and minimum phase transfer function $D(s)$ and got to Step 1 [20].

3.2 System Uncertainty

Let us assume uncertainty in the mass M and K matrices of the form,

$$\begin{aligned} K &= K_0(I + k_p I_{2n\times 2n}\delta_K) \\ M &= M_0(I + m_p I_{2n\times 2n}\delta_M) \end{aligned} \tag{11.33}$$

Alternatively, since in general the Rayleigh damping assumption is,

$$D = aK + \beta M \tag{11.34}$$

D could be expressed similarly to K, M, as,

$$D = D_0(I + d_p I_{2n\times 2n}\delta_D) \tag{11.35}$$

In this way we introduce uncertainty in the form of percentage variation in the relevant matrices. More detailed correlation of uncertainty with certain properties of the structures (e.g., material constants, flexibility of joints, cracks or delaminations) is possible and will be investigated in the future.

Here it will be assumed,

$$\|\Delta\|_\infty \overset{def}{=} \left\| \left[\begin{array}{c|c} I_{n\times n}\delta_K & 0_{n\times n} \\ \hline 0_{n\times n} & I_{n\times n}\delta_M \end{array}\right] \right\|_\infty < 1 \tag{11.36}$$

hence m_p, k_p are used to scale the percentage value and the zero subscript denotes nominal values (it is reminded here that the norm for a matrix $A_{n\times n}$ is calculated through $\|A\|_\infty = \max_{1\le j\le m} \sum_{j=1}^{n} |a_{ij}|$).

With these definitions Eq. (11.13) becomes,

$$\begin{aligned} & M_0(I + m_p I_{2n\times 2n}\delta_M)\ddot{w}(t) + K_0(I + k_p I_{2n\times 2n}\delta_K)w(t) \\ & \qquad + \left[D_0 + 0.0005[K_0 k_p I_{2n\times 2n}\delta_K + M_0 m_p I_{2n\times 2n}\delta_M]\right]\dot{w}(t) \\ & \qquad = f_m(t) + f_e(t) \\ \Rightarrow \quad & M_0\ddot{w}(t) + D_0\dot{q}(t) + K_0 w(t) \end{aligned}$$

$$
\begin{aligned}
&= -\big[M_0 m_p I_{2n\times 2n}\delta_M \ddot{w}(t) + 0.0005[K_0 k_p I_{2n\times 2n}\delta_K + M_0 m_p I_{2n\times 2n}\delta_M]\dot{w}(t) \\
&\quad + K_0 k_p I_{2n\times 2n}\delta_K w(t)\big] \\
&= f_m(t) + f_e(t) \\
\Rightarrow \quad & M_0\ddot{w}(t) + D_0\dot{w}(t) + K_0 w(t) = \tilde{D}q_u(t) + f_m(t) + f_e(t)
\end{aligned} \tag{11.37}
$$

where,

$$
q_u(t) = \begin{bmatrix} \ddot{w}(t) \\ \dot{w}(t) \\ w(t) \end{bmatrix} \tag{11.38}
$$

$$
\begin{aligned}
\tilde{D} &= -\begin{bmatrix} M_0 m_p & K_0 k_p \end{bmatrix} \left[\begin{array}{c|c} I_{2n\times 2n}\delta_M & 0_{2n\times 2n} \\ \hline 0_{2n\times 2n} & I_{2n\times 2n}\delta_K \end{array}\right] \\
&\quad \times \begin{bmatrix} I_{2n\times 2n} & 0.0005 I_{2n\times 2n} & 0_{2n\times 2n} \\ 0_{2n\times 2n} & 0.0005 I_{2n\times 2n} & I_{2n\times 2n} \end{bmatrix} \\
&= G_1 \cdot \Delta \cdot G_2
\end{aligned} \tag{11.39}
$$

Writing (11.37) in state space form, gives,

$$
\begin{aligned}
\dot{x}(t) &= \begin{bmatrix} 0_{2n\times 2n} & I_{2n\times 2n} \\ -M^{-1}K & -M^{-1}D \end{bmatrix} x(t) + \begin{bmatrix} 0_{2n\times 2n} \\ M^{-1} f_e^* \end{bmatrix} u(t) \\
&\quad + \begin{bmatrix} 0_{2n\times 2n} \\ M^{-1} \end{bmatrix} d(t) + \begin{bmatrix} 0_{2n\times 6n} \\ M^{-1} F_1 \cdot \Delta \cdot G_2 \end{bmatrix} q_u(t) \\
&= Ax(t) + Bu(t) + Gd(t) + G_u G_2 q_u(t)
\end{aligned} \tag{11.40}
$$

In this way we treat uncertainty in the original matrices as an extra uncertainty term. To express our system in the form of Fig. 11.6, consider Fig. 11.7.

The matrices E_1, E_2 are used to extract,

$$
q_u(t) \overset{def}{=} \begin{bmatrix} \ddot{w}(t) \\ \dot{w}(t) \\ w(t) \end{bmatrix} \tag{11.41}
$$

Since,

$$
\gamma = \begin{bmatrix} \dot{w}(t) \\ \ddot{w}(t) \end{bmatrix} \qquad \beta = \int \begin{bmatrix} \dot{w}(t) \\ \ddot{w}(t) \end{bmatrix} dt = \begin{bmatrix} w(t) \\ \dot{w}(t) \end{bmatrix} \tag{11.42}
$$

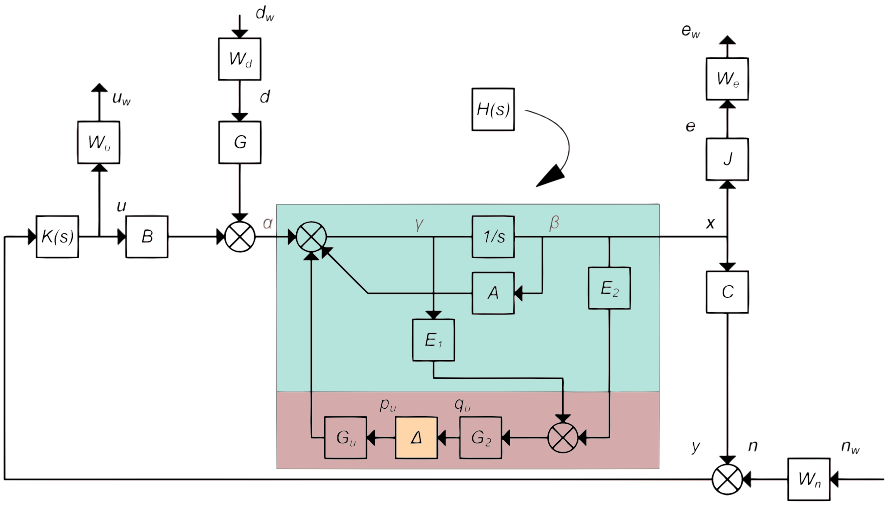

Fig. 11.7 Uncertainty block diagram

appropriate choices for E_1, E_2 are,

$$E_1 = \begin{bmatrix} 0_{2n\times 2n} & \vdots & I_{2n\times 2n} \\ \cdots & \vdots & \cdots \\ I_{2n\times 2n} & \vdots & 0_{2n\times 2n} \\ \cdots & \vdots & \cdots \\ 0_{2n\times 2n} & \vdots & 0_{2n\times 2n} \end{bmatrix}, \qquad E_2 = \begin{bmatrix} 0_{2n\times 2n} & \vdots & 0_{2n\times 2n} \\ \cdots & \vdots & \cdots \\ 0_{2n\times 2n} & \vdots & 0_{2n\times 2n} \\ \cdots & \vdots & \cdots \\ I_{2n\times 2n} & \vdots & 0_{2n\times 2n} \end{bmatrix} \tag{11.43}$$

The idea is to find an N such that,

$$\begin{bmatrix} q_u \\ \cdots \\ e_w \\ u_w \end{bmatrix} = N \begin{bmatrix} p_u \\ \cdots \\ d_w \\ n_w \end{bmatrix},$$

$$N = \begin{bmatrix} N_{p_u q_u} & \vdots & N_{d_w q_u} & N_{n_w q_u} \\ \cdots & \vdots & \cdots & \cdots \\ N_{p_u e_w} & \vdots & N_{d_w e_w} & N_{n_w e_w} \\ N_{p_u u_w} & \vdots & N_{d_w u_w} & N_{n_w u_w} \end{bmatrix} = \begin{bmatrix} N_{11} & N_{12} \\ N_{21} & N_{22} \end{bmatrix} \tag{11.44}$$

or in the notation of Fig. 11.6

$$\begin{bmatrix} q_u \\ w \end{bmatrix} = N \begin{bmatrix} p_u \\ z \end{bmatrix} \tag{11.45}$$

Now $N_{d_w e_w}$, $N_{n_w e_w}$, $N_{n_w u_w}$ are known. For the rest we will use a methodology known as "pulling out the Δ's". To this end, break the loop at points p_u, q_u (which will be used as additional inputs/outputs respectively) and use the auxiliary signals a, β, γ. To get the transfer function $N_{d_w q_u}$ (from d_w to q_u):

$$q_u = G_2(E_2\beta + E_1\gamma) = G_2\left(E_2\frac{1}{s} + E_1\right)\gamma \tag{11.46}$$

$$\gamma = GW_d d_w + Bu + A\frac{1}{s}\gamma = GW_d d_w + BKC\frac{1}{s}\gamma + A\frac{1}{s}\gamma \tag{11.47}$$

$$\Rightarrow \quad \gamma = \left(I - BKC\frac{1}{s} - A\frac{1}{s}\right)^{-1} GW_d d_w \tag{11.48}$$

Hence,

$$N_{d_w q_u} = G_2\left(E_2\frac{1}{s} + E_1\right)\left(I - BKC\frac{1}{s} - A\frac{1}{s}\right)^{-1} GW_d \tag{11.49}$$

Now, $N_{p_u q_u}$, $N_{p_u e_w}$, $N_{p_u u_w}$, are similar to $N_{d_w q_u}$, $N_{d_w e_w}$, $N_{d_w u_w}$, with GW_d replaced by G_u, i.e.,

$$\begin{aligned} N_{p_u q_u} &= G_2\left(E_2\frac{1}{s} + E_1\right)\left(I - BKC\frac{1}{s} - A\frac{1}{s}\right)^{-1} G_u \\ N_{p_u e_w} &= W_y JH\big[I + B\big[K(I - CHBK)^{-1}CH\big]\big]G_u \\ M_{p_u u_w} &= W_u K(I - CHBK)^{-1}CHG_u \end{aligned} \tag{11.50}$$

Finally to find $N_{n_w q_u}$,

$$q_u = G_2(E_2\beta + E_1\gamma) = G_2\left(E_2\frac{1}{s} + E_1\right)\gamma \tag{11.51}$$

$$\begin{aligned} \gamma &= Bu + A\frac{1}{s}\gamma = BK(W_n n_w + y) + A\frac{1}{s}\gamma \\ &= BKW_n n_w + BKC\frac{1}{s}\gamma + A\frac{1}{s}\gamma \end{aligned} \tag{11.52}$$

$$\Rightarrow \quad \gamma = \left(I - BKC\frac{1}{s} - A\frac{1}{s}\right)^{-1} BKW_n n_w \tag{11.53}$$

Hence,

$$N_{n_w q_u} = G_2\left(E_2\frac{1}{+}E_1\right)\left(I - BKC\frac{1}{s} - A\frac{1}{s}\right)^{-1}BKW_n \tag{11.54}$$

Collecting all the above yields N:

$$N = \begin{bmatrix} N_{11} & N_{12} & N_{13} \\ N_{21} & N_{22} & N_{23} \\ N_{31} & N_{32} & N_{33} \end{bmatrix} \tag{11.55}$$

where

$$\begin{aligned}
N_{11} &= G_2\left(E_2\frac{1}{s} + E_1\right)\left(I - BKC\frac{1}{s} - A\frac{1}{s}\right)^{-1}G_u, \\
N_{12} &= G_2\left(E_2\frac{1}{s} + E_1\right)\left(I - BKC\frac{1}{s} - A\frac{1}{s}\right)^{-1}GW_d, \\
N_{13} &= G_2\left(E_2\frac{1}{s} + E_1\right)\left(I - BKC\frac{1}{s} - A\frac{1}{s}\right)^{-1}BKW_u, \\
N_{21} &= W_e JH\big[I + BK(I - CHBK)^{-1}CF\big]G_u, \\
N_{22} &= W_e J(I - HBKC)^{-1}HGW_d, \\
N_{23} &= W_e J(I - HBKC)^{-1}HBKW_u, \\
N_{31} &= W_u K(I - CHBK)^{-1}CFG_u, \\
N_{32} &= W_u(I - KCHB)^{-1}KCHGW_d, \\
N_{33} &= W_u(I - KCHB)^{-1}KW
\end{aligned}$$

Having obtained N for the beam problem, all proposed controllers $K(s)$ can be compared using the structured singular value relations [1, 18, 19].

4 Robustness Issues

The superiority of H_∞ control lies in its ability to take explicitly into account the worst effect of unknown disturbances and noise in the system. Furthermore, at least in theory, it is possible to synthesize an H_∞ controller that is robust to a prescribed amount of modeling errors. Unfortunately, this last possibility is not implementable in some cases, as it will be subsequently illustrated [9, 13].

In what follows, the robustness to modeling errors of the designed H_∞ controller will be analyzed. Furthermore an attempt to synthesize a μ-controller will be presented, and comparisons between the two will be made.

In all simulations, routines from Matlab's Robust Control Toolbox will be used. In particular:

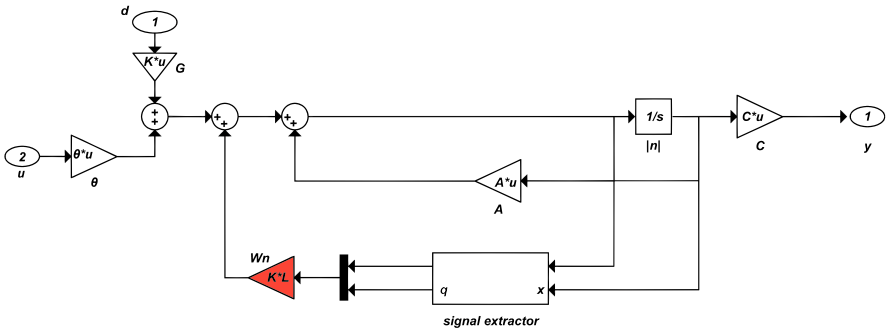

Fig. 11.8 Simulink diagram of uncertain plant

1. For uncertain elements,
2. To calculate bounds on the structured singular value,
3. To calculate a μ-controller,

Numerical models used in all simulations, are implemented in three ways:

1. Through Eq. (11.56)

$$\begin{aligned} K &= K_0(I + k_p I_{2n\times 2n}\delta_K) \\ M &= M_0(I + m_p I_{2n\times 2n}\delta_M) \\ D &= D_0 + 0,0005[K_0 k_p I_{2n\times 2n}\delta_K + M_0 m_p I_{2n\times 2n}\delta_M] \end{aligned} \tag{11.56}$$

   and subsequent evaluation of matrix N for specific values of k_p, m_p.
2. By use of Matlab's "uncertain element object". As explained, this form is needed in the D-K robust synthesis algorithm.
3. By Simulink implementation of Fig. 11.8.

4.1 Inputs-Loading

Loading corresponds to the wind excitation. The function $y(t)$ has been obtained from the wind velocity record, through the relation

$$f_m(t) = y(t), \quad \text{where } y(t) = 0.5 p v^2(t) C_v E \tag{11.57}$$

Where $p = 1.125$ kg/m^3 is the air density, C_v is a coefficient that depends on beam cross section, for rectangular cross section $C_v = 1.5$, $v(t)$ is wind velocity and E represents the beam surface area that is exposed to wind (Fig. 11.9).

Moreover, in all simulations random noise has been introduced within a probability interval of $\pm 1\%$ to measurements at the system output locations. Due to small displacements of system nodal points noise amplitude is taken to be small of the order of $5 \cdot 10^{-5}$ (Fig. 11.10).

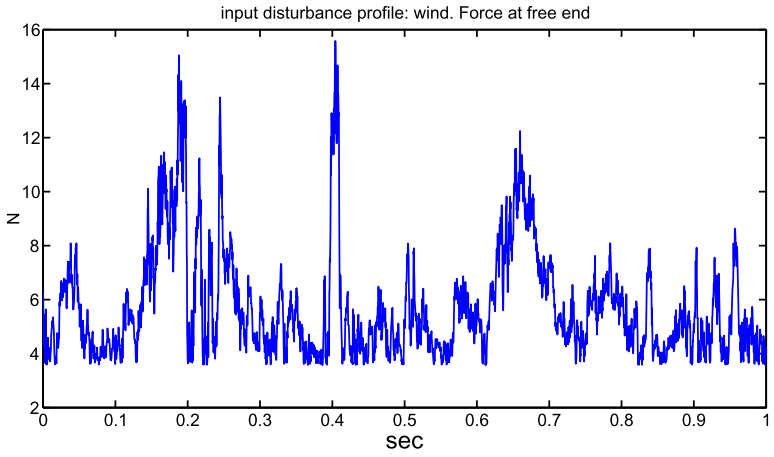

Fig. 11.9 Wind force

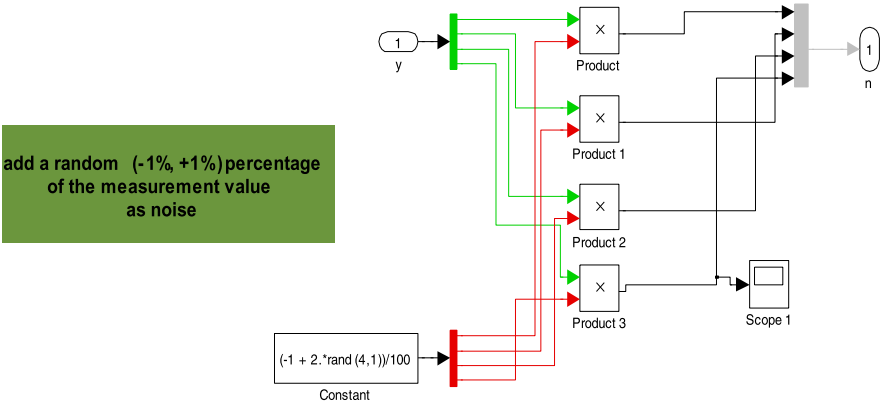

Fig. 11.10 Simulink diagram of noise

4.2 Robust Analysis—Results

Robust analysis is carried out through the relations:

$$\sup_{\omega\in\mathbb{R}} \mu_{\Delta}\big(N_{11}(j\omega)\big) < 1 \tag{11.58}$$

for robust stability, and,

$$\sup_{\omega\in\mathbb{R}} \mu_{\Delta_a}\big(N(j\omega)\big) < 1 \tag{11.59}$$

for robust performance.

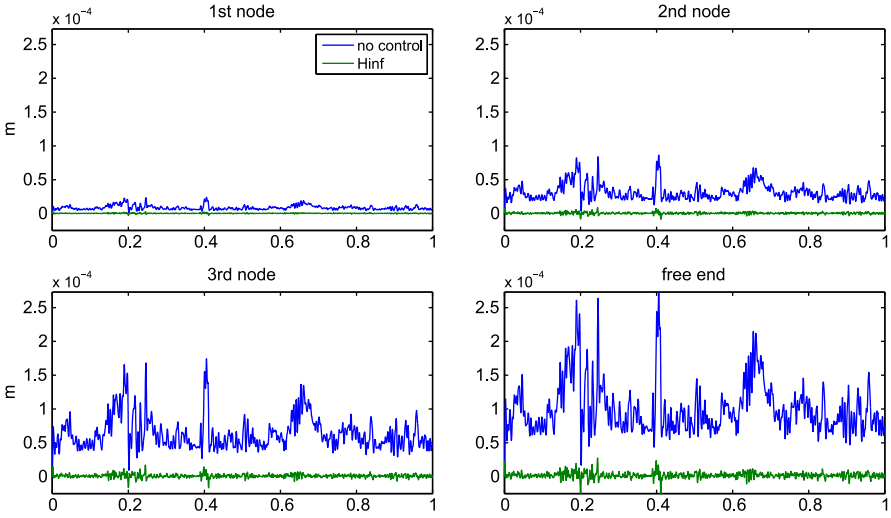

Fig. 11.11 Displacement response with and without $H\infty$ control for the four rodes of the beam

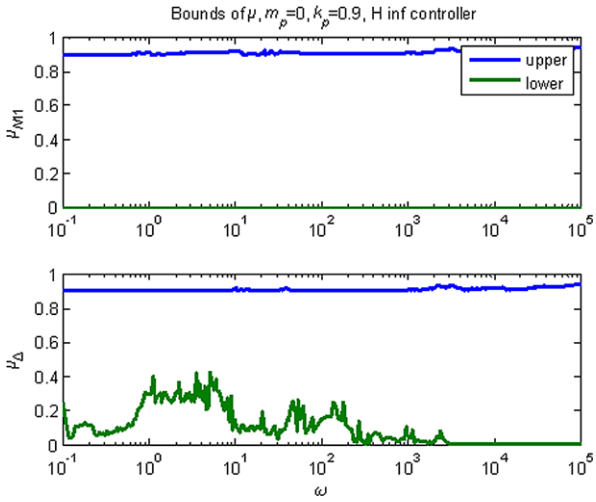

Fig. 11.12 μ-bounds of the H_∞ controller for $m_p = 0$, $k_p = 0.9$

For the H_∞ found, robust analysis was performed for the following values of m_p, k_p.

1. $m_p = 0, k_p = 0.9$. This corresponds to a $\pm 90\%$ variation from the nominal value of the stiffness matrix K.

   In Fig. 11.11 the displacement responses for this controller for the mechanical input are shown. In Fig. 11.12 are shown the bounds on the μ values. As seen the system remains stable and exhibits robust performance, since the upper bounds of both values remain below 1 for all frequencies of interest. This result is validated

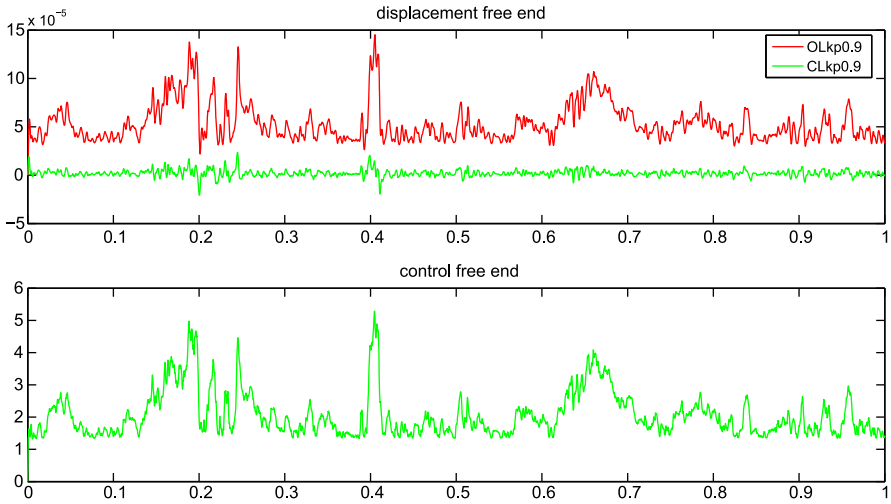

Fig. 11.13 Displacement and control at free end for the H_∞ controller with $m_p = 0$, $k_p = 0.9$ (extreme values)

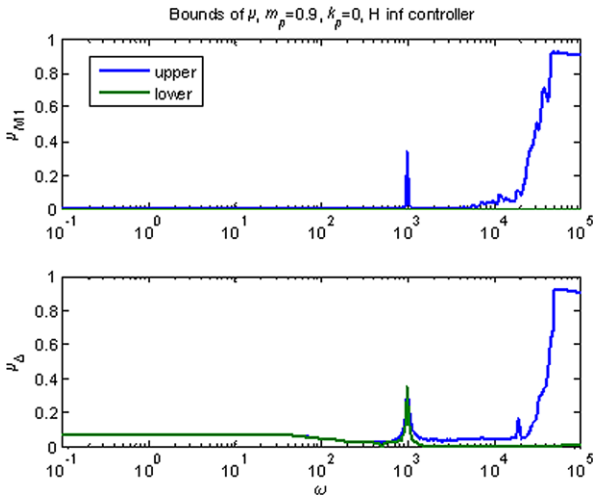

Fig. 11.14 μ-bounds of the H_∞ controller for $m_p = 0.9$, $k_p = 0$

in Fig. 11.13, where the displacement of the free end and the voltage applied are shown at the extreme uncertainty. Comparison with the open loop response for the same plant shows the good performance of the nominal controller.

2. $m_p = 0.9$, $k_p = 0$. This corresponds to a $\pm 90\%$ variation from the nominal value of the mass matrix M.

In Fig. 11.14 are shown the bounds on the μ values. As seen the system remains stable and exhibits robust performance, since the upper bounds of both values remain below 1 for all frequencies of interest. This result is validated in

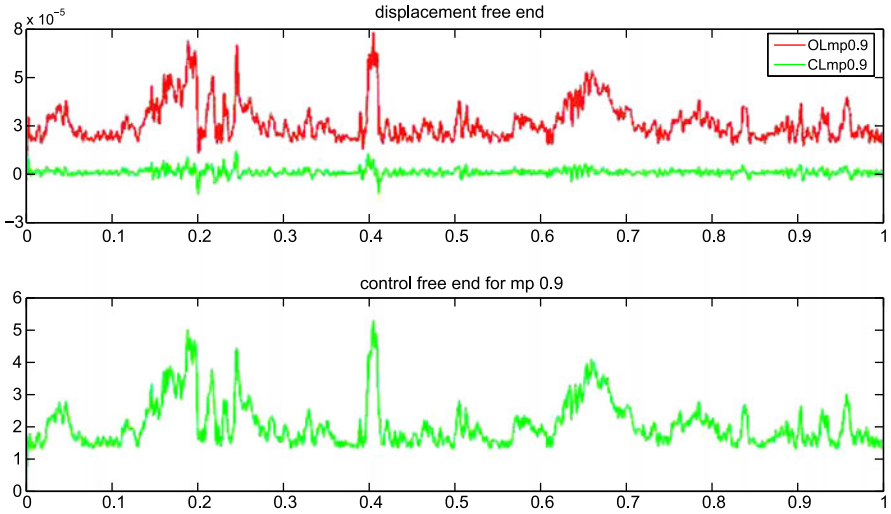

Fig. 11.15 Displacement and control at free end for the H_∞ controller with $m_p = 0.9$, $k_p = 0$ (extreme values)

Fig. 11.16 Displacement and control at free end for the H_∞ controller with $m_p = 0.9$, $k_p = 0$ (extreme values)

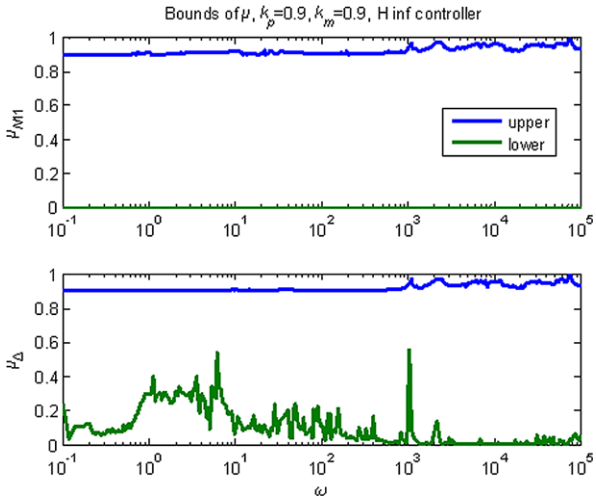

Fig. 11.15, where the displacement of the free end and the voltage applied are shown. Comparison with the open loop response for the same plant shows the good performance of the nominal controller.

3. $m_p = 0.9$, $k_p = 0.9$. This corresponds to a $\pm 90\%$ variation from the nominal values of both the mass and stiffness matrices M, K.

In Fig. 11.16 are shown the bounds on the μ values. As seen the system remains stable and exhibits robust performance, since the upper bounds of both values remain below 1 for all frequencies of interest. This result is validated in

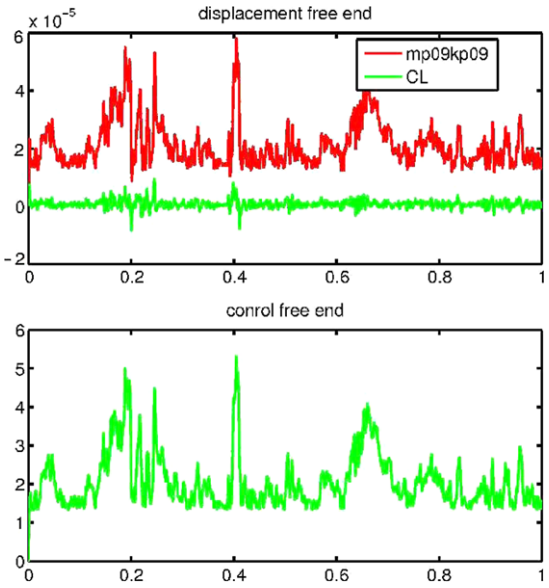

Fig. 11.17 Displacement and control at free end for the H_∞ controller with $m_p = 0.9$, $k_p = 0$ (extreme values)

Fig. 11.17, where the displacement of the free end and the voltage applied are shown. Comparison with the open loop response for the same plant shows the good performance of the nominal controller.

4.3 Robust Synthesis: μ-Controller—Results

A μ-controller can be synthesized via the procedure of D-K iteration As explained, this is an approximate procedure, providing bounds on the μ-value. To facilitate comparison with the H_∞ controller, similar bounds for the uncertainty will be used. In all the simulations that follow the disturbance is 10 N at the free end of the beam.

1. $m_p = 0, k_p = 0.9$. This corresponds to a $\pm 90\%$ variation from the nominal value of the stiffness matrix K. In Fig. 11.18 -values of the calculated controller are shown. As seen the controller is robust in most frequencies. In Fig. 11.19 performance of the μ and H_∞ controllers is compared at the free end (this is indicative of overall performance). As seen the H_∞ controller performs better at the expense of increased control effort. Figure 11.20 (the top two panels) verifies this result, where it is seen that the H_∞ controller fares better at the extreme value. This could be due to numerical difficulties in the calculation of the μ-controller arising from the bad condition number of the plant. It could also be due to the high order of the μ-controller. In any case, further investigation is needed.

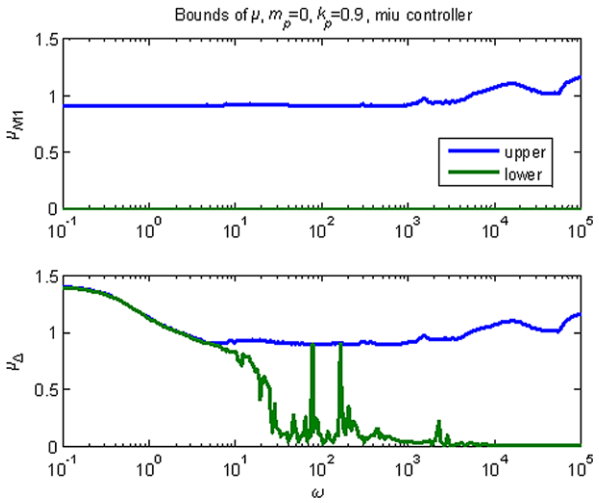

Fig. 11.18 μ-bounds of the μ-controller for $mp = 0$, $kp = 0.9$

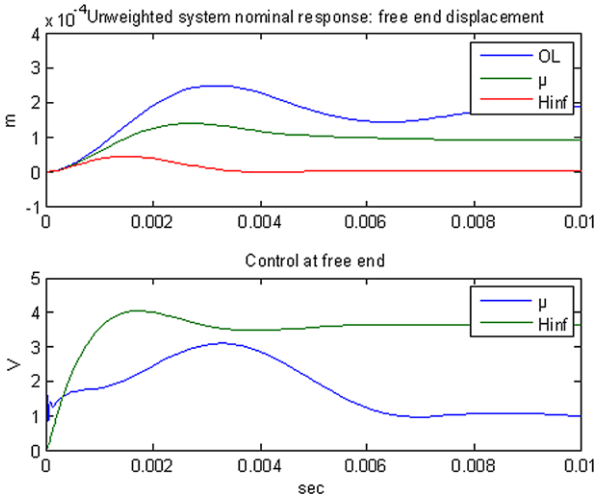

Fig. 11.19 Comparison of H_∞ and μ-controller

5 Conclusions

A finite element based model for a representative smart structure, namely a smart beam, including uncertainties has been presented. Based on this model H_∞ and μ-controller has been designed which effectively suppress the vibrations of the smart beam under stochastic load. The advantage of the H_∞ criterion is its ability to take into account the worst influence of uncertain disturbances or noise in the system. It is possible to synthesize a H_∞ controller which will be robust with respect to a prespecified number of errors in the model. The vibration suppression is achieved by the application of H_∞ controller. The system remains stable and exhibits robust performance, for all frequencies of interest. In addition a ro-

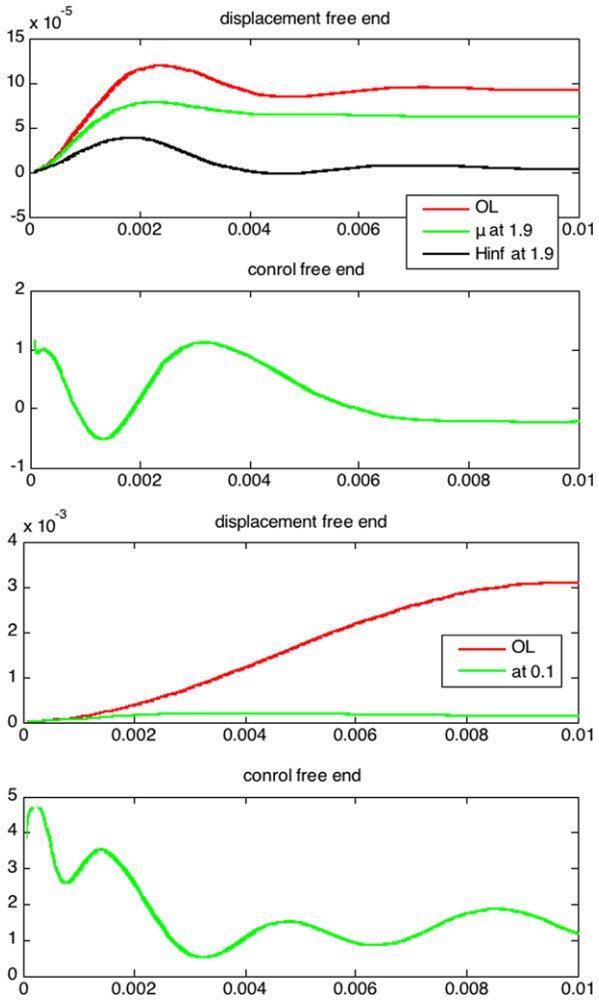

Fig. 11.20 Displacement and control at free end for μ-controller with $m_p = 0$, $k_p = 0.9$ (extreme values)

bust μ-controller was analyzed and synthesized, using the D-K Iterative method. The results are compared and commented. The results are very good: the oscillations were suppressed, with the voltages of the piezoelectric components' lying within their endurance limits. The above findings indicate that modern robust control techniques combined with classical finite element modelling provide us a powerful tool for applicable structural control design. Further work in this direction, including specialization for given damage-related uncertainties, investigation of different excitations as well as experimental verification, seems to be very promising.

References

1. Arvanitis, K.G., Zacharenakis, E.C., Soldatos, A.G., Stavroulakis, G.E.: New trends in optimal structural control. In: Selected Topics in Structronic and Mechatronic System, pp. 321–415. World Scientific, Singapore (2003)
2. Bosgra, O., Kwakernaak, H.: Design methods for control systems. Course notes, Dutch Institute for Systems and Control, p. 69 (2001)
3. Burke, J.V., Henrion, D., Lewis, A.S., Overton, M.L.: HIFOO—a MATLAB package for fixed-order controller design and H_∞ optimization. In: Proceedings of the IFAC Symposium on Robust Control Design, Toulouse, France (2006). www.cs.nyu.edu/overton/software/hifoo
4. Burke, J.V., Henrion, D., Lewis, A.S., Overton, M.L.: Stabilization via nonsmooth, nonconvex optimization. IEEE Trans. Autom. Control **5**(11), 1760–1769 (2006)
5. Foutsitzi, G., Marinova, D., Hadjigeorgiou, E., Stavroulakis, G.: Finite element modelling of optimally controlled smart beams. In: Venkov, G., Marinov, M. (eds.) 28th Summer School: Applications of Mathematics in Engineering and Economics, Sozopol, Bulgaria (2002)
6. Foutsitzi, G., Marinova, D., Hadjigeorgiou, E., Stavroulakis, G.: Robust H2 vibration control of beams with piezoelectric sensors and actuators. In: Proceedings of Physics and Control Conference (PhyCon03), St. Petersburg, Russia, 20–22 August, vol. I, pp. 158–163 (2003)
7. Hou, M., Muller, P.C.: Design of observers for linear systems with unknown inputs. IEEE Trans. Autom. Control **37**, 871–875 (1992)
8. Huang, W.S., Park, H.C.: Finite element modelling of piezoelectric sensors and actuators. AIAA J. **31**, 930–937 (1993)
9. Marinova, D., Stavroulakis, G.E., Foutsitzi, D., Hadjigeorgiou, E., Zacharenakis, E.C.: Robust design of smart structures taking into account structural defects. In: Indeitsev, D.A. (ed.) Summer School Conference Advanced Problems in Mechanics, Russian Academy of Sciences, pp. 288–292 (2004)
10. Miara, B., Stavroulakis, G., Valente, V. (eds.): Topics on Mathematics for Smart Systems: Proceedings of the European Conference, Rome, Italy, 26–28 October 2006. World Scientific, Singapore (2007)
11. Moutsopoulou, A., Stavroulakis, G., Pouliezos, A.: Model uncertainties in smart structures. In: Papadrakakis, M., Fragiadakis, M., Plevris, V. (eds.) 3rd Thematic Conference on Computational Methods in Structural Dynamics and Earthquake Engineering, Corfu, Greece (2011)
12. Packard, A., Doyle, J., Balas, G.: Linear, multivariable robust control with a perspective. J. Dyn. Syst. Meas. Control **115**(2b), 310–319 (1993)
13. Pouliezos, A.: MIMO control systems. Class notes (2008). http://pouliezos.dpem.tuc.gr
14. Shahian, B., Hassul, M.: Control System Design Using MATLAB. Prentice Hall, New York (1994)
15. Sisemore, C., Smaili, A., Houghton, R.: Passive damping of flexible mechanism system: experimental and finite element investigation. In: The 10th World Congress of the Theory of Machines and Mechanisms, Oulu, Finland, vol. 5, pp. 2140–2145 (1999)
16. Stavroulakis, G.E., Foutsitzi, G., Hadjigeorgiou, E., Marinova, D., Baniotopoulos, C.C.: Design and robust optimal control of smart beams with application on vibrations suppression. Adv. Eng. Softw. **36**(11–12), 806–813 (2005)
17. Tiersten, H.F.: Linear Piezoelectric Plate Vibrations. Plenum Press, New York (1969)
18. Tits, A.L., Yang, Y.: Globally convergent algorithms for robust pole assignment by state feedback. IEEE Trans. Autom. Control **41**, 1432–1452 (1996)
19. Ward, R.C.: Balancing the generalized eigenvalue problem. SIAM J. Sci. Stat. Comput. **2**, 141–152 (1981)
20. Young, P., Newlin, M., Doyle, J.: Practical computation of the mixed problem. In: Proceedings of the American Control Conference, pp. 2190–2194 (1992)
21. Zhang, N., Kirpitchenko, I.: Modelling dynamics of a continuous structure with a piezoelectric sensor/actuator for passive structural control. J. Sound Vib. **249**, 251–261 (2002)

Chapter 12
Robust Structural Health Monitoring Using a Polynomial Chaos Based Sequential Data Assimilation Technique

George A. Saad and Roger G. Ghanem

Abstract With the recent technological advances and the evolution of advanced smart systems for damage detection and signal processing, Structural Health Monitoring (SHM) emerged as a multidisciplinary field with wide applicability throughout the various branches of engineering, mathematics and physical sciences. However, significant challenges associated with modeling the physical complexity of systems comprising these structures remain. This is mainly due to the fact that numerous uncertainties associated with modeling, parametric and measurement errors could be introduced. In cases where these uncertainties are significant, standard identification and damage detection techniques are either unsuitable or inefficient. This study presents a robust data assimilation approach based on a stochastic variation of the Kalman Filter where polynomial functions of random variables are used to represent the inherent process uncertainties. The presented methodology is combined with a non-parametric modeling technique to tackle structural health monitoring of a four-story shear building. The structure is subject to a base motion specified by a time series consistent with the El-Centro earthquake and undergoes a preset damage in the first floor. The purpose of the problem is localizing the damage in both space and time, and tracking the state of the system throughout and subsequent to the damage time. The application of the introduced data assimilation technique to SHM enhances the latter's applicability to a wider range of structural problems with strongly nonlinear dynamical behavior and with uncertain and complex governing laws.

G.A. Saad (✉)
American University of Beirut, Beirut, Lebanon
e-mail: george.saad@aub.edu.lb

R.G. Ghanem
University of Southern California, Los Angeles, CA, USA
e-mail: ghanem@usc.edu

M. Papadrakakis et al. (eds.), *Computational Methods in Stochastic Dynamics*,
Computational Methods in Applied Sciences 26,
DOI 10.1007/978-94-007-5134-7_12, © Springer Science+Business Media Dordrecht 2013

1 Introduction

With the recent technological advances and the evolution of advanced smart systems for damage detection and signal processing, Structural Health Monitoring (SHM) emerged as a multidisciplinary field with wide applicability throughout the various branches of engineering, mathematics and physical sciences. Typically, the SHM problem can be addressed as a statistical pattern recognition paradigm with three main components:

1. A numerical model that accurately represents the governing system dynamics
2. Real-time data acquisition and management system
3. A sequential data assimilation technique that relies on a set of observational data to calibrate and update the underlying dynamic principles governing the system under observation.

In such context, numerous uncertainties associated with modeling, parametric and measurement errors could be introduced. In cases where these uncertainties are significant, standard identification and damage detection techniques are either unsuitable or inefficient. Therefore, the need rises for robust system identification algorithms that can tackle the aforementioned challenges. This has been a very active research area over the past decade [3–5, 8, 9, 11, 12].

Sequential data assimilation has been widely used for structural health monitoring and system identification problems. Many extensions of the Kalman Filter were developed as adaptations to important classes of these problems. While the Extended Kalman Filter may fail in the presence of high non-linearities, Monte Carlo based Kalman Filters usually give satisfactory results. The Ensemble Kalman Filter (EnKF) [1, 2] was recently used for damage detection in strongly nonlinear systems [4], where it is combined with non-parametric modeling techniques to tackle structural health monitoring for non-linear systems. The EnKF uses a Monte Carlo Simulation scheme for characterizing the noise in the system, and therefore allows representing non-Gaussian perturbations. Although this combination gives good results, it requires a relatively accurate representation of the nonlinear system dynamics. It also requires a large ensemble size to quantify the non-Gaussian uncertainties in such systems and consequently imposes a high computational cost.

This study presents a system identification approach based on coupling robust non-parametric non-linear models with the Polynomial Chaos methodology in the context of the Kalman Filtering techniques [10]. The proposed approach uses a Polynomial Chaos expansion [6, 7] of the nonparametric representation of the system's non-linearity to statistically characterize the system's behavior. A filtering technique that allows the propagation of a stochastic representation of the unknown variables using Polynomial Chaos is used to identify the chaos coefficients of the unknown parameters in the model. The introduced filter is a modification of the EnKF that uses the Polynomial Chaos methodology to represent uncertainties in the system. This allows the representation of non-Gaussian uncertainties in a simpler, less taxing way without the necessity of managing a large ensemble. It also allows obtain-

ing the probability density function of the model state or parameters at any instant in time by simply simulating the Polynomial Chaos basis.

2 The Polynomial Chaos Kalman Filter (PCKF)

The Kalman Filter is an optimal sequential data assimilation method for linear dynamics and measurement processes with Gaussian error statistics. The PCKF builds on the mathematics of the original Kalman Filter to allow the propagation of a stochastic representation of the unknown variables using Polynomial Chaos. In the PCKF, the model state is given by,

$$x = \sum_{i=0}^{P} x_i \psi_i(\xi), \tag{12.1}$$

where, $P+1$ is the number of terms in the Polynomial expansion of the state vector, $\{\psi_i\}$ is set of Hermite polynomials function of the Gaussian random variable, ξ. Consequently, the covariance matrix of the model state is defined around the mean, the zero order term, of the stochastic representation,

$$\begin{aligned}
\mathbf{P} &\approx \left\langle \left(\sum_{i=0}^{P} x_i \psi_i - x_0 \right) \left(\sum_{i=0}^{P} x_i \psi_i - x_0 \right)^T \right\rangle \\
&\approx \left\langle \left(\sum_{i=1}^{P} x_i \psi_i \right) \left(\sum_{i=1}^{P} x_i \psi_i \right)^T \right\rangle \\
&\approx \sum_{i=1}^{P} x_i x_i^T \langle \psi_i^2 \rangle,
\end{aligned} \tag{12.2}$$

where, $\mathbf{P}$ is the covariance matrix, and $\langle\rangle$ denotes the mathematical expectation. The Polynomial Chaos representation depicts all the information available through the complete probability density function, and therefore allows the propagation of all the statistical moments of the unknown parameters and variables.

The observations are also treated as random variables represented via a Polynomial Chaos expansion with a mean equal to the first-guess observations. Since the model and measurement errors are assumed to be independent, the latter is represented as a Markov process.

2.1 Analysis Scheme

For computational efficiency, the dimensionality and order of the Polynomial Chaos expansion are homogenized through out the solution. These parameters are initially defined based on the uncertainty within the problem at hand and are assumed to

be constant thereafter. Since the model state and measurement vectors are assumed independent, the Polynomial Chaos representation of these variables has a sparse structure.

Let **A** be the matrix holding the chaos coefficients of the state vector x,

$$\mathbf{A} = (x_0, x_1, \ldots, x_P) \in R^{n\times(P+1)}, \tag{12.3}$$

where P + 1 is the total number of terms in the Polynomial Chaos representation of x and n is the size of the model state vector. The mean of x is stored in the first column of **A** and is denoted by x_0. The state perturbations are given by the higher order terms stored in the remaining columns. Consequently, the state error covariance matrix **P** is defined as:

$$\mathbf{P} = \sum_{i=1}^{P} x_i x_i^T \langle \psi_i^2 \rangle \in R^{n\times n} \tag{12.4}$$

Given a vector of measurements $d \in R^m$, with m being the number of measurements at each occurrence, a Polynomial chaos representation of the measurements is defined as

$$d = \sum_{j=0}^{P} d_j \psi_j(\xi), \tag{12.5}$$

where the mean d_0 is given by the actual measurement vector, and the higher order terms represent the measurement uncertainties. The representation d can be stored in matrix form as:

$$\mathbf{B} = (d_0, d_1, \ldots, d_P) \in R^{m\times(P+1)}. \tag{12.6}$$

Based on Eq. (12.5), the measurement error covariance matrix, **R**, is defined as:

$$\mathbf{R} = \sum_{i=1}^{P} d_i d_i^T \langle \psi_i^2 \rangle \in R^{m\times m} \tag{12.7}$$

The Kalman Filter forecast step is carried out by employing a stochastic Galerkin scheme, and the assimilation step consists of the traditional Kalman Filter correction step applied on the Polynomial Chaos expansion of the model state vector,

$$\sum_{i=0}^{P} x_i^a \psi_i = \sum_{i=0}^{P} x_i^f \psi_i + \mathbf{P}\mathbf{H}^T \left(\mathbf{H}\mathbf{P}\mathbf{H}^T + \mathbf{R}\right)^{-1} \left(\sum_{i=0}^{P} d_i \psi_i - \mathbf{H} \sum_{i=0}^{P} x_i^f \psi_i \right) \tag{12.8}$$

where **H** is the observation matrix, and the superscripts f and a represent the forecast and analysis states respectively. Projecting the above equation on an approximating space spanned by the Polynomial Chaos $\{\psi_i\}_{i=0}^{P}$ yields,

$$x_i^a = x_i^f + \mathbf{P}\mathbf{H}^T \left(\mathbf{H}\mathbf{P}\mathbf{H}^T + \mathbf{R}\right)^{-1} \left(d_i - \mathbf{H}x_i^f\right) \quad \forall i = 0, 1, \ldots, P. \tag{12.9}$$

In matrix form, the assimilation step is expressed as:

$$\mathbf{A}^a = \mathbf{A}^f + \mathbf{P}\mathbf{H}^T \left(\mathbf{H}\mathbf{P}\mathbf{H}^T + \mathbf{R}\right)^{-1} \left(\mathbf{B} - \mathbf{H}\mathbf{A}^f\right) \tag{12.10}$$

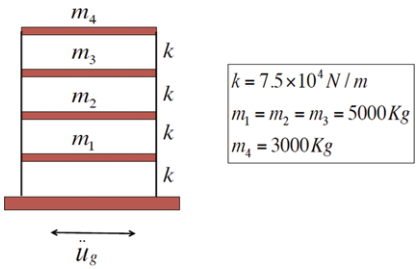

Fig. 12.1 Shear building under analysis

Table 12.1 Bouc–Wen model coefficients

Model Coefficient	Pre-Change	Post-Change
α	0.15	0.15
β	0.1	10
n	1	1
Υ	0.1	10
A	1	1

3 Numerical Example

The efficiency of the presented method is assessed by applying it to the structural health monitoring of the four-story shear building shown in Fig. 12.1. This model has a constant stiffness on each floor and a 5% damping ratio in all modes. All structural elements of this frame are assumed to involve hysteretic behavior, and it is supposed that a change in the hysteretic loop of the first floor element occurs at some point. It is of utmost importance to localize that point in time and track the state of the system throughout and subsequent to that point.

A synthetically generated dataset representing measurements of the displacements and velocities at each floor is obtained by representing the hysteretic restoring force by the Bouc–Wen model, which is therefore considered as the exact hysteretic behavior of the system. Thus, the equation of motion of the system is given by,

$$\mathbf{M}\ddot{u}(t) + \mathbf{C}\dot{u}(t) + \alpha\mathbf{K}_{\text{el}}u(t) + (1-\alpha)\mathbf{K}_{\text{in}}z(x,t) = -\mathbf{M}\tau\ddot{u}_g(t) \tag{12.11}$$

where, $\mathbf{M}$, $\mathbf{C}$, $\mathbf{K}_{\text{el}}$, and $\mathbf{K}_{\text{in}}$ are the mass, damping, elastic and inelastic stiffness matrices respectively; α is the ratio of the post yielding stiffness to the elastic stiffness, τ is the influence vector, u is the displacement vector, x is the inter-story drift vector, and z is an n-dimensional evolutionary hysteretic vector whose i^{th} component is give by the Bouc–Wen model as,

$$\dot{z}_i = A_i\dot{x}_i - \beta|\dot{x}_i||z_i|^{n_i-1} - \gamma_i\dot{x}_i|z_i|^{n_i}, \quad i = 1,\ldots,n \tag{12.12}$$

A, β, and Υ are the Bouc–Wen model parameters. The adopted values for these parameters are shown in Table 12.1.

The structure is subject to a base motion specified by a time series consistent with the 1940 El-Centro earthquake shown in Fig. 12.2, and a change of the first

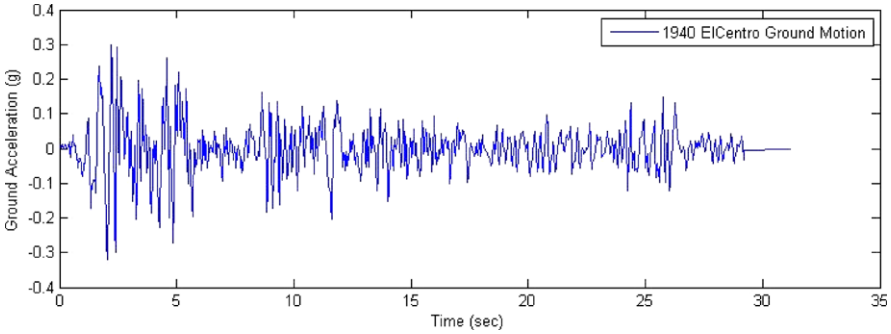

Fig. 12.2 The 1940 ElCentro excitation applied to the structure

floor hysteretic behavior is assumed to take place five seconds after the excitation. A monitoring scenario where it is assumed that measurements are available every 5 time steps is adopted. A nonparametric representation of the system nonlinearity is adopted, and the filtering technique is used to characterize the latter representation in order to capture any ambiguous behavior of the structure examined.

4 Non-parametric Representation of the Non-linearity

The proposed filtering methodology is combined with a non-parametric modeling technique to tackle structural health monitoring of non-linear systems but instead of adopting a deterministic nonparametric representation of the non-linearity, a stochastic representation via Polynomial Chaos is used. The basic idea behind the non-parametric identification technique used is to determine an approximating analytical function $\hat{F}$ that approximates the actual system non-linearities, with the form of $\hat{F}$ including suitable basis functions that are adapted to the problem at hand [8]. For general non-linear systems, a suitable choice of basis would be the list of terms in the power series expansion in the doubly indexed series,

$$S = \sum_{i=0}^{i_{max}} \sum_{j=0}^{j_{max}} u^i \dot{u}^j \tag{12.13}$$

where u and $\dot{u}$ are used to represent the system's displacement and velocity respectively. Therefore, if $i_{max} = 3$ and $j_{max} = 3$, the basis functions become:

$$\begin{aligned} basis = \{&1, \dot{u}, \dot{u}^2, \dot{u}^3, u, u\dot{u}, u\dot{u}^2, u\dot{u}^3, u^2, u^2\dot{u}, u^2\dot{u}^2, u^2\dot{u}^3, \\ &u^3, u^3\dot{u}, u^3\dot{u}^2, u^3\dot{u}^3\} \end{aligned} \tag{12.14}$$

In the proposed method the displacements and velocities are stochastic processes represented by their Polynomial Chaos expansion. Thus, the approximating function

is also expressed as a stochastic process via a Polynomial Chaos representation. The model adopted within the Kalman Filter is hence given by

$$M\ddot{u}(t) + F(u, \dot{u}) = -M\tau\ddot{u}_g(t) \tag{12.15}$$

where, F is the non-parametric representation of the non-linearity whose i^{th} floor component is given by

$$\begin{aligned}
F^i &\approx \sum_j F_j^i(u, \dot{u})\psi_j \\
&\approx \sum_j a_j^i \psi_j \left(\sum_k (u_k - u_k^{i-1})\psi_k \right) + \sum_j a_j^{i+1} \psi_j \left(\sum_k (u_k^i - u_k^{i+1})\psi_k \right) \\
&\quad + \sum_j b_j^i \psi_j \left(\sum_k (u_k^i - u_k^{i-1})\psi_k \right)^2 + \sum_j b_j^{i+1} \psi_j \left(\sum_k (u_k^i - u_k^{i+1})\psi_k \right)^2 \\
&\quad + \sum_j c_j^i \psi_j \left(\sum_k (\dot{u}_k^i - \dot{u}_k^{i-1})\psi_k \right) + \sum_j c_j^{i+1} \psi_j \left(\sum_k (\dot{u}_k^i - \dot{u}_k^{i+1})\psi_k \right) \\
&\quad + \sum_j d_j^i \psi_j \left(\sum_k (u_k^i - u_k^{i-1})\psi_k \right) \left(\sum_l (\dot{u}_l^i - \dot{u}_l^{i-1})\psi_l \right) \\
&\quad + \sum_j d_j^{i+1} \psi_j \left(\sum_k (u_k^i - u_k^{i+1})\psi_k \right) \left(\sum_l (\dot{u}_l^i - \dot{u}_l^{i+1})\psi_l \right)
\end{aligned} \tag{12.16}$$

In the above equation, $\{a_j\}$, $\{b_j\}$, $\{c_j\}$, and $\{d_j\}$ represent the chaos coefficients of the unknown parameters to be identified. The fourth order Runge–Kutta method is used for the time stepping and a stochastic Galerkin approach is employed to solve the system at each time step.

5 Results

In the numerical example, it is assumed that observations of displacements and velocities from all floors are available. The noise signals perturbing both the model and measurements are modeled as first order, one dimensional, independent, Polynomial Chaos expansions having zero-mean and an RMS of 0.05 and 0.001 respectively. The parametric uncertainties on the other hand, are modeled as second order, one dimensional, Polynomial Chaos expansions whose coefficients are to be determined in accordance with the available observations. This is done to incorporate the possibility that the unknown parameters may deviate from Gaussianity. Furthermore, it is assumed that the first floor undergoes a change in its hysteretic behavior 5 seconds after the ground excitation. The purpose of the application is to detect this behavioral change.

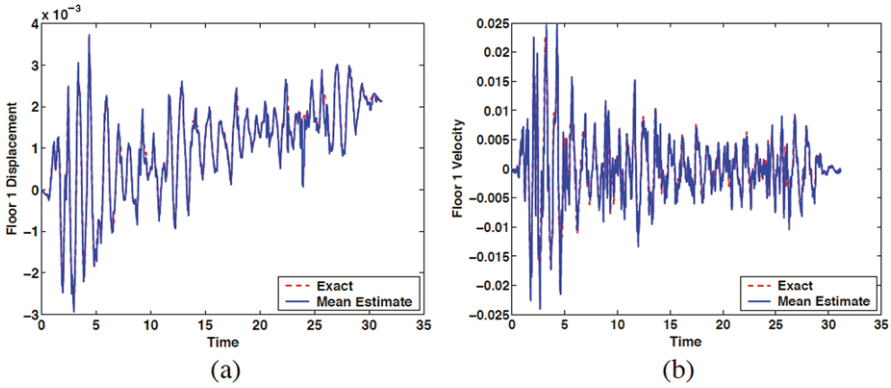

Fig. 12.3 Estimate of the first floor parameters, (**a**) displacement, (**b**) velocity

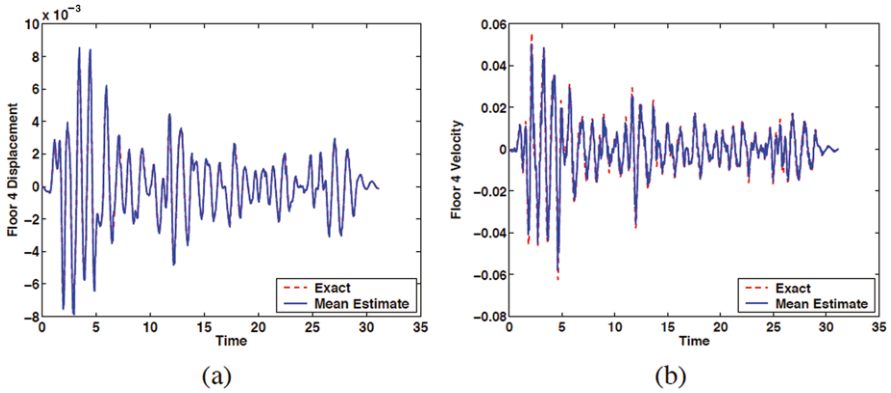

Fig. 12.4 Estimate of the fourth floor parameters, (**a**) displacement, (**b**) velocity

Fig. 12.3 and Fig. 12.4 describe the tracking of the displacement and velocity for the first and fourth floor respectively. Excellent match between the results estimated using the Polynomial Chaos based Kalman Filter and the true state is observed.

Fig. 12.5 presents the evolution of the mean of the unknown parameters identified by the proposed filtering technique. Error bars representing the scatter in the estimated parameters are also present in Fig. 12.5. The different jumps within the parameters are associated with the perks in the corresponding excitation.

Further investigation of the parameters indicates that the main changes take place in the first floor following the 5 s time interval. Note that the parameters a and c in floors 1 and 2 undergo the greatest jumps since they are associated with inter-story drift and velocity, respectively. One of the main advantages of using the Polynomial Chaos Kalman filter is that it provides a scatter around the estimated parameters. This is represented by the probability density functions corresponding to each of

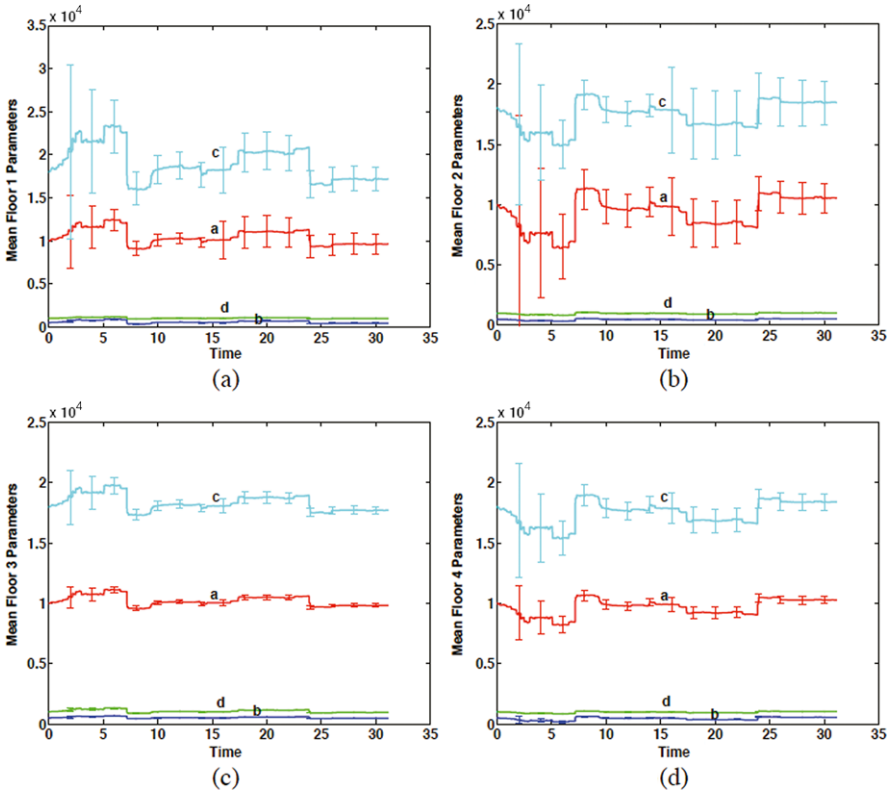

Fig. 12.5 Estimate of the mean floor parameters

the estimated parameters. Fig. 12.6 presents the probability density functions of the estimated floor 1 parameters.

6 Conclusions

The combination of Polynomial Chaos with the Ensemble Kalman Filter renders an efficient data assimilation methodology that competes with other Kalman Filtering techniques while maintaining a relatively low computational cost. Although the proposed method employs traditional Kalman Filter updating schemes, it preserves all the error statistics, and hence allows the computation of the probability density function of the uncertain parameters and variables at all time steps. This is achieved by simply simulating the Polynomial Chaos representation of these parameters. Together with the non-parametric representation of the nonlinearities, the approach constitutes an effective system identification technique that accurately detects any changes in the systems behavior. The Polynomial Chaos representation of the non-parametric model for the nonlinearities is a robust innovative approach that per-

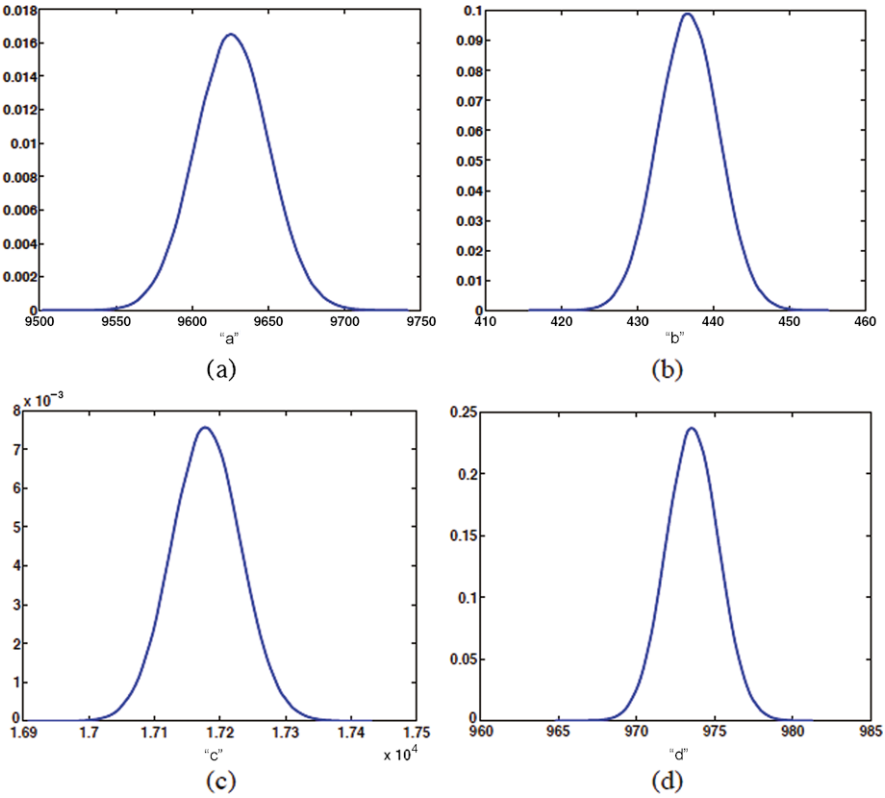

Fig. 12.6 Probability density functions of the estimated floor 1 parameters

mits damage identification and tracking the dynamical state beyond that point. Using Polynomial Chaos, the uncertainty associated with the assumed non-parametric model is inherently present and thus represents the actual nonlinearity in a more accurate way.

References

1. Evensen, G.: Sequential data assimilation with a nonlinear quasi-geostrophic model using Monte Carlo to forecast error statistics. J. Geophys. Res. **99**, 10143–10162 (1994)
2. Evensen, G.: The ensemble Kalman filter: theoretical formulation and practical implementation. Ocean Dyn. **53**, 343–367 (2003)
3. Franco, G., Betti, R., Lus, S.: Identification of structural systems using an evolutionary strategy. J. Eng. Mech. **130**, 1125–1139 (2005)
4. Ghanem, R., Ferro, G.: Health monitoring for strongly non-linear systems using the ensemble Kalman filter. Struct. Control Health Monit. **13**, 245–259 (2002)
5. Ghanem, R., Shinozuka, M.: Structural systems identification I, theory. J. Eng. Mech. **121**, 255–264 (1995)

6. Ghanem, R., Spanos, P.: Stochastic Finite Elements: A Spectral Approach, revised edn. Dover, New York (2003)
7. Ghanem, R., Saad, G., Doostan, A.: Efficient solution of stochastic systems: application to the embankment dam problem. Struct. Saf. **29**, 238–251 (2007)
8. Masri, S., Caffrey, J.P., Caughey, T.K., Smyth, A.W., Chassiakos, A.G.: Identification of the state equation in complex non-linear systems. Int. J. Non-Linear Mech. **39**, 1111–1127 (2004)
9. Masri, S., Ghanem, R., Arrate, F., Caffrey, J.P.: A data based procedure for analyzing the response of uncertain nonlinear systems. Struct. Control Health Monit. **16**, 724–750 (2009)
10. Saad, G., Ghanem, R.: Characterization of reservoir simulation models using a polynomial chaos based ensemble Kalman filter. Water Resour. Res. **45**, W04417 (2009)
11. Saad, G., Ghanem, R., Masri, S.: Robust system identification of strongly non-linear dynamics using a polynomial chaos-based sequential data assimilation technique. In: 48th AIAA/ASME/ASCE/AHS/ASC Structures, Structural Dynamics, and Materials Conference, Honolulu, Hawaii (2007)
12. Zhang, H., Foliente, G., Yang, Y., Ma, F.: Parametric identification of elastic structures under dynamic loads. Earthquake Eng. Struct. Dyn. **31**, 1113–1130 (2002)

Chapter 13
Efficient Model Updating of the GOCE Satellite Based on Experimental Modal Data

B. Goller, M. Broggi, A. Calvi, and G.I. Schuëller

Abstract The accurate prediction of the structural response of spacecraft systems during launch and ascent phase is a crucial aspect in design and verification stages which requires accurate numerical models. The enhancement of numerical models based on experimental data is denoted model updating and focuses on the improvement of the correlation between finite element (FE) model and test structure. In aerospace industry the examination of the agreement between model and real structure involves the comparison of the modal properties of the structure. Model updating techniques have to handle several difficulties, like incomplete experimental data, measurement errors, non-unique solutions and modeling uncertainties. To cope with the computational challenges associated with the large-scale FE-models involving up to over one million degrees of freedom (DOFs), enhanced strategies are required. A large-scale numerical example, namely a satellite model, will be used for demonstrating the applicability of the employed updating procedure to complex aerospace structures.

1 Introduction

The dynamic loads acting on a spacecraft during the launch and ascent phase are modeled by the spacecraft-launcher coupled dynamic analysis. The accuracy of the

G.I. Schuëller is deceased.

B. Goller (✉)
Institute of Engineering Mechanics, University of Innsbruck, Technikerstr. 13, 6020 Innsbruck, Austria
e-mail: barbara.goller@uibk.ac.at

M. Broggi
Institute for Risk and Uncertainty, University of Liverpool, Warrington, WA4 4AD, UK
e-mail: matteo.broggi@liverpool.ac.uk

A. Calvi
Structures Section TEC-MSS, European Space Agency/ESTEC, P.O. Box 299, 2200 AG Noordwijk, The Netherlands
e-mail: adriano.calvi@esa.int

M. Papadrakakis et al. (eds.), *Computational Methods in Stochastic Dynamics*, Computational Methods in Applied Sciences 26,
DOI 10.1007/978-94-007-5134-7_13,

structural response in this low-frequency mechanical environment depends on the quality of the underlying mechanical model of the spacecraft. Therefore, it is mandatory to ensure that the FE-model represents the real structure accurately enough. This level of accuracy to be reached for aerospace structures is defined in [1] and is based on the agreement of experimentally and computationally determined modal properties, respectively. Possible sources for discrepancies between test data and respective computed values are e.g. uncertainties in the modeling process arising from inadequate theory for some system behaviors, simplifying assumptions made in order to reduce the complexity of the model and uncertainties about model parameter values. Hence, the need for improving the mechanical model based on experimental data arises which is referred to as model updating and the consecutive corroboration of the model by means of modal properties is denoted by validation [2–4].

The use of deterministic updating procedures does not allow for a quantification of the involved uncertainties in the design and verification processes which will subsequently affect the accuracy of the predictive structural response. Probabilistic methods for model updating provide a means for tackling these problems and for avoiding a wrong conclusion about the fit of the experimental data and analytical results [5]. A significant obstacle in the consideration of uncertainties when performing model updating of complex structures is posed by the associated computational efforts. Therefore, the most frequently used approaches for model updating performed by industry are deterministic approaches (see e.g. [6–9]). While stochastic methods have been developing successfully in this research field, applications in industry are relatively limited (see e.g. [10]). Hence, in this work it is aimed at a computationally efficient application of a stochastic model updating procedure to complex aerospace models.

The thereby adopted updating process is the Bayesian approach which is based on updating the initial engineering knowledge about the ranges of the adjustable parameters using experimental data [11–13]. In this way, a revised information about the parameters is obtained, which is expressed by posterior probability density functions. Probability is therefore not interpreted in the usual frequentist sense, where it refers to the relative frequency of occurrence in case of many events, but it is based on the idea of reasonable expectation, i.e. probability is interpreted as a measure of plausibility of the hypothesis. This interpretation makes it possible to extend the application of probability theory to fields where the frequentist interpretation may not be directly intuitive, as it is the case for one-of-a-kind structures, where no ensemble exists, and also in the case of limited data, where classical statistics is of limited applicability. Therefore, Bayesian statistics makes it possible to deal with the usual situation in aerospace industry, where a large amount of experimental data is infeasible due to the enormous costs associated with test campaigns, and it provides a means for making decisions based on limited, incomplete information.

The computational tools for the Bayesian updating procedure are sampling-based algorithms, where a multi-level Markov chain Monte Carlo algorithm is adopted in this approach [14]. As a remedy for the large computational efforts associated with the Bayesian updating procedure, the application of a surrogate model (a so-called "meta-model") is proposed. This meta-model is formulated with respect to the repeated analysis tasks, which are the eigensolutions in case of model updating based

on modal data. Hence, a simple relation between the input data and output quantity of interest has to be established in order to replace the computationally intensive evaluation of a full finite element analysis by a function evaluation at low computational costs. Several techniques, e.g. linear or polynomial regression, kriging and the radial basis functions have been developed in this context (see e.g. [15]), where in this work neural networks [16, 17] will be adopted in order to approximate the modal properties of the structure.

This manuscript will demonstrate the feasibility of the application of Bayesian model updating procedures on spacecraft structures using eigenfrequencies and mode shape vectors. Section 2 is devoted to the presentation of the basic steps of Bayesian model updating, and in Sect. 3 the algorithm for the generation of samples in the solution space is summarized. Computational aspects will be addressed in the following (Sect. 4), where the basic concepts of neural networks are discussed. In order to apply these outlined concepts to an FE-model of a spacecraft structure, the use of a surrogate model within the updating process is adopted for the FE-model of the GOCE satellite (Sect. 5).

2 Bayesian Model Updating

2.1 Introduction

The fundamental rule that governs the Bayesian updating procedure is Bayes' Theorem, which is formulated in general terms as [18]

$$P(H|\mathscr{D}, I) = \frac{P(\mathscr{D}|H, I)P(H|I)}{P(\mathscr{D}|I)}, \tag{13.1}$$

where H is any hypothesis to be tested, $\mathscr{D}$ denotes the data and I is the available background information. Bayes' Theorem provides a means to update the prior probability density function (PDF) of H, $P(H|I)$, by using the data in the likelihood function $P(\mathscr{D}|H, I)$ in order to obtain the posterior distribution of H, $P(H|\mathscr{D}, I)$. The denominator $P(\mathscr{D}|I)$ is a normalizing constant and does not affect the shape of the posterior PDF. All probabilities in Eq. (13.1) are conditional on I, which means that the outcome of the updating procedure depends on the available information.

2.2 Bayesian Updating Using Modal Data

If applying Bayes' Theorem for structural model updating [11, 12], the hypothesis H is interpreted as the vector of unknown (i.e. adjustable) parameters, which will be referred to as θ in the following, and $\mathscr{D}$ denotes the experimental data, which consist of the measured modal properties of the investigated structure. The available information I is interpreted as the experience and knowledge of the engineer which

is reflected by the established model itself and is therefore denoted as $\mathscr{M}$. This leads to the following form of Eq. (13.1):

$$p(\theta|\mathscr{D},\mathscr{M}) = \frac{p(\mathscr{D}|\theta,\mathscr{M})\,p(\theta|\mathscr{M})}{p(\mathscr{D}|\mathscr{M})}. \tag{13.2}$$

The prior distribution $p(\theta|\mathscr{M})$ expresses the initial knowledge about the adjustable parameters. The choice of the distribution can be based on the principle of maximum entropy [19]. In this case, the PDF used for describing the initial uncertainty maximizes the uncertainty subject to the prescribed constraints, which can be given by e.g. imposing moment constraints. The likelihood function $p(\mathscr{D}|\theta,\mathscr{M})$ gives a measure of the agreement between the system data and the corresponding structural model output. This measure of the data fit of each model defined by the parameters vector θ, is given by the probability model established for the system output. The derivation of the likelihood function for modal data will be summarized in Sect. 2.3. The posterior distribution $p(\theta|\mathscr{D},\mathscr{M})$ expresses the revised knowledge about the parameters θ conditional on the initial knowledge and the experimental data.

2.3 Formulation of the Likelihood Function for Modal Data

In general terms, the connection between the model output $q(\theta)$ and the corresponding system output y is given by the prediction error e in the form of

$$y = q(\theta) + e. \tag{13.3}$$

The choice for the probability model of the prediction error e, which is the difference between the model output for a certain value of θ and the corresponding system output, is based on the maximum entropy principle [19] which yields a multidimensional Gaussian distribution with zero mean and covariance matrix Σ. The Gaussian PDF arises because it gives the largest amount of uncertainty among all probability distributions for a real variable whose first two moments are specified. Hence, the predictive PDF for the system output conditional on the parameter vector θ is given by

$$p(y|\theta,\mathscr{M}) = \frac{1}{(2\pi)^{N/2}|\Sigma|^{1/2}} \exp\left[-\frac{1}{2}\big(y-q(\theta)\big)^T \Sigma^{-1}\big(y-q(\theta)\big)\right], \tag{13.4}$$

where N denotes the length of the vector y, i.e. the number of observed points. If a set of measured output $\mathscr{D} = \{y_j : j = 1,\ldots,N_s\}$ is available, then the likelihood function can be constructed as $p(\mathscr{D}|\theta,\mathscr{M}) = \prod_{j=1}^{N_s} p(y_j|\theta,\mathscr{M})$ if the prediction errors are modeled as statistically independent.

The formulation of the likelihood function using modal data is derived in [20] and is summarized in the following. The experimental data $\mathscr{D}$ from the structure is assumed to consist of N_s sets of modal data, $\mathscr{D} = \{\hat{\omega}_{1,j}\cdots\hat{\omega}_{N_m,j}, \hat{\Psi}_{1,j}\cdots\hat{\Psi}_{N_m,j}\}_{j=1}^{N_s}$ comprised of N_m modal frequencies $\hat{\omega}_r$ and N_m incomplete mode shape vectors $\hat{\Psi}_r \in \mathbb{R}^{N_0}$, where N_0 is the number of observed DOFs. The model output $q(\theta)$ is

the set of corresponding modal properties of the structural model, i.e. eigenfrequencies $\omega_r(\theta)$ and partial eigenvectors $\psi_r(\theta)$, $r = 1, \ldots, N_m$, defined by the parameter vector $\theta \in \Theta \in \mathbb{R}^{N_p}$.

The probability model conditional on the parameter vector θ is chosen to have statistical independence between the mode shape vectors and modal frequencies, between the different modes, and between one data set to another. Therefore, the likelihood function can be written as the product of the probability density functions for the modal frequencies and mode shape components:

$$p(\mathscr{D}|\theta, \mathscr{M}) = \prod_{j=1}^{N_s} \prod_{r=1}^{N_m} p\big(\hat{\omega}_{r,j}^2|\theta, \mathscr{M}\big)\, p(\hat{\psi}_{r,j}|\theta, \mathscr{M}), \tag{13.5}$$

where $p(\hat{\omega}_{r,j}^2|\theta, \mathscr{M})$ and $p(\hat{\psi}_{r,j}|\theta, \mathscr{M})$, $r = 1, \ldots, N_m$ and $j = 1, \ldots, N_s$, are, respectively, the PDFs for the squared modal frequency and the mode shape vector of the rth mode in the jth data set.

In the first step, the likelihood function for the mode shape vectors is formulated by rewriting Eq. (13.3) as

$$\hat{\psi}_{r,j} = a_r \psi_r(\theta) + e_{\psi_r}, \tag{13.6}$$

where a_r is an optimal scaling factor to relate the scaling of the model mode shape vector $\psi_r(\theta)$ to that of the experimental mode shape vector $\hat{\psi}_{r,j}$, which is assumed to be normalized so that its Euclidean norm $\|\hat{\psi}_{r,j}\| = 1$. Since the latter is usually constituted by an incomplete set of observed DOFs N_0, the corresponding model mode shape vector is given by $\psi_r = \Gamma \phi_r$, where the matrix Γ picks the observed degrees of freedom from the complete model eigenvector ϕ_r. Using a Gaussian distribution for the probabilistic characterization of the prediction error for the mode shape vector, the likelihood function for the mode shape vector, after some algebraic manipulation, may be written as:

$$p(\hat{\psi}_{r,j}|\theta, \mathscr{M}) = c_1 \exp\left(\frac{\psi_r^T (I - \hat{\psi}_{r,j}\hat{\psi}_{r,j}^T)\psi_r}{2\delta_r^2 \|\psi_r\|^2}\right) \tag{13.7}$$

$$= c_1 \exp\left(\frac{1}{2\delta_r^2}\left[1 - \frac{|\psi_r^T \hat{\psi}_{r,j}|^2}{(\psi_r^T \psi_r)^2}\right]\right) \tag{13.8}$$

where I is the identity matrix of dimension N_m and $\delta_r^2 I$ denotes the mode shape prediction error covariance matrix for the rth mode. The equality in Eq. (13.7) shows that the probability density function for $\hat{\psi}_{r,j}$ involves the MAC (Modal Assurance Criterion) between $\hat{\psi}_{r,j}$ and $\psi_r(\theta)$, the experimental and model partial mode shapes of the rth mode, respectively.

Secondly, Eq. (13.3) is formulated for the squared modal frequencies, which yields

$$\hat{\omega}_{r,j}^2 = \omega_r^2(\theta) + e_{\omega_r^2}. \tag{13.9}$$

Using again a Gaussian probability model for the prediction error of the modal frequencies, the likelihood function for the modal frequencies is given by

$$p\left(\hat{\omega}_{r,j}^2|\theta,\mathscr{M}\right) = c_2 \exp\left[-\frac{1}{2}\left(\frac{1-\hat{\omega}_{r,j}^2/\omega_r^2}{\varepsilon_r}\right)^2\right], \tag{13.10}$$

where ε_r^2 denotes the variance of the prediction error of the squared r-th eigenfrequency, i.e. of $e_{\omega_r^2}$. Using the probability distributions for the mode shape vectors and modal frequencies given in Eqs. (13.7) and (13.10), the likelihood function in Eq. (13.5) can be written as

$$p(\mathscr{D}|\theta,\mathscr{M}) = c_3 \exp\left(-\frac{1}{2}\sum_{r=1}^{N_m} J_r(\theta)\right), \tag{13.11}$$

where the modal measure of fit $J_r(\theta)$ is defined by

$$J_r(\theta) = \sum_{j=1}^{N_s}\left[\left(\frac{1-\hat{\omega}_{r,j}^2/\omega_r^2}{\varepsilon_r}\right)^2 + \left(1-\frac{|\psi_r^T\hat{\psi}_{r,j}|^2}{(\psi_r^T\psi_r)^2}\right)/\delta_r^2\right] \tag{13.12}$$

3 Transitional Markov Chain Monte Carlo Algorithm

The evaluation of Eq. (13.2) requires the computation of high-dimensional integrals for the determination of the normalizing constant of the posterior PDF, which cannot be tackled analytically or numerically. Recently, efficient stochastic simulation algorithms have been proposed which generate samples of the posterior distribution and which hence identify the parameter regions with the highest posterior probability mass. In this work, the so-called Transitional Markov Chain Monte Carlo (TMCMC) algorithm [14] is applied whose basic steps are discussed in the following.

The main idea of this algorithm is to iteratively proceed from the prior to the posterior distribution. It starts with the generation of samples from the prior PDF in order to populate the space in which also the most probable regions of the posterior distribution lie. Then, some intermediate PDFs are defined, where the shape does not change remarkably from the intermediate PDF $p[j]$ to the next $p[j+1]$. The small change of the shape makes it possible to efficiently sample according to $p[j+1]$ if samples according to $p[j]$ have been generated. The intermediate distributions are defined by

$$p[j+1] \propto p(\mathscr{D}|\theta,\mathscr{M})^{\beta_j}\, p(\theta|\mathscr{M}), \tag{13.13}$$

with $j = 0,\ldots,m$ as the step index and $0 = \beta_0 < \beta_1 < \cdots < \beta_m = 1$. Hence, the exponent β_j can be interpreted as the percentage of the total information provided by the experimental data which is incorporated in the jth iteration of the updating procedure: $\beta_0 = 0$ corresponds to the prior distribution and for $\beta_m = 1$ the samples are generated from the posterior distribution.

Samples of the subsequent intermediate distribution $p[j+1]$ are obtained by generating Markov chains where the lead samples are selected from the distribution $p[j]$ by computing their probability weights with respect to $p[j+1]$, which are given by

$$w\big(\theta_j^{(l)}\big) = \frac{p(\mathscr{D}|\theta,\mathscr{M})^{\beta_{j+1}}\, p(\theta|\mathscr{M})}{p(\mathscr{D}|\theta,\mathscr{M})^{\beta_j}\, p(\theta|\mathscr{M})} = p(\mathscr{D}|\theta,\mathscr{M})^{\beta_{j+1}-\beta_j}, \tag{13.14}$$

where the upper index $l = 1,\ldots,N_j$ denotes the sample number in the jth iteration step. Each sample of the current step is generated using the Metropolis–Hastings algorithm [21, 22]: the starting point of a Markov chain is a sample from the previous step that is selected according to the probability equal to its normalized weight

$$\overline{w}\big(\theta_j^{(l)}\big) = \frac{w(\theta_j^{(l)})}{\sum_{l=1}^{N_j} w(\theta_j^{(l)})} \tag{13.15}$$

and the proposal density for the Metropolis–Hastings algorithm is a Gaussian distribution centered at the preceding sample of the chain and with a covariance matrix Σ_0 which is equal to the scaled version of the estimated covariance matrix of the current intermediate PDF:

$$\Sigma_0 = c^2 \sum_{l=1}^{N_j} \overline{w}\big(\theta_j^{(l)}\big)\big(\theta_j^{(l)} - \overline{\theta}_j\big)^T\big(\theta_j^{(l)} - \overline{\theta}_j\big), \tag{13.16}$$

where

$$\overline{\theta}_j = \sum_{l=1}^{N_j} \overline{w}\big(\theta_j^{(l)}\big)\theta_j^{(l)}. \tag{13.17}$$

The parameter c is a scaling parameter that is used to control the rejection rate of the Metropolis–Hastings algorithm at each step. These steps are repeated until $\beta_j = 1$ is reached, i.e. until the samples are generated from the posterior distribution.

4 Computational Aspects

4.1 General Remarks

Due to the repeated execution of the normal mode analysis of the FE-model, the computational effort of the Bayesian updating method might become infeasible for large FE-models. Hence, in order to reduce the wall clock time, i.e. the time between submitting the updating analysis and its completion, a strategy based on the reduction of the computational efforts associated with the normal mode analysis of the full FE-model is applied in this manuscript. This strategy is based on the use of neural networks for the modal parameters, which will be addressed in the following.

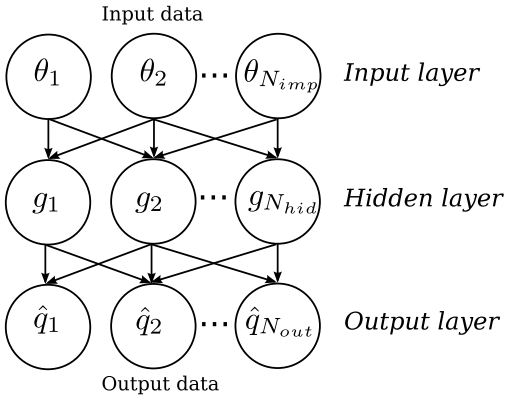

Fig. 13.1 Schematic representation of the concept of neural networks

4.2 Neural Networks

An Artificial Neural Network (ANN) is a machine-learning algorithm that tries to simulate the structure and functional aspects of biological networks of neurons in order to approximate a relation $f : \theta \to q$ by a simple mathematical model at low computational efforts. It consists of an interconnected group of computational units, called neurons or nodes, and processes information using consecutively connected layers of neurons. In the following, the most widely used neural network, namely the so-called feed-forward neural network, is discussed (see e.g. [23, 24]). It is composed of a multi-layered structure, with a first layer of nodes, called input layer, one or more intermediate layers, called hidden, and a final output layer. For simplicity, but without loss of generality, the scheme is discussed when using one single hidden layer.

Each layer is characterized by a different number of neurons, indicated by N_{inp}, N_{hid} and N_{out} for the input, hidden and output layers, respectively. Each node of the hidden layer receives as input a linear combination $\sum_{i=1}^{N_{inp}} w_{i,j}\theta_i$ of the input values θ_i of all the nodes of the input layer, scaled by a so-called connection weight $w_{i,j}$, where j denotes the number of the hidden node. Then, the node proceeds this function value through a non-linear function K, which is called activation function and which is of the form $g_j = K(\sum_{i=1}^{N_{inp}} w_{i,j}\theta_i)$. This collection of function values $(g_1, \ldots, g_{N_{hid}})$ is then sent to all the nodes of the subsequent, i.e. output, layer, where the approximated model output $\hat{q}_k(\theta) = K(\sum_{j=1}^{N_{hid}} w_{j,k}y_j)$, $k = 1, \ldots, N_{out}$ is evaluated. A schematic representation of this algorithm is shown in Fig. 13.1.

Hence, the connection weights act as parameters of the meta-model which have to be adapted through a calibration procedure of supervised learning, called also training, by means of e.g. the error back-propagation algorithm. In this calibration phase, the network, which is initialized with random weights, is fed with a set of input/output values which is called calibration set and which is obtained from the target physical model. The network processes the inputs and produces then an estimation of the outputs; such outputs are compared with the real outputs through a

predefined error measurement (typically, a sum of the squared errors of each output). The training consists thus of an optimization problem which aims to minimize the error of the network in the output prediction. Such optimization is carried out by computing the gradient of the error with respect to the connection weights, and it is interrupted when a target error is reached or when a certain number of input/output pairs have been processed.

An important indicator of the goodness of the network after training is the coefficient of determination R^2, defined as

$$R^2 = 1 - \frac{\sum_{i=1}^{N_{data}} (q_i - \hat{q}_i)^2}{\sum_{i=1}^{N_{data}} (q_i - \overline{q}_i)^2} \tag{13.18}$$

where q_i are the real outputs of the physical model, $\overline{q}_i = \frac{1}{N_{data}} \sum_{i=1}^{N_{data}} q_i$ and $\hat{q}_i$ are the output values predicted by the meta-model. The accuracy of the output prediction of the neural network can be judged by the closeness of the value R^2 to the target value of 1.0, which expresses an exact match of the network prediction and the output of the full model. This quantity is computed both using the calibration set and a new set of input/output values, called validation or verification set. In the latter case, a qualitative indication of the generalization capabilities of the network is obtained.

The freely available Fast Artificial Neural Network (FANN) library [25], which is an implementation of the here discussed Neural Network and learning algorithm, has been used for the approximation of the modal properties in the following numerical example.

5 Numerical Example: GOCE Satellite

5.1 Problem Statement

The use of a meta-model within the Bayesian updating procedure is illustrated using the Gravity Field and Steady-State Ocean Circulation Explorer (GOCE) satellite. The mission of the GOCE satellite is to determine the geoid and to measure the gravitational field of Earth with a very high degree of accuracy in a low Earth orbit. The particularities of the GOCE are its arrow-shape with winglets and its ion propulsion engine, used to compensate the air-drag induced orbit-decay. The total length of the satellite is 5.3 m, and the mass amounts to approximately 1,000 kg including the fuel of the propulsion system.

Figure 13.2 shows the FE model of the satellite, provided by Thales Alenia Space (Italy) for use within the commercial FE code MSC.Nastran [26]. Approximately 360,000 DOFs and 74,000 elements compose the FE model, with half of the elements used in the main satellite platform and half in the gravitational gradiometer.

In the main GOCE platform, quadrilateral (QUAD4) and triangular (TRIA3) shell elements are used to model the body panels, the wings and the winglets, the

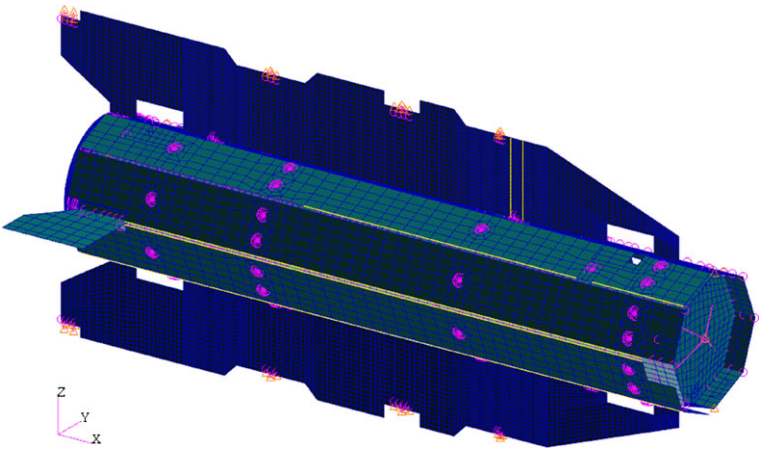

Fig. 13.2 FE model of the GOCE satellite (courtesy of Thales Alenia Space Italy)

internal floors and the solar panels. Beam elements (BAR, ROD and BEAM) constitute the connections of the wings to the main structure and of the instrumentation to the floors. Solid elements (HEXA and PENTA) are used in the Launch Vehicle Adapter (LVA) ring, and scalar spring elements (CELAS2) represent the connection between the solar panels and the structure, as well as the fixing of the wing to the main octagonal body.

A total number of 18 groups combining 3047 structural parameters are defined according to the type and location of the respective materials or geometric specifications (see Table 13.1). This grouping is carried out with the purpose of remarkably reducing the number of parameters to be used within the Bayesian updating procedure since an independent processing of all involved parameters might become infeasible. Hence, the updating procedure is carried out with the goal of identifying as to which changes have to be performed to the single parameter groups in order to obtain a better agreement of the numerical model with the real satellite structure.

5.2 Experimental Modal Data

The experimental data used for model updating consists of $N_s = 1$ set of 7 modal frequencies and partial mode shapes vectors (83 components) which have been determined from the vibration responses during the GOCE structural model qualification test. The dynamic qualification test was performed on the multi-axis vibration test facility of ESA/ESTEC in Noordwijk (The Netherlands). The correlation of the experimental and computed eigenvectors of the initial model is shown by means of the MAC matrix in Fig. 13.3 and the initial comparison of the eigenfrequencies can be found in Table 13.2. The large discrepancies, especially for the first two modes, arise the need for model updating which will be discussed in the following.

Table 13.1 Definition of the groups of parameters of the GOCE satellite

Group no.	Parameters
1	Young's modulus of isotropic materials
2	Poisson's ratio of isotropic materials
3	Young's modulus in the principal direction of orthotropic materials
4	Young's modulus in the secondary direction of orthotropic materials
5	Poisson's ratio of orthotropic materials
6	In-plane shear modulus of orthotropic materials
7	First out-of-plane shear modulus of orthotropic materials
8	Second out-of-plane shear modulus of orthotropic materials
9	Densities of the materials
10	Thicknesses of the shells
11	Linear elastic connections of panels to the main satellite structure
12	Linear elastic connections of panels to the satellite wings
13–18	Linear elastic connections of the wings to the main satellite structure

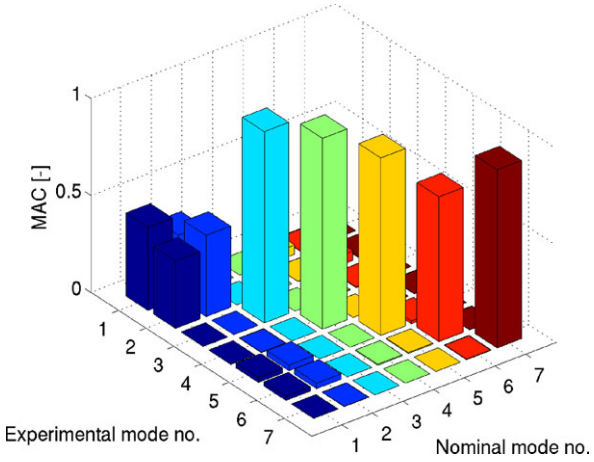

Fig. 13.3 Initial MAC values obtained with the nominal model and the experimental data $\hat{\psi}$

5.3 Accuracy Analysis of the Neural Network

A set of $N_{data} = 2{,}000$ finite element simulations have been performed using Gaussian distributions with the mean values equal to the nominal values and coefficients of variation of 10%. Out of these samples, 1,900 have been dedicated to calibrate the neural networks, and 100 have been kept to verify the generalization capabilities of the networks after training. Each of the 14 neural networks, constituted by $N_{inp} = 18$ inputs and $N_{out} = 1$ output, predicts either one of the eigenfrequencies or one of the diagonal terms of the MAC matrix.

Table 13.2 Comparison of the analytical eigenfrequencies f_a and the experimental data f_e

Mode no.	f_a [Hz]	f_e [Hz]	Δ [%]
1	18.43	15.98	13.29
2	18.37	16.40	10.69
3	28.84	29.59	−2.60
4	34.96	33.33	4.66
5	46.90	48.91	−4.28
6	49.13	51.61	−5.04
7	65.81	61.35	6.77

An automated training procedure has been implemented such that various network topologies are tested and the best networks, characterized by the highest R^2 value (see Eq. (13.18)) obtained with the verification data, are kept. As an indication of the accuracy of the network, Fig. 13.4 shows the regression plots for the neural network of the first eigenfrequency, using the calibration and verification data, respectively. Moreover, the values of R^2 of all the networks obtained with the verification data are listed in Table 13.3.

5.4 Bayesian Model Updating

The prior distributions assigned to the 18 groups of parameters to be updated are all Gaussian with the moments as specified for the calibration of the neural networks. For these ranges, the neural networks of the considered modal properties show high accuracy as discussed in the previous section and are therefore applied for substituting the full FE-analysis when evaluating the likelihood function within the updating process.

The results of the updating procedure are shown exemplary for three parameter groups, namely the thickness, the Young's moduli of the orthotropic materials and the group of stiffnesses of joints between the wings and the main structure (groups no. 10, 3 and 14 in Table 13.1). The prior and posterior histograms of these parameters, which are all transformed in standard normal space, are depicted in Figs. 13.5, 13.6 and 13.7. This representation in standard normal space is advantageous due to the fact that these figures do not show one single parameter each but a parameter group, where the members of each group may have different initial values. Hence, in order to obtain the posterior values in physical space, a back-transformation has to be performed for each parameter of a group, which is achieved by

$$\theta_i = \theta_i^* \sigma_i + \theta_{i,\mathrm{nom}}, \tag{13.19}$$

where θ_i denotes the i-th parameter in the physical space, θ_i^* the value in the standard normal space, σ_i the prior standard deviation and $\theta_{i,\mathrm{nom}}$ the prior (nominal) mean of this parameter.

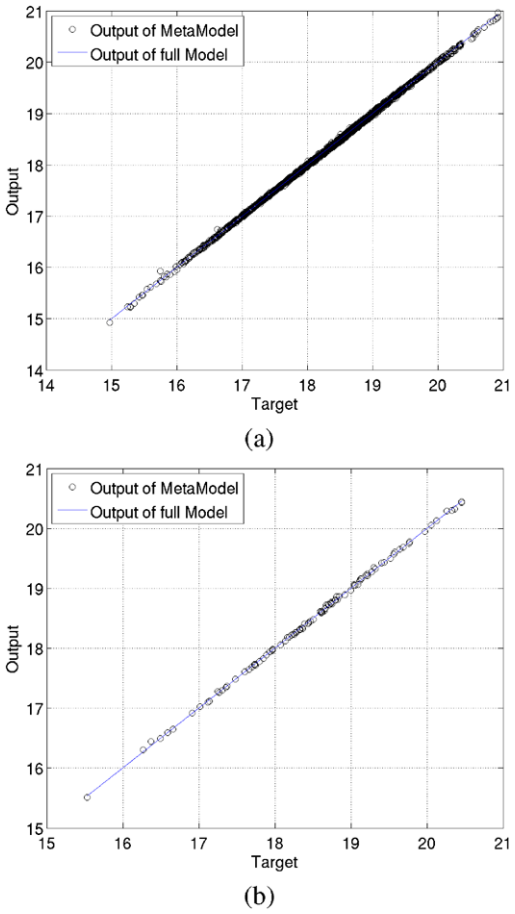

Fig. 13.4 Regression plot of the output of the neural network of the first eigenfrequency for (**a**) calibration data and (**b**) verification data

In Fig. 13.5, the prior and posterior histograms of the thickness of shell elements are depicted. This figure leads to the conclusion that the information contained in the experimental data suggests a decrease of these values. A reduction of approximately 10% of the mean value of the prior distribution leads to a better fit with the experimental modal properties. Also for the Young's modulus of the orthotropic material in the longitudinal direction (material card MAT8 in the MCS.Nastran input file), the updating process suggests a decrease of the mean values (see Fig. 13.6). As opposed to these two parameter groups, all other 16 out of 18 parameter groups used in the updating process show small changes if compared to the prior distribution. As an example, the stiffness values of the joints of the main structure to the wings (used for the specification of the CELAS2 elements in the MCS.Nastran input file) is shown in Fig. 13.7. Due to the information extracted from the experimental values, the prior uncertainty about these parameters could be reduced which is visible through the smaller variation of the posterior distribution.

Table 13.3 R^2 values of the 14 neural networks

Neural network output	R^2 of verification data
Frequency 1	0.99960
Frequency 2	0.99966
Frequency 3	0.99968
Frequency 4	0.99957
Frequency 5	0.88299
Frequency 6	0.97804
Frequency 7	0.95822
$MAC_{1,1}$	0.99886
$MAC_{2,2}$	0.99782
$MAC_{3,3}$	0.99577
$MAC_{4,4}$	0.99861
$MAC_{5,5}$	0.94947
$MAC_{6,6}$	0.97623
$MAC_{7,7}$	0.82779

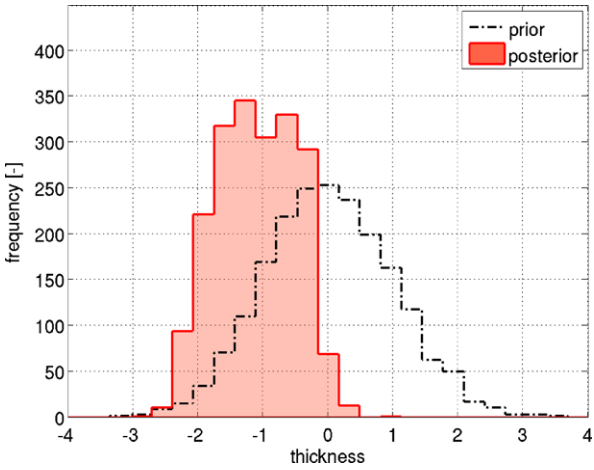

Fig. 13.5 Histograms of the prior and posterior samples of the group of thicknesses (group no. 10 in Table 13.1)

The effect of the choice of the prior on the posterior distribution has not been investigated in this example, however a few remarks will be added in this context: in general, the influence of the prior distribution on the results decreases with increasing amount of experimental data. This is due to the fact that the likelihood function becomes the dominant term in comparison to the prior distribution in Eq. (13.2). In this case, also values in the tails of the prior distribution can be identified and only values with zero probability (e.g. values out of the interval of uniform distributions) cannot be reached since they are excluded from the possible solution space due to the prior knowledge. In case of limited data the selection of the prior distribution clearly has an influence on the results. The prior distribution can therefore be seen

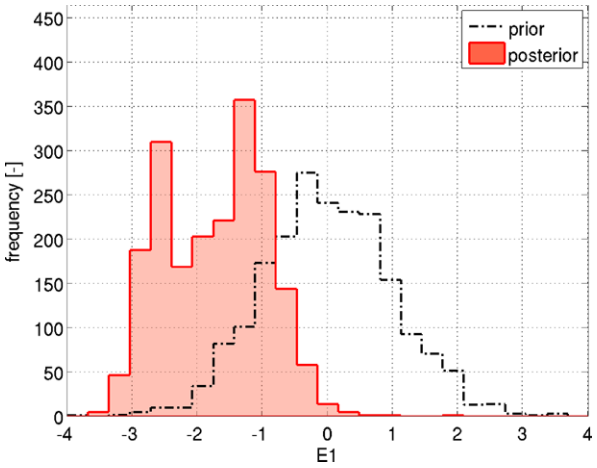

Fig. 13.6 Histograms of the prior and posterior samples of the group of Young's moduli of the orthotropic materials (group no. 3 in Table 13.1)

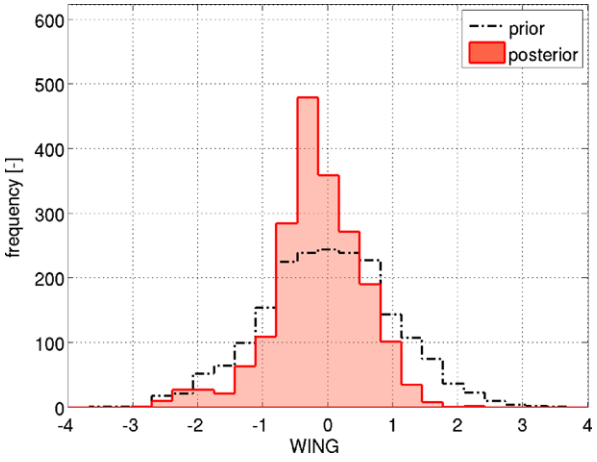

Fig. 13.7 Histograms of the prior and posterior samples of the group of stiffnesses of the joints between wings and main structure (group no. 14 in Table 13.1)

as a means to incorporate initial knowledge about parameter ranges into the identification process and it is subjective in the sense that people with different experience may use different priors leading to broader ranges of the solution in case smaller amount of prior information is available. The selection can therefore be seen as part of the modeling process since also the model itself is affected by a certain amount of subjectivity of the designer. However, the probability content of the prior PDF is updated by the data and if one felt uncomfortable with the choice of the prior distribution the effect of different prior PDFs on the posterior PDF can be studied.

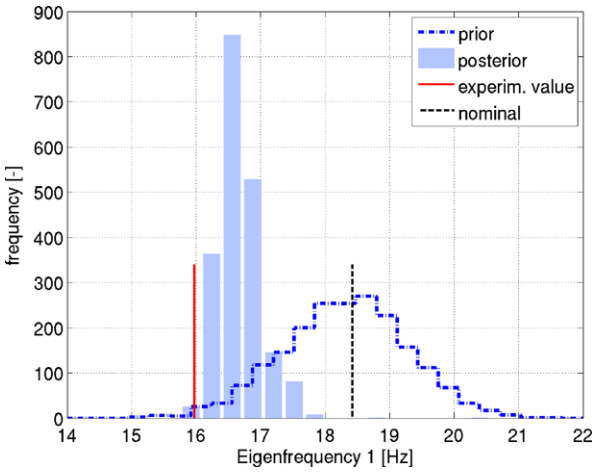

Fig. 13.8 Prior (*dashed-dotted line*) and posterior (*shaded bars*) histograms of the 1st eigenfrequency with experimental value (*solid line*) and nominal value (*dashed line*)

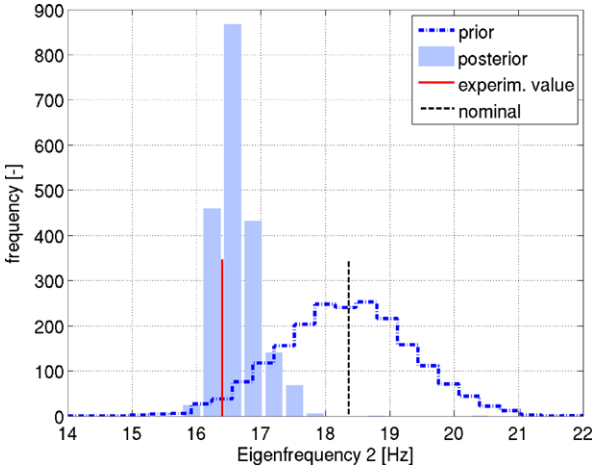

Fig. 13.9 Prior (*dashed-dotted line*) and posterior (*shaded bars*) histograms of the 2nd eigenfrequency with experimental value (*solid line*) and nominal value (*dashed line*)

5.5 Effect on the Correlation of Modal Data

The effect of the updating procedure on the correlation of the experimental and computed modal properties is shown exemplary for the two lowest and highest considered modes. Figures 13.8, 13.9, 13.10 and 13.11 are devoted to the eigenfrequencies and Fig. 13.12 to the corresponding diagonal MAC-values. The figures show that a successful shift of the PDFs towards the experimental values could be achieved, as it can be seen for modes 1, 2 and 7, where it shall be annotated that the correlation of the eigenvector no. 7 with respect to the corresponding experimental data reveals to be high already for the initial model (initial $\mathrm{MAC}_{7,7} = 0.92$).

However, for the 6th eigenfrequency and eigenvector no improvement could be achieved. The reasons might lie in the fact that there is no parameter combination possible which affects an improvement of the fit with respect to all 14 target values

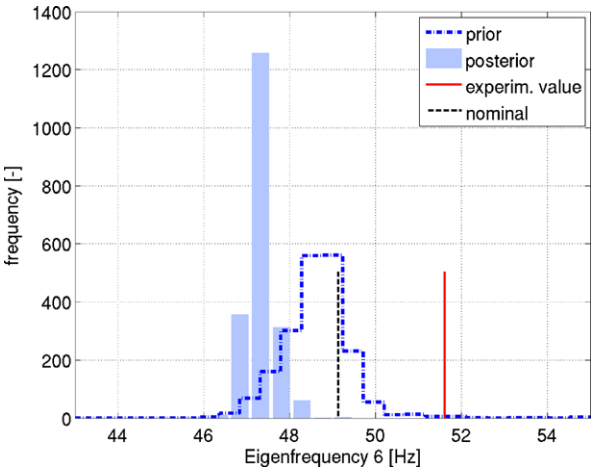

Fig. 13.10 Prior (*dashed-dotted line*) and posterior (*shaded bars*) histograms of the 6th eigenfrequency with experimental value (*solid line*) and nominal value (*dashed line*)

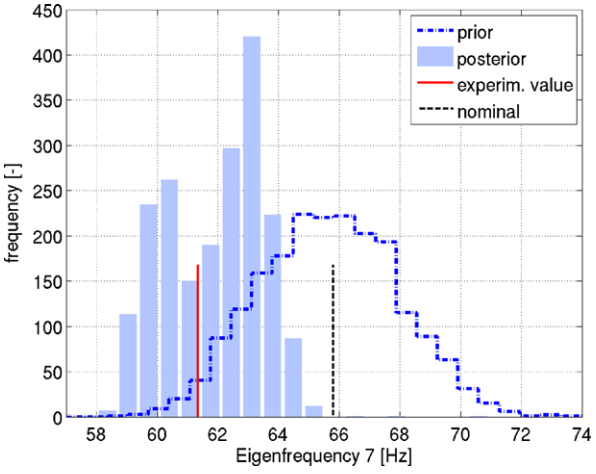

Fig. 13.11 Prior (*dashed-dotted line*) and posterior (*shaded bars*) histograms of the 7th eigenfrequency with experimental value (*solid line*) and nominal value (*dashed line*)

defined by the first 7 modal frequencies and mode shape vectors. Only a revision of the model itself might lead to the situation where the prior distributions span the full solution space, meaning that posterior samples provoke a high correlation with all targets. This example uses real experimental data in the Bayesian updating procedure, thus a fit with respect to all targets might not be possible without revising the FE-model itself.

5.6 Computational Aspects

In this example, the eigensolution of the full FE-model is replaced by an approximate relation at low computational costs which is given by a neural network for

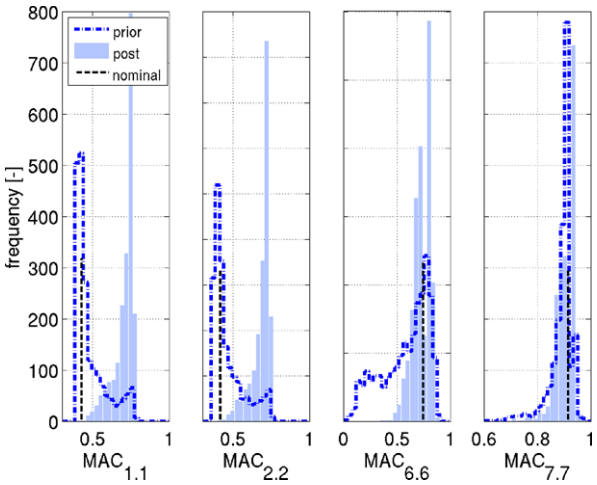

Fig. 13.12 Prior (*dashed-dotted line*) and posterior (*shaded bars*) histograms of the diagonal terms of the MAC matrix corresponding to modes no. 1, 2, 6 and 7 and nominal values (*dashed lines*)

each modal property. If considering that on the above described dual quad-core Xeon server (i) the replacement of the nominal parameter values θ_{nom} by the current value θ in the FE-input file, the normal mode analysis of the full model performed with MSC.Nastran and the import of the modal quantities into Matlab [27] requires 220 s (please see the Appendix for details on the interaction of Matlab with MSC.Nastran), (ii) the updating process of the present model involves approximately 32 iterations $\times$ 2,000 eigensolutions and (iii) the remaining part of the updating process lasts for about 96 min, then the total time amounts up to a theoretical value of

$$t_{\text{full}} = 64{,}000 \cdot 220 \text{ s} + 96 \cdot 60 \text{ s} \approx 160 \text{ days}.$$

The computational time of 220 s of a normal mode analysis of the full FE-model is replaced by the evaluation of the neural networks which takes 0.0014 s. Hence, in this way the analysis time can be remarkably reduced to

$$t_{\text{NN}} = 64{,}000 \cdot 0.0014 \text{ s} + 96 \cdot 60 \text{ s} \approx 100 \text{ min}.$$

However, it shall be noted that in addition 2,000 calibration samples have been generated (see Sect. 5.3), which require evaluations of the full FE-model lasting for a total time of approximately 5 days if performed sequentially (please refer to the Appendix for the interaction with 3rd party software).

6 Conclusions

In this manuscript, the basic steps of model updating within the Bayesian framework using modal data have been summarized and strategies for reducing the analysis time are proposed. The numerical example shows the applicability of the Bayesian updating procedure on complex aerospace structures. It demonstrates that

```
MAT1, 1, <cossan name="E" format="%8.2e" original="7.e+10"/>,,
<cossan name="nu" format="%8.2e" original="0.33"/>,
<cossan name="rho" format="%8.2e" original="2000."/>,
2.40E-5, 20.0000
```

Fig. 13.13 Excerpt of a master input file with identifiers

```
MAT1, 1, 6.13e+10,, 3.98e-01, 2.22e+03, 2.40E-5, 20.0000
```

Fig. 13.14 Excerpt of a stochastic analysis input file with sampled values

ill-conditioned inverse problems in the high-dimensional parameter space can be tackled and that the limited, incomplete data can be used for reducing the initial uncertainty about the adjustable parameters. As a remedy for the large computational efforts of model updating the establishment of a surrogate model has been proposed which approximates the modal properties at a low computational cost. In this way, model updating of a finite element model of a full satellite structure of a size of approximately 360,000 DOFs becomes feasible as shown in the numerical example.

Acknowledgements This research was partially supported by the European Space Agency (ESA) under Contract No. 20829/07/NL/EM, which is gratefully acknowledged by the authors. The authors thank Thales Alenia Space Italy for the FE-model of the GOCE satellite and the experimental modal data. The first author is a recipient of a DOC-fForte-fellowship of the Austrian Academy of Science at the Institute of Engineering Mechanics (University of Innsbruck).

Appendix: Interaction with 3rd Party Software

FE models are defined uniquely by one or more ASCII input files. These files contain the definition of the nodes and elements constituting the model, as well as the structural parameters and boundary and loading conditions in form of fixed numerical values. However, in a stochastic analysis some of these values change, since they are samples from a given probability distribution function. Thus, it is envisioned to automatically manipulate the input files such that in each simulation the respective sample values are inserted into the FE-input file. For this purpose, XML-like tags, called identifiers, are inserted into the master input files in order to define the parameters which have to be changed in each simulation, as shown in Fig. 13.13. An identifier defines the name of the random variable used within the stochastic analysis, the format in which the number is written into the file as well as the original value of the parameter.

The code used to drive the simulation is COSSAN-X, a software for computational stochastic structural analysis [28]. This code parses the master input files in order to identify the positions and the insertion formats of all variables. In each analysis, these identifiers are replaced by sampled numerical values, obtaining a valid input file which is then used for the finite element analysis (see Fig. 13.14). It shall be noted that this software is not restricted to a particular FE-code, but it is applicable to any FE-solver which uses ASCII input files.

References

1. European Cooperation for Space Standardization: Space engineering: modal survey assessment. ECSS-E-ST-32-11C (2008)
2. The American Institute of Aeronautics and Astronautics: Guide for the verification and validation of computational fluid dynamics simulations. AIAA Standards Series G-077 (1998)
3. The American Society of Mechanical Engineers: Guide for verification and validation in computational solid mechanics. ASME V&V (10) (2006)
4. Göge, D., Link, M.: Assessment of computational model updating procedures with regard to model validation. Aerosp. Sci. Technol. **7**, 47–61 (2003)
5. Calvi, A., Garcia de Paredes, S., Roy, N., Lefevre, Y.: On the development of a stochastic approach for the validation of spacecraft structural dynamic models. In: Proceedings of the European Conference on Spacecraft Structures, Materials and Mechanical Testing (CD-ROM), Toulouse, France (2002)
6. Friswell, M., Mottershead, J.: Finite Element Model Updating in Structural Dynamics. Kluwer Academic, Norwell (1995)
7. Girard, A., Roy, N.: Structural Dynamics in Industry. Wiley, New York (2008)
8. Buffe, F.: Application of updating methods on the finite element model of Picard. In: European Conference on Spacecraft Structures, Materials and Mechanical Testing (ECSSMMT 2009 CD-ROM), Toulouse, France (2009)
9. Göge, D., Link, M.: Results obtained by minimizing natural frequencies and mode shape errors of a beam model. Mech. Syst. Signal Process. **17**(1), 21–27 (2003)
10. Calvi, A.: Uncertainty-based loads analysis for spacecraft: finite element model validation and dynamic responses. Comput. Struct. **83**(14), 1103–1112 (2005)
11. Beck, J., Katafygiotis, L.: Updating models and their uncertainties. I: Bayesian statistical framework. J. Eng. Mech. **124**(4), 455 (1998)
12. Katafygiotis, L., Beck, J.: Updating models and their uncertainties. II: model identifiability. J. Eng. Mech. **124**(4), 463 (1998)
13. Yuen, K.-V.: Bayesian Methods for Structural Dynamics and Civil Engineering. Wiley, New York (2010)
14. Ching, J., Chen, Y.-C.: Transitional Markov chain Monte Carlo method for Bayesian updating, model class selection, and model averaging. J. Eng. Mech. **133**, 816–832 (2007)
15. Kleijnen, J., Sargent, R.: A methodology for fitting and validating metamodels in simulation. Eur. J. Oper. Res. **124**(1), 14–29 (2000)
16. Rumelhart, D., McClelland, J.: Parallel Distributed Processing, Exploration in the Microstructure of Cognition, vol. 1. MIT Press, Cambridge (1986)
17. Rumelhart, D., McClelland, J.: Parallel Distributed Processing, Exploration in the Microstructure of Cognition, vol. 2. MIT Press, Cambridge (1986)
18. Bayes, T.: An essay towards solving a problem in the doctrine of chances. Philos. Trans. R. Soc. Lond. **53**, 370–418 (1763)
19. Jaynes, E.: Probability Theory: The Logic of Science. Cambridge University Press, Cambridge (2003)

20. Vanik, M., Beck, J., Au, S.-K.: Bayesian probabilistic approach to structural health monitoring. J. Eng. Mech. **126**, 738–745 (2000)
21. Metropolis, N., Rosenbluth, A., Rosenbluth, M., Teller, A., Teller, E.: Equations of state calculations by fast computing machines. J. Chem. Phys. **21**(6), 1087–1092 (1953)
22. Hastings, W.: Monte Carlo sampling methods using Markov chains and their applications. Biometrika **57**(1), 97–109 (1970)
23. Anderson, J.: Introduction to Neural Network. MIT Press, Cambridge (1995)
24. Bishop, C.: Neural Networks for Pattern Recognition. Oxford University Press, London (1995)
25. Nissen, S.: Implementation of a fast artificial neural network library (fann). Technical report, Department of Computer Science University of Copenhagen (DIKU) (2003)
26. MSC.Software Corporation: MSC.NASTRAN, version 2007.1.0. Santa Ana, CA, USA (2007)
27. The MathWork: Matlab R2009b. Natick, MA, USA (2009)
28. COSSAN-X: COmputational Stochastic Structural ANalysis. Chair of Engineering Mechanics, University of Innsbruck, Innsbruck, Austria, EU (2010)

Chapter 14
Identification of Properties of Stochastic Elastoplastic Systems

Bojana V. Rosić and Hermann G. Matthies

Abstract This paper presents the parameter identification in a Bayesian setting for the elastoplastic problem, mathematically speaking the variational inequality of a second kind. The inverse problem is formulated in a probabilistic manner in which unknown quantities are embedded in a form of the probability distributions reflecting their uncertainty. With the help of the stochastic functional analysis the update procedure is introduced as a direct, purely algebraic way of computing the posterior, which is comparatively inexpensive to evaluate. Such formulation involves the process of solving the convex minimisation problem in a stochastic setting for which the extension of classical optimization algorithm in predictor-corrector form as the solution procedure is proposed. A validation study of identification procedure is done through a series of virtual experiments taking into account the influence of the measurement error and the order of approximation on the posterior estimate.

Keywords Linear Bayesian update · Stochastic Galerkin method · Stochastic elastoplasticity · Stochastic convex minimisation

1 Introduction

In recent years several mathematical models have been proposed to predict the yielding and elastoplastic behavior of heterogeneous materials. Even though these models carry some confidence as to own fidelity, they can not be taken as realistic as the most of quantities entering the model are only incompletely known, i.e. uncertain. In order to give the more reliable description we try to identify these quantities from the given experimental data (system response). However such identification is often regarded as ill-posed due to limited size of the measurement data. In order to resolve this problem various approaches have been proposed, from which the most often uti-

B.V. Rosić (✉) · H.G. Matthies
Institut für Wissenschaftliches Rechnen, TU Braunschweig, Braunschweig, Germany
e-mail: bojana.rosic@tu-bs.de

H.G. Matthies
e-mail: wire@tu-bs.de

M. Papadrakakis et al. (eds.), *Computational Methods in Stochastic Dynamics*, Computational Methods in Applied Sciences 26,
DOI 10.1007/978-94-007-5134-7_14,

lized is the Bayesian regularisation technique described in [23] together with its all possible variants.

In this work we use the so-called Bayesian type of regularisation, a probabilistic approach employing an additional—prior—information on the material property q next to the measurement data. The prior information is usually posed in a form of a distribution function obtained from the maximum entropy principle [26] under given constraints—known properties of q (e.g. positive definiteness, boundness etc.). In this manner the unknown parameter q is modelled as a random variable whose probabilistic description is further altered with the help of the measurement data to the so-called posterior model.

In order to extract the information from the posterior most estimates take the form of expectations (integrals) w.r.t. the posterior. Higdon et al. [6], Gamerman et al. [3] and Tarantola et al. [27] estimate these integrals with the help of the Markov chain Monte Carlo (MCMC) method. By letting the Markov chain to run sufficiently long time the posterior distribution is approached in an asymptotic manner. Regarding this the asymptotic approach is relatively simple and straightforward, though the obtained samples are not any more independent. As opposite to simplicity the MCMC computational efficiency is not so satisfactory due to slow convergence rates; and hence for an efficient run the method requires fewer simulations of the prior model. This can be achieved by a polynomial chaos (PC) [5, 28] or a Karhunen–Loève (KL) approximation [4, 7, 13] of the prior distribution and corresponding observations as presented in [10, 12].

The approaches mentioned above require a large number of samples in order to obtain satisfactory results. In contrast to this the main idea here is to do the Bayesian update directly on the polynomial chaos expansion (PCE) without any sampling [15, 17, 22, 23]. This idea has appeared independently in [1] in a simpler context, whereas in [24] it appears as a variant of the Kalman filter (e.g. [8]). A PCE for a push-forward of the posterior measure is constructed in [16].

The paper is organized as follows: in Sect. 2 we briefly describe the Bayesian formulation of the inverse problem, which is then reduced to a linear update formula in Sect. 3 with the help of the theory of conditional expectations and minimum variance estimation. Such update procedure is based on the polynomial chaos approximation of the system response obtained via stochastic Galerkin method as presented in Sect. 4. Finally in Sect. 5 we test the update procedure on two numerical examples in plain strain conditions.

2 Bayesian Updating

The elastoplastic system is modelled by an evolution equation for its state:

$$\frac{\partial}{\partial t}u(t) + A\big(p; u(t)\big) = f(p; t), \tag{14.1}$$

where $u(t) \in \mathcal{U}$ describes the state of the system at time $t \in [0, T]$ lying in a Hilbert space $\mathcal{U}$ (for the sake of simplicity), A is the nonlinear operator modelling the physics of the system, and $f \in \mathcal{U}^*$ is some external influence (action/excitation/loading). The model depends on a set of parameters $p \in \mathcal{P}$ with corresponding subset $q \subset p$ representing the material properties such as yield stress σ_y, bulk K and shear G modulus.

The process of identifying q by observing a function of the state $Y(u(q), q) \in \mathcal{Y}$ (e.g. the stress, strain etc.) is called the inverse problem. As one can only observe a finite number of quantities the space $\mathcal{Y}$ is finite dimensional and hence the mapping $q \mapsto Y(q)$ is usually not invertible. However, in practice that is not the case as the parameter set q is only incompletely known (uncertain). Regarding this we may model it as a mapping $q(\omega) : \Omega \to \mathcal{Q}$ (i.e. random variable) on a probability space $(\Omega, \mathfrak{A}, \mathbb{P})$ with Ω being the set of all events, $\mathfrak{A}$ a σ-algebra of subsets of Ω and $\mathbb{P}$ a probability measure. This a priori information originates from the maximum entropy principle [26] based on the available information we have on properties of q (i.e. K, G and σ_y). In addition to this, the measurement data y in real experiments are "polluted" by some kind of noise ε, often assumed to be of additive type, i.e. $y = z + \varepsilon$, where $z := Y(q)$.

Only with the previous assumptions in mind the inverse problem becomes well-posed and reduces to a comparison of the forecast obtained from the forward problem (the system response on prior q) with the actual information—so-called Bayesian inference. Its practical realisation generally classifies into two groups: the one performing by changing the probability measure $\mathbb{P}$ and leaving the mapping $q(\omega)$ as it is, whereas the other set of methods leaves the probability measure unchanged and updates the function $q(\omega)$. See [23] for synopsis.

3 Linear Bayesian Update

The probability of an event is the same as the expected value of the indicator variable for that event, which may help us to reformulate the full Bayesian update

$$\mathbb{P}(I_q|M_y) = \frac{\mathbb{P}(M_y|I_q)}{\mathbb{P}(M_y)}\mathbb{P}(I_q), \tag{14.2}$$

in terms of conditional expectations. According to [9] the conditional probability $\mathbb{P}(I_q|M_y)$ is equal to conditional expectation $\mathbb{E}(\chi_q|y)$ where M_y is the information provided by a measurement and χ_q is the characteristic function of some subset of possible q's. Defining the conditional expectation $\mathbb{E}(q|\sigma(Y))$ measurable w.r.t. $\sigma(Y)$ for the sub-σ-algebra $\mathfrak{S} = \sigma(Y)$ generated by Y, we may state that $\mathbb{E}(q|\sigma(Y)) = H(Y)$ for some measurable $H \in \mathcal{L}(\mathcal{Y}; \mathcal{Q}) \subset L_0(\mathcal{Y}; \mathcal{Q})$ according to *Doob–Dynkin* lemma [2]. Here we limit ourselves to the vector space $\mathcal{L}(\mathcal{Y}; \mathcal{Q})$ of linear measurable maps from $\mathcal{Y}$ to $\mathcal{Q}$. The more general case is considered in [23].

Following previous statements the linear approximation of the full Bayesian update derived in [17, 22, 23] can be written as the orthogonal projection $P_{\mathcal{Q}_l}$ of q onto

the subspace $\mathcal{Q}_l = \overline{\text{span}}\{H(Y(q)) \in \mathcal{Q} | H \in \mathcal{L}(\mathcal{Y}; \mathcal{Q})\} \subset \mathcal{Q} := \mathcal{Q} \otimes L_2(\Omega)$, i.e.:

$$\begin{aligned} K &= \mathbb{E}\big(q|\sigma(Y)\big) = P_{\mathcal{Q}_l}(q) \\ &= \underset{\tilde{q}\in\mathcal{Q}_l}{\arg\min} \|q - \tilde{q}\|^2_{\mathcal{Q}} \\ &= \underset{H\in\mathcal{L}(\mathcal{Y},\mathcal{Q})}{\arg\min} \big\|q - H\big(Y(q)\big)\big\|^2_{\mathcal{Q}}. \end{aligned} \tag{14.3}$$

The optimal K is not hard to find by taking the derivative in Eq. (14.3) w.r.t. the linear map H (see e.g. [8, 11]) and requiring the derivative to vanish. This further leads to the formula (see e.g. [18, 22]):

$$q_a = q_f + K(y - z_f) \tag{14.4}$$

representing the so-called linear Bayesian update. Note that Eq. (14.4) in the mean reduces to the familiar Kalman filter formula [8, 18].

Finally, the update in Eq. (14.4) employs the measurement data y and assimilates it with both, the prior (forecast) information q_f and the measurement forecast z_f, to the posterior value q_a through the Kalman gain K. The gain[1] is computed as

$$K = C_{q,z}(C_z + C_\varepsilon)^\dagger \tag{14.5}$$

where the corresponding covariances are given as

$$\begin{aligned} C_{q,z} &= \mathbb{E}\big(\big(q - \mathbb{E}(q)\big) \otimes \big(Y(q,u) - \mathbb{E}\big(Y(q,u)\big)\big)\big) \\ C_z &= \mathbb{E}\big(\big(Y(q,u) - \mathbb{E}\big(Y(q,u)\big)\big) \otimes \big(Y(q,u) - \mathbb{E}\big(Y(q,u)\big)\big)\big) \end{aligned} \tag{14.6}$$

together with C_ε being the covariance of the measurement noise ε. The last one is often assumed to be of Gaussian type i.e. $C_\varepsilon = \sigma^2_\varepsilon I$.

3.1 Sampling Free Update

In order to numerically compute the linear formula in Eq. (14.4) one has to discretise the space $\mathcal{Q} := \mathcal{Q} \otimes \mathcal{S}$, $\mathcal{S} := L_2(\Omega)$. This is performed by taking the finite element discretisation $\mathcal{Q}_M$ of $\mathcal{Q}$ and a finite subset $\mathcal{S}_J = \text{span}\{H_{\boldsymbol{\alpha}} : \boldsymbol{\alpha} \in \mathcal{J}\}$ of $\mathcal{S}$, where $\mathcal{J}$ is the finite set of multi-indices with cardinality $J = |\mathcal{J}|$ and $H_{\boldsymbol{\alpha}}$ the multivariate Hermite polynomial in Gaussian random variables $\boldsymbol{\theta}$. The orthogonal projection P_J onto $\mathcal{S}_J$ is then simply

$$P_J : \mathcal{Q}_M \otimes \mathcal{S} \ni \sum_{\boldsymbol{\alpha}\in\mathcal{N}} \boldsymbol{q}^{\boldsymbol{\alpha}} H_{\boldsymbol{\alpha}} \mapsto \sum_{\boldsymbol{\alpha}\in\mathcal{J}} \boldsymbol{q}^{\boldsymbol{\alpha}} H_{\boldsymbol{\alpha}} \in \mathcal{Q}_M \otimes \mathcal{S}_J, \tag{14.7}$$

[1] The Moore–Penrose pseudo-inverse † is used as a general inverse in case $C_z + C_\varepsilon$ is not invertible or close to singularity.

where $\sum_{\boldsymbol{\alpha}\in\mathcal{N}} \boldsymbol{q}^{\boldsymbol{\alpha}} H_{\boldsymbol{\alpha}}$ denotes the polynomial chaos expansion (PCE) of a random variable q. Elements of the discretised space $\mathcal{Q}_{M,J} = \mathcal{Q}_M \otimes \mathcal{S}_J \subset \mathcal{Q}$ thus may be written as $\sum_{m=1}^{M} \sum_{\boldsymbol{\alpha}\in\mathcal{J}} q^{\boldsymbol{\alpha},m} \rho_m H_{\boldsymbol{\alpha}}$ and the tensor representation of parameter set as $\mathbf{q} := (q^{\boldsymbol{\alpha},m}) = \sum_{\boldsymbol{\alpha}\in\mathcal{J}} \boldsymbol{q}^{\boldsymbol{\alpha}} \otimes \boldsymbol{e}^{\boldsymbol{\alpha}}$, where $\boldsymbol{e}^{\boldsymbol{\alpha}}$ are the unit vectors in $\mathbb{R}^J$. With the previous notation the update Eq. (14.4) is simply computed in the PCE representation without any sampling as:

$$\mathbf{q}_a = \mathbf{q}_f + \mathbf{K}(\mathbf{y} - \mathbf{z}_f), \tag{14.8}$$

where $\mathbf{K} = \boldsymbol{K} \otimes \boldsymbol{I}$. The gain $\mathbf{K}$ follows from the formula given in Eq. (14.5), where the covariance $\boldsymbol{C}_{q,z}$ is evaluated via PCE in the following manner

$$\boldsymbol{C}_{q,z} = \sum_{\boldsymbol{\alpha}\in\mathcal{N},\boldsymbol{\alpha}\neq 0} (\boldsymbol{\alpha}!)\boldsymbol{q}^{\boldsymbol{\alpha}} \otimes \boldsymbol{z}^{\boldsymbol{\alpha}} \approx \sum_{\boldsymbol{\alpha}\in\mathcal{J},\boldsymbol{\alpha}\neq 0} (\boldsymbol{\alpha}!)\boldsymbol{q}^{\boldsymbol{\alpha}} \otimes \boldsymbol{z}^{\boldsymbol{\alpha}}, \tag{14.9}$$

and similarly C_z and C_ε.

4 Elastoplastic Problem

Let be given the state variable $w = (u, \varepsilon_p, v) \subset \mathcal{Z} := \mathcal{U} \times \mathcal{P} \times \mathcal{C}$ describing the infinitesimal quasi-static von Mises elasto-plastic behaviour with mixed hardening. Here u denotes the displacement vector, ε_p the plastic deformation and v the appropriate internal hardening variable. Their spaces of definition are $\mathcal{U} := \mathcal{U} \otimes \mathcal{S} = H_0^1(\mathcal{G}) \otimes L_2(\Omega)$, $\mathcal{P} \subset \mathcal{E} = L_2(\mathcal{G}) \otimes \mathcal{S}$ and $\mathcal{C} \subset \mathcal{E}$ respectively. In this notation the variational form of a quasi-static problem in Eq. (14.1) is described by a $\mathcal{Z}$-elliptic and bounded bilinear form

$$a(w, v) = \langle\!\langle \boldsymbol{A} : \big(\varepsilon(u) - \varepsilon_p\big), \varepsilon(u_1) - \varepsilon_p \rangle\!\rangle + \langle\langle \boldsymbol{H} : \eta, \mu \rangle\rangle, \tag{14.10}$$

where $\langle\langle \cdot, \cdot \rangle\rangle$ denotes the duality pairing

$$\langle\langle \boldsymbol{H} : \eta, \mu \rangle\rangle = \int_\Omega \int_\mathcal{G} \boldsymbol{H} : \eta : \mu \, \mathrm{d}x\mathbb{P}(\mathrm{d}\omega), \tag{14.11}$$

ε the total deformation, $\boldsymbol{A}$ the elastic and $\boldsymbol{H}$ the hardening positive-definite constitutive tensor. In a similar manner after multiplication of Eq. (14.1) with the test functions and integration its right hand side transforms to the following functional of a linear type:

$$\ell : \mathcal{Z} \to \mathbb{R} : \quad \ell(v) = \langle\langle f, v \rangle\rangle. \tag{14.12}$$

The definitions Eq. (14.11) and Eq. (14.12) correspond to the conservation law of the momentum balance. However, additionally to this law the system has to satisfy the second law of thermodynamics describing the energy of a system. In a Clausius–Duhelm form the energy law introduces the dissipation functional $j(v)$ also supposed to be the support functional of a closed, non-empty, convex set $\mathcal{K} \subset \mathcal{Z}$ [20].

Thus, following the definition of its sub-differential:

$$\partial j(\dot{w}) := \left\{ w^* \in \mathcal{Z}^* : j(v) \geq j\big(w(t)\big) + \big\langle\!\big\langle w^*(t), v - w(t) \big\rangle\!\big\rangle, \forall v \in \mathcal{Z} \right\} \tag{14.13}$$

after few mathematical steps one may arrive to the mixed variational formulation of the elastoplastic problem (see [20]):

Proposition 1 *Find unique functions* $w \in H^1(\mathcal{T}, \mathcal{Z}^*)$ *and* $w^* \in H^1(\mathcal{T}, \mathcal{Z}^*)$ *with* $w(0) = 0$ *and* $w^*(0) = 0$ *such that the equilibrium equation*

$$a\big(w(t), v\big) + \big\langle\!\big\langle w^*(t), v \big\rangle\!\big\rangle = \big\langle\!\big\langle f(t), v \big\rangle\!\big\rangle \tag{14.14}$$

and the flow rule

$$\forall v^* \in \mathcal{K} : \quad \big\langle\!\big\langle \dot{w}(t), v^* - w^*(t) \big\rangle\!\big\rangle \leq 0 \tag{14.15}$$

are satisfied almost surely on Ω *and for all* $t \in \mathcal{T}$.

Proof The proof of existence, uniqueness and stability of the solution, as well as complete derivation can be found in Rosić et al. [20]. □

Here $w^* \in H^1(T, \mathcal{Z}^*)$ denotes the dual variable $(g, \sigma, \chi) \in \mathcal{U}^* \times \mathcal{R} \times \mathcal{C}$ with g being the force-like variable, σ the Cauchy stress and $\chi := (\varsigma, \zeta)$ the hardening stress with the back-stress ς (kinematic hardening) and the isotropic stress ζ as components.

4.1 Minimisation

The variational inequality Eq. (14.14) may be equivalently formulated as a standard minimisation problem of a convex objective function Φ. In particular we look at a continuous (or bounded $a(v_1, v_2) \leq c\|v_1\|\|v_2\|$), symmetric and $\mathcal{Z}$-elliptic ($a(v, v) \geq c\|v\|^2$) bilinear form $a : \mathcal{Z} \times \mathcal{Z} \to \mathbb{R}$ and an element $\varrho \in \mathcal{Z}^*$ such that the solution w^* in $\mathcal{K}$ is the closest point to ϱ in the a^* metric (*closest point projection*) [20]:

$$w^* = \arg\min_{v^* \in \mathcal{K}} \Phi = \arg\min_{v^* \in \mathcal{K}} \frac{1}{2} a^*\big(\varrho - v^*, \varrho - v^*\big) \tag{14.16}$$

and that there exists some $w \in \mathcal{Z}$ satisfying

$$\forall v \in \mathcal{Z} : \quad a(w, v) = \big\langle\!\big\langle \varrho - w^*, v \big\rangle\!\big\rangle. \tag{14.17}$$

As a and ϱ are continuous and Gâteaux-differentiable, and as a is $\mathcal{Z}$-elliptic, Φ has all desired properties. To handle the dissipation, we have to allow for a second convex functional j on $\mathcal{Z}$, which may not be Gâteaux differentiable everywhere.

4.2 Discretisation

As the elastoplastic problem is time dependent the implicit Euler procedure is used for its discretisation by taking the time step $h := t_n - t_{n-1}$ to be constant over time. Regarding to this the total deformation ε, the Cauchy stress σ, the hardening stress χ and the plastic deformation ε_p are assumed to be known at time t_{n-1}. The goal is to find those variables at time t_n by initially assuming that the increment of the total strain $\Delta\varepsilon_n$ is purely elastic. Note that in such situation the equilibrium Eq. (14.14) depends only on the increment of displacement Δu_n as unknown variable. Moreover, one may rewrite it to the corresponding residual of a nonlinear type:

$$r := \langle\!\langle A[q_n; \Delta u_n], v \rangle\!\rangle - \ell_n(f, v) = 0, \quad \forall v \in \mathcal{U} \tag{14.18}$$

where the nonlinear operator A depends on the parameter set q and the displacement u. Finally, following the residual one may define the measurement operator as

$$z_f = Y(u_n, q_n) = Y(q_n). \tag{14.19}$$

For notational simplicity the index n is dropped from the further text.

Before solving Eq. (14.18) one may notice that the spaces $\mathcal{U}$ and $\mathcal{Z}$ are infinite dimensional, as is the space $\mathcal{S} = L_2(\Omega)$. Thus, for further analysis their finite approximation has to be introduced. In an analogous fashion to Sect. 3.1, let us choose an N-dimensional subspace $\mathcal{U}_N = \text{span}\{\upsilon_j : j = 1, \ldots, N\} \subset \mathcal{U}$ with the piecewise linear basis $\{\upsilon_j\}_{j=1}^N$. Then an element of $\mathcal{U}_N$ can be represented by the vector $\boldsymbol{u} = (u^1, \ldots, uj^N)^T \in \mathbb{R}^N$ such that $\sum_{j=1}^N u^j \upsilon_j \in \mathcal{U}_N$. Similarly, the spaces $\mathcal{P}$ and $\mathcal{C}$ are discretised by piecewise constant functions such that $\mathcal{Z}_N = \mathcal{U}_N \times \mathcal{P}_N \times \mathcal{C}_N$ is appropriate subspace of $\mathcal{Z}$. By inserting those ansatzes into Eq. (14.18) the residual becomes:

$$\boldsymbol{r}(\boldsymbol{u}) := \langle\!\langle A[\boldsymbol{q}; \Delta\boldsymbol{u}], \boldsymbol{v} \rangle\!\rangle - \ell(\boldsymbol{f}, \boldsymbol{v}) = \boldsymbol{0}, \quad \forall \boldsymbol{v} \in \mathcal{U}_N := \mathcal{U}_N \otimes \mathcal{S} \tag{14.20}$$

and the measurement operator:

$$\boldsymbol{z}_f = \boldsymbol{Y}(\boldsymbol{u}, \boldsymbol{q}) = \boldsymbol{Y}(\boldsymbol{q}). \tag{14.21}$$

However, Eq. (14.20), and subsequently Eq. (14.21), are only semi-discretised due to the dependence on the uncertain parameter ω. For MCMC or any other Monte Carlo method [10, 12], Eq. (14.20) has to be solved for each sample point ω_z to obtain $\boldsymbol{u}(\omega_z)$. This then can be used to predict the measurement $\boldsymbol{z}_f(\omega_z) = \boldsymbol{Y}(\boldsymbol{u}(\omega_z), \boldsymbol{q}(\omega_z))$, which may be computationally quite costly. Thus we take another approach by assuming the PCE ansatz for the solution in a form:

$$\boldsymbol{u}(\omega) = \sum_{\alpha \in \mathcal{J}} \boldsymbol{u}^{(\alpha)} H_\alpha\big(\boldsymbol{\theta}(\omega)\big) \tag{14.22}$$

and projecting the residual in a Galerkin manner onto the finite dimensional subspace $\mathcal{S}_J$ according to:

$$\mathbf{r}(\mathbf{u}) = \left[\ldots, \mathbb{E}\left(H_\alpha(\cdot)\boldsymbol{r}(\cdot)\left[\sum_\alpha \boldsymbol{u}_\beta H_\beta\right]\right), \ldots\right] = \mathbf{0}, \tag{14.23}$$

where the block-version of the residual is denoted as $\mathbf{r}(\mathbf{u}) = (\ldots, \boldsymbol{r}^{(\alpha)}(\mathbf{u})^T, \ldots)^T$. In this manner the process of solving the residual Eq. (14.20) reduces to the evaluation of a possibly high-dimensional integral.

The integration of $\mathbb{E}(H_\alpha(\cdot)\boldsymbol{r}(\cdot)[\sum_\alpha \boldsymbol{u}_\beta H_\beta])$ can be done directly via PCE algebra as presented in [21] (Galerkin method) or numerically via high-dimensional integration (pseudo-Galerkin method). Whether we use the first or second approach the computational time of integration drastically reduces in comparison to the direct integration techniques. As the direct algebraic approach is already considered in [21] in this work we choose the pseudo-Galerkin (collocation) approach and compute:

$$\int_\Omega H_\alpha \boldsymbol{r}(\omega)\left[\sum_\beta \boldsymbol{u}^{(\beta)} H_\beta\right] \mathrm{d}\mathbb{P}(\omega) \approx \sum_{z=1}^{L} w_z H_\alpha(\boldsymbol{\theta}_z)\boldsymbol{r}(\boldsymbol{\theta}_z)\left[\sum_\beta \boldsymbol{u}^{(\beta)} H_\beta(\boldsymbol{\theta}_z)\right], \tag{14.24}$$

via the set of integration points $\Theta = \{\boldsymbol{\theta}_z, 1 \le z \le L\}$, $\boldsymbol{\theta} = \{\theta_1, \ldots, \theta_M\}$ with the corresponding weights $\boldsymbol{w} := \{w_z\}_{z=1}^L$. Note that the evaluation of the integral requires L evaluations of the residual, $\boldsymbol{r}(\boldsymbol{\theta}_z)$, $z = 1, \ldots, L$, each corresponding to the numerical integration over the spatial domain $\mathcal{G} \subset \mathbb{R}^d$ done in a classical FEM way. This could be seen as an advantage compared to the intrusive Galerkin method [21], as the FEM code is used in a black-box fashion. On other side, the number of calls of the deterministic software increases drastically with the stochastic dimension which may lead to the expensive or almost impractical procedures.

Once the solution of Eq. (14.20) is found the following procedure collapses to the (iterative) solution of a convex mathematical programming problem, which has for a goal to find the closest distance in the energy norm of a trial state to a convex set $\mathcal{K}$, known as a closest point projection. In other words, one search for the solution of:

$$\Sigma(\omega) = \underset{\Sigma(\omega)\in\mathcal{K}}{\arg\min} \Phi(\omega) \tag{14.25}$$

where

$$\Phi := \underset{\Sigma(\omega)\in\mathcal{K}}{\arg\min}\left[\frac{1}{2}\left\langle\!\left\langle \Sigma^{trial} - \Sigma, \boldsymbol{A}^{-1} : \left(\Sigma^{trial} - \Sigma\right)\right\rangle\!\right\rangle\right] \tag{14.26}$$

and

$$\mathcal{K} := \left\{\Sigma := \left(\sigma(\omega), \chi(\omega)\right) \in \mathcal{R} \times \mathcal{C} \mid \varphi(\Sigma) \le 0 \text{ a.s. in } \Omega\right\}. \tag{14.27}$$

Here $\Sigma := (\sigma(\omega), \chi(\omega))$ denotes the so-called generalised stress and $\Sigma^{trial} = \Sigma_n + \boldsymbol{A} : \Delta\varepsilon$ its corresponding trial stress in time n. Note that the minimisation is done

over the convex set $\mathcal{K}$ described by a von Mises yield function φ which must be non-positive almost surely. However, in order to perform the numerical computation one has first to spatially discretise the problem via $\mathcal{W}_N := \mathcal{R}_N \times \mathcal{C}_N$ and then to relax the almost sure condition by introduction of the discretised substitute of $\mathcal{K}$:

$$\mathcal{K}^\star = \left\{ \Sigma \in \mathcal{W}_N \otimes \mathcal{S}_J \mid \boldsymbol{\varphi}\big(\Sigma(\boldsymbol{\theta}_z)\big) \leq 0, \forall \boldsymbol{\theta}_z \in \Theta \right\}. \tag{14.28}$$

Here the set $\mathcal{K}^\star$ is taken as a set of "deterministic" constraints on a finite number of the integration points Θ. Such construction allows the decoupling of the problem in Eq. (14.25) into L smaller problems, which may be solved independently. Note that each of them corresponds to the normal deterministic optimization problem as presented in [25], for which the closest point projection consists of two steps called the predictor and the corrector step respectively.

Predictor Step The predictor step evaluates the displacement $\boldsymbol{u}_n(\boldsymbol{\theta}_z)$ by solving the equilibrium equation Eq. (14.20) [14, 19] and the strain increment $\Delta\boldsymbol{\varepsilon}_n(\boldsymbol{\theta}_z) = \nabla_s \Delta\boldsymbol{u}_n(\boldsymbol{\theta}_z)$ via linear symmetric mapping ∇_s. Once the increment of strain is computed one may define the trial stress $\boldsymbol{\Sigma}_n^{trial}(\boldsymbol{\theta}_z)$ assuming $\Delta\boldsymbol{\varepsilon}_n(\boldsymbol{\theta}_z)$ to be purely elastic. By checking if the stress $\boldsymbol{\Sigma}_n^{trial}(\boldsymbol{\theta}_z)$ lies outside of the admissible region $\mathcal{K}^*(\boldsymbol{\theta}_z)$ we proceed with the corrector step. Otherwise, $\boldsymbol{\Sigma}_n(\boldsymbol{\theta}_z) = \boldsymbol{\Sigma}_n^{trial}(\boldsymbol{\theta}_z)$ is our solution and we may proceed to the next step.

Corrector Step The purpose of the corrector step is to project the stress outside of admissible region back onto a point in $\mathcal{K}^*(\boldsymbol{\theta}_z)$. To do this, we define the corresponding Lagrangian to a minimisation problem Eq. (14.25):

$$\mathcal{L}(\boldsymbol{\theta}_z) = \Phi_n(\boldsymbol{\theta}_z) + \boldsymbol{\lambda}_n(\boldsymbol{\theta}_z)\varphi_n(\boldsymbol{\Sigma})(\boldsymbol{\theta}_z), \tag{14.29}$$

with $\varphi_n(\Sigma)(\boldsymbol{\theta}_z)$ being the yield function describing the convex set. The solution $\boldsymbol{\lambda}_n(\boldsymbol{\theta}_z)$ is then simply found by taking the derivative

$$\mathbf{0} \in \partial_\Sigma \mathcal{L} = \partial_\Sigma \Phi_n(\boldsymbol{\theta}_z) + \boldsymbol{\lambda}_n(\boldsymbol{\theta}_z)\partial_\Sigma \boldsymbol{\varphi}(\boldsymbol{\theta}_z) \tag{14.30}$$

and solving the corresponding system of equations. Once $\boldsymbol{\lambda}_n(\boldsymbol{\theta}_z)$ is known one may compute the update of the stress- and strain-like variables.

5 Numerical Results

The method considered in this paper is numerically tested on the example of a flat plate containing a circular hole. The plate is constrained on the left edge, and subjected to uniform tension f on the right edge as shown in Fig. 14.1. The material properties describing the elastoplastic behaviour are taken in two different scenarios: homogeneous and heterogeneous case. The homogeneous random quantities q

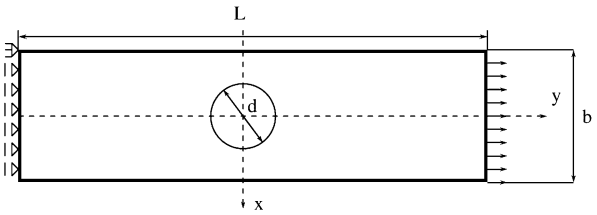

Fig. 14.1 Experimental set up. Here $b = 20$, $L = 56$ and $d = 10$

are modelled as a random variables of lognormal type, more precisely a modified lognormal random variable:

$$\kappa = \kappa_0 + \kappa_1 \exp(\mu + \sigma\theta), \tag{14.31}$$

where κ_0 and κ_1 are constants and θ the standard Gaussian random variable. On other side the heterogeneous case is specified by properties modelled as a lognormal random field (positive-definite):

$$\kappa(x,\omega) = \exp\big(\mu(x) + \sigma(x)\gamma(x,\omega)\big) \tag{14.32}$$

where $\gamma(x,\omega)$ represents the standard Gaussian random field with zero mean and unit variance. In case that one chooses $\mu(x)$ and $\sigma(x)$ as appropriate constants the random field becomes homogeneous in a mean sense, but locally in each realisation heterogeneous.

Due to the lack of the measurement data, the reality is simulated via computer by assuming the true values for q and running the corresponding finite element analysis. For simplicity reasons the truth is taken to be deterministic even though one realisation of some positive definite random field would be more appropriate. Additionally the obtained response is polluted by a Gaussian noise with zero mean and the standard deviation σ_ε.

5.1 Random Variable Update

In this particular example the prior elastoplastic behaviour is described by the random yield stress σ_y and bulk modulus K. Due to their positive definiteness, the mentioned properties are modelled according to Eq. (14.31) by taking for σ_{yf}: $\kappa_0 = 0.1$, $\kappa_1 = 0.25$, $\mu = 0$ and $\sigma = 0.3$ and for K_f: $\kappa_0 = 10$, $\kappa_1 = 15$, $\mu = 1$ and $\sigma = 0.3$. For such chosen probability distributions the corresponding forward response is computed with the help of the pseudo-Galerkin method (and Gauss–Hermite sparse grid) with the polynomial chaos expansion of the maximum order equal to four. More than that is not necessary to take as the input can be already accurately described by polynomial order 3. On other side, the first order polynomial expansion (i.e. Gaussian distribution) is not considered due to the violence of positive-definite requirements on K_f and σ_{yf}.

Table 14.1 The relative mean error ε_m [%] and relative variance ε_v [%] as a function of the PCE order and the number of the measurement points. The measurement is the first stress component

	Bulk modulus							Yield stress						
	p	2	3	4	5	6	7	p	2	3	4	5	6	7
ε_m	2	6.70	6.70	4.81	4.02	2.50	2.50	2	30.62	30.76	20.54	16.32	0.50	0.27
	3	6.70	6.70	4.79	3.92	2.47	2.43	3	30.73	30.79	20.60	16.42	0.78	0.11
	4	6.69	6.69	4.78	3.92	2.46	2.41	4	30.73	30.54	20.62	16.36	0.76	0.10
ε_v	2	14.68	14.31	11.92	9.65	7.35	7.38	2	99.42	97.66	87.65	82.37	48.32	44.06
	3	14.81	14.63	12.23	9.95	7.10	7.14	3	99.37	97.37	87.16	82.12	48.24	44.10
	4	14.80	14.72	12.25	9.96	7.09	7.07	4	99.37	99.37	87.12	82.08	48.12	44.03

In order to simulate the virtual measurement the true values $\sigma_y = 0.5$ and $K = 80$ are adopted together with the uniform tension $f = 10 \cdot t$ in three equal time steps $h = 1$. Further, the finite element analysis is performed by discretising the domain with the different number of elements than the one corresponding to the forward problem in order to escape the violation of the inverse law. The obtained response is then polluted by a Gaussian noise with σ_ε taking the values in a set $\{0.1, 0.01, 0.001\}$. As any kind of response (stress, strain, etc.) can be declared as the measurement quantity, in this work we choose the stress components (as a more abstract than real experiment) or the displacement (corresponding to the experiments performed in reality). In each of these cases the response is measured in 2 up to 7 measurement points mostly concentrated around the hole (where the measurements in reality are expected to be performed).

With respect to the previous description the results after the update are plotted in Table 14.1 for the measurement of the first stress component and noise $\sigma_\varepsilon = 0.01$. As the error estimates we adopt the relative mean error of posterior compared to the truth $\varepsilon_m = 100 \cdot |\mathbb{E}(\kappa_a) - \mathbb{E}(\kappa_t)|/|\mathbb{E}(\kappa_t))$ and the reduction of the variance compared to the prior $\varepsilon_v = 100(\operatorname{var}\kappa_a / \operatorname{var}\kappa_f)$. In Table 14.1 clearly is visible that the bulk modulus K approaches the truth in circa 6% of the mean error already with only two measurement points. This continues to drop to 2% with the number of the measurement points. Similar is valid for the reduction of variance ε_v. In addition to this, the slight decrease of ε_m and ε_v can be observed in the direction of the polynomial order increase. However, this improvement is not very drastic as the second order approximation already accurately describes the prior. Similar results are characterizing the update of the stress variable σ_y, though the errors drop much faster than in a case of K. The reason for this are the placements of the measurement points. Namely, the more points are lying in the plastic area the more informative data for σ_y enter the update process. It is interesting to notice that the mean error becomes smaller than 1%, while the variance more slowly reduces. For this one need more measurement points or possibly nonlinear approximation of Bayesian estimate. Namely, due to the nonlinear relationship between the parameter and data, the linear update as presented in Sect. 3 is not optimal for σ_y.

Table 14.2 The relative mean error ε_m [%] with respect to the number of the measurements in different experiments

Bulk modulus							Yield stress						
z	2	3	4	5	6	7	z	2	3	4	5	6	7
σ_{xx}	6.79	6.73	4.88	4.01	2.57	2.51	σ_{xx}	30.62	30.76	20.54	16.32	0.50	0.27
σ_{yy}	8.70	8.71	5.02	3.73	3.69	2.91	σ_{yy}	31.74	32.10	16.26	8.49	9.19	3.02
σ_{xy}	7.88	7.75	4.68	3.81	3.18	2.80	σ_{xy}	31.21	30.81	15.18	11.29	6.81	2.84
u	39.94	7.59	8.48	7.93	7.85	7.83	u	5.27	2.43	1.98	2.12	2.13	2.13

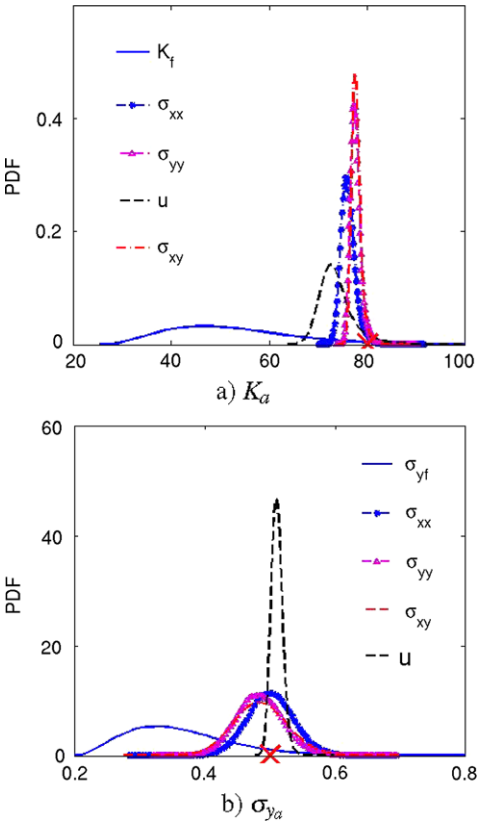

Fig. 14.2 (**a**) The posterior probability density function of bulk modulus in different experiments. (**b**) The posterior density function of yield stress in different experiments. The truth is denoted with *red X*

Following previous discussion in Table 14.2 are studied the results obtained by measuring different quantities such as σ_{xx}, σ_{yy} and σ_{xy} stress components as well as the displacement u (see Fig. 14.2). Here it is interesting to note that the stress measurement brings smaller errors in posterior for K than for yield stress, in both ε_m and ε_v (the later one gathered in Table 14.3). In contrast to this the displacement is more suitable measurement for the value of σ_y. More importantly the higher reduction in the variance is observed (see Table 14.3).

Table 14.3 The relative variance ε_v [%] with respect to the number of the measurements in different experiments

Bulk modulus							Yield stress						
z	2	3	4	5	6	7	z	2	3	4	5	6	7
σ_{xx}	14.68	14.31	11.92	9.65	7.35	7.38	σ_{xx}	99.42	97.66	87.65	82.37	48.32	44.06
σ_{yy}	14.64	18.41	13.47	10.11	9.94	8.79	σ_{yy}	98.80	95.87	80.19	60.23	59.77	45.46
σ_{xy}	17.06	16.67	12.33	9.68	8.14	7.86	σ_{xy}	99.10	98.66	78.22	70.9	63.20	52.42
u	96.92	43.54	33.34	29.35	29.34	18.10	u	28.31	18.55	12.32	11.28	11.27	11.27

Table 14.4 The relative mean ε_m [%] and variance ε_v [%] with respect to the measurement noise

Mean							Variance						
σ_ε	2	3	4	5	6	7	σ_ε	2	3	4	5	6	7
1e-1	9.98	9.95	6.74	5.8	5.65	5.54	1e-1	36.99	36.89	21.74	16.34	16.23	15.91
1e-2	6.79	6.73	4.88	4.01	2.57	2.51	1e-2	14.68	14.31	11.92	9.65	7.35	7.38
1e-3	6.75	6.79	0.95	1.14	1.98	1.31	1e-3	14.23	11.72	6.94	6.65	6.94	6.61

Besides the influence of the polynomial order on the update procedure, one may investigate the influence of the corresponding measurement error. As shown in Table 14.4 the mean error ε_m and the variance reduction ε_v for the bulk modulus are decreasing with smaller values of σ_ε as expected. The smaller measurement error is, the more we are certain about the experimental data (and hence the truth) and thus the better is update.

5.2 Random Field Update

The previous example was rather simple as the number of random variables representing the problem is relatively small. In order to properly investigate the update of material properties in this example we consider the identification of shear modulus G priory modelled as a lognormal random field with $\mu = 3.50 \cdot 10^4$ and $\sigma = 0.1\mu$ according to Eq. (14.32). The field has exponential correlation function with the correlation lengths equal to $l_c = 10$. The same geometrical problem (see Fig. 14.1) as before is considered with slightly different loading conditions, i.e. $f = 25$. In addition both, the purely elastic and nonlinear response are studied due to the comparison purposes. Due to the lack of the measurement data, the reality is simulated by modelling the shear modulus $G_t = 2.8 \cdot 10^4$ as a point-wise constant function, and measuring the values of the shear stress σ_{xy} in 30% of nodal points (including boundary conditions). The collected data are then disturbed by a central Gaussian noise with the diagonal covariance $\sigma_\varepsilon^2 \boldsymbol{I}$, where σ_ε is approximately equal to 1% of the measured value.

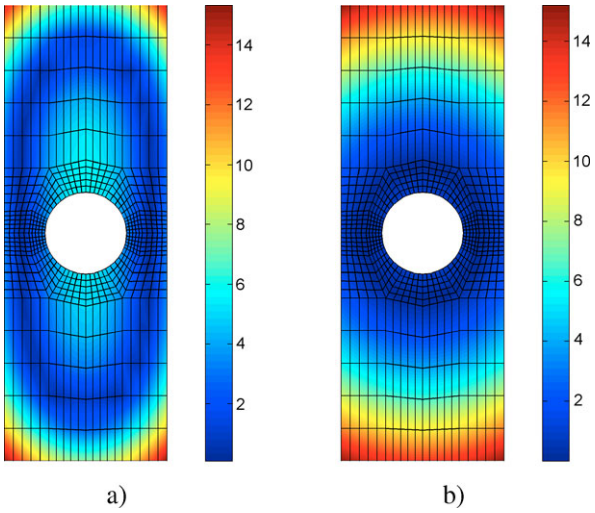

Fig. 14.3 The relative error ε_a [%] of updated shear modulus G via (**a**) linear model (elasticity) (**b**) nonlinear model (elasto-plasticity). For PCE is used order $p = 3$ in $M = 10$ random variables

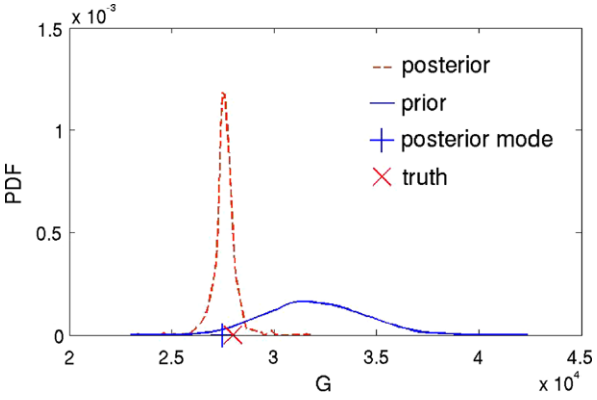

Fig. 14.4 Posterior probability distribution compared to the prior for the nonlinear model. The update is obtained by linear Bayesian method with third order PCE and $M = 10$ random variables

As the plots of the relative root mean square error

$$\varepsilon_a = 100 \cdot \frac{\|G_a - G_t\|_{L_2(\Omega)}}{\|G_f - G_t\|_{L_2(\Omega)}} \tag{14.33}$$

in Fig. 14.3 show the direct linear update performs better in a case of linear than the nonlinear model as expected. The 2% error region E_r in linear case spreads from the central part to the boundary resulting in much wider region than in nonlinear case. In contrast to this, the nonlinear model produces reduced E_r region strictly in the central plastifying zone. For the point in this domain the update performs well, i.e. the variance reduces, the mean moves in the direction of the truth and the truth is almost coinciding with the mode, see Fig. 14.4. However, in other nodes outside of E_r this may not be the case. This behaviour is expected as the linear Bayesian approximation is not optimal for the nonlinear models.

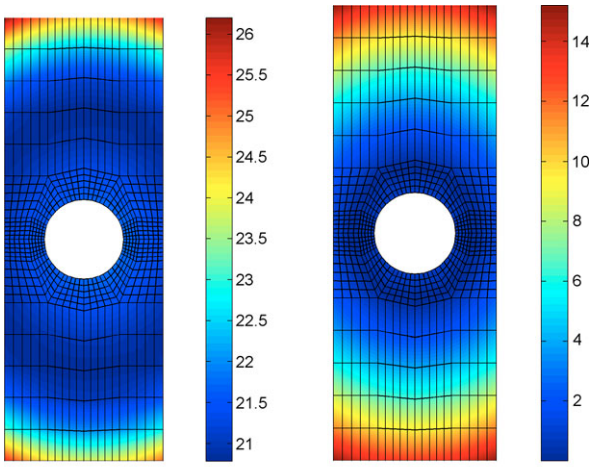

Fig. 14.5 Shear modulus G via elasto-plastic response, the relative error ε_a [%]: (**a**) EnKF result (**b**) direct PCE result. For PCE is used $p = 3$ and $M = 10$ random variables, while for EnKF 100 ensemble members

Besides the direct PCE update procedure the identification of the shear modulus for the nonlinear model is also done with the help of ensemble Kalman filter (EnKF) method (see [17, 18]) with 100 ensemble members. The comparison of results in Fig. 14.5 shows that the direct update produces much smaller value of the relative error ε_a. This can be explained by relatively small number of ensemble members. On other side the EnKF identifies G in a more unified way, i.e. the region of the minimal error is covering almost the whole computational area in contrast to PCE where it is placed around the hole edge.

In previous experiments the update results are influenced by the values of the different quantities such as the order of PCE, number of terms in truncated KLEs, etc. However, until now we did not consider the influence of the measured quantity on the update process. We assumed that the shear stress σ_{xy} is the most appropriate measurement. In order to investigate this, we substituted σ_{xy} in previous experiment by a stress σ_{yy}. This change significantly influences the update results by increasing the relative root mean square error three times as shown in Fig. 14.6 for nonlinear model.

6 Conclusion

In this paper is studied the problem of identifying parameters or quantities in elasto-plastic computational model by comparison with virtual reality models (e.g. more refined models). The introduced Bayesian approach starts from the idea that the choice of parameters should be such as to minimise a certain error functional. In other words, the update setting embeds the unknown quantity in a probability distribution, where the spread of the probability distribution should reflect the uncertainty about that quantity. Reformulating the classical Bayesian approach via conditional

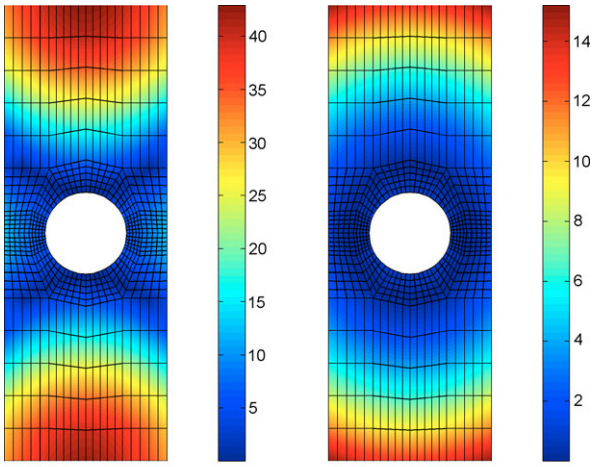

Fig. 14.6 The relative error ε_a [%] of updated shear modulus G (nonlinear model) with the help of (**a**) σ_{yy} measurement (**b**) σ_{xy} measurement. For PCE is used $p = 3$ and $M = 10$

expectation and the minimisation of variance as its background the Bayesian update reduces to the simple linear formula, containing the well-known Kalman filter as a special case.

The identification problem here considered is a very difficult one, an elasto-plastic system, or mathematically speaking a variational inequality of a second kind. The non-smoothness inherent in such problems makes the update procedure more complex and difficult to perform. However, as presented in numerical results the PCE based methods still succeed to preform well. Regarding this the PCE methods show great promise for the future parameter identification in nonlinear problems.

Acknowledgements The authors would like to acknowledge the financial support of Technical University Braunschweig, DAAD and DFG (Deutsche Forschungsgemeinschaft).

References

1. Blanchard, E.D., Sandu, A., Sandu, C.: A polynomial chaos-based Kalman filter approach for parameter estimation of mechanical systems. J. Dyn. Syst. Meas. Control **132**(6), 061404 (2010)
2. Bobrowski, A.: Functional Analysis for Probability and Stochastic Processes: An Introduction. Wiley Series in Probability and Statistics. Cambridge University Press, Cambridge (2005)
3. Gamerman, D., Lopes, H.F.: Markov Chain Monte Carlo: Stochastic Simulation for Bayesian Inference. Chapman & Hall, London (2006)
4. Ghanem, R.G., Spanos, P.D.: Stochastic Finite Elements: A Spectral Approach. Springer, New York (1991)
5. Hida, T., Kuo, H.-H., Potthoff, J., Streit, L.: White Noise Analysis—An Infinite Dimensional Calculus. Kluwer, Dordrecht (1993)
6. Higdon, D., Lee, H., Holloman, C.: Markov chain Monte Carlo-based approaches for inference in computationally intensive inverse problems. Bayesian Stat. **7**, 181–197 (2003)

7. Holden, H., Øksendal, B., Ubøe, J., Zhang, T.-S.: Stochastic Partial Differential Equations. Birkhäuser, Basel (1996)
8. Kalman, R.E.: A new approach to linear filtering and prediction problems. J. Basic Eng. **82**, 35–45 (1960)
9. Kolmogorov, A.: Foundations of the Theory of Probability, 2nd edn. Chelsea, New York (1956)
10. Kučerová, A., Matthies, H.G.: Uncertainty updating in the description of heterogeneous materials. Tech. Mech. **30**(1–3), 211–226 (2010)
11. Luenberger, D.G.: Optimization by Vector Space Methods. Wiley, New York (1969)
12. Marzouk, Y.M., Xiu, D.: A stochastic collocation approach to Bayesian inference in inverse problems. Commun. Comput. Phys. **6**(4), 826–847 (2009)
13. Matthies, H.G.: Stochastic finite elements: computational approaches to stochastic partial differential equations. Z. Angew. Math. Mech. **88**(11), 849–873 (2008)
14. Matthies, H.G., Rosić, B.: Inelastic media under uncertainty: stochastic models and computational approaches. In: Reddy, D. (ed.) IUTAM Symposium on Theoretical, Computational and Modelling Aspects of Inelastic Media. IUTAM Bookseries, vol. 11, pp. 185–194 (2008)
15. Matthies, H.G., Litvinenko, A., Pajonk, O., Rosić, B., Zander, E.: Parametric and uncertainty computations with tensor product representations. Technical report, Institut für Wissenschaftliches Rechnen, TU Braunschweig (2011)
16. El Moselhy, T., Marzouk, Y.M.: Bayesian inference with optimal maps. J. Comput. Phys. (2011). doi:10.1016/j.jcp.2012.07.022
17. Pajonk, O., Rosić, B.V., Litvinenko, A., Matthies, H.G.: A deterministic filter for non-Gaussian Bayesian estimation—Applications to dynamical system estimation with noisy measurements. Physica D **241**(7), 775–788 (2012)
18. Pajonk, O., Rosić, B.V., Matthies, H.G.: Deterministic linear Bayesian updating of state and model parameters for a chaotic model. Informatikbericht 2012-01, Institut für Wissenschaftliches Rechnen, Technische Universität. Braunschweig (2012)
19. Rosić, B., Matthies, H.G.: Computational approaches to inelastic media with uncertain parameters. J. Serbian Soc. Comput. Mech. **2**, 28–43 (2008)
20. Rosić, B.V., Matthies, H.G.: Stochastic plasticity—a variational inequality formulation and functional approximation approach I: the linear case. Technical Report 2012-02, Institut für Wissenschaftliches Rechnen (2012)
21. Rosić, B.V., Matthies, H.G., Živković, M.: Uncertainty quantification of infinitesimal elastoplasticity. Sci. Tech. Rev. **61**(2), 3–9 (2011)
22. Rosić, B.V., Pajonk, O., Litvinenko, A., Matthies, H.G.: Sampling-free linear Bayesian update of polynomial chaos representations. J. Comput. Phys. **231**(17), 5761–5787 (2012)
23. Rosić, B.V., Kučerová, A., Sýkora, J., Pajonk, O., Litvinenko, A., Matthies, H.G.: Parametric identification in a probabilistic setting. Technical report, Institut für Wissenschaftliches Rechnen, TU Braunschweig (2012)
24. Saad, G., Ghanem, R.: Characterization of reservoir simulation models using a polynomial chaos-based ensemble Kalman filter. Water Resour. Res. **45**, W04417 (2009)
25. Simo, J.C., Hughes, T.J.R.: Computational Inelasticity. Springer, New York (1998)
26. Soize, C.: Maximum entropy approach for modeling random uncertainties in transient elastodynamics. J. Acoust. Soc. Am. **109**(5I), 1979–1996 (2001)
27. Tarantola, A.: Popper, Bayes and the inverse problem. Nat. Phys. **2**(8), 492–494 (2006)
28. Wiener, N.: The homogeneous chaos. Am. J. Math. **60**, 1936–1938 (1938)

Chapter 15
SH Surface Waves in a Half Space with Random Heterogeneities

Chaoliang Du and Xianyue Su

Abstract Horizontally polarized shear waves (SH waves) do not exist in a homogeneous half space according to the traditional elastic wave theory. However, in this study, we proved both theoretically and numerically that there will be surface waves in a half space which has small, random density, but the mean value of the density is homogeneous. Historically, this type of half space is often treated as a homogeneous one with deterministic methods. In this investigation, a closed-form dispersion equation was derived stochastically, and the frequency spectrum, dispersion equation, phase/group velocity were plotted numerically to study how the random inhomogeneities will affect the dispersion properties of the half space with random density. This research may find its application in seismology, non-destructive test/evaluation, etc.

1 Introduction

In this study, the dispersion and attenuation properties of waves propagating in a half space (see Fig. 15.1) with random heterogeneities are investigated.

Shear horizontal surface waves (SHSW) are the most destructive waves in an earth quake and they can propagate through a very long distance without much loss of its energy. But, scientists have proved long ago that there is no SHSW in a homogeneous isotropic linearly elastic half-space [1]. However, in 1911, love predicted

C. Du
Department of Mechanics and Aerospace Engineering, College of Engineering, Peking University, Beijing, 100871, P.R. China

C. Du (✉)
Beijing Aeronautical Science and Technology Research Institute, COMAC, The Olympic Building, No.267 Middle Section of North 4th Ring Road, Beijing, 100083, P.R. China
e-mail: duchaoliang@comac.cc

X. Su
LTCS and Department of Mechanics and Aerospace Engineering, College of Engineering, Peking University, Beijing, 100871, P.R. China
e-mail: xyswsk@pku.edu.cn

M. Papadrakakis et al. (eds.), *Computational Methods in Stochastic Dynamics*, Computational Methods in Applied Sciences 26,
DOI 10.1007/978-94-007-5134-7_15,

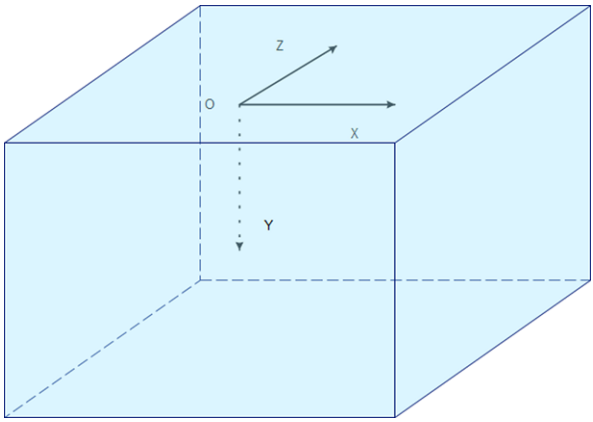

Fig. 15.1 Coordinate system of the half space

mathematically that SHSW could exist if the half-space is covered by a layer of a different material.

Since then, SHSW in a half space was mostly explained theoretically by Love's theory or its variant theories. But we know that the earth's surface is very complex. It is a mixture of many kinds of rocks, sands, soil, water, etc., and more complicatedly, these materials do not often distribute in deterministic ways, but distribute randomly. So do SHSW exist in such a complex, random half space?

Similar problems have been explored by some scientists. B. Collet et al. [2] studied SHSW in a Functionally Graded Material of which some material constants share the same depth-dependent function , and derived some of the depth-dependent functions which could be solved exactly. Using their solutions, they studied the influence of different inhomogeneity functions on the properties of SHSW. J. Achenbach et al. [3] studied SHSW in a purely elastic half-space whose shear modulus and mass density depend arbitrarily on the depth and gave a general solution that is quite exact for high frequencies. T.C.T. Ting [4] recently investigated SHSW in a half space of which C_{44} and ρ have the same function form, and C_{55}, C_{45} are correlated. Here, $C_{\alpha\beta}$ is the elastic stiffness in the contracted notation. Ting also got an asymptotic solution of general graded materials for large wave number k. Anti-plane shear waves for anisotropic graded materials have been considered for periodic half-spaces by A. Shuvalov et al. [5] and for a single plate by A. Shuvalov et al. [6]. Shear horizontal waves in functionally graded piezoelectric materials are also greatly studied by Tianjian Lu et al. [7–9].

But these researches haven't given an explicit solution of dispersion and attenuation of SHSW in a half space with random density in the depth direction by strict stochastic methods. In this study, we get the explicit dispersion equation by the first order smoothing approximation (FOSA) method. And we then analyze the dispersion and attenuation properties using the dispersion equation.

In this study we proved mathematically and numerically that SHSW could exist in a stochastically homogeneous half space. Some interesting properties of dispersion and attenuation found in this study could promote our understanding of waves propagating in a half space with random heterogeneities, e.g. earth's upper crust,

alloys or composites. It will also help us to do the inverse problems, for example, to use seismic waves to detect the earth's crust structure, and to use ultrasonic waves to evaluate a structure with randomly distributed micro-cracks or heterogeneities.

2 Modeling and Mathematical Analysis

The fundamental dynamic equation system for statistically homogeneous, isotropic, linearly elastic solid is

$$\tau_{ij,j} + \rho f_i = \rho \ddot{u}_i \tag{15.1}$$

$$\tau_{ij} = \lambda \varepsilon_{kk} \delta_{ij} + 2\mu \varepsilon_{ij} \tag{15.2}$$

$$\varepsilon_{ij} = \frac{1}{2}(u_{i,j} + u_{j,i}) \tag{15.3}$$

To account for the random heterogeneities, the constants ρ, μ, λ in the equation system are changed to random processes of space.

Consider SH waves propagating in x direction in a half space (see Fig. 15.1).

It is known that for anti-plane waves that $u_x = u_y = 0$ and $\partial/\partial z = 0$. And if we assume that there is no body force, the equation system reduces to

$$\tau_{zj,j} = \rho \ddot{u}_z \tag{15.4}$$

$$\tau_{zj} = \mu u_{z,j} \tag{15.5}$$

in which, $j = x, y$.

So the dynamic equation for SH waves in a random half space is

$$(\mu u_{z,j})_{,j} = \rho \ddot{u}_z \tag{15.6}$$

And the boundary condition is

$$\tau_{zy}|_{y=0} = 0 \quad \text{i.e.} \tag{15.7}$$

$$\mu u_{z,y}|_{y=0} = 0 \tag{15.8}$$

Assume here that there is randomness only in the y direction. Consider an harmonic wave motion of the form

$$u_z = f(y) \exp\left[i(k_1 x - \omega t)\right] \tag{15.9}$$

in which, $f(y)$ is a random process. To study the surface shear wave, we assume the averaged $f(y)$ to be

$$\left\langle f(y) \right\rangle = Ae^{-by}, \tag{15.10}$$

in which $b > 0$. Thus the mean wave motion $\langle u_z \rangle$ could be written as

$$\langle u_z \rangle = Ae^{-by} e^{i(k_1 x - \omega t)} \tag{15.11}$$

If there is no random heterogeneities in the solid, a solution of Eq. (15.6) would be of the form [1]

$$u_z = Ae^{-by}e^{i(k_1 x-\omega t)} \tag{15.12}$$

Substituting Eq. (15.12) into Eq. (15.6), we find

$$\frac{\omega^2}{C_s^2} - k_1^2 + b^2 = 0 \tag{15.13}$$

In which, C_s is the shear velocity of the homogeneous material without random heterogeneities,

$$C_s = \sqrt{\frac{\mu_0}{\rho_0}} \tag{15.14}$$

For a free surface, the boundary condition at $y = 0$ is

$$\frac{\mathrm{d}u_z}{\mathrm{d}y} = 0 \tag{15.15}$$

The boundary condition Eq. (15.15) can be satisfied only if either $A = 0$ or $b = 0$. Therefore, there is no surface SH wave in an homogeneous, isotropic, linearly elastic half space.

Firstly, we consider that random heterogeneities are only on the surface (as a practical example, the roughness of the earth surface could be viewed as a half space but with random heterogeneities on the surface). Under this circumstance, the boundary condition will be

$$\mu\frac{\partial u_z}{\partial y}\bigg|_{y=0} = 0 \quad \Rightarrow \quad (\mu_0 + \varepsilon\mu_1)\frac{\partial(\langle u_z\rangle + \varepsilon u_{z1})}{\partial y}\bigg|_{y=0} = 0 \tag{15.16}$$

in which, $\varepsilon\mu_1$ and εu_{z1} represent the surface roughness. Averaging both sides of Eq. (15.16), we get

$$\left\{\mu_0\frac{\mathrm{d}\langle u_z\rangle}{\mathrm{d}y} + \varepsilon^2\left\langle\mu_1\frac{\partial u_{z1}}{\partial y}\right\rangle\right\}\bigg|_{y=0} = 0 \tag{15.17}$$

ε is an averaging measure of how the properties of random heterogeneities deviate from the averaged properties, and we assume it to be small and take it as the small parameter. The randomness of the surface takes effect through the term $\varepsilon^2\langle\mu_1\frac{\partial u_{z1}}{\partial y}\rangle$. We assume here that

$$\varepsilon^2\left\langle\mu_1\frac{\partial u_{z1}}{\partial y}\right\rangle\bigg|_{y=0} = \mu_0 A\beta e^{i(k_1 x-\omega t)} \tag{15.18}$$

in which, β is the surface parameter. Substituting Eqs. (15.18) and (15.11) into Eq. (15.17), we get

$$b = \beta \tag{15.19}$$

Considering Eq. (15.13), the dispersion equation for SH waves in a half space with random heterogeneities only on the surface is

$$\frac{\omega^2}{C_s^2} - k_1^2 + \beta^2 = 0 \tag{15.20}$$

Next, we will investigate the problem of the half space with random heterogeneities in the whole depth direction. Substituting Eq. (15.9) in Eq. (15.6) gives

$$\left(\rho\omega^2 - \mu k_1^2\right) f + (\mu f_{,y})_{,y} = 0 \tag{15.21}$$

Assuming that ρ, μ differ slightly from the mean value of them, ρ, μ can be written as

$$\rho(y) = \rho_0 + \varepsilon\rho_1(y) \qquad \mu(y) = \mu_0 + \varepsilon\mu_1(y) \tag{15.22}$$

where, ε is a small parameter, and

$$\langle\rho_1\rangle = \langle\mu_1\rangle = 0 \tag{15.23}$$

Substituting Eq. (15.22) in Eq. (15.21), we have

$$\left(\rho_0\omega^2 - \mu_0 k_1^2\right) f + \mu_0 f_{,yy} + \varepsilon\left(\left(\rho_1\omega^2 - \mu_1 k_1^2\right) f + (\mu_1 f_{,y})_{,y}\right) = 0 \tag{15.24}$$

According to FOSA theory, the deterministic operator of Eq. (15.21) is

$$L_0(y) = \mu_0\left(k_0^2 + \frac{\partial^2}{\partial y^2}\right) \tag{15.25}$$

in which,

$$k_0^2 = \frac{\omega^2}{C_s^2} - k_1^2 \tag{15.26}$$

And the first order random operator of Eq. (15.21) is

$$L_1(y) = P(y) + \mu_1(y)_{,y}\frac{\partial}{\partial y} + \mu_1(y)\frac{\partial^2}{\partial y^2} \tag{15.27}$$

in which,

$$P(y) = \rho_1(y)\omega^2 - \mu_1(y)k_1^2 \tag{15.28}$$

Considering Eq. (15.23), we can see that $\langle L_1\rangle = 0$.

For steady waves, the Green function G_0 of the deterministic operator L_0 is

$$G_0(y_1, y_2) = -\frac{1}{2k_0\mu_0}\sin\left(k_0|y_1 - y_2|\right) \tag{15.29}$$

According to stochastic theory, the FOSA equation is

$$L_0\langle f(y_1)\rangle - \varepsilon^2\left\langle L_1(y_1)\int G_0(y_1, y_2)L_1(y_2)\langle f(y_2)\rangle \mathrm{d}y_2\right\rangle = 0 \tag{15.30}$$

To solve Eq. (15.30), let's calculate $L_1(y_1)G_0(y_1, y_2)$ first,

$$\begin{aligned} L_1(y_1)G_0(y_1, y_2) = &-\left(P(y_1) + \mu_1(y_1)_{,y_1}\frac{\partial}{\partial y_1} + \mu_1(y_1)\frac{\partial^2}{\partial y_1^2}\right) \\ &\times \frac{1}{2k_0\mu_0}\sin\big(k_0|y_1 - y_2|\big) \end{aligned} \tag{15.31}$$

When $y_2 < y_1$

$$\begin{aligned} L_1(y_1)G_0(y_1, y_2) &= Q_1\sin\big(k_0(y_1 - y_2)\big) + Q_2\cos\big(k_0(y_1 - y_2)\big) \\ &= M(y_1, y_2) \end{aligned} \tag{15.32}$$

in which,

$$Q_1 = \left(\frac{\mu_1(y_1)k_0}{2\mu_0} - \frac{P(y_1)}{2k_0\mu_0}\right) \tag{15.33}$$

$$Q_2 = -\frac{\mu_1(y_1), y_1}{2\mu_0} \tag{15.34}$$

and, when $y_2 > y_1$

$$L_1(y_1)G_0(y_1, y_2) = -M(y_1, y_2) \tag{15.35}$$

Then, using Eq. (15.10), $L_1(y_2)\langle f(y_2)\rangle$ can be expressed as

$$\begin{aligned} L_1(y_2)\langle f(y_2)\rangle &= \left(P(y_2) + \mu_1(y_2)_{,y_2}\frac{\partial}{\partial y_2} + \mu_1(y_2)\frac{\partial^2}{\partial y_2^2}\right)Ae^{-by_2} \\ &= A\big(P(y_2) - \mu_1(y_2)_{,y_2}b + \mu_1(y_2)b^2\big)e^{-by_2} = N(y_2) \end{aligned} \tag{15.36}$$

If we assume that $\mu_1 = 0$, we could study the influence of the randomness of the density on the dispersion properties of the half space.

The random process $\rho_1(y_1; \gamma)$ is taken as Uhlenbeck–Ornstein process [10]. Although its correlation function is not mean-square differentiable, this process has been used in a number of investigations because it fits experimental data the best [11]. This process is a centered and stationary random process [10] and its correlation function is

$$\begin{aligned} R_{\rho_1(y_1;\gamma)\rho_1(y_2;\gamma)} &= \int \rho_1(y_1; \gamma)\rho_1(y_2; \gamma)\,\mathrm{d}\gamma \\ &= \zeta^2 e^{-|y_1 - y_2|/R_c} = R(y_1 - y_2) \end{aligned} \tag{15.37}$$

In which, $\zeta = \sqrt{\langle{\rho_1}^2\rangle}$ and it is the standard deviation of the random density function; γ is a random variable. And R_c is the integral radius (the correlation length)

of the correlation function, which physically means the scale of heterogeneity [12], and it should be positive.

From Eq. (15.10), we have

$$L_0\langle f(y_1)\rangle = \mu_0\left(k_0^2 + \frac{\partial^2}{\partial y^2}\right)Ae^{-by_1} = \mu_0\left(k_0^2 + b^2\right)Ae^{-by_1} \tag{15.38}$$

Substituting Eqs. (15.31), (15.36) and (15.38) into Eq. (15.30), we get the dispersion equation,

$$k_0^2 + b^2 - \frac{\omega^4\zeta^2\varepsilon^2 b}{2k_0\mu_0^2}\left(\frac{1}{(b+1/R_c)^2+b^2} + \frac{1}{(b-1/R_c)^2+b^2}\right) = 0 \tag{15.39}$$

It could be seen from the dispersion equation Eq. (15.39) that if there is no random fluctuation, i.e. $\varepsilon = 0$ or $\zeta = 0$ then $k_0^2 + b^2 = 0$—the equation becomes the dispersion equation without random heterogeneities;

Considering the surface condition Eq. (15.19), the dispersion equation could be written as,

$$k_0^2 + \beta^2 - \frac{\omega^4\zeta^2\varepsilon^2\beta}{2k_0\mu_0^2}\left(\frac{1}{(\beta+1/R_c)^2+\beta^2} + \frac{1}{(\beta-1/R_c)^2+\beta^2}\right) = 0 \tag{15.40}$$

If β is zero, then ε will be zero too according to Eq. (15.18), that is, there will be no heterogeneities in the half space. So if β is zero, the half space will be homogeneous, and there will be no SH surface waves according to Eq. (15.40). In the future, we may consider another model that, if β is zero, ε will not be zero, to study the interesting case which has randomness only below the surface.

To conveniently evaluate numerically the effect of random heterogeneities, the dispersion equation Eq. (15.40) is transformed into a dimensionless equation in the following. h is a symbol for the characteristic length and it could be the correlation length of the random heterogeneities. Introduce new dimensionless variables as,

$$\begin{aligned} \overline{\omega} &= \frac{2h\omega}{\pi C_s} \qquad \overline{k} = \frac{2hk_1}{\pi} \\ \overline{R_c} &= \frac{\pi R_c}{2h} \qquad \overline{\zeta} = \frac{\varepsilon\zeta}{\rho_0} \\ \overline{\mu_0} &= \frac{\mu_0}{\rho_0 C_s^2} = 1 \qquad \overline{\beta} = \frac{2h\beta}{\pi} \end{aligned} \tag{15.41}$$

From Eqs. (15.26) and (15.41), we get

$$k_0^2 = \frac{\omega^2}{C_s^2} - k_1^2 = \left(\frac{\pi}{2h}\right)^2\left(\overline{\omega}^2 - \overline{k}^2\right) \tag{15.42}$$

so the dimensionless k_0 is defined as,

$$\overline{k_0}^2 = \overline{\omega}^2 - \overline{k}^2 \tag{15.43}$$

Using Eqs. (15.41), we could get the dimensionless dispersion equation from Eq. (15.20),

$$\overline{\omega}^2 - \overline{k_1}^2 + \overline{\beta}^2 = 0 \tag{15.44}$$

Using Eqs. (15.41) and (15.43), the dimensionless dispersion equation of Eq. (15.40) is,

$$\overline{k_0}^2 + \overline{\beta}^2 - \Lambda = 0 \tag{15.45}$$

Λ denote the random term,

$$\Lambda = \frac{\overline{\omega}^4 \overline{\zeta}^2 \overline{\beta}}{2\overline{k_0}} \left(\frac{1}{(\overline{\beta} + 1/\overline{R_c})^2 + \overline{\beta}^2} + \frac{1}{(\overline{\beta} - 1/\overline{R_c})^2 + \overline{\beta}^2} \right) \tag{15.46}$$

3 Numerical Results and Analysis

The SH surface waves propagating in a half space with random densities is further studied numerically. The dimensionless dispersion equation Eq. (15.45) is used to compute the curves. The numerical results are explained and discussed in the following.

3.1 Random Heterogeneities Only on the Surface

The geomorphy of the earth's surface is always very complex. The reason for this complexness can come from both natural and man-made actions. In this study, we model the complex geomorphy by giving a surface parameter β. So in this section, we will study the dispersion properties for half spaces with random heterogeneities only on the surface. The dispersion curves are plotted according to Eq. (15.20).

From Fig. 15.2, it can be seen that the phase velocity will grow to 1 slowly, but for $\overline{k} < 2$, the phase velocity will be 0, i.e. the waves become standing waves in this circumstance.

From Fig. 15.3, it can be seen that, given a wave number, the phase velocity will decrease to 0 as the surface parameter $\overline{\beta}$ grows, i.e. the waves propagate more and more slowly when the surface becomes more and more rough, and all the waves will be blocked when $\overline{\beta}$ is large enough.

3.2 Frequency Spectrum Analysis

In the following, we will study the dispersion properties for half spaces with random heterogeneities not only on the surface but also in the whole half space. The related parameters are set to $\varepsilon = 0.1$, $\overline{\zeta} = 2$, $\overline{R_c} = 0.4$, $\overline{\beta} = 2$ respectively.

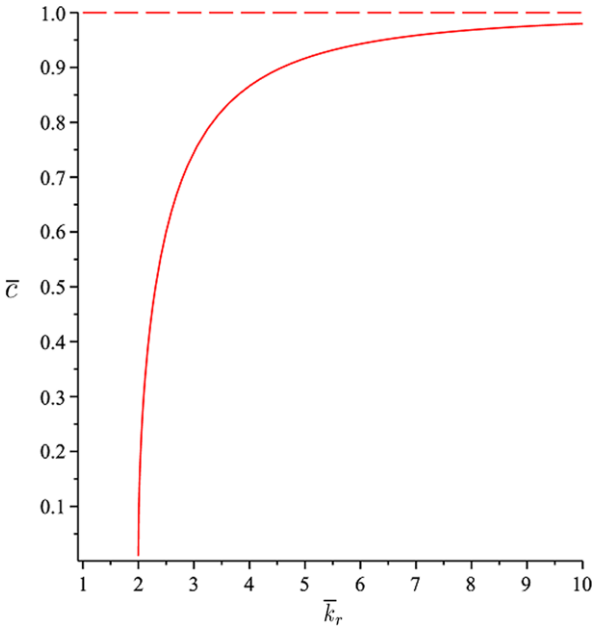

Fig. 15.2 Normalized phase velocity—normalized wave number. $\overline{\beta} = 2$

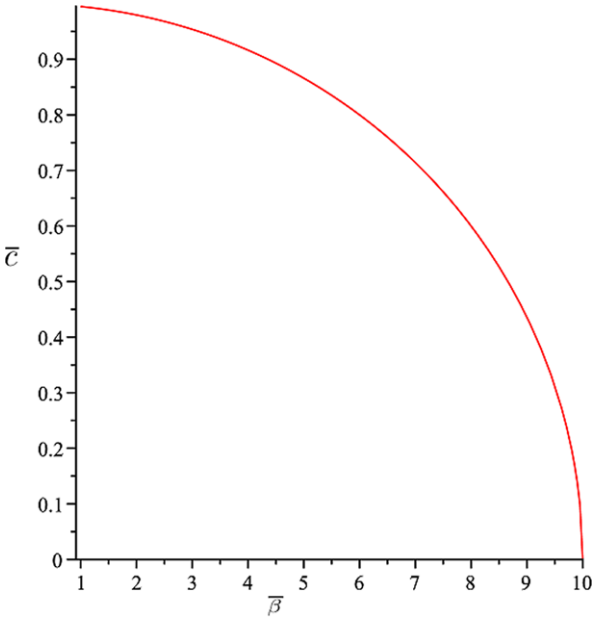

Fig. 15.3 Normalized phase velocity—normalized surface parameter. $\overline{k} = 10$

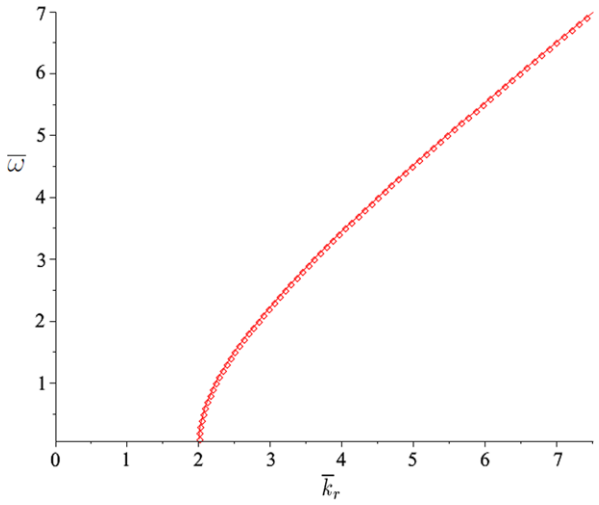

Fig. 15.4 Normalized circular frequency—normalized wave number

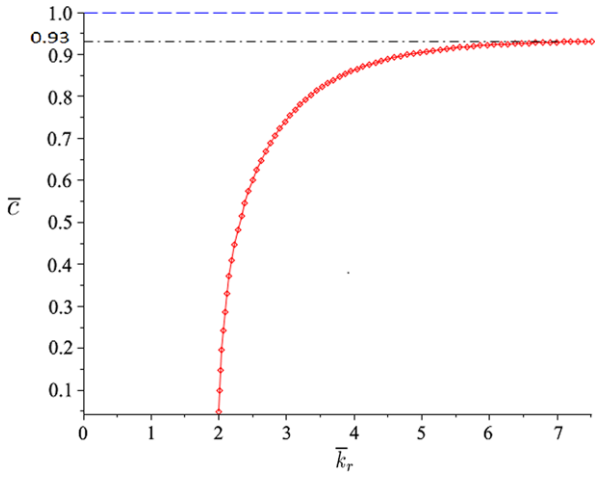

Fig. 15.5 Normalized phase velocity—normalized wave number

From Figs. 15.4, 15.5 and 15.6, we can see that

1. As the wave number grows, the velocity will grow to a value—approximately 0.93 in this case. The reason that it can not reach to 1 could be that the waves are reflected and scattered by the random heterogeneities.
2. The wave number does not start from 0, but 2. We can call this value the cut-off wave number. 2 is also the value of $\overline{\beta}$. From Eq. (15.45), we can see that the cut-off wave number equals the surface parameter.

Also, from Fig. 15.5, it can be seen that the phase velocity will decrease to 0 when the wave number decreases. This phenomenon agrees with the common knowledge that when the wave number decreases (the wave length increases), the effect of the random heterogeneities will be averaged out gradually, that is, the stochastically

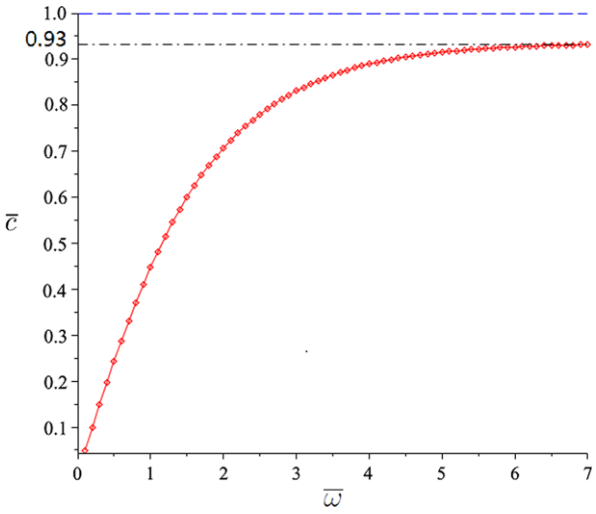

Fig. 15.6 Normalized phase velocity—normalized circular frequency

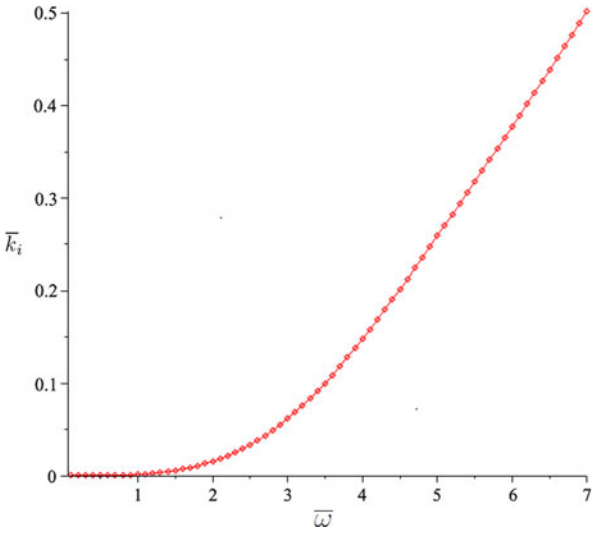

Fig. 15.7 Normalized imaginary wave number—normalized circular frequency

homogeneous half space will be more and more like a homogeneous half space, and we know that SHSW could not exist in a homogeneous half space, therefore, the phase velocity will decrease gradually to 0.

The imaginary wave number represents the attenuation rate. Therefore, we know from Fig. 15.7 that the bigger the circular frequency is, the faster the wave attenuates. This phenomenon should be caused by reflection and scattering. And from Fig. 15.4 we see that the wave length will decrease as the circular frequency grows. It is known that the smaller the wave length is, the easier the waves can be reflected or scattered by the random heterogeneities. Thus the wave should attenuates more fast as the frequency grows.

4 Conclusion

In this study, we proved that SHSW could exist in a stochastically homogeneous half space. The dispersion properties of SHSW in an half space with random density in the depth direction or only near the surface have been investigated both theoretically and numerically. The first order smoothing approximation method is used to solve the random differential equation. The dimensionless dispersion equation is obtained. And the dispersion properties is further studied numerically. The phase velocity is found increasing to an asymptotic value when the wave number is bigger than a critical value—the cut-off wave number, below which the phase velocity is 0. The interesting properties of dispersion and attenuation found here will help us understanding properties of waves in a half space with random heterogeneities, e.g. the earth's crust. It will also help us to do the inverse problems, for example, to use seismic waves to detect the earth's upper crust structure, and to extract information more exactly from the acoustic testing results.

Acknowledgements This study is supported by the National Natural Science Foundation of China under Grant no. 90916007.

References

1. Achenbach, J.: Wave Propagation in Elastic Solids. North-Holland, Amsterdam (1973)
2. Collet, B., Destrade, M., Maugin, G.: Bleustein–Gulyaev waves in some functionally graded materials. Eur. J. Mech. A, Solids **25**(5), 695 (2006)
3. Achenbach, J.D., Balogun, O.: Anti-plane surface waves on a half-space with depth dependent properties. Wave Motion **47**(1), 59 (2010)
4. Ting, T.: Existence of anti-plane shear surface waves in anisotropic elastic half-space with depth-dependent material properties. Wave Motion **47**(6), 350 (2010)
5. Shuvalov, A.L., Poncelet, O., Golkin, S.V.: Existence and spectral properties of shear horizontal surface acoustic waves in vertically periodic half-spaces. Proc. R. Soc., Math. Phys. Eng. Sci. **465**(2105), 1489 (2009)
6. Shuvalov, A., Poncelet, O., Kiselev, A.: Shear horizontal waves in transversely inhomogeneous plates. Wave Motion **45**(5), 605 (2008)
7. Qian, Z., Jin, F., Lu, T., Kishimoto, K.: Transverse surface waves in functionally graded piezoelectric materials with exponential variation. Smart Mater. Struct. **17**, 065005 (2008)
8. Eskandari, M., Shodja, H.: Love waves propagation in functionally graded piezoelectric materials with quadratic variation. J. Sound Vib. **313**(1–2), 195 (2008)
9. Cao, X., Jin, F., Wang, Z., Lu, T.: Bleustein–Gulyaev waves in a functionally graded piezoelectric material layered structure. Sci. China Ser. G, Phys. Mech. Astron. **52**(4), 613 (2009)
10. Frisch, U.: Wave Propagation in Random Media. Probabilistic Methods in Applied Mathematics. Academic Press, San Diego (1970)
11. Chen, K., Soong, T.: Covariance properties of waves propagating in a random medium. J. Acoust. Soc. Am. **49**, 1639 (1971)
12. Belyaev, A., Ziegler, F.: Uniaxial waves in randomly heterogeneous elastic media. Probab. Eng. Mech. **13**(1), 27 (1998)

Chapter 16
Structural Seismic Fragility Analysis of RC Frame with a New Family of Rayleigh Damping Models

Pierre Jehel, Pierre Léger, and Adnan Ibrahimbegovic

Abstract Structural seismic vulnerability assessment is one of the key steps in a seismic risk management process. Structural vulnerability can be assessed using the concept of fragility. Structural fragility is the probability for a structure to sustain a given damage level for a given input ground motion intensity, which is represented by so-called fragility curves or surfaces. In this work, we consider a moment-resisting reinforced concrete frame structure in the area of the Cascadia subduction zone, that is in the South-West of Canada and the North-West of the USA. According to shaking table tests, we first validate the capability of an inelastic fiber beam/column element, using a recently developed concrete constitutive law, for representing the seismic behavior of the tested frame coupled to either a commonly used Rayleigh damping model or a proposed new model. Then, for each of these two damping models, we proceed to a structural fragility analysis and investigate the amount of uncertainty to be induced by damping models.

Keywords Damping · Inelastic time-history analysis · Structural fragility · Fiber beam element · Reinforced concrete frame structure · Earthquake

P. Jehel (✉)
MSSMat, École Centrale Paris/CNRS, Grande Voie des Vignes, 92295 Châtenay-Malabry Cedex, France
e-mail: pierre.jehel@ecp.fr

P. Léger
Department of Civil Engineering, École Polytechnique of Montreal, University of Montreal Campus, P.O. Box 6079, Station CV, Montreal, QC, Canada H3C 3A7
e-mail: pierre.leger@polymtl.ca

A. Ibrahimbegovic
LMT-Cachan, ENS Cachan/CNRS/UPMC/PRES UniverSud Paris, 61 avenue du Président Wilson, 94235 Cachan Cedex, France
e-mail: ai@lmt.ens-cachan.fr

M. Papadrakakis et al. (eds.), *Computational Methods in Stochastic Dynamics*, Computational Methods in Applied Sciences 26,
DOI 10.1007/978-94-007-5134-7_16,

1 Introduction

Decision makers are interested in seismic risk analyses for predicting the post-earthquake situation in a given geographical region, so as to anticipate the human, social and economical impact of a major earthquake. For building structures, seismic risk assessment requires three main steps. (i) A seismic hazard analysis has first to be performed. It can be either deterministic or probabilistic. In the latter case, the seismic hazard is often expressed as an intensity measure—often the peak ground acceleration (*PGA*)—with a certain probability of being exceeded in a certain number of years. (ii) Then, the seismic fragility of the building considered has to be estimated: it corresponds to the conditional probability $P_{ij} = P[DI \geq DI_i | IM = IM_j]$ of the building to sustain a given damage index DI_i for a unique—or a set of—given input ground motion intensity measures IM_j. The probability to attain a damage index DI_i can then be computed as

$$P_i = \sum_j P[DI \geq DI_i | IM = IM_j] \cdot P[IM = IM_j]. \tag{16.1}$$

These damage indices have to be related to building performance requirements. (iii) Finally, the exposure of the buildings and populations has to be determined.

Structural seismic fragility analysis thus is a key step in the overall earthquake risk management process. This task is commonly achieved by constructing fragility curves from inelastic time-history analyses that take into account the variability in the seismic input motion alone or in both the input motion and the structural model. The main ingredients for fragility analyses are: (i) A set of seismic time-history records representative of the seismic hazard in the geographical region of interest for the project; (ii) An inelastic structural model along with a damping model; (iii) A mapping between damage indices and structural performance levels; and (iv) Statistical tools to analyze fragility curves.

In [1], Hwang and Huo present a methodology for constructing fragility curves accounting for uncertainties in the seismic, site, and structural parameters. On the one hand, 8 scenario earthquakes corresponding to different *PGA*, annual exceedance probabilities, magnitudes, and source-to-site distances are considered; for each scenario, 50 samples of ground motion time histories are generated using a seismological model that takes into account uncertainties in seismic and soils parameters. On the other hand, 50 samples of each of 6 random structural parameters are generated and then combined using the Latin Hypercube sampling technique to eventually generate 50 samples of the inelastic structural model. Then, for each earthquake scenario, the 50 ground motion samples are combined with the 50 structural samples to establish 50 earthquake-site-structure samples. Finally, for each earthquake scenario, 50 values of the damage index are computed from inelastic analyses and fragility curves are constructed.

The preceding approach defines a fully probabilistic approach in the sense that it takes into account uncertainty sources in both the seismic input motions and the inelastic structural behavior. It can however also be worth considering only uncertainties in ground motions. To that purpose, there exists, following Jalayer and Beck

[2], an alternative to the *IM-based approach* considered in this work: the *probabilistic ground motion time history approach*. This latter method is based on a stochastic ground motion model pertaining to seismic source parameters, which has to circumvent the most difficult drawback to be tackled in the *IM*-based approach, namely whether the selected set of *IM* thoroughly represent the input signal characteristics. On another hand, the recent work of Rosić *et al.* [3] considers the uncertain structural response of inelastic media and deterministic loading to provide maps of the probability for a component of the stress tensor to reach a given value at a given point.

The concept of fragility curve reduces the vulnerability analysis to the consideration of a unique intensity measure. This limitation has been pointed out in research work where the concept of fragility surfaces emerged. In a study dedicated to the analyze of the limitations of commonly used intensity measures for fragility analysis of single-degree-of-freedom linear and nonlinear systems [4], Kafali and Grigoriu propose to construct fragility surfaces instead of curves for assessing the seismic performance of nonlinear systems. For a given state of damage in the structure, the proposed fragility surface is the graphical representation of the relationship between the failure probability and the set of intensity parameters (m, r) constituted of the moment magnitude m and source-to-site distance r. This concept of fragility surface is also used in [5] by Seyedi *et al.* who extend it to other intensity measures. Indeed, they construct fragility surfaces that provide the probability for an inelastic reinforced concrete structure to sustain a given inter-story drift ratio, according to the spectral displacement at both eigenperiod T_1 and T_2. They finally conclude that when dealing with uncertainties propagation, fragility surfaces allow for estimating the variability of structural fragility due to a second *IM*, which should lead to more accurate seismic risk analyses.

Fragility curves have been used as a baseline to deal with a wide range of issues pertaining to earthquake engineering. In [6], Sáez *et al.* study the effect of considering inelastic dynamic soil-structure interaction on the seismic vulnerability analysis. They construct fragility curves from a very large number of artificially generated input earthquakes. They also introduce the so-called Fisher information concept which allows for measuring the amount of information contained in the seismic ground motions and thus provide a tool for the statistical analysis of fragility curves. In [7], Saxena *et al.* address the issue of assuming identical support ground motion in the analysis of the seismic response of long, multi-span, reinforced concrete bridges. Analyzing fragility curves, they show that considering spatial variation of earthquake ground motions is of first importance. In [8], Popescu *et al.* construct fragility curves to present the results of deterministic and both 2D and 3D stochastic analyses of the seismic liquefaction potential of saturated soil deposits. In the context of design rules assessments, Lagaros [9] computes fragility curves to analyze the seismic performance of multi-story RC buildings designed according to Greek and European building codes. The fragility curves are plotted from 10,000 simulations based on Monte Carlo techniques to take into account both uncertainty in the seismic signal and in key structural parameters for assessing structural stability.

There is a likely source of uncertainty in inelastic seismic time history analyses which is only rarely considered in fragility analyses, namely damping added to

the inelastic structural model so as to introduce in the simulations an amount of energy dissipation coming from inelastic mechanisms that are not explicitly accounted for in the structural model. In [1], the critical viscous damping ratio added for the seismic analyses of a reinforced concrete frame building is described by the uniform distribution restricted to the range 2%–4%. In [10], the structural damping is described by a lognormal distribution with a mean of 2% and a coefficient of variation of 0.62 for the purpose of steel frame fragility analysis. In both these works, Rayleigh damping is added and the uncertainty pertaining to additional damping thus stems from the critical damping ratio, not from the damping model type—Rayleigh in this case. Because it has been shown that it can be difficult to control the amount of damping generated by common Rayleigh damping models throughout inelastic time history analyses [11–13], the main purpose of the work presented in this chapter is to investigate the likely amount of uncertainty introduced by the damping model, in the context of fragility analysis.

To that aim, we proceed as follows. In the next section, we first present a reinforced concrete moment-resisting frame structure—simply referred to as "RC frame" throughout this chapter—which was tested on a shaking table. We use the corresponding experimental data as a reference to validate the developments that we present all along this chapter. Then, we detail in Sect. 3 the numerical model that we use to perform inelastic seismic time-history analyses of the RC frame. The issue of modeling damping is discussed and a new family of Rayleigh damping models is proposed. Results from simulations performed with both a "classical" Rayleigh damping model and the proposed new damping model are compared to the shaking table test results so as to validate the capability of the proposed combination of hysteretic with additional damping models for representing the behavior of the RC frame. The proposed new family of Rayleigh damping models can rely on a physical background which often lacks to commonly used Rayleigh damping models. In Sect. 4, we proceed to the selection of a set of real seismic ground motion records compatible with the seismic hazard in the Cascadia subduction zone. A seismic fragility analysis of the RC frame in this geographical region is then carried out in Sect. 5: fragility curves, along with their statistical analysis, as detailed in [6], are constructed for every damping models considered so as to investigate the amount of uncertainty these latter could bring in structural fragility analyses.

2 RC Frame Tested on a Shaking Table

The test structure considered throughout this chapter is represented in Fig. 16.1. It was designed at a reduced scale of $1/2$ according to the provisions of the National Building Code of Canada [14] and of the Canadian concrete standard [15]. The structure was assumed to have a nominal ductility, which corresponds to a force reduction factor $R = 2$ to compute the design base shear. The various assumptions and parameters used in the design of the this structure can be found in [16]. Four inverted U-shape concrete blocks attached in each span of the beams were used to

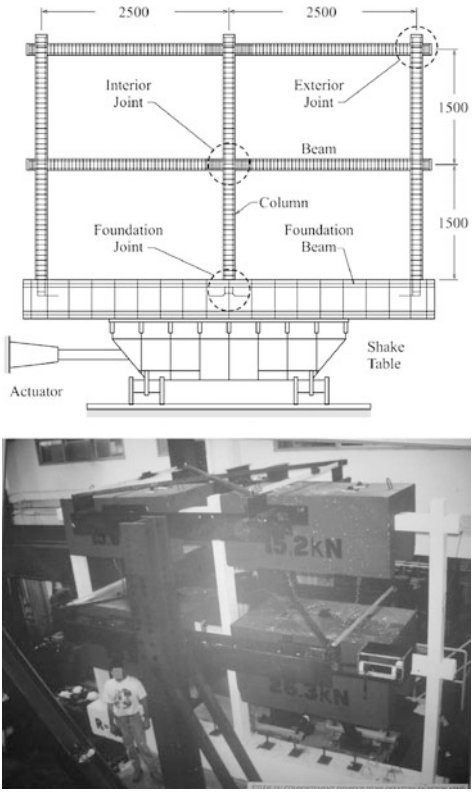

Fig. 16.1 RC frame structure tested on the shaking table at École Polytechnique in Montreal. Dimensions are in [mm]

simulate concentrated gravity loads from framing joints. The centers of gravity of the added masses were computed such that they coincide with the center of gravity of the beams. Service cracks were induced by these added masses. The total weight of the frame was 95 kN. The fundamental period T_1 of the structure with added masses was measured at 0.36 s in a free-vibration test. Mode 1 excites 91% of the total mass of the structure and when mode 2 is also considered approximately all the mass is excited.

The structure was assumed to be located in a seismic zone 4 in Canada, as depicted in the 1985 seismic zoning map of the National Building Code of Canada. The seismic hazard in this zone is such that peak horizontal ground acceleration between 0.16 g and 0.23 g is likely to be observed with 10% probability of exceedance in 50 years. Such seismic zones can be found in Western, Eastern and Northern Canada. The ground motion record that was selected for the test program corresponds to the N04W component of the accelerogram recorded in Olympia, Washington on April 13, 1949. Figure 16.2 presents the feedback record measured during the test initially scaled to a peak ground acceleration $PGA = 0.21\ g$ as well as the corresponding elastic response spectrum with 5% viscous damping ratio.

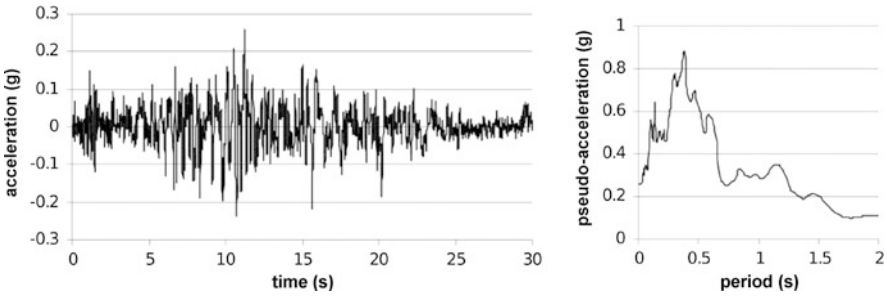

Fig. 16.2 Acceleration time history recorded on the shaking table during the test and corresponding elastic response spectrum with a critical viscous damping ratio of 5%

3 Seismic Inelastic Time History Analysis of the RC Frame

The set of equations of motion for the discretized structure is written as:

$$\mathbf{M}\ddot{\mathbf{d}}(t) + \mathbf{C}(t)\dot{\mathbf{d}}(t) + \mathbf{F}_R(t) = -\mathbf{M}\boldsymbol{\Delta}\ddot{u}_g(t) \tag{16.2}$$

where $\mathbf{d}(t)$ is the vector containing the nodal displacements, $\mathbf{M}$ is the mass matrix, $\mathbf{C}(t)$ is the damping matrix, $\mathbf{F}_R(t)$ is the inelastic resisting forces vector, $\boldsymbol{\Delta}\ddot{u}_g(t)$ is the vector of the rigid body acceleration induced by the ground displacement $u_g(t)$. In this section, we first present the inelastic structural model used to compute $\mathbf{F}_R(t)$, then we define two damping models: a "classical" Rayleigh model $\mathbf{C}_1(t)$ and a new model $\mathbf{C}_2(t)$, and we finally validate the capability of the two models for representing the behavior of the RC frame presented in the previous section.

3.1 Fiber Beam/Column Element

The inelastic structural model is based on a fiber frame element suitably implemented in the framework of a displacement-based formulation so that it can integrate the uniaxial concrete behavior law recently developed by the authors [17] and briefly presented in this section. This constitutive model is capable of representing the main energy dissipative phenomena likely to occur in concrete: appearance of permanent deformation, strain hardening and softening, stiffness degradation, local hysteresis loops, appearance of cracks. Its theoretical development and numerical implementation are based on thermodynamics with internal variables [18, 19] and on the finite element method with embedded strong discontinuities [20–22]. FEAP [23] is the finite element program used for the numerical implementation of the developments presented in this section.

Enhanced Kinematics The first ingredient of this model is the definition of an enhanced kinematics that takes strong discontinuities into account. This is done, as depicted in Fig. 16.3 by writing the displacement field $u(\mathbf{x}, t)$ as the sum of

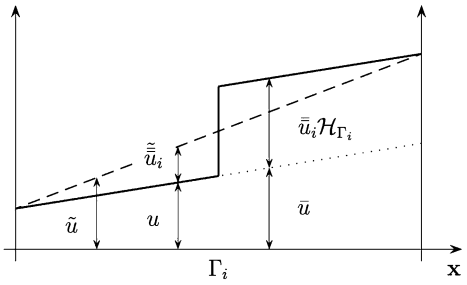

Fig. 16.3 Construction of an enhanced displacement field $u(\mathbf{x}, t)$ as the sum of a continuous displacement $\bar{u}(\mathbf{x}, t)$ and of a displacement jump $\bar{\bar{u}}_i(t)\mathcal{H}_{\Gamma_i}(\mathbf{x})$ pertaining to discontinuity Γ_i

a continuous displacement $\bar{u}(\mathbf{x}, t)$—that is the displacement as it would be in the absence of strong discontinuity—and of displacement jumps $\bar{\bar{u}}_i(t)$ in sections Γ_i of the solid domain Ω:

$$u(\mathbf{x}, t) = \bar{u}(\mathbf{x}, t) + \sum_{i=1}^{n_{dis}} \bar{\bar{u}}_i(t)\mathcal{H}_{\Gamma_i}(\mathbf{x}) \tag{16.3}$$

where $\mathcal{H}_{\Gamma_i}(\mathbf{x})$ is the Heaviside's function which, for a left-to-right oriented domain, is null on the left side of the discontinuity Γ_i and unity on its right side.

With the hypothesis of small transformation, we have the following expression for the normal strain field:

$$\epsilon_{xx}(\bar{u}, \bar{\bar{u}}_i, t) = \frac{\partial \bar{u}(\mathbf{x}, t)}{\partial \mathbf{x}} + \sum_{i=1}^{n_{dis}} \bar{\bar{u}}_i(t)\delta_{\Gamma_i}(\mathbf{x}) \tag{16.4}$$

where $\delta_{\Gamma_i}(\mathbf{x})$ is the Dirac's function.

Stored Energy Function When the Lagrange's variational principle is for instance chosen to derive the governing equations of the system (see Eq. (16.2) for the corresponding discretized form), the internal potential energy U^{int} as to be written:

$$\begin{aligned} U^{int}(\bar{u}, \boldsymbol{\alpha}, t) &= \int_{\Omega} \psi(\bar{u}, \boldsymbol{\alpha}, t)\, d\Omega \\ &= \sum_{f=1}^{n^c_{fib}} \int_{\Omega^c_f} \psi^c\left(\bar{u}, \boldsymbol{\alpha}^c, t\right) d\Omega^c_f + \sum_{f=1}^{n^s_{fib}} \int_{\Omega^s_f} \psi^s\left(\bar{u}, \boldsymbol{\alpha}^s, t\right) d\Omega^s_f \end{aligned} \tag{16.5}$$

where $n^{c,s}_{fib}$ is the total number of concrete or steel fibers, $\Omega^{c,s}_f$ is the volume of the fiber, $\psi^{c,s}$ is the stored energy function for concrete or steel which depends on the continuous displacement field $\bar{u}(\mathbf{x}, t)$ and on the set of internal variables $\boldsymbol{\alpha}^{c,s}$. Normal stresses are computed from these functions as

$$\sigma_{xx} = \frac{\partial \psi}{\partial \epsilon_{xx}}. \tag{16.6}$$

Set of Internal Variables The set of internal variables $\boldsymbol{\alpha}$ is defined to characterize the evolution of the main energy dissipative—inelastic—mechanisms which develop in the system. These internal variables are the memory of the system. The

$\boldsymbol{\alpha}$	Phenomenological analogy
$\bar{\epsilon}^p$	plastic deformation
$\bar{\xi}^p$	plastic isotropic strain hardening
$\bar{\lambda}^p$	plastic kinematic strain hardening
$\bar{D}$	damaged elastic compliance
$\bar{\xi}^d$	damage isotropic strain hardening
$\bar{\bar{u}}^p$	localized plastic displacement
$\bar{\bar{\xi}}^p$	strain softening due to displacement localization

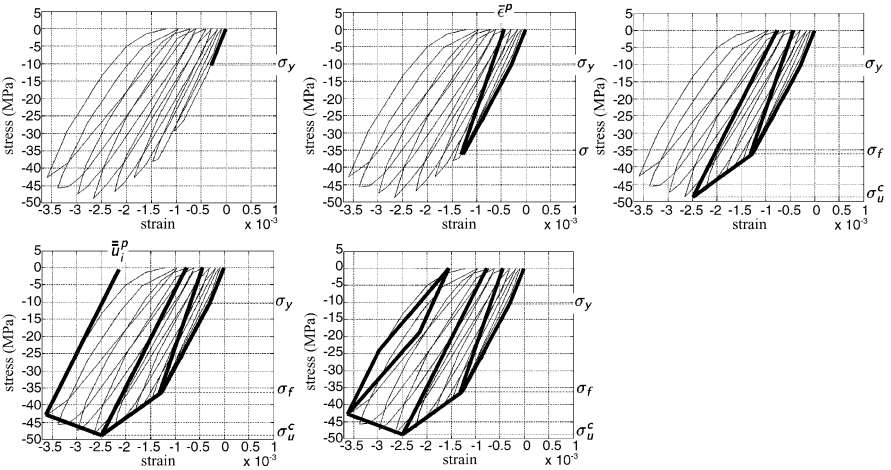

Fig. 16.4 Internal variables for compression and their phenomenological interpretation. [*top, left*] Elastic response until yield stress σ_y is reached. [*top, centre*] In the plastic domain, plastic deformation ($\bar{\epsilon}^p$) and strain hardening ($\bar{\xi}^p$) develop. [*top, right*] Once the limit stress σ_f is reached, damage mechanisms are activated too, leading to a degradation of stiffness ($\bar{D}$) and a change in the strain hardening evolution ($\bar{\xi}^d$). [*bottom, left*] Once the ultimate stress σ_u is reached, deformation localizes ($\bar{\bar{u}}^p$) and strain-softening is observed ($\bar{\bar{\xi}}^p$). [*bottom, center*] Local hysteresis loops are represented with kinematic hardening in the plastic domain ($\bar{\lambda}^p$). Note that each parameter of this model has a clear interpretation regarding the constitutive law to be identified

physical interpretation of each of them is provided in Fig. 16.4. Note that the constitutive law used here can handle different behavior in compression and tension, and can also reproduce a visco-elastic response (see [17] for a full description). Viscosity is not considered in this work and, for the sake of conciseness, we only focus on the compressive part of the behavior law in Fig. 16.4. The local admissible state of the system is expressed according to criteria functions in the stress-like domain of the set of variables dual to $\boldsymbol{\alpha}$. When irreversible mechanisms are activated in the structure, internal variables have to be updated and their evolution is governed by the principle of maximum dissipation. From the computational point of view, because we only consider linear hardening and softening laws, there is no need for

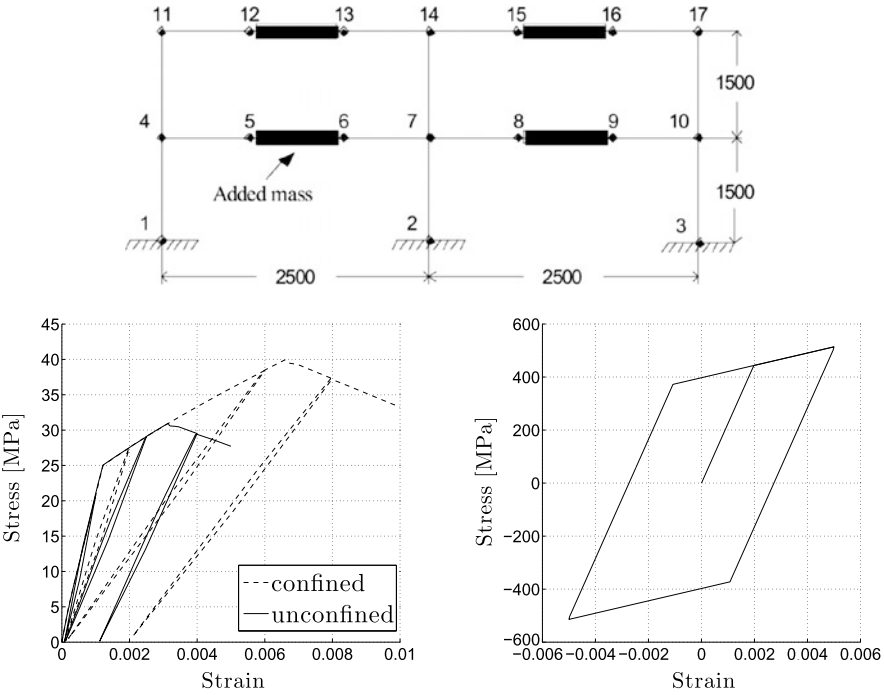

Fig. 16.5 Finite element mesh (dimensions in [mm]) and material constitutive laws for the inelastic structural modeling. [*bottom left*] Confined and unconfined concrete behavior laws. [*bottom right*] Steel constitutive law

local iteration when internal variables are updated, except for transitions between hardening and softening regimes, which leads to an efficient resolution procedure.

3.2 Inelastic Structural Model

The finite element mesh and the uniaxial constitutive laws for steel and both confined and unconfined concrete fibers used for the inelastic structural model of the RC frame are shown in Fig. 16.5. Material behavior laws have been identified to fit experimental monotonic ($\sigma_{xx} - \epsilon_{xx}$) curves. The structure is assumed fixed at its base. Rigid end zones are defined to model the beam-to-column connections and rebar slip in surrounding concrete is not represented. These later hypotheses are questionable because the connections exhibit inelastic behavior during the test. This obvious limitations of the structural model has to be reminded when damping model is added in the simulation.

The loading time history consists in two successive phases: (i) Static dead load is first applied step by step and then kept constant; (ii) The seismic loading is applied. A first validation check of the inelastic structural model is carried out by simulating

a free vibration test. Before dead load is applied, the elastic fundamental period of the structure is computed as $T_1^{ela} = 0.28$ s; then, due to the inelastic behavior of the structure, the elongated period is evaluated as $T_1^{ini} = 0.36$ s when dead load is completely applied. Both T_1^{ela} and T_1^{ini} coincide with the experimental values.

3.3 Proposition of a New Family of Rayleigh Damping Models

Basic Definitions In the context of inelastic time history numerical analysis, the definition of damping might differ according to the reference cited. On the one hand, in [24], damping consists in both (i) *inherent damping* resulting from the dissipation of energy by inelastic structural elements, and (ii) *additional viscous damping* added in the simulation to take into account inherent energy dissipation sources not otherwise explicitly considered in the inelastic structural model. On the other hand, in [25], damping is defined as "the portion of energy dissipation that is not captured in the hysteretic response of components that have been included in the model", and it is then suggested in [25] to use "un-modeled energy dissipation" as a more appropriate terminology for damping.

Because, in experimental investigations, measured damping results from all the energy dissipative phenomena, we herein decide to define damping as the combination of both *hysteretic damping* due to the energy dissipated by all the inelastic phenomena explicitly accounted for in the structural model and *additional viscous damping* that should be consistent with the inelastic structural model namely, that does not introduce energy dissipation already accounted for in the inelastic structural model.

Problems Encountered with Rayleigh Damping Controlling the amount of additional viscous damping energy dissipated in inelastic time history analyses is a very challenging task [11–13]. This is especially the case for commonly used Rayleigh proportional damping models, that is when the damping matrix is computed, in its most general form, as

$$\mathbf{C}(t) = \alpha(t)\mathbf{M} + \beta(t)\mathbf{K}(t), \tag{16.7}$$

where $\mathbf{K}(t)$ is the tangent stiffness matrix. Several researchers have provided insight in the comprehension of Rayleigh damping regarding the inelastic structural model it is coupled to, have highlighted limitations, and have eventually provided recommendations to cope with them [11–13]. Nevertheless, adding damping and controlling its consistency with the inelastic structural model still remains an issue to be addressed.

Three Common Phases in Seismic Response We now discuss in a qualitative way the notion of *consistency* for additional viscous damping. To that purpose, we start by stating that seismic structural response is composed by three main consecutive phases, as illustrated in Fig. 16.6. Both inelastic structural model and additional damping model must then be capable of representing the salient phenomena

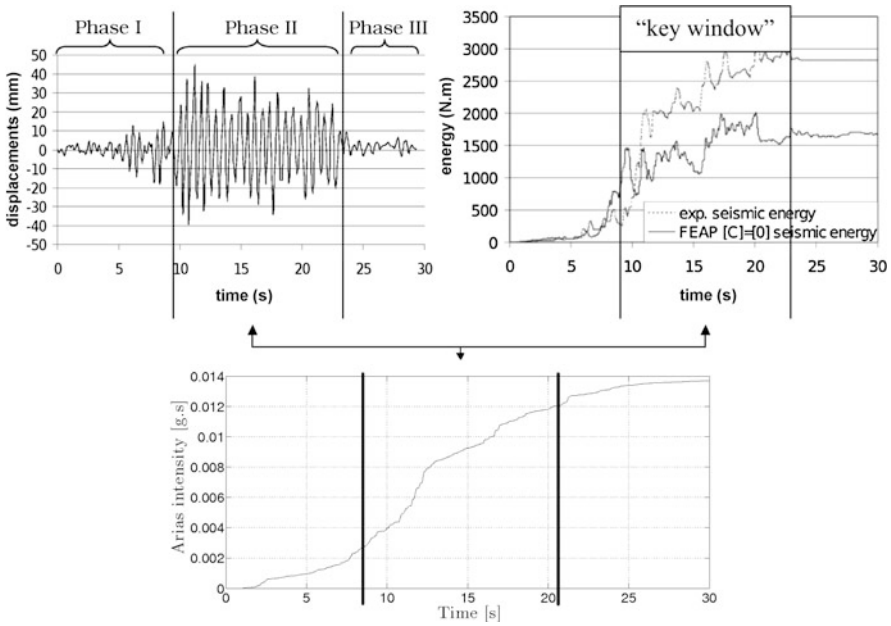

Fig. 16.6 Three common phases in the seismic response and the concept of "key window". [*top left*] Structural relative displacement time-history. [*top right*] Total relative seismic energy time-history in the structure. [*bottom*] Arias intensity of the seismic signal: $AI(t) = \frac{\pi}{2g} \int_0^t \ddot{u}_g^2(\tau)\, d\tau$

corresponding to each of these three phases. Foremost has to be properly modeled what we call here the "key window", namely the time interval within which the major inelastic modifications for structural performance assessment develop. For instance, key mechanisms that control near-collapse structural behavior are listed in [26]: degradation of strength and stiffness, and structure P-delta effects. From experimental results, we know that strain rate is another major issue.

A consistent additional damping model should be adapted to each of these three phases as follows:

- Phase 1: None or only few incursions in the inelastic domain occur. Energy dissipation in phase 1 thus comes from the friction in the cracks that appeared when applying dead load and from many other mechanisms always present in mechanical systems. When used, visco-elasticity and constitutive laws with local hysteresis [17, 27] in the structural model could account for these energy dissipation sources but a small amount of additional damping usually has to be added. For the RC frame considered in this work, a free-vibration test was carried out after dead load had been applied and a first modal damping ratio of 3.3% was measured [16].
- Phase 2: As the ground motion becomes stronger (at around 8 s in Fig. 16.6), an important amount of seismic energy is imparted to the structure and some parts of the structure then exhibit inelastic behavior. Inelastic structural models

are designed to explicitly model part of the numerous inherent nonlinear energy dissipative mechanisms involved in the structural response. The energy dissipation due to the mechanisms not explicitly accounted for in the inelastic structural model has to be introduced with the additional damping model.

- Phase 3: The structure has suffered irreversible degradations that modified its dynamic properties. Thus, even if the seismic demand is again as low as in phase 1, the energy dissipative mechanisms are different because of frictions in the cracks that appeared within phase 2 or at degraded bound between steel and concrete. Here again, visco-elasticity and behavior laws with local hysteresis [17, 27] in the structural model could account for these damping sources, but it generally has to be completed by additional damping.

Proposition of a New Family of Rayleigh Damping Models In the following, two damping models will be used:

- A commonly used Rayleigh model based on tangent stiffness matrix and with two constant coefficients

$$\mathbf{C}_1(t) = \alpha\mathbf{M} + \beta\mathbf{K}(t); \tag{16.8}$$

- We propose a new family of models that is directly dependent on both the two key notions in the definition of the three phases introduced above: the capacity of the inelastic structural model to absorb energy and the seismic demand. The model is based on Rayleigh damping with tangent stiffness matrix and with coefficients adapted to each of the three phases:

$$\mathbf{C}_2(t) = \alpha(t)\mathbf{M} + \beta(t)\mathbf{K}(t) \tag{16.9}$$

The idea of adapting Rayleigh damping to the capabilities of the inelastic structural model for dissipating energy is present in the use of the tangent stiffness rather than the initial one: it is expected that the choice of tangent stiffness dependent damping will have the main advantage of providing the significant additional source of damping only in the domains/modes that are not accounted for by inelastic model. Such a choice allows to provide the physically based damping phenomena interpretation, which leads to damping coefficients that are easier to identify. The same idea has been further exploited in [28] where 1% viscous damping is added to an inelastic dam model before cracking and 10% after cracking to represent localized high dissipation by friction between crack lips. Another instance is the work presented in [29] where viscous damping is added only in the shear wall zones which remain elastic, while no damping is added in the inelastic zones where the structural model is let alone to dissipate the seismic energy.

In spite of its stronger physical background, implementing damping model $\mathbf{C}_2(t)$ is not as straightforward as damping model $\mathbf{C}_1(t)$. First, three sets of Rayleigh coefficients $(\alpha_p, \beta_p)_{p=1,2,3}$ corresponding to each of the three phases p have to be identified to define the appropriate damping ratios ξ. Second, the instants which delimit the three phases have to be determined, which can be automatically accomplished by the computer program that is capable of detecting the activation of significant inelastic behavior.

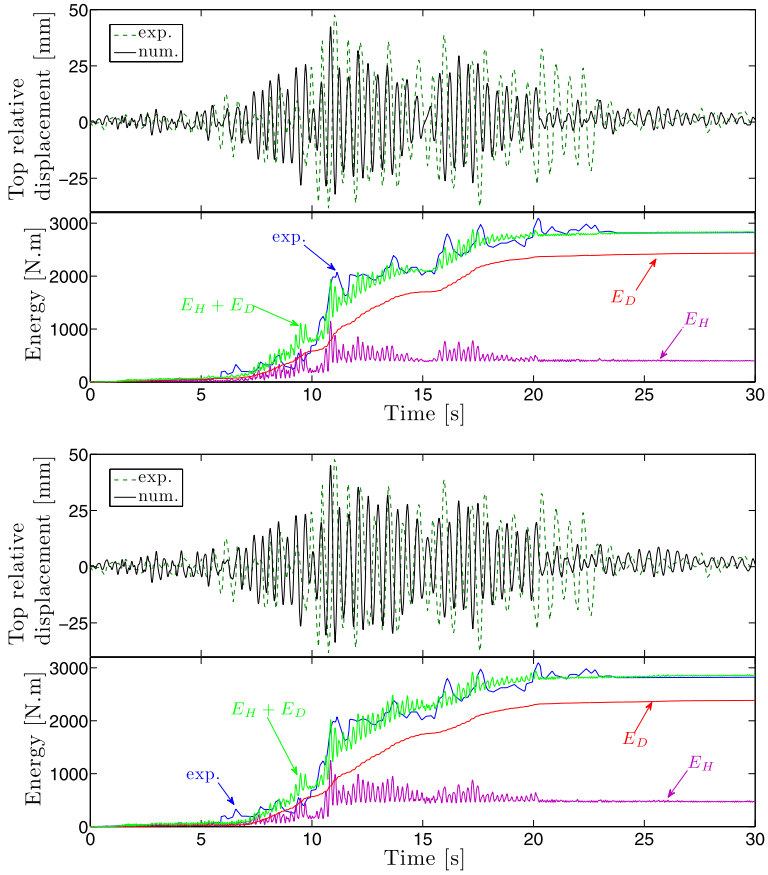

Fig. 16.7 Experimental and simulated top-displacement; simulated hysteretic plus elastic energies (E_H), simulated additional damping energy (E_D), and both experimental and simulated total internal work. [*top*] With common added damping model $\mathbf{C}_1(t)$; [*bottom*] With the proposed new family of Rayleigh damping models $\mathbf{C}_2(t)$. The structural responses shown here for damping models $\mathbf{C}_1(t)$ and $\mathbf{C}_2(t)$ looks very similar because both models have been calibrated to experimental data; however, model $\mathbf{C}_2(t)$ has more capability for representing transient evolution of added damping

3.4 Calibration and Validation of the Models

Seismic inelastic time history analyses of the RC frame have been carried out with the inelastic structural model presented above coupled to either additional damping model $\mathbf{C}_1(t)$ or $\mathbf{C}_2(t)$. The implicit Newmark integration scheme with parameters $\beta = 0.25$ and $\gamma = 0.5$ is used with a time step of 0.005 s. Figure 16.7 shows a comparison between the simulated top-displacement and energies time histories and the respective experimental results reproduced from [30]. Good agreement between simulated and experimental data can be observed. Moreover, there is very good agreement between the hysteretic plus elastic (E_H) and damping (E_D) energy

quantities computed with the models proposed here and an analogous Perform3D [31] simulation we carried out for comparison purpose, namely $E_H \approx 550$ N.m and $E_D \approx 2250$ N.m, corresponding to approximately 20% and 80% of the total work done by the structure during seismic motions. Last, the fundamental period of the RC frame in post-earthquake conditions is estimated by a free-vibration test performed at the end of the seismic signal and it is observed that simulated value is $T_1^{sim} = 0.45$ s whereas the experimental measure comes to $T_1^{exp} = 0.55$ s. This shows, as expected by regarding the limitations of the structural model used (elastic beam to column connections and no rebar slip), that not all structural stiffness degradation mechanisms are always well represented by the inelastic structural model. In particular, the joints and supports often need special attention and more elaborate models.

For damping model $\mathbf{C}_1(t)$, the good results shown in Fig. 16.7 have been obtained with α and β computed so that $\xi_1 = \xi_2 = 3.3\%$. For damping model $\mathbf{C}_2(t)$, curves plotted in Fig. 16.7 have been obtained with the following parameters identified so as to obtain good match between experimental and simulated responses:

- Phase 1: from $0 \leq t \leq t_1$, $\xi_1 = \xi_2 = 1.0\%$. t_1 is defined such that two conditions are satisfied. First, the hysteretic energy which is dissipated by the inelastic response of the structural model has to reach—for the frame considered in this work—150 N.m. Then, the seismic demand must be such that the increase in Arias intensity AI [32] within the time range $[t_1; t_1 + 10 \times T_1^{ini}]$ is larger than 0.0025 g.s; T_1^{ini} is the fundamental period of the structure after dead load has been applied and before the earthquake ($T_1^{ini} = 0.36$ s for the structure considered here).
- Phase 2: from $t_1 \leq t \leq t_2$, $\xi_1 = \xi_2 = 4.0\%$. t_2 is defined as $t_2 = t_1 + 10 \times T_1^{ini}$.
- Phase 3: from $t_2 \leq t \leq \bar{T}$, $\xi_1 = \xi_2 = 2.5\%$, where $\bar{T}$ is the duration of the seismic signal.

It might happen that one of these two criteria is never satisfied within the earthquake duration. In such a case, only phase 1 is effectively active throughout the analysis.

In the rest of this chapter, we focus only on the new model with changing coefficients, for it is very likely to deliver better prediction from the standard Rayleigh damping models given its more sound physical basis. The damping parameters defined above are expected to be suitable to model the response of the frame structure for every seismic signal that will be used in the next sections, as we usually proceed with damping model $\mathbf{C}_1(t)$. In the next sections, we then investigate likely consequences of using damping model $\mathbf{C}_2(t)$ instead of $\mathbf{C}_1(t)$ when it comes to structural fragility analysis.

4 Selection of a Set of Real Ground Motions

Following [33], there are three basic options available for obtaining accelerograms for inelastic time-history analysis: (i) to use spectrum-compatible synthetic ac-

celerograms with realistic energy, duration and frequency content; (ii) to use synthetic accelerograms generated from seismological source model and accounting for path and site effects; and (iii) to use real accelerograms recorded during earthquakes. We chose this latter option and present in the following how we proceed to select ground motion time histories in the PEER ground motion database [34].

4.1 Likely Earthquake Scenarios in the Cascadia Subduction Zone

Ground motion time history recorded from the Olympia, Washington 1949 earthquake has been used for the shaking table test at École Polytechnique of Montreal [16]. It is then assumed that the frame structure considered in this investigation is located in the Cascadia subduction zone. The Western margin of the North American plate—from the North of California state up to Vancouver island, British Columbia, Canada—is characterized by the so-called Cascadia subduction zone, where it is subducted by the Juan de Fuca plate beneath the Pacific ocean.

The seismic activity in the Cascadia subduction zone has been investigated for several decades [35–38]. Three types of earthquakes are produced in this zone:

- *Shallow crustal earthquakes* are associated to surface faults in the American continental plate with magnitude M_w larger than 7.0 and hypocenter depth less than 30 km;
- *Thrust interplate or interface earthquakes* are due to differential motion in the interface between the Juan de Fuca and the North American plates. They happen offshore with surface hypocenter, generally with depth less than 30 km. The Cascadia subduction zone has the potential to produce a large event of $M_w = 8.3 \pm 0.5$;
- *Intraplate or intraslab earthquakes* occur deep within the Cascadia subduction zone (depth $>$ 40 km) beneath the Puget Sound of Western Washington state. These types of earthquakes have occurred frequently including in 1949 Olympia ($M_w = 6.8$), 1965 Seattle–Tacoma ($M_w = 6.8$), 1999 Satsop ($M_w = 5.9$) and 2001 Nisqually ($M_w = 6.8$);
- No seismicity has been observed for depth larger than 100 km.

4.2 Search for a Real Ground Motions Dataset

To that purpose, we use the PEER ground motion database with its Web application [34]. Currently, this database is limited to recorded time series from shallow crustal earthquakes only. A basic criterion used by the Web application to select a representative acceleration time history is that its elastic response spectrum provides a good match to a user target spectrum over a range of periods of interest. We define the target spectrum as the elastic response spectrum corresponding to the feedback accelerogram recorded on the shaking table during the test (see

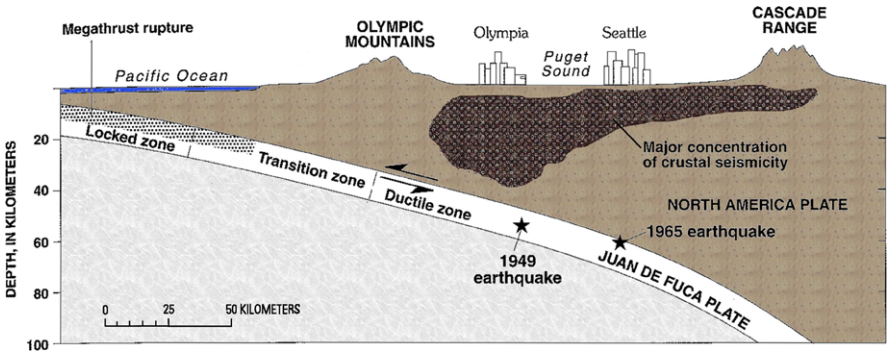

Fig. 16.8 Cross section of the Cascadia subduction zone (adapted from [36])

Table 16.1 Geologic profile for the Olympic Highway Test Lab strong-motion recording site in Washington [36]. v_s is the shear wave velocity and ρ the density

Depth [m]	Geology	Description	v_s [m/s]	ρ [kg/m^3]
0–3	Fill	Loose sand	165	1500
3–12	Deposits	Medium dense fine to medium sand	220	1500
12–20	Deposits	Interbedded very stiff to hard sandy silt and very dense silty fine to medium sand	270	1500
20–41	Deposits	(*same as layer just above*)	330	1500

Fig. 16.2). The Web application allows for assigning different weights to different period ranges so that the matching process is guided by the period ranges with the higher weights. In our case, the response of the structure is governed by its first eigenmode and the fundamental period was experimentally measured to vary within the range $0.36\ \text{s} \leq T_1 \leq 0.55\ \text{s}$ corresponding to the pre- and post-seismic states. We consequently favor the target and actual spectra to match within this period range.

Then, several parameters—or acceptance criteria—can be input into the Web application to characterize the likely earthquake scenarios of interest for the study. According to (i) what was stated in the previous Sect. 4.1, (ii) the cross section of the Cascadia subduction zone depicted in Fig. 16.8, and (iii) the geological profile of the Puget Sound region described in Table 16.1, we define suitable ranges for these parameters as summarized in Table 16.2. Practically, due to the above-mentioned current limitation of the PEER database, we only look for ground motion records corresponding to shallow crustal earthquakes.

Because a first search with these criteria led to a selection of around 20 earthquakes only, we proceeded to a second search with the range of allowed moment magnitudes extended to $6.0 \leq M_w \leq 9.0$. Then, we only retained 48 earthquakes which had the best fitting coefficients with the target response spectrum and finally multiply each of them by a scale factor of 5.0. Note that PEER ground motion database provides the fault normal (FN) and fault parallel (FP) components of the

Table 16.2 Acceptance criteria for initial ground motions search with the PEER database Web application [34]. M_w is the moment magnitude, R_{JB} is the Joyner–Boore distance, R_{rup} is the closest distance to rupture plane and v_{s30} is the average shear wave velocity in the top 30 meters of the site. All fault types are considered

Earthquake:	crustal	interface	intraslab
M_w	[7.0, 9.0]	[7.8, 8.8]	[5.5, 7.0]
R_{JB} [km]	[0, 150]	[30, 200]	[30, 200]
R_{rup} [km]	[0, 150]	[30, 100]	[30, 100]
v_{s30} [m/s]	[0, 200]	[0, 200]	[0, 200]

seismic signal and that the 48 records we selected either corresponds to the FN or FP component pertaining to 48 different earthquakes.

5 Seismic Fragility Analysis

In this section, we focus on the vulnerability analysis of the test RC frame structure presented in Sect. 2. Uncertainty is only considered in the seismic loading: the selected time-history ground motions that are likely to occur in the Cascadia subduction zone are used as inputs of inelastic time-history deterministic simulations to compute fragility curves. The damping model—either $\mathbf{C}_1(t)$ or $\mathbf{C}_2(t)$—is the only variable considered in the RC frame model.

5.1 Theoretical Background

Structural vulnerability analysis is evaluated here by computing fragility curves which provide the conditional probability for a structure to sustain a given damage level for a given earthquake intensity. Following [39], it is assumed that the fragility curve can be expressed in the form of a two-parameter lognormal distribution function. The estimation of these two parameters is then performed with the maximum likelihood method.

Let consider a sample of n independent observations x_j that can be classified in two classes as "success" ($x_j = 1$) and "failure" ($x_j = 0$). Let also consider that each realization x_j has a relative frequency of success equal to $F(IM_j, \theta)$, that is a function that depends on the intensity measure IM_j associated to each realization x_j and of a set of parameters θ. Then, the probability of observing a set of realizations $\mathbf{x} = (x_1, \ldots, x_n)$ composed of p successes $x_1, \ldots, x_p$ and $n - p$ failures $x_{p+1}, \ldots, x_n$, whatever the order, is ([40], p. 77):[1]

[1] Henri Poincaré (1854–1912) is a French mathematician, physician and philosopher. This year is the hundredth anniversary of his death.

$$f(\mathbf{x}|\theta) = \frac{n!}{p!(n-p)!}\big(F(IM_j,\theta)\big)^p \cdot \big(1 - F(IM_j,\theta)\big)^{n-p} \tag{16.10}$$

The problem one has to solve can be expressed as: *Given the observed data* $\mathbf{x}$*, find the set of parameters* θ *that is most likely to have produced these observed data*. To solve this inverse problem, we define the likelihood function as a function of θ given $\mathbf{x}$:

$$\mathcal{L}(\theta|\mathbf{x}) = f(\mathbf{x}|\theta). \tag{16.11}$$

The principle of maximum likelihood estimation states that: given the data $\mathbf{x}$ actually observed, the set of parameters θ looked for is the one that makes $\mathbf{x}$ the most likely data to be observed. θ can thus be identified by maximizing the likelihood function $\mathcal{L}$. For computational convenience, the log-likelihood $\ln \mathcal{L}(\theta|\mathbf{x})$ is introduced and maximized, which provides the same estimators because $\ln x$ is a monotonic function. The problem one has to solve thus reads:

$$\theta_e = \arg\max_{\theta} \ln \mathcal{L}(\theta|\mathbf{x}) \tag{16.12}$$

Under the lognormal assumption, the fragility curve for a particular damage index DI_i—defining what is "success" and "failure"—is defined as:

$$F(IM_j,\theta_e) = \phi\left(\frac{1}{\zeta_e}\ln\frac{IM_j}{c_e}\right) = P[DI \geq DI_i|IM_j] \tag{16.13}$$

where $\theta_e = \{\zeta_e, c_e\}$ is the set of estimated parameters and $\phi(\cdot)$ is the standardized normal distribution function.

Constructing fragility curves in such a framework raises issues concerning their statistical significance. In [39], Shinozuka *et al.* provide tools to test the goodness of fit between the inferred fragility curve and the realization of the random variable X_j following Bernoulli distribution: $X_j = 1$ when the damage index is reached and $X_j = 0$ otherwise. They also present a Monte Carlo technique they use to demonstrate the extent of the statistical variations in the estimators θ. Another very important contribution for the statistical analysis of fragility curves is the work of Sáez *et al.* [6]. They show how to compute the amount of Fisher information about the set of parameters θ—the terms of the Fisher information matrix being by definition $\mathcal{F}_{ij}(\theta) = \mathrm{cov}(\frac{\partial \ln \mathcal{L}}{\partial \theta_i}; \frac{\partial \ln \mathcal{L}}{\partial \theta_j})$, where $\mathrm{cov}(\cdot)$ denotes the covariance—which is provided by the ground motions used to construct fragility curves, and then how to compute a lower bound for the standard deviation of the elements of θ_e. This method thus provides a way to somehow measure the ability of the data to estimate θ.

5.2 Intensity Measures and Structural Damage Indices

To characterize the seismic ground motion time-histories used for structural vulnerability analysis, they are assigned intensity measures (*IM*). 18 of them are reviewed in [41] in the context of the issue of selecting earthquakes for incremental

dynamic analysis of inelastic steel frame structures. 44 *IM* are reviewed or proposed for masonry structures in [42]. Among the most common *IM*, one finds: the peak ground acceleration (*PGA*); the acceleration at the fundamental period $S_A(T_1, 5\%)$; the Arias intensity (*AI*) which is effectively a measure of the total energy in the ground motion and computed as

$$AI(t) = \frac{\pi}{2g} \int_0^t \ddot{u}_g^2(\tau)\, d\tau; \tag{16.14}$$

the significant duration D_{5-95}, which the time needed to build up between 5% and 95% of the total Arias intensity. Other measures are: the root mean square of acceleration (RMSA) computed as [41]:

$$RMSA = \sqrt{\frac{1}{\tau_d} \frac{2g}{\pi} AI}, \tag{16.15}$$

where τ_d is an effective duration of the record, taken here as D_{5-95}; spectrum intensities such as [42]:

$$SI_V = \int_{T_a}^{T_b} S_V(T, \xi)\, dT, \tag{16.16}$$

where S_V is the spectral velocity at period T and with damping ξ. Here, we take $T_A = 0.36$ s and $T_B = 0.55$ s which are the fundamental periods in pre- and post-earthquake conditions. For fragility surfaces, Seyedi *et al.* [5] chose the spectral displacement $S_D(T_1)$ and $S_D(T_2)$ where T_1 and T_2 are the two main eigenperiods in the direction along which the ground motions are applied.

Then, to characterize the structural response, damage indices (*DI*) are used. One can distinguish between three categories: (i) *DI* computed from energy quantities such as the Park–Ang–Wen damage accumulation model [43] or the normalized hysteretic energy used in [44] or [41]; (ii) Other *DI* based on quantities directly related to the structural inelastic response such as the ductility demand [41], the cumulative ductility index as defined in [44] or the maximum strength degradation ratio [42]; (iii) Other quantities not necessarily pertaining to—but affected by—the inelastic structural behavior such as the maximum relative roof displacement (*MRD*) or the maximum inter-story drift ratio (*MISDR*). To these two latter indices, because particular attention is paid in this work on the energy dissipated by both the damping and the inelastic structural models, we also compute the amount of hysteretic energy (E_H) dissipated by the inelastic mechanisms explicitly accounted for in the structural model and the amount of damping energy (E_D), as well as their respective ratio $E_{H,D}R = E_{H,D}/(E_H + E_D)$.

5.3 Fragility Curves

We first investigate in Table 16.3 the correlation between the intensity measures and damage indices considered in this work, when a linear model is used to predict a

Table 16.3 Square of the coefficient of correlation R^2 (in %) between actual *DI* and *DI* obtained from a linear model between *IM* and *DI*, for added damping models $\mathbf{C}_1(t)/\mathbf{C}_2(t)$

	MRD	*MISDR*	$E_{D/H}R$	E_D	E_H
PGA	73/71	71/69	3.5/0.6	51/52	36/37
AI	68/68	68/68	9.1/5.9	86/83	61/62
D_{5-95}	8/7	8/7	1.3/1.0	1/1	2/2
RMSA	75/73	74/73	8.2/4.5	57/55	43/45
$S_{A,V,D}(T_1, 5\%)$	85/82	84/82	5.7/2.6	68/68	53/55
$SI_{A,V,D}(5\%)$	77/74	77/75	8.5/4.6	57/57	48/51

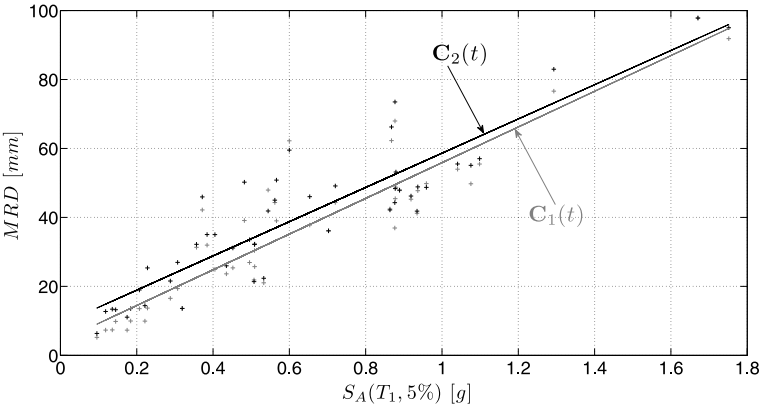

Fig. 16.9 Linear model between $S_A(T_1, 5\%)$ and *MRD* for both damping models $\mathbf{C}_1(t)$ and $\mathbf{C}_2(t)$

DI from an *IM*. Correlation is the lowest for intensity measure D_{5-95} because there is no explicit influence of the earthquake duration in the various *DI* considered. The correlation for the energy ratios is poor for all the *IM* considered, which is not the case for the dissipated energy quantities where, in particular, correlation is good with the energy contained in the seismic signal (*AI*). The very good correlated maximum roof displacement and spectral displacement at fundamental period T_1 with 5% viscous damping—as depicted in Fig. 16.9—will be used in the following to construct fragility curves.

In Fig. 16.9, one can see an obvious tendency to obtain larger maximum roof displacement with damping model $\mathbf{C}_2(t)$. Constructing fragility curves for a given *MRD* level along with a proper statistical analysis provides another way to infer some likely consequences of using a damping model instead of another. To that purpose, Fig. 16.10 shows the fragility curves (solid lines) pertaining to *DI MRD* ≥ 40 mm obtained with both damping models $\mathbf{C}_1(t)$ and $\mathbf{C}_2(t)$. Dashed lines approximately represent the smallest area the fragility curves would describe when its parameters $\theta = \{\zeta, c\}$ varies around $\theta_e = \{\zeta_e, c_e\}$ plus or minus their standard de-

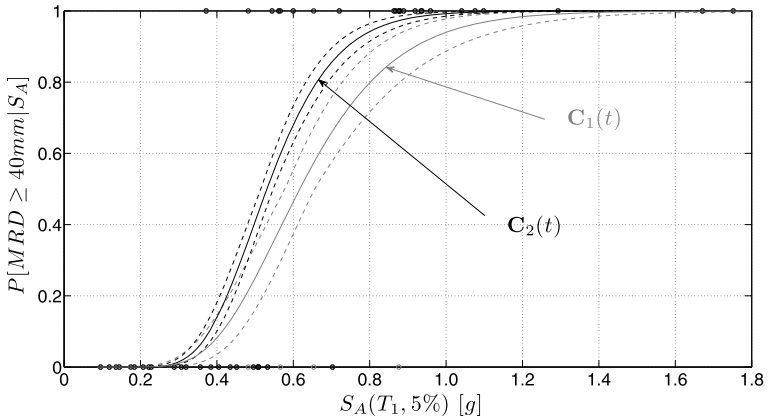

Fig. 16.10 Structural fragility curves (*solid lines*) for both damping models $\mathbf{C}_1(t)$ and $\mathbf{C}_2(t)$. *Dashed lines* are plotted according to the method presented in [6] and show that, for the *DI* level considered here, the fragility curves are constructed from a number of ground motions which is sufficient for drawing pertinent conclusions from this comparative study. *Circles* represent the realizations of the Bernoulli random variable $X_i = 1$ when $RMD_i \geq 40$ mm and $X_i = 0$ otherwise, $i \in [1; 48]$

viation. Dashed lines are constructed as in [6], relying on the inverse of the Fisher information matrix provided by the selected ground motion about θ.

From Fig. 16.10, one can infer that the additional damping model entails very significant uncertainty in structural fragility analysis of inelastic RC frame structures. Figure 16.11 is shown to provide better insight into the discrepancies one can expect to observe in the structural response when either damping model $\mathbf{C}_1(t)$ or $\mathbf{C}_2(t)$ is used. Both seismic signals considered have the same intensity measure $S_A(T_1, 5\%) = 0.51\ g$. For the analysis in concern on the left part of Fig. 16.11, either the maximum capacity of the structure to store hysteretic energy $E_H = 150$ N.m or the minimum seismic demand $0.0025/(t_2 - t_1)$ is not reached, so that, for damping model $\mathbf{C}_2(t)$, only the phase 1 with $\xi_1 = \xi_2 = 1\%$ is effectively active throughout the analysis; this makes both damping models analogous but with critical damping ratios in sharp contrast—3.3% against 1%—leading to very different structural responses. For the analysis in concern on the right part of Fig. 16.11, phase 2 begins at $t_1 = 15.4$ s until $t_2 = 19$ s. Both models predict almost identical *MRD* but oscillation amplitude is more rapidly attenuated for model $\mathbf{C}_1(t)$.

6 Conclusions and Perspectives

The inelastic structural response in seismic loading results from the combination of an inelastic structural model with an added damping model. The damping model has to be consistent with the inelastic structural model, which implies that it has, and only has, to model the energy dissipation sources not otherwise explicitly accounted

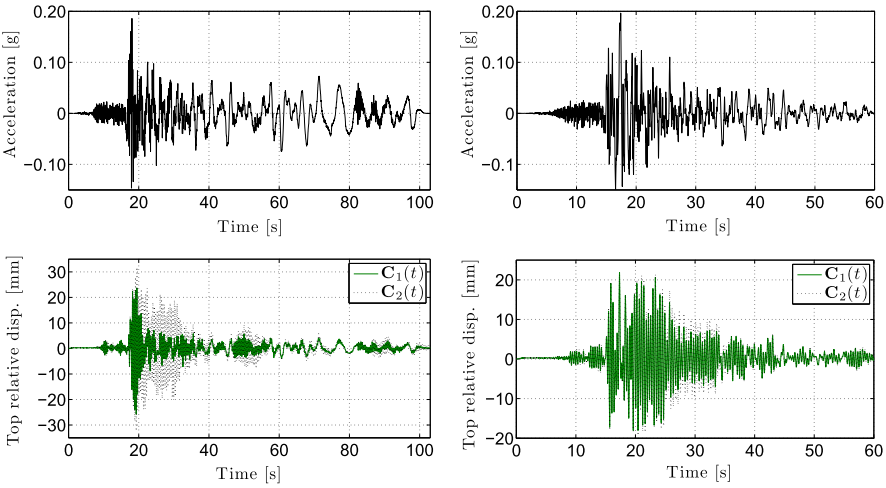

Fig. 16.11 [*left*] Analysis where only phase 1 is activated for damping model $\mathbf{C}_2(t)$. [*right*] Analysis where three phases are accounted for in damping model $\mathbf{C}_2(t)$. [*top*] Ground motion time-history. [*bottom*] Top relative displacement time-history; Model $\mathbf{C}_1(t)$ with $\xi_1 = \xi_2 = 3.3\%$ all along the simulation; [*bottom left*] Model $\mathbf{C}_2(t)$ with $\xi_1 = \xi_2 = 1\%$ all along the simulation; [*bottom right*] Model $\mathbf{C}_2(t)$ with $\xi_1 = \xi_2 = 1\%$ for $0 \leq t \leq 15.4$ s, $\xi_1 = \xi_2 = 4\%$ for 15.4 s $\leq t \leq 19$ s and $\xi_1 = \xi_2 = 2.5\%$ for 19 s $\leq t \leq 60$ s

for in the inelastic structural model, nothing more or less. Rayleigh damping models are the most commonly used for earthquake engineering applications, although it is well established that controlling the amount of energy dissipation these models introduce throughout inelastic time history simulations is difficult to achieve.

On another hand, inelastic time history analyses are widely used for structural fragility assessment in seismic loading. Uncertainties arising from the seismic signal likely to excite a building in a given geographical region as well as from the lack of knowledge on the structural parameters which characterize the inelastic structural model have both been considered in structural fragility analyses. On the opposite, the damping model is scarcely considered as a source of uncertainty; moreover, when it is the case, the damping ratio is assigned a probabilistic distribution but whether commonly used added damping models are suitable or not is an issue that is not regarded. This is the issue addressed in the work presented above.

In this chapter, we propose a new family of Rayleigh damping models that relies both on the capacity of the inelastic structural model to absorb energy and on the seismic demand and compare it to a commonly used Rayleigh model in the context of the fragility analysis of a RC moment-resisting frame. Its inelastic response is modeled by fiber elements using a constitutive law recently developed by the authors [17]. The structure is supposed to be built in the Cascadia subduction zone, a seismically active zone in the South-West of Canada and the North-West of the USA. From this comparative analysis, it can be inferred that the added damping model entails very significant uncertainty in structural fragility analysis of inelastic RC frame structures.

As a further development, we seek the proposed new family of Rayleigh damping models to be confronted to other experimental evidence, criticized and improved. Albeit constructed on a stronger physical basis than commonly used damping models, there is yet no clear guarantee that this model remains consistent with the inelastic structural model it is coupled to, throughout inelastic time history analysis. Finally, such a proposition for a damping model should not eclipse the need for further improvement of the inelastic structural model, which would, for the case treated in this work, at least involve explicitly accounting for the inelastic response of the beam to column connections.

Acknowledgements The authors thank Pr. André Filiatrault for providing the data from the shaking table tests used in this work. The first author benefited from partial funding from Électricité de France (EDF) within the research project "MARS" ("Modèles Avancés pour le Risque Sismique").

References

1. Howard, H.H.M., Huo, J.-R.: Generation of hazard-consistent fragility curves. Soil Dyn. Earthq. Eng. **13**(5), 345–354 (1994)
2. Jalayer, F., Beck, J.L.: Effects of two alternative representations of ground-motion uncertainty on probabilistic seismic demand assessment of structures. Earthquake Eng. Struct. Dyn. **37**, 61–79 (2008)
3. Rosic, B.V., Matthies, H.G., Zikovic, M., Ibrahimbegovic, A.: Formulation and computational application of inelastic media with uncertain parameters. In: Oñate, E., Owen, D.R.J. (eds.) Proceedings of the 10th International Conference on Computational Plasticity (COMPLAS X), CIMNE, Barcelona (2009)
4. Kafali, C., Grigoriu, M.: Seismic fragility analysis: application to simple linear and nonlinear systems. Earthquake Eng. Struct. Dyn. **36**, 1885–1900 (2007)
5. Seyedi, D.M., Gehl, P., Douglas, J., Davenne, L., Mezher, N., Ghavamian, S.: Development of seismic fragility surfaces for reinforced concrete buildings by means of nonlinear time-history analysis. Earthquake Eng. Struct. Dyn. **39**, 91–108 (2010)
6. Sáez, E., Lopez-Caballero, F., Modaressi-Farahmand-Razavi, A.: Effect of the inelastic dynamic soil-structure interaction on the seismic vulnerability assessment. Struct. Saf. **33**(1), 51–63 (2011)
7. Saxena, V., Deodatis, G., Shinozuka, M., Feng, M.Q.: Development of fragility curves for multi-span reinforced concrete bridges. In: Proceedings of International Conference on Monte Carlo Simulation, Monte-Carlo, Monaco (2000)
8. Popescu, R., Prevost, J.H., Deodatis, G.: 3d effects in seismic liquefaction of stochastically variable soil deposits. Géotechnique **55**(1), 21–31 (2005)
9. Lagaros, N.D.: Probabilistic fragility analysis: a tool for assessing design rules of rc buildings. Earthq. Eng. Eng. Vib. **7**(1), 45–56 (2008)
10. Ellingwood, B.R.: Earthquake risk assessment of building structures. Reliab. Eng. Syst. Saf. **74**, 251–262 (2001)
11. Léger, P., Dussault, S.: Seismic-energy dissipation in MDOF structures. J. Struct. Eng. **118**(6), 1251–1267 (1992)
12. Hall, J.F.: Problems encountered from the use (or misuse) of Rayleigh damping. Earthquake Eng. Struct. Dyn. **35**, 525–545 (2006)
13. Charney, F.A.: Unintended consequences of modeling damping in structures. J. Struct. Eng. **134**(4), 581–592 (2008)

14. Associate Committee on the National Building Code: National building code of Canada. Technical report, National Research Council of Canada, Ottawa, Ontario, Canada (1995)
15. Design of concrete structures for buildings. Standard CAN-A23.3-94, Canadian Standards Association, Rexdale, Ontario, Canada (1994)
16. Filiatrault, A., Lachapelle, É., Lamontagne, P.: Seismic performance of ductile and nominally ductile reinforced concrete moment resisting frames. I. Experimental study. Can. J. Civ. Eng. **25**, 331–341 (1998)
17. Jehel, P., Davenne, L., Ibrahimbegovic, A., Léger, P.: Towards robust viscoelastic-plastic-damage material model with different hardenings/softenings capable of representing salient phenomena in seismic loading applications. Comput. Concr. **7**(4), 365–386 (2010)
18. Germain, P., Nguyen, Q.S., Suquet, P.: Continuum thermodynamics. J. Appl. Mech. **50**, 1010–1020 (1983)
19. Maugin, G.A.: The Thermodynamics of Nonlinear Irreversible Behaviors—An Introduction. World Scientific, Singapore (1999)
20. Garikipati, K., Hughes, T.J.R.: A study of strain localization in a multiple scale framework—the one-dimensional problem. Comput. Methods Appl. Mech. Eng. **159**, 193–222 (1998)
21. Ibrahimbegovic, A., Brancherie, D.: Combined hardening and softening constitutive model of plasticity: precursor to shear slip line failure. Comput. Mech. **31**, 89–100 (2003)
22. Oliver, J., Huespe, A.E.: Theoretical and computational issues in modelling material failure in strong discontinuity scenarios. Comput. Methods Appl. Mech. Eng. **193**, 2987–3014 (2004)
23. Taylor, R.L.: FEAP: A Finite Element Analysis Program, User Manual and Programmer Manual, Version 7.4. University of California Press, Berkeley (2005)
24. Applied Technology Council: Quantification of building seismic performance factors. Technical Report FEMA P695, Federal Emergency Management Agency, Washington, DC (June 2009)
25. Applied Technology Council: Modeling and acceptance criteria for seismic design and analysis of tall buildings. Technical Report PEER 2010/111 or PEER/ATC-72-1, Pacific Earthquake Engineering Research Center, Richmond, CA (October 2010)
26. Krawinkler, H.: Importance of good nonlinear analysis. Struct. Des. Tall Spec. Build. **15**, 515–531 (2006)
27. Ragueneau, F., La Borderie, C., Mazars, J.: Damage model for concrete-like materials coupling cracking and friction, contribution towards structural damping: first uniaxial applications. Mech. Cohes.-Frict. Mater. **5**, 607–625 (2000)
28. Tinawi, R., Léger, P., Leclerc, M., Cipolla, G.: Seismic safety of gravity dams: from shake table experiments to numerical analyses. J. Struct. Eng. **126**(4), 518–529 (2000)
29. Luu, H., Ghorbanirenani, I., Léger, P., Tremblay, R.: Structural dynamics of slender ductile reinforced concrete shear walls. In: EURODYN 2011 (2011)
30. Filiatrault, A., Lachapelle, É., Lamontagne, P.: Seismic performance of ductile and nominally ductile reinforced concrete moment resisting frames. II. Analytical study. Can. J. Civ. Eng. **25**, 342–351 (1998)
31. CSI: Perform3D User's manual. Technical report, California (2007)
32. Arias, A.: A measure of earthquake intensity. In: Seismic Design for Nuclear Power Plants, pp. 438–483. MIT Press, Cambridge (1970)
33. Bommer, J.J., Acevedo, A.B.: The use of real earthquake accelerograms as input to dynamic analysis. J. Earthq. Eng. **8**(S1), 43–91 (2004)
34. Users manual for the PEER ground motion database web application. Technical report, Pacific Earthquake Engineering Research Center (November 2011)
35. Baker, G.E., Langston, C.: Source parameters of the 1949 magnitude 7.1 South Puget Sound, Washington, earthquake as determined from long-period body waves and strong ground motion. Bull. Seismol. Soc. Am. **77**, 1530–1557 (1987)
36. Silva, W.J., Wong, I.G., Darragh, R.B.: Engineering characterization of earthquake strong motions in the Pacific Northwest. In: Assessing Earthquake Hazards and Reducing Risk in the Pacific Northwest, vol. 2. U.S. Geological Survey Professional Paper 1560, pp. 313–324. United States Government Printing Office, Washington (1998)

37. Saragoni, G.R., Concha, P.: Damaging capacity of Cascadia subduction earthquakes compared with Chilean subduction. In: 13th World Conference on Earthquake Engineering, Vancouver, BC, Canada, August 1–6 (2004)
38. Wiest, K.R., Doser, D.I., Velasco, A.A., Zollweg, J.: Source investigation and comparison of the 1939, 1946, 1949 and 1965 earthquakes, Cascadia subduction zone, western Washington. Pure Appl. Geophys. **164**, 1905–1919 (2007)
39. Shinozuka, M., Feng, M.Q., Jongheon, L., Naganuma, T.: Statistical analysis of fragility curves. J. Eng. Mech. **126**(12), 1224–1231 (2000)
40. Poincaré, H.: Calcul des Probabilités. Cours de la Faculté des Sciences de Paris—Cours de Physique mathématique, 2nd edn. Gauthier-Villars, Paris (1912) (in French)
41. Léger, P., Kervégant, G., Tremblay, R.: Incremental dynamic analysis of nonlinear structures: selection of input ground motions. In: Proceedings of the 9th U.S. National and 10th Canadian Conference on Earthquake Engineering, Toronto, Ontario, Canada, July 25–29 (2010)
42. Bommer, J., Magenes, G., Hancock, J., Penazzo, P.: The influence of strong-motion duration on the seismic response of masonry structures. Bull. Earthq. Eng. **2**, 1–26 (2004). doi:10.1023/B:BEEE.0000038948.95616.bf
43. Park, Y.J., Ang, A.H.S., Wen, Y.K.: Seismic damage analysis of reinforced concrete buildings. J. Struct. Eng. **111**(4), 740–757 (1985)
44. Castiglioni, C.A., Pucinotti, R.: Failure criteria and cumulative damage models for steel components under cyclic loading. J. Constr. Steel Res. **65**, 751–765 (2009)

Chapter 17
Incremental Dynamic Analysis and Pushover Analysis of Buildings. A Probabilistic Comparison

Yeudy F. Vargas, Luis G. Pujades, Alex H. Barbat, and Jorge E. Hurtado

Abstract Capacity-spectrum-based-methods are also used for assessing the vulnerability and risk of existing buildings. Capacity curves are usually obtained by means of nonlinear static analysis. Incremental Dynamic Analysis is another powerful tool based on nonlinear dynamic analysis. This method is similar to the pushover analysis as the input is increasingly enlarged but it is different as it is based on dynamic analysis. Moreover, it is well known that the randomness associated to the structural response can be significant, because of the uncertainties involved in the mechanical properties of the materials, among other uncertainty sources, and because the expected seismic actions are also highly stochastic. Selected mechanical properties are considered as random variables and the seismic hazard is considered in a probabilistic way. A number of accelerograms of actual European seismic events have been selected in such a way that their response spectra fit well the response spectra provided by the seismic codes for the zone where the target building is constructed. In this work a fully probabilistic approach is tackled by means of Monte Carlo simulation. The method is applied to a detailed study of the seismic response of a reinforced concrete building. The building is representative for office buildings in Spain but the procedures used and the results obtained can be extended to other types of buildings. The main purposes of this work are (1) to analyze the differences when static and dynamic techniques are used and (2) to obtain a measure of the uncertainties involved in the assessment of the vulnerability of structures. The results show that static based procedures are somehow conservative and that uncertainties increase with the severity of the seismic actions and with the damage. Low dam-

Y.F. Vargas (✉) · L.G. Pujades
Department of Geotechnical Engineering and Geosciences, Technical University of Catalonia (BarnaTech), Jordi Girona 1-3, Building D2, Campus Norte UPC, 08034 Barcelona, Spain
e-mail: yeudy.felipe.vargas@upc.edu

A.H. Barbat
Structural Mechanics Department, Technical University of Catalonia (BarnaTech), Jordi Girona 1-3, Building C1, Campus Norte UPC, 08034 Barcelona, Spain

J.E. Hurtado
National University of Colombia, Apartado 127, Manizales, Colombia

M. Papadrakakis et al. (eds.), *Computational Methods in Stochastic Dynamics*, Computational Methods in Applied Sciences 26,
DOI 10.1007/978-94-007-5134-7_17,

age state fragility curves have little uncertainty while high damage grades fragility curves show great scattering.

1 Introduction

To prevent the seismic risk, it is necessary to assess the vulnerability of existing structures. To do that, several methods have been proposed, starting from different approaches. One is the vulnerability index method in which the action is defined by EMS-98 macroseismic intensities and structural behaviour through a vulnerability index [1, 2]. Another highly used method is based on the capacity spectrum. In this, the seismic action is defined by means of the 5% damped elastic response spectra and the vulnerability or fragility of the building by using the capacity curve. Capacity curves are calculated from an incremental nonlinear static analysis, commonly known as "Pushover Analysis" (PA) [3–5]. Another tool used to evaluate the performance of structures against seismic actions is the Incremental Dynamic Analysis (IDA) proposed by Vamvatsikos & Cornell [6]. The purpose of IDA is to obtain a measure of damage in the structure by increasing the intensity of the action record, in this case the peak ground acceleration. Vamvatsikos & Cornell makes an interesting analogy between PA and IDA, as both procedures are based on incremental increases of the loads on the structure and on the measure of its response in terms of a control variable which usually is the maximum displacement at the roof or the maximum inter storey drift, among others. Furthermore IDA allows obtaining the dynamic response of a structure for increasing seismic actions. On the other hand, most of the parameters involved in the structural response are random variables. In this work only the randomness due to the mechanical properties of the materials and the seismic action is considered. The randomness expected in the vulnerability and fragility of the building is analysed by means of Monte Carlo techniques. Therefore, a probabilistic comparison between the PA and the IDA is performed when calculating the fragility and expected damage of an existing reinforced concrete building. The main result of this work is the quantitative assessment of the expected randomness of the structural response, defined by its capacity curve, as well as of the fragility curves and the expected damage, which can be given in terms of mean values and standard errors. The damage assessment through nonlinear static procedures is tested against the results of fully nonlinear dynamic analyses. One of the main conclusions of this work is the importance of measuring the vulnerability of structures taking into account that the variables involved are random. Furthermore, this approach incorporates detailed information about the building and uses powerful tools to analyze the structure such as the PA and the IDA, providing valuable key information that can hardly be obtained with other simplified methods in which the building and the seismic actions are defined by only one parameter.

Fig. 17.1 Picture of the block of buildings omega located in the Technical University of Catalonia (BarnaTech) (*above*) and sketch of the 2D structural model (*below*)

2 Building Description

This paper analyzes a reinforced concrete structure, consisting of columns and waffle slabs, which is part of the North Campus of the Technical University of Catalonia in Barcelona, Spain. It has 7 stories and 4 spans, the height is 24.35 m and the width is 22.05 m. Figure 17.1 shows a block of four buildings as the analyzed one. In the first building 5 levels can be clearly seen; the other two stories are under the ground. The fundamental period of the building is 0.97 seconds. This value is higher when compared to that of conventional reinforced concrete buildings, because in the numerical model, the waffle slabs are approximated with beams of equivalent inertia and, therefore, are structural elements wide and flat leading to a reduction of the lateral stiffness of the structure. In the calculation model, the structural elements (equivalent beams and columns) follow an elasto-plastic constitutive law, which does not take into account either hardening or softening. Yielding surfaces are defined by the bending moment-axial load interaction diagram in columns and by the bending moment-angular deformation interaction diagram in beams.

Table 17.1 Parameters defining the Gaussian random variables considered in this work

	Mean Value (kPa)	Standard deviation (kPa)	Coefficient of variation
fc	25000	2500	0.1
fy	500000	50000	0.1

3 Damage Index Based on Pushover Analysis

Pushover analysis is the tool more often used to evaluate the behaviour of the structures against seismic loads. This numerical tool consists in applying horizontal loads to the structure, according to a certain pattern of forces and increasing its value until the structural collapse is reached. The result is a relationship between the displacement at the roof of the building and the base shear, called capacity curve. In this article, due to the probabilistic approach, the PA is performed repeatedly, therefore, it is appropriate to apply a procedure for obtaining automatically the horizontal load limit. To do that, Satyarno [7] proposes the adaptive incremental nonlinear analysis that establishes the horizontal load limit as a function of the tangent fundamental frequency, i.e. the frequency associated with the first mode of vibration, which is being calculated for each load increment. Therefore, the first mode of vibration to determine the shape of the load in height is calculated in each step. A detailed description of this procedure is found in the manuals of the program Ruaumoko [8] used here for calculating the static and dynamic nonlinear structural response. As mentioned above, the mechanical properties of the materials are considered as random variables. The impact of epistemic uncertainties in the structural response has been treated by Crowley et al. in [9] by considering the variation of the ground floor storey height, column depth and beam length, among others. The aim of that article is to generalize the results for a structural typology. In the present study, the aim is to obtain a measure of the uncertainties in the structural response for one building and, for this reason, we consider only the epistemic uncertainties associated to the compressive strength of concrete and the yield strength of steel. Thus, the values used in the structural design for concrete compressive strength *fc*, and the tensile strength associated with steel yielding strength *fy*, are considered as random variables assuming they follow a Gaussian probability function whose parameters are shown in Table 17.1. For the Monte Carlo analysis 1000 random samples are generated by means of the inversion method of the cumulative probability distribution curve. This method warranties the homogeneous distribution of the samples. Figure 17.2 shows the capacity curves obtained by means of the PA analysis.

The capacity curves shown in Fig. 17.2 are transformed into capacity spectra, which relate the spectral displacement to spectral acceleration by means of the following equations [10]:

$$sd_i = \frac{\delta_i}{PF_1}; \qquad sa_i = \frac{V_i/W}{\alpha_i} \tag{17.1}$$

The subscript i in Eq. (17.1) refers to the applied load increments on the structure during the PA; sd_i is the spectral displacement; δ_i is the displacement at the roof of

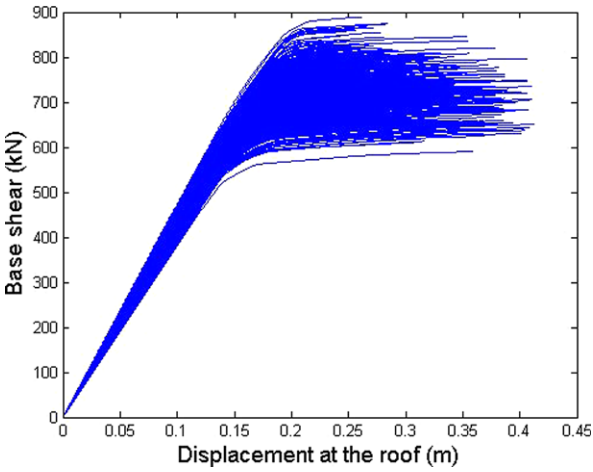

Fig. 17.2 Capacity curves obtained from the PA, taking into account the uncertainty in the mechanical properties of materials

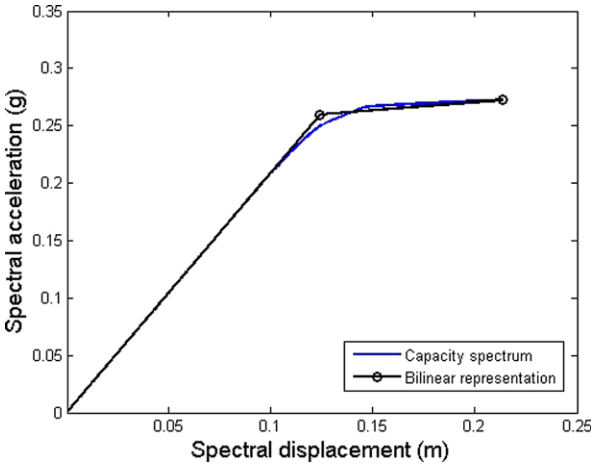

Fig. 17.3 Capacity spectrum and the bilinear representation

the building; PF_i is the modal participation factor of the first mode of vibration; sa_i is the spectral acceleration; V_i is the base shear; W is the weight of the building and α_i is the modal mass coefficient of the first mode of vibration.

On the other hand, the capacity spectrum can be represented in a bilinear form, which is defined completely by the yielding (Dy, Ay) and ultimate (Du, Au) capacity points. As we will see later on, this simplified form is useful for defining damage state thresholds in a straightforward manner; see also [5]. Assumptions to build the bilinear capacity spectrum are: (1) the area under the bilinear curve must be equal to the area of the original curve; (2) the coordinates of the point of maximum displacement must be the same in both curves; (3) the slope of the initial branch should be equal in both curves. Figure 17.3 shows an example of the bilinear representation of the capacity spectrum. Different studies have been proposed to calculate the damage of the structure from the definition of damage states (ds), which are a description of

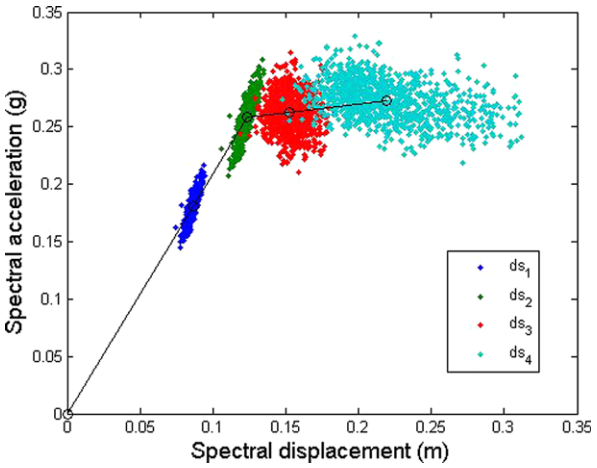

Fig. 17.4 Damage states as random variables

the damage in the structure for a given spectral displacement. For example, FEMA [11] and Risk UE [12], define 4 *ds*, namely *slight*, *moderate*, *extensive* and *complete*. Description of the damage states depends on the type of structure. For instance, according to FEMA [11], in the case of reinforced concrete structures, the *ds slight* is described as: "*beginning of cracking due to bending moment or shear in beams and columns*". *Collapse* state considers that the structure reaches an imminent risk of collapse. Risk UE defines the damage states in simplified form, starting from the capacity spectrum in its bilinear representation.

Based on the values (Dy, Ay) and (Du, Au), the spectral displacements for the four damage states threshold ds_i are obtained according to the following equations:

$$\begin{aligned} ds_1 &= 0.7 * Dy \\ ds_2 &= Dy \\ ds_3 &= Dy + 0.25 * (Du - Dy) \\ ds_4 &= Du \end{aligned} \tag{17.2}$$

Therefore, after calculating the capacity spectrum in bilinear representation and applying Eq. (17.2), it is possible to obtain the damage states thresholds as random variables, as is shown in Fig. 17.4. The mean, standard deviation and coefficient of variation of the damage states are shown in Table 17.2. It is worth noting how the co-

Table 17.2 Mean value, standard deviation and coefficient of variation of the damage states

	ds_1 (cm)	ds_2 (cm)	ds_3 (cm)	ds_4 (cm)
μ_{ds}	8.6	12.3	15.2	21.9
σ_{ds}	0.27	0.38	1.00	3.25
c.o.v.	0.03	0.03	0.06	0.15

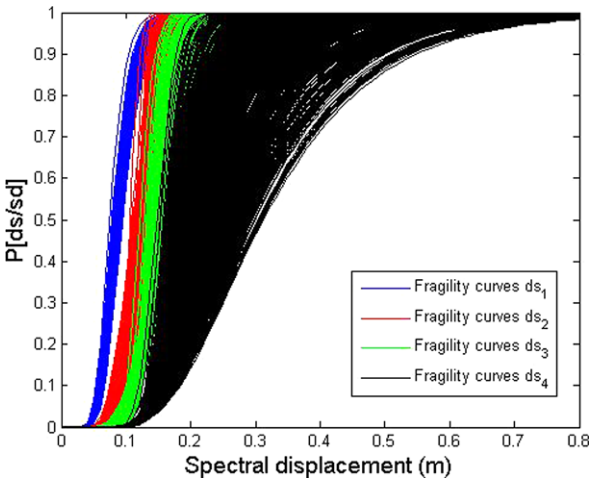

Fig. 17.5 Fragility curves as random variables

efficient of variation of the damage state 4 is greater than those of the input variables. This effect is due to the fact that this type of systems is not robust, mainly because of the nonlinearity of the problem. In addition, these results show the importance of the probabilistic approach in this type of analysis as the expected uncertainties in the output can be greater than those of the input variables. After obtaining the damage states as random variables it is also possible to calculate the fragility curves which, for each damage state, represent the probability of reaching or exceeding the corresponding damage state. Fragility curves are represented as a function of a parameter representing the seismic action, for instance spectral displacement, PGA, etc.

The following simplified assumptions to construct fragility curves from damage states thresholds are considered: (1) the probability that the spectral displacements in each damage state threshold, ds_i, equals or exceeds the damage state is 50%; (2) for each damage state ds_i, the corresponding fragility curve, follows a lognormal cumulative probability function described by the following equation:

$$P[ds_i/sd] = \phi\left[\frac{1}{\beta_{ds_i}}\,\mathrm{Ln}\left(\frac{sd}{ds_i}\right)\right] \tag{17.3}$$

where sd is the spectral displacement and β_{ds_i} is the standard deviation of natural logarithm of the damage state ds_i; (3) the expected seismic damage in buildings follows a binomial probability distribution. Figure 17.5 shows all fragility curves calculated after applying the described procedure.

Since the probabilities of occurrence of each damage state are easily obtained from the fragility curves, one can calculate the expected damage index, *DI*, which is the normalized mean damage state. *DI* can be interpreted as a measure of the overall expected damage in the structure.

$$DI = \frac{1}{n}\sum_{i=0}^{n} i\,P(ds_i) \tag{17.4}$$

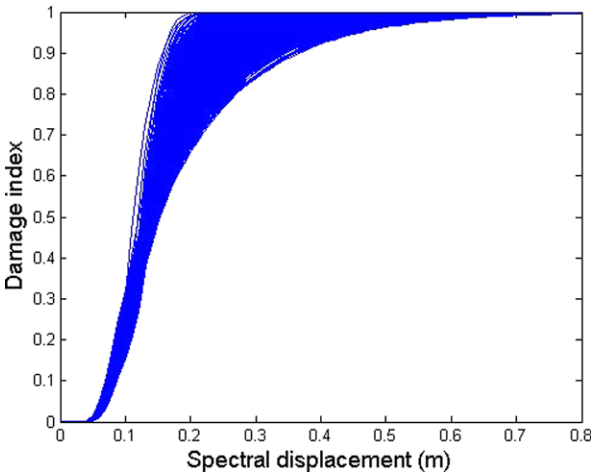

Fig. 17.6 Damage index curves obtained starting from the PA, considering the mechanical properties of the materials as random variables

where n is the number of damage states considered, in this case 5 (four non-null) and $P(ds_i)$ is the probability of occurrence of ds_i. Figure 17.6 shows the DI calculated from the fragility curves of Fig. 17.5. The curves of Fig. 17.6 must be interpreted as random vulnerability curves. These curves are an important result of this work as they allow linking PA and IDA procedures by comparing the obtained results.

4 Damage Index Based on the Incremental Dynamic Analysis

Dynamic analysis allows obtaining the time history of the response of a structure to an earthquake action. In IDA, the earthquake is scaled to various PGA, allowing obtaining the maximum response as a function, for instance, of PGA. As mentioned above, the main purpose of this article is to compare the results obtained with PA and IDA. An important element of the uncertainty related to the seismic response of structures is the random variability in the ground-motion prediction, whose influence has been studied in [13]. According to the probabilistic approach it is necessary to obtain the seismic action as a random variable. To do that, 20 earthquakes have been selected from two databases, one from Spain and the other from Europe [14], whose elastic response spectra are compatible with elastic response spectrum taken from EuroCode 8 (EC8) [15]. In this case, the elastic spectrum type 1 and soil D is selected. This spectrum corresponding to great earthquakes and soft soils has been chosen in order to submit the structure to strong enough seismic actions to obtain significant damage. Figure 17.7 shows the spectra of the selected earthquakes, their median value, and the spectrum type 1 soil D, taken from EC8. After selecting the accelerograms, the dynamic response of the structure is calculated for different PGA increasing at intervals of 0.04 g, until the value that causes the collapse. This value is 0.8 g. In each run of the nonlinear dynamic analysis, the damage index proposed by Park & Ang [16] and the maximum displacement at the roof of the building are calculated, allowing comparing these results with those of the PA analysis. Fig-

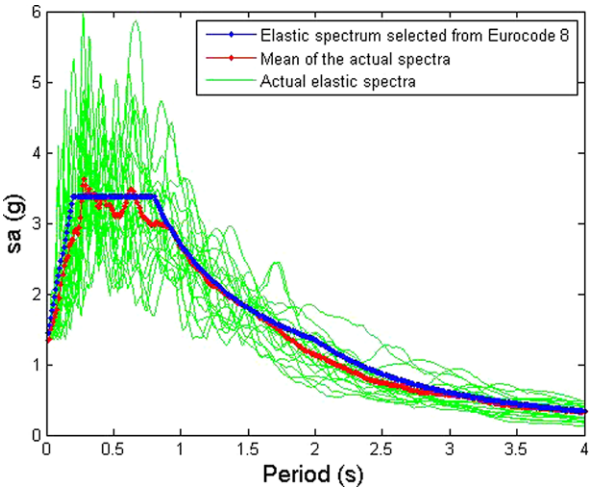

Fig. 17.7 Selected spectra of the accelerograms that are compatible with spectrum type 1 soil D of Eurocode 8

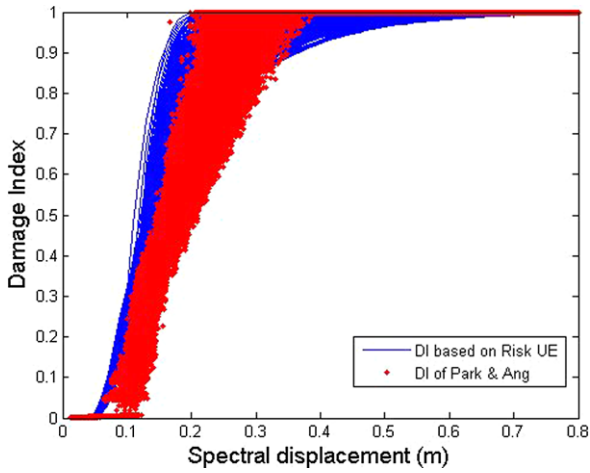

Fig. 17.8 Damage index obtained with static and dynamic procedures

ure 17.8 shows the results obtained. It is important to note the large scatter in both cases, showing the importance of assessing the vulnerability of structures from a probabilistic perspective, whichever procedure is used.

Figure 17.8 shows that the damage index obtained with the procedure based on the PA is conservative. However, for extreme cases when the damage index is close to 0 and 1, which correspond to the *null* and *collapse* damage states, similar values are obtained with both procedures. On the other hand, it can be seen that the curves obtained with the PA procedure are somehow conservative, as the structural damage begins for a smaller spectral displacement. PA based curves are shifted with respect to the IDA based curves. This behavior can be attributed to the fact that the damage state thresholds ds_1 and ds_3 in Eq. (17.2) are based on expert opinion. A little change in these values would avoid this shift. The use of constant coefficients, namely of 0.7

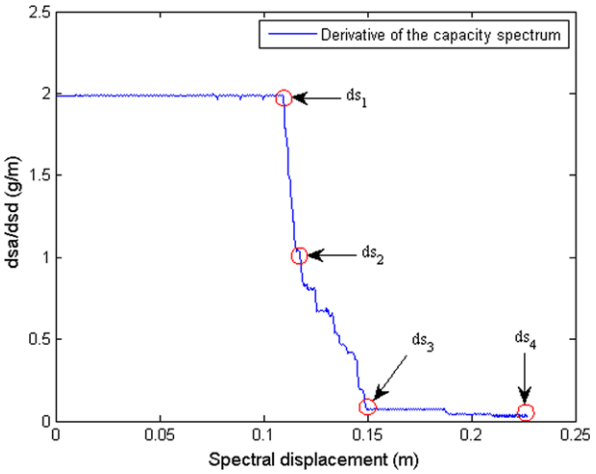

Fig. 17.9 Derivative of a capacity spectrum and new damage states

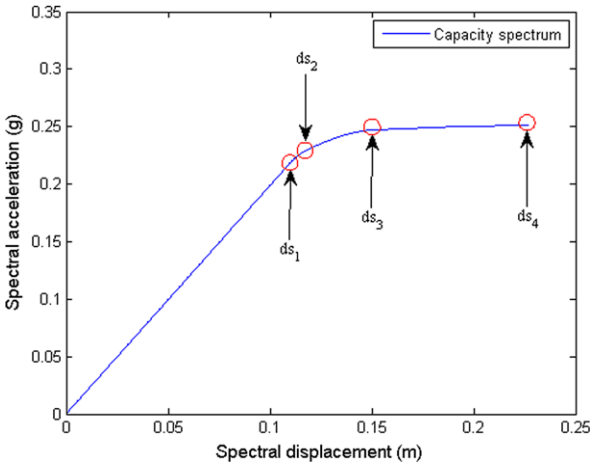

Fig. 17.10 Capacity spectrum and new damage states

and 0.25, in these equations are useful for massive large scale assessments. In this type of studies [5] a great amount of buildings is evaluated based on the use of simplified structural typologies owing to the difficulty to obtain specific capacity curves and coefficients for each building. This approach leads to reasonably good results in average sense. A new method for estimating the damage state thresholds is proposed here. This method is based on an accurate analysis of the variation of the slope of the capacity curve, namely of its derivative. It is worth noting too that, as we will see below, the new procedure of assessing the ds_1 and ds_3 thresholds avoids the shifting between PA and IDA based damage curves of Fig. 17.8.

Figure 17.9 shows an example of the derivative function of the capacity spectrum plotted in Fig. 17.10. In both figures the new damage states thresholds are shown.

In fact, the derivative function is related to the degradation of the stiffness as it gives the actual stiffness of the structure as a function of the spectral displacement

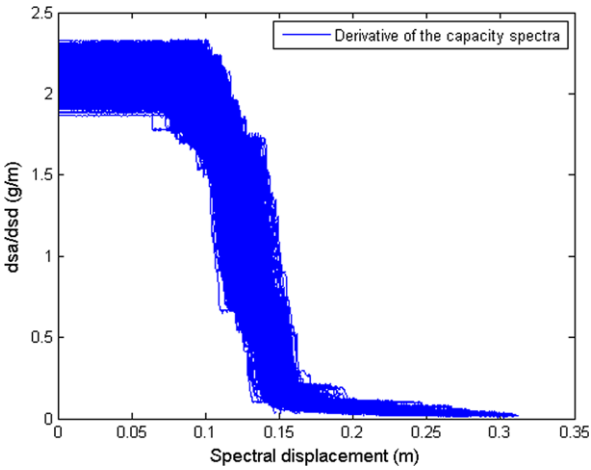

Fig. 17.11 Derivative functions of all capacity spectra

caused by lateral load increases in the pushover analysis. Then, ds_1 is defined by the spectral displacement where the lateral stiffness start to decrease; in other words, the point where the damage starts to increase. At this stage of the method, ds_2 has been defined as the spectral displacement corresponding to a reduction of 50% of the initial stiffness. ds_3 is defined by the spectral displacement where the derivative tends to be constant, indicating the end of the degradation of the stiffness which remains almost constant till the displacement of collapse. Finally, ds_4 is maintained as the spectral displacement corresponding to the ultimate point. It is worth noting that the shapes, but not the values, of the derivative functions are very similar for all the 1000 capacity spectra analyzed. See Fig. 17.11. Therefore, the new damage states based on the stiffness degradation and the damage states calculated via Risk UE approach, which will be called $ds_{i\text{-}S}$ and $ds_{i\text{-}R}$ respectively, are compared. In order to characterize the statistical properties of the distribution of the old (see Fig. 17.4) and new defined damage states, the Kolmogorov–Smirnov test [17] has shown that the damage states calculated with both approaches follow a Gaussian distribution. Figure 17.12 shows the comparison between both probability density functions. For the damage states different to *extensive* and *collapse*, the mean values and the standard deviations of the $ds_{i\text{-}S}$ are higher than those of $ds_{i\text{-}R}$. Then, the procedure described above for obtaining the fragility curves and damage indices was applied again by using the new damage states. Figure 17.13 shows the obtained results. For comparison purposes, the damage indices obtained by means of the dynamic analyses are also plotted in this figure. This figure allows comparing new and old damage index functions as well as each of these functions with the results of the dynamic analyses.

Concerning PA results, blue and black colour curves, a clear shift towards increasing spectral displacements of the new damage functions can be seen, indicating that the Risk UE choice is somehow conservative. Furthermore, new black curves fit better the IDA results (red points).

In order to quantitatively improve this comparison, Fig. 17.14 and Fig. 17.15 compare respectively the first and second moments of these distributions. These sta-

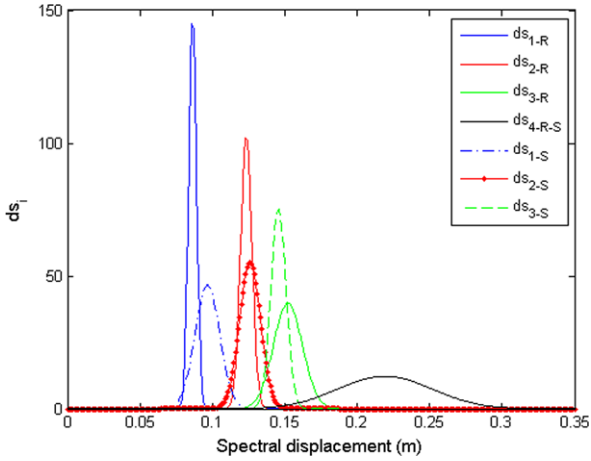

Fig. 17.12 Comparison between damage states based on Risk UE and stiffness degradation approach

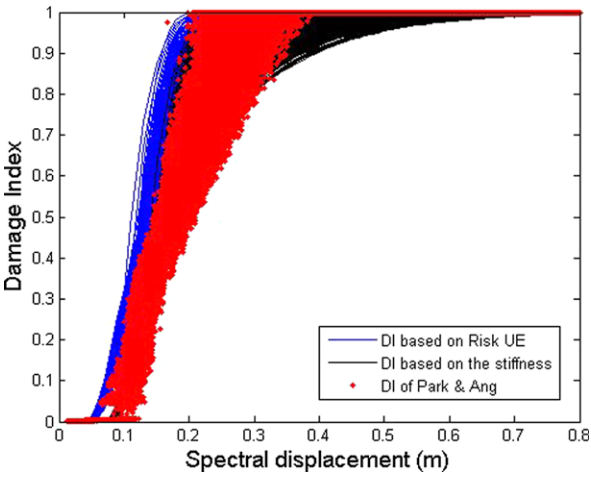

Fig. 17.13 Comparison between damage indices obtained with all methodologies

tistical properties, namely the mean values and standard deviations are computed for each spectral displacement by using the corresponding random ordinates. It can be clearly seen in Fig. 17.14 how the mean of the random variable obtained with the derivative approach fits quite well the mean of the damage index obtained via non-linear dynamic analysis. Figure 17.15 shows that, for spectral displacements in the range 0.1 to 0.3 m, the standard deviation corresponding to PA results is lower than one corresponding to IDA results. This effect is attributed to the fact that PA results do not consider the seismic actions leading to lower uncertainties. To consider the uncertainties of the seismic action, we use a simplified method allowing obtaining the expected displacement as a function of PGA for a given seismic input, represented by the 5% damped elastic response spectrum. Obviously, the building in this analysis is defined by its capacity spectrum. In this procedure, the elastic response spectrum is reduced based on the ductility of the building which is calculated from

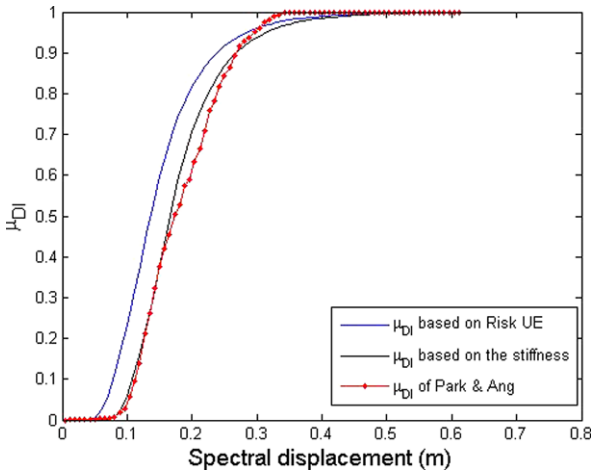

Fig. 17.14 Mean of the damage indices

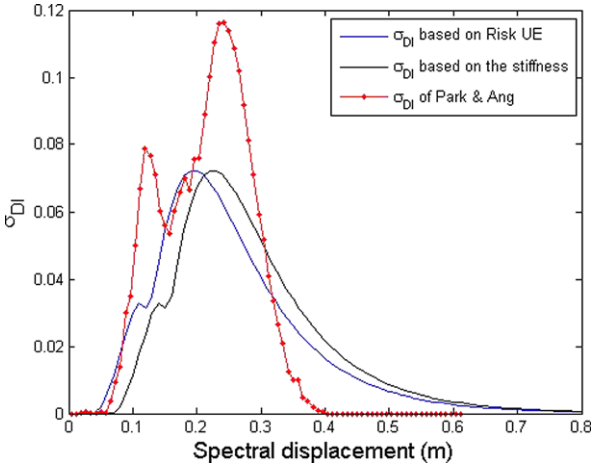

Fig. 17.15 Standard deviations of the damage indices

the capacity spectrum as the ratio between the spectral displacements of the ultimate capacity point (Du) and that of the yielding point (Dy) (see Fig. 17.3). An extended explanation of this technique can be found in [9] and has been also used in [18], it has been initially proposed by [19] and its development has been reviewed in [20]. In this way, increasing the PGA at intervals of 0.04 g between 0.04 and 0.8 g, as in the IDA, a relation between the PGA and the spectral displacement, sd, is obtained for each spectrum corresponding to each of the 20 accelerograms used and for each of the 1000 capacity spectra. Therefore, a total of 20000 relations between sd and PGA are obtained.

Figure 17.16 and Fig. 17.17 show the mean and the standard deviation curves of the damage indices as a function of PGA for PA, by using the new defined damage states, and IDA results.

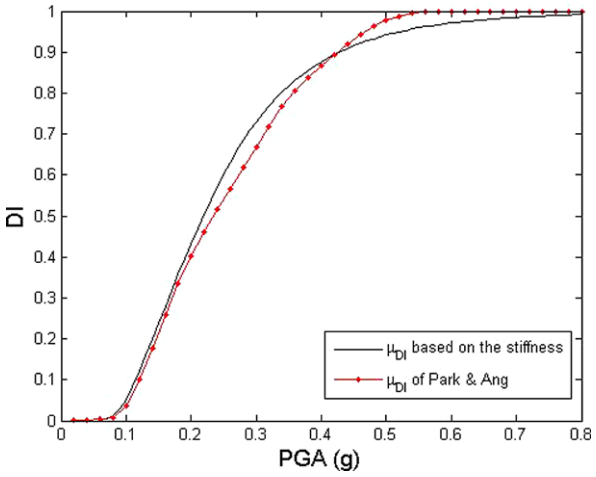

Fig. 17.16 Mean of the damage indices as a function of the PGA

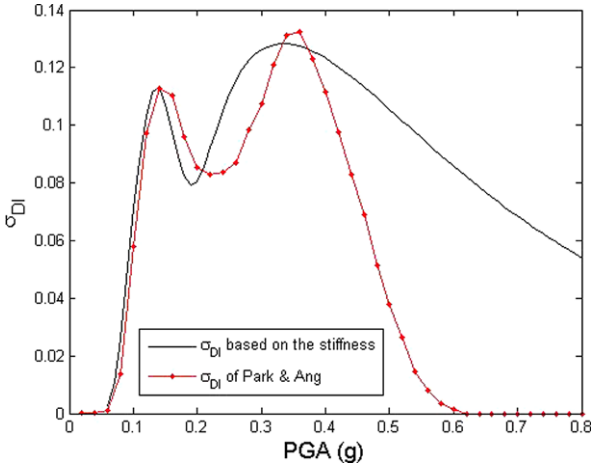

Fig. 17.17 Standard deviation of the damage indices as a function of the PGA

It can be seen how, in the range between 0 and 0.4 g, the mean values and the standard deviations show a good agreement. Note that now the uncertainties in the seismic actions are included in both curves. For greater values, standard deviations in the new PA approach are larger than for the IDA approach but both decrease because damage indices greater than one were not allowed. The fact of the better agreement between the PA and IDA results, when using the new damage states thresholds, indicates that this proposal based on the stiffness degradation, obtained from the derivatives of the capacity curves, should be preferred to the expert-opinion based one as proposed in the Risk UE approach. Furthermore, the damage index calculated in this way is able to represent, not only the expected damage obtained via nonlinear dynamic analysis, but also the uncertainties associated to the mechanical properties of the materials and the seismic action. Finally, it is important to note that in the case study building analysed here the Risk UE approach is a little conservative

as the damage appears before the new approach. This is so because the new damage states thresholds are greater. Obviously the spectral displacements of the damage states thresholds can coincide but if the new defined grades are smaller, the Risk UE approach may underestimate the expected damage. In any case, the new approach to determine damage state thresholds capture better the degradation of the buildings strength as indicated by the agreement with the IDA results.

5 Conclusions

In this work, the vulnerability of a real reinforced concrete structure, with columns and waffle slabs has been assessed, taking into account that the input variables are random. Only the randomness of the concrete compressive and the steel yielding strengths has been taking into account but the seismic action has been also considered in a stochastic way. Two approaches to evaluate the expected damage of the building have been used. The first one is based on the pushover analysis and the second one is based on the incremental dynamic analysis. An important conclusion is that, despite working with advanced structural analysis, these procedures show significant uncertainties when taking into account the randomness of the variables associated with the problem. It should be emphasized that in this work relatively small coefficients of variation for input variables have been considered taking into account the uncertainties that may exist in older structures that did not have quality control and have not been designed according to the earthquake-resistant criteria. The results obtained give support to the idea that static procedures are conservative when compared with the dynamic analysis. Furthermore, for expected damage analysis, a new procedure has been proposed to define the damage states thresholds. The technique is based on the degradation of the stiffness which can be observed in the derivative function of the capacity curve. The results using this new approach show a better agreement with the dynamic analysis than the obtained ones when using damage states thresholds based on expert-opinion.

Probably one of the most relevant conclusions of this work is that whichever procedure is used to evaluate the expected seismic damage of a structure, the input parameters of the structural problem to be treated, must be considered as random variables. We have seen how the probabilistic consideration of a few of these parameters produces significant uncertainties in the seismic response. Simplified deterministic procedures based on characteristic values usually lead to conservative results but some abridged assumptions on the definition of the seismic actions and on the estimation of the seismic damage states and thresholds can lead also to underestimate the real damage that can occur in a structure.

Acknowledgements This work was partially funded by the Geologic Institute of Catalonia (IGC), by the ministry of science and innovation of Spain and by the European Commission through research projects CGL-2005-04541-C03-02/BTE, CGL2008-00869/BTE, CGL2011-23621 INTERREG: POCTEFA 2007-2013/ 73/08 y MOVE—FT7-ENV-2007-1-211590. The first author has a scholarship funded by a bilateral agreement between the IGC and the Polytechnic University of Catalonia (BarnaTech).

References

1. Barbat, A.H., Yépez Moya, F., Canas, J.A.: Damage scenarios simulation for risk assessment in urban zones. Earthq. Spectra **2**(3), 371–394 (1996)
2. Barbat, A.H., Mena, U., Yépez, F.: Evaluación probabilista del riesgo sísmico en zonas urbanas. Revista internacional de métodos numéricos para cálculo y diseño en ingeniería **14**(2), 247–268 (1998)
3. Borzi, B., Phino, R., Crowley, H.: Simplified pushover analysis for large-scale assessment of RC buildings. Eng. Struct. **30**, 804–820 (2008)
4. Barbat, A.H., Pujades, L.G., Lantada, N., Moreno, R.: Seismic damage evaluation in urban areas using the capacity spectrum method: application to Barcelona. Soil Dyn. Earthq. Eng. **28**, 851–865 (2008)
5. Lantada, N., Pujades, L.G., Barbat, A.H.: Vulnerability index and capacity spectrum based methods for urban seismic risk evaluation. A comparison. Nat. Hazards **51**, 501–524 (2009)
6. Vamvatsikos, D., Cornell, C.A.: The incremental dynamic analysis. Earthquake Eng. Struct. Dyn. **31**(3), 491–514 (2002)
7. Satyarno, I.: Pushover analysis for the seismic assessment of reinforced concrete buildings. Dissertation, University of Canterbury (1999)
8. Carr, A.J.: Ruaumoko—inelastic dynamic analisys program. Dept. of Civil Engineering, Univ. of Canterbury, Christchurch, New Zealand (2000)
9. Crowley, H., Bommer, J.J., Pinho, R., Bird, J.F.: The impact of epistemic uncertainty on an earthquake loss model. Earthquake Eng. Struct. Dyn. **34**(14), 1635–1685 (2005)
10. ATC-40: Seismic evaluation and retrofit of concrete buildings. Applied Technology Council, Redwood City, California (1996)
11. FEMA: HAZUS99 technical manual. Federal Emergency Management Agency, Washington, DC, USA (1999)
12. RISK-UE: An advanced approach to earthquake risk scenarios with applications to different European towns. Project of the European Commission (2004)
13. Bommer, J.J., Crowley, H.: The influence of ground motion variability in earthquake loss modelling. Bull. Earthq. Eng. **4**(3), 231–248 (2006)
14. Ambraseys, N., Smit, P., Sigbjornsson, R., Suhadolc, P., Margaris, B.: Internet-site for European strong-motion data. European Commission, Research-Directorate General, Environment and Climate Programme. http://www.isesd.hi.is/ESD_Local/frameset.htm. Accesed 17 Apr 2011
15. Eurocode 8: Design of structures for earthquake resistance. Part 1: general rules, seismic actions and rules for building (2002)
16. Park, Y.J., Ang, A.H.S.: Mechanistic seismic damage model for reinforced concrete. J. Struct. Eng. **111**(4), 722–757 (1985)
17. Lilliefors, H.W.: On the Kolmogorov–Smirnov test for normality with mean and variance unknown. J. Am. Stat. Assoc. **318**, 399–402 (1967)
18. Vargas, Y.F., Pujades, L.G., Barbat, A.H., Hurtado, J.E.: Evaluación probabilista de la capacidad, fragilidad y daño sísmico en edificios de hormigón armado. Revista internacional de métodos numéricos para cálculo y diseño en ingeniería **29**(1) (2013, to appear)
19. Freeman, S.A., Nicoletti, J.P., Tyrell, J.V.: Evaluation of existing buildings for seismic risk—a case study of Puget Sound Naval Shipyard, Bremerton, Washington. In: Proceedings of U.S. National Conference on Earthquake Engineering, Berkeley, USA, pp. 113–122 (1975)
20. Freeman, S.A.: Review of the development of the capacity spectrum method. ISET J. Earthq. Technol. **41**, 1–13 (2004)

Chapter 18
Stochastic Analysis of the Risk of Seismic Pounding Between Adjacent Buildings

Enrico Tubaldi and Michele Barbato

Abstract Seismic pounding can induce severe damage and losses in buildings. The corresponding risk is particularly relevant in densely inhabited metropolitan areas, due to the inadequate clearance between buildings. In order to mitigate the seismic pounding risk, building codes provide simplified procedures for determining the minimum separation distance between adjacent buildings. The level of safety corresponding to the use of these procedures is not known a priori and needs to be investigated. The present study proposes a reliability-based procedure for assessing the level of safety corresponding to a given value of the separation distance between adjacent buildings exhibiting linear elastic behaviour. The seismic input is modelled as a nonstationary random process, and the first-passage reliability problem corresponding to the pounding event is solved employing analytical techniques involving the determination of specific statistics of the response processes. The proposed procedure is applied to estimate the probability of pounding between linear single-degree-of-freedom systems and to evaluate the reliability of simplified design code formulae used to determine building separation distances. Furthermore, the capability of the proposed method to deal with complex systems is demonstrated by assessing the effectiveness of the use of viscous dampers, according to different retrofit schemes, in reducing the probability of pounding between adjacent buildings modelled as multi-degree-of-freedom systems.

1 Introduction

Earthquake ground motion excitation can induce pounding in adjacent buildings with inadequate separation distance. The corresponding risk is particularly relevant

E. Tubaldi (✉)
Department of Architecture, Construction and Structures, Marche Polytechnic University, Via Brecce Bianche, 60131, Ancona, Italy
e-mail: etubaldi@libero.it

M. Barbato
Department of Civil & Environmental Engineering, Louisiana State University and A&M College, Nicholson Extension, Baton Rouge, LA 70803, USA
e-mail: mbarbato@lsu.edu

M. Papadrakakis et al. (eds.), *Computational Methods in Stochastic Dynamics*, Computational Methods in Applied Sciences 26,
DOI 10.1007/978-94-007-5134-7_18,

in densely inhabited metropolitan areas, due to the need of maximizing the land use and the consequent limited separation distance between adjacent buildings.

The problem of seismic pounding has been investigated by several researchers in the last two decades. A significant number of early studies focused on the definition of simplified rules, such as the Double Difference Combination (DDC) rule, for determining the peak relative displacement response of adjacent buildings at the potential pounding locations [1–3]. A critical separation distance (CSD) was defined and set equal to the mean peak relative displacement between adjacent buildings, by neglecting the associated probability of pounding. In the same context, considerable research effort was devoted to the assessment of the accuracy of code rules (e.g., the absolute sum (ABS) and square-root-of-the-sums-squared (SRSS) rules [4, 5]) in determining the mean peak relative displacement response (i.e., the CSD) of adjacent buildings.

More recent studies have proposed a probabilistic approach for the assessment of the seismic pounding risk. In Lin [6], a method was developed to estimate the first two statistical moments of the random variables describing the peak relative displacement response between linear elastic structures subjected to stationary base excitation. In Lin and Weng [7], a numerical simulation approach was suggested to evaluate the pounding probability, over a 50-year design lifetime, of adjacent buildings separated by the code-specified CSD. The latter study considered both the uncertainty affecting the seismic input intensity (by using a proper hazard model) and the record-to-record variability (by using artificially generated spectrum-compatible ground acceleration time histories as input loading). The buildings were modelled as multi-degree of freedom systems with inelastic behaviour and deterministic properties. In Hong et al. [8], a procedure was developed to assess the fractiles of the CSD between linear elastic systems with deterministic and uncertain structural properties subjected to stationary base excitation. The previous study was later extended by Wang and Hong [9] to include non-stationary seismic input.

Despite the numerous studies available in the literature on seismic pounding, to the best of the authors' knowledge, a reliability-based methodology for the evaluation of the safety levels associated with specified CSDs is still needed. In addition, the gradual progress of seismic design codes from a prescriptive to a performance-based design philosophy generates a significant need for new advanced, accurate, and computationally efficient reliability-based methodologies for the assessment and mitigation of seismic pounding risk.

This paper presents a fully probabilistic methodology for assessing the seismic pounding risk between adjacent buildings with linear behaviour. This methodology is consistent with and can be easily incorporated into a performance-based earthquake engineering (PBEE) paradigm such as the Pacific Earthquake Engineering Research centre (PEER) framework [10, 11]. The presented methodology considers the uncertainty affecting both the seismic input (i.e., site hazard and record-to-record variability) and the parameters used to describe the structural systems of interest (i.e., material properties, geometry, and damping properties). The seismic input is modelled as a nonstationary random process. The seismic pounding risk is computed from the solution of a first-passage reliability problem. While the approach proposed is general, the methodology presented here is specialized to linear

elastic systems subjected to Gaussian loading. Under these assumptions, approximate analytical solutions and efficient simulation techniques can be used to solve the relevant first-passage reliability problem. Thus, this methodology is appropriate for structural systems that remain in their linear elastic behaviour range before pounding (which is a very common condition for low values of the CSDs and, thus, high seismic pounding risk), although it can be extended to account for nonlinear behaviour of the considered structural systems.

2 PBEE Framework for Seismic Pounding Risk Assessment

The PEER PBEE framework is a general probabilistic methodology, based on the total probability theorem, for risk assessment and design of structures subjected to seismic hazard [10, 11]. The PEER PBEE methodology involves four probabilistic analysis components: (1) probabilistic seismic hazard analysis (PSHA), (2) probabilistic seismic demand analysis (PSDA), (3) probabilistic seismic capacity analysis (PSCA), and (4) probabilistic seismic loss analysis (PSLA). PSHA provides the probabilistic description of an appropriate ground motion intensity measure (*IM*), usually expressed as mean annual frequency (MAF), $\nu_{IM}(im)$, of exceedance of a specific value *im*. PSDA provides the statistical description of structural response parameters of interest, usually referred to as engineering demand parameters (*EDP*s), conditional to the value of the seismic intensity *IM*. PSCA consists in computing the probability of exceeding a specified physical limit-state, defined by structure-specific damage measures (*DM*s), and conditional to the values of the *EDP*s. Finally, PSLA provides the probabilistic description of a decision variable (*DV*), which is a measurable attribute of a specific structural performance and can be defined in terms of cost/benefit for the users and/or the society.

The reliability-based procedure developed in this paper consists in computing the MAF of pounding, ν_p, between two adjacent buildings. This procedure is a specialization for the seismic pounding problem of the first three steps of the general PEER PBEE framework (i.e., PSLA is beyond the scope of this paper). It is noteworthy that the proposed approach is conceptually very different from the computation of the CSD, which does not explicitly provide the probability of pounding associated with a given separation distance. The computation of the MAF of pounding can be expressed as

$$\nu_p = \int_{edp} \int_{im} G_{DM|EDP}(dm|edp) \cdot \left|\mathrm{d}G_{EDP|IM}(edp|im)\right| \cdot \left|\mathrm{d}\nu_{IM}(im)\right| \qquad (18.1)$$

in which, $G_{DM|EDP}(dm|edp) =$ complementary cumulative distribution function of variable *DM* conditional to $EDP = edp$, and $G_{EDP|IM}(edp|im) =$ complementary cumulative distribution function of variable *EDP* conditional to $IM = im$, where upper case symbols indicate random variables and lower case symbols denote specific values assumed by the corresponding random variable. The *IM* must be selected so that it can be readily related to the stochastic description of an appropriate random

process model for the input ground motion. This selection must also account for sufficiency and efficiency of the *IM* in describing the effects of the ground motion excitation on the structural response [12]. However, an exhaustive selection of appropriate *IM*s for different types of structures and structural performances is beyond the scope of this paper.

The maximum value $U_{rel,\max}$ of the relative distance $U_{rel}(t)$ between the adjacent buildings observed during the seismic event (i.e., for $t \in [0, t_{\max}]$, with $t =$ time and $t_{\max} =$ duration of the seismic event) is assumed here as *EDP*. The probabilistic distribution of $U_{rel,\max}$ reflects the record-to-record variability of the ground motions expected to occur at the site for a given intensity, as well as the effects of the uncertainty in the parameters used to describe the structural model. Finally, the pounding event is assumed as the controlling limit-state in PSCA, by using the following limit-state function, g:

$$g = \Xi - U_{rel,\max} \tag{18.2}$$

in which $\Xi =$ random variable describing the building separation distance, and the pounding event corresponds to $g \leq 0$. Thus, $G_{EDP|IM}(epd|im) = P[U_{rel,\max} \geq u|IM = im]$ and $G_{DM|EDP}(dm|edp) = P[g < 0|U_{rel,\max} = u]$. An important intermediate result of the procedure is the convolution of PSCA and PSDA, also called fragility analysis, which yields a fragility curve. Fragility curves describe the probability $P_{p|IM}$ of pounding conditional on the seismic intensity, i.e.,

$$P_{p|IM} = \int_{edp} G_{DM|EDP}(dm|edp) \cdot \left| \mathrm{d}G_{EDP|IM}(edp|im) \right| \tag{18.3}$$

The MAF of pounding, ν_p, can be used to compute the MAF of exceeding a specified value of *DV*, e.g., the MAF of repair cost due to pounding damage. The computation of the latter quantity requires the definition of a realistic loss model, based on appropriate structural response models (e.g., dynamic impact between adjacent systems) and damage models (e.g., damage produced by floor-to-floor and floor-to-column pounding). Structural response and damage models involve the definition of other *EDP*s and *DM*s, respectively, in addition to those already employed in this paper for assessing the pounding risk. Several structural response and damage models available in the literature could be employed to define an appropriate loss model [13–16].

In addition, ν_p can be directly used to determine the pounding risk, $P_p(t_L)$, for a given structure over its design life, t_L (e.g., 50 years). Assuming that the occurrence of a pounding event can be described by a Poisson process and that the buildings are immediately restored to their original condition after pounding occurs, $P_p(t_L)$ can be easily computed as

$$P_p(t_L) = 1 - e^{-\nu_p \cdot t_L} \tag{18.4}$$

3 Seismic Pounding Risk Assessment Methodology

Fragility analysis is the most computationally challenging component of the probabilistic PBEE framework. A simple and general approach for fragility analysis in

seismic pounding assessment is provided by Monte Carlo simulation (MCS) [5, 7]. For any given value of *IM*, MCS-based fragility analysis requires (1) the definition of a set of ground motions that are selected from an appropriate database of real records or generated from an appropriate random process, (2) the sampling of the structural parameters that define the structural systems and of their separation distances, (3) the numerical simulation of the structural response for each ground motion time history and each set of structural parameters and separation distances, and (4) the evaluation of $P_{p|IM}$ as the ratio between the number of failures and the number of samples. However, the computational cost associated with MCS can be very high and even prohibitive when small failure probabilities need to be estimated by numerically simulating the time history response of complex multi-degree-of-freedom (MDOF) systems.

In this paper, an efficient combination of analytical and simulation techniques is proposed for the calculation of $P_{p|IM}$ under the assumptions of linear elastic behaviour for the buildings and of Gaussian input ground motion. The methodology is described first for linear elastic systems with deterministic structural properties and separation distance, and then generalized to stochastic linear systems.

It is noteworthy that, for low values of the building separation distance, ξ, the buildings are expected to behave elastically before pounding occurs, while the assumption of linear behaviour of the buildings before pounding becomes less realistic for larger values of ξ. If the buildings are expected to enter their nonlinear behaviour before pounding, the methodology described in the remainder of this paper needs to be extended to nonlinear systems, e.g., by using statistical linearization techniques [17] or subset simulation [18]. This extension is beyond the scope of this paper.

3.1 Linear Systems with Deterministic Structural Properties

The computation of the conditional failure probability $P_{p|IM}$ can be expressed in the form of a single-barrier first-passage reliability problem as [5, 9]

$$P_{p|IM} = P\left\{\max_{0\le t\le t_{\max}}\left[U_{rel}(t)\right] \ge \xi \,|IM = im\right\} \tag{18.5}$$

in which $U_{rel}(t) = U_{\mathrm{A}}(t) - U_{\mathrm{B}}(t)$, $U_{\mathrm{A}}(t)$ and $U_{\mathrm{B}}(t)$ = displacement response of the adjacent buildings A and B at the (most likely) pounding location, and ξ = deterministic value of the building separation distance (Fig. 18.1).

Under the hypotheses of deterministic linear elastic systems subjected to Gaussian loading processes and deterministic threshold, several analytical approximations of $P_{p|IM}$ exist in the literature [19–22]. These analytical approximations require computing the following statistics of the relative displacement process $U_{rel}(t)$ for a given $IM = im$: $\sigma^2_{U_{rel}}(t)$ = variance of $U_{rel}(t)$, $\sigma^2_{\dot{U}_{rel}}(t)$ = variance of the relative velocity process $\dot{U}_{rel}(t)$, $\rho_{U_{rel}\dot{U}_{rel}}(t)$ = correlation coefficient between $U_{rel}(t)$ and $\dot{U}_{rel}(t)$, and $q_{U_{rel}}(t)$ = bandwidth parameter of $U_{rel}(t)$.

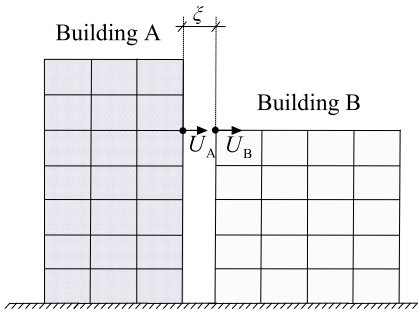

Fig. 18.1 Geometric description of the pounding problem between adjacent buildings

These statistics can be obtained from the spectral characteristics of order zero to two of process $U_{rel}(t)$ [23–25].

Following the methodology described in Barbato and Conte [24], a state-space formulation of the equations of motion for the two buildings is employed to compute exactly and in closed-form the required spectral characteristics. The seismic input is modelled as a time-modulated Gaussian colored noise process. For this specific input ground motion process, the spectral characteristics of the displacement processes (and of any response process obtained as a linear combination of the displacement processes) are available in exact closed-form for single-degree-of-freedom (SDOF) systems and both classically and non-classically damped MDOF systems [25].

The equations of motion for the linear system constituted by two non-connected adjacent buildings can be expressed as follows:

$$\mathbf{m} \cdot \ddot{\mathbf{U}}(t) + \mathbf{c} \cdot \dot{\mathbf{U}}(t) + \mathbf{k} \cdot \mathbf{U}(t) = \mathbf{p} \cdot F(t) \tag{18.6}$$

in which $\mathbf{m} = \begin{pmatrix} \mathbf{m}_A & \mathbf{0} \\ \mathbf{0} & \mathbf{m}_B \end{pmatrix}$, $\mathbf{c} = \begin{pmatrix} \mathbf{c}_A & \mathbf{0} \\ \mathbf{0} & \mathbf{c}_B \end{pmatrix}$, $\mathbf{k} = \begin{pmatrix} \mathbf{k}_A & \mathbf{0} \\ \mathbf{0} & \mathbf{k}_B \end{pmatrix}$, $\mathbf{U} = \begin{pmatrix} \mathbf{U}_A \\ \mathbf{U}_B \end{pmatrix}$, $\mathbf{m}_i$, $\mathbf{k}_i$, $\mathbf{c}_i$ and $\mathbf{U}_i$ = mass matrix, damping matrix, stiffness matrix, and vector of nodal displacements of building i, respectively ($i = \mathrm{A}, \mathrm{B}$), $\mathbf{p}$ = load distribution vector, $F(t)$ = scalar function describing the time-history of the external loading (input random process), and a superposed dot denotes differentiation with respect to time. It is noteworthy that connections between the two buildings (e.g., damping devices interposed between the building to mitigate seismic pounding risk) can be easily modelled by introducing the appropriate terms in matrix $\mathbf{c}$. The response process of interest $U_{rel}(t)$ can be related to the displacement response vector $\mathbf{U}(t)$ by means of a linear operator $\mathbf{b}$ as $U_{rel}(t) = \mathbf{b} \cdot \mathbf{U}(t)$.

The probability of pounding conditional on $IM = im$ is given by

$$P_{p|IM} = 1 - P\left[U_{rel}(t=0) < \xi | IM = im\right] \times \exp\left\{ - \int_0^{t_{\max}} h_{U_{rel}|IM}(\xi, \tau) \cdot \mathrm{d}\tau \right\} \tag{18.7}$$

in which $P[U_{rel}(t=0) < \xi | IM = im]$ = probability that the random process $U_{rel}(t)$ is below the threshold ξ at time $t = 0$, and $h_{U_{rel}|IM}(\xi, t)$ = time-variant hazard function (i.e., up-crossing rate of threshold ξ conditioned on zero up-crossings be-

fore time t) conditional on $IM = im$. For systems with at rest initial conditions, $P[U_{rel}(t=0) < \xi | IM = im] = 1$.

To date, no exact closed-form expressions exist for the time-variant hazard function $h_{U_{rel}|IM}(\xi, t)$. However, several approximate solutions are available in the literature, e.g., Poisson's (P), $h^{(\mathrm{P})}_{U_{rel}|IM}(\xi, t) = \nu_{U_{rel}|IM}(\xi, t)$, classical Vanmarcke's (cVM), $h^{(\mathrm{cVM})}_{U_{rel}|IM}(\xi, t)$, and modified Vanmarcke's (mVM), $h^{(\mathrm{mVM})}_{U_{rel}|IM}(\xi, t)$, approximations [22, 26]. These analytical approximations can be readily computed based on the closed-form expressions of the spectral characteristics of process $U_{rel}(t)$, as shown in Barbato and Vasta [25]. In addition, for linear elastic systems subjected to Gaussian loading, $P_{p|IM}$ can be efficiently and accurately estimated by using the Importance Sampling using Elementary Events (ISEE) method [27].

3.2 Linear Systems with Uncertain Structural Properties and Separation Distance

In addition to the uncertainty in the seismic input, significant uncertainty can be found in geometrical, mechanical, and material properties characterizing the structural systems and their models. Hereinafter, the uncertainty in geometrical, mechanical, and material properties of the structural models, as well as in their separation distance, Ξ, is referred to as model parameter uncertainty (MPU). MPU can significantly modify the structural performance and, thus, must be considered in the assessment of seismic pounding risk.

In order to include the effects of MPU, the total probability theorem is employed to compute the conditional probability of pounding as follows:

$$P_{p|IM} = \int_{\mathbf{X}} P_{p|IM,\mathbf{X}}(\mathbf{x}) \cdot f(\mathbf{x}) \cdot \mathrm{d}\mathbf{x} = E_{\mathbf{X}}[P_{p|IM,\mathbf{X}}] \tag{18.8}$$

in which $\mathbf{X}$ = vector of uncertain model parameters (including the uncertain separation distance Ξ) with joint probability density function $f_{\mathbf{X}}(\mathbf{x})$, $P_{p|IM,\mathbf{X}}(\mathbf{x})$ = probability of pounding conditional on $\mathbf{X}$ and IM, and $E_{\mathbf{X}}[\ldots]$ = expectation operator with respect to vector $\mathbf{X}$.

MCS, or any variance reduction technique such as stratified sampling, can be employed to evaluate $P_{p|IM}$ in Eq. (18.8). For example, Latin hypercube sampling (LHS) can be employed for its computational efficiency [28]. The samples of vector $\mathbf{X}$ generated by using LHS can be used to define a set of deterministic linear elastic models with deterministic separation distance, for which the conditional probability of pounding can be computed as in Eq. (18.7).

4 Application Examples

In this section, the proposed methodology is applied to: (1) compute the pounding risk for SDOF systems with deterministic model parameters, (2) evaluate the re-

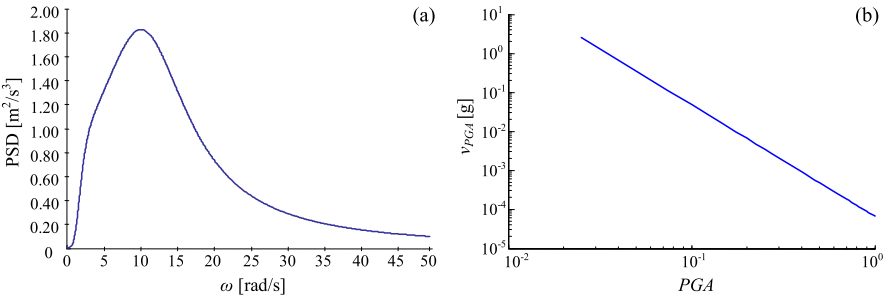

Fig. 18.2 Input ground motion: (**a**) PSD function of the embedded stationary process, and (**b**) site hazard curve

liability of simplified design code formulae used to determine building separation distance, and (3) to evaluate the effectiveness of different retrofit solutions using viscous dampers in reducing the pounding risk for deterministic MDOF models of multi-storey buildings. In all the application examples considered here, the input ground acceleration is modelled by a time-modulated Gaussian process. The time-modulating function, $I(t)$, is represented by the Shinozuka–Sato's function [29], i.e.,

$$I(t) = c \cdot \left(e^{-b_1 \cdot t} - e^{-b_2 \cdot t}\right) \cdot H(t) \tag{18.9}$$

in which $b_1 = 0.045\pi$ s^{-1}, $b_2 = 0.050\pi$ s^{-1}, $c = 25.812$, and $H(t) =$ unit step function. A duration $t_{\max} = 30$ s is considered for the seismic excitation.

The power spectral density (PSD) of the embedded stationary process is described by the widely-used Kanai–Tajimi model, as modified by Clough and Penzien [30], i.e.,

$$S_{CP}(\omega) = S_0 \frac{\omega_g^4 + 4\xi_g^2\omega^2\omega_g^2}{[\omega_g^2 - \omega^2]^2 + 4\xi_g^2\omega^2\omega_g^2} \cdot \frac{\omega^4}{[\omega_f^2 - \omega^2]^2 + 4\xi_f^2\omega^2\omega_f^2} \tag{18.10}$$

in which $S_0 =$ spectral amplitude of the bedrock excitation (considered to be a white noise process), ω_g and $\xi_g =$ fundamental circular frequency and damping factor of the soil, respectively, and ω_f and $\xi_f =$ parameters describing the Clough–Penzien filter. The values of the parameters employed for all the applications are $\omega_g = 12.5$ rad/s, $\xi_g = 0.6$, $\omega_f = 2$ rad/s, and $\xi_f = 0.7$. The PSD function in Eq. (18.10) is shown in Fig. 18.2(a) for $S_0 = 1$.

The peak ground acceleration, *PGA*, is assumed as *IM*. In order to derive the fragility curves in terms of the selected *IM*, the relationship between the parameter S_0 of the Kanai–Tajimi spectrum and the *PGA* at the site is assessed empirically. A set of 500 synthetic stationary ground motion records are generated using the spectral representation method [31] based on the PSD function given in Eq. (18.10) with $S_0 = 1$. Each ground motion realization is then modulated in time using the function defined in Eq. (18.9). The peak ground acceleration corresponding to $S_0 = 1$, $PGA_{S_0=1}$, is estimated as the mean of the *PGA*s of the sampled ground

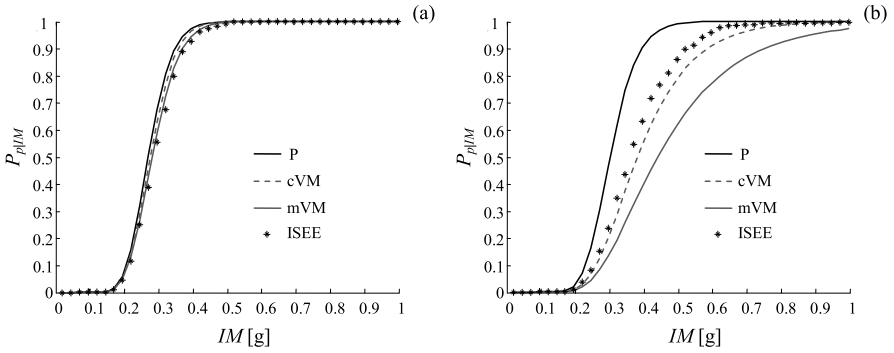

Fig. 18.3 Fragility curves for $\xi = 0.1$ m: (**a**) $t_A = 1.0$ s and $t_B = 0.5$ s, and (**b**) $t_A = 1.0$ s and $t_B = 0.9$ s

motion time histories. The values of S_0 corresponding to different values of PGA are obtained as follows:

$$S_0 = \left(\frac{PGA}{PGA_{S_0=1}} \right)^2 \tag{18.11}$$

In this study, the site hazard curve is expressed in the approximate form used in Cornell et al. [32], i.e.,

$$\nu_{IM}(im) = P[IM \geq im | 1yr] = k_0 \cdot im^{-k_1} \tag{18.12}$$

in which k_0 and k_1 = parameters obtained by fitting a straight line through two known points of the site hazard curve in logarithmic scale. The site hazard curve is taken from Eurocode 8-Part 2 [33], assuming that, for the site of interest, $PGA =$ 0.3 g corresponds to a return period of 475 years. Using $k_1 = 2.857$ [34], the site hazard curve becomes (see Fig. 18.2(b)).

$$\nu_{PGA}(pga) = 6.734 \cdot 10^{-5} \cdot pga^{-2.857} \tag{18.13}$$

4.1 Pounding Risk for Linear SDOF Systems with Deterministic Model Parameters

The first application example consists in the assessment of the pounding risk between two adjacent buildings modelled as deterministic linear elastic SDOF systems with periods t_A and t_B, and damping ratios $\zeta_A = \zeta_B = 5\%$. The conditional probability of pounding $P_{p|IM}$ is calculated using the approximate analytical hazard functions $h^{(P)}_{U_{rel}|IM}(\xi, t)$, $h^{(cVM)}_{U_{rel}|IM}(\xi, t)$, and $h^{(mVM)}_{U_{rel}|IM}(\xi, t)$, for a deterministic distance between the buildings $\xi = 0.1$ m and for two different combinations of natural periods of the two systems, i.e., (1) $t_A = 1.0$ s and $t_B = 0.5$ s, referred to as well separated natural periods (Fig. 18.3(a)), and (2) $t_A = 1.0$ s and $t_B = 0.9$ s, referred

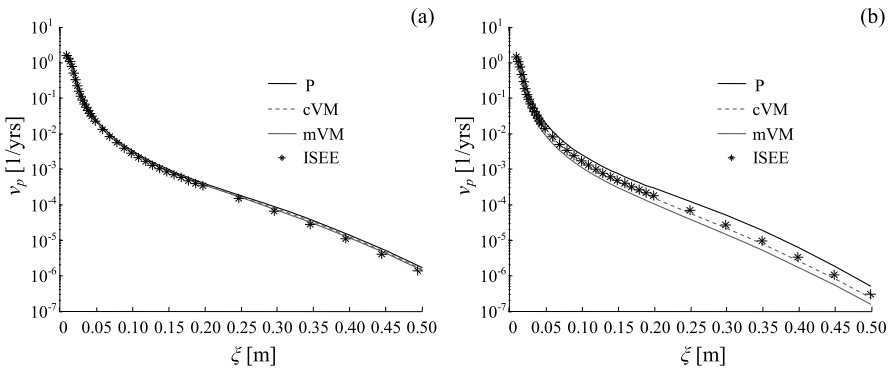

Fig. 18.4 MAF of pounding for varying separation distance: (**a**) $t_A = 1.0$ s and $t_B = 0.5$ s, and (**b**) $t_A = 1.0$ s and $t_B = 0.9$ s

to as close natural periods (Fig. 18.3(b)). The obtained conditional probabilities are presented in Fig. 18.3 as fragility curves and compared with the corresponding results obtained using ISEE method [27], which are assumed as reference solution.

In the case of well separated natural periods for the structures (Fig. 18.3(a)), the fragility curves estimated using the P, cVM, and mVM approximations are very similar and close to the fragility curves obtained using the ISEE method. In the case of close natural periods (Fig. 18.3(b)), the fragility curves estimated with the approximate analytical methods show significant differences, and only the cVM approximation provides results that are close to the fragility curves estimated using the ISEE method. The observed result can be explained by recognizing that the relative displacement process $U_{rel}(t)$ can be interpreted as a response process of a two-degree-of-freedom system. This multi-modal characteristic of $U_{rel}(t)$ can significantly affect the accuracy of the different approximations of the time-variant hazard function $h_{U_{rel}|IM}(\xi, t)$ [35]. In the case of well separated natural periods, the contribution of the higher period vibration mode to $U_{rel}(t)$ is significantly larger than the contribution of the lower period vibration mode. By contrast, in the case of close natural periods, both vibration modes provide a significant contribution to the response process.

Figure 18.4 shows the MAF of pounding, ν_p, as a function of the building separation distance ξ (in semi-logarithmic scale) for the cases of well separated natural periods (Fig. 18.4(a)) and of close natural periods (Fig. 18.4(b)), respectively. The estimates of the MAF of pounding obtained using the analytical approximations (P, cVM, and mVM) of the hazard function are compared to the corresponding estimate obtained using the ISEE method. Figure 18.5 plots (in semi-logarithmic scale) the pounding risk for a design lifetime of 50 years, evaluated according to Eq. (18.4), for the same two cases of well separated and close natural periods. Considerations similar to the ones made for the fragility curves can be made also for the MAF of pounding and the 50-year pounding risk, i.e., the analytical approximations provide very accurate results for the case of well separated natural periods and less accu-

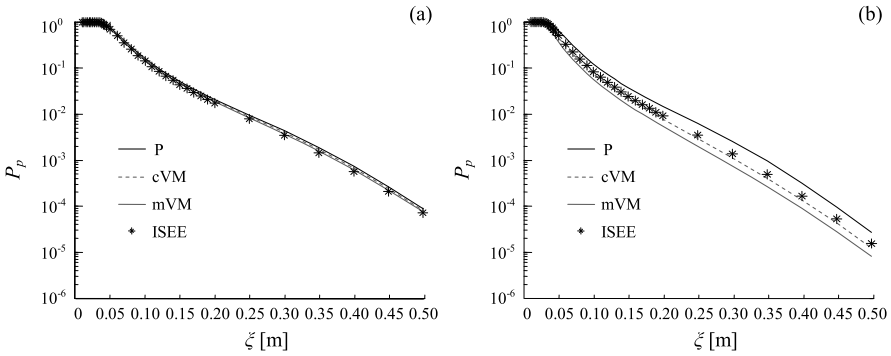

Fig. 18.5 50-year pounding risk for varying separation distance: (**a**) $t_A = 1.0$ s and $t_B = 0.5$ s, and (**b**) $t_A = 1.0$ s and $t_B = 0.9$ s

rate results for the case of close natural periods, with the exception of the cVM approximation, which is accurate in both cases.

It is observed that the P approximation of the time-variant hazard function always yields conservative results, while the mVM approximation underestimates the risk computed using the ISEE method for the case of close natural periods. Similar results have been documented for the first-passage reliability problem of SDOF and MDOF systems subjected to time-modulated white and colored noise excitations [26].

4.2 Reliability of Formulae Used in Seismic Design Codes

The proposed methodology is applied here to evaluate the pounding risk corresponding to the separation distance prescribed by anti-seismic design codes. In order to avoid pounding between new adjacent buildings, current seismic design codes (e.g., [4, 33]) prescribe a minimum clearance to be provided between the structures. This minimum clearance between two adjacent buildings is assumed equal to the expected value of the peak relative displacement, for a given site-specific earthquake action and a value of the seismic intensity (hazard level) corresponding to a given probability of exceedance. Given the seismic input, the peak relative displacement is obtained by combining (using simplified combination rules) the values of the peak displacements of the two adjacent structural systems, which are computed using (deterministic) structural analysis. The most commonly employed rules are the ABS method or the slightly more accurate SRSS method. The major limit of these approximate rules is that they neglect the response phase differences between the adjacent structures. In order to overcome this drawback, the use of the Double Difference Combination rule for determining the CSD has been proposed and investigated by several researchers [1–3].

In the application presented here, the values of the CSD according to the ABS, SRSS, and DDC rules are calculated following the procedure described in [5]. This

Table 18.1 Critical separation distance and corresponding 50-year pounding risk using different combination rules

	$t_A = 1.0$ s and $t_B = 0.5$ s				$t_A = 1.0$ s and $t_B = 0.9$ s		
	ABS	SRSS	DDC		ABS	SRSS	DDC
ξ [m]	0.1379	0.1049	0.1042	ξ [m]	0.1832	0.1298	0.0946
P_p	0.0620	0.1351	0.1376	P_p	0.0106	0.0334	0.0857

procedure involves (1) generating a set of 500 samples of input ground motion time histories for the reference value of the peak ground acceleration (i.e., $PGA = 0.3$ g, corresponding to a probability of exceedance of 10% in 50 years), (2) computing the corresponding 500 peak displacement responses of systems A and B ($U_{A,max}$ and $U_{B,max}$), (3) computing the sample means $\bar{U}_{A,max}$ and $\bar{U}_{B,max}$ of $U_{A,max}$ and $U_{B,max}$, respectively, and (4) combining $\bar{U}_{A,max}$ and $\bar{U}_{B,max}$ using the ABS, the SRSS, and the DDC rule to derive estimate of the peak relative displacement $\overline{U}_{rel,max}$.

Table 18.1 shows the values of the separation distance computed according to different combination rules and the corresponding 50-year probability of failure, computed based on the cVM approximation of the time-variant hazard function. It is observed that the CSDs obtained using simplified combination rules yield inconsistent values of the failure probability, which are also strongly dependent on the natural periods of the two adjacent buildings. Thus, it is concluded that a methodology is still needed to determine the CSD between adjacent buildings corresponding to consistent safety levels for different combinations of the buildings' natural periods and location's seismic hazard.

4.3 MDOF Models of Multi-storey Buildings Retrofitted by Means of Viscous Dampers

As a third application, the proposed methodology is employed to assess the risk of pounding between two adjacent multi-storey buildings modelled as linear MDOF systems, before and after retrofit with viscous dampers (Fig. 18.6(a)). Different retrofit solutions are considered and their effectiveness in reducing the seismic pounding risk is compared (Fig. 18.6(b)). The considered buildings are steel moment-resisting frames with shear-type behaviour. The properties of the buildings are taken from Lin [36]. Building A is a six-story building with story stiffness $k_A = 548{,}183$ kN/m (equal for every story) and floor mass $m_A = 454.545$ tons (equal for each floor). Building B is a four-story building with story stiffness $k_B = 470{,}840$ kN/m and floor mass $m_B = 454.545$ tons. A Rayleigh-type damping matrix $\mathbf{c}_R$ is used to model the inherent buildings' damping and is built by considering a damping ratio $\zeta_R = 2\%$ for the first two vibration modes of each system. MPU is not considered in this application. The fundamental vibration periods of building A and B are $t_A = 0.751$ s and $t_B = 0.562$ s, respectively.

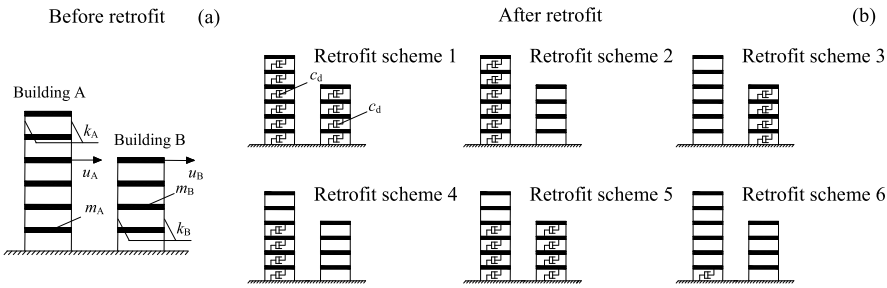

Fig. 18.6 Pounding between adjacent multi-storey buildings: (**a**) building A and B before retrofit, and (**b**) different retrofit schemes considered in this study

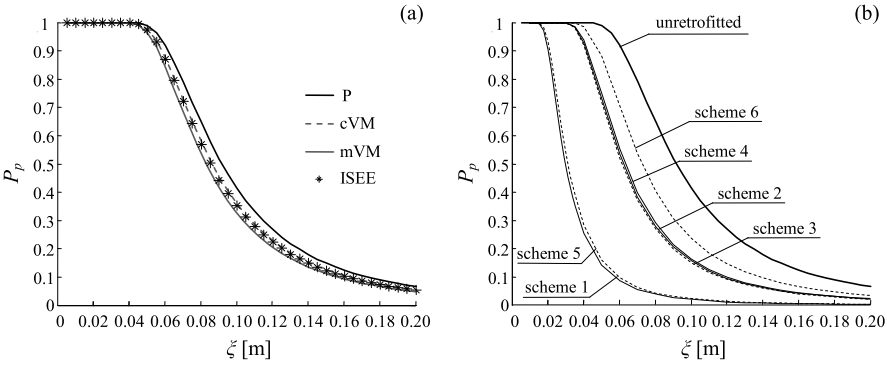

Fig. 18.7 Pounding risk between multi-storey buildings A and B: (**a**) comparison of different analytical solution and ISEE results, and (**b**) comparison of different retrofit schemes

The following six different retrofit solutions, based on the use of braces with purely viscous behaviour [37], are considered: (1) braces located at each story of both buildings (retrofit scheme 1), (2) braces located at all stories of the tall building only (retrofit scheme 2), (3) braces located at all stories of the short building only (retrofit scheme 3), (4) braces located at the lower four stories of the tall building only (retrofit scheme 4), (5) braces located at the lower four stories of both buildings, and (6) a single brace located at the first story of the tall building only. The two buildings before retrofit are shown in Fig. 18.6(a), while the six retrofit schemes are shown in Fig. 18.6(b). The viscous braces provide an additional source of damping, modelled by means of a damping matrix $\mathbf{c_v}$. The total damping matrix for the two buildings' systems becomes $\mathbf{c} = \mathbf{c_R} + \mathbf{c_v}$. The damping coefficient corresponding to the dampers at each floor of buildings A and B is $c_d = 10{,}000$ kN·s/m. The systems corresponding to retrofit schemes 4, 5, and 6 are non-classically damped and their analysis requires the use of the complex modal analysis technique [25].

Figure 18.7(a) shows three different analytical estimates (P, cVM, and mVM approximations) of the 50-year probability of pounding between the two un-retrofitted buildings, for different values of the separation distance. Figure 18.7 also reports the

50-year probability of pounding obtained using the ISEE method, which is considered as reference solution. The analytical estimates provide a very good approximation of the pounding risk for a wide range of separation distances. In this particular case, the results obtained using the cVM hazard function give the best approximation of the ISEE results.

Figure 18.7(b) compares the 50-year probability of pounding of the un-retrofitted buildings and of the buildings retrofitted following the six different retrofit solutions considered in this application example. The results presented in Fig. 18.7(b) are obtained using the cVM approximation of the hazard function.

It is observed that the use of viscous dampers can be very effective in reducing the risk of pounding between the two buildings. Furthermore, the introduction of viscous braces according to scheme 3, scheme 5, and scheme 6 (corresponding to the dotted lines in Fig. 18.7(b)) is a very efficient retrofit solution, since it obtains a significant reduction of the pounding risk at a significantly lower retrofit cost when compared with other retrofit schemes. In particular, retrofit scheme 3 appears to achieve a very good compromise between retrofit cost and reduction of pounding risk.

5 Possible Applications and Future Work

The innovative performance-based approach proposed in this paper for estimating the risk of pounding between adjacent buildings under earthquake excitation presents several practical applications. A first application is the evaluation of the safety levels corresponding to current seismic code provisions for building separation distance under different design conditions. The current code provisions are affected by several limitations: (1) they do not provide an explicit control on the performance of the structures [38]; (2) they do not account for uncertainties in the model properties of the structures; (3) they consider only a single value of the seismic event intensity instead of a continuous representation of the site seismic hazard [39]; and (4) they are based on simplified rules for combining the peak responses of the buildings [5], the accuracy of which is limited. Although these limitations have already been pointed out in many studies (including the present paper), an extensive parametric study involving a wide range of building properties and seismic input models is required to assess their effects on the performance and reliability of adjacent buildings subjected to seismic pounding hazard.

As an additional application, the proposed assessment methodology can be used as a first step toward improved code provisions and/or a performance-based design methodology for the separation distances between adjacent buildings. A performance-based design methodology should aim to obtain a target (sufficiently small and consistent for different design conditions) probability of pounding between two adjacent systems. The computation of the separation distance corresponding to the target pounding probability can be regarded as an inverse reliability problem, i.e., a problem in which one is seeking to determine the values to assign to design parameters such that target reliability levels are attained for the limit state

considered. Possible design parameters that can be varied in the design are the separation distance between the two buildings, for newly design buildings, or the properties of viscous or viscoelastic dampers in the buildings or between the buildings in the case of existing buildings with a given insufficient separation distance.

An efficient solution to this design problem can be sought by recasting the inverse reliability problem as a zero-finding problem:

$$\mathbf{y}^* = \text{Zero}\left[P_p(\mathbf{y}, t_L) - \bar{P}_p\right] \tag{18.14}$$

where $\mathbf{y}$ = vector collecting the design parameters, the functional expression Zero[...] = zero of the function in the parentheses, and $P_p(\mathbf{x}, t_L)$ = probability of pounding in the design life-time t_L. This zero-finding problem can be solved efficiently using classical iterative constrained optimization algorithms.

6 Conclusions

This paper presents a fully probabilistic performance-based methodology for assessment of the seismic pounding risk between adjacent buildings. This methodology, which is consistent with the PEER PBEE framework, is able to account for all pertinent sources of uncertainty that can affect the pounding risk, e.g., uncertainty in the seismic input (i.e., site hazard and record-to-record variability) and in the parameters used to describe the structural systems of interest (i.e., material properties, geometry, damping properties, separation distance).

An efficient combination of analytical and simulation techniques is proposed for the calculation of the pounding risk under the assumptions of linear elastic behaviour for the buildings and of non-stationary Gaussian input ground motion. The pounding problem is recast as a first-passage reliability problem, which is solved analytically by using the spectral characteristics (up to the second order) of the non-stationary stochastic process representing the relative displacement between the buildings. Three different analytical approximations of the time-variant hazard function are used: (1) the Poisson's approximation, (2) the classical Vanmarcke's approximation, and (3) the modified Vanmarcke's approximation. Results obtained by employing the importance sampling using elementary events method are assumed as reference solutions to evaluate the absolute and relative accuracy of the three analytical approximations considered here. The effects of uncertainty in the model parameters are efficiently included by means of the total probability theorem and the Latin hypercube sampling technique.

The proposed methodology is applied in this paper to investigate the risk of pounding between SDOF systems with deterministic properties. With reference to this specific application example, the following observations are made:

(1) The proposed combination of analytical and simulation techniques provides sufficiently accurate estimates of the pounding risk when the classical Vanmarcke's approximation is used to estimate the time-variant hazard function.

(2) The accuracy of the analytical approximations of the time-variant hazard function depends on the ratio between the natural periods of the adjacent buildings. Higher accuracy is reached when the natural periods of the two buildings are well separated.
(3) The Poisson's approximation of the time-variant hazard function yields always conservative estimates of the risk.
(4) The simplified combination rules suggested in modern seismic design codes for calculating the critical separation distance yield inconsistent values of the pounding probability, which are also strongly dependent on the natural periods of the adjacent buildings.

In addition, the capabilities of the proposed method are demonstrated in a second application example by assessing the effectiveness of the use of viscous dampers, according to different retrofit schemes, in reducing the pounding probability of two adjacent multi-story buildings modelled as linear elastic multi-degree-of-freedom systems. Based on the results presented, the following considerations are made:

(1) The analytical approximations provide very accurate estimates of the pounding risk, due to the fact that the fundamental periods of the two buildings are well separated.
(2) The use of viscous dampers can dramatically reduce the risk of pounding between the two systems for any given separation distance.
(3) The use of viscous braces in the lower levels of the taller building is a very efficient and cost-effective technique for minimizing the pounding risk.

Acknowledgements The authors gratefully acknowledge support of this research by (1) the Louisiana Board of Regents (LA BoR) through the Pilot Funding for New Research (Pfund) Program of the National Science Foundation (NSF) Experimental Program to Stimulate Competitive Research (EPSCoR) under Award No. LEQSF(2011)-PFUND-225; (2) the LA BoR through the Louisiana Board of Regents Research and Development Program, Research Competitiveness (RCS) subprogram, under Award No. LESQSF(2010-13)-RD-A-01; (3) the Longwell's Family Foundation through the Fund for Innovation in Engineering Research (FIER) Program; and (4) the LSU Council on Research through the 2009–2010 Faculty Research Grant Program. Any opinions, findings, conclusions or recommendations expressed in this publication are those of the authors and do not necessarily reflect the views of the sponsors.

References

1. Jeng, V., Kasai, K., Maison, B.F.: A spectral difference method to estimate building separations to avoid pounding. Earthq. Spectra **8**, 201–223 (1992)
2. Kasai, K., Jagiasi, R.A., Jeng, V.: Inelastic vibration phase theory for seismic pounding. J. Struct. Eng. **122**, 1136–1146 (1996)
3. Penzien, J.: Evaluation of building separation distance required to prevent pounding during strong earthquake. Earthquake Eng. Struct. Dyn. **26**, 849–858 (1997)
4. International Conference of Building Officials (ICBO): Uniform Building Code, Whittier, California (1997)
5. Lopez-Garcia, D., Soong, T.T.: Assessment of the separation necessary to prevent seismic pounding between linear structural systems. Probab. Eng. Mech. **24**, 210–223 (2009)

6. Lin, J.H.: Separation distance to avoid seismic pounding of adjacent buildings. Earthquake Eng. Struct. Dyn. **26**, 395–403 (1997)
7. Lin, J.H., Weng, C.C.: Probability analysis of seismic pounding of adjacent buildings. Earthquake Eng. Struct. Dyn. **30**, 1539–1557 (2001)
8. Hong, H.P., Wang, S.S., Hong, P.: Critical building separation distance in reducing pounding risk under earthquake excitation. Struct. Saf. **25**, 287–303 (2003)
9. Wang, S.S., Hong, H.P.: Quantiles of critical separation distance for nonstationary seismic excitations. Eng. Struct. **28**, 985–991 (2006)
10. Porter, K.A.: An overview of PEER's performance-based earthquake engineering methodology. In: 9th International Conference on Application of Statistics and Probability in Civil Engineering (ICASP9), San Francisco, California (2003)
11. Zhang, Y., Acero, G., Conte, J., Yang, Z., Elgamal, A.: Seismic reliability assessment of a bridge ground system. In: 13th World Conference on Earthquake Engineering, Vancouver, Canada (2004)
12. Luco, N., Cornell, C.A.: Structure-specific scalar intensity measures for near-source and ordinary earthquake ground motions. Earthq. Spectra **23**, 357–392 (2007)
13. Karayannis, C.G., Favvata, M.J.: Earthquake-induced interaction between adjacent reinforced concrete structures with non-equal heights. Earthquake Eng. Struct. Dyn. **34**, 1–20 (2005)
14. Jankowski, R.: Non-linear viscoelastic modelling of earthquake-induced structural pounding. Earthquake Eng. Struct. Dyn. **34**, 595–611 (2005)
15. Muthukumar, S., DesRoches, R.: A Hertz contact model with nonlinear damping for pounding simulation. Earthquake Eng. Struct. Dyn. **35**, 811–828 (2006)
16. Cole, G., Dhakal, R., Carr, A., Bull, D.: An investigation of the effects of mass distribution on pounding structures. Earthquake Eng. Struct. Dyn. **40**, 641–659 (2010)
17. Roberts, J.B., Spanos, P.D.: Random Vibrations and Statistical Linearization. Dover, New York (1993)
18. Au, S., Beck, J.L.: Estimation of small failure probabilities in high dimensions by subset simulation. Probab. Eng. Mech. **16**, 263–277 (2001)
19. Crandall, S.H.: First-crossing probabilities of the linear oscillator. J. Sound Vib. **12**, 285–299 (1970)
20. Wen, Y.K.: Approximate methods for nonlinear time-variant reliability analysis. J. Eng. Mech. **113**, 1826–1839 (1987)
21. Vanmarcke, E.H.: On the distribution of the first-passage time for normal stationary random processes. J. Appl. Mech. **42**, 215–220 (1975)
22. Barbato, M.: Use of time-variant spectral characteristics of nonstationary random processes in structural reliability and earthquake engineering applications. In: Computational Methods in Stochastic Dynamics. Springer, Berlin (2011)
23. Michaelov, G., Sarkani, S., Lutes, L.D.: Spectral characteristics of nonstationary random processes—a critical review. Struct. Saf. **21**, 223–244 (1999)
24. Barbato, M., Conte, J.P.: Spectral characteristics of non-stationary random processes: theory and applications to linear structural models. Probab. Eng. Mech. **23**, 416–426 (2008)
25. Barbato, M., Vasta, M.: Closed-form solutions for the time-variant spectral characteristics of non-stationary random processes. Probab. Eng. Mech. **25**, 9–17 (2010)
26. Barbato, M., Conte, J.P.: Structural reliability applications of spectral characteristics of nonstationary random processes. J. Eng. Mech. **137**, 371–382 (2011)
27. Au, S.K., Beck, J.L.: First excursion probabilities for linear systems by very efficient importance sampling. Probab. Eng. Mech. **16**, 193–207 (2001)
28. Iman, R.L., Conover, W.J.: Small sample sensitivity analysis techniques for computer models, with an application to risk assessment. Commun. Stat. **A9**, 1749–1842 (1980)
29. Shinozuka, M., Sato, Y.: Simulation of nonstationary random processes. J. Eng. Mech. Div. **93**(EM1), 11–40 (1967)
30. Clough, R.W., Penzien, J.: Dynamics of Structures. McGraw-Hill, New York (1993)
31. Shinozuka, M., Deodatis, G.: Simulation of stochastic processes by spectral representation. Appl. Mech. Rev. **44**, 191–203 (1991)

32. Cornell, A.C., Jalayer, F., Hamburger, R.O.: Probabilistic basis for 2000 SAC federal emergency management agency steel moment frame guidelines. J. Struct. Eng. **128**, 526–532 (2002)
33. European Committee for Standardization (ECS): Eurocode 8—design of structures for earthquake resistance, EN1998. Brussels, Belgium (2005)
34. Lubkowski, Z.A.: Deriving the seismic action for alternative return periods according to Eurocode 8. In: 14th European Conference on Earthquake Engineering, Ohrid, Macedonia (2010)
35. Toro, G.R., Cornell, C.A.: Extremes of Gaussian processes with bimodal spectra. J. Eng. Mech. **112**, 465–484 (1986)
36. Lin, J.H.: Evaluation of seismic pounding risk of buildings in Taiwan. J. Chin. Inst. Eng. **28**, 867–872 (2005)
37. Occhiuzzi, A.: Additional viscous dampers for civil structures: analysis of design methods based on effective evaluation of modal damping ratios. Eng. Struct. **31**, 1093–1101 (2009)
38. Collins, K.R., Wen, Y.K., Foutch, D.A.: Dual-level seismic design: a reliability-based methodology. Earthquake Eng. Struct. Dyn. **25**, 1433–1467 (1996)
39. Krawinkler, H., Miranda, E.: Performance-based earthquake engineering. In: Bozorgnia, Y., Bertero, V.V. (eds.) Earthquake Engineering: From Engineering Seismology to Performance-Based Engineering. CRC Press, Boca Raton (2004)

Chapter 19
Intensity Parameters as Damage Potential Descriptors of Earthquakes

Anaxagoras Elenas

Abstract This paper provides a methodology to quantify the interrelationship between the seismic intensity parameters and the structural damage. First, a computer-supported elaboration of the accelerograms provides several peak, spectral and energy seismic parameters. After that, nonlinear dynamic analyses are carried out to provide the structural response for a set of seismic excitations. Among the several response characteristics, the overall structure damage indices after Park/Ang and the maximum inter-storey drift ratio are selected to represent the structural response. Correlation coefficients are evaluated to express the grade of interrelation between seismic acceleration parameters and the structural damage. The presented methodology is applied to a six-story reinforced concrete frame building, designed according to the rules of the recent Eurocodes. As seismic input for the nonlinear dynamic analysis, a set of spectrum-compatible synthetic accelerograms has been used. As the numerical results have shown, the spectral and energy parameters provide strong correlation to the damage indices. Due to this reason, spectral and energy related parameters are better qualified to be used for the characterization of the seismic damage potential.

1 Introduction

It is well-known that seismic accelerograms are ground acceleration time-histories that cannot be described analytically. Several seismic parameters have been presented in the literature during the last decades. These can be used to express the intensity of the seismic excitations and to simplify its description. Post-seismic field observations and numerical investigations have indicated the interdependency between the seismic parameters and the damage status of buildings after earthquakes [1, 2]. The latter can be expressed by proper damage indices, while the interdependency between the considered quantities can be quantified numerically by appropri-

A. Elenas (✉)
Institute of Structural Mechanics and Earthquake Engineering, Democritus University of Thrace, 67100 Xanthi, Greece
e-mail: elenas@civil.duth.gr

M. Papadrakakis et al. (eds.), *Computational Methods in Stochastic Dynamics*, Computational Methods in Applied Sciences 26,
DOI 10.1007/978-94-007-5134-7_19,

ate correlation coefficients. Their values deliver the correlation grade (low, medium or high) between the examined quantities.

This paper provides a method for quantifying the interrelationship between the seismic parameters and global damage indices. First, a computer analysis of the accelerograms provided several peak ground motion, spectral and energy seismic parameters. After that, nonlinear dynamic analyses were carried out to provide the structural response for a set of seismic excitations and a given reinforced concrete frame structure. Keeping in mind that most of the seismic loading parameters are characterized by a single numerical value, single-value damage indicators have also been selected to represent the structural response. Thus, the overall structural damage index (OSDI) after Park/Ang ($DI_{G,PA}$) and the maximum inter-storey drift ratio (MISDR) are selected to represent the structural response. Finally, correlation coefficients are evaluated to express the grade of interdependency between seismic acceleration parameters and the used damage indices. The presented methodology is applied to a six-story reinforced concrete frame building subjected to several artificial accelerograms.

2 Seismic Intensity Parameters

In general, the intensity parameters can be classified with peak, spectral and energy parameters. In this work the following parameters have been selected to represent the seismic intensity: peak ground acceleration PGA, peak ground velocity PGV, the term PGA/PGV, spectral acceleration (SA), spectral velocity (SV), spectral displacement (SD), central period (CP), absolute seismic input energy (E_{inp}), Arias intensity (I_A), strong motion duration after Trifunac/Brady (SMD_{TB}), seismic power ($P_{0.90}$), root mean square acceleration (RMS_a), intensity after Fajfar/Vidic/Fischinger (I_{FVF}), spectral intensities after Housner (SI_H), after Kappos (SI_K) and after Martinez-Rueda (SI_{MR}). They have been chosen from all three of the seismic parameter categories. Table 19.1 provides an overview of the used parameters and their literature references, respectively. The definition of each parameter is presented in the mentioned literature.

3 Seismic Acceleration Time Histories

The seismic excitations used for the dynamic analyses in this study are based on artificial accelerograms created to be compatible with the design spectra of the current Greek antiseismic code (2004). The reason for choosing this approach rather than relying on natural accelerograms was dictated by the need to have a sufficiently large database for statistical reasons. For the creation of the aforementioned artificial accelerograms the program SIMQKE [14] has been utilized. As artificial accelerogram creation parameters the PGA, the total duration (TD) and the design spectra for all three Greek seismic regions (nominal PGA equal to 0.16 g, 0.24 g and 0.36 g) have

Table 19.1 Seismic parameters

No	Seismic parameters	Reference	No	Seismic parameters	Reference
1	PGA	[3]	9	I_A	[7]
2	PGV	[3]	10	SMD_{TB}	[8]
3	PGA/PGV	[3]	11	$P_{0.90}$	[9]
4	SA	[4]	12	RMS_a	[3]
5	SV	[4]	13	I_{FVF}	[10]
6	SD	[4]	14	SI_H	[11]
7	CP	[5]	15	SI_K	[12]
8	E_{inp}	[6]	16	SI_{MR}	[13]

been used. All created for subsoil category B, as described in Eurocode 8 (EC8) [15] and the Greek Antiseismic Code [16]. This subsoil category belongs to deep deposits of medium dense sand or over-consolidated clay at least 70 m thick. In order to cover most types of Greek region seismic activity, an artificial accelerogram creation procedure has been devised comprising the creation of 5 random artificial accelerograms for each of the 15 preselected PGA values that were assigned for the three different Greek seismic regions. Thus, 75 different synthetic accelerograms have been compiled, which ensures that the overall structural damages of the examined structure will cover all the possible damage grades, from low to severe, in order to cover statistical demands as well.

4 Global Damage Indices

As explained previously, attention is focused on damage indicators that consolidate all member damage into one single value that can be easily and accurately be used for the statistical exploration of the interrelation with the also single-value seismic parameters in question. Thus, in the OSDI model after Park/Ang [17] the global damage is obtained as a weighted average of the local damage at the ends of each element. The local damage index is a linear combination of the damage caused by excessive deformation and that contributed by the repeated cyclic loading effect that occurs during seismic excitation. Thus, the local DI is given by the following relation:

$$DI_{L,PA} = \frac{\theta_m - \theta_r}{\theta_u - \theta_r} + \frac{\beta}{M_y \theta_u} E_T \tag{19.1}$$

where, $DI_{L,PA}$ is the local damage index, θ_m the maximum rotation attained during the load history, θ_u the ultimate rotation capacity of the section, θ_r the recoverable rotation at unloading, β a strength degrading parameter, M_y the yield moment of the section and E_T the dissipated hysteretic energy. The Park/Ang damage index is a linear combination of the maximum ductility and the hysteretic energy dissipation demand imposed by the earthquake on the structure.

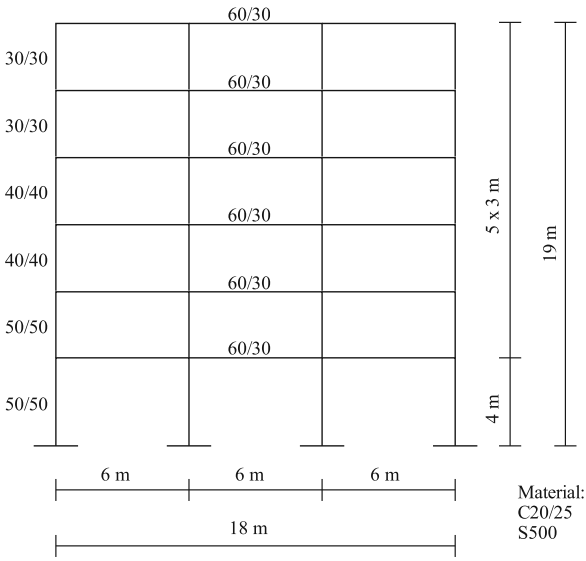

Fig. 19.1 Reinforced concrete frame structure

The global damage index after Park/Ang [17] takes into account the local damages of all elements of the examined structure (e.g. beams and columns of a frame). Thus, it depends both, the distribution and the severity of the localized damage and is given by the following relation:

$$DI_{G,PA} = \frac{\sum_{i=1}^{n} DI_{L,PA} E_i}{\sum_{i=1}^{n} E_i} \tag{19.2}$$

where, $DI_{G,PA}$ is the global damage index, $DI_{L,PA}$ the local damage index after Park/Ang, E_i the energy dissipated at location i and n the number of locations at which the local damage is computed.

The MISDR [18, 19] is a simple overall structural damage index that describes satisfactorily various forms of damages after an earthquake. The post-seismic damage degree can be classified according to this index. Equation (19.3) defines the maximum inter-storey drift ratio (MISDR) as the ratio of the maximum absolute inter-storey drift $|u|_{max}$ to the inter-storey height h:

$$MISDR = \frac{|u|_{max}}{h} 100\ [\%] \tag{19.3}$$

5 Application

The six-storey reinforced concrete frame structure shown in Fig. 19.1 has been detailed in agreement with the rules of the recent Eurocodes for structural concrete and antiseismic structures, Eurocode 2 (EC2) and Eurocode 8 (EC8) [15, 20], respectively. According to the EC8 Eurocode, the structure shown in Fig. 19.1, has

been considered as an "importance class II, ductility class M"-structure with a subsoil category B (deep deposits of medium dense sand or over-consolidated clay at least 70 m thick). The building belongs on a seismic zone with nominal seismic design acceleration equal to 0.16 g. The cross-sections of the beams are considered as T-beams with 30 cm width, 20 cm slab thickness, 60 cm total beam height and 1.45 m effective slab width. The distances between each frame of the structure is equal to 6 m while the ground floor has a 4 m height and all subsequent floors 3 m. The eigenperiod of the frame was 1.0 s. In addition to the seismic load, live, snow and wind loads have also been taken into account as well as the eccentricity of structural element from verticality. The numerical values of loads, safety factors as well as load combinations have been chosen in accordance with the current design codes (Eurocodes).

After the design procedure of the reinforced concrete frame structure, a nonlinear dynamic analysis evaluates the structural seismic response, using the computer program IDARC [21]. A three-parameter Park model specifies the hysteretic behavior of beams and columns at both ends of each member. This hysteretic model incorporates stiffness degradation, strength deterioration, slip-lock and a tri-linear monotonic envelope. Experimental results of cyclic force-deformation characteristics of typical components of the studied structure, specifies the parameter values of the above degrading parameters. This study uses the nominal parameter for stiffness degradation. Among the several response parameters, the focus is on the overall structural damage indices (OSDI) described in the previous section.

6 Results

The first step was the creation of the aforementioned set of 75 synthetic accelerograms using the SIMQKE program. This program generates baseline corrected acceleration-time histories. The next step was a computer supported evaluation of 16 seismic parameters as presented in Table 19.1. Nonlinear dynamic analyses has been performed for the reinforced concrete frame building under question, including all artificial acceleration-time histories, in order to obtain the structural damage indices after Park/Ang and the MISDR. Statistical procedures provide the correlation coefficients after Pearson and Spearman [22], between all the evaluated seismic parameters and damage indices. The Pearson correlation shows how well the data fit a linear relationship, while the Spearman correlation shows how close the examined data are to monotone ranking. The latter coefficient is more important in the present study. Table 19.2 summarizes the results of the correlation study.

It is supposed that correlation coefficients up to 0.5 means low correlation, coefficients between 0.5 and 0.8 means medium correlations, while coefficients greater than 0.8 means strong correlation between the two variables. Table 19.2 presents the correlation coefficients after Pearson and the rank correlation coefficients after Spearman among all the examined seismic parameters presented and the examined the damage indices. Thus, the results show low Pearson and Spearman correlation

Table 19.2 Correlation coefficients between the seismic parameters and the OSDIs

Seismic parameters	Pearson correlation		Spearman rank correlation	
	$DI_{G,PA}$	MISDR	$DI_{G,PA}$	MISDR
PGA	0.568	0.523	0.635	0.631
PGV	0.657	0.659	0.788	0.795
PGA/PGV	−0.355	−0.367	−0.393	−0.394
SA	0.711	0.678	0.803	0.806
SV	0.724	0.696	0.804	0.804
SD	0.738	0.706	0.849	0.845
CP	−0.342	−0.326	−0.351	−0.332
E_{inp}	0.668	0.667	0.812	0.821
I_A	0.682	0.659	0.824	0.821
SMD_{TB}	0.103	0.086	0.155	0.145
$P_{0.90}$	0.685	0.662	0.823	0.820
RMS_a	0.713	0.677	0.824	0.821
I_{FVF}	0.655	0.656	0.789	0.796
SI_H	0.703	0.664	0.796	0.795
SI_K	0.702	0.670	0.802	0.806
SI_{MR}	0.614	0.558	0.725	0.725

between the term PGA/PGV, CP, SMD_{TB} and the examined damage indices. All the remaining seismic parameters provided medium Pearson correlation with the examined damage indices. On the other hand, high rank correlation is observed between SA, SV, SD, E_{inp}, I_A, $P_{0.90}$, RMS_a, SI_K and the used damage indices. In addition, medium rank correlation is observed between PGA, PGV, I_{FVF}, SI_H, SI_{MR} and the damage indices.

Thus, spectral (SA, SV, SD, SI_K) and energy (E_{inp}, I_A, $P_{0.90}$, RMS_a) seismic intensity parameters provided high correlation with the examined overall structural damage indices. These parameters are appropriate descriptors of the damage potential of a seismic excitation. Finally, the seismic parameters show the same correlation grade with the global damage index of Park/Ang ($DI_{G,PA}$) and with the maximum inter-storey drift ratio (MISDR) in all the cases. All the seismic parameters show the same correlation grade for both, Pearson and Spearman correlation, with exception the cases with high rank correlation. There, the Pearson correlation grade is medium.

7 Conclusions

In this paper a methodology for the value estimation of the interdependence between seismic acceleration intensity parameters and damage indices has been presented.

Peak, spectral and energy parameters have been considered. The global damage index after Park/Ang and the MISDR represented the post-seismic structural damage status. The degree of the interrelationship between seismic parameters and damage indices has been expressed by the Pearson correlation coefficient and by the Spearman rank correlation coefficient.

The results show low Pearson and Spearman correlation between the term PGA/PGV, CP, SMD_{TB} and the examined damage indices. Medium correlation is observed between PGA, PGV, I_{FVF}, SI_H, SI_{MR} and the damage indices, in all the cases. High rank correlation is observed between SA, SV, SD, E_{inp}, I_A, $P_{0.90}$, RMS_a, SI_K and the damage indices. In all these cases, the corresponding Pearson correlation grade was medium. The seismic parameters show the same correlation grade with $DI_{G,PA}$ with MISDR in all the cases.

All these results lead to conclude that the spectral and energy seismic parameters are reliable descriptors of the seismic damage potential and to recommend them as appropriate descriptors of the seismic damage potential.

References

1. Elenas, A.: Correlation between seismic acceleration parameters and overall structural damage indices of buildings. Soil Dyn. Earthq. Eng. **20**, 93–100 (2000)
2. Elenas, A., Meskouris, K.: Correlation study between seismic acceleration parameters and damage indices of structures. Eng. Struct. **23**, 698–704 (2001)
3. Meskouris, K.: Structural Dynamics. Ernst & Sohn, Berlin (2000)
4. Chopra, A.K.: Dynamics of Structures. Prentice Hall, New York (1996)
5. Vanmarcke, E.H., Lai, S.S.P.: Strong-motion duration and RMS amplitude of earthquake records. Bull. Seismol. Soc. Am. **70**, 1293–1307 (1980)
6. Uang, C.M., Bertero, V.V.: Evaluation of seismic energy in structures. Earthquake Eng. Struct. Dyn. **19**, 77–90 (1990)
7. Arias, A.: A measure of earthquake intensity. In: Hansen, R.J. (ed.) Seismic Design for Nuclear Power Plants, pp. 438–483. MIT Press, Cambridge (1970)
8. Trifunac, M.D., Brady, A.G.: A study on the duration of strong earthquake ground motion. Bull. Seismol. Soc. Am. **65**, 581–626 (1975)
9. Jennings, P.C.: Engineering seismology. In: Kanamori, H., Boschi, E. (eds.) Earthquakes: Observation, Theory and Interpretation, pp. 138–173. Italian Physical Society, Varenna (1982)
10. Fajfar, P., Vidic, T., Fischinger, M.: A measure of earthquake motion capacity to damage medium-period structures. Soil Dyn. Earthq. Eng. **9**, 236–242 (1990)
11. Housner, G.W.: Spectrum intensities of strong motion earthquakes. In: Proceedings of Symposium on Earthquake and Blast Effects on Structures, pp. 20–36. EERI, Oakland (1952)
12. Kappos, A.J.: Sensitivity of calculated inelastic seismic response to input motion characteristics. In: Proceedings of the 4th U.S. National Conference on Earthquake Engineering, pp. 25–34. EERI, Oakland (1990)
13. Martinez-Rueda, J.E.: Definition of spectrum intensity for the scaling and simplified damage potential evaluation of earthquake records. In: Proceedings of the 11th European Conference on Earthquake Engineering, CD-ROM. Balkema, Rotterdam (1998)
14. Gasparini, D.A., Vanmarcke, E.H.: SIMQKE, a Program for Artificial Motion Generation, User's Manual and Documentation. Publication R76-4. MIT Press, Cambridge (1976),
15. EC8: Eurocode 8: design of structures for earthquake resistance—part 1: general rules, seismic actions, and rules for buildings. European Committee for Standardization, Brussels, Belgium (2004)

16. EAK: National Greek antiseismic code. Earthquake Planning and Protection Organization (OASP) Publication, Athens (2003)
17. Park, Y.J., Ang, A.H.S.: Mechanistic seismic damage model for reinforced concrete. J. Struct. Eng. **111**, 722–739 (1985)
18. Structural Engineers Association of California (SEAOC): Vision 2000: performance based seismic engineering of buildings. Sacramento, California (1995)
19. Rodriguez-Gomez, S., Cakmak, A.S.: Evaluation of seismic damage indices for reinforced concrete structures. Technical Report NCEER-90-0022, State University of New York, Buffalo (1990)
20. EC2: Eurocode 2: design of concrete structures—part 1: general rules and rules for buildings. European Committee for Standardization, Brussels, Belgium (2000)
21. Valles, R.E., Reinhorn, A.M., Kunnath, S.K., Li, C., Madan, A.: IDARC 2D version 4.0: a program for inelastic damage analysis of buildings. Technical Report NCEER-96-0010, State University of New York, Buffalo (1996)
22. Ryan, T.P.: Modern Engineering Statistics. Wiley, Hoboken (2007)

Chapter 20
Classification of Seismic Damages in Buildings Using Fuzzy Logic Procedures

Anaxagoras Elenas, Eleni Vrochidou, Petros Alvanitopoulos, and Ioannis Andreadis

Abstract It is well-known that damage observations on buildings after severe earthquakes exhibit interdependence with the seismic intensity parameters. Numerical elaboration of structural systems quantified the interrelation degree by correlation coefficients. Further, the seismic response of buildings is directly depended on the ground excitation. Consequently, the seismic response of buildings is directly depended on the used accelerogram and its intensity parameters. Among the several response quantities, the focus is on the overall damage. Thus, the Maximum Inter-Storey Drift Ratio and the damage index of Park/Ang are used. Intervals for the values of the damage indices are defined to classify the damage degree in low, medium, large and total. This paper presents an Adaptive Neuro-Fuzzy Inference System for the damage classification. The seismic excitations are simulated by artificial accelerograms. Their intensity is described by seismic parameters. The proposed system was trained and tested on a reinforced concrete structure. The results have shown that the proposed fuzzy technique contributes to the development of an efficient blind prediction of seismic damages. The recognition scheme achieves correct classification rates over 90%.

A. Elenas (✉)
Institute of Structural Mechanics and Earthquake Engineering, Democritus University of Thrace, 67100 Xanthi, Greece
e-mail: elenas@civil.duth.gr

E. Vrochidou · P. Alvanitopoulos · I. Andreadis
Laboratory of Electronics, Department of Electrical and Computer Engineering, Democritus University of Thrace, 67100 Xanthi, Greece

E. Vrochidou
e-mail: evrochid@ee.duth.gr

P. Alvanitopoulos
e-mail: palvanit@ee.duth.gr

I. Andreadis
e-mail: iandread@ee.duth.gr

M. Papadrakakis et al. (eds.), *Computational Methods in Stochastic Dynamics*, Computational Methods in Applied Sciences 26,
DOI 10.1007/978-94-007-5134-7_20,

1 Introduction

Seismic accelerograms are records of ground acceleration versus time during earthquakes that cannot be described analytically. However, several seismic parameters have been presented in the literature during the last decades that can be used to express the intensity of a seismic excitation and to simplify its description. Post-seismic field observations and numerical investigations have indicated the interdependency between the seismic parameters and the damage status of buildings after earthquakes [1, 2]. The latter can be expressed by proper damage indices (DIs). The Maximum Inter-Storey Drift Ratio (MISDR) and the global damage index as defined by Park/Ang ($DI_{G,PA}$) characterize effectively the structural damage caused to buildings during earthquakes and thus, are used as metrics to classify the damage degree into 4 categories, low, medium, large and total. In this context, the damage degrees denote undamaged or minor damage-repairable damage-irreparable damage-partial or total collapse of the building, respectively.

This paper suggests a technique based on an Adaptive Neuro-Fuzzy Inference System (ANFIS) for seismic structural damage classification. A total set of 200 artificial accelerograms has been used and were correctively assigned to one of the above four categories with performances up to 90% and 87% of accuracy, for MISDR and $DI_{G,PA}$, respectively. High classification rates indicate that the proposed methodology is suitable for adaptive predictive control of the behavior of the concrete construction used, for any unknown seismic signal. The proposed method is applied to an eight-story reinforced concrete frame building, designed after the rules of the recent Eurocodes.

2 Damage Indices

MISDR is an overall structural damage index (OSDI) that can define the level of post-seismic corruption in a building [3, 4] and can be evaluated by Eq. (20.1):

$$\mathrm{MISDR} = \frac{|\mathrm{u}|_{\max}}{\mathrm{h}} 100[\%] \tag{20.1}$$

where $|\mathrm{u}|_{\max}$ is the absolute maximum inter-storey drift and h the inter-storey height.

Additionally, the OSDI after Park/Ang ($DI_{L,PA}$) is used to describe the structural damage [5]. First, the local damage index according to Park/Ang is calculated. The local damage index is a linear combination of the damage caused by excessive deformation and that contributed by the repeated cyclic loading effect that happens during an earthquake. The local DI is given by the relation:

$$\mathrm{DI}_{\mathrm{L,PA}} = \frac{\theta_{\mathrm{m}} - \theta_{\mathrm{r}}}{\theta_{\mathrm{u}} - \theta_{\mathrm{r}}} + \frac{\beta}{\mathrm{M_y}\theta_{\mathrm{u}}} \mathrm{E_T} \tag{20.2}$$

where θ_{m} is the maximum rotation during the load history, θ_{u} is the ultimate rotation capacity of the section, θ_{r} is the recoverable rotation at unloading, β is a strength

Table 20.1 Structural damage classification according to MISDR and $DI_{G,PA}$

Structural Damage Indices	Structural Damage Degree			
	Low	Medium	Large	Total
MISDR	≤ 0.5	$0.5 < MISDR \leq 1.5$	$1.5 < MISDR \leq 2.5$	> 2.5
$DI_{G,PA}$	≤ 0.3	$0.3 < DI_{G,PA} \leq 0.6$	$0.6 < DI_{G,PA} \leq 0.8$	> 0.8

degrading parameter (0.1–0.15), M_y is the yield moment of the section and E_T is the dissipated hysteretic energy.

The global damage index after Park/Ang is a combination of the maximum ductility and the hysteretic energy dissipation demand forced by the earthquake on the structure. Thus, the global damage index after Park/Ang ($DI_{G,PA}$) is given by:

$$DI_{G,PA} = \frac{\sum_{i=0}^{n} DI_L E_i}{\sum_{i=0}^{n} E_i} \tag{20.3}$$

where E_i is the energy dissipated at location i and n is the number of locations at which the local damage is calculated.

The two used DIs are utilized extensively in earthquake engineering, as they are experimentally proved to express the behavior of structures [5–12]. In Table 20.1, intervals for the values of the DIs are defined to classify the damage degree in low, medium, large and total [11]. These categories refer to minor, reparable damage, irreparable damage and severe damage or collapse of buildings, respectively.

3 Seismic Intensity Parameters

It is well-known that seismic intensity parameters are simple descriptors of the complex seismic accelerogram and they exhibit interdependency with observed post-seismic damages. Correlation studies manifested the interrelation degree between seismic intensity parameters and the damage indicators [1, 2]. Therefore, the following parameters are evaluated: peak ground acceleration PGA, peak ground velocity PGV, the term PGA/PGV, spectral acceleration (SA), spectral velocity (SV), spectral displacement (SD), central period (CP), absolute seismic input energy (E_{inp}), Arias intensity (I_A), strong motion duration after Trifunac/Brady (SMD_{TB}), seismic power ($P_{0.90}$), root mean square acceleration (RMS_a), intensity after Fajfar/Vidic/Fischinger (I_{FVF}), spectral intensities after Housner (SI_H), after Kappos (SI_K) and after Martinez-Rueda (SI_{MR}), effective peak acceleration (EPA), maximum EPA (EPA_{max}), cumulative absolute velocity (CAV) and destructiveness potential after Araya/Saragoni (DP_{AS}). Table 20.2 presents the examined intensity parameters and their literature references, respectively.

Table 20.2 Seismic intensity parameters

No	Seismic Intensity Parameter	References
1	Peak Ground Acceleration (PGA)	[13, 14]
2	Peak Ground Velocity (PGV)	[13, 14]
3	PGA to PGV ratio (PGA/PGV)	[13, 14]
4	Spectral Velocity (SV)	[13, 14]
5	Spectral Acceleration (SA)	[13, 14]
6	Spectral Displacement (SD)	[13, 14]
7	Central Period (CP)	[15]
8	Seismic Energy Input (E_{inp})	[16]
9	Arias Intensity (I_A)	[17]
10	Strong Motion Duration after Trifunac/Brady (SMD_{TB})	[18]
11	Power ($P_{0.90}$)	[19]
12	Root Mean Square Acceleration (RMS_a)	[13]
13	Seismic Intensity after Fajfar/Vidic/Fischinger (I_{FVF})	[20]
14	Spectrum Intensity after Housner (SI_H)	[21]
15	Spectrum Intensity after Kappos (SI_K)	[22]
16	Spectrum Intensity after Martinez-Rueda (SI_{MR})	[23]
17	Effective Peak Acceleration (EPA)	[24, 25]
18	Cumulative Absolute Velocity (CAV)	[26]
19	Maximum EPA (EPA_{max})	[24, 25]
20	Destructiveness Potential after Araya/Saragoni (DP_{AS})	[27]

4 Structural Model

Figure 20.1 presents the examined reinforced concrete structure. The eigenfrequency of the frame is 0.85 Hz. The design of the 8-storey building is based on the recent Eurocode rules EC2 and EC8 [28, 29]. The cross-sections of the beams are T-beams with 40 cm width, 20 cm slab thickness, 60 cm total beam height and 1.45 m effective slab width. The distance between the frames of the structure is 6 m. The structure has been characterized as an "importance class II-ductility class medium" structure according to the EC8 Eurocode. The subsoil is of type C and the region seismicity of category 2 after the EC8 Eurocode (design around acceleration value equal to 0.24 g). External loads are taken under consideration and are incorporated into load combinations due to the rules of EC2 and EC8. With the help of the IDARC software, the characteristics of the building are inserted into the program and a dynamic analysis is taking place, so as to estimate the structural behaviour of the building [7].

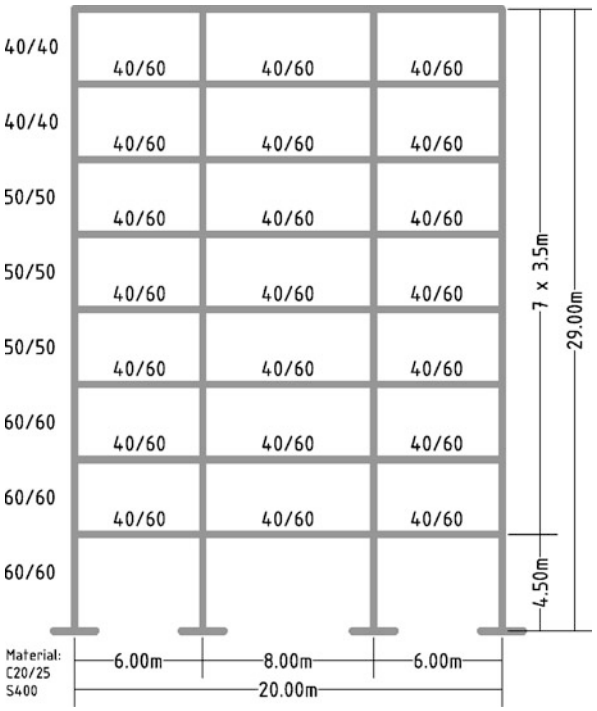

Fig. 20.1 Reinforced concrete frame structure

5 ANFIS Algorithm

ANFIS was introduced in 1993. ANFIS is able to extract a set of fuzzy "if-then" rules and define the membership functions in order to establish the association between inputs and outputs. Its structure is shown in Fig. 20.2. Basically, ANFIS suggests a method that, through the training procedure, can estimate the membership function parameters that serve the fuzzy inference system (FIS) to consequently specify the desired output for a certain given input [30].

ANFIS creates a fuzzy inference system in order to relate a certain input to the appropriate output. FIS interprets inputs into a set of fuzzy membership values and similarly the output membership functions to outputs. During the learning process, all parameters which define the membership functions will change. In order to optimize the model, these parameters are evaluated. Usually a gradient vector is used and an optimization routine could be applied in order to tune the parameters, so as to lead the model to a better generalization performance.

In this work, 20 seismic parameters are used as input data to describe the damage caused by one seismic event, and a total of 200 seismic events are used to train the system. All 20 seismic features have been normalized to belong in the interval [0, 1]. The 200 seismic events are distributed equally to all four damage categories in order to create a uniform data set.

First, inputs are related to membership functions (MFs) (Fig. 20.3 shows the initial MF for one of the seismic parameters), to rules to outputs MFs, by using

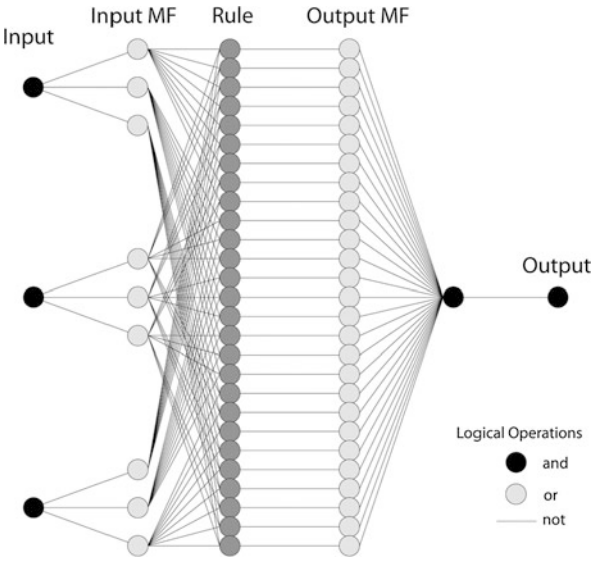

Fig. 20.2 ANFIS structure

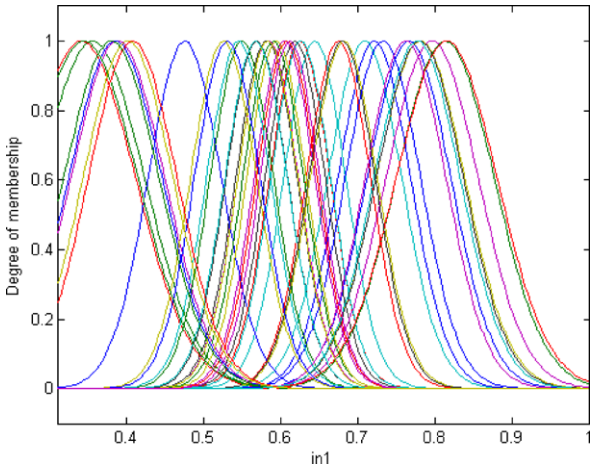

Fig. 20.3 Initial membership function on input 1

Fuzzy C-Means (FCM) technique [31, 32], which is analyzed later in this section. Next, the input/output data, which is a uniform set of 100 accelerograms, is used for training the model. The membership function parameters are tuned through the training process.

After the training, a model validation procedure is performed. During this procedure, an unknown input data set is presented to the trained fuzzy model for simulation. Thus, it can be evaluated the efficiency of the model. When a checking data set is presented to ANFIS, the fuzzy model selects the appropriate parameters associated with the minimum checking data model error. One crucial point with model validation, is selecting a suitable data set. This set must be representative of the

Table 20.3 Classification results based on the structural damage indices MISDR and $DI_{G,PA}$

Structural Damage Index	MISDR	$DI_{G,PA}$
Correct Classification Percentage (%)	90%	87%

data that the model is trying to simulate, and at the same time distinguishable from the training data. If a large amount of samples is collected, then all possible cases are contained and thus, the training set is more representative. In our case, a total number of 200 seismic excitations are considered as the data set.

FCM is a wildly used data clustering technique. Each data point is assigned to a cluster with a membership grade that is specified by a membership grade. It provides a method that shows how to group data points that populate some multidimensional space into a specific number of different clusters. The purpose of data clustering is to discover similarities between input patterns from a large data set, in order to design an effective classification system. At first; the FCM algorithm selects randomly the cluster centers. This initial choice for these centers is not always the appropriate. Furthermore, the variation of the cluster centers leads to different membership grades for each one of the clusters. Through the iteration process of the FCM algorithm, the cluster centers are gradually moved towards to their proper location. This is achieved by minimizing the weighted distance between any data point and the cluster centre. Finally, FCM function defines the cluster centers and the membership grades for every data point.

6 Results

The results are summarized in Table 20.3. The structural damage is presented by means of the two used DIs, MISDR and $DI_{G,PA}$, and the algorithm was tested for both DIs. The results indicate that the MISDR leads to higher performance, up to 90%, compared with the results when using $DI_{G,PA}$ which rates up to 87%.

In Figs. 20.4 and 20.5, blue circles represent the seismic signals that have been misclassified with ANFIS algorithm using MISDR and $DI_{G,PA}$ respectively.

7 Conclusions

This paper presents an efficient algorithm based on ANFIS techniques for seismic signal classification. A number of 20 seismic parameters and a set of 200 artificial accelerograms with known damage effects were used. For each seismic excitation the induced structural damage of the examined building is estimated and quantified according to two widely used damage indices, MISDR and $DI_{G,PA}$. The structural damage is expressed in the form of 4 damage categories. The 4 damage categories (classes) are defined through threshold values of the used damage indices.

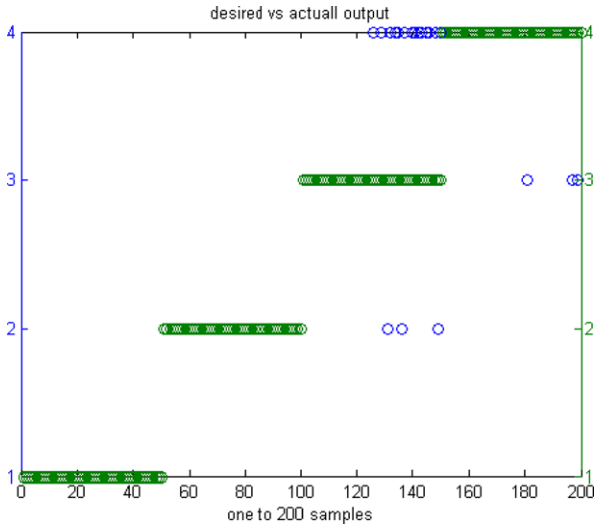

Fig. 20.4 Classification of 200 seismic signals into 4 damage classes with MISDR as metric. Correct classification percentage: 90%

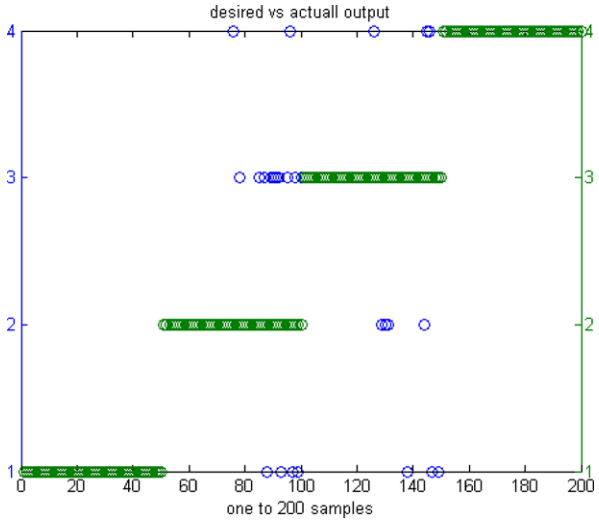

Fig. 20.5 Classification of 200 seismic signals into 4 damage classes with $DI_{G,PA}$ as metric. Correct classification percentage: 87%

An ANFIS model is trained and tested. The classification results reveal the effectiveness of the proposed system to estimate the earthquake's impact (damage category) on the examined structure. Classification rates up to 90% in the case of MISDR and 87% in the case of $DI_{G,PA}$ are achieved. The high percentage of correct classification in both cases, prove the efficiency of the method and show that the fuzzy technique that is implemented, contributes to the development of a competent blind prediction of the seismic damage potential that an accelerogram possesses.

References

1. Elenas, A.: Correlation between seismic acceleration parameters and overall structural damage indices of buildings. Soil Dynamics and Earthquake. Engineering **20**, 93–100 (2000)
2. Elenas, A., Meskouris, K.: Correlation study between seismic acceleration parameters and damage indices of structures. Eng. Struct. **23**, 698–704 (2001)
3. Structural Engineers Association of California (SEAOC): Vision 2000: performance based seismic engineering of buildings. Sacramento, California (1995)
4. Rodriguez-Gomez, S., Cakmak, A.S.: Evaluation of seismic damage indices for reinforced concrete structures. Technical Report NCEER-90-0022, State University of New York, Buffalo (1990)
5. Park, Y.J., Ang, A.H.S.: Mechanistic seismic damage model for reinforced concrete. J. Struct. Eng. **111**, 722–739 (1985)
6. Altoontash, A.: Simulation and damage models for performance assessment of reinforced concrete beam-column joints. Dissertation, Stanford University, Stanford (2004)
7. Valles, R.E., Reinhorn, A.M., Kunnath, S.K., Li, C., Madan, A.: IDARC 2D version 4.0: a program for inelastic damage analysis of buildings. Technical Report NCEER-96-0010, State University of New York, Buffalo (1996)
8. Freeman, S.A.: Drift limits: are they realistic. Earthq. Spectra **1**, 355–362 (1985)
9. CEB-FIP: Displacement-based design of reinforced concrete buildings. State-of-Art report, Fédération Internationale du Béton, Lausanne (2003)
10. Toussi, S., Yao, J.T.P.: Assessment of structural damage using the theory of evidence. Struct. Saf. **1**, 107–121 (1982)
11. Gunturi, S.K.V., Shah, H.C.: Building specific damage estimation. In: Proceedings of the l0th World Conference on Earthquake Engineering, pp. 6001–6006. Balkema, Rotterdam (1992)
12. Andreadis, I., Tsiftzis, Y., Elenas, A.: Intelligent seismic acceleration signal processing for structural damage classification. IEEE Trans. Instrum. Meas. **56**, 1555–1564 (2007)
13. Meskouris, K.: Structural Dynamics. Ernst & Sohn, Berlin (2000)
14. Chopra, A.K.: Dynamics of Structures. Prentice Hall, New York (1996)
15. Vanmarcke, E.H., Lai, S.S.P.: Strong-motion duration and RMS amplitude of earthquake records. Bull. Seismol. Soc. Am. **70**, 1293–1307 (1980)
16. Uang, C.M., Bertero, V.V.: Evaluation of seismic energy in structures. Earthquake Eng. Struct. Dyn. **19**, 77–90 (1990)
17. Arias, A.: A measure of earthquake intensity. In: Hansen, R.J. (ed.) Seismic Design for Nuclear Power Plants, pp. 438–483. MIT Press, Cambridge (1970)
18. Trifunac, M.D., Brady, A.G.: A study on the duration of strong earthquake ground motion. Bull. Seismol. Soc. Am. **65**, 581–626 (1975)
19. Jennings, P.C.: Engineering seismology. In: Kanamori, H., Boschi, E. (eds.) Earthquakes: Observation, Theory and Interpretation, pp. 138–173. Italian Physical Society, Varenna (1982)
20. Fajfar, P., Vidic, T., Fischinger, M.: A measure of earthquake motion capacity to damage medium-period structures. Soil Dyn. Earthq. Eng. **9**, 236–242 (1990)
21. Housner, G.W.: Spectrum intensities of strong motion earthquakes. In: Proceedings of Symposium on Earthquake and Blast Effects on Structures, pp. 20–36. EERI, Oakland (1952)
22. Kappos, A.J.: Sensitivity of calculated inelastic seismic response to input motion characteristics. In: Proceedings of the 4th U.S. National Conference on Earthquake Engineering, pp. 25–34. EERI, Oakland (1990)
23. Martinez-Rueda, J.E.: Definition of spectrum intensity for the scaling and simplified damage potential evaluation of earthquake records. In: Proceedings of the 11th European Conference on Earthquake Engineering, CD-ROM. Balkema, Rotterdam (1998)
24. ATC 3-06 Publication: Tentative provisions for the development of seismic regulations for buildings. Applied Technology Council, Redwood City, CA (1978)
25. Lungu, D., Aldea, A., Zaicenco, A., Cornea, T.: PSHA and GIS technology tools for seismic hazard macrozonation in Eastern Europe. In: Proceedings of the 11th European Conference on Earthquake Engineering, CD-ROM. Balkema, Rotterdam (1998)

26. Cabanas, L., Benito, B., Herraiz, M.: An approach to the measurement of the potential structural damage of earthquake ground motions. Earthquake Eng. Struct. Dyn. **26**, 79–92 (1997)
27. Araya, R., Saragoni, G.R.: Earthquake accelerograms destructiveness potential factor. In: Proceedings of the 8th World Conference on Earthquake Engineering, pp. 835–842. EERI, San Francisco (1984)
28. EC2: Eurocode 2: design of concrete structures—part 1: general rules and rules for buildings. European Committee for Standardization, Brussels, Belgium (2000)
29. EC8: Eurocode 8: design of structures for earthquake resistance—part 1: general rules, seismic actions, and rules for buildings. European Committee for Standardization, Brussels, Belgium (2004)
30. Duda, R.O., Hart, P.E., Stock, D.G.: Pattern Classification. Wiley, New York (2001)
31. Kurian, C.P., George, V.I., Bhat, J., Aithal, R.S.: ANFIS model for time series prediction of interior daylight illuminance. ICGST Int. J. Artif. Intell. Mach. Learn. (Online) **6**, 35–40 (2006)
32. Theodoridis, S., Koutroumbas, K.: Pattern Recognition. Academic Press, Kidlington (2009)

Chapter 21
Damage Identification of Masonry Structures Under Seismic Excitation

G. De Matteis, F. Campitiello, M.G. Masciotta, and M. Vasta

Abstract In the present paper, a spectral based damage identification technique is addressed on historical masonry structures. The seismic behavior of a physical 1:5.5 scaled model of the church of the Fossanova Abbey (Italy) is investigated by means of numerical and experimental analyses. Aiming at defining the seismic vulnerability of such a structural typology a wide experimental campaign was carried out. The achieved experimental results lead to the definition of a refined FE model reproducing the dynamic behavior of the whole structural complex. Then, the central transversal three-central bays of the church, as it mostly influences the seismic vulnerability of the Abbey, was investigated in a more detail by means of a shaking table test on a 1:5.5 scaled physical model in the Laboratory of the Institute for Earthquake Engineering and Engineering Seismology in Skopje. In the present paper a brief review of the numerical activity related to the prediction of the shaking table test response of the model is first proposed. Then, the identification of frequency decay during collapse is performed through decomposition of the measured power spectral density matrix. Finally, the localization and evolution of damage in the structure is analyzed. The obtained results shown that a very good agreement is achieved between the experimental data and the predictive/interpretative numerical analyses.

Keywords Masonry structures · Earthquake engineering · Shaking table tests · Power spectral matrix decomposition · Dynamic damage identification

1 Introduction

Gothic architecture spread as from the 12th Century and broke out during the Middle Ages in the cultural and religious area of the Christianity of Western Europe, with some trespasses in the Middle East and in the Slavic–Byzantine Europe. Many important abbeys were built in those areas, providing a key impulse to the regional

G. De Matteis · F. Campitiello · M.G. Masciotta · M. Vasta (✉)
Engineering Department, University "G. D'Annunzio" of Chieti-Pescara, Viale Pindaro 42, 65123 Pescara, Italy
e-mail: mvasta@unich.it

M. Papadrakakis et al. (eds.), *Computational Methods in Stochastic Dynamics*, Computational Methods in Applied Sciences 26,
DOI 10.1007/978-94-007-5134-7_21,

economy and contributing to a general social, economic and cultural development. The most interested areas sprawl from the northern Countries (England) to those facing the Mediterranean Basin (Italy), but also spread out from the Western (Portugal) to the Eastern Countries, as Poland and Hungary. Monastic orders and in particular the Cistercian one, with its monasteries, had an important role for broaden the new architectonic message, adapting to the local traditions the technical and formal heritage received by the Gothic style [1, 2] and [3].

Gothic cathedrals may result particularly sensitive to earthquake loading. Therefore, within the European research project "Earthquake Protection of Historical Buildings by Reversible Mixed Technologies" (PROHITECH), this structural typology has been investigated by means of shaking table tests on large scale models [4]. Based on a preliminary study devoted to define typological schemes and geometry which could be assumed as representative of many cases largely present in the seismic prone Mediterranean Countries, the Fossanova cathedral, which belongs to the Cistercian abbatial complex built in a small village in the central part of Italy, close to the city of Priverno (LT), has been selected as an interesting and reference example of pre-Gothic style church [5]. In order to assess the vulnerability of the church against seismic actions a wide numerical and experimental activity was developed. Firstly, the identification of the geometry of the main constructional parts as well as of the mechanical features of the constituting materials of the cathedral was carried out. Then, Ambient Vibration Tests were performed in order to characterize the dynamic behavior of the church and to calibrate refined FE models developed using the ABAQUS code [5]. To this purpose elastic FEM analyses were performed to predict the behavior of the three-central bays of the church, which were detected as the key-part of the structural complex [6, 7]. The recognized resistant unit about transversal direction was designed in length scale 1:5.5 according to "true replica" modeling principles and tested on the shaking table in the IZIIS Laboratory in Skopje [8]. The physical model was tested and the as-built model was loaded until heavy damage occurred. The structural response of the tested physical model has been deeply investigated by means of non-linear numerical analyses that has shown good agreements with experimental measurements [8].

In this paper, the identification of frequency decay during collapse is performed through decomposition of the measured power spectral density matrix. Finally, the localization and evolution of damage in the structure is analyzed. The obtained results has shown that a very good agreement is achieved between the experimental data and the predictive/interpretative numerical analyses.

2 The Fossanova Abbey: Model and Experimental Test

The Fossanova Abbey (Fig. 21.1) was built in the XII century and opened in 1208. The architectural complex presents three rectangular aisles with seven bays, a transept and a rectangular apse. Between the main bay and the transept raises the skylight turret with a bell tower. The main dimensions are 69.85 m (length), 20.05 m

Fig. 21.1 The Fossanova church

Fig. 21.2 The vaulted system of the Fossanova church

(height), and 23.20 m (width). The nave, the aisles, the transept and the apse are covered by ogival cross vaults. Detailed information on the main dimensions of the bays are provided in De Matteis et al. [6].

The previously mentioned vaulted system does not present ribs, but only ogival arches transversally oriented with respect to the span and ogival arches placed on the confining walls (Fig. 21.2). The ridge-poles of the covering wood structure is supported by masonry columns placed on the boss of the transversal arches of the nave and apse. The crossing between the main bay and the transept is covered by a wide ogival cross vault with diagonal ribs sustained by four cross shaped columns delimiting a span with the dimensions of 9.15×8.85 m.

The main structural elements constituting the central nave and the aisles are four longitudinal walls (West–East direction). The walls delimiting the nave are sustained by seven couples of cross-shaped piers (with dimensions of 1.80×1.80 m) with small columns laying on them and linked to the arches. The bays are delimited inside the church by columns with adjacent elements having a capital at the top. The columns-capital system supports the transversal arches of the nave. The external of the clearstory walls are delimited by the presence of buttresses with a hat on the top that reaches the height of 17.90 m. The walls of the clearstory present large splayed windows and oval openings that give access to the garret of the aisles. Also the walls that close the aisles present seven coupled column-buttresses systems reaching the height of 6.87 m and further splayed windows.

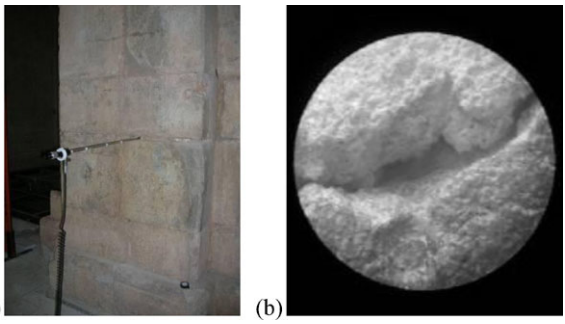

Fig. 21.3 Endoscope tests

During the centuries, the complex suffered some aesthetic modifications: the main prospect was modified since the narthex was eliminated installing an elaborate portal with a large rose-window; a part of the roof and of the lantern were rebuilt, introducing a Baroque style skylight turret; additional modifications on the roofing of the church were applied, with the reduction of the slope of pitches and with the restoration of the same slope as in the original form.

In order to determine the actual geometry and the mechanical features of the main constructional elements, an accurate experimental activity has been developed. In particular, both in situ inspection and laboratory tests have been carried out [5, 6].

It has been determined that the basic material constituting the constructional elements of the church is a very compact sedimentary limestone. In particular, columns and buttresses are made of plain stones with fine mortar joints (thickness less than 1 cm). The lateral walls (total thickness 120 cm) consist of two outer skins of good coursed ashlar (the skins being 30 cm thick) with an internal cavity with random rubble and mortar mixture fill.

In order to inspect the hidden parts of the constituting structural elements, endoscope tests have been executed on the right and left columns of the first bay, on the third buttress of the right aisle, on the wall of the main prospect and at the end on the filling of the vault covering the fourth bay of the nave. The test on the columns (Fig. 21.3a) allowed the exploration of the internal nucleus of the pier, relieving a total lack of internal vacuum, with the predominant presence of limestone connected with continuum joints of mortar (Fig. 21.3b). The test on the buttress was performed at the level of 143 cm, reaching the centre of the internal wall. The presence of regular stone blocks having different dimensions and connected to each other with mortar joints without any significant vacuum was detected. The tests on the wall put into evidence the presence of a two skins and rubble fill. The test made on the extrados of the vault, with a drilling depth of 100 cm, allowed a first layer of 7 cm made of light concrete and then a filling layer of irregular stones and mortar with the average thickness of 10 cm to be identified.

In order to define the mechanical features of the material, original blocks of stone were taken from the cathedral and submitted to compression tests (Fig. 21.4a). In total, 10 different specimens having different sizes have been tested, giving rise to an average ultimate strength of about 140 MPa and an average density $\gamma = 1700\ \text{kg/m}^3$.

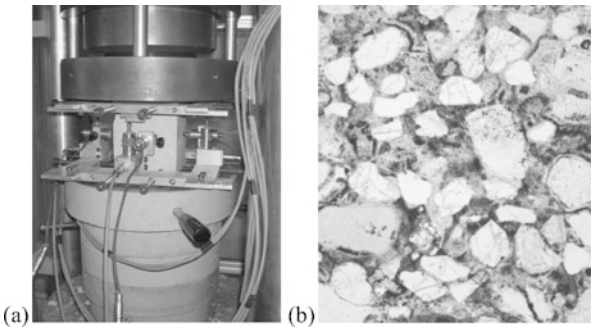

Fig. 21.4 Compression tests on limestone (**a**) and microscope analysis on mortar (**b**)

Besides, based on the results obtained for three different specimens, a Young's modulus equal to 42.600 MPa has been assessed, while a Poisson's ratio equal to 0.35 has been estimated.

Also, mortar specimens were extracted from the first column placed on the left of the first bay, from the wall of the aisle on the right and from the wall on the northern side of the transept. The specimens were catalogued as belonging to either the external joints (external mortar) or to the filling material (internal mortar). Compression tests have been carried out according to the Italian provisions (UNI EN 1926:2001), relieving a noticeable reduction of the average compressive strength for the specimens belonging to the external mortar (3.33 MPa) with respect to the internal ones (10.30 MPa). Besides, the Young's modulus has been determined on three different mortar specimens, according to the UNI EN 1015-11:2001 provisions, providing values ranging from 8.33 MPa to 12.16 MPa.

Chemical and petrography analyses have been also performed on the mortar specimens. In particular, chemical tests were made by X rays diffractometer analysis, according to the UNI 11088:2003 provisions. The prevalence of three material, namely, quartz crystal SiO_2, crystallized calcium carbonate $CaCO_3$ and some traces of felspate, was noticed. Also, a petrography study on thin sections of mortar specimens have been done by using two electronic microscopes, according to the UNI EN 932-3:1998 provisions (Fig. 21.4b). The analysis relieved the presence of quartz crystal sand end felspate, without any significant presence of crystallized calcium carbonate. The binding was quantified with a percentage of 60% of the total volume.

A FE model of the entire Abbey was calibrated on the basis of the in-situ experimental activity. The seismic analyses on such a model revealed that the more important structural part of the structural complex was to be recognized in the three-central bays of the main nave shown in Fig. 21.5 [7]. For the above reason a physical model of the key-structural part was designed and constructed in the IZIIS Laboratory in Skopje (Fig. 21.6). The model was executed in a 1:5.5 scale ratio (length) which was the maximum value compatible with the capacity of the shaking table.

The Buckingham's theorem was followed to define all the physical parameters needed to the construction of the model, according to the "true replica" modeling principles. All the involved quantities was scaled on the base of the three main parameters Length ($L_r = 1/5.5$), Mass Density ($\rho_r = 1$) and Acceleration ($a_r = 1$)

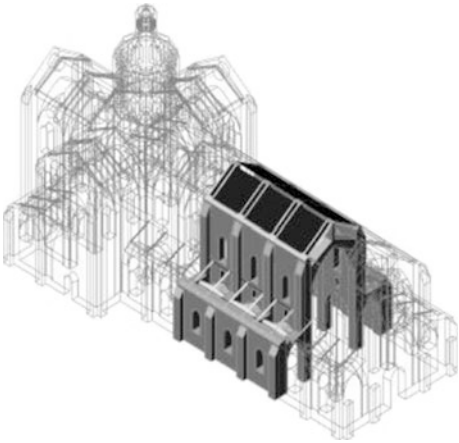

Fig. 21.5 Recognized seismic resistant unit in transversal direction

Fig. 21.6 Fossanova physical model (UPM) in scale 1:5.5 tested on shaking table

so that for the stresses a scaling ratio $\sigma_r = 0.18$ is obtained. The dimensions of the model were 3.97×4.44 m at the base, 3.67 m was the maximum height.

Some simplifications were adopted in the construction of the prototype: free edges was left in longitudinal direction, in fact no boundary restrains was applied on the fronts, neglecting the longitudinal continuity as it is in the reality. Then, the wooden roof structure wasn't realized because it wasn't considered as an active element in the evaluation of the seismic vulnerability [7].

The input signal of the test was assumed to be the scaled natural Calitri record (North–South direction) of Irpinia (Italy) 1980 earthquake record. The main feature of the selected earthquake are a maximum acceleration of 0.155 g (compatible with seismic hazard of the site), a quite long duration time (80 s), a high input energy for the relevant frequency (0.5 Hz–10 Hz) and typical two peak accelerations (or two strong motions). The record and the derived elastic spectra (with damping ratio $\zeta = 5\%$) are shown in Fig. 21.7a, b. The shaking table test was performed by considering three phases: phase 1, phase 2A and phase 2B. In the first phase the as-built unreinforced physical model (UPM) was tested and heavy damaged at the end. In the second phase (2A) the model was repaired and reinforced with carbon fiber ties.

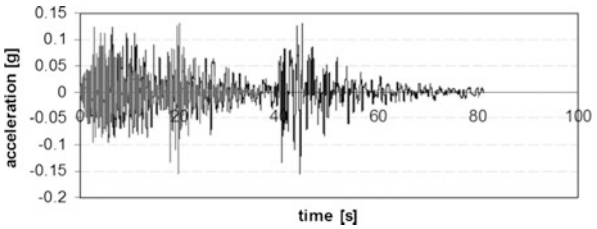

a. Calitri North-South record (scaled and not scaled)

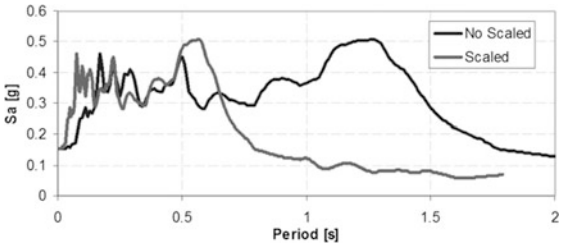

b. Relevant elastic response spectra

Fig. 21.7 The accelerometric record (Irpinia, 1980)

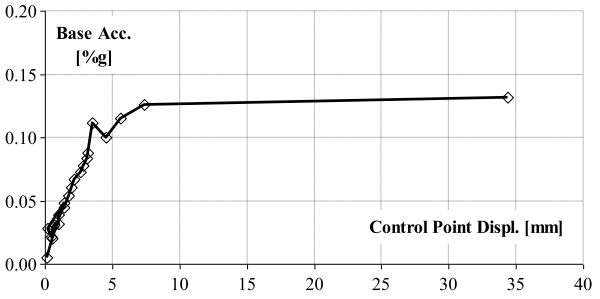

Fig. 21.8 Equivalent capacity curve of the tested model

Finally, in the phase 2B, the reinforcing system was modified and the model was loaded until failure. Even though the examination of the reinforced systems is not the object of the present paper, in the following the level of input intensity which provoked serious damage to the model for every phase is listed:

- 0.14 g for the original model (phase 1);
- 0.28 g for the strengthened model (phase 2A);
- 0.40 g for the strengthened model (phase 2B);

In particular, the maximum acceleration measured at the base of the shaking table, by means of the accelerometer "CH1" [9], versus the maximum absolute displacement measured at the top of the buttresses at each step of the phase 1 (unreinforced physical model) is shown in Fig. 21.8. The curve can be assumed as an equivalent capacity curve for the tested UPM [8].

3 Dynamic Damage Identification

Assuming in first instance linearity under earthquake condition, the following equations of motion holds for the structure

$$\boldsymbol{M}\ddot{\boldsymbol{X}} + \boldsymbol{C}\dot{\boldsymbol{X}} + \boldsymbol{K}\boldsymbol{X} = a_g(t)\boldsymbol{V} \tag{21.1}$$

where $\boldsymbol{X}$(t) is the nodal structural response process, $\boldsymbol{M}$, $\boldsymbol{C}$ and $\boldsymbol{K}$ are $n \times n$ mass, damping and stiffness matrices respectively, $\boldsymbol{V}$ a $n \times 1$ vector while $a_g(t)$ represent the ground acceleration.

A more suitable representation of the structural response may be achieved by means of the decomposition in fully coherent independent vectors. Despite the non Gaussianity of the structural response vector $\mathbf{X}(t) = [X_i(t)]$ $(i = 1, \ldots, n)$, collecting the nodal response processes, its main characteristics can be represented by the knowledge of the second order spectral properties. Let us consider the power spectral density (PSD) matrix of $\boldsymbol{X}(t)$

$$\mathbf{S}_X(\omega) = \begin{bmatrix} S_{X_1}(\omega) & S_{X_1X_2}(\omega) & \cdots & S_{X_1X_n}(\omega) \\ S_{X_2X_1}(\omega) & S_{X_2}(\omega) & \cdots & S_{X_2X_n}(\omega) \\ \vdots & & \ddots & \vdots \\ S_{X_1X_n}(\omega) & \cdots & \cdots & S_{X_n}(\omega) \end{bmatrix} \tag{21.2}$$

The elements of $\mathbf{S}_X(\omega)$ are the direct and cross power spectral densities, defined as the Fourier transform of the correlation components

$$S_{X_1X_j}(\omega) = \frac{1}{2\pi}\int_{-\infty}^{+\infty} R_{X_1X_j}(\tau)e^{-j\omega\tau}\,d\tau \tag{21.3}$$

For finite length measurements of the process $\mathbf{X}(t)$ the elements of the spectral matrix becomes

$$S_{X_1X_j}(\omega, T) = \frac{E[X_i(\omega, T)X_j^*(\omega, T)]}{2\pi T} \tag{21.4}$$

where $X_i(\omega, T)$ denotes the Fourier transform of $X_i(t)$ over the observation time T

$$X_i(\omega, T) = \int_0^T X_i(t)e^{-j\omega t}\,dt \tag{21.5}$$

The input–output spectral relationship can be written as

$$\boldsymbol{S}_{\boldsymbol{X}}(\omega, T) = \mathrm{S}_a(\omega, T)\left[\boldsymbol{H}^{*T}(\omega)\boldsymbol{V}^T\boldsymbol{V}\boldsymbol{H}(\omega)\right] \tag{21.6}$$

where $\mathrm{S}_a(\omega, T)$ represent the input ground acceleration PSD while $\boldsymbol{H}(\omega)$ is the transfer matrix

$$\boldsymbol{H}(\omega) = \left[\boldsymbol{K} + i\omega\boldsymbol{C} - \omega^2\boldsymbol{M}\right]^{-1} \tag{21.7}$$

Dividing both members of Eq. (21.6) by $\mathrm{S}_a(\omega, T)$

$$\boldsymbol{S}(\omega) = \frac{\boldsymbol{S}_{\boldsymbol{X}}(\omega, T)}{\mathrm{S}_a(\omega, T)} = \boldsymbol{H}^{*T}(\omega)\boldsymbol{V}^T\boldsymbol{V}\boldsymbol{H}(\omega) \tag{21.8}$$

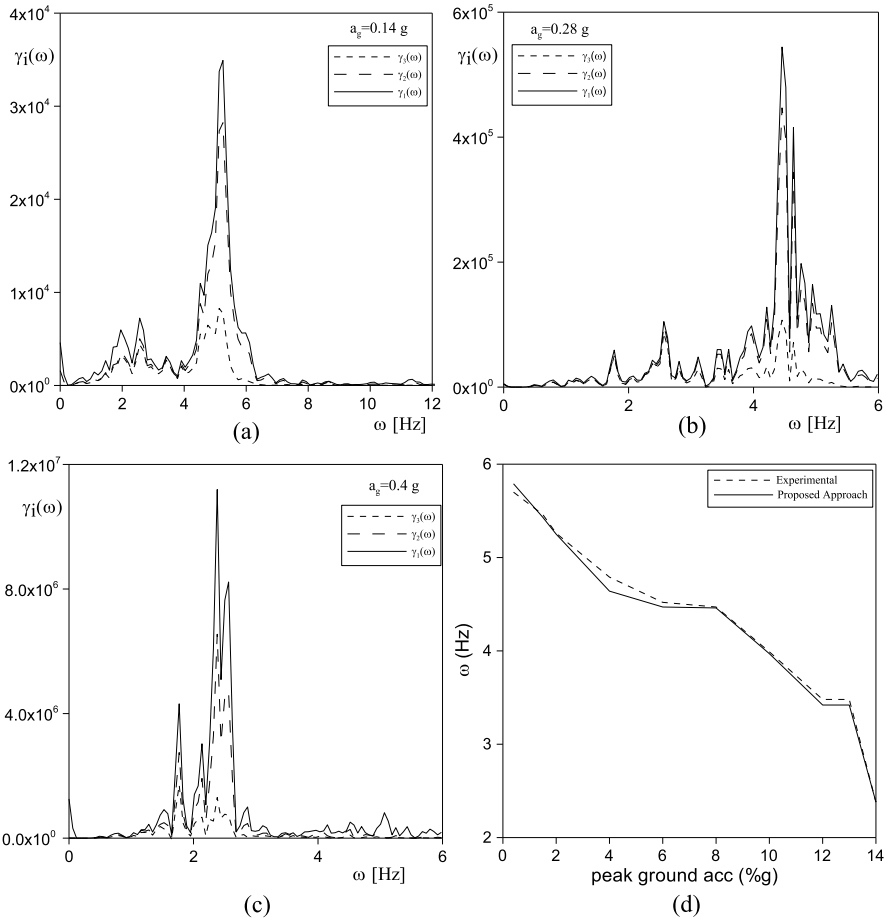

Fig. 21.9 Response spectral eigenvalues $\gamma_i(\omega)$ increasing peak ground acceleration: (**a**) $a_g = 0.14$ g; (**b**) $a_g = 0.28$ g; (**c**) $a_g = 0.4$ g; (**d**): Comparison between experimental and identified frequency decay curves for different values of ground peak acceleration

we observe that the matrix $\boldsymbol{S}(\omega)$ does not depend on the observation time T and, as well as the response PDF matrix $\boldsymbol{S}_{\boldsymbol{X}}(\omega, T)$, is Hermitian and non-negative definite, thus its eigenvalues $\boldsymbol{\Gamma}(\omega) = \text{diag}(\gamma_1(\omega)\gamma_2(\omega)\cdots\gamma_n(\omega))$ are real and non-negative, with orthonormal complex eigenvectors $\boldsymbol{\Psi}(\omega) = [\boldsymbol{\psi}_1(\omega)\boldsymbol{\psi}_2(\omega)\cdots\boldsymbol{\psi}_n(\omega)]$

$$\boldsymbol{\Psi}(\omega)^{*T}\boldsymbol{\Psi}(\omega) = \boldsymbol{I}, \qquad \boldsymbol{\Psi}(\omega)^{*T}\boldsymbol{S}(\omega)\boldsymbol{\Psi}(\omega) = \boldsymbol{\Gamma}(\omega) \tag{21.9}$$

$$\boldsymbol{S}(\omega)\boldsymbol{\Psi}(\omega) = \boldsymbol{\Psi}(\omega)\boldsymbol{\Gamma}(\omega) \tag{21.10}$$

The eigenvalues $\gamma_i(\omega)$ $(i = 1, \ldots, n)$ may be sorted in decreasing order, and their importance in principal component analysis is usually limited to a reduced numbers.

Figures 21.9a–c show the response spectral eigenvalues for different intensities of ground peak acceleration $a_g = 0.14$ g, $a_g = 0.28$ g and $a_g = 0.4$ g. In the fre-

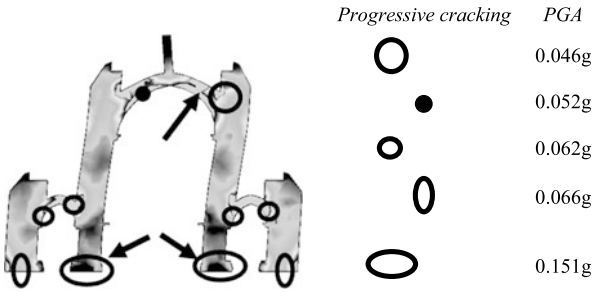

Fig. 21.10 Progressive damage of the model with increasing PGA

quency axis, the abscissa of the peak of the maximum eigenvalue $\gamma_1(\omega)$ allows for the identification of the frequency decay curve by varying a_g, as shown in Fig. 21.9d in comparison with experimental results.

Damage localization has been performed using the Parameter Method (PM) proposed by Dong et al. [10, 11] using a combination of frequency and mode shapes. The expression for the PM method is

$$\Delta\varphi = \sum_{j=1}^{n}\left[\phi_j^d\left(\frac{\omega_j^u}{\omega_j^d}\right) - \phi_j^u\right] \tag{21.11}$$

where ϕ is the structural mode, n the mode number while upper script u, d stands for undamaged and damage state respectively.

In Fig. 21.10 the progressive development of the cracks with increasing PGA is shown. Firstly, tensile stress is attained in both the arches for quite the same value of the PGA (0.046 g ÷ 0.062 g). Then, stress peaks were observed in the lateral buttresses for a PGA value equal to 0.066 g. Finally, the collapse mechanism was identified for a PGA of 0.151 g, when also the base sections of the internal piers exceed the adopted conventional limit state.

The experimental evidence of the collapse mode and crack evolution as shown in Fig. 21.10 can be identified by the PM method considering a simplified 2D model of the structure. In Fig. 21.11a the 2D finite element model is shown allowing the evaluation of the modes of the damaged and undamaged structure [12]. Once the evolutionary modes are known, damage location was performed by the PM method as shown in Fig. 21.11b–d were damage evolutionary localization is identified in the nodes of the 2D model.

4 Conclusions

The seismic behavior of a physical 1:5.5 scaled model of the church of the Fossanova Abbey has been investigated by means of numerical and experimental analyses. The achieved experimental results lead to the definition of a refined FE model reproducing the dynamic behavior of the whole structural complex. Then, the central transversal three-central bays of the church, as it mostly influences the seismic

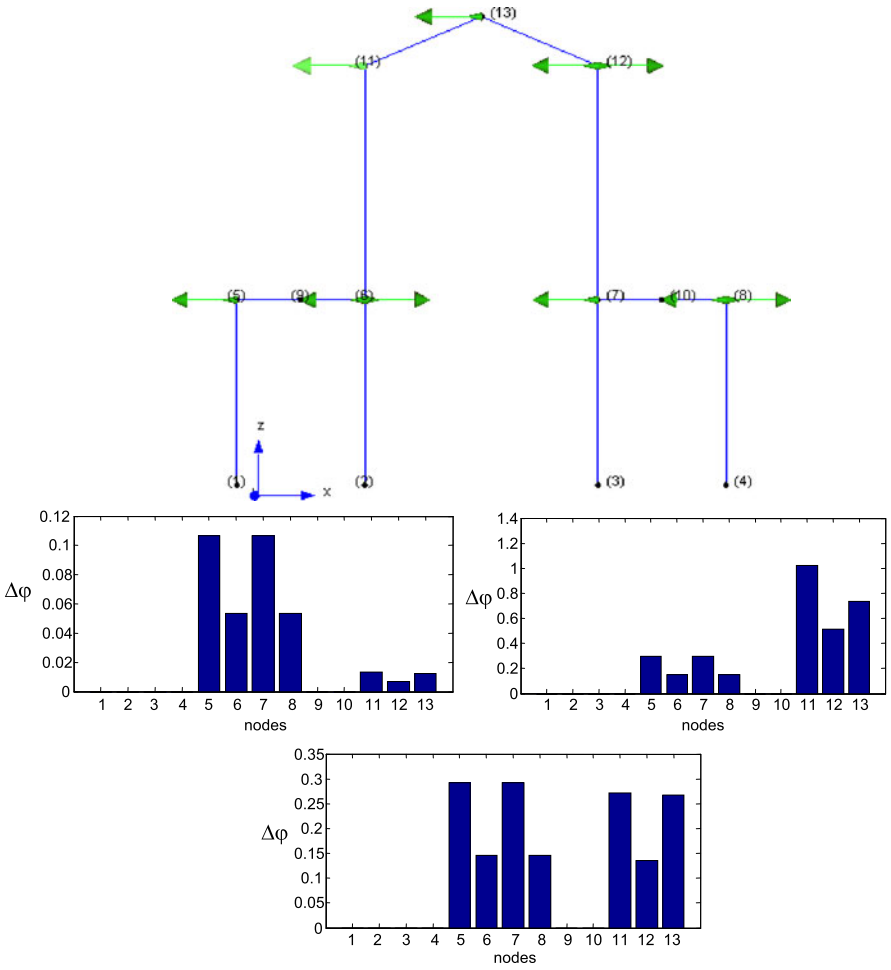

Fig. 21.11 (**a**) 2D finite element model, *arrows* symbol for measured displacement, (**b**) Progressive damage of the model with increasing PGA—PM method identification

vulnerability of the Abbey, was investigated in a more detail by means of a shaking table test on a 1:5.5 scaled physical model in the Laboratory of the Institute for Earthquake Engineering and Engineering Seismology in Skopje. In the present paper a brief review of the numerical activity related to the prediction of the shaking table test response of the model is first proposed. Then, the identification of frequency decay during collapse is performed through decomposition of the measured power spectral density matrix. Finally, the localization and evolution of damage in the structure is analyzed using a simplified 2D FEM model of the structure. The obtained results shown that a very good agreement is achieved between the experimental data and the predictive/interpretative numerical analyses.

References

1. Grodecki, L.: L'architettura gotica. Mondadori, Milan (1976) (in Italian)
2. Gimpel, J.: I costruttori di cattedrali. Jaca Book, Milan (1982) (in Italian)
3. De Longhi, F.: L'architettura delle chiese cistercensi Italiane. Ceschina, Milan (1958) (in Italian)
4. Mazzolani, F.M.: Earthquake protection of historical buildings by reversible mixed technologies. In: Proceedings of Behaviour of Steel Structures in Seismic Areas (STESSA 2006), pp. 11–24. Taylor & Francis, London (2006)
5. De Matteis, G., Colanzi, F., Mazzolani, F.M.: La chiesa abbaziale di Fossanova: indagini sperimentali per la valutazione della vulnerabilità sismica. In: Proceedings of the Workshop on Design for Rehabilitation of Masonry Structures (Wondermasonry 2), Ischia, Italy, 11–12 October (2007)
6. De Matteis, G., Langone, I., Colanzi, F., Mazzolani, F.M.: Experimental and numerical modal identification of the Fossanova Gothic cathedral. In: Proceedings of the 7th International Conference on Damage Assessment of Structures (DAMAS 2007), Torino, Italy, 25–27 June (2007)
7. De Matteis, G., Colanzi, F., Langone, I., Eboli, A., Mazzolani, F.M.: Numerical evaluation of the seismic response of the Fossanova cathedral based on experimental dynamic identification. In: Proceedings of the Third International Conference on Structural Engineering, Mechanics and Computation (SEMC 2007), Cape Town, South Africa, 10–12 September (2007)
8. De Matteis, G., Campitiello, F., Eboli, A., Mazzolani, F.M.: Analisi sismica della chiesa abbaziale di Fossanova mediante modelli numerici e sperimentali. In: L'Ingegneria Sismica in Italia, SM7.6, ANIDIS, Bologna (2009)
9. De Matteis, G., Mazzolani, F.M., Krstevska, L., Tashkov, Lj.: Seismic analysis and strengthening intervention of the Fossanova Gothic church: numerical and experimental activity. In: Urban Habitat Construction Under Catastrophic Events, COST C26, Malta, pp. 247–254 (2008)
10. Dong, C., Zhang, P.Q., Feng, W.Q., Huang, T.C.: The sensitivity study of the modal parameters of a cracked beam. In: Proceedings of the 12th International Modal Analysis Conference, pp. 98–104 (1994)
11. Ramos, L.F., De Roeck, G., Lourenco, P.B., Campos-Costa, A.: Damage identification on arched masonry structures using ambient and random impact vibrations. Eng. Struct. **32**, 146–162 (2010)
12. ARTeMIS version 5.2. Structural Vibration Solution A/S, NOVI Science Park